

NONLINEAR  
PHYSICAL  
SCIENCE

Albert C.J. Luo  
Valentin Afraimovich  
*Editors*



Hamilton  
Chaos Be

# **NONLINEAR PHYSICAL SCIENCE**

# NONLINEAR PHYSICAL SCIENCE

*Nonlinear Physical Science* focuses on recent advances of fundamental theories and principles, analytical and symbolic approaches, as well as computational techniques in nonlinear physical science and nonlinear mathematics with engineering applications.

Topics of interest in *Nonlinear Physical Science* include but are not limited to:

- New findings and discoveries in nonlinear physics and mathematics
- Nonlinearity, complexity and mathematical structures in nonlinear physics
- Nonlinear phenomena and observations in nature and engineering
- Computational methods and theories in complex systems
- Lie group analysis, new theories and principles in mathematical modeling
- Stability, bifurcation, chaos and fractals in physical science and engineering
- Nonlinear chemical and biological physics
- Discontinuity, synchronization and natural complexity in the physical sciences

## SERIES EDITORS

### **Albert C.J. Luo**

Department of Mechanical and Industrial  
Engineering  
Southern Illinois University Edwardsville  
Edwardsville, IL 62026-1805, USA  
Email: aluo@siue.edu

### **Nail H. Ibragimov**

Department of Mathematics and Science  
Blekinge Institute of Technology  
S-371 79 Karlskrona, Sweden  
Email: nib@bth.se

## INTERNATIONAL ADVISORY BOARD

**Ping Ao**, University of Washington, USA; Email: aoping@u.washington.edu

**Jan Awrejcewicz**, The Technical University of Lodz, Poland; Email: awrejcew@p.lodz.pl

**Eugene Benilov**, University of Limerick, Ireland; Email: Eugene.Benilov@ul.ie

**Eshel Ben-Jacob**, Tel Aviv University, Israel; Email: eshel@tamar.tau.ac.il

**Maurice Courbage**, Université Paris 7, France; Email: maurice.courbage@univ-paris-diderot.fr

**Marian Gidea**, Northeastern Illinois University, USA; Email: mgidea@neu.edu

**James A. Glazier**, Indiana University, USA; Email: glazier@indiana.edu

**Shijun Liao**, Shanghai Jiaotong University, China; Email: sjliao@sjtu.edu.cn

**Jose Antonio Tenreiro Machado**, ISEP-Institute of Engineering of Porto, Portugal; Email: jtm@dee.isep.ipp.pt

**Nikolai A. Magnitskii**, Russian Academy of Sciences, Russia; Email: nmag@isa.ru

**Josep J. Masdemont**, Universitat Politècnica de Catalunya (UPC), Spain; Email: josep@barquins.upc.edu

**Dmitry E. Pelinovsky**, McMaster University, Canada; Email: dmpeli@math.mcmaster.ca

**Sergey Prants**, V.I.Ilichev Pacific Oceanological Institute of the Russian Academy of Sciences, Russia;  
Email: prants@poi.dvo.ru

**Victor I. Shrira**, Keele University, UK; Email: v.i.shrira@keele.ac.uk

**Jian Qiao Sun**, University of California, USA; Email: jqsun@ucmerced.edu

**Abdul-Majid Wazwaz**, Saint Xavier University, USA; Email: wazwaz@sxu.edu

**Pei Yu**, The University of Western Ontario, Canada; Email: pyu@uwo.ca

Albert C.J. Luo  
Valentin Afraimovich

# Hamiltonian Chaos Beyond the KAM Theory

Dedicated to George M. Zaslavsky (1935–2008)

With 114 figures, 8 of them in color

 高等教育出版社  
HIGHER EDUCATION PRESS

 Springer

*Editors*

Albert C.J. Luo  
Department of Mechanical and Industrial Engineering  
Southern Illinois University Edwardsville  
Edwardsville, IL 62026-1805, USA  
E-mail: aluo@siue.edu

Valentin Afraimovich  
IICO-UASLP, Av. Karakorum 1470  
Lomas 4a Seccion, San Luis Potosi  
SLP 78210, Mexico  
E-mail: valentin@cactus.iico.uaslp.mx

ISSN 1867-8440

e-ISSN 1867-8459

Nonlinear Physical Science

ISBN 978-7-04-029187-2

Higher Education Press, Beijing

ISBN 978-3-642-12717-5

e-ISBN 978-3-642-12718-2

Springer Heidelberg Dordrecht London New York

Library of Congress Control Number: 2010925492

© Higher Education Press, Beijing and Springer-Verlag Berlin Heidelberg 2010

This work is subject to copyright. All rights are reserved, whether the whole or part of the material is concerned, specifically the rights of translation, reprinting, reuse of illustrations, recitation, broadcasting, reproduction on microfilm or in any other way, and storage in data banks. Duplication of this publication or parts thereof is permitted only under the provisions of the German Copyright Law of September 9, 1965, in its current version, and permission for use must always be obtained from Springer. Violations are liable to prosecution under the German Copyright Law.

The use of general descriptive names, registered names, trademarks, etc. in this publication does not imply, even in the absence of a specific statement, that such names are exempt from the relevant protective laws and regulations and therefore free for general use.

*Cover design:* Frido Steinen-Broo, EStudio Calamar, Spain

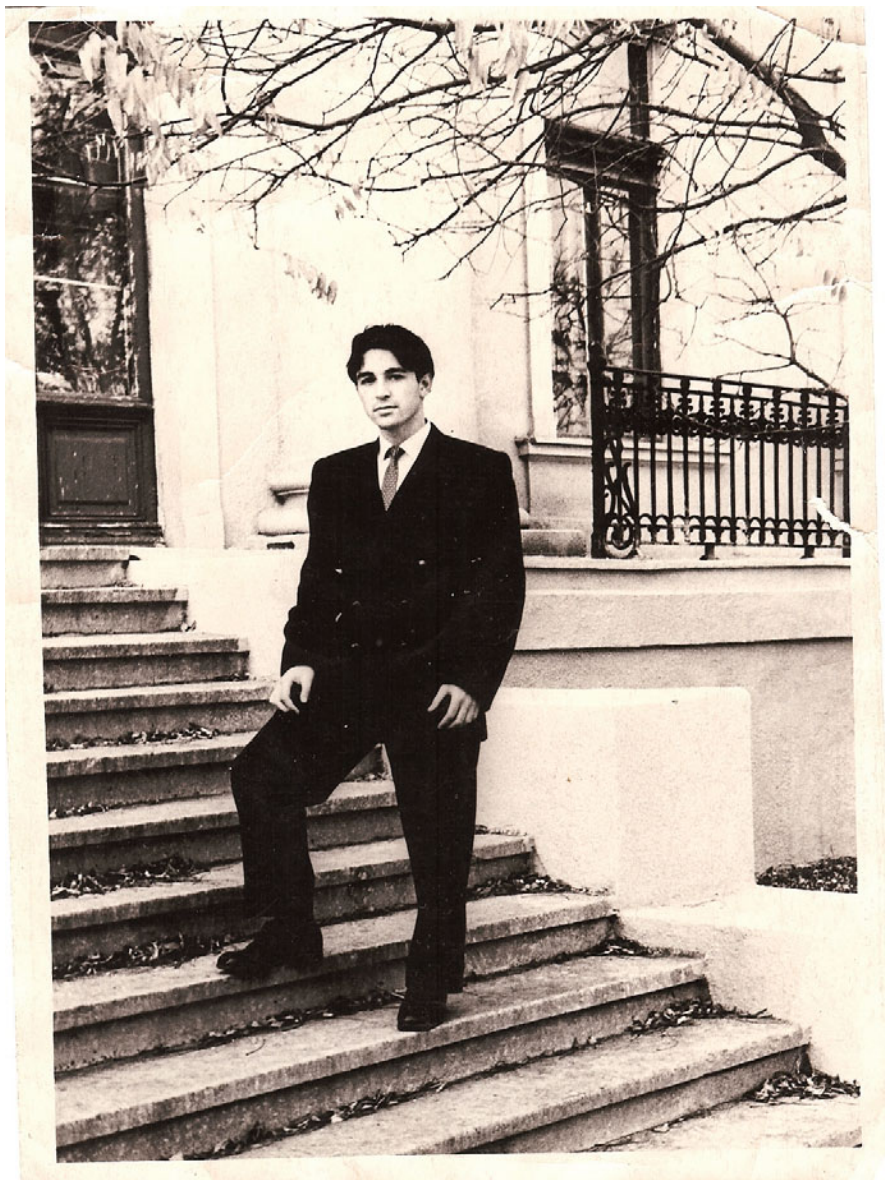
Printed on acid-free paper

Springer is part of Springer Science+Business Media ([www.springer.com](http://www.springer.com))

*To the memory of George M. Zaslavsky*



*Dedicated to George M. Zaslavsky, your significant achievements on Science will leave to the entire society forever.*





# Preface

George M. Zaslavsky was born in Odessa, Ukraine in 1935 in a family of an artillery officer. He received education at the University of Odessa and moved in 1957 to Novosibirsk, Russia. In 1965, George joined the Institute of Nuclear Physics where he became interested in nonlinear problems of accelerator and plasma physics. Roald Sagdeev and Boris Chirikov were those persons who formed his interest in the theory of dynamical chaos. In 1968 George introduced a separatrix map that became one of the major tools in theoretical study of Hamiltonian chaos. The work “Stochastical instability of nonlinear oscillations” by G. Zaslavsky and B. Chirikov, published in *Physics Uspekhi* in 1971, was the first review paper “opened the eyes” of many physicists to power of the theory of dynamical systems and modern ergodic theory. It was realized that very complicated behavior is possible in dynamical systems with only a few degrees of freedom. This complexity cannot be adequately described in terms of individual trajectories and requires statistical methods. Typical Hamiltonian systems are not integrable but chaotic, and this chaos is not homogeneous. At the same values of the control parameters, there coexist regions in the phase space with regular and chaotic motion. The results obtained in the 1960s were summarized in the book “Statistical Irreversibility in Nonlinear Systems” (Nauka, Moscow, 1970).

The end of the 1960s was a hard time for George. He was forced to leave the Institute of Nuclear Physics in Novosibirsk for signing letters in defense of some Soviet dissidents. George got a position at the Institute of Physics in Krasnoyarsk, not far away from Novosibirsk. There he founded a laboratory of the theory of nonlinear processes which exists up to now. In Krasnoyarsk George became interested in the theory of quantum chaos. The first rigorous theory of quantum resonance was developed in 1977 in collaboration with his co-workers. They introduced the important notion of quantum break time (the Ehrenfest time) after which quantum evolution began to deviate from a semiclassical one. The results obtained in Krasnoyarsk were summarized in the book “Chaos in Dynamical Systems” (Nauka, Moscow and Harwood, Amsterdam, 1985).

In 1984, R. Sagdeev invited George to the Institute of Space Research in Moscow. There he has worked on the theory of degenerate and almost degenerate Hamilto-

nian systems, anomalous chaotic transport, plasma physics, and theory of chaos in waveguides. The book “Nonlinear Physics: from the Pendulum to Turbulence and Chaos” (Nauka, Moscow and Harwood, New York, 1988), written with R. Sagdeev, has been a classical textbook for everybody who studies chaos theory. When studying interaction of a charged particle with a wave packet, George with colleagues from the Institute discovered that stochastic layers of different separatrices in degenerated Hamiltonian systems may merge producing a stochastic web. Unlike the famous Arnold diffusion in non-degenerated Hamiltonian systems, that appears only if the number of degrees of freedom exceeds 2, diffusion in the Zaslavsky webs is possible at one and half degrees of freedom. This diffusion is rather universal phenomenon and its speed is much greater than that of Arnold diffusion. Beautiful symmetries of the Zaslavsky webs and their properties in different branches of physics have been described in the book “Weak chaos and Quasi-Regular Structures” (Nauka, Moscow, 1991 and Cambridge University Press, Cambridge, 1991) coauthored with R. Sagdeev, D. Usikov and A. Chernikov.

In 1991, George emigrated to the USA and became a Professor of Physics and Mathematics at Physical Department of the New York University and at the Courant Institute of Mathematical Sciences. The last 17 years of his life he devoted to principal problems of Hamiltonian chaos connected with anomalous kinetics and fractional dynamics, foundations of statistical mechanics, chaotic advection, quantum chaos, and long-range propagation of acoustic waves in the ocean. In his New York period George published two important books on the Hamiltonian chaos: “Physics of Chaos in Hamiltonian Systems” (Imperial College Press, London, 1998) and “Hamiltonian chaos and Fractional Dynamics” (Oxford University Press, New York, 2005). His last book “Ray and wave chaos in ocean acoustics: chaos in waveguides” (World Scientific Press, Singapore, 2010), written with D. Makarov, S. Prants, and A. Virovlynsky, reviews original results on chaos with acoustic waves in the underwater sound channel.

George was a very creative scientist and a very good teacher whose former students and collaborators are working now in America, Europe and Asia. He authored and co-authored 9 books and more than 300 papers in journals. Many of his works are widely cited. George worked hard all his life. He loved music, theater, literature and was an expert in good wines and food. Only a few people knew that he loved to paint. In the last years he has spent every summer in Provence, France working, writing books and papers and painting in water-colors. The album with his water-colors was issued in 2009 in Moscow.

George Zaslavsky was one of the key persons in the theory of dynamical chaos and made many important contributions to a variety of other subjects. His books and papers influenced very much in advancing modern nonlinear science.

Sergey Prants  
Albert C.J. Luo  
Valentin Afraimovich

March, 2010

# Contents

## 1 Stochastic and Resonant Layers in Nonlinear Hamiltonian Systems

<i>Albert C.J. Luo</i> .....	1
1.1 Introduction .....	1
1.2 Stochastic layers .....	4
1.2.1 Geometrical description .....	5
1.2.2 Approximate criterions .....	9
1.3 Resonant layers .....	17
1.3.1 Layer dynamics .....	19
1.3.2 Approximate criterions .....	23
1.4 A periodically forced Duffing oscillator .....	27
1.4.1 Approximate predictions .....	28
1.4.2 Numerical illustrations .....	34
1.5 Discussions .....	47
References .....	48

## 2 A New Approach to the Treatment of Separatrix Chaos and Its Applications

<i>S.M. Soskin, R. Mannella, O.M. Yevtushenko, I.A. Khovanov,</i> <i>P.V.E. McClintock</i> .....	51
2.1 Introduction .....	52
2.1.1 Heuristic results .....	52
2.1.2 Mathematical and accurate physical results .....	53
2.1.3 Numerical evidence for high peaks in $\Delta E(\omega_f)$ and their rough estimations .....	54
2.1.4 Accurate description of the peaks and of the related phenomena .....	54
2.2 Basic ideas of the approach .....	55
2.3 Single-separatrix chaotic layer .....	60
2.3.1 Rough estimates. Classification of systems .....	61
2.3.2 Asymptotic theory for systems of type I .....	62
2.3.3 Asymptotic theory for systems of type II .....	71
2.3.4 Estimate of the next-order corrections .....	79

2.3.5	Discussion .....	83
2.4	Double-separatrix chaos .....	85
2.4.1	Asymptotic theory for the minima of the spikes .....	89
2.4.2	Theory of the spikes' wings .....	108
2.4.3	Generalizations and applications .....	114
2.5	Enlargement of a low-dimensional stochastic web .....	117
2.5.1	Slow modulation of the wave angle .....	119
2.5.2	Application to semiconductor superlattices .....	120
2.5.3	Discussion .....	121
2.6	Conclusions .....	121
2.7	Appendix .....	122
2.7.1	Lower chaotic layer .....	122
2.7.2	Upper chaotic layer .....	137
	References .....	138

### **3 Hamiltonian Chaos and Anomalous Transport in Two Dimensional Flows**

	<i>Xavier Leoncini</i> .....	<b>143</b>
3.1	Introduction .....	143
3.2	Point vortices and passive tracers advection .....	145
3.2.1	Definitions .....	145
3.2.2	Chaotic advection .....	146
3.3	A system of point vortices .....	148
3.3.1	Definitions .....	148
3.4	Dynamics of systems with two or three point vortices .....	150
3.4.1	Dynamics of two vortices .....	150
3.4.2	Dynamics of three vortices .....	151
3.5	Vortex collapse and near collapse dynamics of point vortices .....	152
3.5.1	Vortex collapse .....	153
3.5.2	Vortex dynamics in the vicinity of the singularity .....	153
3.6	Chaotic advection and anomalous transport .....	155
3.6.1	A brief history .....	156
3.6.2	Definitions .....	157
3.6.3	Anomalous transport in incompressible flows .....	160
3.6.4	Tracers (passive particles) dynamics .....	162
3.6.5	Transport properties .....	169
3.6.6	Origin of anomalous transport .....	174
3.6.7	General remarks .....	180
3.7	Beyond characterizing transport .....	180
3.7.1	Chaos of field lines .....	180
3.7.2	Local Hamiltonian dynamics .....	180
3.7.3	An ABC type flow .....	182
3.8	Targeted mixing in an array of alternating vortices .....	185
3.9	Conclusion .....	189
	References .....	189

<b>4 Hamiltonian Chaos with a Cold Atom in an Optical Lattice</b>	
<i>S.V. Prants</i> .....	<b>193</b>
4.1 Short historical background .....	194
4.2 Introduction .....	195
4.3 Semiclassical dynamics .....	196
4.3.1 Hamilton-Schrödinger equations of motion .....	196
4.3.2 Regimes of motion .....	198
4.3.3 Stochastic map for chaotic atomic transport .....	200
4.3.4 Statistical properties of chaotic transport .....	202
4.3.5 Dynamical fractals .....	204
4.4 Quantum dynamics .....	208
4.5 Dressed states picture and nonadiabatic transitions .....	209
4.5.1 Wave packet motion in the momentum space .....	211
4.6 Quantum-classical correspondence and manifestations of dynamical chaos in wave-packet atomic motion .....	219
References .....	221
<b>5 Using Stochastic Webs to Control the Quantum Transport of Electrons in Semiconductor Superlattices</b>	
<i>T.M. Fromhold, A.A. Krokhin, S. Bujkiewicz, P.B. Wilkinson,     D. Fowler, A. Patané, L. Eaves, D.P.A. Hardwick, A.G. Balanov,     M.T. Greenaway, A. Henning</i> .....	<b>225</b>
5.1 Introduction .....	226
5.2 Superlattice structures .....	228
5.3 Semiclassical electron dynamics .....	231
5.4 Electron drift velocity .....	234
5.5 Current-voltage characteristics: theory and experiment .....	236
5.6 Electrostatics and charge domain structure .....	238
5.7 Tailoring the SL structure to increase the number of conductance resonances .....	240
5.8 Energy eigenstates and Wigner functions .....	243
5.9 Summary and outlook .....	247
References .....	249
<b>6 Chaos in Ocean Acoustic Waveguide</b>	
<i>A.L. Virovlyansky</i> .....	<b>255</b>
6.1 Introduction .....	255
6.2 Basic equations .....	258
6.2.1 Parabolic equation approximation .....	259
6.2.2 Geometrical optics. Hamiltonian formalism .....	260
6.2.3 Modal representation of the wave field .....	262
6.2.4 Ray-based description of normal modes .....	263
6.3 Ray chaos .....	264
6.3.1 Statistical description of chaotic rays .....	264
6.3.2 Environmental model .....	266

6.3.3	Wiener process approximation .....	267
6.3.4	Distribution of ray parameters.....	269
6.3.5	Smoothed intensity of the wave field .....	270
6.4	Ray travel times.....	272
6.4.1	Timefront .....	272
6.4.2	Statistics of ray travel times .....	274
6.5	Modal structure of the wave field under conditions of ray chaos ...	278
6.5.1	Coarse-grained energy distribution between normal modes.	278
6.5.2	Transient wave field.....	280
6.6	Conclusion .....	287
	References.....	289

# Contributors

**A.G. Balanov** Department of Physics, Loughborough University, Leicestershire, LE11 3TU, UK, e-mail: a.balanov\_@\_lboro.ac.uk

**S. Bujkiewicz** Centre for Biostatistics and Genetic Epidemiology, Department of Health Sciences, University of Leicester, University Road, Leicester LE1 7RH, UK, e-mail: sb309@leicester.ac.uk

**L. Eaves** School of Physics & Astronomy, University of Nottingham, Nottingham NG7 2RD, UK, e-mail: laurence.eaves@nottingham.ac.uk

**T.M. Fromhold** School of Physics & Astronomy, University of Nottingham, Nottingham NG7 2RD, UK, e-mail: mark.fromhold@nottingham.ac.uk

**M.T. Greenaway** School of Physics & Astronomy, University of Nottingham, Nottingham NG7 2RD, UK, e-mail: ppxmg@nottingham.ac.uk

**D.P.A. Hardwick** School of Physics & Astronomy, University of Nottingham, Nottingham NG7 2RD, UK.

**A. Henning** School of Physics & Astronomy, University of Nottingham, Nottingham NG7 2RD, UK, e-mail: ppxah@nottingham.ac.uk.

**I.A. Khovanov** School of Engineering, University of Warwick, Coventry CV4 7AL, UK, e-mail: i.khovanov@warwick.ac.uk

**A.A. Krokhin** Department of Physics, University of North Texas, P.O. Box 311427, Denton, TX 76203, USA, e-mail: arkady@unt.edu

**Xavier Leoncini** Centre de Physique Thorique, Luminy Case 907, 13288 Mar-seille Cedex 9, France, e-mail: Xavier.Leoncini@cpt.univ-mrs.fr

**Albert C. J. Luo** Department of Mechanical and Industrial Engineering Southern Illinois University Edwardsville Edwardsville, Illinois 62026-1805, USA, Tel: 618-650-5389, Fax: 618-650-2555, e-mail: aluo@siue.edu

**R. Mannella** Dipartimento di Fisica, Università di Pisa, 56127Pisa, Italy, e-mail: mannella@df.unipi.it

**P.V.E. McClintock** Physics Department, Lancaster University, Lancaster LA1 4YB, UK, e-mail: p.v.e.mcclintock@lancaster.ac.uk

**D. Fowler** School of Physics & Astronomy, University of Nottingham, Nottingham NG7 2RD, UK, e-mail: daivid.fowler\_@\_ief.u-psud.fr

**A. Patanè** School of Physics & Astronomy, University of Nottingham, Nottingham NG7 2RD, UK, e-mail: amalia.patane@nottingham.ac.uk

**S.V. Prants** Laboratory of Nonlinear Dynamical Systems, Pacific Oceanological Institute of the Russian Academy of Sciences, 43 Baltiiskaya st., 690041 Vladivostok, Russia, e-mail:prants@poi.dvo.ru

**S.M. Soskin** Institute of Semiconductor Physics, National Academy of Sciences of Ukraine, 03028 Kiev, Ukraine, e-mail: ssoskin@ictp.it

**A.L. Virovlyansky** Institute of Applied Physics, Russian Academy of Science, 46 Ul'yanov Street, 603950 Nizhny Novgorod, Russia, e-mail: viro@hydro.appl.sci-nnov.ru

**P.B. Wilkinson** British Geological Survey, Kingsley Dunham Centre, Keyworth NG12 5GG, UK, e-mail: pbw@bgs.ac.uk

**O.M. Yevtushenko** Physics Department, Ludwig-Maximilians-Universität München, D-80333 München, Germany, e-mail: bom@ictp.it

# Chapter 1

## Stochastic and Resonant Layers in Nonlinear Hamiltonian Systems

Albert C.J. Luo

**Abstract** In this chapter, stochastic and resonant layers in 2-dimensional nonlinear Hamiltonian systems are presented. The chaos in the stochastic layer is formed by the primary resonance interaction in nonlinear Hamiltonians systems. However, the chaos in the resonant layer is formed by the sub-resonance interaction. The chapter presented herein is to memorize Professor George M. Zaslavsky for his contributions in stochastic layers.

### 1.1 Introduction

The modern theory of dynamics originates from Poincaré's qualitative analysis. Poincaré (1892) discovered that the motion of nonlinear a coupled oscillator is sensitive to the initial condition, and qualitatively presented that the inherent characteristics of the motion in the vicinity of unstable fixed points of nonlinear oscillation systems may be *stochastic* under regular applied forces. In addition, Poincaré developed the perturbation theory for periodic motions in planar dynamical systems. Birkhoff (1913) continued Poincaré's work, and provided a proof of Poincaré's geometric theorem. Birkhoff (1927) showed that both stable and unstable fixed points of nonlinear oscillation systems with 2-degrees of freedom must exist whenever their frequency ratio (or called *resonance*) is rational. The sub-resonances in periodic motions of such systems change the topological structures of phase trajectories, and the island chains are obtained when the dynamical systems renormalized with fine scales are used. The work of Poincaré and Birkhoff implies that the complexity of topological structures in phase space exists for nonlinear dynamic systems. The question is whether the complicated trajectory can fill the entire phase space or not.

---

Albert C.J. Luo

Department of Mechanical and Industrial Engineering, Southern Illinois University Edwardsville, Edwardsville, Illinois 62026-1805, USA, Tel: 618-650-5389, Fax: 618-650-2555, e-mail: aluo@siue.edu

The formal and normal forms in the vicinity of equilibrium are developed through the Taylor series to investigate the complexity of trajectory in the neighborhood of the equilibrium. Since the trajectory complexity exists in the vicinity of hyperbolic points, one focused on investigating the dynamics in such vicinity of hyperbolic points.

From a topological point of view, Smale's horseshoe was presented in Smale (1967). Further, a differentiable dynamical system theory was developed. Such a theory has been extensively used to interpret the homoclinic tangle phenomenon in nonlinear dynamics. Smale found the infinite, many periodic motions, and a perfect minimal Cantor set near a homoclinic motion can be formed. However, Smale's results cannot apply to Hamiltonian systems with more than 2-degrees of freedom. Because the differentiable dynamical system theory is based on the linearization of dynamical systems at hyperbolic points, it may not be adequate to explain the complexity of chaotic motions in nonlinear dynamical systems. To continue Birkhoff's formal stability, Glimm (1963) investigated the formal stability of an equilibrium (or a periodic solution) of Hamiltonian systems through the rational functions instead of the power series expansion. Such an investigation just gave another kind of approximation. Though those theories are extensively applied in nonlinear dynamical systems, such analyses based on the formal and normal forms are still the local analyses in the vicinity of equilibrium. Those theories cannot be applied for the global behaviors of nonlinear dynamical systems.

To understand the complexity of motion in nonlinear Hamiltonian systems, based on the non-rigorous theory of perturbation, Kolmogorov (1954) postulated the KAM theorem. In the KAM theorem, Kolmogorov suggested a procedure which ultimately led to the stability proof of the periodic solutions of the Hamiltonian systems with 2-degrees of freedom. This problem is intimately connected with the difficulty of small divisors. The aforementioned theorem was proved under different restrictions (e.g., Arnold, 1963; Moser, 1962). Further, Arnold (1964) investigated the instability of dynamical systems with several degrees of freedom, and the diffusion of motion along the generic separatrix was discussed. The results of Arnold (1964) extended Kolmogorov's results to the Hamiltonian system with several degrees of freedom system. The stability in the sense of Lyapunov cannot be inferred. The KAM theory is based on the separable oscillators with weak interactions. In fact, once the perturbation exists, the dynamics of the perturbed Hamiltonian systems may not be well-behaved to the separable dynamical systems. In physical systems, the interaction between two oscillators in a nonlinear dynamical system cannot be very small. The KAM theorem may provide an acceptable prediction only when the interaction perturbation is very weak. The KAM theory is based on separable, integrable Hamiltonian systems. In fact, the complexity of motions in non-integrable, nonlinear Hamiltonian systems is much beyond what the KAM theory stated.

The instability zone (or *stochastic layer*) of Hamiltonian systems, as investigated in Arnold (1964), is a domain of chaotic motion in the vicinity of the generic separatrix. Even if the width of the separatrix splitting was estimated, the dynamics of the separatrix splitting was not developed. Henon and Heiles (1964) gave a numerical investigation on the nonlinear Hamiltonian systems with 2-degrees of freedom

in order to determine whether or not a well-behaved constant of the motion exists for such Hamiltonian Systems. Izrailev and Chirikov (1966) first pointed out that the periodically forced, nonlinear Hamiltonian system with 1-degree of freedom exhibits a KAM instability leading to the stochastic behavior (or stochastic and resonance layers). Walker and Ford (1969) investigated the amplitude instability and ergodic behavior for nonlinear Hamiltonian systems with 2-degrees of freedom to develop the verifiable scheme for prediction of the onset of the amplitude instability. Isolated resonance and double resonance were investigated and the resonance was determined through the transformed coordinates. Such ergodic behavior in nonlinear Hamiltonian system originates from Birkhoff (1927). In other words, to investigate the enormous complexity of non-special motions in dynamical systems from geodesic flows, Birkhoff (1927) presented that the set of non-special motions (or chaotic motions) is measurable in the sense of Lebesgue, and the set of the special motions (or regular motion) is of zero measure. Furthermore, the ergodic theory had been developed in the 20<sup>th</sup> century and it is as a fundamental base for fractal theory. The thorough study of the geodesic flows in the ergodic theory can be found in Hopf (1937). Those ideas were generalized by Anosov (1962) to study a class of differential equations, which can be also referenced to (Sinai,1976). Even though the ergodic theory is a foundation for fractality of chaotic motions in nonlinear dynamical systems, such a theory still cannot provide enough hopes to understand the complexity of chaotic motions in nonlinear dynamics.

For a nonlinear Hamiltonian system with  $n$ -degrees of freedom, it is very difficult to understand the mechanism of chaotic motions. To date, such a problem is unsolved. Around (1960) considered extremely simple, nonlinear Hamiltonian systems to investigate such a mechanism. Melnikov (1962) used the concept in Poincaré (1892) to investigate the behavior of trajectories of perturbed systems near autonomous Hamiltonian systems. Melnikov (1963) further investigated the behavior of trajectories of perturbed Hamiltonian systems and the width of the separatrix splitting were approximately estimated. The width gives the domain of the chaotic motion in the vicinity of the generic separatrix. Even if the width of the separatrix splitting was approximately estimated, the dynamics of the separatrix splitting was not developed. From a physical point of view, Chirikov (1960) investigated the resonance processes in magnetic traps, and the resonance overlap was presented initially. Zaslavsky and Chirikov (1964) discussed the mechanism of 1-dimensional Fermi acceleration and determined the stochastic property of such a system. Rosenblut et al. (1966) investigated the appearance of a stochastic instability (or chaotic motion) of trapped particles in the magnetic field of a traveling wave under a perturbation. Filonenko et al. (1967) further discussed the destruction of magnetic surface generated by the resonance harmonics of perturbation. The destruction of such a magnetic surface demonstrates the formation and destruction of the resonant surface. Zaslavsky and Filonenko (1968) gave a systematic investigation of the stochastic instability of trapped particles through the separatrix map (or whisker motion in Arnold (1964)), and the fractional equation for diffusion was developed. Zaslavsky and Chirikov (1972) further presented the stochastic instability of nonlinear oscillations. Chirikov (1979) refined the resonance overlap criterion to predict the onset

of chaos in stochastic layers. In addition, the most important achievements for prediction of the appearance of chaotic motions were summarized. Escande and Doveil (1981) used the resonance overlap concept and gave a criterion through a renormalization group method (also see, Escande, 1985). The details for the resonance overlap theory and renormalization group scheme can be referred to references (e.g., Lichtenberg and Lieberman, 1992; Reichl, 1992). Though the resonant overlap criterion can provide a rough prediction of the onset of chaotic motion in the stochastic layers, the mechanism of the chaotic motion in the stochastic layers still cannot be fully understood until now.

Luo (1995) proposed the resonance theory for chaotic motions in the vicinity of generic separatrix in nonlinear Hamiltonian systems (also see, Luo and Han, 2001), and it was asserted that chaotic motions in nonlinear Hamiltonian systems are caused by the resonant interaction. Furthermore, the mechanism for the formation, growth and destruction of stochastic layers in nonlinear Hamiltonian systems was discussed in Luo and Han (2001). In Luo et al. (1999), the resonant webs formed in the stochastic layer were presented, and it was observed that the webs are similar to the stochastic layer of the parametrically forced pendulum system. The recent investigations (e.g., Han and Luo, 1998; Luo, 2001b, c, 2002) discovered that the resonance interaction generates the resonant separatrix, and the chaotic motion forms in vicinity of such a resonant separatrix. The corresponding criteria were presented for analytical predictions of chaotic motions in 1-DOF nonlinear Hamiltonian systems with periodic perturbations. The maximum and minimum energy spectrum methods were developed for numerical predictions of chaotic motions in nonlinear Hamiltonian systems (also see, Luo et al., 1999; and Luo, 2002). The energy spectrum approach is applicable not only for small perturbations but for the large perturbation. The recent achievements for stochastic layers in periodically forced Hamiltonians with 1-degree of freedom were summarized in Luo (2004). Luo (2006a) investigated quasi-periodic and chaotic motions in  $n$ -dimensional nonlinear Hamiltonian systems. The energy spectrum method was systematically presented for arbitrary interactions of the integrable nonlinear Hamiltonian systems. The internal resonance was discussed analytically for weak interactions, and the chaotic and quasi-periodic motions can be predicted. From a theory for discontinuous dynamical system in Luo (2006b), Luo (2007a) presented a general theory for  $n$ -dimensional nonlinear dynamical systems. The global tangency and transversality to the separatrix were discussed from the first integral quantity. The first integral quantity increment was introduced to investigate the periodic and chaotic flows. In this chapter, only the stochastic and resonant layers in nonlinear Hamilton systems will be presented. For more materials, readers can refer to Luo (2008).

## 1.2 Stochastic layers

In this section, the stochastic layers in nonlinear Hamiltonian systems will be described geometrically, and the approximate criteria for onset and destruction of the stochastic layers will be presented.

### 1.2.1 Geometrical description

Consider a 2-dimensional Hamiltonian system with a time periodically perturbed vector field, i.e.,

$$\dot{\mathbf{x}} = \mathbf{f}(\mathbf{x}, \boldsymbol{\mu}) + \mu \mathbf{g}(\mathbf{x}, t, \boldsymbol{\pi}); \quad \mathbf{x} = (x, y)^T \in \mathbb{R}^2, \quad (1.1)$$

where  $\mathbf{f}(\mathbf{x}, \boldsymbol{\mu})$  is an unperturbed Hamiltonian vector field on  $\mathbb{R}^2$  and  $\mathbf{g}(\mathbf{x}, t)$  is a periodically perturbed vector field with period  $T = 2\pi/\Omega$ , and

$$\mathbf{f}(\mathbf{x}, \boldsymbol{\mu}) = (f_1(\mathbf{x}, \boldsymbol{\mu}), f_2(\mathbf{x}, \boldsymbol{\mu}))^T \text{ and } \mathbf{g}(\mathbf{x}, t, \boldsymbol{\pi}) = (g_1(\mathbf{x}, t, \boldsymbol{\pi}), g_2(\mathbf{x}, t, \boldsymbol{\pi}))^T \quad (1.2)$$

are sufficiently smooth ( $C^r, r \geq 2$ ) and bounded on a bounded set  $D \subset \mathbb{R}^2$  in phase space.  $f_1 = \partial H_0(x, y)/\partial y$ ,  $f_2 = -\partial H_0(x, y)/\partial x$ ;  $g_1 = \partial H_1(x, y, \Omega t)/\partial y$ ,  $g_2 = -\partial H_1(x, y, \Omega t)/\partial x$ . If the perturbation (or forcing term)  $\mathbf{g}(\mathbf{x}, t)$  vanishes, Equation (1.1) reduces to a 2-dimensional autonomous system  $\dot{\mathbf{x}} = \mathbf{f}(\mathbf{x}, \boldsymbol{\mu})$  corresponding to a 1-degree of freedom system in nonlinear Hamiltonian systems. Therefore the total Hamiltonian of Eq. (1.1) can be expressed by

$$H(x, y, t, \mathbf{p}) = H_0(x, y, \boldsymbol{\mu}) + \mu H_1(x, y, \Omega t, \boldsymbol{\pi}), \quad (1.3)$$

with excitation frequency  $\Omega$  and strength  $\mu$  of the perturbed Hamiltonian  $H_1(x, y, t, \boldsymbol{\pi})$  as well. For comparison with the other approximate analysis, such a perturbation parameter is introduced herein. The Hamiltonian of the integrable system in Eq. (1.1) is  $H_0(x, y, \boldsymbol{\mu})$ . Once the initial condition is given, the Hamiltonian  $H_0(x, y)$  is invariant (i.e.,  $H_0(x, y, \boldsymbol{\mu}) = E$ ), which is the first integral manifold.

To restrict this investigation to the 2-dimensional stochastic layer, four assumptions for Eq.(1.1) are introduced as follows:

- (H1) The unperturbed system of Eq.(1.1) possesses a bounded, closed separatrix  $q_0(t)$  with at least one hyperbolic point  $p_0 : (x_h, y_h)$ .
- (H2) The neighborhood of  $q_0(t)$  for the point  $p_0 : (x_h, y_h)$  is filled with at least three families of periodic orbits  $q_\sigma(t)$  ( $\sigma = \alpha, \beta, \gamma$ ) with  $\alpha, \beta, \gamma \in (0, 1]$ .
- (H3) For the Hamiltonian energy  $E_\sigma$  of  $q_\sigma(t)$ , its period  $T_\sigma$  is a differentiable function of  $E_\sigma$ .
- (H4) The perturbed system of Eq.(1.1) possesses a *perturbed* orbit  $q(t)$  in the neighborhood of the *unperturbed* separatrix  $q_0(t)$ .

From the foregoing hypothesis, the phase portrait of the unperturbed Hamiltonian system in the vicinity of the separatrix is sketched in Fig.1.1. The following point sets and the corresponding Hamiltonian energy are introduced, i.e.,

$$\Gamma_0 \equiv \{(x, y) | (x, y) \in q_0(t), t \in \mathbb{R}\} \cup \{p_0\} \text{ and } E_0 = H_0(q_0(t)) \quad (1.4)$$

for the separatrix,

$$\Gamma_\sigma \equiv \{(x,y) | (x,y) \in q_\sigma(t), t \in \mathbb{R}\} \text{ and } E_\sigma = H_0(q_\sigma(t)) \quad (1.5)$$

for the unperturbed,  $\sigma$ -periodic orbit and

$$\Gamma = \{(x,y) | (x,y) \in q(t), t \in \mathbb{R}\} \text{ and } E = H_0(q(t)) \quad (1.6)$$

for the perturbed orbit  $q(t)$ .

The Hamiltonian energies in Eqs. (1.4) and (1.5) are constant for any periodic orbit of the unperturbed system but the Hamiltonian energy in Eq. (1.6) varies with  $(x,y) \in q(t)$  of the perturbed system. Note that the unperturbed Hamiltonian  $H_0(q_\sigma(t))$  ( $\sigma = \alpha, \beta, \gamma$ ) and  $H_0(q_0(t))$  are  $C^r$  ( $r \geq 2$ ) smooth in Luo and Han (2001). The hypotheses (H2)–(H3) imply that  $T_\sigma \rightarrow \infty$  monotonically as  $\sigma \rightarrow 0$  (i.e., the periodic orbit  $q_\sigma(t)$  approaches to  $q_0(t)$  as  $\sigma \rightarrow 0$ ).

The  $\delta$ -sets of the first integral quantity (or the energy) of the unperturbed Eq. (1.1) in  $\Gamma_\sigma$  ( $\sigma = \alpha, \beta, \gamma$ ), are defined as

$$N_\sigma^\delta(E_0) = \{E_\sigma | |E_\sigma - E_0| < \delta_\sigma, \text{ for small } \delta_\sigma > 0\} \quad (1.7)$$

and the union of the three  $\delta$ -sets with  $E_0$  is

$$N^\delta(E_0) = \bigcup_\sigma N_\sigma^\delta(E_0) \cup \{E_0\}. \quad (1.8)$$

For some time  $t$ , there is a point  $\mathbf{x}_\sigma = (x_\sigma(t), y_\sigma(t))^T$  on the orbit  $q_\sigma(t)$  and this point is also on the normal  $\mathbf{f}^\perp(\mathbf{x}_0) = (-f_2(\mathbf{x}_0), f_1(\mathbf{x}_0))^T$  of the tangential vector of the separatrix  $q_0(t)$  at a point  $\mathbf{x}_0 = (x_0(t), y_0(t))^T$ , as shown in Fig. 1.2. Therefore, the distance is defined as

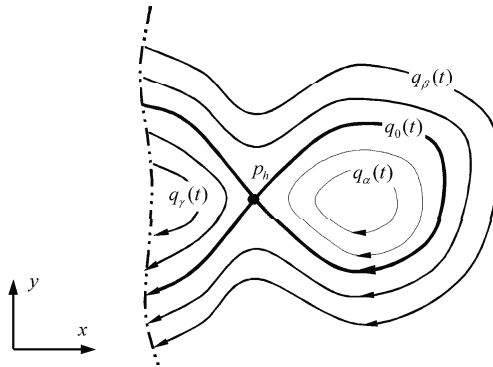


**Fig. 1.1** The phase portrait of the unperturbed system of Eq. (1.1) near a hyperbolic point  $p_h$ .  $q_0(t)$  is a separatrix going through the hyperbolic point and splitting the phase into three parts near the hyperbolic point, and the corresponding orbits  $q_\sigma(t)$  are termed the  $\sigma$ -orbit ( $\sigma = \{\alpha, \beta, \gamma\}$ ).

$$\begin{aligned} \|q_\sigma(t) - q_0(t)\| &= \max_{t \in \mathbb{R}} \|\mathbf{x}_\sigma(t) - \mathbf{x}_0(t)\| \\ &= \max_{t \in \mathbb{R}} \sqrt{[x_\sigma(t) - x_0(t)]^2 + [y_\sigma(t) - y_0(t)]^2}. \end{aligned} \quad (1.9)$$

**Lemma 1.1** For Eq. (1.1) with (H1)–(H4),  $\forall \varepsilon > 0, \exists \delta_\sigma > 0$  ( $\sigma = \alpha, \beta, \gamma$ ) so that  $\|q_\sigma(t) - q_0(t)\| < \varepsilon$  for  $E_\sigma \in N^\delta(E_0)$  at a specific time  $t$ .

*Proof.*  $\forall \varepsilon > 0$ , let  $\delta_\sigma = \varepsilon \|H_0\| > 0$  satisfying

$$|E_\sigma - E_0| = |H_0(q_\sigma) - H_0(q_0)| \leq \|H_0\| \cdot \|q_\sigma - q_0\| < \delta_\sigma,$$

where

$$\|H_0\| \equiv \sup_{\sigma \neq 0} [ |H_0(q_\sigma) - H_0(q_0)| / \|q_\sigma - q_0\| ].$$

Since the unperturbed Hamiltonian  $H_0$  of orbits  $q_\sigma$  and  $q_0$  is  $C^r$ -smooth ( $r \geq 2$ ) and  $0 < \|H_0\| < \infty$  for bounded and closed orbits. Therefore, one obtains

$$\|q_\sigma(t) - q_0(t)\| < \delta_\sigma / \|H_0\| = \varepsilon.$$

This lemma is proved. ■

The  $\varepsilon$ -neighborhood of orbit  $q_0(t)$  is formed by the three  $\varepsilon$ -sets of  $\Gamma_0$  for the  $\sigma$ -orbits ( $\sigma = \alpha, \beta, \gamma$ ), as shown in Fig. 1.2. The bold solid curves denote the separatrix  $q_0(t)$  and the  $\varepsilon$ -neighborhood boundaries,  $q_\sigma^\varepsilon(t)$  ( $\sigma = \alpha, \beta, \gamma$ ), is determined

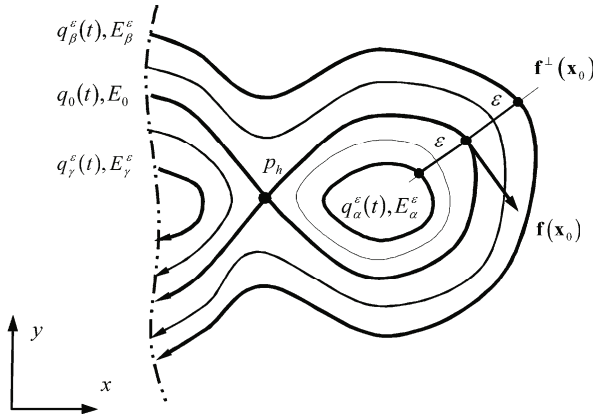


**Fig. 1.2** The  $\varepsilon$ -neighborhood of orbit  $q_0(t)$ . The bold solid curves represent the separatrix  $q_0(t)$  and the  $\varepsilon$ -neighborhood boundaries  $q_\sigma^\varepsilon(t)$  determined by  $\max_{t \in [0, \infty)} \|q_\sigma^\varepsilon(t) - q_0(t)\| = \varepsilon$  ( $\sigma = \alpha, \beta, \gamma$ ).

The solid curves depict all orbits  $q_\sigma(t)$  in the  $\varepsilon$ -neighborhood. The energies on the boundary orbits are given through  $E_\sigma^\varepsilon = H_0(q_\sigma^\varepsilon(t))$ .

through  $\max_{t \in [0, \infty)} \|q_\sigma^\varepsilon(t) - q_0(t)\| = \varepsilon$  when  $E_\sigma^\varepsilon = H_0(q_\sigma^\varepsilon(t))$ . The solid curves represent all the  $\sigma$ -orbits  $q_\sigma(t)$  in the  $\varepsilon$ -neighborhood.

The three  $\varepsilon$ -sets of  $\Gamma_0$  for the  $\sigma$ -orbits ( $\sigma = \alpha, \beta, \gamma$ ) are defined by

$$\Gamma_\sigma^\varepsilon = \{(x, y) | (x, y) \in q_\sigma(t), \|q_\sigma(t) - q_0(t)\| < \varepsilon, t \in \mathbb{R}\}. \quad (1.10)$$

Furthermore, from Eq.(1.8), the unions of the  $\varepsilon$ -sets with  $\Gamma_0$  are

$$\Gamma_0^\varepsilon = \bigcup_\sigma \Gamma_\sigma^\varepsilon \bigcup \Gamma_0, \quad \Gamma_{\sigma 0}^\varepsilon = \Gamma_\sigma^\varepsilon \bigcup \Gamma_0. \quad (1.11)$$

The Poincaré map  $P : \Gamma^P \rightarrow \Gamma^P$ , where the Poincaré mapping set in phase space is:

$$\Gamma^P \equiv \left\{ (x_N, y_N) \left| (x_N, y_N) \in q(t), t_N = \frac{2\pi N}{\Omega} + t_0, N = 0, 1, \dots \right. \right\} \subset \Gamma, \quad (1.12)$$

where  $t_0$  is the initial time. Using the above notations, a stochastic layer is defined through the Poincaré mapping set with nonzero measure as follows:

**Definition 1.1** The Poincaré mapping set  $\Gamma^P$  is termed the stochastic layer in the  $\varepsilon$ -sense if the compact, dense set  $\Gamma^P$  belongs to  $\Gamma_0^\varepsilon$  (or  $\Gamma^P \subset \Gamma_0^\varepsilon$ ) for  $t_N = 2N\pi/\Omega + t_0$  ( $N = 0, 1, \dots$ ). Similarly, the Poincaré mapping subset  $U_\sigma \subset \Gamma^P$  is the  $\sigma$ -stochastic layer if  $U_\sigma \subset \Gamma_{\sigma 0}^\varepsilon$  for  $t_N = 2N\pi/\Omega + t_0$ .

A stochastic layer of system in Eq. (1.1) is formed through the Poincaré mapping set of  $q(t)$  in the  $\varepsilon$ -neighborhood for time  $t \in [0, \infty)$ , as shown in Fig. 1.3. The separatrix of the stochastic layer by the separatrix gives three sub-stochastic layers shaded. The sub-layers relative to the  $\sigma$ -orbits ( $\sigma = \alpha, \beta, \gamma$ ) are termed the  $\sigma$ -stochastic layer. The more detail description can be referred to Luo (2008).

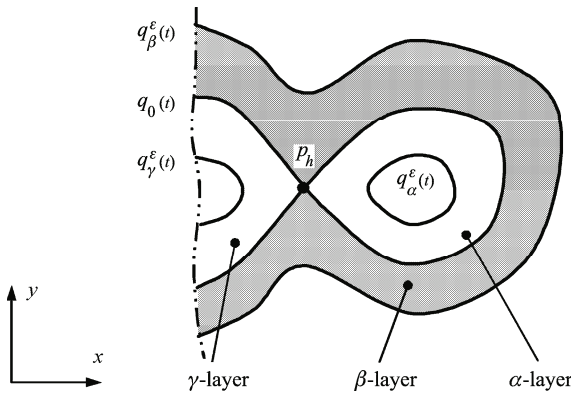


**Fig. 1.3** A stochastic layer of Eq. (1.1) formed by the Poincaré mapping set of  $q(t)$  in the  $\varepsilon$ -neighborhood of  $q_0(t)$  for  $t \in [0, \infty)$ . The separatrix separates the stochastic layer into three sub-stochastic layers (i.e.,  $\alpha$ -layer and  $\beta$ -layer and  $\gamma$ -layer).

### 1.2.2 Approximate criterions

The approximate predictions of resonance in the stochastic layer of a 2-dimensional nonlinear Hamiltonian system will be presented. The incremental energy technique will be presented first from the approximate first integral quantity increment (or approximate energy increment). The whisker mapping will be obtained, and the corresponding criterion will be presented. The linearization of the whicker mapping, the improved standard mapping will be presented and the approximate prediction of chaos onset will be given. Based on the exact first integral quantity, the energy spectrum technique will be developed for a numerical prediction of resonances in the stochastic layer.

#### A. An incremental energy method

As in Luo and Han (2001), the incremental energy method will be presented for understanding the resonant mechanism of chaos in the stochastic layer.

**Lemma 1.2** *For the dynamical system in Eq. (1.1) with (H1)–(H4), if a point  $(x, y) \in \Gamma \cap \Gamma_\sigma$  for some  $\sigma = \{\alpha, \beta, \gamma\}$ , then  $H_0(q(t)) = H_0(q_\sigma(t))$  for some time  $t$ .*

*Proof.* If the perturbed orbit  $q(t)$  in the set  $\Gamma$  is intersected with an unperturbed orbit  $q_\sigma(t)$  in the set  $\Gamma_\sigma$  for some  $\sigma \in \{\alpha \in [-1, 0), \beta \in (0, 1], \gamma \in [-1, 0)\}$  at time  $t$ , there is a single point  $(x, y) \in \Gamma \cap \Gamma_\sigma$ . Therefore, for  $(x, y) \in \Gamma \cap \Gamma_\sigma$ , we have  $(x, y) \in q_\sigma(t)$  and  $(x, y) \in q(t)$ . Thus,  $H_0(q(t)) = H_0(x, y) = H_0(q_\sigma(t))$ , which implies that the conservative energy is equal for the same point in phase space. This lemma is proved.  $\blacksquare$

The detailed discussion is given as follows. Because the conservative energy  $H_0$  is the first integral quantity, for the  $\sigma$ -layer, the map describing the changes of both energy  $H_0$  and phase  $\varphi$  for time transition from  $t_i$  to  $t_i + T_\sigma$  in Eq. (1.1) is obtained, i.e.,

$$E_{i+1} = E_i + \Delta H^\sigma(\varphi_i) \text{ and } \varphi_{i+1} = \varphi_i + \Delta \varphi^\sigma(E_{i+1}), \quad (1.13)$$

where  $E_i = H(q(t_i))$ ,  $\varphi_i = \varphi(q(t_i))$ . For a specific external frequency  $\Omega$ , the initial phase is defined by  $\varphi_i = \Omega t_i$ . Notice that the energy relationship in the foregoing can be expressed through the action variable. As in Chirikov (1979) or Lichtenberg and Lieberman (1992), the phase and energy changes,  $\Delta \varphi^\sigma(E_{i+1})$  and  $\Delta H^\sigma(\varphi_i)$ , are approximately computed by

$$\begin{aligned} \Delta \varphi^\sigma(E_{i+1}) &\approx \Omega T_\sigma(E_{i+1}), \text{ and} \\ \Delta H^\sigma(\varphi_i) &\approx \mu \int_{t_i}^{T_\sigma(E_i) + t_i} \{H_0, H_1\} dt = \mu \int_{t_i}^{T_\sigma(E_i) + t_i} (f_1 g_2 - f_2 g_1) dt. \end{aligned} \quad (1.14)$$

The energy and phase changes in Eq. (1.14) for the system in Eq. (1.1) over one period  $T_\sigma$  of the  $\sigma$ -orbit are sketched in Fig. 1.4. If  $E_i = E_0$  expresses the energy of the separatrix, Equation (1.13) becomes a generalized separatrix map (or a general-

ized whisker map). When the  $\sigma$ -orbit ( $\sigma = \alpha, \beta, \gamma$ ) is close to the separatrix (i.e.,  $T_\sigma \rightarrow \infty$ ), the energy increment reduces to the one along the separatrix in Luo and Han (2001):

$$\Delta H^h(\varphi_i) \approx \lim_{T_\sigma \rightarrow \infty} \mu \int_{t_i}^{T_\alpha(E_i)+t_i} \{H_0, H_1\} dt = \lim_{T_\sigma \rightarrow \infty} \mu \int_{t_i}^{T_\sigma(E_i)+t_i} (f_1 g_2 - f_2 g_1) dt \quad (1.15)$$

which can also be obtained through the Melnikov function with a small parameter  $\mu$ , i.e.,  $\Delta H^h(\varphi_i) = \mu M(t_i)$  (e.g., Rom-Keder, 1990, 1994, 1995; Zaslavsky and Abdullaev, 1995; Abdullaev and Zaslavsky, 1995, 1996; Ahn et al., 1996; Iomin and Fishman, 1996).

After the KAM torus in the vicinity of separatrix is destroyed, the stochastic layer (or the instability zone) will form in such vicinity, and the resonant-separatrix webs appear as in Luo et al. (1999). Such resonance-separatrix webs are generated by the interaction of resonances between the unperturbed perturbed orbits and the periodic forcing in the stochastic layer. In this section, the prediction of the onset of the primary resonance in the stochastic layer will be of great interest. Such resonant interactions in the  $\varepsilon$ -neighborhood of the separatrix are qualitatively illustrated in Fig. 1.5. The hollow circles depict intersection points of the perturbed and unperturbed orbits. When the perturbed orbit arrived to the  $(m_\sigma : n_\sigma)$  primary resonant unperturbed orbit of Eq. (1.1), the resonance between the unperturbed Hamiltonian and perturbation appears, and the resonant condition for a periodically forced system with 1-degree of freedom is obtained from Eq. (1.3), i.e.,

$$m_\sigma \omega_\sigma = n_\sigma \Omega, \quad m_\sigma, n_\sigma \in \mathbb{N} \text{ are irreducible}, \quad (1.16)$$

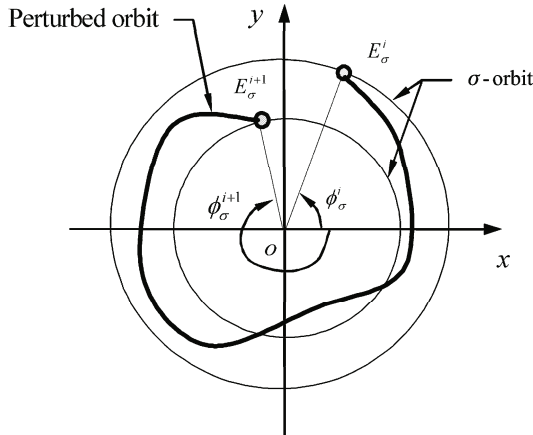


**Fig. 1.4** The energy and phase changes of a perturbed orbit over one period  $T_\alpha$  based on  $E_\sigma^i$ .

where  $\omega_\sigma = 2\pi T_\sigma$  is a frequency of the  $\sigma$ -orbit,  $\Omega$  is the excitation frequency and  $\mathbb{N}$  is the natural number set. For the  $(i+1)^{\text{th}}$  iteration of Eq. (1.13), if  $q(t_{i+1}) = (x_{i+1}, y_{i+1})$  is on the unperturbed, resonant orbit, the phase change in the second of Eq.(1.13) becomes  $\varphi_{i+1} - \varphi_i = 2\pi m_\sigma/n_\sigma$  and  $E_{i+1}$  is replaced by  $E^{(m_\sigma:n_\sigma)}$ . The perturbed orbit  $q(t)$  relative to the  $(m_\sigma : n_\sigma)$ -resonance is represented by  $q^{(m_\sigma:n_\sigma)}(t)$ . Since  $\omega_\sigma = 2\pi/T_\sigma$  depends on the corresponding energy  $E_\sigma$ , the resonant conditions can be directly expressed through  $E_\sigma$  and  $\Omega$ , as shown in Fig. 1.6. In Fig. 1.6(a),  $E_\alpha^{(m_\alpha:n_\alpha)}$  is an unperturbed Hamiltonian energy relative to the  $(m_\alpha : n_\alpha)$ -resonant orbit and  $E_\beta^{(m_\beta:n_\beta)}$  is the Hamiltonian energy pertaining to the  $(m_\beta : n_\beta)$ -resonant orbit. The resonant number sets in the stochastic layer for  $\sigma = \alpha, \beta, \gamma$  are introduced:

$$R_\sigma^\varepsilon = \left\{ (m_\sigma : n_\sigma) \left| \begin{array}{l} m_\sigma \omega_\sigma = n_\sigma \Omega, m_\sigma, n_\sigma \in \mathbb{N} \text{ are irreducible,} \\ \text{and } \|q_\sigma(t) - q_0(t)\| < \varepsilon \end{array} \right. \right\} \quad (1.17)$$

For a given external frequency  $\Omega$  with a constant  $n_\sigma$ , the frequency  $\omega_\sigma$  is relative to  $E_\sigma$ . In Fig. 1.6(b), the zoomed view of the resonant relations in the neighborhood of the separatrix with energy  $E = E_0$  at a specific excitation frequency  $\Omega$  is illustrated through the  $\alpha$ - and  $\beta$ -layers. Once the resonance energy is close to the energy of the separatrix, the density of the resonance separatrix increases in the stochastic layer because of the rapid change of elliptic modulus function. Namely, as  $E_\sigma \rightarrow E_0$ , we have  $\omega_\sigma \rightarrow 0$ . Therefore, from Eq. (1.17), one obtains  $m_\sigma \rightarrow \infty$ . A resonance with large  $m_\sigma$  will be included in the stochastic layer. For each  $m_\sigma$ , the  $(m_\sigma : n_\sigma)$ -resonant separatrix possesses  $m_\sigma$ -center points and  $m_\sigma$ -hyperbolic points under the  $n_\sigma$ -external periods. In the stochastic layer, for  $E_\sigma \rightarrow E_0$ , the number for

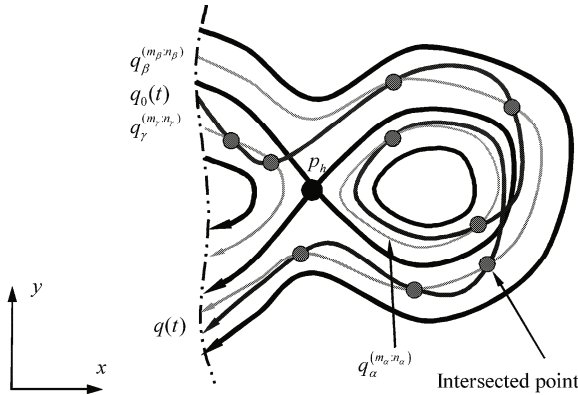


**Fig. 1.5** A perturbed orbit  $q(t)$  for Eq.(1.1) and the resonant interactions with the unperturbed orbits. The circles denote intersections between the perturbed and unperturbed orbits.  $q_\sigma^{(m_\sigma:n_\sigma)}$  ( $\sigma = \alpha, \beta, \gamma$ ) represents an unperturbed orbit having the  $(m_\sigma : n_\sigma)$ -resonant interaction with the perturbed orbit.

center points and hyperbolic points will approach the infinity. When the energy  $E_\sigma$  arbitrarily approaches  $E_0$ , there are infinite centers and infinite hyperbolic points on the resonant separatrix. Such an issue in resonant layers will be discussed in detail. As popularly accepted (e.g., Lu, 2007), the chaos is formed by infinite stable periodic solutions and infinite unstable periodic solutions. The total resonant separatrix number is the summation of the resonant orbit relative to the  $(m_\sigma : n_\sigma)$ -condition with  $m_\sigma \in [\min\{m_\sigma\}, \infty) \subset \mathbb{N}$ . This implies that the infinite resonances exist in the  $\sigma$ -layer ( $\sigma = \alpha, \beta, \gamma$ ). The stochastic layer complexity will be formed by the resonant-web, which can be referred to Luo et al. (1999).

When the perturbation becomes stronger, the perturbed orbit will pass over more and more unperturbed, periodic orbits, as shown in Fig. 1.5. Therefore, the interaction between the Hamiltonian system and its perturbation increases with increasing

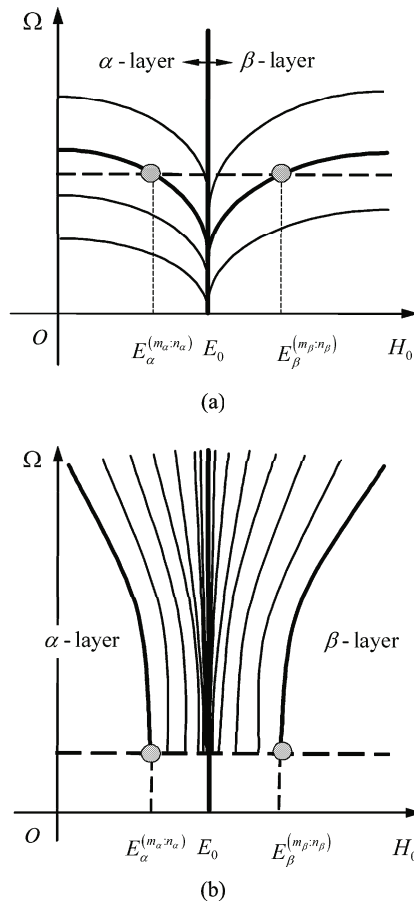


**Fig. 1.6** (a) Resonant conditions of the perturbed system in the stochastic layer and (b) a zoomed view of resonant conditions in neighborhood of separatrix.

perturbation strength. The resonant interaction leads to a new resonant overlap, and such resonant overlap generates a new stochastic layer different in the old stochastic layer because a new, specific resonant-separatrix web is formed in the stochastic layer. Thus, the prediction of the onset of a specific resonant-separatrix web in the stochastic layer is given by the following theorems.

**Theorem 1.1** *For a perturbed Hamiltonian Eq. (1.1) with (H1)–(H4), for an arbitrarily small  $\varepsilon_\sigma > 0$ , there exists  $\delta_\sigma > 0$ , so that if for  $(m_\sigma : n_\sigma) \in R_\sigma^\varepsilon (\sigma = \alpha, \beta, \gamma)$ ,*

$$|\Delta H^\sigma(\varphi_i)| = |E_\sigma^{(m_\sigma : n_\sigma)} - E_0| \leq \delta_\sigma, \quad (1.18)$$

*then  $\|q^{(m_\sigma : n_\sigma)}(t_i) - q_0(t_i)\| < \varepsilon_\sigma$  for all the time  $t_i$ , i.e., the Poincaré mapping set of  $q^{(m_\sigma : n_\sigma)}(t)$  is in a  $\sigma$ -stochastic layer as  $t \in [0, \infty)$ .*

*Proof.* Consider Eq.(1.1) with (H1)–(H4). If  $q^{(m_\sigma : n_\sigma)}(t_{i+1}) = (x_{i+1}, y_{i+1}) \in \Gamma \cap \Gamma_{\sigma 0}^\varepsilon$ , for  $\sigma \in \{\alpha, \beta, \gamma\}$ , Lemma 1.2 gives

$$E_{i+1} = H_0(q^{(m_\sigma : n_\sigma)}(t_{i+1})) = H_0(q_\sigma^{(m_\sigma : n_\sigma)}(t_{i+1})) = E_\sigma^{(m_\sigma : n_\sigma)}.$$

Similarly, if  $q^{(m_\sigma : n_\sigma)}(t_i) = (x_i, y_i) \in \Gamma \cap \Gamma_0$ , then

$$E_i = H_0(q_0(t_i)) = E_0 = H_0(q_0(t_{i+1})),$$

where  $q_0(t_{i+1}) = (x_{i+1}^0, y_{i+1}^0) \in q_0(t)$  and the normal of its tangential vector intersects with  $q_\sigma^{(m_\sigma : n_\sigma)}(t)$  at  $(x_{i+1}, y_{i+1})$ . From Eq. (1.13),

$$|\Delta H^\sigma(\varphi_0)| = |E_{i+1} - E_i| = |E_\sigma^{(m_\sigma : n_\sigma)} - E_0|.$$

$\forall \varepsilon > 0$ , let  $\delta_\sigma = \varepsilon \|H_0\| > 0$  satisfying

$$|E_\sigma^{(m_\sigma : n_\sigma)} - E_0| \leq \|H_0\| \cdot \|q_\sigma^{(m_\sigma : n_\sigma)}(t_{i+1}) - q_0(t_{i+1})\| \leq \varepsilon \|H_0\| = \delta_\sigma.$$

Since the unperturbed Hamiltonian  $H_0$  of orbits  $q_\sigma$  and  $q_0$  is  $C^r$  ( $r \geq 2$ ) smooth,

$$0 < \|H_0\| \equiv \sup_{\sigma \neq 0} \|\|H_0(q(t)) - H_0(q_0(t))\| / \|q(t) - q_0(t)\|\| < \infty,$$

for bounded and closed orbits Therefore, one obtains

$$\|q^{(m_\sigma : n_\sigma)}(t_{i+1}) - q_0(t_{i+1})\| < \delta_\sigma / \|H_0\| = \varepsilon$$

for all  $t_{i+1}$ , that is,

$$\|q^{(m_\sigma : n_\sigma)}(t_{i+1}) - q_0(t_{i+1})\| < \varepsilon.$$

This theorem is proved. ■

In Eq. (1.18), the incremental energy  $\Delta H^\sigma(\varphi_0)$  is a function of the amplitude and frequency of perturbation. The conservative energy  $E_\sigma^{(m_\sigma : n_\sigma)}$  relative to the unper-

turbed resonant orbit is determined by the resonant condition given in Eq. (1.16). With  $\max_{t \in [0, \infty)} |H(q^{(m_\sigma^{(1)}, n_\sigma^{(1)})}(t)) - E_0| = \delta_\sigma^{(1)}$ , the foregoing theorem gives the following corollary.

**Corollary 1.1** *For a perturbed Hamiltonian in Eq. (1.1) with (H1)–(H4), for an arbitrarily small  $\varepsilon_\sigma > 0$ , there exists  $\delta_\sigma^{(1)} > 0$ , so that if for  $(m_\sigma^{(1)} : n_\sigma^{(1)}) \in R_\sigma^\varepsilon(\sigma = \alpha, \beta, \gamma)$ ,*

$$\max_{\sigma \in \{\alpha, \beta, \gamma\}} |\Delta H^\sigma(\varphi_i)| = \max_{R_\sigma^\varepsilon} |E_\sigma^{(m_\sigma : n_\sigma)} - E_0| = |E_\sigma^{(m_\sigma^{(1)}, n_\sigma^{(1)})} - E_0| \leq \delta_\sigma^{(1)}, \quad (1.19)$$

then  $\|q^{(m_\sigma^{(1)}, n_\sigma^{(1)})}(t) - q_0(t)\| < \varepsilon$ , i.e., the Poincaré mapping sets of  $q^{(m_\sigma^{(1)}, n_\sigma^{(1)})}(t) \in \Gamma$  is the last one absorbed in the  $\varepsilon$ -stochastic layer.

*Proof.* Consider Eq.(1.1) with (H1)–(H4). For a  $\sigma$ -resonant orbit  $q^{(m_\sigma : n_\sigma)}(t) \in \Gamma^\varepsilon$ ,  $\forall \varepsilon > 0$ , choosing  $\delta_\sigma > 0$ , find  $(m_\sigma^{(1)} : n_\sigma^{(1)}) \in R_\sigma^\varepsilon$  satisfying

$$\max_{R_\sigma^\varepsilon} |E_\sigma^{(m_\sigma : n_\sigma)} - E_0| \leq |E_\sigma^{(m_\sigma^{(1)}, n_\sigma^{(1)})} - E_0| = \delta_\sigma.$$

Let  $\delta = \max_{\sigma \in \{\alpha, \beta, \gamma\}} \{\delta_\sigma\} > 0$ , we have

$$\max_{\sigma \in \{\alpha, \beta, \gamma\}} \max_{R_\sigma^\varepsilon} |E_\sigma^{(m_\sigma : n_\sigma)} - E_0| \leq \max_{\sigma \in \{\alpha, \beta, \gamma\}} |E_\sigma^{(m_\sigma^{(1)}, n_\sigma^{(1)})} - E_0| = \delta.$$

Therefore, from Theorem 1.1,

$$\|q^{(m_\sigma^{(1)}, n_\sigma^{(1)})}(t) - q_0(t)\| < \varepsilon.$$

This corollary is proved. ■

After a new stochastic layer is formed, the stochastic layer becomes thicker and thicker with increasing the perturbation strength until its destruction occurs. The increase of perturbation strength also leads to the energy increment not satisfying Eq. (1.18), and then, the enlarged stochastic motion domain is termed *the global stochastic layer* in the  $\varepsilon$ -sense. For an approximate prediction of resonant-separatrix webs in the global stochastic layer, we have the following theorem:

**Theorem 1.2** *For a perturbed Hamiltonian in Eq. (1.1) with (H1)–(H4), for an arbitrarily small  $\varepsilon_\sigma > 0$ , there exists  $\delta_\sigma > 0$ , so that if for  $(m_\sigma : n_\sigma) \notin R_\sigma^\varepsilon(\sigma = \alpha, \beta, \gamma)$ ,*

$$|\Delta H^\sigma(\varphi_0)| = |E_\alpha^{(m_\sigma : n_\sigma)} - E_0| \geq \delta_\sigma, \quad (1.20)$$

then  $\|q^{(m\sigma:n\sigma)}(t_i) - q_0(t_i)\| > \varepsilon_\sigma$ .

*Proof.* The proof of contradiction is used herein. This theorem can be proved in a same manner as for Theorem 1.1. ■

The criterion in Eq. (1.18) can be expressed through the action and natural frequency of unperturbed Hamiltonian system. The onset of a specified resonance in the stochastic layer is predicted through the incremental energy approach. This approach is also applicable for strong excitations when the energy increments still maintain in good accuracy. For the more accurate predictions of the resonance interaction in the stochastic layer, a new computational method for the energy increment should be developed because the sub-resonance is not considered. If the exact energy increment is given, the above theorems give the exact prediction of the resonance in the stochastic layer.

## B. Accurate standard-mapping technique

Luo (2001) developed the accurate standard mapping technique to determine the resonant mechanism of the stochastic layer. For linearization of the second equation in Eq.(1.13) at the period-1 fixed point on the  $(m_\sigma : n_\sigma)$ -resonance, for  $E_{i+1} = E_i = E_\sigma^{(m\sigma:n\sigma)}$  and  $\varphi_{i+1} = \varphi_i + 2\pi m_\sigma/n_\sigma = \varphi^{(m\sigma:n\sigma)} + 2\pi m_\sigma/n_\sigma$ , equation (1.13) gives:

$$\Delta H_0^\sigma(\varphi_\sigma^{(m\sigma:n\sigma)}) = 0, \text{ and } 2\pi m_\sigma/n_\sigma = \Delta\varphi^\sigma(E_\sigma^{(m\sigma:n\sigma)}). \quad (1.21)$$

From Eq. (1.21),  $\varphi_\sigma^{(m\sigma:n\sigma)}$  and  $E_\sigma^{(m\sigma:n\sigma)}$  can be obtained. A near energy is

$$E_i = E_\sigma^{(m\sigma:n\sigma)} + \Delta E_i, \text{ and } I_i = G_\sigma^{(m\sigma:n\sigma)} \Delta E_i, \quad (1.22)$$

where  $G_\sigma^{(m\sigma:n\sigma)} = \partial(\Delta\varphi(E_{i+1}))/\partial E_{i+1}|_{E_{i+1}=E_\sigma^{(m\sigma:n\sigma)}}$ . With Eq. (1.22), the linearization of the second equation of Eq.(1.13) leads to

$$I_{i+1} = I_i + G_\sigma^{(m\sigma:n\sigma)} \Delta H_0^\sigma(\varphi_i), \text{ and } \varphi_{i+1} \approx \varphi_i + I_{i+1}, \quad (1.23)$$

which gives a generalized standard map. In the above derivation, no approximations of the period are required. The criteria for the  $(m_\sigma : n_\sigma)$ - resonance in the stochastic layer can be obtained through the transition from the local stochasticity to global stochasticity in Eq. (1.23). Setting  $G_\sigma^{(m\sigma:n\sigma)} \Delta H_0^\sigma(\varphi_i) = K \sin \varphi_i$ , such an equation presents a standard map (or the Chirikov-Taylor map), i.e.,

$$I_{i+1} = I_i + K \sin \varphi_i, \text{ and } \varphi_{i+1} \approx \varphi_i + I_{i+1}. \quad (1.24)$$

Greene (1968, 1979) developed a method to numerically determine the strength of the stochasticity parameter when the transition to global stochasticity for Eq. (1.23) occurs. Therefore, for the special case, the perturbation strength of Eq. (1.1) is estimated from

$$|G_\sigma^{(m\sigma:n\sigma)} \Delta H^\sigma(\varphi_i)| \approx 0.9716 \dots. \quad (1.25)$$

Other estimates for the strength of stochasticity parameter can be referred to the references (e.g., Chirikov, 1979; Lichtenberg and Lieberman, 1992). Luo (2001) developed an accurate standard map approach based on the accurate whisker map for such a prediction of the resonance in the stochastic layer. Luo et al. (1999) developed an energy spectrum approach (numerical method) for prediction of the onset of resonance in the stochastic layer. A comparison of analytical and numerical predictions was presented in Luo and Han (2000). From numerical results, the previous approaches presented in Luo and Han (2000a) are not very accurate for strong excitations. When the excitation strength is very weak, the accurate and approximate standard-map methods are in good agreement, and the accurate one is applicable to nonlinear systems with strong excitations. However, the further improvement should be completed for a more accurate, analytical prediction of the onset of a new resonant-overlap in stochastic layers of nonlinear Hamiltonian systems with periodical excitations. The energy spectrum is based on the exact energy increments. Thus, the energy spectrum will be discussed in next section and the corresponding layer width can be estimated.

### C. Energy spectrum and layer width

For the numerical prediction of resonances in the stochastic layer, Luo et al. (1999) developed an energy spectrum technique, and the resonant characteristics in stochastic layers are investigated through the energy spectra. This technique computes the maximum and minimum energies of the Poincaré mapping points as in Eq. (1.3). From Lemma 1.2, the perturbed energy can be measured by the unperturbed Hamiltonian. Thus, the unperturbed Hamiltonian for each Poincaré mapping point of Eq. (1.1) is

$$H_0^{(N)} = H_0(\mathbf{x}_N, \boldsymbol{\mu}) \equiv H_0(x_N, y_N, \boldsymbol{\mu}), \quad (1.26)$$

and its minimum and maximum energies are determined by

$$E_{\max} = \max_{N \rightarrow \infty} \{H_0^{(N)}\} \text{ and } E_{\min} = \min_{N \rightarrow \infty} \{H_0^{(N)}\}. \quad (1.27)$$

The minimum layer width defined in Luo et al. (1999) is

$$w \equiv \min_{t \in [0, \infty)} \|\mathbf{x}(E^{\max}, t) - \mathbf{x}(E^{\min}, t)\| \equiv \|\mathbf{x}^{\max} - \mathbf{x}^{\min}\|, \quad (1.28)$$

where  $\|\cdot\|$  is a norm. Two points  $\mathbf{x}^{\max}$  and  $\mathbf{x}^{\min}$  on the normal vector  $\mathbf{f}^\perp(\mathbf{x}_0) = (-f_2(\mathbf{x}_0), f_1(\mathbf{x}_0))^T$  of the tangential vector of separatrix at point  $\mathbf{x}_0$  are the closest between the maximum and minimum energy orbits  $\mathbf{x}(E_{\max}, t)$  and  $\mathbf{x}(E_{\min}, t)$  which can be obtained by Eq. (1.27) with  $E_{\max}$  and  $E_{\min}$ , as shown in Fig. 1.2.

### 1.3 Resonant layers

Consider a 2-dimensional Hamiltonian system as

$$\dot{\mathbf{x}} = \mathbf{f}(\mathbf{x}, \boldsymbol{\mu}) + \mathbf{g}(\mathbf{x}, t, \boldsymbol{\pi}); \quad \mathbf{x} = (x, y)^T \in \mathbb{R}^2, \quad (1.29)$$

where  $\mathbf{f}(\mathbf{x}, \boldsymbol{\mu})$  is a Hamiltonian vector field defined on  $\mathbb{R}^2$  and  $\mathbf{g}(\mathbf{x}, t, \boldsymbol{\pi})$  is a  $T2\pi/\Omega$ -periodic (fixed period) Hamiltonian vector field in time  $t$ , and  $\Omega$  denotes excitation frequency. Specifically, they are of the form

$$\mathbf{f}(\mathbf{x}, \boldsymbol{\mu}) = (f_1(\mathbf{x}, \boldsymbol{\mu}), f_2(\mathbf{x}, \boldsymbol{\mu}))^T \text{ and } \mathbf{g}(\mathbf{x}, t, \boldsymbol{\pi}) = (g_1(\mathbf{x}, t, \boldsymbol{\pi}), g_2(\mathbf{x}, t, \boldsymbol{\pi}))^T \quad (1.30)$$

and are assumed to be sufficiently smooth ( $C^r, r \geq 2$ ) and bounded on bounded sets  $D \subset \mathbb{R}^2$  in phase space. The total energy of such a system is,

$$H(x, y, t, \mathbf{p}) = H_0(x, y, \boldsymbol{\mu}) + H_1(x, y, t, \boldsymbol{\pi}), \quad (1.31)$$

where  $H_0(x, y, \boldsymbol{\mu})$  and  $H_1(x, y, t, \boldsymbol{\pi})$  are energy functions of the conservative and perturbed Hamiltonians, respectively.

To restrict the discussion on the 2-dimensional resonant layer (or band) in perturbed nonlinear Hamiltonian systems, the following hypothesis will be used.

- (A1a) There is a bounded open domain  $D \subset \mathbb{R}^2$  and in such a domain, there is only one center equilibrium  $p_c: (x_c, y_c)$  around which a family of periodic flows  $q_\alpha(t) = (x_\alpha(t), y_\alpha(t)) (\alpha \in [1, \infty))$  of the unperturbed Hamiltonian exists.
- (A1b) There is an open domain  $D \subset \mathbb{R}^2$  bounded by a separatrix (i.e.,  $q_0(t) = (x_0(t), y_0(t)): \mathbf{x}_0 \in q_0(t)$ ) with hyperbolic points, and then in such a domain there is a center equilibrium  $p_c: (x_c, y_c)$  around which a family of periodic flows (i.e.,  $\mathbf{x}_\alpha \in q_\alpha(t)$  for  $\alpha \in (0, 1]$ ) of unperturbed Hamiltonian with  $\limsup_{\alpha \rightarrow 0} \inf_{t \in \mathbb{R}} \inf_{\mathbf{x}_0 \in q_0(t), \mathbf{x} \in q_\alpha(t)} \|\mathbf{x}_\alpha(t) - \mathbf{x}_0(t)\| = 0$  exists.
- (A1c) There is an open domain  $D \subset \mathbb{R}^2$  bounded by an internal boundary formed by a separatrix (i.e.,  $\mathbf{x}_0 \in q_0(t)$ ) with hyperbolic points. On the outside of the separatrix, a family of periodic flows (i.e.,  $\mathbf{x}_\alpha \in q_\alpha(t)$  for  $\alpha \in (0, \infty)$ ) of the unperturbed Hamiltonian exists.  $\limsup_{\alpha \rightarrow 0} \inf_{t \in \mathbb{R}} \inf_{\mathbf{x}_0 \in q_0(t), \mathbf{x} \in q_\alpha(t)} \|\mathbf{x}_\alpha - \mathbf{x}_0\| = 0$ .
- (A2)  $H_0(q(t)) = E_\alpha$  and  $T_\alpha$  is the period of  $q_\alpha(t)$  and its frequency  $\omega_\alpha$  is greater than zero (i.e.  $\omega_\alpha > 0$ ). The frequency is a differentiable function of  $E_\alpha$  (i.e.,  $d\omega_\alpha/dE_\alpha \neq 0$ ). Namely,  $d\omega_\alpha/dE_\alpha > 0$ ,  $d\omega_\alpha/dE_\alpha < 0$  and  $d\omega_\alpha/dE_\alpha > 0$  are for cases in (A1a), (A1b) and (A1c), respectively.

Without loss of generality, consider the second type of domain is bounded by the separatrix, as shown in Fig. 1.7(a). In this domain, there is a center point. The separatrix is sketched by a dashed curve. All the periodic flows in this domain will be formed around the center point in Fig. 1.7(b). The natural frequency at the center point is maximum. With increasing energy, the frequency will decrease (i.e.,  $d\omega_\alpha/dE_\alpha < 0$ ) or the flow period will increase (i.e.,  $dT_\alpha/dE_\alpha > 0$ ). When a peri-

odic flow in the family of periodic flows in such a domain approach the separatrix, the natural frequency will approach zero (i.e.,  $\lim_{E_\alpha \rightarrow E_0} \omega_\alpha = 0$ ) or the corresponding period approaches infinity (i.e.,  $\lim_{E_\alpha \rightarrow E_0} T_\alpha = \infty$ ).

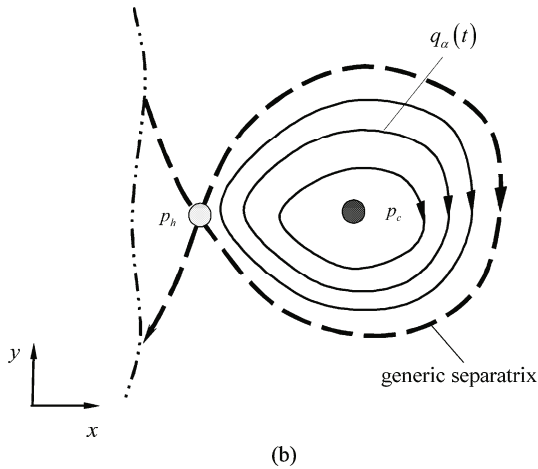
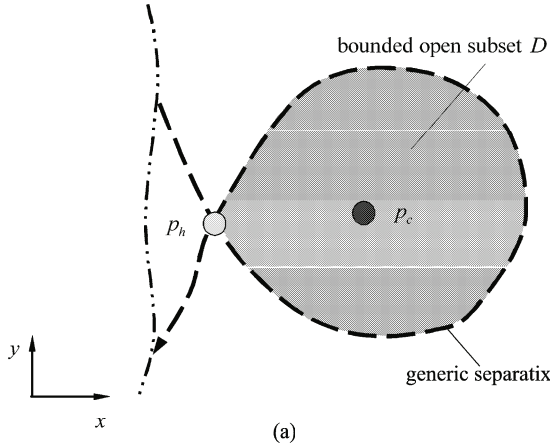


**Fig. 1.7** (a) An open domain  $D$  bounded by the separatrix and (b) periodic flow of the unperturbed system of Eq.(1.1).  $q_\alpha(t)$  is the periodic flow of the unperturbed system in domain  $D \subset \mathbb{R}^2$ . This periodic flow existing on the inside of separatrix can be called the librational (or local) periodic flows.

### 1.3.1 Layer dynamics

To investigate chaotic motions in a resonant separatrix layer, for a given energy  $E_\alpha$ , the Hamiltonian is

$$H_0(x_\alpha, y_\alpha) = E_\alpha \quad (1.32)$$

from which

$$y_\alpha = y_\alpha(x_\alpha, E_\alpha). \quad (1.33)$$

The action variable is defined by

$$J_\alpha = \oint y_\alpha dx_\alpha. \quad (1.34)$$

So we have

$$H_0(J_\alpha) = E_\alpha. \quad (1.35)$$

The angle variable is defined by

$$\theta_\alpha = \omega_\alpha t + \theta_{\alpha 0}, \quad (1.36)$$

with

$$\dot{\theta}_\alpha = \frac{\partial H_0(J_\alpha)}{\partial J_\alpha} = \omega_\alpha. \quad (1.37)$$

From the foregoing hypotheses, the periodic flow  $q_\alpha(t) = (x_\alpha(t), y_\alpha(t))$  in the domain  $D$  can be expressed by

$$x_\alpha = x_\alpha(J_\alpha, \theta_\alpha) \text{ and } y_\alpha = y_\alpha(J_\alpha, \theta_\alpha). \quad (1.38)$$

Substitution of Eq.(1.38) into Eq.(1.30) and using Fourier expansion give

$$\begin{aligned} H(J_\alpha, \theta_\alpha, t) &= H_0(J_\alpha) + H_1(J_\alpha, \theta_\alpha, \Omega t) \\ &= H_0(J_\alpha) + \sum_n \sum_m \left\{ H_{1(m;n)}^{(-)}(J_\alpha) \cos(m\omega_\alpha t - n\Omega t + \psi_{\alpha n}^{(-)}) \right. \\ &\quad \left. + H_{1(m;n)}^{(+)}(J_\alpha) \cos(m\omega_\alpha t + n\Omega t + \psi_{\alpha n}^{(+)}) \right\}. \end{aligned} \quad (1.39)$$

Letting  $\varphi_\alpha = (m\omega_\alpha - n\Omega)t$ , we have

$$\begin{aligned} H(J_\alpha, \theta_\alpha, t) &= H_0(J_\alpha) + H_1(J_\alpha, \theta_\alpha, \Omega t) \\ &= H_0(J_\alpha) + \sum_n \sum_{m_1} \left\{ H_{1(m_1;n)}^{(-)}(J_\alpha) \cos \left[ \frac{m_1}{m} \varphi_\alpha + \frac{n(m_1 - m)}{m} \Omega t + \psi_{\alpha n}^{(-)} \right] \right. \\ &\quad \left. + H_{1(m_1;n)}^{(+)}(J_\alpha) \cos \left[ \frac{m_1}{m} \varphi_\alpha + \frac{n(m_1 + m)}{m} \Omega t + \psi_{\alpha n}^{(+)} \right] \right\}. \end{aligned} \quad (1.40)$$

If the following resonance condition holds as

$$m\omega_\alpha = n\Omega, \quad (1.41)$$

then we have

$$J_\alpha = J_\alpha^{(m:n)} \text{ and } E_\alpha = E_\alpha^{(m:n)}. \quad (1.42)$$

To define a generating function, we have

$$\begin{aligned} & H_0(J_\alpha, \theta_\alpha, t) + \frac{\partial G}{\partial t} \\ &= H_0(J_\alpha^{(m:n)}) + \frac{\partial H_0(J_\alpha)}{\partial J_\alpha} \Big|_{J_\alpha=J_\alpha^{(m:n)}} (J_\alpha - J_\alpha^{(m:n)}) + \frac{\partial G}{\partial t} \\ & \quad + \frac{1}{2} \frac{\partial^2 H_0(J_\alpha)}{\partial J_\alpha^2} \Big|_{J_\alpha=J_\alpha^{(m:n)}} (J_\alpha - J_\alpha^{(m:n)})^2 + \dots + h.o.t. \end{aligned} \quad (1.43)$$

$$\begin{aligned} & H_1(J_\alpha, \theta_\alpha, t) \\ &= \sum_n \sum_{m_1} \left\{ H_{1(m_1:n)}^{(-)}(J_\alpha) \cos \left[ \frac{m_1}{m} \varphi_\alpha + \frac{n(m_1 - m)}{m} \Omega t + \psi_{\alpha n}^{(-)} \right] \right. \\ & \quad \left. + H_{1(m_1:n)}^{(+)}(J_\alpha) \cos \left[ \frac{m_1}{m} \varphi_\alpha + \frac{n(m_1 + m)}{m} \Omega t + \psi_{\alpha n}^{(+)} \right] \right\}. \end{aligned} \quad (1.44)$$

Letting

$$\frac{\partial H_0(J_\alpha)}{\partial J_\alpha} (J_\alpha - J_\alpha^{(m:n)}) = -\frac{\partial G}{\partial t}, \quad (1.45)$$

the generating function can be defined as

$$G = -\omega_\alpha t (J_\alpha - J_\alpha^{(m:n)}) = -\frac{(\varphi_\alpha + n\Omega t)}{m} (J_\alpha - J_\alpha^{(m:n)}). \quad (1.46)$$

Furthermore, we have a new coordinate  $(\bar{p}_\alpha, \varphi_\alpha)$

$$\bar{p}_\alpha = -\frac{\partial G}{\partial \varphi_\alpha} = \frac{1}{m} (J_\alpha - J_\alpha^{(m:n)}) \text{ and } \theta_\alpha = \omega_\alpha t = -\frac{\partial G}{\partial J_\alpha} = \frac{1}{m} (\varphi_\alpha + n\Omega t). \quad (1.47)$$

If  $\bar{p}_\alpha = 0$ , we have  $J_\alpha = J_\alpha^{(m:n)}$ . The variable  $\bar{p}_\alpha$  gives the difference between the instant  $J_\alpha$  and the resonance  $J_\alpha^{(m:n)}$ , which defines the gap of the resonant se-paratrix layer. Because the natural frequency  $\omega_\alpha$  is a function of energy  $E_\alpha$  or the action variable  $J_\alpha$ , the relation between the resonance frequency and energy is illustrated in Fig. 1.8 from the resonance relation in Eq. (1.41). The resonant frequency distributions along the conservative energy are different for four resonant layers. Further, their resonant structures are distinguishing from each other. The specific  $(m:n)$ -resonant frequency and natural frequency are expressed by  $\Omega^{(m:n)}$  and  $\omega_\alpha^{(m:n)}$ , respectively. The corresponding resonant condition in Eq. (1.41) becomes,

$$m\omega_\alpha^{(m:n)} = n\Omega^{(m:n)}. \quad (1.48)$$

To guarantee the resonant layers in a certain gap, consider a neighborhood of a natural frequency  $\omega_\alpha$  close to  $\omega_\alpha^{(m:n)}$ , i.e.,

$$\begin{aligned} |\omega_\alpha - \omega_\alpha^{(m:n)}| &= \left| \omega_\alpha - \frac{n}{m} \Omega^{(m:n)} \right| \leq \varepsilon \text{ and} \\ T(E_\alpha^{(m:n)}) &= \frac{2\pi}{\omega_\alpha^{(m:n)}}, T(E_\alpha) = \frac{2\pi}{\omega_\alpha}, \end{aligned} \tag{1.49}$$

where  $\varepsilon \ll 1$  and  $T(E)$  is the nonlinear period. From the foregoing condition, with Eqs.(1.43) and (1.44), we obtain

$$\begin{aligned} H(J_\alpha, \theta_\alpha, t) + \frac{\partial G}{\partial t} &\approx E_\alpha^{(m:n)} + \frac{1}{2} \frac{\partial^2 H_0(J_\alpha)}{\partial J_\alpha^2} \Big|_{J_\alpha=J_\alpha^{(m:n)}} m^2 \bar{p}_\alpha^2 \\ &+ \sum_n \sum_{m_1} \left\{ H_{1(m_1:n)}^{(-)}(J_\alpha^{(m:n)}, \bar{p}_\alpha) \cos \left[ \frac{m_1}{m} \varphi_\alpha + \frac{n(m_1 - m)}{m} \Omega t + \psi_{\alpha n}^{(-)} \right] \right. \\ &\left. + H_{1(m_1:n)}^{(+)}(J_\alpha^{(m:n)}, \bar{p}_\alpha) \cos \left[ \frac{m_1}{m} \varphi_\alpha + \frac{n(m_1 + m)}{m} \Omega t + \psi_{\alpha n}^{(+)} \right] \right\} \end{aligned} \tag{1.50}$$

Rescaling gives the following variables as

$$\begin{aligned} \bar{H}(J_\alpha, \theta_\alpha, t) &= H(J_\alpha, \theta_\alpha, t) + \frac{\partial G}{\partial t} - E_\alpha, B = \frac{\partial^2 H_0(J_\alpha)}{\partial J_\alpha^2} \Big|_{J_\alpha=J_\alpha^{(m:n)}} \\ mB\bar{p}_\alpha &= p_\alpha, H(p_\alpha, \varphi_\alpha, t) = B\bar{H}(J_\alpha, \theta_\alpha, t), \Omega_1 = 2n\Omega \\ U_{(m:n)}^{(+)} &= BH_{1(m:n)}^{(+)}(J_\alpha^{(m:n)}, p_\alpha), U_{(m:n)}^{(-)} = BH_{1(m:n)}^{(-)}(J_\alpha^{(m:n)}, p_\alpha). \end{aligned} \tag{1.51}$$

The new Hamiltonian becomes

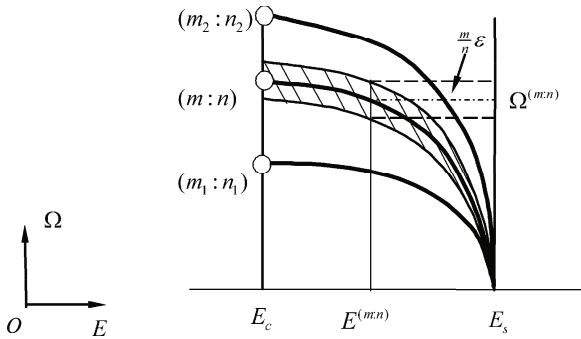


**Fig. 1.8** The neighborhood of the  $(m : n)$ -resonant frequency for the inside separatrix.

$$\begin{aligned}
H(p_\alpha, \varphi_\alpha, t) \approx & \frac{1}{2} p_\alpha^2 + U_{1(m:n)}^{(-)} \cos(\varphi_\alpha + \psi_{\alpha n}^{(-)}) \\
& + U_{1(m:n)}^{(+)} \cos(\varphi_\alpha + 2n\Omega t + \psi_{\alpha n}^{(+)}) \\
& + \sum_{n_1} \sum_{m_1} \left\{ U_{1(m_1:n_1)}^{(-)} \cos \left[ \frac{m_1}{m} \varphi_\alpha + \frac{n_1(m_1 - m)}{m} \Omega t + \psi_{\alpha n_1}^{(-)} \right] \right. \\
& \left. + U_{1(m_1:n_1)}^{(+)} \cos \left[ \frac{m_1}{m} \varphi_\alpha + \frac{n_1(m_1 + m)}{m} \Omega t + \psi_{\alpha n_1}^{(+)} \right] \right\}. \quad (1.52)
\end{aligned}$$

Because the primary resonance is relatively isolated, herein the other resonance terms in Eq. (1.52) is ignored except for the  $(m : n)$ -resonance, the approximate Hamiltonian is expressed by

$$\begin{aligned}
H(p_\alpha, \varphi_\alpha, t) \\
\approx & \frac{1}{2} p_\alpha^2 + U_{1(m:n)}^{(-)} \cos(\varphi_\alpha + \psi_{\alpha n}^{(-)}) + U_{1(m:n)}^{(+)} \cos(\varphi_\alpha + \Omega_1 t + \psi_{\alpha n}^{(+)}). \quad (1.53)
\end{aligned}$$

It is assumed that the two parameters  $U_{1(m:n)}^{(-)}$  and  $U_{1(m:n)}^{(+)}$  are independent of  $p_\alpha$ , and the corresponding dynamical system is

$$\begin{aligned}
\dot{\varphi}_\alpha &= p_\alpha, \\
\dot{p}_\alpha &= -U_{1(m:n)}^{(-)} \sin(\varphi_\alpha + \psi_{\alpha n}^{(-)}) - U_{1(m:n)}^{(+)} \sin(\varphi_\alpha + \Omega_1 t + \psi_{\alpha n}^{(+)}). \quad (1.54)
\end{aligned}$$

This equation represents a kind of parametrically excited pendulum. The dynamics in the neighborhood of the  $(m : n)$ -resonant separatrix can be investigated through Eq. (1.54). The resonance effects of Eq. (1.52) give the sub-resonance for the  $(m : n)$ -resonance. Without the perturbation of  $U_{1(m:n)}^{(+)}$ , the separatrix of such a parametric pendulum can be illustrated in Fig.1.9(a). The red and yellow circles are the center and hyperbolic points of the unperturbed pendulum in Eq.(1.54), respectively. The two thin dash curves are the inner and outer boundaries of the resonant separatrix layer. Because  $U_{1(m:n)}^{(-)}$  is relative to external excitation and energy orbit, the resonant separatrix will be changed with frequency and amplitude. The sub-resonance can be obtained from the perturbed system in Eq. (1.53). On the other hand, from the differential equation, the self-similar structure may not exist. The sub-resonant structure is strongly dependent on the energy analysis of Eq. (1.54). Based on a certain sub-resonance in the  $(m : n)$ -resonant separatrix layer, the sub-sub-resonance can be obtained by repeating the same procedure to obtain a new equation similar to Eq.(1.54). Such a sub-resonant structure is sketched in Fig.1.9(b). This renormalization procedure cannot lead to a self-similar sub-resonance structure. Indeed, the sub-resonant structure in the resonant layer is relative to the corresponding parent-resonance separatrix of Eq.(1.54), but such a sub-resonant structure cannot be generated by simply copying from its parent primary-resonance. From the foregoing discussion, the dynamics of the parametric pendulum is a key to understand the mechanism of stochasticity in a neighborhood of the  $(m : n)$ -resonant separatrix.

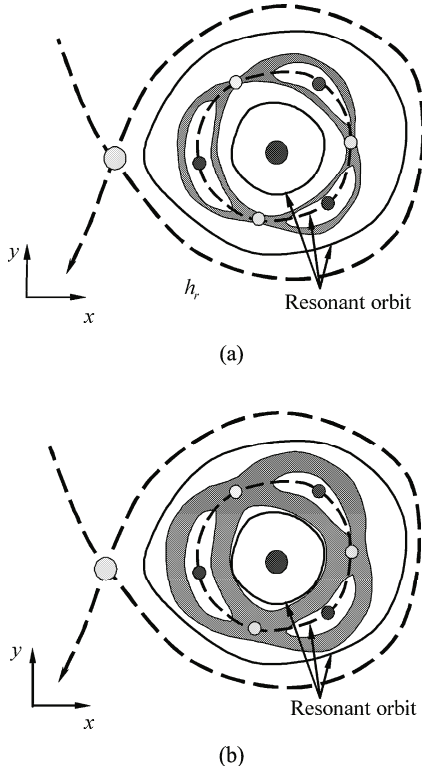


**Fig. 1.9** Resonant layer in nonlinear Hamiltonian systems with separatrix: (a) appearance and (b) disappearance. The solid and hollow circles represent the center and hyperbolic points. The irregular small circles are the sub-resonances in the neighborhood of the primary resonance (color plot in the book end).

### 1.3.2 Approximate criterions

To develop the criterions for appearance, growth and destruction of primary resonance layers, consider an  $(m_1 : n_1)$ -primary resonance closest to the  $(m : n)$ -resonant separatrix. In the Chirikov overlap criterion and renormalization technique, from Eq. (1.52), the following new energy form is considered.

$$\begin{aligned}
 H(p_\alpha, \varphi_\alpha, t) \approx & \frac{1}{2} p_\alpha^2 + U_{1(m:n)}^{(-)} \cos(\varphi_\alpha + \psi_{\alpha n}^{(-)}) \\
 & + U_{1(m_1:n_1)}^{(-)} \cos \left[ \frac{m_1}{m} \varphi_\alpha + \frac{n_1(m_1 - m)}{m} \Omega t + \psi_{\alpha n_1}^{(-)} \right]. \quad (1.55)
 \end{aligned}$$

As in Chirikov (1979) and Reichl (2002), the corresponding Chirikov resonance overlap criterion becomes

$$\sqrt{U_{1(m:n)}^{(-)}} + \sqrt{U_{1(m_1:n_1)}^{(-)}} = 1. \quad (1.56)$$

From renormalization, the criterion becomes

$$\sqrt{U_{1(m:n)}^{(-)}} + \sqrt{U_{1(m_1:n_1)}^{(-)}} \approx 0.7. \quad (1.57)$$

From author's points of view, once the  $(m : n)$ -resonant separatrix is formed, with increasing excitation strength, the sub-resonance in its neighborhood will be developed first from Eq. (1.54). Of course, from Eq. (1.52), the other primary resonance may have a certain effect as external excitations. Until such a resonant layer approaches an unperturbed orbit from which the  $(m_1 : n_1)$ -primary resonance can be formed, the  $(m : n)$ -resonant layer almost cannot be destroyed, and the effects of the  $(m_1 : n_1)$ -primary resonance to the  $(m : n)$ -resonant layer are very small compared to the  $U_{1(m:n)}^{(+)}$ -term. In other words, before such a resonant layer is destroyed, the  $(m_1 : n_1)$ -primary resonance will not be strongly involved in the  $(m : n)$ -resonant layer. Therefore, it is very doubtful that the criterions in Eqs. (1.56) and (1.57), given by the Chirikov overlap criterion and the renormalization technique, can provide a reasonable prediction of the global stochasticity of the resonant layer. In addition, it is not clear that the two existing criteria can be used for the appearance or disappearance of the resonant layer.

### A. Onset conditions

To discuss the appearance, growth and destruction of the  $(m : n)$ -resonant layer, The geometrical intuitions of both just after onset and just before destruction of the resonant layer are sketched. Two kinds of resonant layers are sketched in Figs.1.8 and 1.9. The  $(m : n)$ -resonant layer is formed in the neighborhood of its primary resonant separatrix. With increasing excitation strength, the width of the resonant layer will increase.

For an approximate estimate of the resonant layer width, the theorem given in Luo (2008) is adopted. In other words, if the farthest energy boundary of the primary  $(m : n)$ -resonant layer is the energy of the  $(m_1 : n_1)$ -primary resonant orbit, the primary  $(m : n)$ -resonant layer will be destroyed. However, the onset of the primary resonant layer will be estimated through the standard mapping technique. To understand the formation mechanism of the primary resonant layer, the onset of the primary  $(m : n)$ -resonant layer will be discussed first as follows.

The energy increment along the  $(m : n)$ -resonant orbit of the perturbed conservative system is approximated by

$$\begin{aligned} \Delta H_0 &= \int_{t_i}^{T\alpha(E_i)+t_i} \frac{dH(x, y, t)}{dt} dt = \int_{t_i}^{T\alpha(E_i)+t_i} \{H_0, H_1\}_{\text{Poisson}} dt \\ &= \int_{t_i}^{T\alpha(E_i)+t_i} (f_1 g_2 - f_2 g_1) dt = U_0 f(\varphi_i), \end{aligned} \quad (1.58)$$

where  $t_i$  is the initial time and  $f(\phi_i)$  is a bounded and periodic function. Without loss of generality, in Eq. (1.58), consider the following form,

$$\Delta H_0 = U_0 \sin \phi_i, \quad (1.59)$$

in which  $U_0$  is a system parameter function excluding the initial phase angle  $\phi_i = \Omega t_i$ . For a perturbed orbit in the neighborhood of the prescribed resonant orbit, the change of phase angle over one period is

$$\Delta \phi = \phi_{i+1} - \phi_i = \Omega T(E_{i+1}) = V_0(E_{i+1}), \quad (1.60)$$

where  $V_0$  is a function associated with energy  $E_i$ . To calculate this new energy iteratively, we introduce the following notation:  $E_{i+1} = w_{i+1}$  at the  $(i+1)^{\text{th}}$  period and the corresponding phase angle is  $\phi_{i+1}$ . Equations (1.59) and (1.60) can now be written as,

$$w_{i+1} = w_i + U_0 \sin \phi_i \text{ and } \phi_{i+1} = \phi_i + V_0(w_{i+1}). \quad (1.61)$$

The resonant separatrix layer can be investigated by iteration of the mapping in Eq. (1.61). Although this mapping is not based on the accurate energy increment, it is enough good as an approximate, analytical expression because the exact computation of the energy increment only can be done numerically. In the neighborhood of the resonant separatrix layer, Equation (1.61) can be linearized about a fixed point and the standard mapping can be obtained. Considering a period-1 of the iterative map for a specific resonance of  $(m : n)$ , its fixed point can be easily determined by  $w_{i+1} = w_i = w_0$  and  $\phi_{i+1} = \phi_i + 2m\pi/n = \phi_0 + 2m\pi/n$ . This implies,

$$U_0 \sin \phi_0 = 0, V_0(w_0) = \frac{2\pi m}{n}. \quad (1.62)$$

Defining a new dimensionless energy

$$I_i = \left. \frac{\partial V_0(w_{i+1})}{\partial w_{i+1}} \right|_{w_{i+1}=w_0} (w_i - w_0), \quad (1.63)$$

and linearization of Eq. (1.60) about the fixed point yields

$$I_{i+1} = I_i + \Xi \sin \phi_i \text{ and } \phi_{i+1} = \phi_i + I_{i+1}, \quad (1.64)$$

where  $\Xi = U_0 \partial V_0 / \partial w_{i+1} |_{w_{i+1}=w_0}$ . From Eq. (1.64), the mechanism involved in the transition to the global stochasticity in a nonlinear Hamiltonian system is very clear. The coefficient  $\Xi$  is the only control parameter for the characterization of the KAM tori. For the standard map, a critical value of  $\Xi$  is attained when  $\Xi = \Xi^* = 0.9716354 \dots$ . At this value, the last remaining KAM torus is broken. When this happens, we have

$$U_0 \frac{\partial V_0}{\partial w_0} = \Xi^*. \quad (1.65)$$

The transition from the local stochasticity to global stochasticity implies chaos appears in such a standard mapping. This appearance condition is as a condition for the appearance of resonant layers in the neighborhood of the  $(m : n)$ -resonant separatrix. For a generalized case in Eq. (1.61), it can be discussed in a similar fashion. The corresponding criteria can be developed for the global stochasticity of motion in the primary resonant layer.

## B. Vanishing conditions

Once this resonant separatrix layer is formed, with increasing the excitation, the other sub-resonant separatrix layers will merge in the resonant layer until they come into contact the closest resonant orbit. When this case occurs, the resonant layer will be destroyed, and a new stochastic motion near that resonant orbit will be involved in, and suddenly, the width of the resonant layer will become large. The two primary resonant layers will be overlapped each other. Based on this reason, the Chirikov resonant overlap criterion and the renormalized criterion may be used as a condition for the destruction of a certain, primary resonant layer. Such a mechanism is qualitatively sketched in Fig. 1.9. Again it is postulated that when the resonant layer is destroyed, the energy increment in Eq.(1.28) is given by the energy difference between the two closest resonant orbits, one of which is associated with the destroyed resonant layer. From Luo (2008), we have

$$\min \left( |E_{\alpha}^{(m_2:n_2)} - E_{\alpha}^{(m:n)}|, |E_{\alpha}^{(m_1:n_1)} - E_{\alpha}^{(m:n)}| \right) = |\Delta H_0^{(m:n)}| \approx U_0 |f(\varphi_0)|. \quad (1.66)$$

Equation (1.66) constitutes the critical condition for the disappearance of the  $(m : n)$ -resonant separatrix layer. From the foregoing equation, the excitation strength for *disappearance* of the resonant layer can be computed. To determine the excitation strength for *appearance* of the resonant layer, equation (1.65) will be used. For a better prediction of resonant layers, the effects of the secondary resonances should be considered in the vicinity of the primary resonant layer. Because the energy increment is computed by an approximate expression, with increasing excitation strength, such a prediction is not accurate. To verify the valid of the approximate prediction, the numerical prediction should be completed through the energy increment for non-linear Hamiltonian systems.

## C. Energy increment spectrum

The exact energy increment can be computed numerically. Luo et al. (1999) developed the energy spectrum approach, which was used for the numerical prediction of the onset of resonance in the stochastic layer. In the energy spectrum, the maximum and minimum conservative energies are computed through the Poincaré mapping section. As discussed in Section 1.2.2C, the energy spectrum for resonant layer can be determined by the energy increment spectrum. Using the Poincaré map section in Eq. (1.29), the Poincaré map is defined by  $P : \Sigma \rightarrow \Sigma$ . Such a technique computes the maximum and minimum energies of the Poincaré mapping points as in Eq. (1.31). The unperturbed Hamiltonian energy for each Poincaré mapping point

of Eq. (1.29) is

$$H_0^{(N)} = H_0(\mathbf{x}_N, \boldsymbol{\mu}) \equiv H_0(x_N, y_N, \boldsymbol{\mu}). \quad (1.67)$$

However, in computation of conservative energy for a specified resonant layer, the energy changes in energy spectrums cannot be observed clearly. To observe the energy changes caused by the sub-resonance for the specified resonant layer, the minimum and maximum energy increments with respect to the unperturbed resonant orbit are introduced herein. On the other hand, the initial condition is chosen from the specific resonant orbit. The initial energy is  $H_0(\mathbf{x}_0, \boldsymbol{\mu}) = E_\alpha^{(m:n)}$ , so the energy increment (or the first integral quantity increment) should be computed by

$$L(t_0, kT) = \Delta H_0(t_0, kT) = H_0^{(N)}(\mathbf{x}_N, \boldsymbol{\mu}) - H_0(\mathbf{x}_0, \boldsymbol{\mu}),$$

that is,

$$\Delta E_{\max} = \max_{N \rightarrow \infty} \left\{ H_0^{(N)} - E_\alpha^{(m:n)} \right\} \text{ and } \Delta E_{\min} = \min_{N \rightarrow \infty} \left\{ H_0^{(N)} - E_\alpha^{(m:n)} \right\}. \quad (1.68)$$

For the appearance and disappearance of the resonant layer for a specific resonance, the maximum or minimum energy increment will have a big jump between the two closest resonant separatrices. From the minimum and maximum energy increment spectra, The width of a resonant separatrix layer is computed like the one of a stochastic layer in Luo et al. (1999), i.e.,

$$w \equiv \min_{t \in [0, \infty)} \|\mathbf{x}(E_\alpha^{\max}, t) - \mathbf{x}(E_\alpha^{\min}, t)\| \equiv \|\mathbf{x}_\alpha^{\max} - \mathbf{x}_\alpha^{\min}\|, \quad (1.69)$$

where  $\|\cdot\|$  is a norm and the minimum and maximum energies are computed by  $E_\alpha^{\max} = \Delta E_{\max} + E_\alpha^{(m:n)}$ ,  $E_\alpha^{\min} = \Delta E_{\min} - E_\alpha^{(m:n)}$ . Two points  $\mathbf{x}_\alpha^{\max}$  and  $\mathbf{x}_\alpha^{\min}$  on the normal vector  $\mathbf{f}^\perp(\mathbf{x}_\alpha^{(m:n)}) = (-f_2(\mathbf{x}_\alpha^{(m:n)}), f_1(\mathbf{x}_\alpha^{(m:n)}))^T$  of the tangential vector of unperturbed resonant orbit at point  $\mathbf{x}_\alpha^{(m:n)}$  are the closest between the maximum and minimum energy orbits  $\mathbf{x}(E_\alpha^{\max}, t)$  and  $\mathbf{x}(E_\alpha^{\min}, t)$ , which can be obtained from Eq. (1.31) with  $E_\alpha^{\max}$  and  $E_\alpha^{\min}$ . The detailed discussion on the energy increment spectrum can be referred to Luo (2002).

## 1.4 A periodically forced Duffing oscillator

In this section, the stochastic resonant layers in a periodically forced Duffing oscillator will be presented as an example to show how to apply the theory of stochastic and resonant layers, presented in the previous sections.

### 1.4.1 Approximate predictions

Consider a periodically forced Duffing oscillator with twin-well potentials

$$\ddot{x} - \alpha_1 x + \alpha_2 x^3 = Q_0 \cos \Omega t, \quad (1.70)$$

where  $\alpha_1 > 0$  and  $\alpha_2 > 0$  are system parameters,  $Q_0$  and  $\Omega$  are the excitation strength and frequency, respectively. The total energy for Eq. (1.70) is

$$H(x, y) = H_0(x, y) + H_1(x, y), \quad (1.71)$$

and the time-independent  $H_0$  (unperturbed) and time-dependent  $H_1$  (perturbation) in the Hamiltonian of Eq. (1.71) are

$$H_0 = \frac{1}{2}x^2 - \frac{1}{2}\alpha_1 x^2 + \frac{1}{4}\alpha_2 x^4, \quad H_1 = -\frac{1}{2}x^2 Q_0 \cos \Omega t. \quad (1.72)$$

For the unperturbed system of Eq. (1.69), there is a generic separatrix (homoclinic orbit) pertaining to the saddle point  $(0, 0)$  for  $H_0 = E_0 = 0$ . For the given energies, a phase portrait for the unperturbed Duffing with twin-well potentials is illustrated in Fig. 1.10. In the potential well, the orbit is termed the small motion orbit (or s-orbit), and the orbit outside the potential wells is termed the large motion orbit (or l-orbit), and the separatrix between the two orbits is termed the homoclinic orbit as well. The chaos in vicinity of the homoclinic separatrix and resonant separatrices

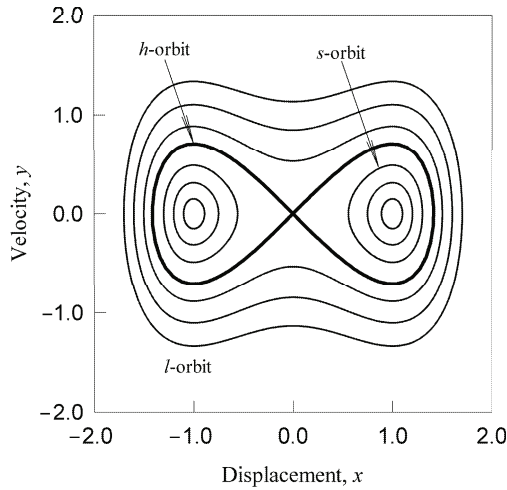


**Fig. 1.10** Phase portrait for an unperturbed Duffing with twin-potential wells. In the potential wells, the orbit is termed the small motion orbit (or s-orbit) and the orbit outside the potential wells is termed the large motion orbit (or l-orbit) and the separatrix between the two orbits is the homoclinic orbit.

inside and outside the homoclinic separatrix will be presented, which will be called the stochastic and resonant layers of the periodically forced Duffing oscillator.

### A. Resonant layers inside separatrix

For a given energy  $E_s$  satisfying  $H_0 = E_s < E_0$  in the two potential wells, the solution of the small motion orbit is

$$\begin{aligned} x^0 &= \pm e_s \operatorname{dn} \left[ \frac{K(k_s) \omega_s t}{\pi}, k_s \right], \\ y^0 &= \dot{x}^0 = \sqrt{\frac{\alpha_2}{2}} e_s^2 k_s^2 \operatorname{sn} \left[ \frac{K(k_s) \omega_s t}{\pi}, k_s \right] \operatorname{cn} \left[ \frac{K(k_s) \omega_s t}{\pi}, k_s \right]. \end{aligned} \quad (1.73)$$

where  $\operatorname{cn}$ ,  $\operatorname{sn}$  and  $\operatorname{dn}$  are the Jacobi-elliptic functions,  $K(k_s)$  the complete elliptic integral of the first kind, and  $k_s$  the modulus of the Jacobi-elliptic function. The modulus  $k_s$ , the response amplitude  $e_s$  and the natural frequency  $\omega_s$  are:

$$k_s = \sqrt{\frac{2(\alpha_1^2 + 4\alpha_2 E_s)^{1/2}}{\alpha_1 + (\alpha_1^2 + 4\alpha_2 E_s)^{1/2}}}, \quad e_s = \sqrt{\frac{2\alpha_1}{(2 - k_s^2)\alpha_2}}, \quad \omega_s = \frac{\sqrt{\alpha_2} e_s \pi}{\sqrt{2} K(k_s)}. \quad (1.74)$$

Once an external force exerts to the unperturbed Duffing oscillator, the total energy  $H(x, y)$  changes around the initially given energy  $H = H_0 = E_s$ . For a small external force, an approximate estimate of the energy is given by

$$H(x, y) \approx H_0(x^0, y^0) + H_1(x^0, y^0), \quad (1.75)$$

and

$$H_1(x, y) = -\frac{1}{2} x^2 Q_0 \cos \Omega t \approx -\frac{1}{2} (x^0)^2 Q_0 \cos \Omega t. \quad (1.76)$$

Substitution of Eq. (1.73) into Eq. (1.76), and use of Fourier series expansion lead to

$$\begin{aligned} H_1(x, y) &\approx -\frac{\pi e_s Q_0}{2K} \left\{ \cos \Omega t + \sum_{m=1}^{\infty} \operatorname{sech} \left[ \frac{m\pi K'}{K} \right] \right. \\ &\quad \left. \times [\cos(m\omega_s - \Omega)t + \cos(m\omega_s + \Omega)t] \right\}. \end{aligned} \quad (1.77)$$

From Eq. (1.77), the resonant condition is

$$m\omega_s = \Omega. \quad (1.78)$$

Because all other terms in  $H_1(x, y)$  will average to zero over one period  $T = 2\pi/\Omega$  except for the term of the  $(m : 1)$  primary resonance (i.e., an averaging of Hamiltonian in Eq. (1.77)), its magnitude  $\bar{H}_1$  in the potential well is:

$$\bar{H}_1 \approx \frac{\sqrt{2}\Omega Q_0}{2m\pi\sqrt{\alpha_2}} \operatorname{sech} \left[ \frac{m\pi K'(k_s^{(m:1)})}{K(k_s^{(m:1)})} \right], \quad (1.79)$$

where  $K'(k_s^{(m:1)}) = K(k_s^{(m:1)})$ ,  $k_s^{(m:1)} = \sqrt{1 - (k_s^{(m:1)})^2}$  and  $k_s^{(m:1)}$  is obtained from Eq. (1.74) with the resonant condition, i.e.,

$$k_s^{(m:1)} = \sqrt{\frac{2\sqrt{\alpha_1^2 + 4\alpha_2 E_s^{(m:1)}}}{\alpha_1 + \sqrt{\alpha_1^2 + 4\alpha_2 E_s^{(m:1)}}}}, \quad (1.80)$$

in which  $E_s^{(m:1)}$  is a  $(m : 1)$  resonant energy.

The energy increment  $\Delta H = H(x, y) - H_0(x^0, y^0) \approx H_1(x^0, y^0)$  is caused by excitation, and the averaging of energy increment is computed by  $\Delta \bar{H} = \bar{H}_1$ . The energy increment in the one of twin wells along the  $(m : 1)$  resonant orbit is computed by

$$\begin{aligned} \Delta H_0^s(\varphi_i) &= \int_{t_i}^{T_s+t_i} (f_1 g_2 - f_2 g_1) dt \\ &\approx \int_{t_i}^{T_s+t_i} x_s^{(0)} y_s^{(0)} Q_0 \cos \Omega t dt = Q_0 Q_s^{(m:1)} \sin \varphi_i, \end{aligned} \quad (1.81)$$

where  $\varphi_i = \Omega t_i$  and

$$\begin{aligned} f_1 &= y = \dot{x}, g_1 = \alpha_1 x - \alpha_2 x^3, \\ f_2 &= 0, g_2 = x Q_0 \cos \Omega t; \end{aligned} \quad (1.82)$$

$$Q_s^{(m:1)} = \sqrt{\frac{2}{\alpha_2} \pi \Omega \operatorname{sech} \left[ \frac{m\pi K'(k_s^{(m:1)})}{K(k_s^{(m:1)})} \right]}. \quad (1.83)$$

The phase change from Eq. (1.74) is:

$$\Delta \varphi^s(E_s) = \frac{2\pi\Omega}{\omega_s} = \frac{2\Omega\sqrt{2 - k_s^2 K(k_s)}}{\sqrt{\alpha_1}}. \quad (1.84)$$

From the energy increment in Eq. (1.81) and phase change, the accurate whisker map for the  $(m : 1)$ -resonant layer of the Duffing oscillator is

$$\begin{aligned} E_s^{(i+1)} - E_s^{(i)} &\approx Q_0 Q_s^{(m:1)} \sin \varphi_i, \\ \varphi_{i+1} - \varphi_i &= \frac{2\pi\Omega}{\omega_s} = \frac{2\Omega\sqrt{2 - (k_s^{(m:1)})^2} K(k_s^{(m:1)})}{\sqrt{\alpha_1}}. \end{aligned} \quad (1.85)$$

Therefore, the excitation strength for the onset of the  $(m : 1)$ -resonant layer in the potential wells is approximately estimated by

$$Q_0 \approx \frac{0.9716}{Q_s^{(m:1)} G_s^{(m:1)}}, \quad (1.86)$$

where

$$G_s^{(m:1)} = -\frac{\Omega\alpha_2 \left[2 - (k_s^{(m:1)})^2\right]^{5/2}}{(k_s^{(m:1)})^4 \alpha_1^2 \sqrt{\alpha_1}} \left\{ 2K(k_s^{(m:1)}) - \frac{2 - (k_s^{(m:1)})^2}{1 - (k_s^{(m:1)})^2} E(k_s^{(m:1)}) \right\}. \quad (1.87)$$

As in Section 1.3, from Eq.(1.81), the approximate condition for the destruction of the  $(m : 1)$ -resonant layer in the potential wells is

$$Q_0 = \min \frac{1}{Q_s^{(m:1)}} \left\{ |E_s^{(m:1)} - E_s^{(m+1:1)}|, |E_s^{(m:1)} - E_s^{(m-1:1)}| \right\}. \quad (1.88)$$

Based on this condition, the  $(m + 1 : 1)$  or  $(m - 1 : 1)$ -resonant motion will be interacted with the  $(m : 1)$ -resonant layer.

### B. Resonant layers outside separatrix

For the given energy  $E_l$  satisfying  $H_0 = E_l > E_0$ , the solution of the large motion orbit in Luo and Han (1998) is

$$\begin{aligned} x^0 &= e_l \operatorname{cn} \left[ \frac{2K(k)}{\pi} \omega_l t, k_l \right], \\ y^0 &= \dot{x}^0 = \pm \sqrt{\frac{\alpha_2}{2}} \frac{e_l^2}{k_l} \operatorname{sn} \left[ \frac{2K(k_l)}{\pi} \omega_l t, k_l \right] \operatorname{dn} \left[ \frac{2K(k_l)}{\pi} \omega_l t, k_l \right]. \end{aligned} \quad (1.89)$$

The modulus  $k_l$ , the response amplitude  $e_l$ , the natural frequency  $\omega_l$  are

$$k_l = \sqrt{\frac{\alpha_1 + \sqrt{\alpha_1^2 + 4\alpha_2 E_l}}{2\sqrt{\alpha_1^2 + 4\alpha_2 E_l}}}, \quad e_l = \sqrt{\frac{2k^2 \alpha_1}{(2k^2 - 1)\alpha_2}}, \quad \omega_l = \frac{\sqrt{\alpha_2} e_l \pi}{2\sqrt{2} k_l K(k_l)}. \quad (1.90)$$

Substitution of Eq.(1.89) into Eq.(1.76) and using Fourier series expansion lead to

$$\begin{aligned} H_1(x, y) &\approx -\frac{\pi e_s Q_0}{2kK} \left\{ \sum_{m=1}^{\infty} \operatorname{sech} \left[ (2n-1) \frac{\pi K'}{2K} \right] \right. \\ &\quad \left. \times [\cos[(2n-1)\omega_l - \Omega]t + \cos[(2n-1)\omega_l + \Omega]t] \right\}. \end{aligned} \quad (1.91)$$

The resonant condition for the corresponding resonant separatrix layer is

$$(2n-1)\omega_l = \Omega \quad (1.92)$$

and the magnitude  $\bar{H}_1$  for the  $(2n-1 : 1)$ - resonant layer outside the homoclinic orbit is

$$\Delta \bar{H} \approx \bar{H}_1 \approx \frac{\sqrt{2}\Omega Q_0}{(2n-1)\pi\sqrt{\alpha_1}} \operatorname{sech} \left[ (2n-1) \frac{\pi K'(k_l^{(2n-1:1)})}{2K(k_l^{(2n-1:1)})} \right], \quad (1.93)$$

where

$$k_l^{(2n-1:1)} = \sqrt{\frac{\alpha_1 + \sqrt{\alpha_1^2 + 4\alpha_2 E_l^{(2n-1:1)}}}{2\sqrt{\alpha_1^2 + 4\alpha_2 E_l^{(2n-1:1)}}}}, \quad (1.94)$$

and  $E_l^{(2n-1:1)}$  is a resonant energy. The energy increment along the  $(2n-1:1)$  resonant orbit outside the potential well is

$$\Delta H_0^l(\varphi_i) \approx \int_{t_i}^{T_l+t_i} y_i^{(0)} Q_0 \cos(\Omega t) dt = Q_0 Q_l^{(2n-1:1)} \sin \varphi_i, \quad (1.95)$$

where

$$Q_l^{(2n-1:1)} \approx \frac{2\sqrt{2}\pi\Omega Q_0}{\sqrt{\alpha_2}} \operatorname{sech} \left[ (2n-1) \frac{\pi K'(k_l^{(2n-1:1)})}{2K(k_l^{(2n-1:1)})} \right]. \quad (1.96)$$

Similarly, the excitation strength for the onset of the  $(2n-1:1)$ -resonant layer outside the potential well is

$$Q_0 \approx \frac{0.9716}{Q_l^{(2n-1:1)} G_l^{(2n-1:1)}}, \quad (1.97)$$

where

$$G_l^{(2n-1:1)} = \frac{2\Omega\alpha_2 \left[ 2(k_l^{(2n-1:1)})^2 - 1 \right]^{5/2}}{(k_l^{(2n-1:1)})^2 \alpha_1^2 \sqrt{\alpha_1}} \cdot \left[ K(k_l^{(2n-1:1)}) - \frac{1 - 2(k_l^{(2n-1:1)})^2}{1 - (k_l^{(2n-1:1)})^2} E(k_l^{(2n-1:1)}) \right]. \quad (1.98)$$

The approximate destruction condition for the  $(2n-1:1)$ -resonant separatrix layer is

$$Q_0 = \min \frac{1}{Q_l^{(2n-1:1)}} \left\{ |E_l^{(2n+1:1)} - E_l^{(2n-1:1)}|, |E_l^{(2n-3:1)} - E_l^{(2n-1:1)}| \right\}. \quad (1.99)$$

### C. Stochastic layer

Due to the presence of the two symmetric wells in the unperturbed Eq. (1.70), the energy increments of the perturbed orbit should be computed through the two inner orbits possessing the same energy in the stochastic layer. Therefore, the energy increment along the inner  $(m:1)$  resonant orbit is computed from Eq. (1.70), i.e.,

$$\begin{aligned} \Delta \tilde{H}^s(\varphi_i) &= 2 \int_{t_i}^{T_s+t_i} (f_1 g_2 - f_2 g_1) dt \\ &\approx \frac{2\sqrt{2}\pi Q_0 \Omega}{\sqrt{\alpha_2}} \operatorname{sech} \left[ \frac{m\pi K'(k_s^{(m:1)})}{K(k_s^{(m:1)})} \right] \sin \varphi_i, \end{aligned} \quad (1.100)$$

where  $\varphi_0 = \Omega t_0$ ,  $K'(k_s^m) = K(k_s^m)$  and  $k_s^m = \sqrt{1 - (k_s^m)^2}$  are related to the  $(m : 1)$ -resonance, and

$$f_1 = y, f_2 = \alpha_1 x - \alpha_2 x^3; g_1 = 0, g_2 = Q_0 \cos(\Omega t). \quad (1.101)$$

In a same manner, the energy increment along the  $((2n - 1) : 1)$  resonant orbit is

$$\begin{aligned} \Delta \tilde{H}^l(\varphi_i) &= \int_{t_i}^{T_i+t_i} (f_1 g_2 - f_2 g_1) dt \\ &\approx \frac{2\sqrt{2}\pi\Omega Q_0}{\alpha_2} \operatorname{sech} \left[ (2n-1) \frac{\pi K'(k_l^{(2n-1:1)})}{2K(k_l^{(2n-1:1)})} \right] \sin \varphi_i. \end{aligned} \quad (1.102)$$

where  $K'(k_l^{(2n-1:1)}) = K(k_l^{(2n-1:1)})$  and  $k_l^{(2n-1:1)} = \sqrt{1 - (k_l^{(2n-1:1)})^2}$  are related to the  $(2n - 1 : 1)$ -resonance. From Eq. (1.70), the energy increment along the homoclinic orbit is

$$\begin{aligned} \Delta H^h(\varphi_i) &= \lim_{T_s \rightarrow \infty} \Delta \tilde{H}^s(\varphi_i) = \lim_{T_l \rightarrow \infty} \Delta \tilde{H}^l(\varphi_i) \\ &= \int_{t_0}^{\infty} (f_1 g_2 - f_2 g_1) dt \approx \frac{2\sqrt{2}Q_0\pi\Omega}{\sqrt{\alpha_2}} \operatorname{sech} \left[ \frac{\pi\Omega}{2\sqrt{\alpha_1}} \right] \sin \varphi_i. \end{aligned} \quad (1.103)$$

From Theorem 1.1 and  $E_0 = 0$ , the condition for the onset of the  $(m : 1)$  resonant-separatrix web in the inner stochastic layer is

$$|\Delta \tilde{H}^s(\varphi_i)| = |E_s^{(m:1)}|. \quad (1.104)$$

Substitution of Eq. (1.100) into Eq. (1.104) yields the excitation strength for the onset of the  $(m : 1)$  resonant-separatrix web in the inner stochastic layer:

$$Q_0 = \frac{|E_s^{(m:1)}|}{2\pi\Omega} \sqrt{\frac{\alpha_2}{2}} \cosh \left[ \frac{m\pi K'(k_s^{(m:1)})}{K(k_s^{(m:1)})} \right]. \quad (1.105)$$

If  $\Delta \tilde{H}^s(\varphi_i)$  is replaced by  $\Delta H^h(\varphi_0)$  in Eq.(1.103), the excitation strength is predicted approximately from

$$Q_0 = \frac{|E_\alpha^{(m:1)}|}{2\pi\Omega} \sqrt{\frac{\alpha_2}{2}} \cosh \left[ \frac{\pi\Omega}{2\sqrt{\alpha_1}} \right]. \quad (1.106)$$

In the vicinity of separatrix, equations (1.105) and (1.106) give very close predictions of the resonance in the stochastic layers.

From Theorem 1.1 and  $E_0 = 0$ , the condition for the onset of the  $((2n - 1) : 1)$  resonant-separatrix web in the outer stochastic layer is

$$|\Delta \tilde{H}^l(\varphi_i)| = |E_l^{(2n-1:1)}|. \quad (1.107)$$

Substitution of Eq. (1.102) into Eq. (1.107) yields the excitation strength for the onset of the  $((2n - 1) : 1)$  resonant-separatrix web, i.e.,

$$Q_0 = \frac{|E_l^{(2n-1:1)}|}{2\pi\Omega} \sqrt{\frac{\alpha_2}{2}} \cosh \left[ (2n-1) \frac{\pi K'(k_l^{(2n-1:1)})}{2K(k_l^{(2n-1:1)})} \right]. \quad (1.108)$$

If  $\Delta\tilde{H}^l(\varphi_i)$  is replaced by  $\Delta H^h(\varphi_i)$ , the excitation strength is given by

$$Q_0 = \frac{|E_l^{(2n-1:1)}|}{2\pi\Omega} \sqrt{\frac{\alpha_2}{2}} \cosh \left[ \frac{\pi\Omega}{2\sqrt{\alpha_1}} \right]. \quad (1.109)$$

The predictions of resonance in the stochastic layers can be given by the approximate and accurate standard mapping approaches, which can be referred to Luo (1995), Luo and Han (1998), and Luo (2008).

## 1.4.2 Numerical illustrations

From the theoretical conditions, numerical illustrations for chaos in the periodic forced Duffing oscillator will be given. Energy spectrum method will be employed for numerical predictions, and analytical and numerical predictions will be given. Stochastic and resonant layers will be illustrated by Poincaré mapping sections.

### A. Stochastic layers

For a better understanding of the above definitions, a resonant-separatrix web of the 5<sup>th</sup>-order in the outer stochastic layer for  $\alpha_1 = \alpha_2 = 1.0$ ,  $\Omega = 4.0$  and  $Q_0 = 0.45$  is shown. The layer width, minimum and maximum energy orbits for that resonant separatrix web are illustrated in Fig. 1.11. For the Duffing oscillator, the layer width is  $|\mathbf{x}^{\max} - \mathbf{x}^{\min}|$  at  $y = 0$  which can be determined numerically. Using the above definition, the maximum and minimum energy spectra are shown in Fig. 1.12 for  $Q_0 = 0.2$  and  $\alpha_1 = \alpha_2 = 1.0$  in Eq. (1.70). The maximum and minimum energy are computed from 10,000 iterations of Poincaré map for each excitation frequency.  $\Omega^{\alpha(m:1)}$  (or  $\Omega^{\beta(2n-1:1)}$ ) denotes a maximum value of excitation frequency when the  $(m:1)$ -order inner (or  $(2n-1:1)$ -order outer) resonant separatrix disappears in the stochastic layer. To view the energy jump clearly, four specific areas in the spectra are zoomed. The energy jumps occur at  $\Omega^{\beta(1:1)} = 1.33, \Omega^{\beta(3:1)} = 2.73, \Omega^{\beta(5:1)} = 3.51$  for the outer stochastic layer and, at  $\Omega^{\alpha(2:1)} = 2.67$  and  $\Omega^{\alpha(3:1)} = 3.39$  for the inner stochastic layer. The specific values are critical excitation frequencies for the disappearance of the resonance in the stochastic layer. For instance, if an excitation frequency chosen for  $Q_0 = 0.2$  is greater than  $\Omega^{\beta(3:1)} = 2.73$ , then, the resonant-separatrix of lower than 5<sup>th</sup> order in the outer-layer and of lower than 3<sup>rd</sup> order in the inner-layer will not appear. For  $Q_0 = 0.2$ , the resonant-separatrix of the first order in the inner stochastic layer cannot be observed because the Hamiltonian arrives at the

minimum energy  $E_\alpha = -0.25$  (for  $\alpha_1 = \alpha_2 = 1.0$ ) until this resonant separatrix appears. Based on the minimum and maximum energies in Fig. 1.12, the width of the stochastic layer is computed, as shown in Fig. 1.13. The numerical and analytical predictions of excitation strengths for the inner and outer resonant-separatrices appearing in the stochastic layer are illustrated in Fig. 1.14(a) and (b), respectively. The solid curves denote the analytical predictions and the hollow-circle curves represent the numerical predictions. The two predictions are in a good agreement. However, in the derivation of analytical conditions, only the primary resonance is used and the incremental energy is approximately computed by the unperturbed orbits rather than the perturbed ones. The aforementioned reasons are two major factors to cause the difference between the analytical and numerical predictions of excitation strength.

For numerical simulations of the resonant-separatrix webs in the stochastic layer, we use a 2<sup>nd</sup>-order symplectic scheme (e.g., Feng and Qin, 1991; McLachlan and Atela, 1992) with time step  $\Delta t = 10^{-5} \sim 10^{-7}T$ , where  $T = 2\pi/\Omega$ , and a precision of  $10^{-6}$ . For  $\alpha_1 = \alpha_2 = 1.0$  and  $\Omega = 4.0$ , the resonant-separatrix webs in the stochastic layers generated by 20,000 Poincaré mapping points of Eq. (1.70) are illustrated in Fig.1.15 for  $Q_0 = 0.98$  and  $Q_0 = 0.2$ . As discussed in Luo and Han (2001), the stochastic layer of Duffing oscillator is separated into the inner and outer stochastic layers by the homoclinic orbit, as shown in Fig.1.15, and the resonant structures of the inner and outer stochastic layers are very distinguishing owing to the different resonance. In Fig.1.15(a), the (3:1) and (5:1)-order resonant separatrix webs are in the outer stochastic layer at  $Q_0 = 0.98$ , and the subresonant separatrix in the vicinity of the (5:1)-order resonant separatrix is also clearly observed. When the excitation

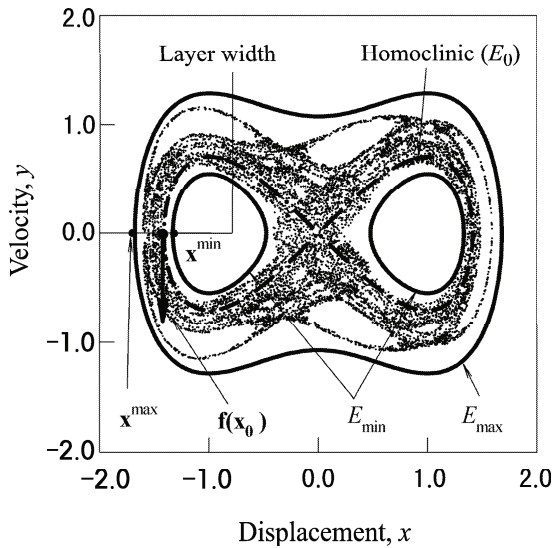


**Fig. 1.11** A description of layer width, minimum and maximum energy through an outer resonant-separatrix web of the 5<sup>th</sup>-order in the stochastic layer for the twin-well Duffing oscillator at  $Q_0 = 0.45$  and  $\Omega = 4.0$ .

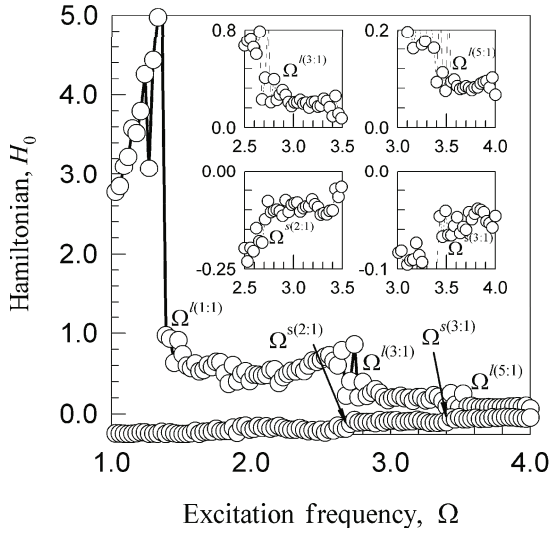


**Fig. 1.12** Minimum and Maximum energy spectra for the stochastic layer in the twin-well Duffing oscillator at  $Q_0 = 0.2$  and  $\alpha_1 = \alpha_2 = 1.0$ .

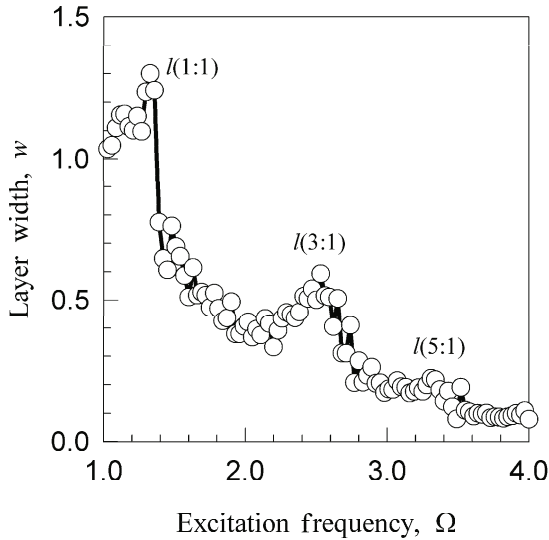
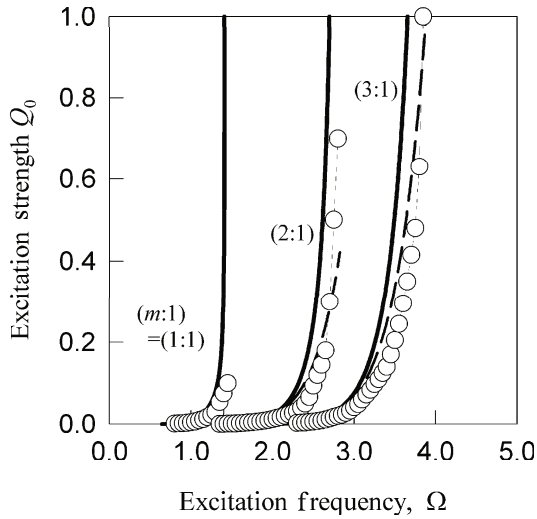
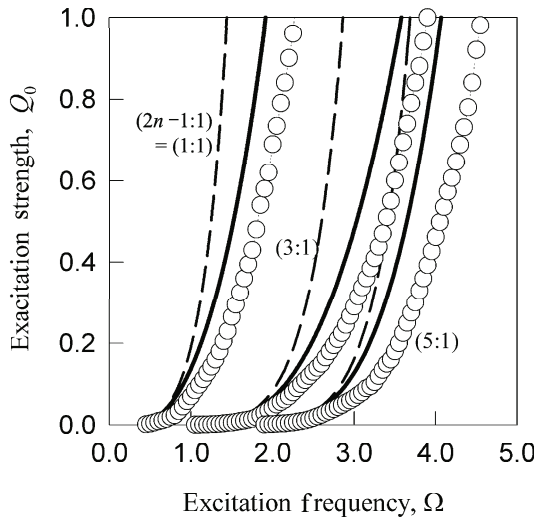


**Fig. 1.13** The width of the stochastic layer in the twin-well Duffing oscillator for  $\alpha_1 = \alpha_2 = 1.0$  and  $Q_0 = 0.2$ .

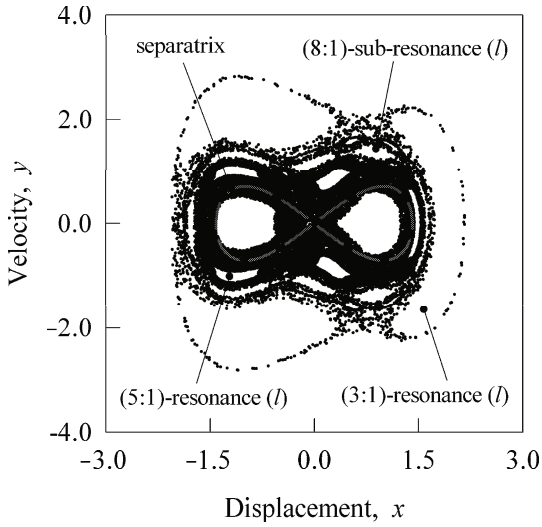


(a)

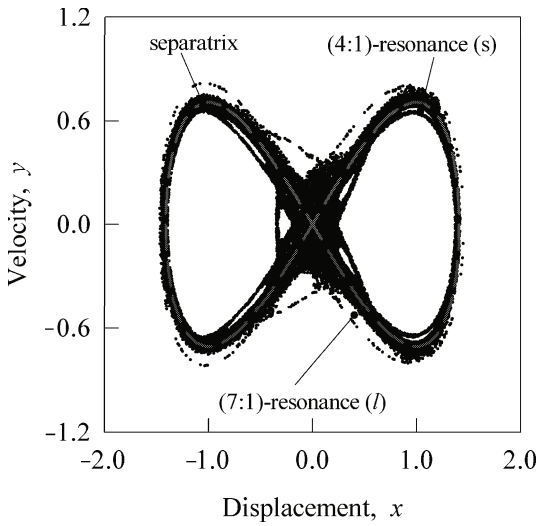


(b)

**Fig. 1.14** Excitation strength for the onset of a specific resonant-separatrix in the stochastic layer of the twin-well Duffing oscillator: (a) inside separatrix and (b) outside separatrix at  $\alpha_1 = \alpha_2 = 1.0$ . Solid and dashed curves represent the analytical conditions based on the small (or large) orbit and the homoclinic orbit, respectively. The circular symbol curves give the numerical prediction of the resonance from the energy spectrum method.



(a)



(b)

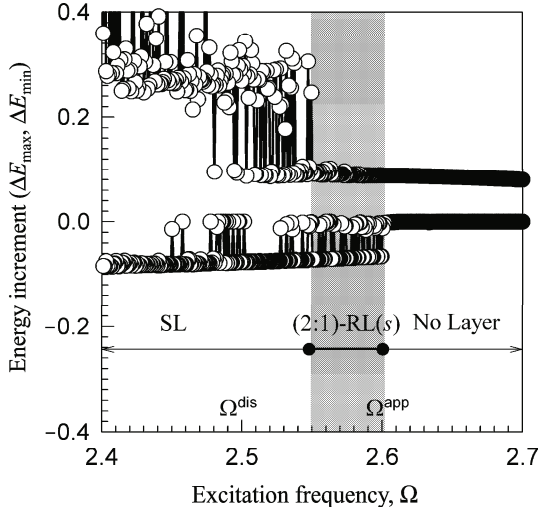
**Fig. 1.15** Poincaré mapping sections of resonant-separatrix webs in the stochastic layer at  $\Omega = 4.0$ . (a) The outer resonance of the (3:1)- and (5:1)-order for  $Q_0 = 0.98$  (upper), and (b) the outer resonance of the (7:1)-order and the inner resonance of the (4:1)-order for  $Q_0 = 0.2$  (lower). The dashed curve is the homoclinic orbit.

strength decreases to  $Q_0 = 0.2$ , the (7:1)-order resonant separatrix appears in the outer stochastic layer, and the (4:1)-order resonant separatrix in the inner stochastic layer is observed in Fig. 1.15(b). From the above observations, the appearance of a new resonant-separatrix in the stochastic layer depends on excitation strength, and the width of the stochastic layer increases with excitation strength.

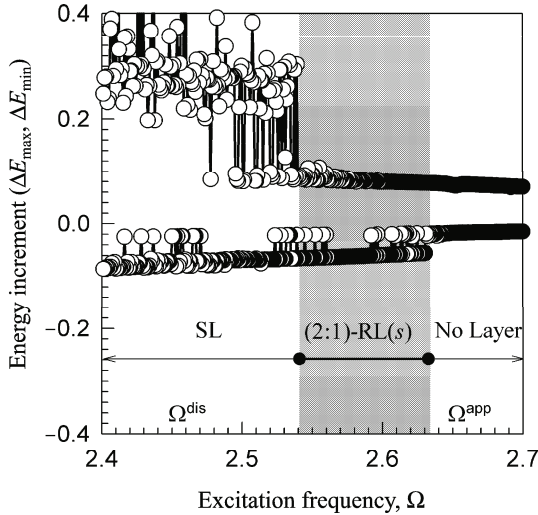
## B. Resonant layers

In the two potential wells, the critical conditions for the onset and disappearance of the resonant layer are different. The onset, developing and destruction of resonant layers are investigated through the maximum and minimum incremental energy spectrums. For the excitation strength  $Q_0 = 0.1$ , the critical values for the appearance of the (2:1)-resonant layer are quite different (i.e.,  $\Omega_{cr}^{app(2:1)} \approx 2.600112249$  (left) and  $\Omega_{cr}^{app(2:1)} \approx 2.641554784$  (right)), but for the disappearance of the two (2:1)-resonant layers, the two critical values are very close (i.e.,  $\Omega_{cr}^{dis(2:1)} \approx 2.550274844$  (left) and  $\Omega_{cr}^{dis(2:1)} \approx 2.547076114$  (right)), as shown in Fig.1.16. However, the resonant layer relative to the large motion is also investigated through the incremental energy spectrum in Fig.1.17 for  $Q_0 = 0.2$ . The critical values of excitation frequency are  $\Omega_{cr}^{app(3:1)} \approx 2.949933222$  and  $\Omega_{cr}^{dis(3:1)} \approx 2.83580655$  for the (3:1)-resonant layer;  $\Omega_{cr}^{app(5:1)} \approx 4.475239668$  and  $\Omega_{cr}^{dis(5:1)} \approx 3.610528592$  for the (5:1)-resonant layer. Through this numerical investigation, the (1:1)-resonant layer relative to the large motion is very difficult to detect. In summary, once the resonant layer appears at  $\Omega = \Omega_{cr}^{app}$ , the resonant layer grows with decreasing excitation frequency until destroyed at  $\Omega \approx \Omega_{cr}^{dis}$ . During the growing period of the resonant layer, the sub-resonance is developed through the self-similarity and is embedded in the resonant layer.

The analytical and numerical predictions of the critical conditions for the appearance and disappearance of resonant layers are also presented in Figs.18 and 19. The solid and dashed curves represent the analytical predictions of the appearance and disappearance of resonant layers, respectively. The solid and hollow circular symbol curves give the numerical predictions of predictions of the appearance and disappearance of resonant layers, respectively. In Fig.1.18(a), the analytical and numerical predictions of the resonant layer appearance in the left well are in very good agreement. For weak excitation, the agreement between the two predictions is much better than for strong excitation. However, for the disappearance conditions, the analytical and numerical estimates do not match very well due to the sub-resonant self-similarity. With excitation amplitude increase, the curves for numerical prediction are not very smooth since the sub-resonance effects become more important. In Fig.1.18(b), for relatively weak excitations, the two predictions are totally different due to the intermittency between two closet resonant layers. Since excitation is not strong enough to produce the interaction between the two resonant layers. Such a resonant layer is isolated. With increasing excitation, the two isolated resonant layers will grow, and finally they merge together. In the right well, higher-order resonant layers cannot be observed through this incremental energy spectrum ap-

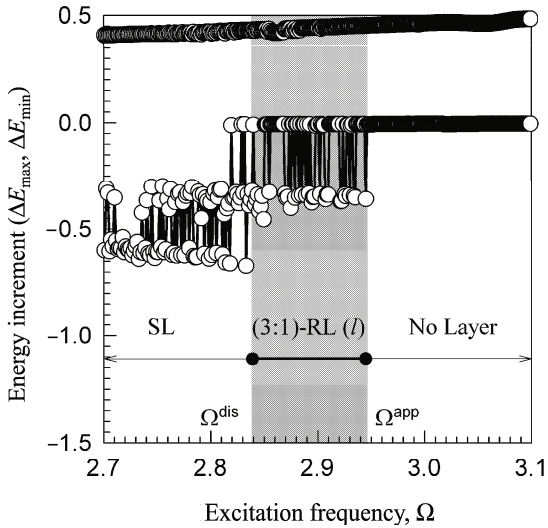


(a)

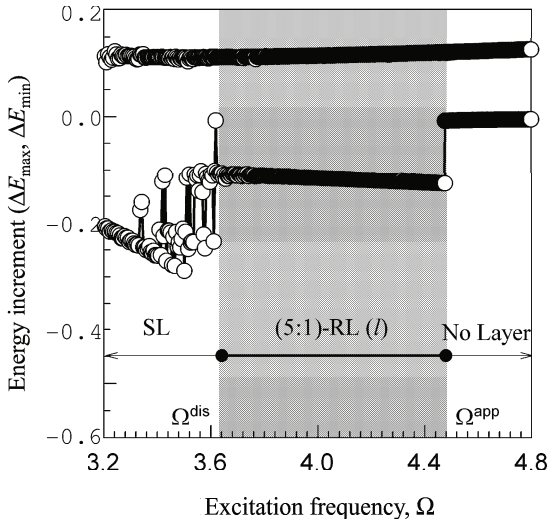


(b)

**Fig. 1.16** The maximum and minimum incremental energy spectra relative to the small motion for the (2:1)-resonant separatrix layer in (a) the left well and (b) the right well ( $Q_0 = 0.1$ ).  $\Omega^{\text{app}}$  and  $\Omega^{\text{dis}}$  are the critical values for the resonant layer appearance and disappearance, respectively.  $\Omega_{\text{cr}}^{\text{app}(2:1)} \approx 2.600112249$  and  $\Omega_{\text{cr}}^{\text{dis}(2:1)} \approx 2.550274844$  (left)  $\Omega_{\text{cr}}^{\text{app}(2:1)} \approx 2.641554784$  and  $\Omega_{\text{cr}}^{\text{dis}(2:1)} \approx 2.547076114$  (right).

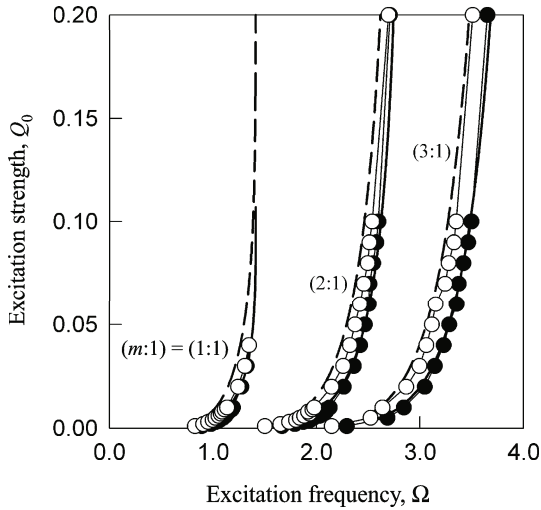


(a)

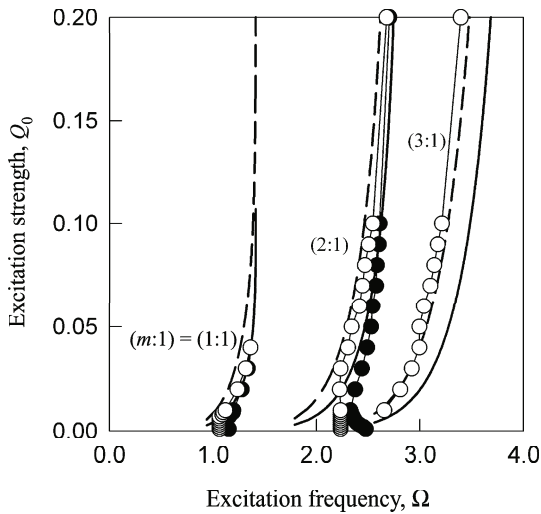


(b)

**Fig. 1.17** The maximum and minimum incremental energy spectra relative to the large motion ( $Q_0 = 0.2$ ) for (a) the (3:1)-resonant separatrix layer, and (b) the (5:1)-resonant separatrix layer.  $\Omega^{\text{app}}$  and  $\Omega^{\text{dis}}$  are the critical values for the resonant layer appearance and disappearance, respectively.  $\Omega_{\text{cr}}^{\text{app}(3:1)} \approx 2.949933222$  and  $\Omega_{\text{cr}}^{\text{dis}(3:1)} \approx 2.83580655$ ;  $\Omega_{\text{cr}}^{\text{app}(5:1)} \approx 4.475239668$  and  $\Omega_{\text{cr}}^{\text{dis}(5:1)} \approx 3.610528592$ .



(a)



(b)

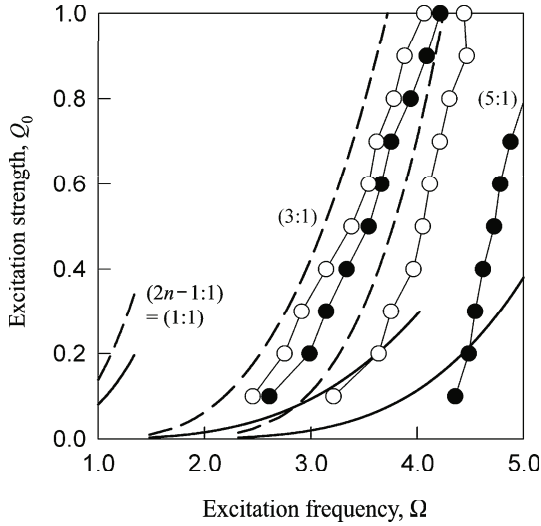
**Fig. 1.18** The critical conditions for the appearance and disappearance of  $(m : 1)$  resonant layers relative to the small motion in (a) the left potential well and (b) the right potential well. The solid and dashed curves represent the analytical predictions of the appearance and disappearance of resonant layers, respectively. The solid and hollow, circular symbol curves represents the numerical predictions of the appearance and disappearance of resonant layers, respectively.

proach since the stochastic layer appears before the higher-order resonant layers are formed.

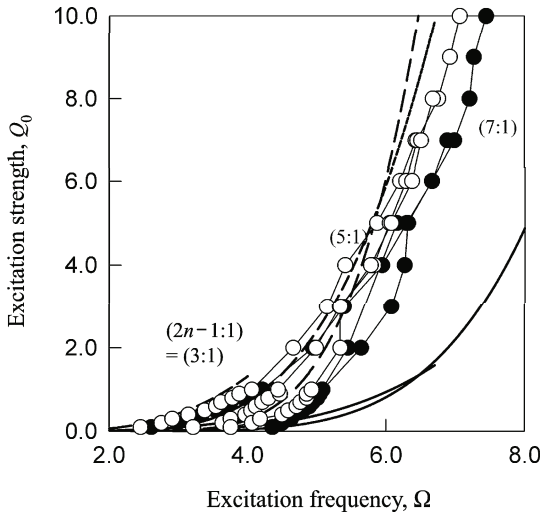
In Fig.1.19, the critical conditions for  $(2n - 1 : 1)$  resonant layers relative to the large motion are shown. No any  $(1:1)$ -resonant layer can be detected through this incremental energy spectrum. For weak excitation, the critical conditions for the appearance and disappearance are plotted in Fig.1.19(a). In Fig.1.19(b), the conditions for relatively strong excitation are presented. The analytical and numerical predictions provide the similar pattern of the critical conditions. The further analytical method needs to be developed for a better understanding of the mechanism of the resonant layers.

From the phase portrait in Fig.1.10, chaotic motions exist in the two wells. To investigate the dynamics of chaos in resonant layers, the Poincaré mapping sections for onset and destruction of resonant layers in potential wells are illustrated. For numerical simulations of chaotic motion in the resonant layer, a 2<sup>nd</sup>-order symplectic scheme (e.g., Feng and Qin, 1991) is used again with time step  $\Delta t = 10^{-6} \sim 10^{-7}T$ , where  $T = 2\pi/\Omega$ , and a precision of  $10^{-8}$ .  $\alpha_1 = \alpha_2 = 1.0$  is used herein. The  $(2:1)$ -resonant layers in the potential wells are presented in Fig. 1.20 for  $Q_0 = 0.1$ . The dashed lines depict the homoclinic orbit (i.e., homoclinic) and small motion orbit in the potential well. The solid and hollow circular symbols represent the center and hyperbolic points for the resonant layers, respectively. It is obviously observed that the resonant layer is not symmetric in the two-wells. With decreasing the external frequency, such a resonant layer will be developed, and the sub-resonance will be embedded in the resonant layer. Fig.1.20(a) shows the onset of such two resonant layers in the potential wells. Since the critical external frequencies for the onset of resonant layers are quite different in the two wells, the two frequencies are used. In the left well,  $\Omega = 2.600112249$  ( $\Omega_{cr}^{app(2:1)} \approx 2.600112249$ ) is used here and the initial conditions are  $x_0 = -0.891618894$  and  $y_0 = 0.403713106$ . In the right well, a different frequency and the corresponding initial conditions are  $\Omega = 2.641554784 \leq \Omega_{cr}^{app(2:1)}$  ( $\Omega_{cr}^{app(2:1)} \approx 2.641554784$ ),  $x_0 = 0.665750376$  and  $y_0 = 0$ . It is observed that the hyperbolic points of the resonant layers deviate from the unperturbed orbit (i.e., s-orbit). This phenomenon needs to be further investigated theoretically. Similarly, with decreasing external frequency, the  $(2:1)$ -resonant layer will grow until it destroys. Consider the external frequency  $\Omega = 2.559774525 > \Omega_{cr}^{dis(2:1)}$  (i.e.,  $\Omega_{cr}^{dis(2:1)} \approx 2.550274844$ ) with the initial conditions  $x_0 = -0.872307555$  and  $y_0 = 0.426521382$  in the left well, and in the right well,  $\Omega = 2.555042597 > \Omega_{cr}^{dis(2:1)}$  (i.e.,  $\Omega_{cr}^{dis(2:1)} \approx 2.547076114$ ) plus the initial conditions  $x_0 = 0.588682962$  and  $y_0 = 0$ .

In a similar fashion, the  $(3:1)$ -resonant layer outside the two potential wells are illustrated in Fig.1.21. The appearance and disappearance of the  $(3:1)$ -resonant layer are shown through Poincaré mapping sections for  $Q_0 = 0.2$  with the two sets of input parameters ( $\Omega \approx 2.949933222 \approx \Omega_{cr}^{app(3:1)}$ ,  $x_0 = 0.622626565$ ,  $y_0 = 1.253204801$ : appearance) and ( $\Omega = 2.839895688 > \Omega_{cr}^{dis(3:1)}$ ,  $x_0 = 0.603644624$ ,  $y_0 = 1.177284164$ : disappearance), respectively.  $\Omega_{cr}^{app(3:1)} \approx 2.949933222$  and  $\Omega_{cr}^{dis(3:1)} \approx 2.83580655$ . It is observed that the resonant layer starts to be formed



(a)



(b)

**Fig. 1.19** The critical conditions for the appearance and disappearance of  $(2n-1:1)$  resonant layers relative to the large motion: (a) weak excitation and (b) strong excitation. The solid and dashed curves represent the analytical predictions of the appearance and disappearance of resonant layers, respectively. The solid and hollow circular symbol curves represent the numerical predictions of the appearance and disappearance of resonant layers, respectively.

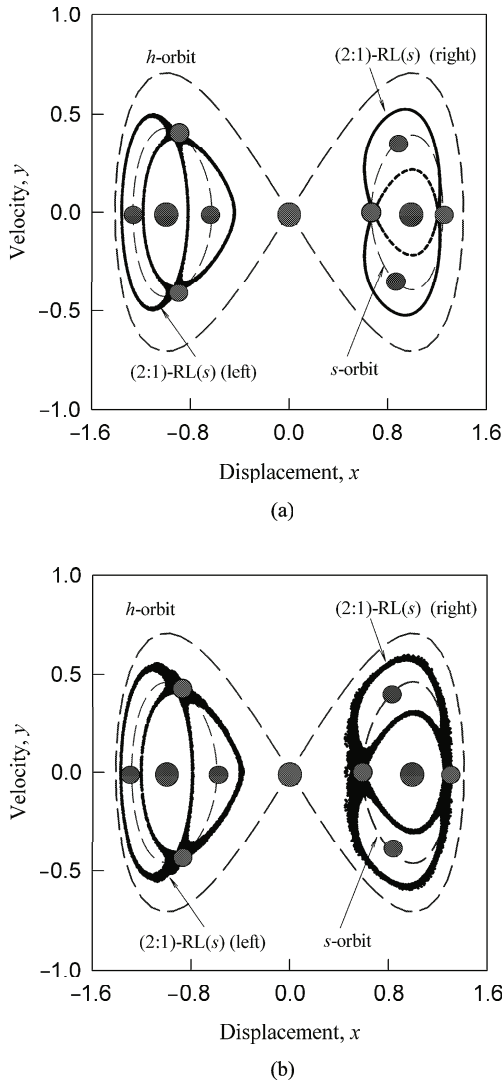
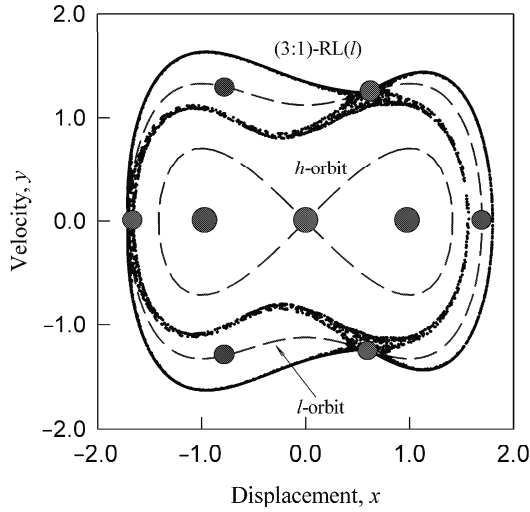
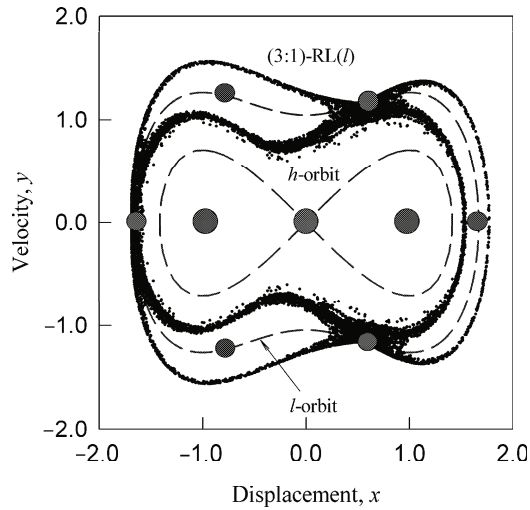


**Fig. 1.20** The (2:1)-resonant layers relative to the small motion orbit ( $Q_0 = 0.1$ ): (a) appearance (left:  $\Omega = 2.600112249$ ,  $x_0 = -0.891618894$ ,  $y_0 = 0.403713106$ ,  $\Omega_{cr}^{app(2:1)} \approx 2.600112249$ ; right:  $\Omega = 2.641554784$ ,  $x_0 = 0.665750376$ ,  $y_0 = 0$ ,  $\Omega_{cr}^{app(2:1)} \approx 2.641554784$ ), (b) disappearance (left:  $\Omega = 2.559774525$ ,  $x_0 = -0.872307555$ ,  $y_0 = 0.426521382$ ,  $\Omega_{cr}^{dis(2:1)} \approx 2.550274844$ ; right:  $\Omega = 2.555042597$ ,  $x_0 = 0.588682962$ ,  $y_0 = 0$ ,  $\Omega_{cr}^{dis(2:1)} \approx 2.547076114$ ). The dashed lines represent the small motion orbit and homoclinic orbit. The solid and hollow circular symbols depict the center and hyperbolic points for the resonant layer, respectively. RL: resonant layer. s-orbit: small orbit. h-orbit: Homoclinic orbit.



(a)



(b)

**Fig. 1.21** The (3:1)-resonant layer related to the large motion orbit ( $Q_0 = 0.2$ ): (a) appearance ( $\Omega = 2.949933222$ ,  $x_0 = 0.622626565$ ,  $y_0 = 1.253204801$ ), (b) disappearance ( $\Omega = 2.839895688$ ,  $x_0 = 0.603644624$ ,  $y_0 = 1.177284164$ ). The dashed lines represent the large motion orbit and homoclinic orbit. The solid and hollow circular symbols depict the center and hyperbolic points for the resonant layer, respectively.  $\Omega_{\text{cr}}^{\text{app}(3:1)} \approx 2.949933222$  and  $\Omega_{\text{cr}}^{\text{dis}(3:1)} \approx 2.83580655$ . RL: resonant layer.  $l$ -orbit: large orbit.  $h$ -orbit: Homoclinic orbit.

in Fig.1.21(a). The sub-resonance appears on the resonant layer before the resonant layer is destroyed.

## 1.5 Discussions

In this chapter, the stochastic and resonant layers in 2-dimensional perturbed nonlinear Hamiltonian systems were presented. This criterion presented in this chapter is applicable to any periodically forced, 2-dimensional nonlinear Hamiltonian system. Since the exact first integral increment (or energy increment) is very difficult to compute analytically, the approximate expressions of the energy increment is derived for analytical prediction of the stochastic and resonant layers. Based on the approximate energy increment, several analytical criteria were developed for the onset of resonance in the stochastic layer. In the energy spectrum method, the minimum and maximum energies are equal to exact computing minimum and maximum energy increments because the initial energy is given. That is,

$$\begin{aligned} E_{\max} &= \max_{N \in \mathbb{N}} H_0^{(N)}(\mathbf{x}_N, \boldsymbol{\mu}) = \max_{N \in \mathbb{N}} \{ \Delta H_0(t_0, NT) + H_0(\mathbf{x}_0, \boldsymbol{\mu}) \} \\ &= \max_{N \in \mathbb{N}} \{ \Delta H_0(t_0, kT) \} + H_0(\mathbf{x}_0, \boldsymbol{\mu}), \end{aligned} \quad (1.110)$$

$$\begin{aligned} E_{\min} &= \min_{N \in \mathbb{N}} H_0^{(N)}(\mathbf{x}_N, \boldsymbol{\mu}) = \min_{N \in \mathbb{N}} \{ \Delta H_0(t_0, NT) + H_0(\mathbf{x}_0, \boldsymbol{\mu}) \} \\ &= \min_{N \in \mathbb{N}} \{ \Delta H_0(t_0, kT) \} + H_0(\mathbf{x}_0, \boldsymbol{\mu}). \end{aligned} \quad (1.111)$$

If  $H_0(\mathbf{x}_0, \boldsymbol{\mu}) = 0$ , we have

$$E_{\max} = \max_{N \in \mathbb{N}} \{ \Delta H_0(t_0, kT) \} \text{ and } E_{\min} = \min_{N \in \mathbb{N}} \{ \Delta H_0(t_0, kT) \}. \quad (1.112)$$

Based on the maximum and minimum energies, the width of the stochastic layer was computed, which is much better than the estimate of the layer width, given by (Melnikov, 1963).

As in Luo (2008), the onset of a specified resonance in stochastic layer is exactly predicted through the incremental energy approach if the energy increment is exactly computed. Therefore, this approach is also applicable for strong excitations when the energy increments still maintain in good accuracy. The accurate standard mapping approach gives a very good prediction compared to the numerical predictions for the resonant separatrix with the low order of resonance. The chaotic motion in the stochastic layer is formed by the primary resonance interaction. The subresonance in the vicinity of the primary resonance is developed through a renormalization. Therefore, chaotic motion in the stochastic layer is the resonance interaction structure instead of the Smale's horseshoe structure. The Smale's horseshoe structure is based on the linearization of the hyperbolic point along the separatrix for one to imagine the topological structure. However, chaotic motion in the stochastic layer exists in the vicinity of the separatrix rather than the separatrix only. The difference

between Smale's horseshoe structure and the resonance interaction structure is similar to the one between the resonance and beat phenomena in periodically forced linear oscillation.

## References

- Ahn T., Kim G. and Kim S., 1996, Analysis of the separatrix map in Hamiltonian systems, *Physica D*, **89**, 315–328.
- Anosov D.A., 1962, Structural stability of geodesic flows on compact Riemannian manifolds of negative curvature, *Doklady Akademicheskikh Nauk SSSR*, **145**, 707–709.
- Arnold V.I., 1963, Small denominators and the problem of stability of motion in classical and celestial mechanics, *Russian Mathematical Surveys*, **18**, 85–192.
- Arnold V.I., 1964, Instability of dynamical systems with several degrees of freedom, *Soviet Mathematics Doklady*, **5**, 581–585.
- Birkhoff G.D., 1913, Proof of Poincaré's geometric theorem, *Transactions on American Mathematical Society*, **14**, 14–22.
- Birkhoff G.D., 1927, *Dynamical Systems*, American Mathematical Society, Providence.
- Chirikov B.V., 1960, Resonance processes in magnetic traps, *Journal of Nuclear Energy, Part C Plasma*, **1**, 253–260.
- Chirikov B.V., 1979, A universal instability of many-dimensional oscillator systems, *Physics Reports*, **52**, 263–379.
- Escande D.F. and Doveil F., 1981, Renormalization method for the onset of stochasticity in a Hamiltonian system, *Physical Letter*, **83A**, 307–310.
- Escande D.F., 1985, Stochasticity in classic Hamiltonian systems: universal aspects, *Physics Reports*, **121**, 165–261.
- Feng K. and Qin M.Z., 1991, Hamiltonian algorithms for Hamiltonian systems and a comparative numerical study, *Computer Physics Communications*, **65**, 173–187.
- Filonenko N.N., Sagdeev R.Z. and Zaslavsky G.M., 1967, Destruction of magnetic surfaces by magnetic field irregularities: Part II, *Nuclear Fusion*, **7**, 253–266.
- Glimm J., 1963, Formal stability of Hamiltonian systems, *Communications on Pure and Applied Mathematics*, **16**, 509–526.
- Greene, J.M., 1968, Two-dimensional measure-preserving mappings, *Journal of Mathematical Physics*, **9**, 760–768.
- Greene J.M., 1979, A method for computing the stochastic transition, *Journal of Mathematical Physics*, **20**, 1183–1201.
- Han R.P.S. and Luo A.C.J., 1998, Resonant layers in nonlinear dynamics, *ASME Journal of Applied Mechanics*, **65**, 727–736.
- Henon M. and Heiles C., 1964, The applicability of the third integral motion: some numerical experiments, *Astronomical Journal*, **69**, 73–79.
- Hopf E., 1937, *Ergodentheorie*, Ergebnisse der Mathematics und ihrer Grenzgebiete, Springer, Berlin.

- Iomin A. and Fishman S., 1996, Semiclassical quantization of a separatrix map, *Physical Review E*, **54**, R1–R5.
- Izrailev F.M. and Chirikov B.V., 1966, Statistical properties of a nonlinear string, *Doklady Akademicheskoy Nauk SSSR*, **166**, 57–59.
- Kolmogorov A.N., 1954, The conservation of conditionally periodic motions under a small perturbations of the Hamiltonian, *Doklady Akademicheskoy Nauk SSSR*, **98**, 527–530.
- Lichtenberg A.J. and Leiberman M.A., 1992, *Regular and Chaotic Dynamics*, 2nd Edition, Springer, New York.
- Lu C., 2007, Chaos of a parametrically excited undamped pendulum, *Communications in Nonlinear Science and Numerical Simulation*, **12**, 45–57.
- Luo A.C.J., 1995, Analytical modeling of bifurcations, chaos and multifractals in nonlinear dynamics, *Ph.D. Dissertation*, University of Manitoba, Winnipeg, Manitoba, Canada.
- Luo A.C.J., 2001, Resonant-overlap phenomena in stochastic layers of nonlinear Hamiltonian systems with periodical excitations, *Journal of Sound and Vibration*, **240**, 821–836.
- Luo A.C.J., 2002, Resonant layers in a parametrically excited pendulum, *International Journal of Bifurcation and Chaos*, **12**, 409–419.
- Luo A.C.J., 2004, Nonlinear Dynamics theory of stochastic layers in nonlinear Hamiltonian, *Applied Mechanics Review*, **57**, 161–172.
- Luo A.C.J., 2006a, Predictions of quasi-periodic and chaotic motions in nonlinear Hamiltonian systems, *Chaos, Solitons and Fractals*, **28**, 627–649.
- Luo A.C.J., 2006b, *Singularity and Dynamics on Discontinuous Vector Fields*, Elsevier, Amsterdam.
- Luo A.C.J., 2008, *Global Transversality, Resonance and Chaotic Dynamics*, World Scientific, Singapore.
- Luo A.C.J. and Gu K., 2003, On Resonant separatrix bands of a Duffing oscillator with twin-well potentials, *Chaos, Solitons and Fractals*, **15**, 771–782.
- Luo A.C.J., Gu K. and Han R.P.S., 1999, Resonant-separatrix webs in stochastic layers of the twin-well Duffing oscillator, *Nonlinear Dynamics*, **19**, 37–48.
- Luo A.C.J. and Han R.P.S., 2000, Investigations of stochastic layers in nonlinear dynamics, *Journal of Vibration and Acoustics*, **122**, 36–41.
- Luo A.C.J. and Han R.P.S., 2001, The resonance theory for stochastic layers in nonlinear dynamical systems, *Chaos, Solitons and Fractals*, **12**, 2493–2508.
- McLachlan, R. and Atela P., 1992, The accuracy of symplectic integrators, *Nonlinearity*, **5**, 541–562.
- Melnikov V.K., 1962, On the behavior of trajectories of system near to autonomous Hamiltonian systems, *Soviet Mathematics-Doklady*, **3**, 109–112.
- Melnikov V.K., 1963, On the stability of the center for time periodic perturbations, *Transaction Moscow Mathematical Society*, **12**, 1–57.
- Moser J., 1962, On the invariant curves of area-preserving mapping on an annulus, *Nachr. Akad. Wiss. Goettingen Math. Phys. Kl.*, **1**, 1–20.
- Poincaré H., 1890, Sur La Probleme des Trois Corps et les Equations de la Dynamique, *Acta Mathematica*, **13**, 1–271.

- Poincaré H., 1892, *Les Methods Nouvelles de la Mechanique Celeste*, Gauthier-Villars, Paris.
- Reichl L.E., 1992, *The Transition to Chaos in Conservative Classic System: Quantum Manifestations*, Springer, New York.
- Rom-Kedar V., 1990, Transport rates of a class of two-dimensional maps and flow, *Physica D*, **43**, 229–268.
- Rom-Kedar V., 1994, Homoclinic tangles-classification and applications, *Nonlinearity*, **7**, 441–473.
- Rom-Kedar V., 1995, Secondary homoclinic bifurcation theorems, *Chaos*, **5**, 385–401.
- Rosenbluth M.N., Sagdeev R.Z., Taylor J.B. and Zaslavsky G.M., 1966, Destruction of magnetic surfaces by magnetic field irregularities, *Nuclear Fusion*, **6**, 297–300.
- Sinai Y.G., 1976, *Introduction to Ergodic Theory*, Princeton University Press, Princeton.
- Smale S., 1967, Differentiable dynamical systems, *Bull. American Mathematical Society*, **73**, 747–817.
- Walker G.H. and Ford J., 1969, Amplitude instability and ergodic behavior for conservative nonlinear oscillator systems, *Physical Review*, **188**, 416–432.
- Zaslavsky G.M. and Chirikov B.V., 1964, On the mechanism of one-dimensional Fermi acceleration, *Doklady of Akademy Nauk*, **159**, 306–309 (Translation: Soviet Physics-Doklady 1965, **9**, 989–992).
- Zaslavsky G.M. and Filonenko N.N., 1968, Stochastic instability of trapped particles and conditions of application of the quasi-linear approximation, *Soviet Physics JETP*, **27**, 851–857.
- Zaslavsky G.M. and Chirikov B.V., 1972, Stochastic Instability of nonlinear oscillations, *Soviet Physics USP*, **52**, 263–272.
- Zaslavsky G.M. and Abdullaev S.S., 1995, Scaling properties and anomalous transport of particles inside the stochastic layer, *Physical Review E*, **51**, 3901–3910.

## Chapter 2

# A New Approach to the Treatment of Separatrix Chaos and Its Applications

S.M. Soskin, R. Mannella, O.M. Yevtushenko, I.A. Khovanov, P.V.E. McClintock

**Abstract** We consider time-periodically perturbed 1D Hamiltonian systems possessing one or more separatrices. If the perturbation is weak, then the separatrix chaos is most developed when the perturbation frequency lies in the logarithmically small or moderate ranges: this corresponds to the involvement of resonance dynamics into the separatrix chaos. We develop a method matching the discrete chaotic dynamics of the separatrix map and the continuous regular dynamics of the resonance Hamiltonian. The method has allowed us to solve the long-standing problem of an accurate description of the maximum of the separatrix chaotic layer width as a function of the perturbation frequency. It has also allowed us to predict and describe new phenomena including, in particular: (i) a drastic facilitation of the onset of global chaos between neighbouring separatrices, and (ii) a huge increase in the size of the low-dimensional stochastic web.

---

S.M. Soskin

Institute of Semiconductor Physics, 03028 Kiev, Ukraine,  
e-mail: ssoskin@ictp.it

R. Mannella

Dipartimento di Fisica, Università di Pisa, 56127 Pisa, Italy,  
e-mail: mannella@df.unipi.it

O.M. Yevtushenko

Physics Department, Ludwig-Maximilians-Universität München, D-80333 München, Germany,  
e-mail: bom@ictp.it

I.A. Khovanov

School of Engineering, University of Warwick, Coventry CV4 7AL, UK,  
e-mail: i.khovanov@warwick.ac.uk

P.V.E. McClintock

Physics Department, Lancaster University, Lancaster LA1 4YB, UK,  
e-mail: p.v.e.mcclintock@lancaster.ac.uk

## 2.1 Introduction

Separatrix chaos is the germ of Hamiltonian chaos (Zaslavsky, 2007). Consider an integrable Hamiltonian system possessing a saddle, i.e. a hyperbolic point in the one-dimensional case, or a hyperbolic invariant torus, in higher-dimensional cases. The stable (incoming) and unstable (outgoing) manifolds of the saddle are called *separatrices* (Gelfreich and Lazutkin, 2001): they separate trajectories that have different phase space topologies. If a weak time-periodic perturbation is added, then the separatrix is destroyed; it is replaced by a *separatrix chaotic layer* (SCL) (Zaslavsky, 2007; Gelfreich and Lazutkin, 2001; Lichtenberg and Lieberman, 1992; Piftankin and Treschev, 2007). Even if the unperturbed system does not possess a separatrix, the resonant part of the perturbation generates a separatrix in the auxiliary resonance phase space while the non-resonant part of the perturbation destroys this separatrix, replacing it with a chaotic layer (Zaslavsky, 2007; Gelfreich and Lazutkin, 2001; Lichtenberg and Lieberman, 1992; Chirikov, 1979). Thus separatrix chaos is of a fundamental importance for Hamiltonian chaos.

One of the most important characteristics of SCL is its width in energy (or expressed in related quantities). It can be easily found *numerically* by integration of the Hamiltonian equations with a set of initial conditions in the vicinity of the separatrix: the space occupied by the chaotic trajectory in the Poincaré section has a higher dimension than that for a regular trajectory, e.g. in the 3/2D case the regular trajectories lie on lines i.e. 1D objects while the chaotic trajectory lies within the SCL i.e. the object outer boundaries of which limit a 2D area.

On the other hand, it is important to be able to describe *theoretically* both the outer boundaries of the SCL and its width. There is a long and rich history of such studies. The results may be classified as follows.

### 2.1.1 Heuristic results

Consider a 1D Hamiltonian system perturbed by a weak time-periodic perturbation:

$$\begin{aligned} H &= H_0(p, q) + hV(p, q, t), \\ V(p, q, t + 2\pi/\omega_f) &= V(p, q, t), \quad h \ll 1, \end{aligned} \quad (2.1)$$

where  $H_0(p, q)$  possesses a separatrix and, for the sake of notational compactness, all relevant parameters of  $H_0$  and  $V$ , except possibly for  $\omega_f$ , are assumed to be  $\sim 1$ .

Physicists proposed a number of different heuristic criteria (Zaslavsky and Filonenko, 1968; Chirikov, 1979; Lichtenberg and Lieberman, 1992; Zaslavsky et al., 1991; Zaslavsky, 2007, 2005) for the SCL width  $\Delta E$  in terms of energy  $E \equiv H_0(p, q)$  which gave qualitatively similar results:

$$\begin{aligned} \Delta E &\equiv \Delta E(\omega_f) \sim \omega_f \delta, \\ \delta &\equiv h|\varepsilon|, \end{aligned}$$

$$\begin{aligned} |\varepsilon| &\lesssim 1 && \text{for } \omega_f \lesssim 1, \\ |\varepsilon| &\propto \exp(-a\omega_f) \ll 1 && (a \sim 1) \quad \text{for } \omega_f \gg 1. \end{aligned} \quad (2.2)$$

The quantity  $\delta \equiv h|\varepsilon|$  is called the *separatrix split* (Zaslavsky, 2007) (see also Eq. (2.4) below): it determines the maximum distance between the perturbed incoming and outgoing separatrices (Zaslavsky and Filonenko, 1968; Chirikov, 1979; Lichtenberg and Lieberman, 1992; Zaslavsky et al., 1991; Zaslavsky, 2007, 2005; Abdullaev, 2006; Gelfreich and Lazutkin, 2001; Piftankin and Treschev, 2007).

It follows from (2.2) that the maximum of  $\Delta E$  should lie in the frequency range  $\omega_f \sim 1$  while the maximum itself should be  $\sim h$ :

$$\Delta E_{\max} \equiv \max_{\omega_f} \{\Delta E(\omega_f)\} \sim h, \quad \omega_f^{(\max)} \sim 1. \quad (2.3)$$

### 2.1.2 Mathematical and accurate physical results

Many papers studied the SCL by mathematical or accurate physical methods.

For the range  $\omega_f \gg 1$ , many works studied the separatrix splitting (see the review (Gelfreich and Lazutkin, 2001) and references therein) and the SCL width in terms of normal coordinates (see the review (Piftankin and Treschev, 2007) and references therein). Though quantities studied in these works differ from those typically studied by physicists (Zaslavsky and Filonenko, 1968; Chirikov, 1979; Lichtenberg and Lieberman, 1992; Zaslavsky et al., 1991; Zaslavsky, 2007, 2005), they implicitly confirm the main qualitative conclusion from the heuristic formula (2.2) in the high frequency range: provided that  $\omega_f \gg 1$  the SCL width is exponentially small.

There were also several works studying the SCL in the opposite (i.e. adiabatic) limit  $\omega_f \rightarrow 0$ : see e.g. (Neishtadt, 1986; Elskens and Escande, 1991; Neishtadt et al., 1997; Soskin et al., 2005, 2010a) and references therein. In the context of the SCL width, it is most important that  $\Delta E(\omega_f \rightarrow 0) \sim h$  for most of the systems (Neishtadt, 1986; Elskens and Escande, 1991; Neishtadt et al., 1997). For a particular class of systems, namely for ac-driven spatially periodic systems (e.g. the ac-driven pendulum), the width of the SCL part above the separatrix diverges in the adiabatic limit (Soskin et al., 2005, 2010a): the divergence develops for  $\omega_f \ll 1/\ln(1/h)$ .

Finally, there is a qualitative estimation of the SCL width for the range  $\omega_f \sim 1$  within the Kolmogorov-Arnold-Moser (KAM) theory (Piftankin and Treschev, 2007). The quantitative estimate within the KAM theory is lacking, apparently being very difficult for this frequency range (Gelfreich, private communication). It follows from the results in (Piftankin and Treschev, 2007) that the width in this range is of the order of the separatrix split, which itself is of the order of  $h$ .

Thus it could seem to follow that, for all systems except ac-driven spatially periodic systems, the maximum in the SCL width is  $\sim h$  and occurs in the range  $\omega_f \sim 1$ , very much in agreement with the heuristic result (2.3). Even for ac-driven spatially periodic systems, this conclusion could seem to apply to the width of the SCL part

below the separatrix over the whole frequency range, and to the width of the SCL part above the separatrix for  $\omega_f \gtrsim 1/\ln(1/h)$ .

### ***2.1.3 Numerical evidence for high peaks in $\Delta E(\omega_f)$ and their rough estimations***

The above conclusion disagrees with several numerical studies carried out during the last decade (see e.g. (Soskin et al., 2005, 2010a; Shevchenko, 1998; Luo et al., 1999; Soskin et al., 2001; Luo, 2004; Vecheslavov, 2004; Shevchenko, 2008)) which have revealed the existence of sharp peaks in  $\Delta E(\omega_f)$  in the frequency range  $1/\ln(1/h) \lesssim \omega_f \lesssim 1$  the heights of which greatly exceed  $h$  (see also Figs. 2.2, 2.3, 2.5, 2.6 below). Thus, the peaks represent the general *dominant feature* of the function  $\Delta E(\omega_f)$ . They were related by the authors of (Shevchenko, 1998; Luo et al., 1999; Soskin et al., 2001; Luo, 2004; Vecheslavov, 2004; Shevchenko, 2008) to the absorption of nonlinear resonances by the SCL. For some partial case, rough heuristic estimates for the position and magnitude of the peaks were made in (Shevchenko, 1998, 2008).

### ***2.1.4 Accurate description of the peaks and of the related phenomena***

Until recently, accurate analytic estimates for the peaks were lacking. It is explicitly stated in (Luo, 2004) that the search for the mechanism through which resonances are involved in separatrix chaos, and for an accurate analytic description of the peaks in the SCL width as function of the perturbation frequency, are being among the most important and challenging tasks in the study of separatrix chaos. The first step towards accomplishing them was taken through the proposal (Soskin et al., 2008a,b) of a new approach to the theoretical treatment of the separatrix chaos in the relevant frequency range. It was developed and applied to the onset of global chaos between two close separatrices. The application of the approach (Soskin et al., 2008a,b) to the commoner single-separatrix case was also discussed. The approach has been further developed (Soskin and Mannella, 2009a,b), including an explicit theory for the single-separatrix case (Soskin and Mannella, 2009b).

The present paper reviews the new approach (Soskin et al., 2008a,b; Soskin and Mannella, 2009a,b) and its applications to the single-separatrix (Soskin and Mannella, 2009b) and double-separatrix (Soskin et al., 2008a,b) cases. We also briefly review application to the enlargement of the low-dimensional stochastic web (Soskin et al., 2010a,b) and discuss other promising applications.

Though the form of our treatment differs from typical forms of mathematical theorems in this subject (cf. (Gelfreich and Lazutkin, 2001; Piftankin and Treschev, 2007)), it yields the *exact* expressions for the leading term in the relevant asymptotic expansions (the parameter of smallness is  $\alpha \equiv 1/\ln(1/h)$ ) and, in some case, even for the next-order term. Our theory is in excellent agreement with results obtained by numerical integration of the equations of motion.

Sect. 2.2 describes the basic ideas underlying the approach. Sect. 2.3 is devoted to the leading-order asymptotic description of the single-separatrix chaotic layers. Sect. 2.4 presents an asymptotic description of the onset of global chaos in between two close separatrices. Sect. 2.5 describes the increase in sizes of a stochastic web. Conclusions are drawn in Sect. 2.6. Sect. 2.7 presents the Appendix, which explicitly matches the separatrix map and the resonance Hamiltonian descriptions for the double-separatrix case.

## 2.2 Basic ideas of the approach

The new approach (Soskin et al., 2008a,b; Soskin and Mannella, 2009a,b) may be formulated briefly as a matching between the discrete chaotic dynamics of the separatrix map in the immediate vicinity of the separatrix and the continuous regular dynamics of the resonance Hamiltonian beyond that region. The present section describes the general features of the approach in more detail.

Motion near the separatrix may be approximated by the *separatrix map* (SM) (Zaslavsky and Filonenko, 1968; Chirikov, 1979; Lichtenberg and Lieberman, 1992; Zaslavsky et al., 1991; Zaslavsky, 2007, 2005; Abdullaev, 2006; Piftankin and Treschev, 2007; Shevchenko, 1998, 2008; Soskin et al., 2008a,b; Rom-Kedar, 1990). This was introduced in (Zaslavsky and Filonenko, 1968) and its various modifications were subsequently used in many studies. It is sometimes known as the *whisker map*. It was re-derived rigorously in (Rom-Kedar, 1990) as the leading-order approximation of motion near the separatrix in the asymptotic limit  $h \rightarrow 0$ , and an estimate of the error was also carried out in (Rom-Kedar, 1990) (see also the review (Piftankin and Treschev, 2007) and references therein).

The main ideas that allow one to introduce the SM (Zaslavsky and Filonenko, 1968; Chirikov, 1979; Lichtenberg and Lieberman, 1992; Zaslavsky et al., 1991; Zaslavsky, 2007, 2005; Abdullaev, 2006; Piftankin and Treschev, 2007; Soskin et al., 2008a,b; Rom-Kedar, 1990) are as follows. For the sake of simplicity, let us consider a perturbation  $V$  that does not depend on the momentum:  $V \equiv V(q, t)$ . A system with energy close to the separatrix value spends most of its time in the vicinity of the saddle(s), where the velocity  $\dot{q}$  is exponentially small. Differentiating  $E \equiv H_0(p, q)$  with respect to time and allowing for the equations of motion of the system (1), we can show that  $dE/dt \equiv \partial V/\partial q \dot{q} \propto \dot{q}$ . Thus, the perturbation can significantly change the energy only when the velocity is not small i.e. during the relatively short intervals while the system is away from the saddle(s): these intervals correspond to *pulses* of velocity as a function of time (cf. Fig. 2.20 in the Appendix

below). Consequently, it is possible to approximate the continuous Hamiltonian dynamics by a discrete dynamics which maps the energy  $E$ , the perturbation angle  $\varphi \equiv \omega_f t$ , and the velocity sign  $\sigma \equiv \text{sgn}(\dot{q})$ , from pulse to pulse.

The actual form of the SM may vary, depending on the system under study, but its features relevant in the present context are similar for all systems. For the sake of clarity, consider the explicit case when the separatrix of  $H_0(p, q)$  possesses a single saddle and two symmetric loops while  $V = q \cos(\omega_f t)$ . Then the SM reads (Soskin et al., 2008a) (cf. Appendix):

$$\begin{aligned}
 E_{i+1} &= E_i + \sigma_i h \varepsilon \sin(\varphi_i), \\
 \varphi_{i+1} &= \varphi_i + \frac{\omega_f \pi (3 - \text{sgn}(E_{i+1} - E_s))}{2\omega(E_{i+1})}, \\
 \sigma_{i+1} &= \sigma_i \text{sgn}(E_s - E_{i+1}), \quad |\sigma_i| = 1, \\
 \varepsilon &\equiv \varepsilon(\omega_f) = \text{sgn} \left( \left. \frac{\partial H_0}{\partial p} \right|_{t \rightarrow -\infty} \right) \int_{-\infty}^{\infty} dt \left. \frac{\partial H_0}{\partial p} \right|_{E_s} \sin(\omega_f t), \\
 E_i &\equiv H_0(p, q)|_{t_i - \Delta}, \quad \varphi_i \equiv \omega_f t_i, \quad \sigma_i \equiv \text{sgn} \left( \left. \frac{\partial H_0}{\partial p} \right|_{t_i} \right),
 \end{aligned} \tag{2.4}$$

where  $E_s$  is the separatrix energy,  $\omega(E)$  is the frequency of oscillation with energy  $E$  in the unperturbed case (i.e. for  $h = 0$ ),  $t_i$  is the instant corresponding to the  $i$ -th turning point in the trajectory  $q(t)$  (cf. Fig. 2.20 in the Appendix below), and  $\Delta$  is an arbitrary value from the range of time intervals which greatly exceed the characteristic duration of the velocity pulse while being much smaller than the interval between the subsequent pulses (Zaslavsky and Filonenko, 1968; Chirikov, 1979; Lichtenberg and Lieberman, 1992; Zaslavsky et al., 1991; Zaslavsky, 2007, 2005; Abdullaev, 2006; Piftankin and Treschev, 2007; Rom-Kedar, 1990). Consider the two most general ideas of our approach.

1. If a trajectory of the SM includes a state with  $E = E_s$  and an arbitrary  $\varphi$  and  $\sigma$ , then this trajectory is chaotic. Indeed, the angle  $\varphi$  of such a state is not correlated with the angle of the state at the previous step of the SM, due to the divergence of  $\omega^{-1}(E \rightarrow E_s)$ . Therefore, the angle at the previous step may deviate from a multiple of  $2\pi$  by an arbitrary value. Hence the energy of the state at the previous step may deviate from  $E_s$  by an arbitrary value within the interval  $[-h|\varepsilon|, h|\varepsilon|]$ . The velocity sign  $\sigma$  is not correlated with that at the previous step either<sup>1</sup>. Given that a regular trajectory of the SM cannot include a step where all three variables change random-like, we conclude that such a trajectory must be chaotic.

Though the above arguments may appear to be obvious, they cannot be considered a mathematically rigorous proof, so that the statement about the chaotic nature of the SM trajectory which includes any state with  $E = E_s$  should be considered as

<sup>1</sup> Formally,  $\text{sgn}(E - E_s)$  is not defined for  $E = E_s$  but, if to shift  $E$  from  $E_s$  for an infinitesimal value,  $\text{sgn}(E - E_s)$  acquires a value equal to either  $+1$  or  $-1$ , depending on the sign of the shift. Given that  $\sigma_{i+1}$  is proportional to  $\text{sgn}(E_s - E_{i+1})$  while the latter is random-like (as it has been shown above),  $\sigma_{i+1}$  is not correlated with  $\sigma_i$  if  $E_{i+1} = E_s \pm 0$ .

a conjecture supported by the above arguments and by numerical iteration of the SM. Possibly, a mathematically rigorous proof should involve an analysis of the Lyapunov exponents for the SM (cf. Lichtenberg and Lieberman, 1992) but this appears to be a technically difficult problem. We emphasize however that a rigorous proof of the conjecture is not crucial for the validity of the main results of the present paper, namely for the *leading* terms in the asymptotic expressions describing (i) the peaks of the SCL width as a function of the perturbation frequency in the single-separatrix case, and (ii) the related quantities for the double-separatrix case. It will become obvious from the next item that, to derive the leading term, it is sufficient to know that the chaotic trajectory does visit areas of the phase space where the energy deviates from the separatrix by values of the order of the separatrix split  $\delta \equiv h|\varepsilon|$ , which is a widely accepted fact (Zaslavsky and Filonenko, 1968; Chirikov, 1979; Lichtenberg and Lieberman, 1992; Zaslavsky et al., 1991; Zaslavsky, 2007, 2005; Abdullaev, 2006; Gelfreich and Lazutkin, 2001; Piftankin and Treschev, 2007).

2. It is well known (Zaslavsky and Filonenko, 1968; Chirikov, 1979; Lichtenberg and Lieberman, 1992; Zaslavsky et al., 1991; Zaslavsky, 2007, 2005; Abdullaev, 2006; Gelfreich and Lazutkin, 2001; Piftankin and Treschev, 2007; Shevchenko, 1998, 2008; Soskin et al., 2008a,b), that, at the leading-order approximation, the frequency of eigenoscillation as function of the energy near the separatrix is proportional to the reciprocal of the logarithmic factor

$$\omega(E) = \frac{b\pi\omega_0}{\ln\left(\frac{\Delta H}{|E - E_s|}\right)}, \quad b = \frac{3 - \text{sgn}(E - E_s)}{2}, \quad (2.5)$$

$$|E - E_s| \ll \Delta H \equiv E_s - E_{st},$$

where  $E_{st}$  is the energy of the stable states.

Given that the argument of the logarithm is large in the relevant range of  $E$ , the function  $\omega(E)$  is nearly constant for a substantial variation of the argument. Therefore, as the SM maps the state  $(E_0 = E_s, \varphi_0, \sigma_0)$  onto the state with  $E = E_1 \equiv E_s + \sigma_0 h \varepsilon \sin(\varphi_0)$ , the value of  $\omega(E)$  for the given  $\text{sgn}(\sigma_0 \varepsilon \sin(\varphi_0))$  is nearly the same for most of the angles  $\varphi_0$  (except in the vicinity of multiples of  $\pi$ ),

$$\omega(E) \approx \omega_r^{(\pm)}, \quad (2.6)$$

$$\omega_r^{(\pm)} \equiv \omega(E_s \pm h), \quad \text{sgn}(\sigma_0 \varepsilon \sin(\varphi_0)) = \pm 1.$$

Moreover, if the deviation of the SM trajectory from the separatrix increases further,  $\omega(E)$  remains close to  $\omega_r^{(\pm)}$  provided the deviation is not too large, namely if  $\ln(|E - E_s|/h) \ll \ln(\Delta H/h)$ . If  $\omega_f \lesssim \omega_r^{(\pm)}$ , then the evolution of the SM (4) may be regular-like for a long time until the energy returns to the close vicinity of the separatrix, where the trajectory becomes chaotic. Such behavior is especially pronounced if the perturbation frequency is close to  $\omega_r^{(+)}$  or  $\omega_r^{(-)}$  or to one of their multiples of relatively low order: the resonance between the perturbation and the eigenoscillation gives rise to an accumulation of energy changes for many steps of

the SM, which results in a deviation of  $E$  from  $E_s$  that greatly exceeds the separatrix split  $h|\varepsilon|$ . Consider a state at the boundary of the SCL. The deviation of energy of such a state from  $E_s$  depends on its position at the boundary. In turn, the maximum deviation is a function of  $\omega_f$ . The latter function possesses the absolute maximum at  $\omega_f$  close to  $\omega_r^{(+)}$  or  $\omega_r^{(-)}$  typically<sup>2</sup>, for the upper or lower boundary of the SCL respectively. This corresponds to the absorption of the, respectively upper and lower, 1st-order nonlinear resonance by the SCL.

The second of these intuitive ideas has been explicitly confirmed (Soskin et al., 2008a) (see Appendix): in the relevant range of energies, the separatrix map has been shown to reduce to two differential equations which are identical to the equations of motion of the auxiliary resonance Hamiltonian describing the resonance dynamics in terms of the conventional canonically conjugate slow variables, action  $I$  and slow angle  $\tilde{\psi} \equiv n\psi - \omega_f t$  where  $\psi$  is the angle variable (Chirikov, 1979; Lichtenberg and Lieberman, 1992; Zaslavsky et al., 1991; Zaslavsky, 2007, 2005; Abdullaev, 2006) (see Eq. (2.16) below) and  $n$  is the relevant resonance number i.e. the integer closest to the ratio  $\omega_f/\omega_r^{(\pm)}$ .

Thus the matching between the discrete chaotic dynamics of the SM and the continuous regular-like dynamics of the resonance Hamiltonian arises in the following way (Soskin et al., 2008a). After the chaotic trajectory of the SM visits any state on the separatrix, the system transits in one step of the SM to a given upper or lower curve in the  $I - \tilde{\psi}$  plane which has been called (Soskin et al., 2008a) the upper or lower *generalized separatrix split* (GSS) curve<sup>3</sup> respectively:

$$E = E_{GSS}^{(\pm)}(\tilde{\psi}) \equiv E_s \pm \delta |\sin(\tilde{\psi})|, \quad \delta \equiv h|\varepsilon|, \quad (2.7)$$

where  $\delta$  is the conventional separatrix split (Zaslavsky, 2007),  $\varepsilon$  is the amplitude of the Melnikov-like integral defined in Eq. (2.4) above (cf. (Zaslavsky and Filonenko, 1968; Chirikov, 1979; Lichtenberg and Lieberman, 1992; Zaslavsky et al., 1991; Zaslavsky, 2007, 2005; Abdullaev, 2006; Gelfreich and Lazutkin, 2001; Piftankin and Treschev, 2007; Shevchenko, 1998; Vecheslavov, 2004; Shevchenko, 2008; Soskin et al., 2008a,b)), and the angle  $\tilde{\psi}$  may take any value either from the range  $[0, \pi]$  or from the range  $[\pi, 2\pi]$ <sup>4</sup>.

After that, because of the closeness of  $\omega_f$  to the  $n$ -th harmonic of  $\omega(E)$  in the relevant range of  $E^5$ , for a relatively long time the system follows the *nonlinear*

<sup>2</sup> For the SM relating to ac-driven spatially periodic systems, the time during which the SM undergoes a regular-like evolution above the separatrix diverges in the adiabatic limit  $\omega_f \rightarrow 0$  (Soskin et al., 2010a), and the width of the part of the SM layer above the separatrix diverges too. However, we do not consider this case here since it is irrelevant to the main subject of the present paper i.e. to the involvement of the resonance dynamics into the separatrix chaotic motion.

<sup>3</sup> The GSS curve corresponds to the step of the SM which follows the state with  $E = E_s$ , as described above.

<sup>4</sup> Of these two intervals, the relevant one is that in which the derivative  $dE/dt$  in the nonlinear resonance equations (see Eq. (2.16) below) is positive or negative, for the case of the upper or lower GSS curve respectively.

<sup>5</sup> I.e.  $E$  determined by Eq. (2.7) for any  $\tilde{\psi}$  except from the vicinity of multiples of  $\pi$ . As shown in (Soskin et al., 2008a), Eq. (2.7) is irrelevant to the boundary of the chaotic layer in the range of

*resonance* (NR) dynamics (see Eq. (2.16) below), during the first half of which the deviation of the energy from the separatrix value grows, greatly exceeding  $\delta$  for most of the trajectory. As time passes,  $\tilde{\psi}$  is moving and, at some point, the growth of the deviation changes for the decrease. This decrease lasts until the system hits the GSS curve, after which it returns to the separatrix just for one step of the separatrix map. At the separatrix, the slow angle  $\tilde{\psi}$  changes random-like, so that a new stage of evolution similar to the one just described occurs, i.e. the nonlinear resonance dynamics starting from the GSS curve with a new (random) value of  $\tilde{\psi}$ .

Of course, the SM cannot describe the variation of the energy during the velocity pulses (i.e. in between instants relevant to the SM): in some cases this variation can be comparable to the change within the SM dynamics. This additional variation will be taken into account below, where relevant.

One might argue that, even for the instants relevant to the SM, the SM describes the original Hamiltonian dynamics only approximately (Rom-Kedar, 1990) and may therefore miss some fine details of the motion: for example, the above picture does not include small windows of stability on the separatrix itself. However these fine details are irrelevant in the present context, in particular the relative portion of the windows of stability on the separatrix apparently vanishes in the asymptotic limit  $h \rightarrow 0$ .

The boundary of the SM chaotic layer is formed by those parts of the SM chaotic trajectory which deviate from the separatrix more than others. It follows from the structure of the chaotic trajectory described above that the upper/lower boundary of the SM chaotic layer is formed in one of the two following ways (Soskin et al., 2008a,b): (i) if there exists a *self-intersecting* resonance trajectory (in other words, the resonance separatrix) the lower/upper part of which (i.e. the part situated below/above the self-intersection) touches or intersects the upper/lower GSS curve while the upper/lower part does not, then the upper/lower boundary of the layer is formed by the upper/lower part of this self-intersecting trajectory (Figs. 2.1(a) and (b)); (ii) otherwise the boundary is formed by the resonance trajectory *tangent* to the GSS curve (Fig. 2.1(c)). It is shown below that, in both cases, the variation of the energy along the resonance trajectory is larger than the separatrix split  $\delta$  by a logarithmically large factor  $\propto \ln(1/h)$ . Therefore, over the boundary of the SM chaotic layer the largest deviation of the energy from the separatrix value,  $\Delta E_{sm}^{(\pm)}$ , may be taken, in the leading-order approximation, to be equal to the largest variation of the energy along the resonance trajectory forming the boundary, while the latter trajectory can be entirely described within the resonance Hamiltonian formalism.

Finally, we mention that, as is obvious from the above description of the boundary,  $\Delta E_{sm}^{(\pm)} \equiv \Delta E_{sm}^{(\pm)}(\omega_f)$  possesses a local maximum  $\Delta E_{\max, sm}^{(\pm)}$  at  $\omega_f$  for which the resonance separatrix just *touches* the corresponding GSS curve (see Fig. 2.1(a)).

---

$\tilde{\psi}$  close to multiples of  $\pi$  while the boundary in this range of  $\tilde{\psi}$  still lies in the resonance range of energies, where  $\omega(E) \approx \omega^{(\pm)}$ .

### 2.3 Single-separatrix chaotic layer

It is clear from Sect. 2.2 above that  $\Delta E_{\max,sm}^{(\pm)}$  is equal in leading order to the width  $\Delta E_{NR}$  of the nonlinear resonance which touches the separatrix. In Sect. 2.3.1 be-

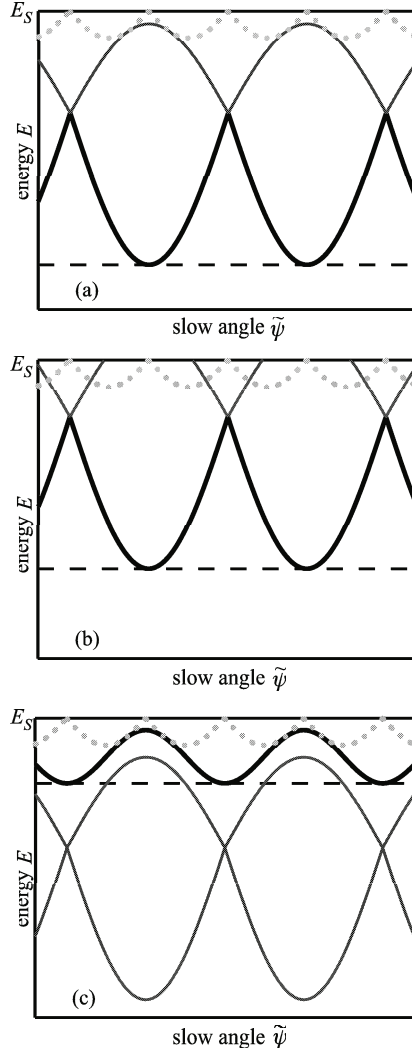


**Fig. 2.1** Schematic figure illustrating the formation of the peak of the function  $\Delta E_{sm}^{(-)}(\omega_f)$ : (a)  $\omega_f = \omega_{\max}$ ; (b)  $\omega_f < \omega_{\max}$ ; (c)  $\omega_f > \omega_{\max}$ . The relevant (lower) GSS curve is shown by the dotted line. The relevant trajectories of the resonance Hamiltonian are shown by solid lines. The lower boundary of the layer is marked by a thick solid line: in (a) and (b) the lower boundary is formed by the lower part of the resonance separatrix while, in (c) it is formed by the resonance trajectory tangent to the GSS curve. The dashed line marks, for a given  $\omega_f$ , the maximal deviation of the lower boundary from the separatrix energy  $E_S$ .

low, we *roughly* estimate  $\Delta E_{NR}$  in order to classify two different types of systems. Sects. 2.3.2 and 2.3.3 present the *accurate* leading-order asymptotic theory for the two types of systems. The *next-order* correction is estimated in Sect. 2.3.4, while a *discussion* is presented in Sect. 2.3.5.

### 2.3.1 Rough estimates. Classification of systems

Let us roughly estimate  $\Delta E_{NR}$ : it will turn out that it is thus possible to classify all systems into two different types. With this aim, we expand the perturbation  $V$  into two Fourier series in  $t$  and in  $\psi$  respectively:

$$V \equiv \frac{1}{2} \sum_l V^{(l)}(E, \psi) e^{-il\omega_f t} + \text{c.c.} \equiv \frac{1}{2} \sum_{l,k} V_k^{(l)}(E) e^{i(k\psi - l\omega_f t)} + \text{c.c.} \quad (2.8)$$

As in standard nonlinear resonance theory (Chirikov, 1979; Lichtenberg and Lieberman, 1992; Zaslavsky et al., 1991; Zaslavsky, 2007, 2005), we single out the relevant (for a given peak) numbers  $K$  and  $L$  for the blind indices  $k$  and  $l$  respectively, and denote the absolute value of  $V_K^{(L)}$  as  $V_0$ :

$$V_0(E) \equiv |V_K^{(L)}(E)|. \quad (2.9)$$

To estimate the width of the resonance roughly, we use the pendulum approximation of resonance dynamics (Chirikov, 1979; Lichtenberg and Lieberman, 1992; Zaslavsky et al., 1991; Zaslavsky, 2007, 2005; Abdullaev, 2006):

$$\Delta E_{NR} \sim \sqrt{8hV_0\omega_f/|d\omega/dE|}. \quad (2.10)$$

This approximation assumes constancy of  $d\omega/dE$  in the resonance range of energies, which is not the case here: in reality,  $\omega(E) \propto 1/\ln(1/|E - E_s|)$  in the vicinity of the separatrix (Zaslavsky and Filonenko, 1968; Chirikov, 1979; Lichtenberg and Lieberman, 1992; Zaslavsky et al., 1991; Zaslavsky, 2007, 2005; Abdullaev, 2006; Piftankin and Treschev, 2007; Shevchenko, 1998; Vecheslavov, 2004; Shevchenko, 2008; Soskin et al., 2008a,b), so that the relevant derivative  $|d\omega/dE| \sim (\omega_r^{(\pm)})^2/(\omega_0|E - E_s|)$  varies strongly within the resonance range. However, for our rough estimate we may use the maximal value of  $|E - E_s|$ , which is approximately equal to  $\Delta E_{NR}$ . If  $\omega_f$  is of the order of  $\omega_r^{(\pm)} \sim \omega_0/\ln(1/h)$ , then Eq. (2.10) reduces to the following approximate asymptotic equation for  $\Delta E_{NR}$ :

$$\Delta E_{NR} \sim V_0(E = E_s \pm \Delta E_{NR})h \ln(1/h), \quad h \rightarrow 0. \quad (2.11)$$

The asymptotic solution of Eq. (2.11) depends on  $V_0(E_s \pm \Delta E_{NR})$  as a function of  $\Delta E_{NR}$ . In this context, all systems can be divided in two types.

**I.** The separatrix of the unperturbed system has *two or more* saddles while the relevant Fourier coefficient  $V^{(L)} \equiv V^{(L)}(E, \psi)$  possesses *different* values on adjacent saddles. Given that, for  $E \rightarrow E_s$ , the system stays most of time near one of the saddles, the coefficient  $V^{(L)}(E \rightarrow E_s, \psi)$  as a function of  $\psi$  is nearly a “square wave”: it oscillates between the values at the different saddles. The relevant  $K$  is typically odd and, therefore,  $V_0(E \rightarrow E_s)$  approaches a well defined non-zero value. Thus, the quantity  $V_0(E = E_s \pm \Delta E_{NR})$  in Eq. (2.11) may be approximated by this non-zero limit, and we conclude therefore that

$$\Delta E_{NR} \propto h \ln(1/h), \quad h \rightarrow 0. \quad (2.12)$$

**II.** Either (i) the separatrix of the unperturbed system has a *single saddle*, or (ii) it has more than one saddle but the perturbation coefficient  $V^{(L)}$  is *identical* for all saddles. Then  $V^{(L)}(E \rightarrow E_s, \psi)$ , as a periodic function of  $\psi$ , significantly differs from its value at the saddle(s) only during a small part of the period in  $\psi$ : this part is  $\sim \omega(E)/\omega_0 \sim 1/\ln(1/|E_s - E|)$ . Hence,  $V_0(E_s \pm \Delta E_{NR}) \propto 1/\ln(1/\Delta E_{NR})$ . Substituting this value in Eq. (2.11), we conclude that

$$\Delta E_{NR} \propto h, \quad h \rightarrow 0. \quad (2.13)$$

Thus, for systems of type I, the maximum width of the SM chaotic layer is proportional to  $h$  times a logarithmically large factor  $\propto \ln(1/h)$  while, for systems of type II, it is proportional to  $h$  times a numerical factor.

As shown below, the variation of energy in between the instants relevant to the SM is  $\sim h$ , i.e. much less than  $\Delta E_{NR}$  (2.12) for systems of the type I, and of the same order as  $\Delta E_{NR}$  (2.13) for systems of type II. Therefore, one may expect that the maximum width of the layer for the original Hamiltonian system (2.1),  $\Delta E^{(\pm)}$ , is at least roughly approximated by that for the SM,  $\Delta E_{sm}^{(\pm)}$ , so that the above classification of systems is relevant to  $\Delta E^{(\pm)}$  too. This is confirmed both by numerical integration of the equations of motion of the original Hamiltonian system and by the accurate theory presented in the next two sub-sections.

### 2.3.2 Asymptotic theory for systems of type I

For the sake of clarity, we consider a particular example of a type I system; its generalization is straightforward.

We choose an archetypal example: the ac-driven pendulum (sometimes referred to as a pendulum subject to a dipole time-periodic perturbation) (Zaslavsky et al., 1991; Soskin et al., 2005, 2010a):

$$\begin{aligned} H &= H_0 + hV, \\ H_0 &= \frac{p^2}{2} - \cos(q), \quad V = -q \cos(\omega_f t), \quad h \ll 1. \end{aligned} \quad (2.14)$$

Fig. 2.2 presents the results of numerical simulations for a few values of  $h$  and several values of  $\omega_f$ . It shows that: (i) the function  $\Delta E^{(-)}(\omega_f)$  indeed possesses sharp peaks whose heights greatly exceed the estimates by the heuristic (Zaslavsky et al., 1991), adiabatic (Elskens and Escande, 1991) and moderate-frequency (Piftankin and Treschev, 2007) theories (see inset); (ii) as predicted by our rough estimates of Sect. 2.3.1, the 1st peak of  $\Delta E^{(-)}(\omega_f)$  shifts to smaller values of  $\omega_f$  while its magnitude grows, as  $h$  decreases. Below, we develop a leading-order asymptotic theory, in which the parameter of smallness is  $1/\ln(1/h)$ , and compare it with results of the simulations.

Before moving on, we note that the SM (approximated in the relevant case by nonlinear resonance dynamics) considers states of the system only at discrete instants. Apart from the variation of energy within the SM dynamics, a variation of energy in the Hamiltonian system also occurs in between the instants relevant to the SM. Given that  $\omega_f \ll 1$ , this latter variation may be considered in adiabatic approximation and it is of the order of  $h$  (Elskens and Escande, 1991; Shevchenko, 2008). It

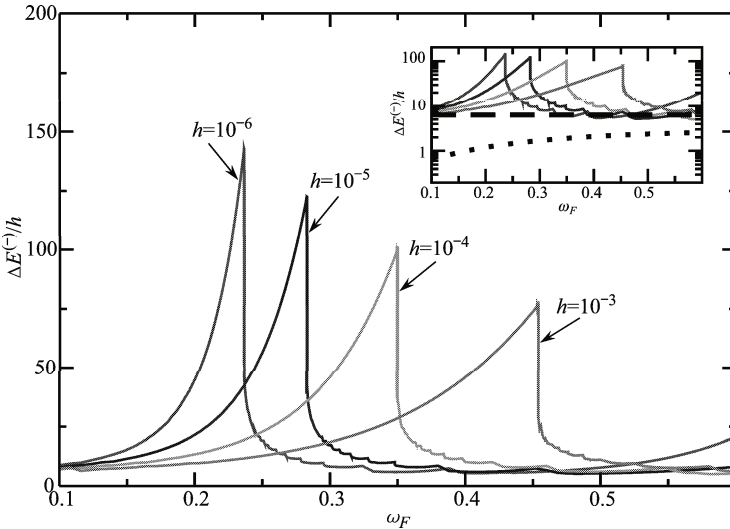


**Fig. 2.2** Computer simulations for the ac driven pendulum (2.14) (an archetypal example of type I): the deviation  $\Delta E^{(-)}$  of the lower boundary of the chaotic layer from the separatrix, normalized by the perturbation amplitude  $h$ , is plotted as a function of the perturbation frequency  $\omega_f$ , for various  $h$ . The inset presents the same data but with a logarithmic ordinate and with the estimates by the heuristic (Zaslavsky et al., 1991), adiabatic (Elskens and Escande, 1991) and moderate-frequency (Piftankin and Treschev, 2007) theories. The heuristic estimate is shown by the dotted line; as an example of the heuristic estimate, we use the formula from (Zaslavsky et al., 1991):  $\Delta E^{(-)}/h = 2\pi\omega_f/\cosh(\pi\omega_f/2)$ . The adiabatic and moderate-frequency estimates are shown by the dashed line: the adiabatic estimate for  $\Delta E^{(-)}(\omega_f)$  is equal approximately to  $2\pi$ ; the estimate following from the results of the work (Piftankin and Treschev, 2007) for  $\omega_f \sim 1$  is of the same order, so that it is schematically represented in the inset in Fig. 2.2 by the same line as for the adiabatic estimate (dashed line). The inset shows explicitly that the simulation results exceed the estimates of the former theories by 1 or 2 orders of magnitude, over a wide range of frequencies.

follows from the above rough estimates, and from the more accurate consideration below, that the variation of energy within the SM dynamics for systems of type I is logarithmically larger i.e. larger by the factor  $\ln(1/h)$ . The variation of energy in between the instants relevant to the SM may therefore be neglected to leading-order for systems of type I:  $\Delta E^{(-)} \simeq \Delta E_{sm}^{(-)}$ . For the sake of notational compactness, we shall henceforth omit the subscript “sm” in this subsection.

For the system (2.14), the separatrix energy is equal to 1, while the asymptotic (for  $E \rightarrow E_s$ ) dependence  $\omega(E)$  is (Zaslavsky et al., 1991):

$$\begin{aligned} \omega(E) &\simeq \frac{\pi}{\ln(32/|E_s - E|)}, \\ E_s &= 1, \quad |E_s - E| \ll 1. \end{aligned} \quad (2.15)$$

Let us consider the range of energies below  $E_s$  (the range above  $E_s$  may be considered in an analogous way) and assume that  $\omega_f$  is close to an odd multiple of  $\omega_r^{(-)}$ . The nonlinear resonance dynamics of the slow variables in the range of approximately resonant energies may be described as follows (Soskin et al., 2008a, 2003) (cf. also (Chirikov, 1979; Lichtenberg and Lieberman, 1992; Zaslavsky et al., 1991; Zaslavsky, 2007, 2005; Abdullaev, 2006)):

$$\begin{aligned} \frac{dI}{dt} &= -\frac{\partial \tilde{H}(I, \tilde{\psi})}{\partial \tilde{\psi}}, \quad \frac{d\tilde{\psi}}{dt} = \frac{\partial \tilde{H}(I, \tilde{\psi})}{\partial I}, \\ \tilde{H}(I, \tilde{\psi}) &= \int_{I(E_s)}^I d\tilde{I} (n\omega - \omega_f) - nhq_n \cos(\tilde{\psi}) \\ &\equiv n(E - E_s) - \omega_f(I - I(E_s)) - nhq_n \cos(\tilde{\psi}), \\ I \equiv I(E) &= \int_{E_{\min}}^E \frac{d\tilde{E}}{\omega(\tilde{E})}, \quad E \equiv H_0(p, q), \\ \tilde{\psi} &= n\psi - \omega_f t, \\ \psi &= \pi + \text{sign}(p)\omega(E) \int_{q_{\min}(E)}^q \frac{d\tilde{q}}{\sqrt{2(E - U(\tilde{q}))}} + 2\pi l, \\ q_n \equiv q_n(E) &= \frac{1}{2\pi} \int_0^{2\pi} d\psi q(E, \psi) \cos(n\psi), \\ |n\omega - \omega_f| &\ll \omega, \quad n \equiv 2j - 1, \quad j = 1, 2, 3, \dots, \end{aligned} \quad (2.16)$$

where  $I$  and  $\psi$  are the canonical variables action and angle respectively (Chirikov, 1979; Lichtenberg and Lieberman, 1992; Zaslavsky et al., 1991; Zaslavsky, 2007, 2005; Abdullaev, 2006);  $E_{\min}$  is the minimal energy over all  $q, p$ ,  $E \equiv H_0(p, q)$ ;  $q_{\min}(E)$  is the minimum coordinate of the conservative motion with a given value of energy  $E$ ;  $l$  is the number of right turning points in the trajectory  $[q(\tau)]$  of the conservative motion with energy  $E$  and given initial state  $(q_0, p_0)$ .

The resonance Hamiltonian  $\tilde{H}(I, \tilde{\psi})$  is obtained in the following way. First, the original Hamiltonian  $H$  is transformed to action-angle variables  $I - \psi$ . Then it is multiplied by  $n$  and the term  $\omega_f I$  is extracted (the latter two operations correspond

to the transformation  $\psi \rightarrow \tilde{\psi} \equiv n\psi - \omega_f t$ ). Finally, the result is being averaged over time i.e. only the resonance term in the double Fourier expansion of the perturbation is kept (it may be done since the effect of the fast-oscillating terms on the dynamics of slow variables is small: see the estimate of the corrections in Sect. 2.3.4 below).

Let us derive asymptotic expression for  $I(E)$ , substituting the asymptotic expression (2.15) for  $\omega(E)$  into the definition of  $I(E)$  (2.16) and carrying out the integration:

$$I(E) \simeq I(E_s) - \frac{E_s - E}{\pi} \left( \ln \left( \frac{32}{E_s - E} \right) + 1 \right). \quad (2.17)$$

As for the asymptotic value  $q_n(E \rightarrow E_s)$ , it can be seen that  $q(E \rightarrow E_s, \psi)$ , as a function of  $\psi$ , asymptotically approaches a “square wave”, oscillating between  $-\pi$  and  $\pi$ , so that, for sufficiently small  $j$ ,

$$\begin{aligned} q_{2j-1}(E \rightarrow E_s) &\simeq (-1)^{j+1} \frac{2}{2j-1}; \\ q_{2j} &= 0, \\ j = 1, 2, \dots &\ll \frac{\pi}{2\omega(E)}. \end{aligned} \quad (2.18)$$

The next issue is the analysis of the phase space of the resonant Hamiltonian (2.16). Substituting  $\tilde{H}$  (2.16) into the equations of motion (2.16), it can be seen that their stationary points have the following values of the slow angle

$$\tilde{\psi}_+ = \pi, \quad \tilde{\psi}_- = 0, \quad (2.19)$$

while the corresponding action is determined by the equation

$$n\omega - \omega_f \mp nh \frac{dq_n}{dI} = 0, \quad n \equiv 2j - 1, \quad (2.20)$$

where the sign “ $\mp$ ” corresponds to  $\tilde{\psi}_{\mp}$  (2.19).

The term  $\propto h$  in (2.20) may be neglected to leading-order (cf. (Chirikov, 1979; Lichtenberg and Lieberman, 1992; Zaslavsky et al., 1991; Zaslavsky, 2007, 2005; Abdullaev, 2006; Soskin et al., 2008a, 2003)), and Eq. (2.20) reduces to the resonance condition

$$(2j - 1)\omega(E_r^{(j)}) = \omega_f, \quad (2.21)$$

the lowest-order solution of which is

$$E_s - E_r^{(j)} \simeq 32 \exp \left( - \frac{(2j - 1)\pi}{\omega_f} \right). \quad (2.22)$$

Eqs. (2.19) and (2.22) together with (2.17) explicitly determine the elliptic and hyperbolic points of the Hamiltonian (2.16). The hyperbolic point is often referred to as a “saddle” and corresponds to  $\tilde{\psi}_+$  or  $\tilde{\psi}_-$  in (2.19) for even or odd  $j$  respectively. The saddle point generates the resonance separatrix. Using the asymptotic relations

(2.17) and (2.18), we find that the resonance Hamiltonian (2.16) takes the following asymptotic value in the saddle:

$$\begin{aligned}\tilde{H}_{saddle} &\simeq \frac{E_s - E_r^{(j)}}{\pi} \omega_f - 2h \\ &\simeq \frac{\omega_f}{\pi} 32 \exp\left(-\frac{\pi(2j-1)}{\omega_f}\right) - 2h.\end{aligned}\quad (2.23)$$

The second asymptotic equality in (2.23) takes into account the relation (2.22).

As explained in Sect. 2.2 above,  $\Delta E^{(-)}(\omega_f)$  possesses a local maximum at  $\omega_f$  for which the resonance separatrix is tangent to the lower GSS curve (Fig. 2.1(a)). For the relevant frequency range  $\omega_f \rightarrow 0$ , the separatrix split (which represents the maximum deviation of the energy along the GSS curve from  $E_s$ ) approaches the following value (Zaslavsky et al., 1991) in the asymptotic limit  $h \rightarrow 0$

$$\delta \simeq 2\pi h, \quad \omega_f \ll 1. \quad (2.24)$$

As shown below, the variation of energy along the relevant resonance trajectories is much larger. Therefore, in the leading-order approximation, the GSS curve may simply be replaced by the separatrix of the unperturbed system i.e. by the horizontal line  $E = E_s$  or, equivalently,  $I = I(E_s)$ . Then the tangency occurs at  $\tilde{\psi}$ , shifted from the saddle by  $\pi$ , so that the condition of tangency is written as

$$\tilde{H}_{saddle} = \tilde{H}(I = I(E_s), \tilde{\psi} = \tilde{\psi}_{saddle} + \pi) \equiv 2h. \quad (2.25)$$

Substituting here  $\tilde{H}_{saddle}$  (2.23), we finally obtain the following transcendental equation for  $\omega_{\max}^{(j)}$ :

$$x \exp(x) = \frac{8(2j-1)}{h}, \quad x \equiv \frac{(2j-1)\pi}{\omega_{\max}^{(j)}}. \quad (2.26)$$

Fig. 2.3(b) demonstrates the excellent agreement between Eq. (2.26) and simulations of the Hamiltonian system over a wide range of  $h$ .

In the asymptotic limit  $h \rightarrow 0$ , the lowest-order explicit solution of Eq. (2.26) is

$$\omega_{\max}^{(j)} \simeq \frac{(2j-1)\pi}{\ln\left(\frac{8(2j-1)}{h}\right)}, \quad j = 1, 2, \dots \ll \ln\left(\frac{1}{h}\right). \quad (2.27)$$

As follows from Eq. (2.26), the value of  $E_s - E_r^{(j)}$  (2.22) for  $\omega_f = \omega_{\max}^{(j)}$  is

$$E_s - E_r^{(j)}(\omega_f = \omega_{\max}^{(j)}) = \frac{4\pi h}{\omega_{\max}^{(j)}}. \quad (2.28)$$

Its leading-order expression is:

$$E_s - E_r^{(j)}(\omega_f = \omega_{\max}^{(j)}) \simeq \frac{4h}{2j-1} \ln\left(\frac{8(2j-1)}{h}\right), \quad h \rightarrow 0. \quad (2.29)$$

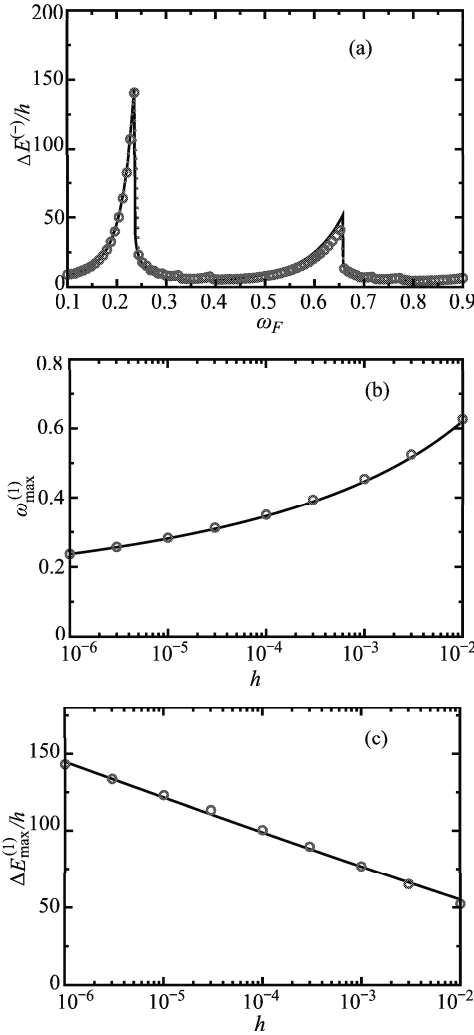


**Fig. 2.3** An archetypal example of a type I system: the ac-driven pendulum (2.14). Comparison of theory (solid lines) and simulations (circles) for: (a) the deviation  $\Delta E^{(-)}(\omega_f)$  of the lower boundary of the chaotic layer from the separatrix, normalized by the perturbation amplitude  $h$ , as a function of the perturbation frequency  $\omega_f$ , for  $h = 10^{-6}$ ; the theory is from Eqs. (2.26), (2.31), (2.32), (2.38), (2.39) and (2.41) (note the discontinuous drop by the factor  $e$  from the maximum to the right wing). (b) The frequency of the 1st maximum in  $\Delta E^{(-)}(\omega_f)$  as a function of  $h$ ; the theory is from Eq. (2.26). (c) The 1st maximum in  $\Delta E^{(-)}(\omega_f)/h$  as a function of  $h$ ; the theory is from Eqs. (2.34) and (2.26).

If  $\omega_f \leq \omega_{\max}^{(j)}$  then, in the chaotic layer, the largest deviation of energy from the separatrix value corresponds to the minimum energy  $E_{\min}^{(j)}$  on the nonlinear resonance separatrix (Fig. 2.1(a,b)), which occurs at  $\tilde{\psi}$  shifted by  $\pi$  from the saddle. The condition of equality of  $\tilde{H}$  at the saddle and at the minimum of the resonance separatrix is written as

$$\tilde{H}_{saddle} = \tilde{H}(I(E_{\min}^{(j)}), \tilde{\psi}_{saddle} + \pi). \quad (2.30)$$

Let us seek its asymptotic solution in the form

$$E_s - E_{\min}^{(j)} \equiv \Delta E_l^{(j)} = (1+y)(E_s - E_r^{(j)}) \simeq (1+y)32 \exp\left(-\frac{\pi(2j-1)}{\omega_f}\right),$$

$$y \gtrsim 1. \quad (2.31)$$

Substituting (2.31) and (2.23) into Eq. (2.30), we obtain for  $y$  the following transcendental equation:

$$(1+y)\ln(1+y) - y = \frac{h}{8(2j-1)} x_f \exp(x_f),$$

$$x_f \equiv \frac{\pi(2j-1)}{\omega_f}, \quad \omega_f \leq \omega_{\max}^{(j)}, \quad y > 0, \quad (2.32)$$

where  $\omega_{\max}^{(j)}$  is given by Eq. (2.26).

Eqs. (2.31) and (2.32) describe the left wing of the  $j$ -th peak of  $\Delta E^{(-)}(\omega_f)$ . Fig. 2.3(a) demonstrates the good agreement between our analytic theory and simulations for the Hamiltonian system.

It follows from Eq. (2.26) that Eq. (2.32) for  $\omega_f = \omega_{\max}^{(j)}$  reduces to the relation  $\ln(1+y) = 1$ , i.e.

$$1 + y(\omega_{\max}^{(j)}) = e. \quad (2.33)$$

It follows from Eqs. (2.33), (2.31) and (2.28) that the maximum for a given peak is:

$$\Delta E_{\max}^{(j)} \equiv E_s - E_{\min}^{(j)}(\omega_{\max}^{(j)}) = \frac{4\pi e h}{\omega_{\max}^{(j)}}. \quad (2.34)$$

Fig. 2.3(c) shows the excellent agreement of this expression with our simulations of the Hamiltonian system over a wide range of  $h$ .

The leading-order expression for  $\Delta E_{\max}^{(j)}$  is:

$$\Delta E_{\max}^{(j)} \simeq \frac{4eh}{2j-1} \ln(8(2j-1)/h), \quad h \rightarrow 0, \quad (2.35)$$

which confirms the rough estimate (2.12).

As  $\omega_f$  decreases, it follows from Eq. (2.32) that  $y$  increases exponentially sharply. In order to understand how  $\Delta E_l^{(j)}$  decreases upon decreasing  $\omega_f$ , it is convenient to rewrite Eq. (2.31) re-expressing the exponent by means of Eq. (2.32):

$$\Delta E_l^{(j)}(\omega_f) = \frac{4\pi h}{\omega_f(\ln(1+y) - y/(1+y))}. \quad (2.36)$$

It follows from Eqs. (2.32) and (2.36) that  $\Delta E_l^{(j)}$  decreases *power-law-like* when  $\omega_f$  is decreased. In particular,  $\Delta E_l^{(j)} \propto 1/(\omega_{\max}^{(j)} - \omega_f)$  at the far part of the wing.

As for the right wing of the peak, i.e. for  $\omega_f > \omega_{\max}^{(j)}$ , over the chaotic layer, the largest deviation of energy from the separatrix value corresponds to the minimum of the resonance trajectory tangent to the GSS curve (Fig. 2.1(c)). The value of  $\tilde{\psi}$  at the minimum coincides with  $\tilde{\psi}_{saddle}$ . In the leading-order approximation, the GSS curve may be replaced by the horizontal line  $I = I(E_s)$ , so that the tangency occurs at  $\tilde{\psi} = \tilde{\psi}_{saddle} + \pi$ . Then the energy at the minimum  $E_{\min}^{(j)}$  can be found from the equation

$$\tilde{H}(I(E_s), \tilde{\psi}_{saddle} + \pi) = \tilde{H}(I(E_{\min}^{(j)}), \tilde{\psi}_{saddle}) \quad (2.37)$$

Let us seek its asymptotic solution in the form

$$E_s - E_{\min}^{(j)} \equiv \Delta E_r^{(j)} = z(E_s - E_r^{(j)}) \simeq 32z \exp\left(-\frac{\pi(2j-1)}{\omega_f}\right) \quad (2.38)$$

$$0 < z < 1, \quad z \sim 1.$$

Substituting (2.38) into (2.37), we obtain for  $z$  the following transcendental equation:

$$z(1 + \ln(1/z)) = \frac{h}{8(2j-1)} x_f \exp(x_f) \quad (2.39)$$

$$x_f \equiv \frac{\pi(2j-1)}{\omega_f}, \quad \omega_f > \omega_{\max}^{(j)}, \quad 0 < z < 1,$$

where  $\omega_{\max}^{(j)}$  is given by Eq. (2.26). Eqs. (2.38) and (2.39) describe the right wing of the  $j$ -th peak of  $\Delta E^{(-)}(\omega_f)$ . Fig. 2.3(a) demonstrates the good agreement between our analytic theory and simulations.

It follows from Eq. (2.26) that the solution of Eq. (2.39) for  $\omega_f \rightarrow \omega_{\max}^{(j)}$  is  $z \rightarrow 1$ , so the right wing starts from the value given by Eq. (2.28) (or, approximately, by Eq. (2.29)). Expressing the exponent in (2.38) from (2.39), we obtain the following equation

$$\Delta E_r^{(j)}(\omega_f) = \frac{4\pi h}{\omega_f(1 + \ln(1/z))}. \quad (2.40)$$

It follows from Eqs. (2.39) and (40) that  $\Delta E_r^{(j)}$  decreases *power-law-like* for increasing  $\omega_f$ . In particular,  $\Delta E_r^{(j)} \propto 1/(\omega_f - \omega_{\max}^{(j)})$  in the far part of the wing. Further analysis of the asymptotic shape of the peak is presented in Sect. 2.3.5 below.

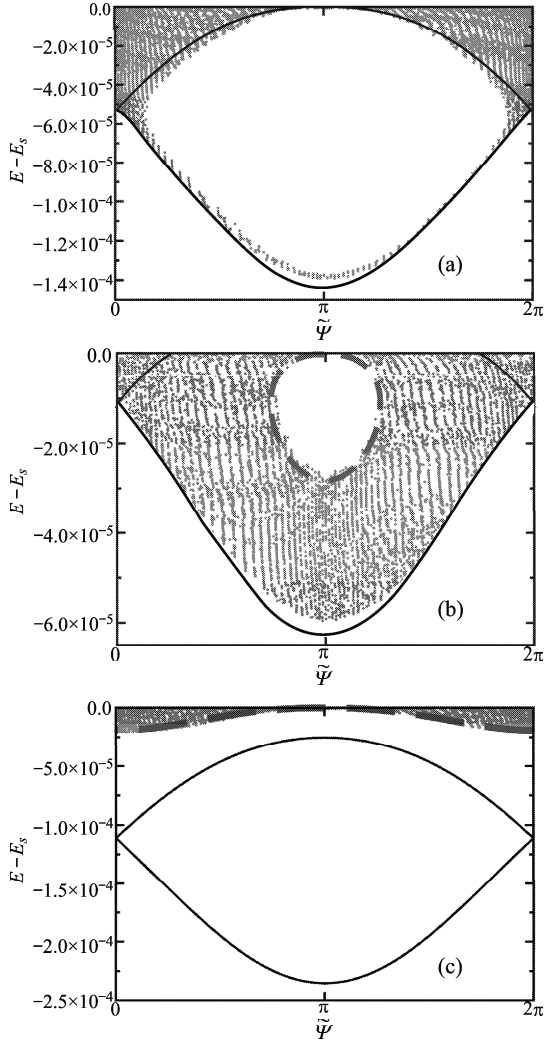


**Fig. 2.4** Some characteristic Poincaré sections in the  $2\pi$ -interval of the energy-angle plane for the system (2.14) with  $h = 10^{-6}$  and  $\omega_f$  equal to: (a) 0.236 (maximum), (b) 0.21 (left wing), (c) 0.25 (right wing). Results of the numerical integration of the equations of motion for the original Hamiltonian (2.14) are shown by (red) dots. The NR separatrix calculated in the leading-order approximation (i.e. by the integration of the resonant equations of motion (2.16) in which  $\omega(E)$ ,  $I(E)$  and  $q_1(E)$  are approximated by the explicit formulæ (2.15), (2.17) and (2.18) respectively) is drawn by the (black) solid line. The NR trajectory (calculated in the leading-order approximation) tangent to the line  $E = E_s$  is drawn by the (blue) dashed line. The outer boundary (marked by a thicker line) is approximated by: the lower part of the NR separatrix in cases (a) and (b), and by the tangent NR trajectory in case (c). The boundary of the island of stability in the cases (a) and (b) is approximated by the tangent NR trajectory (which coincides in the case (a) with the NR separatrix).

Beyond the peaks, the function  $\Delta E^{(-)}(\omega_f)$  is logarithmically small in comparison with the maxima of the peaks. The functions  $\Delta E_l^{(j)}(\omega_f)$  and  $\Delta E_r^{(j)}(\omega_f)$  in the ranges beyond the peaks are also logarithmically small. Hence, nearly any function of  $\Delta E_r^{(j)}(\omega_f)$  and  $\Delta E_l^{(j+1)}(\omega_f)$  which is close to  $\Delta E_r^{(j)}(\omega_f)$  in the vicinity of  $\omega_{\max}^{(j)}$  and to  $\Delta E_l^{(j+1)}(\omega_f)$  in the vicinity of  $\omega_{\max}^{(j+1)}$  while being sufficiently small beyond the peaks may be considered as an approximation of the function  $\Delta E^{(-)}(\omega_f)$  to logarithmic accuracy with respect to the maxima of the peaks,  $\Delta E_{\max}^{(j)}$  and  $\Delta E_{\max}^{(j+1)}$ , in the whole range  $[\omega_{\max}^{(j)}, \omega_{\max}^{(j+1)}]$ . One of the easiest options is the following:

$$\begin{aligned} \Delta E^{(-)}(\omega_f) &= \Delta E_l^{(1)}(\omega_f) && \text{for } \omega_f < \omega_{\max}^{(1)}, \\ \Delta E^{(-)}(\omega_f) &= \max\{\Delta E_r^{(j)}(\omega_f), \Delta E_l^{(j+1)}(\omega_f)\} && \text{for } \omega_{\max}^{(j)} < \omega_f < \omega_{\max}^{(j+1)}, \\ j = 1, 2, \dots &\ll \frac{\pi}{2\omega_{\max}^{(1)}}. && \end{aligned} \quad (2.41)$$

We used this function in Fig. 2.3(a), and the analogous one will also be used in the other cases.

In fact, the theory may be generalized in such a way that Eq. (2.41) would approximate  $\Delta E^{(-)}(\omega_f)$  well in the ranges far beyond the peaks with logarithmic accuracy, even with respect to  $\Delta E^{(-)}(\omega_f)$  itself rather than to  $\Delta E_{\max}^{(j)}$  only (cf. the next section). However, we do not do this in the present case, being interested primarily in the leading-order description of the peaks.

Finally, we demonstrate in Fig. 2.4 that the lowest-order theory describes the boundary of the layers quite well, even in the Poincaré section rather than only in energy/action.

### 2.3.3 Asymptotic theory for systems of type II

We consider two characteristic examples of type II systems, corresponding to the classification given in Sect. 2.3.1. As an example of a system where the separatrix of the unperturbed system possesses a single saddle, we consider an ac-driven Duffing oscillator (Abdullaev, 2006; Gelfreich and Lazutkin, 2001; Piftankin and Treschev, 2007; Soskin et al., 2001). As an example of the system where the separatrix possesses more than one saddle, while the perturbation takes equal values at the saddles, we consider a pendulum with an oscillating suspension point (Abdullaev, 2006; Gelfreich and Lazutkin, 2001; Piftankin and Treschev, 2007; Shevchenko, 1998, 2008). The treatment of these cases is similar in many respects to that presented in Sec. 2.3.2 above. So, we present it in less detail, emphasizing the differences.

### 2.3.3.1 AC-driven Duffing oscillator

Consider the following archetypal Hamiltonian (Abdullaev, 2006; Gelfreich and Lazutkin, 2001; Piftankin and Treschev, 2007; Soskin et al., 2001):

$$H = H_0 + hV, \quad (2.42)$$

$$H_0 = \frac{p^2}{2} - \frac{q^2}{2} + \frac{q^4}{4}, \quad V = -q \cos(\omega_f t), \quad h \ll 1.$$

The asymptotic dependence of  $\omega(E)$  on  $E$  for  $E$  below the separatrix energy  $E_s = 0$  is the following (Abdullaev, 2006; Dykman et al., 1985)

$$\omega(E) \simeq \frac{2\pi}{\ln(16/(E_s - E))}, \quad (2.43)$$

$$E_s = 0, \quad 0 < E_s - E \ll 1.$$

Correspondingly, the resonance values of energies (determined by the condition analogous to (2.21)) are

$$E_s - E_r^{(j)} = 16 \exp\left(-\frac{2\pi j}{\omega_f}\right), \quad j = 1, 2, 3, \dots \quad (2.44)$$

The asymptotic dependence of  $I(E)$  is

$$I(E) \simeq I(E_s) - \frac{E_s - E}{2\pi} \left( \ln\left(\frac{16}{E_s - E}\right) + 1 \right). \quad (2.45)$$

The nonlinear resonance dynamics is described by the resonance Hamiltonian  $\tilde{H}$  which is identical in form to Eq. (2.16). Obviously, the actual dependences  $\omega(E)$  and  $I(E)$  are given by Eq. (2.43) and (2.45) respectively. The most important difference is in  $q_j(E)$ : instead of a non-zero value (see (2.18)), it approaches 0 as  $E \rightarrow E_s$ . Namely, it is  $\propto \omega(E)$  (Abdullaev, 2006; Dykman et al., 1985):

$$q_j(E) \simeq \frac{1}{\sqrt{2}} \omega(E), \quad j = 1, 2, \dots \ll \frac{\pi}{\omega(E)}, \quad (2.46)$$

i.e.  $q_j$  is much smaller than in systems of type I (cf. (2.18)). Due to this, the resonance is “weaker”. At the same time, the separatrix split  $\delta$  is also smaller, namely  $\sim h\omega_f$  (Soskin et al., 2008a) rather than  $\sim h$  as for the systems of type I. That is why the separatrix chaotic layer is still dominated by resonance dynamics while the matching of the separatrix map and nonlinear resonance dynamics is still valid in the asymptotic limit  $h \rightarrow 0$  (Soskin et al., 2008a).

Similarly to the previous section, we find the value of  $\tilde{H}$  in the saddle in the leading-order approximation<sup>6</sup>:

<sup>6</sup> The only essential difference is that  $q_n$  at the saddle is described by Eq. (2.46) rather than by Eq. (2.18).

$$\tilde{H}_{saddle} \simeq \omega_f \left( \frac{E_s - E_r^{(j)}}{2\pi} - \frac{h}{\sqrt{2}} \right), \quad (2.47)$$

where  $E_s - E_r^{(j)}$  is given in (2.44).

As before, the maximum width of the layer corresponds to  $\omega_f$ , for which the resonance separatrix is tangent to the GSS curve (Fig. 2.1(a)). It can be shown (Soskin et al., 2008a) that the angle of tangency asymptotically approaches  $\tilde{\psi}_{saddle} + \pi = \pi$  while the energy still lies in the resonance range. Here  $\omega(E) \approx \omega_r^{(-)} \approx \omega_f/j$ . Using the expressions for  $\tilde{H}(E, \tilde{\psi})$  (cf. (2.16)),  $I(E)$  (2.45),  $q_j(E)$  (2.46), and taking into account that in the tangency  $E < \delta \sim h\omega_f \ll h$ , to leading-order the value of  $\tilde{H}$  at the tangency reads

$$\tilde{H}_{tangency} \simeq \omega_f \frac{h}{\sqrt{2}}. \quad (2.48)$$

Allowing for Eqs. (2.47) and (2.48), the condition for the maximum,  $\tilde{H}_{saddle} = \tilde{H}_{tangency}$ , reduces to

$$E_s - E_r^{(j)}(\omega_{\max}^{(j)}) \simeq 2\pi\sqrt{2}h. \quad (2.49)$$

Thus these values  $E_s - E_r^{(j)}$  are logarithmically smaller than the corresponding values (2.28) for systems of type I.

The values of  $\omega_f$  corresponding to the maxima of the peaks in  $\Delta E^{(-)}(\omega_f)$  are readily obtained from (2.49) and (2.44):

$$\omega_{\max}^{(j)} \simeq \frac{2\pi j}{\ln(4\sqrt{2}/(\pi h))}, \quad j = 1, 2, \dots \ll \ln(1/h). \quad (2.50)$$

The derivation to leading order of the shape of the peaks for the chaotic layer of the separatrix map, i.e. within the nonlinear resonance (NR) approximation, is similar to that for type I. So, we present only the results, marking them with the subscript “NR”.

The left wing of the  $j$ th peak of  $\Delta E_{NR}^{(-)}(\omega_f)$  is described by the function

$$\Delta E_{i,NR}^{(j)}(\omega_f) = 16(1+y) \exp\left(-\frac{2\pi j}{\omega_f}\right) \equiv \frac{2\pi\sqrt{2}h}{\ln(1+y) - y/(1+y)}, \quad (2.51)$$

$$\omega_f \leq \omega_{\max}^{(j)},$$

where  $y$  is the positive solution of the transcendental equation

$$(1+y)\ln(1+y) - y = \frac{\pi h}{4\sqrt{2}} \exp\left(\frac{2\pi j}{\omega_f}\right), \quad y > 0. \quad (2.52)$$

In common with the type I case,  $1 + y(\omega_{\max}^{(j)}) = e$ , so that

$$\Delta E_{\max,NR}^{(j)} = e(E_s - E_r^{(j)}(\omega_{\max}^{(j)})) \simeq 2\pi e\sqrt{2}h. \quad (2.53)$$

Eq. (2.53) confirms the rough estimate (2.13). The right wing of the peak is described by the function

$$\Delta E_{r, NR}^{(j)}(\omega_f) = 16z \exp\left(-\frac{2\pi j}{\omega_f}\right) \equiv \frac{2\pi\sqrt{2}h}{1 + \ln(1/z)}, \quad (2.54)$$

$$\omega_f > \omega_{\max}^{(j)},$$

where  $z < 1$  is the solution of the transcendental equation

$$z(1 + \ln(1/z)) = \frac{\pi h}{4\sqrt{2}} \exp\left(\frac{2\pi j}{\omega_f}\right), \quad 0 < z < 1. \quad (2.55)$$

As in the type I case,  $z(\omega_f \rightarrow \omega_{\max}^{(j)}) \rightarrow 1$ .

It follows from Eqs. (2.49) and (2.53) that the typical variation of energy within the nonlinear resonance dynamics which approximates the separatrix map dynamics is  $\propto h$ . For the Hamiltonian system, the variation of energy in between the discrete instants corresponding to the separatrix map (Zaslavsky et al., 1991; Zaslavsky, 2007, 2005; Abdullaev, 2006; Soskin et al., 2008a; Rom-Kedar, 1990) is also  $\propto h$ . Therefore, unlike the type I case, one needs to take it into account even at the leading-order approximation. Let us consider the right well of the Duffing potential (the results for the left well are identical), and denote by  $t_k$  the instant at which the energy  $E$  at a given  $k$ -th step of the separatrix map is taken: it corresponds to the beginning of the  $k$ -th pulse of velocity (Zaslavsky et al., 1991; Soskin et al., 2008a) i.e. the corresponding  $q$  is close to a left turning point  $q_{lp}$  in the trajectory  $[q(\tau)]$ . Let us also take into account that the relevant frequencies are small so that the adiabatic approximation may be used. Thus, the change of energy from  $t_k$  up to a given instant  $t$  during the following pulse of velocity ( $t - t_k \sim 1$ ) may be calculated as

$$\begin{aligned} \Delta E &= \int_{t_k}^t d\tau \dot{q} h \cos(\omega_f \tau) \simeq h \cos(\omega_f t_k) \int_{t_k}^t d\tau \dot{q} \\ &= h \cos(\omega_f t_k) (q(t) - q_{lp}) \end{aligned} \quad (2.56)$$

For the motion near the separatrix, the velocity pulse corresponds approximately to  $\psi = 0$  (see the definition of  $\psi$  in Eq. (2.16)). Thus, the corresponding slow angle is  $\tilde{\psi} \equiv j\psi - \omega_f t_k \simeq -\omega_f t_k$ .

For the left wing of the peak of  $\Delta E^{(-)}(\omega_f)$  (including also the maximum of the peak), the boundary of the chaotic layer of the separatrix map is formed by the lower part of the NR separatrix. The minimum energy along this separatrix occurs at  $\tilde{\psi} = \pi$ . Taking this into account, and also noting that  $\tilde{\psi} \simeq -\omega_f t_k$ , we conclude that  $\cos(\omega_f t_k) \simeq -1$ . So,  $\Delta E \leq 0$ , i.e. it does lower the minimum energy of the layer of the Hamiltonian system. The maximum reduction occurs at the right turning point  $q_{rp}$ :

$$\max(|\Delta E|) \simeq h(q_{rp} - q_{lp}) = \sqrt{2}h. \quad (2.57)$$

We conclude that the left wing of the  $j$ -th peak is described as follows:

$$\Delta E_l^{(j)}(\omega_f) \simeq \Delta E_{l, NR}^{(j)}(\omega_f) + \sqrt{2}h, \quad \omega_f \leq \omega_{\max}^{(j)}, \quad (2.58)$$

where  $\Delta E_{l, NR}^{(j)}(\omega_f)$  is given by Eqs. (2.51) and (2.52). In particular, the maximum of the peak is:

$$\Delta E_{\max}^{(j)} \simeq (2\pi e + 1)\sqrt{2}h \approx 25.6h. \quad (2.59)$$

For the right wing of the peak, the minimum energy of the layer of the separatrix map occurs when  $\tilde{\psi}$  coincides with  $\tilde{\psi}_{saddle}$  (Fig. 2.1(c)) i.e. is equal to 0. As a result,  $\cos(\omega_f t_k) \simeq 1$  and, hence,  $\Delta E \geq 0$ . So, this variation cannot lower the minimum energy of the layer for the main part of the wing, i.e. for  $\omega_f \leq \omega_{bend}^{(j)}$  where  $\omega_{bend}^{(j)}$  is defined by the condition  $\Delta E_{r, NR}^{(j)} = \max(|\Delta E|) \equiv \sqrt{2}h$ . For  $\omega_f > \omega_{bend}^{(j)}$ , the minimal energy in the layer occurs at  $\tilde{\psi} = \pi$ , and it is determined exclusively by the variation of energy during the velocity pulse (the NR contribution is close to zero at such  $\tilde{\psi}$ ). Thus, we conclude that there is a bending of the wing at  $\omega_f = \omega_{bend}^{(j)}$ :

$$\begin{aligned} \Delta E_r^{(j)}(\omega_f) &= \Delta E_{r, NR}^{(j)}(\omega_f), & \omega_{\max}^{(j)} < \omega_f \leq \omega_{bend}^{(j)}, \\ \Delta E_r^{(j)}(\omega_f) &= \sqrt{2}h, & \omega_f \geq \omega_{bend}^{(j)}, \\ \omega_{bend}^{(j)} &= \frac{2\pi j}{\ln(8\sqrt{2}/h) + 1 - 2\pi}, \end{aligned} \quad (2.60)$$

where  $\Delta E_{r, NR}^{(j)}(\omega_f)$  is given by Eqs. (2.54) and (2.55).

Analogously to the previous case,  $\Delta E^{(-)}(\omega_f)$  may be approximated over the whole frequency range by Eq. (2.41) with  $\Delta E_l^{(j)}$  and  $\Delta E_r^{(j)}$  given by Eqs. (2.58) and (2.60) respectively. Moreover, unlike the previous case, the theory also describes accurately the range far beyond the peaks:  $\Delta E^{(-)}$  is dominated in this range by the velocity pulse contribution  $\Delta E$ , which is accurately taken into account both by Eqs. (2.58) and (2.60).

Fig. 2.5 shows very reasonable agreement between the theory and simulations, especially for the 1st peak<sup>7</sup>.

---

<sup>7</sup> The disagreement between theory and simulations for the magnitude of the 2nd peak is about three times larger than that for the 1st peak, so that the height of the 2nd peak is about 30% smaller than that calculated from the asymptotic theory. This occurs because, for the energies relevant to the 2nd peak, the deviation from the separatrix is much higher than that for the 1st peak. Due to the latter, the Fourier coefficient  $q_2(E)$  for the relevant  $E$  is significantly smaller than that obtained from the asymptotic formula (2.42). In addition, the velocity pulse contribution  $\Delta E$  also significantly decreases while the separatrix split increases as  $\omega_f$  becomes  $\sim 1$ .

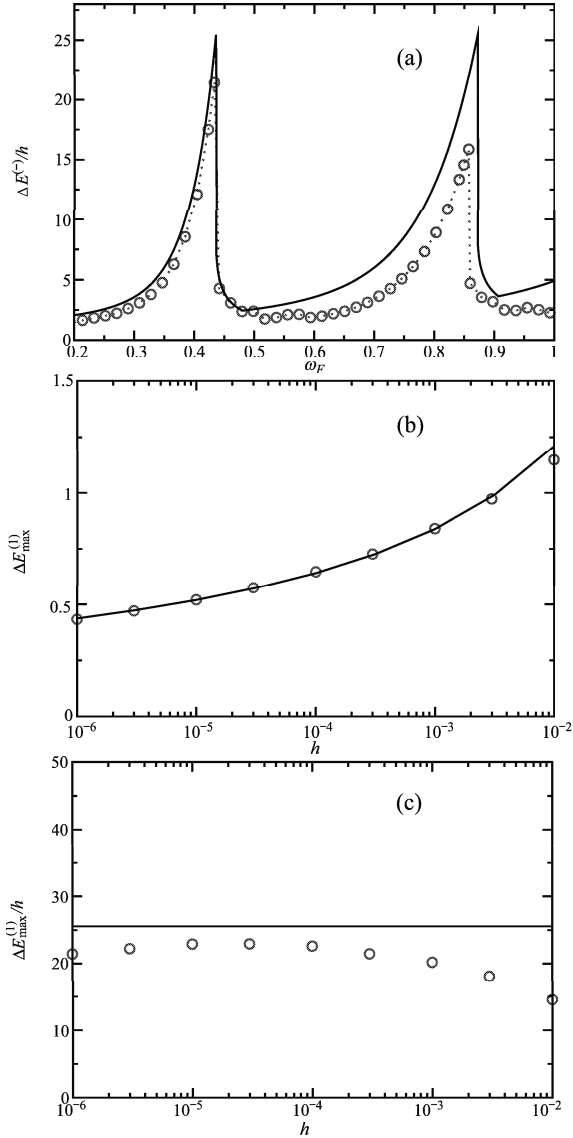


**Fig. 2.5** An archetypal example of a type II system: the ac driven Duffing oscillator (2.42). Comparison of theory (solid lines) and simulations (circles): (a) the deviation  $\Delta E^{(-)}(\omega_f)$  of the lower boundary of the chaotic layer from the separatrix, normalized by the perturbation amplitude  $h$ , as a function of the perturbation frequency  $\omega_f$ , for  $h = 10^{-6}$ ; the theory is from Eqs. (2.41), (2.50), (2.51), (2.52), (2.54), (2.55), (2.58) and (2.60) (note the discontinuous drop from the maximum to the right wing); (b) the frequency of the 1st maximum in  $\Delta E^{(-)}(\omega_f)$  as a function of  $h$ ; the theory is from Eq. (2.50); (c) the 1st maximum in  $\Delta E^{(-)}(\omega_f)/h$  as a function of  $h$ ; the theory is from Eq. (2.59).

### 2.3.3.2 Pendulum with an oscillating suspension point

Consider the archetypal Hamiltonian (Abdullaev, 2006; Gelfreich and Lazutkin, 2001; Piftankin and Treschev, 2007; Shevchenko, 1998, 2008)

$$H = H_0 + hV, \quad (2.61)$$

$$H_0 = \frac{p^2}{2} + \cos(q), \quad V = -\cos(q)\cos(\omega_f t), \quad h \ll 1.$$

Though the treatment is similar to that used in the previous case, there are also characteristic differences. One of them is the following: although the resonance Hamiltonian is similar to the Hamiltonian (2.16), instead of the Fourier component of the coordinate,  $q_n$ , there should be the Fourier component of  $\cos(q)$ ,  $V_n$ , which can be shown as:

$$V_{2j} \simeq (-1)^{j+1} \frac{4}{\pi} \omega(E), \quad E_s - E \ll 1, \quad (2.62)$$

$$V_{2j-1} = 0,$$

$$j = 1, 2, \dots \ll \frac{2\pi}{\omega(E)}, \quad V_n \equiv \frac{1}{2\pi} \int_0^{2\pi} d\psi \cos(q) \cos(n\psi).$$

The description of the chaotic layer of the separatrix map at the lowest order, i.e. within the NR approximation, is similar to that for the ac-driven Duffing oscillator. So we present only the results, marking them with the subscript “NR”.

The frequency of the maximum of a given  $j$ -th peak is:

$$\omega_{\max}^{(j)} \simeq \frac{2\pi j}{\ln(4/h)}, \quad j = 1, 2, \dots \ll \ln(4/h). \quad (2.63)$$

This expression agrees well with simulations for the Hamiltonian system as shown in Fig. 2.6(b). To logarithmic accuracy, Eq. (2.63) coincides with the formula following from Eq. (2.8) of (Shevchenko, 1998) reproduced in (Shevchenko, 2008) as Eq. (2.21) taken in the asymptotic limit  $h \rightarrow 0$  (or, equivalently,  $\omega_{\max}^{(j)} \rightarrow 0$ ). However, the numerical factor in the argument of the logarithm in the asymptotic formula following from the result of (Shevchenko, 1998, 2008) is half our value: this is because the nonlinear resonance is approximated in (Shevchenko, 1998, 2008) by the conventional pendulum model which is not valid near the separatrix (cf. our Sect. 2.3.1 above).

The left wing of the  $j$ th peak of  $\Delta E_{NR}^{(-)}(\omega_f)$  is described by the function

$$\Delta E_{I, NR}^{(j)}(\omega_f) = 32(1+y) \exp\left(-\frac{2\pi j}{\omega_f}\right) \equiv \frac{8h}{\ln(1+y) - y/(1+y)}, \quad (2.64)$$

$$\omega_f \leq \omega_{\max}^{(j)},$$

where  $y$  is the positive solution of the transcendental equation

$$(1+y)\ln(1+y) - y = \frac{h}{4} \exp\left(\frac{2\pi j}{\omega_f}\right), \quad y > 0. \quad (2.65)$$

Similarly to the previous cases,  $1 + y(\omega_{\max}^{(j)}) = e$ . Hence,

$$\Delta E_{\max, NR}^{(j)} = e(E_s - E_r^{(j)}(\omega_{\max}^{(j)})) = 8eh. \quad (2.66)$$

Eq. (2.66) confirms the rough estimate (2.13). The right wing of the peak is described by the function

$$\Delta E_{r, NR}^{(j)}(\omega_f) = 32z \exp\left(-\frac{2\pi j}{\omega_f}\right) \equiv \frac{8h}{1 + \ln(1/z)}, \quad (2.67)$$

$$\omega_f > \omega_{\max}^{(j)},$$

where  $z < 1$  is the solution of the transcendental equation

$$z(1 + \ln(1/z)) = \frac{h}{4} \exp\left(\frac{2\pi j}{\omega_f}\right), \quad 0 < z < 1. \quad (2.68)$$

Similarly to the previous cases,  $z(\omega_f \rightarrow \omega_{\max}^{(j)}) \rightarrow 1$ .

Now consider the variation of energy during a velocity pulse. Though the final result looks quite similar to the case with a single saddle, its derivation has some characteristic differences, and we present it in detail. Unlike the case with a single saddle, the pulse may start close to either the left or the right turning point, and the sign of the velocity in such pulses is opposite (Zaslavsky et al., 1991; Soskin et al., 2008a). The angle  $\psi$  in the pulse is close to  $-\pi/2$  or  $\pi/2$  respectively. So, let us calculate the change of energy from the beginning of the pulse,  $t_k$ , until a given instant  $t$  within the pulse:

$$\begin{aligned} \Delta E &= - \int_{t_k}^t d\tau \dot{q} h \partial V / \partial q = h \int_{t_k}^t d\tau \dot{q} (-\sin(q) \cos(\omega_f \tau)) \\ &\simeq h \cos(\omega_f t_k) \int_{t_k}^t d\tau \dot{q} (-\sin(q)) \simeq h \cos(\omega_f t_k) (\cos(q(t)) - 1). \end{aligned} \quad (2.69)$$

Here, the third equality assumes adiabaticity while the last equality takes into account that the turning points are close to the maxima of the potential i.e. close to a multiple of  $2\pi$ , where the cosine is equal to 1.

The quantity  $\Delta E$  (2.69) takes its maximal absolute value at  $q = \pi$ . So, we shall further consider

$$\Delta E_{\max} = -2h \cos(\omega_f t_k) \equiv -2h \cos(2j\psi_k - \tilde{\psi}_k) = (-1)^{j+1} 2h \cos(\tilde{\psi}_k). \quad (2.70)$$

The last equality takes into account that, as mentioned above, the relevant  $\psi_k$  is either  $-\pi/2$  or  $\pi/2$ . For the left wing, the value of  $\tilde{\psi}$  at which the chaotic layer of

the separatrix map possesses a minimal energy corresponds to the minimum of the resonance separatrix. It is equal to  $\pi$  or 0 if the Fourier coefficient  $V_{2j}$  is positive or negative, i.e. for odd or even  $j$ , respectively: see Eq. (2.63). Thus  $\Delta E_{\max} = -2h$  for any  $j$  and, therefore, it does lower the minimal energy of the boundary. We conclude that

$$\Delta E_l^{(j)}(\omega_f) \simeq \Delta E_{l,NR}^{(j)}(\omega_f) + 2h, \quad \omega_f \leq \omega_{\max}^{(j)}, \quad (2.71)$$

where  $\Delta E_{l,NR}^{(j)}(\omega_f)$  is given by Eqs. (2.64) and (2.65). In particular, the maximum of the peak is:

$$\Delta E_{\max}^{(j)} \simeq (4e + 1)2h \approx 23.7h. \quad (2.72)$$

The expression (2.72) confirms the rough estimate (2.13) and agrees well with simulations shown in Fig. 2.6(c). At the same time, it differs from the formula which can be obtained from Eq. (2.10) of (Shevchenko, 1998) (using also Eqs. (1), (3), (8), (9) of (Shevchenko, 1998)) in the asymptotic limit  $h \rightarrow 0$ : the latter gives for  $\Delta E_{\max}^{(j)}$  the asymptotic value  $32h$ . Though this result (Shevchenko, 1998) (referred to also in (Shevchenko, 2008)) provides for the correct functional dependence on  $h$ , it is quantitatively incorrect because (i) it is based on the pendulum approximation of the nonlinear resonance while this approximation is invalid in the vicinity of the separatrix (see the discussion of this issue in Sect. 2.3.1 above), and (ii) it does not take into account the variation of energy during the velocity pulse.

The right wing, by analogy to the case of the Duffing oscillator, possesses a bend at  $\omega_f = \omega_{\text{bend}}^{(j)}$  where  $\Delta E_{r,NR}^{(j)} = |\Delta E_{\max}| \equiv 2h$ , corresponding to the shift of the relevant  $\tilde{\psi}$  for  $\pi$ . We conclude that:

$$\begin{aligned} \Delta E_r^{(j)}(\omega_f) &= \Delta E_{r,NR}^{(j)}(\omega_f), & \omega_{\max}^{(j)} < \omega_f \leq \omega_{\text{bend}}^{(j)}, \\ \Delta E_r^{(j)}(\omega_f) &= 2h, & \omega_f \geq \omega_{\text{bend}}^{(j)}, \\ \omega_{\text{bend}}^{(j)} &= \frac{2\pi j}{\ln(16/h) - 3}, \end{aligned} \quad (2.73)$$

where  $\Delta E_{r,NR}^{(j)}(\omega_f)$  is given by Eqs. (2.66) and (2.67).

Similarly to the previous case, both the peaks and the frequency ranges far beyond the peaks are well approximated by Eq. (2.41), with  $\Delta E_l^{(j)}$  and  $\Delta E_r^{(j)}$  given by Eqs. (2.71) and (2.73) respectively (Fig. 2.6(a)).

### 2.3.4 Estimate of the next-order corrections

We have calculated explicitly only the leading term  $\Delta E$  in the asymptotic expansion of the chaotic layer width. Explicit calculation of the next-order term  $\Delta E^{(next)}$  is possible, but it is rather complicated and cumbersome: cf. the closely related case

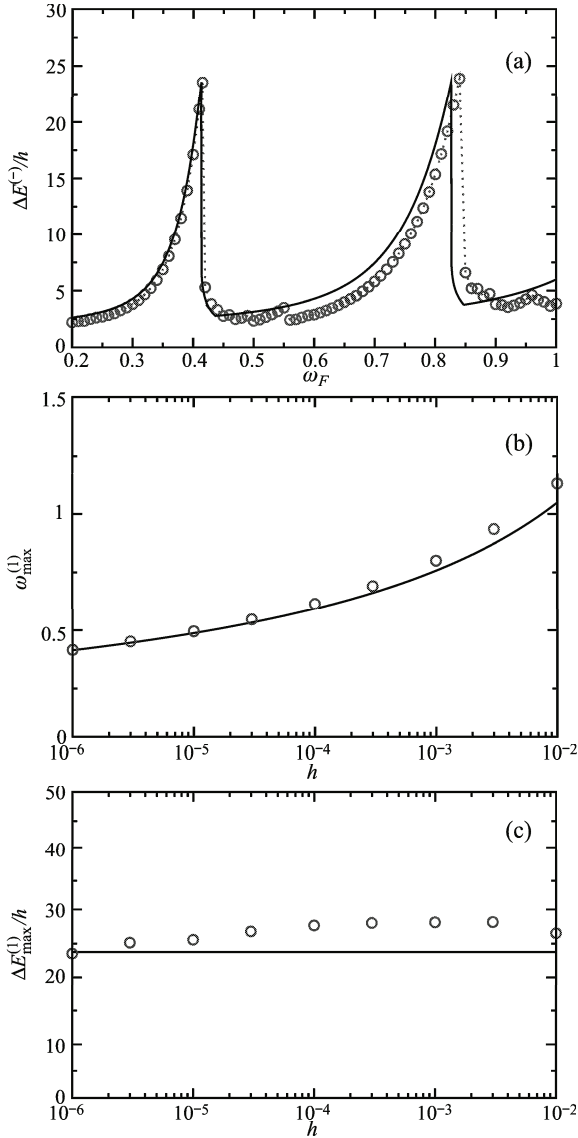


**Fig. 2.6** An archetypal example of a type II system: the pendulum with an oscillating suspension point (2.61). Comparison of theory (solid lines) and simulations (circles): (a) The deviation  $\Delta E^{(-)}(\omega_f)$  of the lower boundary of the chaotic layer from the separatrix, normalized by the perturbation amplitude  $h$ , as a function of the perturbation frequency  $\omega_f$ , for  $h = 10^{-6}$ ; the theory is by Eqs. (2.41), (2.63), (2.64), (2.65), (2.67), (2.68), (2.71) and (2.73) (note the discontinuous drop from the maximum to the right wing). (b) The frequency of the 1st maximum in  $\Delta E^{(-)}(\omega_f)$  as a function of  $h$ ; the theory is from Eq. (2.63). (c) The 1st maximum in  $\Delta E^{(-)}(\omega_f)/h$  as a function of  $h$ ; the theory is from Eq. (2.72).

with two separatrices (Soskin et al., 2008a) (see also Sect. 2.4 below). In the present section, where the perturbation amplitude  $h$  in the numerical examples is 4 orders of magnitude smaller than that in (Soskin et al., 2008a), there is no particular need to calculate the next-order correction quantitatively. Let us estimate it, however, in order to demonstrate that its ratio to the leading term does vanish in the asymptotic limit  $h \rightarrow 0$ .

We shall consider separately the contribution  $\Delta E_w^{(next)}$  stemming from the various corrections *within* the resonance approximation (2.16) and the contribution  $\Delta E_t^{(next)}$  stemming from the corrections *to* the resonance approximation.

The former contribution may be estimated in a similar way to the case considered in (Soskin et al., 2008a): it stems, in particular, from the deviation of the GSS curve from the separatrix (this deviation reaches  $\delta$  at certain angles: see Eq. (2.7)) and from the difference between the exact resonance condition (2.20) and the approximate one (2.21). It can be shown that the absolute value of the ratio between  $\Delta E_w^{(next)}$  and the leading term is logarithmically small (cf. (Soskin et al., 2008a)):

$$\frac{|\Delta E_w^{(next)}|}{\Delta E} \sim \frac{1}{\ln(1/h)}. \quad (2.74)$$

Let us turn to the analysis of the contribution  $\Delta E_t^{(next)}$ , i.e. the contribution stemming from the corrections to the resonance Hamiltonian (2.16). It is convenient to consider separately the cases of the left and right wings of the peak.

As described in Sects. 2.3.2 and 2.3.3 above, the left wing corresponds in the leading-order approximation to formation of the boundary of the layer by the *separatrix* of the resonance Hamiltonian (2.16). The resonance approximation (2.16) neglects time-periodic terms while the frequencies of oscillation of these terms greatly exceed the frequency of eigenoscillation of the resonance Hamiltonian (2.16) around its relevant elliptic point i.e. the elliptic point inside the area limited by the resonance separatrix. As is well known (Gelfreich and Lazutkin, 2001; Lichtenberg and Lieberman, 1992; Piftankin and Treschev, 2007; Zaslavsky, 2007, 2005; Zaslavsky et al., 1991), fast-oscillating terms acting on a system with a separatrix give rise to the onset of an *exponentially narrow* chaotic layer in place of the separatrix. In the present context, this means that the correction to the minimal action  $\tilde{I}$  stemming from fast-oscillating corrections to the resonance Hamiltonian, i.e.  $\Delta E_t^{(next)}$ , is *exponentially small*, thus being negligible in comparison with the correction  $\Delta E_w^{(next)}$  (see (2.74)).

The right wing, described in Sects. 2.3.2 and 2.3.3 above, corresponds in leading-order approximation to the formation of the boundary of the layer by the resonance trajectory *tangent* to the GSS curve. For the part of the right wing exponentially close in frequency to the frequency of the maximum, the tangent trajectory is close to the resonance separatrix, so that the correction stemming from fast-oscillating terms is exponentially small, similarly to the case of the left wing. As the frequency further deviates from the frequency of the maximum, the tangent trajectory further deviates from the resonance separatrix and the correction  $\Delta E_t^{(next)}$  differs from the

exponentially small correction estimated above. It may be estimated in the following way.

It follows from the second-order approximation of the averaging method (Bogolyubov and Mitropolsky, 1961) that the fast-oscillating terms lead, in the second-order approximation, to the onset of additional terms  $h^2 T_{\tilde{I}}(\tilde{I}, \tilde{\psi})$  and  $h^2 T_{\tilde{\psi}}(\tilde{I}, \tilde{\psi})$  in the dynamic equations for slow variables  $\tilde{I}$  and  $\tilde{\psi}$  respectively, where  $T_{\tilde{I}}(\tilde{I}, \tilde{\psi})$  and  $T_{\tilde{\psi}}(\tilde{I}, \tilde{\psi})$  are of the order of the power-law-like function of  $1/\ln(1/h)$  in the relevant range of  $\tilde{I}$ . The corresponding correction to the width of the chaotic layer in energy may be expressed as

$$\Delta E_t^{(next)} = \int_{t_{\min}}^{t_{\max}} dt h^2 T_{\tilde{I}} \omega(\tilde{I}), \quad (2.75)$$

where  $t_{\min}$  and  $t_{\max}$  are instants corresponding to the minimum and maximum deviation of the tangent trajectory from the separatrix of the unperturbed system (cf. Figs. 2.1(c) and 2.4(c)). The interval  $t_{\max} - t_{\min}$  may be estimated as follows:

$$t_{\max} - t_{\min} \sim \frac{\pi}{|\langle \dot{\tilde{\psi}} \rangle|}, \quad (2.76)$$

where  $\langle \dot{\tilde{\psi}} \rangle$  is the value of  $\dot{\tilde{\psi}}$  averaged over the tangent trajectory. It follows from (2.16) that

$$|\langle \dot{\tilde{\psi}} \rangle| \sim \omega_f - \omega(E_s - \delta) \sim \frac{\omega(E_s - \delta)}{\ln(1/h)} \sim \frac{\omega_0}{\ln^2(1/h)}. \quad (2.77)$$

Taking together Eqs. (2.75)–(2.77) and allowing for the fact that  $T_{\tilde{I}}$  is of the order of a power-law-like function of  $1/\ln(1/h)$ , we conclude that

$$\Delta E_t^{(next)} \sim h^2 P(\ln(1/h)), \quad (2.78)$$

where  $P(x)$  is some power-law-like function.

The value  $\Delta E_t^{(next)}$  is still asymptotically smaller than the absolute value of the correction within the resonance approximation,  $|\Delta E_w^{(next)}|$ , which is of the order of  $h$  or  $h/\ln(1/h)$  for systems of type I or type II respectively.

Thus, we conclude that, both for the left and right wings of the peak, (i) the correction  $\Delta E_t^{(next)}$  is determined by the correction within the resonance approximation  $\Delta E_w^{(next)}$ , and (ii) in the asymptotic limit  $h \rightarrow 0$ , the overall next-order correction is negligible in comparison with the leading term:

$$\frac{|\Delta E^{(next)}|}{\Delta E} \equiv \frac{|\Delta E_w^{(next)} + \Delta E_t^{(next)}|}{\Delta E} \approx \frac{|\Delta E_w^{(next)}|}{\Delta E} \sim \frac{1}{\ln(1/h)} \xrightarrow{h \rightarrow 0} 0. \quad (2.79)$$

This estimate well agrees with results in Figs. 2.3–2.6.

### 2.3.5 Discussion

In this section, we briefly discuss the following issues: (i) the *scaled* asymptotic shape of the peaks; (ii) peaks in the range of *moderate* frequencies; (iii) *jumps* in the amplitude dependence of the layer width; (iv) chaotic *transport*; (v) smaller peaks at *rational* frequencies; (vi) other separatrix maps; and (vii) an application to the onset of *global chaos*.

1. Let us analyse the scaled asymptotic shape of the peaks. We consider first systems of type I. The peaks are then described in the leading-order approximation exclusively within separatrix map dynamics (approximated, in turn, by the NR dynamics). It follows from Eqs. (2.32), (2.34), (2.36), (2.39) and (2.40) that most of the peak for given  $j$  can be written in the universal scaled form:

$$\Delta E^{(j)}(\omega_f) = \Delta E_{\max}^{(j)} S \left( \frac{\pi(2j-1)}{(\omega_{\max}^{(j)})^2} (\omega_f - \omega_{\max}^{(j)}) \right), \quad (2.80)$$

where the universal function  $S(\alpha)$  is strongly asymmetric:

$$S(\alpha) = \begin{cases} S_l(\alpha) & \text{for } \alpha \leq 0, \\ S_r(\alpha) & \text{for } \alpha > 0, \end{cases}$$

$$S_l(\alpha) = \frac{1}{e(\ln(1+y) - y/(1+y))}, \quad (1+y)\ln(1+y) - y = \exp(-\alpha), \quad (2.81)$$

$$S_r(\alpha) = \frac{1}{e(1 + \ln(1/z))}, \quad z(1 + \ln(1/z)) = \exp(-\alpha).$$

It is not difficult to show that

$$S_l(\alpha = 0) = 1, \quad S_r(\alpha \rightarrow +0) = e^{-1},$$

$$\frac{dS_l(\alpha = 0)}{d\alpha} = 1 - e^{-1}, \quad \frac{dS_r(\alpha \rightarrow +0)}{d\alpha} \rightarrow -\infty, \quad (2.82)$$

$$S(\alpha \rightarrow \pm\infty) \propto \frac{1}{|\alpha|}.$$

Thus, the function  $S(\alpha)$  is discontinuous at the maximum. To the left of the maximum, it approaches the far part of the wing (which decreases in a power-law-like way) relatively *slowly* while, to the right of the maximum, the function first drops *jump-wise* by a factor  $e$  and then *sharply* approaches the far part of the wing (which again decreases in a power-law-like way).

It follows from Eqs. (2.80), (2.81), (2.82) and (2.27) that the peaks are logarithmically narrow, i.e. the ratio of the half-width of the peak,  $\Delta \omega^{(j)}$ , to  $\omega_{\max}^{(j)}$  is logarithmically small:

$$\frac{\Delta \omega^{(j)}}{\omega_{\max}^{(j)}} \sim \frac{1}{\ln(8(2j-1)/h)}. \quad (2.83)$$

We emphasize that the shape (2.81) is not restricted to the example (2.14): it is valid for any system of type I.

For systems of type II, contributions from the NR and from the variation of energy during the pulse of velocity, in relation to their  $h$  dependence, are formally of the same order but, numerically, the latter contribution is usually much smaller than the former. Thus, typically, the function (2.81) approximates well the properly scaled shape of the major part of the peak for systems of type II too.

2. The quantitative theory presented in the paper relates only to the peaks of *small* order  $n$  i.e. in the range of logarithmically small frequencies. At the same time, the magnitude of the peaks is still significant up to frequencies of order of one. This occurs because, for motion close to the separatrix, the order of magnitude of the Fourier coefficients remains the same up to logarithmically large numbers  $n$ . The shape of the peaks remains the same but their magnitude typically decreases (though in some cases, e.g. in case of the wave-like perturbation (Lichtenberg and Lieberman, 1992; Zaslavsky, 2007, 2005; Zaslavsky et al., 1991) it may even increase in some range of frequencies). The quantitative description of this decrease, together with analyses of more sophisticated cases, requires a generalization of our theory.

3. Apart from the frequency dependence of the layer width, our theory is also relevant to amplitude dependence: it describes the jumps (Soskin et al., 2001) in the dependence of the width on  $h$  and the transition between the jumps and the linear dependence. The values of  $h$  at which the jumps occur,  $h_{jump}^{(j)}$ , are determined by the same condition that determines  $\omega_{max}^{(j)}$  in the frequency dependence of the width. The formulae relevant to the left wings of the peaks in the frequency dependence describe the ranges  $h > h_{jump}^{(j)}$  while the formulae relevant to the right wings describe the ranges  $h < h_{jump}^{(j)}$ .

4. Apart from the description of the boundaries, the approach allows us to describe *chaotic transport* within the layer. In particular, it allows us to describe quantitatively the effect of the stickiness of the chaotic trajectory to boundaries between the chaotic and regular areas of the phase space (Zaslavsky, 2007, 2005). Moreover, the presence of additional (resonance) saddles should give rise to an additional slowing down of the transport, despite a widening of the area of the phase space involved in the chaotic transport.

5. Our approach can be generalized in order to describe smaller peaks at non-integer rational frequencies i.e.  $\omega_f \approx n/m\omega_r^{(\pm)}$  where  $n$  and  $m$  are integer numbers.

6. Apart from Hamiltonian systems of the one and a half degrees of freedom and corresponding Zaslavsky separatrix maps, our approach may be useful in the treatment of other chaotic systems and separatrix maps (see (Piftankin and Treschev, 2007) for the most recent major review on various types of separatrix maps and related continuous chaotic systems).

7. Finally we note that, apart from systems with a separatrix, our work may be relevant to *nonlinear resonances* in any system. If the system is perturbed by a weak time-periodic perturbation, then nonlinear resonances arise and their dynamics is described by the model of the auxiliary time-periodically perturbed pendu-

lum (Chirikov, 1979; Lichtenberg and Lieberman, 1992; Zaslavsky et al., 1991; Zaslavsky, 2007, 2005; Abdullaev, 2006; Gelfreich and Lazutkin, 2001). If the original perturbation has a single harmonic, then the effective perturbation of the auxiliary pendulum is necessarily a high-frequency one, and chaotic layers associated with the resonances are exponentially narrow (Chirikov, 1979; Lichtenberg and Lieberman, 1992; Zaslavsky et al., 1991; Zaslavsky, 2007, 2005; Abdullaev, 2006; Gelfreich and Lazutkin, 2001) while our results are irrelevant. But, if either the amplitude or the angle of the original perturbation is slowly modulated, or if there is an additional harmonic of a slightly shifted frequency, then the effective perturbation of the auxiliary pendulum is a low-frequency one (Soskin et al., 2008a) and the layers become much wider<sup>8</sup> while our theoretical approach becomes relevant. It may allow to find optimal parameters of the perturbation for the facilitation of the onset of global chaos associated with the overlap in energy between different-order nonlinear resonances (Chirikov, 1979): the overlap may be expected to occur at a much smaller amplitude of perturbation in comparison with that one required for the overlap in case of a single-harmonic perturbation.

## 2.4 Double-separatrix chaos

There are many problems in physics where an unperturbed Hamiltonian model possesses two or more separatrices. A weak perturbation of the system typically destroys the separatrices, replacing them by thin chaotic layers. As the magnitude of the perturbation grows, the layers become wider and, at some critical value, they merge with each other: this may be described as the onset of *global chaos* between the separatrices. Such a connection of regions of different separatrices is important for transport in the system.

In the present section, following the paper (Soskin et al., 2008a), we consider the characteristic problem of the onset of global chaos between two close separatrices of a 1D Hamiltonian system perturbed by a time-periodic perturbation. As a characteristic example of a Hamiltonian system with two or more separatrices, we use a spatially periodic potential system with two different-height barriers per period shown in Fig. 72.(a):

$$H_0(p, q) = \frac{p^2}{2} + U(q), \quad U(q) = \frac{(\Phi - \sin(q))^2}{2}, \quad \Phi = \text{const} < 1. \quad (2.84)$$

This model may relate e.g. to a pendulum spinning about its vertical axis (Andronov et al., 1966) or to a classical 2D electron gas in a magnetic field spatially periodic in one of the in-plane dimensions (Yevtushenko and Richter, 1998, 1999).

---

<sup>8</sup> This should not be confused with the widening occurring with the separatrix chaotic layer in the *original* pendulum if an originally single-harmonic perturbation of a high frequency is completed by one more harmonic of a slightly shifted frequency: see (Vechev, 2004) and references therein.

Interest in the latter system arose in the 1990s due to technological advances allowing to manufacture magnetic superlattices of high-quality (Carmona et al., 1995; Ye et al., 1995), and thus leading to a variety of interesting behaviours of the charge carriers in semiconductors (Yevtushenko and Richter, 1998, 1999; Carmona et al., 1995; Ye et al., 1995; Schmidt, 1993; Schmelcher and Shepelyansky, 1994).

Figs. 2.7(b) and 2.7(c) show respectively the separatrices of the Hamiltonian system (2.1) in the  $p-q$  plane and the dependence of the frequency  $\omega$  of its oscillation, often called its *eigenfrequency*, on its energy  $E \equiv H_0(p, q)$ . The separatrices correspond to energies equal to the value of the potential barrier tops  $E_b^{(1)} \equiv (1 - \Phi)^2/2$  and  $E_b^{(2)} \equiv (1 + \Phi)^2/2$  as in Fig. 2.7(a). The function  $\omega(E)$  possesses a local maximum  $\omega_m \equiv \omega(E_m)$ . Moreover,  $\omega(E)$  is close to  $\omega_m$  for most of the range  $[E_b^{(1)}, E_b^{(2)}]$  while sharply decreasing to zero as  $E$  approaches either  $E_b^{(1)}$  or  $E_b^{(2)}$ .

We now consider the addition of a time-periodic perturbation: as an example, we use an AC drive, which corresponds to a dipole (Zaslavsky et al., 1991; Landau and Lifshitz, 1976) perturbation of the Hamiltonian:

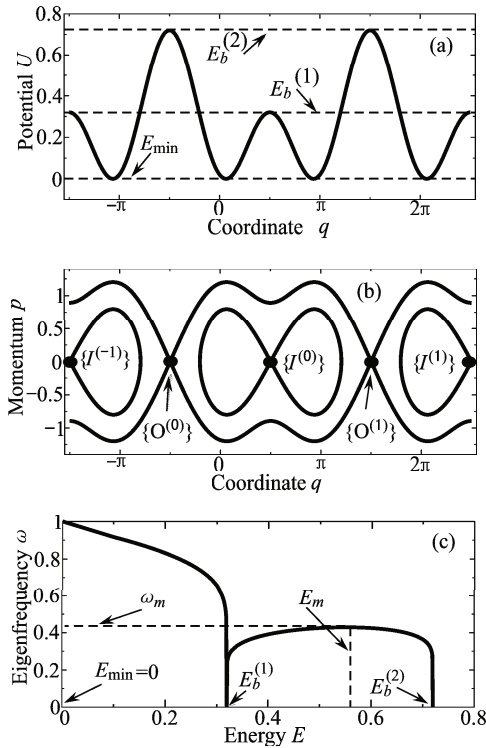


**Fig. 2.7** The potential  $U(q)$ , the separatrices in the phase space, and the eigenfrequency  $\omega(E)$  for the unperturbed system (2.84) with  $\Phi = 0.2$ , in (a), (b) and (c) respectively.

$$\begin{aligned} \dot{q} &= \partial H / \partial p, & \dot{p} &= -\partial H / \partial q, \\ H(p, q) &= H_0(p, q) - hq \cos(\omega_f t). \end{aligned} \quad (2.85)$$

The *conventional* scenario for the onset of global chaos between the separatrices of the system (2.84)–(2.85) is illustrated by Fig. 2.8. The figure presents the evolution of the stroboscopic Poincaré section as  $h$  grows while  $\omega_f$  is fixed at an arbitrarily chosen value *away* from  $\omega_m$  and its harmonics. At small  $h$ , there are two thin chaotic layers around the inner and outer separatrices of the unperturbed system. Unbounded chaotic transport takes place only in the outer chaotic layer i.e. in a *narrow* energy range. As  $h$  grows, so also do the layers. At some critical value  $h_{gc} \equiv h_{gc}(\omega_f)$ , the layers merge. This may be considered as the onset of global chaos: the whole range of energies between the barrier levels is involved, with unbounded chaotic transport. The states  $\{I^{(l)}\} \equiv \{p = 0, q = \pi/2 + 2\pi l\}$  and  $\{O^{(l)}\} \equiv \{p = 0, q = -\pi/2 + 2\pi l\}$  (where  $l$  is any integer) in the Poincaré section are associated respectively with the inner and outer saddles of the unperturbed system, and necessarily belong to the inner and outer chaotic layers, respectively. Thus, the necessary and sufficient condition for global chaos onset may be formulated as the possibility for the system placed initially in the state  $\{I^{(0)}\}$  to pass beyond the neighbourhood of the “outer” states,  $\{O^{(0)}\}$  or  $\{O^{(1)}\}$ , i.e. for the coordinate  $q$  to become  $< -\pi/2$  or  $> 3\pi/2$  at sufficiently large times  $t \gg 2\pi/\omega_f$ .

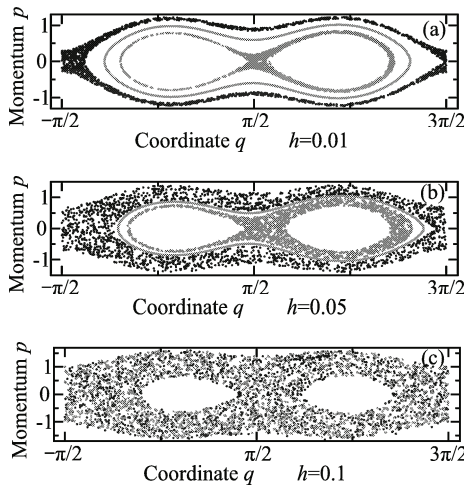


**Fig. 2.8** The evolution of the stroboscopic (at  $t = n2\pi/\omega_f$  with  $n = 0, 1, 2, \dots$ ) Poincaré section of the system (2.84)–(2.85) with  $\Phi = 0.2$  as  $h$  grows while  $\omega_f = 0.3$ . The number of points in each trajectory is 2000. In (a) and (b), three characteristic trajectories are shown: the inner trajectory starts from the state  $\{I^{(0)}\} \equiv \{p = 0, q = \pi/2\}$  and is chaotic but bounded in space; the outer trajectory starts from  $\{O^{(0)}\} \equiv \{p = 0, q = -\pi/2\}$  and is chaotic and unbounded in coordinate; the third trajectory is an example of a regular trajectory separating the two chaotic ones. In (c), the chaotic trajectories mix.

A diagram in the  $h - \omega_f$  plane, based on the above criterion, is shown in Fig. 2.9. The lower boundary of the shaded area represents the function  $h_{gc}(\omega_f)$ . It has deep *spikes* i.e. cusp-like local minima. The most pronounced spikes are situated at frequencies  $\omega_f = \omega_s^{(j)}$  that are slightly less than the odd multiples of  $\omega_m$ ,

$$\omega_s^{(j)} \approx \omega_m(2j - 1), \quad j = 1, 2, \dots \quad (2.86)$$

The deepest minimum occurs at  $\omega_s^{(1)} \approx \omega_m$ : the value of  $h_{gc}$  at the minimum,  $h_s^{(1)} \equiv h_{gc}(\omega_s^{(1)})$ , is approximately 40 times smaller than the value in the neighbouring pronounced local maximum of  $h_{gc}(\omega_f)$  at  $\omega_f \approx 1$ . As  $n$  increases, the  $n$ th minimum becomes shallower. The function  $h_{gc}(\omega_f)$  is very sensitive to  $\omega_f$  in the vicinity of the minima: for example, a reduction of  $\omega_f$  from  $\omega_s^{(1)} \approx 0.4$  of only 1% causes an increase in  $h_{gc}$  of  $\approx 30\%$ .

The origin of the spikes is related to the involvement of the resonance dynamics in separatrix chaos, similar to that considered in Sect. 2.3. In particular, the minima of the spikes correspond to the situation when the resonances almost touch, or slightly overlap with, the separatrices of the unperturbed system while overlapping each other. This is illustrated by the evolution of the Poincaré section as  $h$  grows while  $\omega_f \approx \omega_s^{(1)}$  (Fig. 2.10) and by its comparison with the corresponding evolution of resonance separatrices calculated in the resonance approximation (Fig. 2.11).

Sect. 2.4.1 below presents the self-consistent asymptotic theory of the minima of the spikes, based on an accurate analysis of the overlap of resonances with each other and on the matching between the separatrix map and the resonance Hamiltonian (details of the matching are developed in Appendix). Sect. 2.4.2 presents the theory of the wings of the spikes. Generalizations and applications are discussed in Sect. 2.4.3.

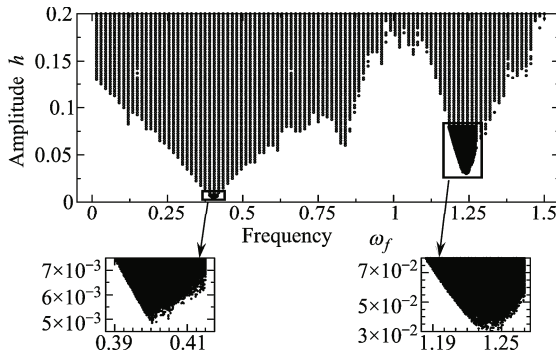


**Fig. 2.9** Diagram indicating the range of perturbation parameters (shaded) for which global chaos exists. The integration time for each point of the grid is  $12000\pi$ .

### 2.4.1 Asymptotic theory for the minima of the spikes

The eigenfrequency  $\omega(E)$  stays close to its local maximum  $\omega_m$  for most of the relevant range  $[E_b^{(1)}, E_b^{(2)}]$  in Fig. 2.7(c). As shown below,  $\omega(E)$  approaches a *rectangular* form in the asymptotic limit  $\Phi \rightarrow 0$ . Hence, if the perturbation frequency  $\omega_f$  is close to  $\omega_m$  or its odd multiples,  $|\omega_f - (2j - 1)\omega_m| \ll \omega_m$ , then the energy widths of nonlinear resonances become comparable to the width of the whole range between the barriers (i.e.  $E_b^{(2)} - E_b^{(1)} \approx 2\Phi$ ) at a rather small perturbation magnitude  $h \ll \Phi$ . Note that  $\Phi$  determines the characteristic magnitude of the perturbation required

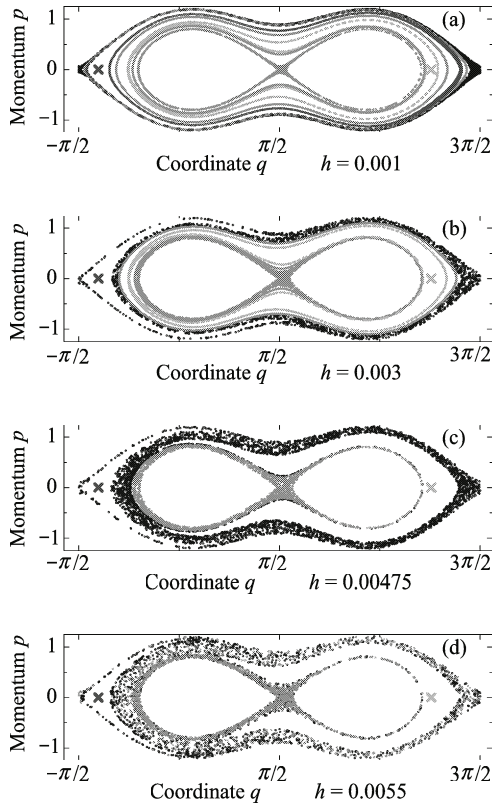


**Fig. 2.10** The evolution of the stroboscopic Poincaré section of the system (84)-(85) with  $\Phi = 0.2$ , as the amplitude  $h$  of the perturbation grows, while the frequency remains fixed at  $\omega_f = 0.401$ . The number of points in each trajectory is 2000. The chaotic trajectories starting from the states  $\{I^{(0)}\}$  and  $\{O^{(0)}\}$  are drawn in green and blue respectively. The stable stationary points of Eq. (2.98) for  $n = 1$  (i.e. for the 1st-order nonlinear resonances) are indicated by the red and cyan crosses. The chaotic layers associated with the resonances are indicated in red and cyan respectively, unless they merge with those associated with the green/blue chaotic trajectories. Examples of regular trajectories embracing the state  $\{I^{(0)}\}$  while separating various chaotic trajectories are shown in brown. (Color version may be found in the online version of (Soskin et al., 2008a) as Fig. 5).

for the conventional overlap of the separatrix chaotic layers, when  $\omega_f$  is not close to any odd multiple of  $\omega_m$  (Fig. 2.8 (c)). Thus, if  $\omega_f \approx \omega_s^{(j)}$ , the nonlinear resonances should play a crucial role in the onset of global chaos (cf. Fig. 2.10).

We note that it is not entirely obvious *a priori* whether it is indeed possible to calculate  $h_s^{(j)} \equiv h_{gc}(\omega_s^{(j)})$  within the resonance approximation: in fact, it is essential for the separatrices of the nonlinear resonances to nearly touch the barrier levels, but the resonance approximation is invalid in the close vicinity of the barriers; furthermore,

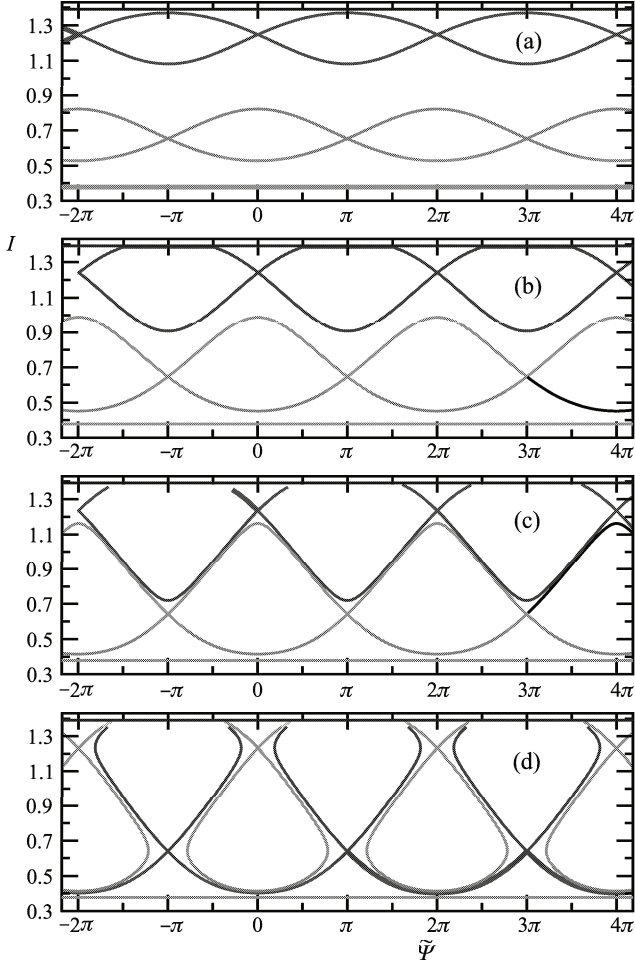


**Fig. 2.11** The evolution of the separatrices of the 1st-order resonances within the resonance approximation (described by (2.16) with  $n = 1$ ) in the plane of action  $I$  and slow angle  $\tilde{\psi}$ , for the same parameters as in Fig. 2.10 (boxes (a), (b), (c), (d) correspond to those in Fig. 2.10). Horizontal levels mark the values of  $I$  corresponding to the barriers. (Color version may be found in the online version of (Soskin et al., 2008a) as Fig. 6).

numerical calculations of resonances show that, if  $\omega_f \approx \omega_s^{(j)}$ , the perturbation amplitude  $h$  at which the resonance separatrix touches a given energy level in the close vicinity of the barriers is very sensitive to  $\omega_f$ , apparently making the calculation of  $h_s^{(j)}$  within the resonance approximation even more difficult.

Nevertheless, we show below in a self-consistent manner that, in the asymptotic limit  $\Phi \rightarrow 0$ , the relevant boundaries of the chaotic layers lie in the range of energies  $E$  where  $\omega(E) \approx \omega_m$ . Therefore, the resonant approximation is valid and it allows us to obtain *explicit* asymptotic expressions both for  $\omega_s^{(j)}$  and  $h_s^{(j)}$ , and for the wings of the spikes in the vicinities of  $\omega_s^{(j)}$ .

The *asymptotic* limit  $\Phi \rightarrow 0$  is the most interesting one from a theoretical point of view because it leads to the strongest facilitation of the onset of global chaos, and it is most accurately described by the self-contained theory. Most of the theory presented below assumes this limit and concentrates therefore on the results to the *lowest* (i.e. leading) order in the small parameter.

On the applications side, the range of *moderately small*  $\Phi$  is more interesting, since the chaos facilitation is still pronounced (and still described by the asymptotic theory) while the area of chaos between the separatrices is not too small (comparable with the area inside the inner separatrix): cf. Figs. 2.7, 2.8 and 2.10. To increase the accuracy of the theoretical description in this range, we estimate the next-order corrections and develop an efficient numerical procedure allowing for further corrections.

### 2.4.1.1 Resonant Hamiltonian and related quantities

Let  $\omega_f$  be close to the  $n$ th odd<sup>9</sup> harmonic of  $\omega_m$ ,  $n \equiv (2j - 1)$ . Over most of the range  $[E_b^{(1)}, E_b^{(2)}]$ , except in the close vicinities of  $E_b^{(1)}$  and  $E_b^{(2)}$ , the  $n$ th harmonic of the eigenoscillation is nearly resonant with the perturbation. Due to this, the (slow) dynamics of the action  $I \equiv I(E) = (2\pi)^{-1} \oint dq p$  and the angle  $\psi$  (Chirikov, 1979; Lichtenberg and Lieberman, 1992; Zaslavsky et al., 1991; Zaslavsky, 2007, 2005; Soskin et al., 2003; Landau and Lifshitz, 1976) can be described by means of a resonance Hamiltonian similar in form to (2.16). The lower integration limit in the expression for  $\tilde{H}$  may be chosen arbitrarily, and it will be convenient for us to use presently  $I(E_m)$  (instead of  $I(E_s)$  in (2.16)) where  $E_m$  is the energy of the local maximum of  $\omega(E)$  shown in Fig. 2.7(c). To avoid confusion, we write the resonance Hamiltonian explicitly below after making this change:

$$\begin{aligned} \tilde{H}(I, \tilde{\psi}) &= \int_{I(E_m)}^I d\tilde{I} (n\omega - \omega_f) - nhq_n \cos(\tilde{\psi}) \\ &\equiv n(E - E_m) - \omega_f(I - I(E_m)) - nhq_n \cos(\tilde{\psi}), \\ I \equiv I(E) &= \int_{E_{\min}}^E \frac{d\tilde{E}}{\omega(\tilde{E})}, \quad E \equiv H_0(p, q), \end{aligned}$$

<sup>9</sup> Even harmonics are absent in the eigenoscillation due to the symmetry of the potential.

$$\begin{aligned}
\tilde{\Psi} &= n\psi - \omega_f t, & (2.87) \\
\psi &= \pi + \text{sign}(p)\omega(E) \int_{q_{\min}(E)}^q \frac{d\tilde{q}}{\sqrt{2(E-U(\tilde{q}))}} + 2\pi l, \\
q_n &\equiv q_n(E) = \frac{2}{\pi} \int_0^{\pi/2} d\psi q(E, \psi) \cos(n\psi), \\
|n\omega - \omega_f| &\ll \omega, \quad n \equiv 2j - 1, \quad j = 1, 2, 3, \dots
\end{aligned}$$

Let us derive explicit expressions for various quantities in (2.87). In the unperturbed case ( $h = 0$ ), the equations of motion (2.85) with  $H_0$  (2.84) can be integrated (Yevtushenko and Richter, 1999), see also Eq. (2.144) below, so that we can find  $\omega(E)$ :

$$\omega(E) = \frac{\pi(2E)^{1/4}}{2K[k]}, \quad k = \frac{1}{2} \sqrt{\frac{(\sqrt{2E} + 1)^2 - \Phi^2}{\sqrt{2E}}}, \quad (2.88)$$

where

$$K[k] = \int_0^{\pi/2} \frac{d\phi}{\sqrt{1 - k^2 \sin^2(\phi)}},$$

is the complete elliptic integral of first order (Abramovitz and Stegun, 1970). Using its asymptotic expression,

$$K[k \rightarrow 1] \simeq \frac{1}{2} \ln \left( \frac{16}{1 - k^2} \right),$$

we derive  $\omega(E)$  in the asymptotic limit  $\Phi \rightarrow 0$ :

$$\begin{aligned}
\omega(E) &\simeq \frac{\pi}{\ln \left( \frac{64}{(\Phi - \Delta E)(\Phi + \Delta E)} \right)}, & (2.89) \\
\Delta E &\equiv E - \frac{1}{2}, \quad |\Delta E| < \Phi, \quad \Phi \rightarrow 0.
\end{aligned}$$

As mentioned above, the function  $\omega(E)$  (2.89) remains close to its maximum

$$\omega_m \equiv \max_{[E_b^{(1)}, E_b^{(2)}]} \{\omega(E)\} \simeq \frac{\pi}{2 \ln(8/\Phi)} \quad (2.90)$$

for most of the interbarrier range of energies  $[1/2 - \Phi, 1/2 + \Phi]$  (note that  $E_b^{(1,2)} \approx 1/2 \mp \Phi$  to first order in  $\Phi$ ); on the other hand, in the close vicinity of the barriers, where either  $|\ln(1/(1 - \Delta E/\Phi))|$  or  $|\ln(1/(1 + \Delta E/\Phi))|$  become comparable with, or larger than,  $\ln(8/\Phi)$ ,  $\omega(E)$  decreases rapidly to zero as  $|\Delta E| \rightarrow \Phi$ . The range where this takes place is  $\sim \Phi^2$ , and its ratio to the whole interbarrier range,  $2\Phi$ , is  $\sim \Phi$  i.e. it goes to zero in the asymptotic limit  $\Phi \rightarrow 0$ : in other words,  $\omega(E)$  approaches a *rectangular* form. As it will be clear from the following, *it is this al-*

most rectangular form of  $\omega(E)$  which determines many of the characteristic features of the global chaos onset in systems with two or more separatrices.

One more quantity which strongly affects  $(\omega_s, h_s)$  is the Fourier harmonic  $q_n \equiv q_n(E)$ . The system stays most of the time very close to one of the barriers. Consider the motion within one of the periods of the potential  $U(q)$ , between neighboring upper barriers  $[q_{ub}^{(1)}, q_{ub}^{(2)}]$  where  $q_{ub}^{(2)} \equiv q_{ub}^{(1)} + 2\pi$ . If the energy  $E \equiv 1/2 + \Delta E$  lies in the relevant range  $[E_b^{(1)}, E_b^{(2)}]$ , then the system will stay close to the lower barrier  $q_{lb} \equiv q_{ub}^{(1)} + \pi$  for a time<sup>10</sup>

$$T_l \approx 2 \ln \left( \frac{1}{\Phi + \Delta E} \right) \quad (2.91)$$

during each period of eigenoscillation, while it will stay close to one of the upper barriers  $q_{ub}^{(1,2)} \equiv q_{lb} \pm \pi$  for most of the remainder of the eigenoscillation,

$$T_u \approx 2 \ln \left( \frac{1}{\Phi - \Delta E} \right) . \quad (2.92)$$

Hence, the function  $q(E, \psi) - q_{lb}$  may be approximated by the following piecewise even periodic function:

$$q(E, \psi) - q_{lb} = \begin{cases} \pi & \text{at } \Psi \in \left[ 0, \frac{\pi}{2} \frac{T_u}{T_l + T_u} \right] \cup \left[ \pi - \frac{\pi}{2} \frac{T_u}{T_l + T_u}, \pi \right], \\ 0 & \text{at } \Psi \in \left[ \frac{\pi}{2} \frac{T_u}{T_l + T_u}, \pi - \frac{\pi}{2} \frac{T_u}{T_l + T_u} \right], \end{cases} \quad (2.93)$$

$$q(E, -\psi) - q_{lb} = q(E, \psi) - q_{lb}, \quad q(E, \psi \pm 2\pi i) = q(E, \psi), \quad i = 1, 2, 3, \dots$$

Substituting the above approximation for  $q(E, \psi)$  into the definition of  $q_n$  in Eq. (2.87), one can obtain:

$$q_{2j-1} \equiv q_{2j-1}(E) = \frac{2}{2j-1} \sin \left( \frac{(2j-1)\pi/2}{1 + \frac{\ln\left(\frac{1}{\Phi + \Delta E}\right)}{\ln\left(\frac{1}{\Phi - \Delta E}\right)}} \right),$$

$$\Phi \rightarrow 0, \quad q_{2j} = 0, \quad j = 1, 2, 3, \dots \quad (2.94)$$

At barrier energies,  $q_{2j-1}$  takes the values

$$q_{2j-1}(E_b^{(1)}) = 0, \quad q_{2j-1}(E_b^{(2)}) = -(-1)^j \frac{2}{(2j-1)}. \quad (2.95)$$

<sup>10</sup> We omit corrections  $\sim (\ln(1/\Phi))^{-1}$  here and in Eq. (2.92) since they vanish in the asymptotic limit  $\Phi \rightarrow 0$ .

As  $E$  varies in between its values at the barriers,  $q_{2j-1}$  varies monotonically if  $j = 1$  and non-monotonically otherwise (cf. Fig. 2.16). But in any case, the significant variations occur mostly in the close vicinity of the barrier energies  $E_b^{(1)}$  and  $E_b^{(2)}$  while, for most of the range  $[E_b^{(1)}, E_b^{(2)}]$ , the argument of the sine in Eq. (2.94) is close to  $\pi/4$  and  $q_{2j-1}$  is then almost constant:

$$q_{2j-1} \approx (-1)^{\lfloor \frac{2j-1}{4} \rfloor} \frac{\sqrt{2}}{2j-1}, \quad j = 1, 2, 3, \dots, \quad (2.96)$$

$$\left| \ln \left( \frac{1 + \Delta E / \Phi}{1 - \Delta E / \Phi} \right) \right| \ll 2 \ln \left( \frac{1}{\Phi} \right),$$

where  $\lfloor \cdot \rfloor$  means the integer part.

In the asymptotic limit  $\Phi \rightarrow 0$ , the range of  $\Delta E$  for which the approximate equality (2.96) for  $q_{2j-1}$  is valid approaches the whole range  $]-\Phi, \Phi[$ .

We emphasize that  $|q_n|$  determines the “strength” of the nonlinear resonances: therefore, apart from the nearly rectangular form of  $\omega(E)$ , the non-smallness of  $|q_n|$  is an important additional factor strongly facilitating the onset of global chaos.

We shall need also an asymptotic expression for the action  $I$ . Substituting  $\omega(E)$  (2.89) into the definition of  $I(E)$  in Eq. (2.87) and carrying out the integration, we obtain

$$I(E) = I(1/2) + \frac{\Delta E \ln \left( \frac{64e^2}{\Phi^2 - (\Delta E)^2} \right) + \Phi \ln \left( \frac{\Phi - \Delta E}{\Phi + \Delta E} \right)}{\pi}, \quad \Phi \rightarrow 0. \quad (2.97)$$

### 2.4.1.2 Reconnection of resonance separatrices

We now turn to analysis of the *phase space* of the resonance Hamiltonian (2.87). The evolution of the Poincaré section (Fig. 2.10) suggests that we need to find a *separatrix* of (2.87) that undergoes the following evolution as  $h$  grows: for sufficiently small  $h$ , the separatrix does not overlap chaotic layers associated with the barriers while, for  $h > h_{gc}(\omega_f)$ , it does overlap them. The relevance of such a condition will be further justified.

Consider  $\omega_f \approx n\omega_m$  with a given odd  $n$ . For the sake of convenience, let us write down the equations of motion (2.87) explicitly:

$$\dot{I} = -\frac{\partial \tilde{H}}{\partial \tilde{\psi}} \equiv -nhq_n \sin(\tilde{\psi}), \quad \dot{\tilde{\psi}} = \frac{\partial \tilde{H}}{\partial I} \equiv n\omega - \omega_f - nh \frac{dq_n}{dI} \cos(\tilde{\psi}). \quad (2.98)$$

Any separatrix necessarily includes one or more unstable stationary points. The system of dynamic equations (2.98) may have several stationary points per  $2\pi$  interval of  $\tilde{\psi}$ . Let us first exclude those points which are irrelevant to a separatrix undergoing the evolution described above.

Given that  $q_n(E_b^{(1)}) = 0$ , there are two unstable stationary points with  $I$  corresponding to  $E = E_b^{(1)}$  and  $\tilde{\psi} = \pm\pi/2$ . They are irrelevant because, even for an infinitely small  $h$ , each of them necessarily lies inside the corresponding barrier chaotic layer.

If  $E \neq E_b^{(1)}$ , then  $q_n \neq 0$ , so  $\dot{I} = 0$  only if  $\tilde{\psi}$  is equal either to 0 or to  $\pi$ . Substituting these values into the second equation of (2.98) and putting  $\tilde{\psi} = 0$ , we obtain the equations for the corresponding actions:

$$X_{\mp}(I) \equiv n\omega - \omega_f \mp nhdq_n/dI = 0, \tag{2.99}$$

where the signs “-” and “+” correspond to  $\tilde{\psi} = 0$  and  $\tilde{\psi} = \pi$  respectively. A typical example of the graphical solution of equations (2.99) for  $n = 1$  is shown in Fig. 2.12. Two of the roots corresponding to  $\tilde{\psi} = \pi$  are very close to the barrier values of  $I$  (recall that the relevant values of  $h$  are small). These roots arise due to the divergence of  $dq/dI$  as  $I$  approaches any of the barrier values. The lower/upper root corresponds to a stable/unstable point, respectively. However, for any  $n$ , both these points and the separatrix generated by the unstable point necessarily lie in the ranges covered by the barrier chaotic layers. Therefore, they are also irrelevant<sup>11</sup>. For  $n > 1$ , the number of roots of (2.99) in the vicinity of the barriers may be larger (due to oscillations of the modulus and sign of  $dq_n/dI$  in the vicinity of the barriers) but they all are irrelevant for the same reason, at least to leading-order terms in the expressions for the spikes’ minima.

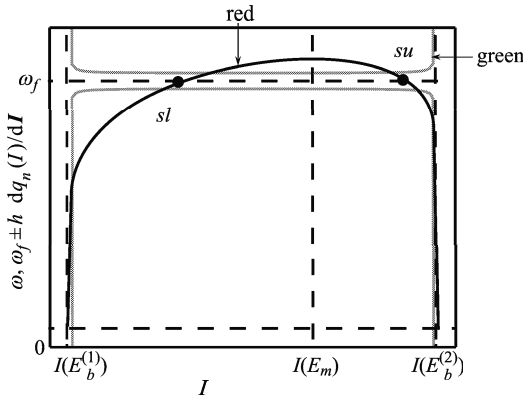


**Fig. 2.12** A schematic example illustrating the graphical solutions of Eqs. (2.99) for  $n = 1$ , as intersections of the curve  $\omega(I)$  (thick solid red line) with the curves  $\omega_f \pm hdq_n(I)/dI$  (thin solid green lines). The solutions corresponding to the lower and upper relevant saddles (defined by Eq. (2.100)) are marked by dots and by the labels  $sl$  and  $su$  respectively (we do not mark other solutions because they are irrelevant). (Color version may be found in the online version of Soskin et al., (2008a) as Fig. 7).

<sup>11</sup> For sufficiently small  $\Phi$  and  $h$ , the separatrix generated by the unstable point forms the boundary of the upper chaotic layer, but this affects only the higher-order terms in the expressions for the spikes minima (see below).

Consider the stationary points corresponding to the remaining four roots of equations (2.99). Just these points are conventionally associated with *nonlinear resonances* (Chirikov, 1979; Lichtenberg and Lieberman, 1992; Zaslavsky et al., 1991; Zaslavsky, 2007, 2005; Soskin et al., 2003). It follows from the analysis of equations (2.98) linearized near the stationary points (cf. (Chirikov, 1979; Lichtenberg and Lieberman, 1992; Zaslavsky et al., 1991; Zaslavsky, 2007, 2005; Soskin et al., 2003)), two of them are stable (elliptic) points<sup>12</sup>, while two others are unstable (hyperbolic) points, often called *saddles*. These saddles are of central interest in the context of our work. They belong to the *separatrices* dividing the  $I - \tilde{\psi}$  plane for regions with topologically different trajectories.

We shall identify the relevant saddles as those with the *lower* action/energy (using the subscript “*sl*”) and *upper* action/energy (using the subscript “*su*”). The positions of the saddles in the  $I - \tilde{\psi}$  plane are defined by the following equations (cf. Figs. 2.11 and 2.12):

$$\begin{aligned} g &\equiv \text{sgn}(q_n(I_{su,sl})) = \text{sgn}\left((-1)^{\lfloor \frac{n}{4} \rfloor}\right), \\ \tilde{\psi}_{sl} &= \pi(1+g)/2, \quad \tilde{\psi}_{su} = \pi(1-g)/2, \\ X_g(I_{sl}) &= X_{-g}(I_{su}) = 0, \quad \frac{dX_g(I_{sl})}{dI_{sl}} > 0, \quad \frac{dX_{-g}(I_{su})}{dI_{su}} < 0, \end{aligned} \quad (2.100)$$

where  $\lfloor \cdot \rfloor$  means an integer part,  $X_{\pm}(I)$  are defined in Eq. (2.99) while  $I_{sl}$  and  $I_{su}$  are closer to  $I(E_m)$  than any other solution of (2.100) (if any) from below and from above, respectively.

Given that the values of  $h$  relevant to the minima of the spikes asymptotically approach 0 in the asymptotic limit  $\Phi \rightarrow 0$ , one may neglect the last term in the definition of  $X_{\mp}$  in Eq. (2.99) in the lowest-order approximation<sup>13</sup>, so that the equations  $X_{\mp} = 0$  reduce to the simplified resonance condition

$$n\omega(I_{su,sl}) = \omega_f. \quad (2.101)$$

Substituting here Eq. (2.89) for  $\omega$ , we obtain explicit expressions for the energies in the saddles:

$$\begin{aligned} E_{su,sl} &\approx \frac{1}{2} \pm \Delta E^{(1)}, \\ \Delta E^{(1)} &\equiv \sqrt{\Phi^2 - 64 \exp\left(-\frac{n\pi}{\omega_f}\right)}, \quad \omega_f \leq n\omega_m. \end{aligned} \quad (2.102)$$

The corresponding actions  $I_{su,sl}$  are expressed via  $E_{su,sl}$  by means of Eq. (2.97).

<sup>12</sup> In the Poincaré sections shown in Fig. 2.10, the points which correspond to such stable points of Eqs. (2.98) are indicated by the crosses.

<sup>13</sup> As will become clear in what follows, the remaining terms are much larger in the asymptotic limit than the neglected term: cf. the standard theory of the nonlinear resonance (Chirikov, 1979; Lichtenberg and Lieberman, 1992; Zaslavsky, 2007, 2005; Zaslavsky et al., 1991).

For  $\omega_f \approx n\omega_m$ , the values of  $E_{su,sl}$  in Eq. (2.102) lie in the range where the expression (2.96) for  $q_n$  holds true. This will be confirmed by the results of calculations based on this assumption.

Using (2.100) for the angles and (2.102) for the energies, and the asymptotic expressions (2.89), (2.96) and (2.97) for  $\omega(E)$ ,  $q_n(E)$  and  $I(E)$  respectively, and allowing for the resonance condition (2.101), we obtain explicit expressions for the values of the Hamiltonian (2.87) at the saddles:

$$\tilde{H}_{sl} = -\tilde{H}_{su} = \frac{\omega_f}{\pi} \left[ 2\Delta E^{(1)} - \Phi \ln \left( \frac{\Phi + \Delta E^{(1)}}{\Phi - \Delta E^{(1)}} \right) \right] + h\sqrt{2}. \quad (2.103)$$

As the analysis of simulations suggests and as it is self-consistently shown further, one of the main conditions which should be satisfied in the spikes is the overlap in phase space between the separatrices of the nonlinear resonances, which is known as *separatrix reconnection* (Soskin et al., 2003; Howard and Hohns, 1984; Howard and Humpherys, 1995; del-Castillo-Negrete et al., 1996; Dullin et al., 2000; Morozov, 2002). Given that the Hamiltonian  $\tilde{H}$  is constant along any trajectory of the system (2.87), the values of  $\tilde{H}$  in the lower and upper saddles of the *reconnected* separatrices are equal to each other:

$$\tilde{H}_{sl} = \tilde{H}_{su}. \quad (2.104)$$

This may be considered as the necessary and sufficient<sup>14</sup> condition for the reconnection. Taking into account that  $\tilde{H}_{sl} = -\tilde{H}_{su}$  in Eq. (2.103), it follows from (2.104) that

$$\tilde{H}_{sl} = \tilde{H}_{su} = 0. \quad (2.105)$$

Explicitly, the relations in (2.105) reduce to

$$h \equiv h(\omega_f) = \frac{\omega_f}{\sqrt{2}\pi} \left[ \Phi \ln \left( \frac{\Phi + \Delta E^{(1)}}{\Phi - \Delta E^{(1)}} \right) - 2\Delta E^{(1)} \right],$$

$$\Delta E^{(1)} \equiv \sqrt{\Phi^2 - 64 \exp\left(-\frac{n\pi}{\omega_f}\right)}, 0 < \omega_m - \omega_f/n \ll \omega_m \equiv \frac{\pi}{2 \ln(8/\Phi)}, \quad (2.106)$$

$$n = 1, 3, 5, \dots$$

The function  $h(\omega_f)$  in Eq (2.106) decreases monotonically to zero as  $\omega_f$  grows from 0 to  $n\omega_m$ , where the line abruptly stops. Fig. 2.15 shows the portions of the lines (2.106) relevant to the left wings of the 1st and 2nd spikes (for  $\Phi = 0.2$ ).

---

<sup>14</sup> Eq. (2.104) is the *sufficient* (rather than just necessary) condition for separatrix reconnection since there is no any other separatrix which would lie in between the separatrices generated by the saddles “sl” and “su”.

### 2.4.1.3 Barrier chaotic layers

The next step is to find the minimum value of  $h$  for which the resonance separatrix overlaps the chaotic layer related to a potential barrier. With this aim, we study how the relevant outer boundary of the chaotic layer behaves as  $h$  and  $\omega_f$  vary. Assume that the relevant  $\omega_f$  is close to  $n\omega_m$  while the relevant  $h$  is sufficiently large for  $\omega(E)$  to be close to  $\omega_m$  at all points of the outer boundary of the layer (the results will confirm these assumptions). Then the motion along the regular trajectory infinitesimally close to the layer boundary may be described within the resonance approximation (2.87). Hence the boundary may also be described as a trajectory of the resonant Hamiltonian (2.87). This is explicitly proved in the Appendix, using a separatrix map analysis allowing for the validity of the relation  $\omega(E) \approx \omega_m$  for all  $E$  relevant to the boundary of the chaotic layer. The main results are presented below. For the sake of clarity, we present them for each layer separately, although they are similar in practice.

#### 1. Lower layer

Let  $\omega_f$  be close to any of the spikes' minima.

One of the key roles in the formation of the upper boundary of the layer is played by the angle-dependent quantity  $\delta_l |\sin(\tilde{\psi})|$  which we call the *generalized separatrix split* (GSS) for the lower layer, alluding to the conventional *separatrix split* (Zaslavsky, 2007) for the lower layer  $\delta_l \equiv |\varepsilon^{(low)}(\omega_f)|h$  with  $\varepsilon^{(low)}$  given by Eq. (2.172)<sup>15</sup> (cf. also (2.4)). Accordingly, we use the term “lower GSS curve” for the following curve in the  $I - \tilde{\psi}$  plane:

$$I = I_{\text{GSS}}^{(l)}(\tilde{\psi}) \equiv I(E_b^{(1)} + \delta_l |\sin(\tilde{\psi})|). \quad (2.107)$$

#### (1) Relatively small values of $h$

If  $h < h_{cr}^{(l)}(\omega_f)$ , where the critical value  $h_{cr}^{(l)}(\omega_f)$  is determined by Eq. (2.125) (its origin will be explained further), then there are differences in the boundary formation for the frequency ranges of *odd* and *even* spikes. We describe these ranges separately.

##### 1) Odd spikes

In this case, the boundary is formed by the trajectory of the Hamiltonian (2.87) *tangent* to the GSS curve, see Fig. 2.22(a); cf. also Figs. 2.1(c), 2.13(a), (b) and (c). There are two tangencies in the angular range  $]-\pi, \pi[$ : they occur at the angles  $\pm \tilde{\psi}_t^{(l)}$  where  $\tilde{\psi}_t^{(l)}$  is determined by Eq. (2.182).

---

<sup>15</sup> The quantity  $\delta_l$  may also be interpreted as the magnitude of the corresponding Melnikov integral (Chirikov, 1979; Lichtenberg and Lieberman, 1992; Zaslavsky et al., 1991; Zaslavsky, 2007, 2005), sometimes called as the Poincaré-Melnikov integral (Piftankin and Treschev, 2007).

In the ranges of  $h$  and  $\omega_f$  relevant to the spike minimum, the asymptotic expressions for  $\delta_l$  and  $\tilde{\psi}_l^{(l)}$  are:

$$\delta_l = \sqrt{2}\pi h, \quad (2.108)$$

$$\tilde{\psi}_l^{(l)} = (-1)^{[n/4]} \sqrt{\frac{n\pi}{8\ln(1/\Phi)}} + \pi \frac{1 - (-1)^{[n/4]}}{2}. \quad (2.109)$$

Hence, the asymptotic value for the deviation of the tangency energy  $E_t^{(l)}$  from the lower barrier reduces to:

$$E_t^{(l)} - E_b^{(1)} \equiv \delta_l \sin(\tilde{\psi}_l^{(l)}) = \frac{\pi^{3/2}}{2} \frac{h}{\sqrt{\ln(1/\Phi)/n}}. \quad (2.110)$$

The minimum energy on the boundary,  $E_{\min}^{(l)}$ , corresponds to  $\tilde{\psi} = 0$  or  $\pi$  for even or odd values of  $[n/4]$  respectively. Thus, it can be found from the equality

$$\tilde{H}\left(I(E_{\min}^{(l)}), \tilde{\psi} = \pi(1 - (-1)^{[n/4]})/2\right) = \tilde{H}\left(I_t^{(l)} \equiv I(E_t^{(l)}), \tilde{\psi}_l^{(l)}\right). \quad (2.111)$$

At  $\Phi \rightarrow 0$ , Eq. (2.111) yields the following expression for the minimal deviation of energy on the boundary from the barrier:

$$\delta_{\min}^{(l)} \equiv E_{\min}^{(l)} - E_b^{(1)} = (E_t^{(l)} - E_b^{(1)})/\sqrt{e} = \frac{\pi^{3/2}}{2\sqrt{e}} \frac{h}{\sqrt{\ln(1/\Phi)/n}}. \quad (2.112)$$

In the context of the onset of global chaos, the most important property of the boundary is that the *maximum* deviation of its energy from the barrier,  $\delta_{\max}^{(l)}$ , greatly exceeds both  $\delta_{\min}^{(l)}$  and  $\delta_l$ . As  $h \rightarrow h_{cr}^{(l)}$ , the maximum of the boundary approaches the saddle “ $sl$ ”.

## 2) Even spikes

In this case, the Hamiltonian (2.87) possesses saddles “ $s$ ” in the close vicinity to the lower barrier (see Fig. 2.22(b)). Their angles differ by  $\pi$  from those of “ $sl$ ”:

$$\tilde{\psi}_s = \pi \frac{1 - (-1)^{[n/4]}}{2} + 2\pi m, \quad m = 0, \pm 1, \pm 2, \dots, \quad (2.113)$$

while the deviation of their energies from the barrier still lies in the relevant (resonant) range and reads, in the lowest-order approximation,

$$\delta_s = \frac{\pi}{2\sqrt{2}} \frac{h}{\ln(\ln(1/\Phi))}. \quad (2.114)$$

The lower whiskers of the separatrix generated by these saddles intersect the GSS curve while the upper whiskers in the asymptotic limit do not intersect it Fig.

2.22(b). Thus, it is the upper whiskers of the separatrix which form the boundary of the chaotic layer in the asymptotic limit. The energy on the boundary takes the minimal value right on the saddle “s”, so that

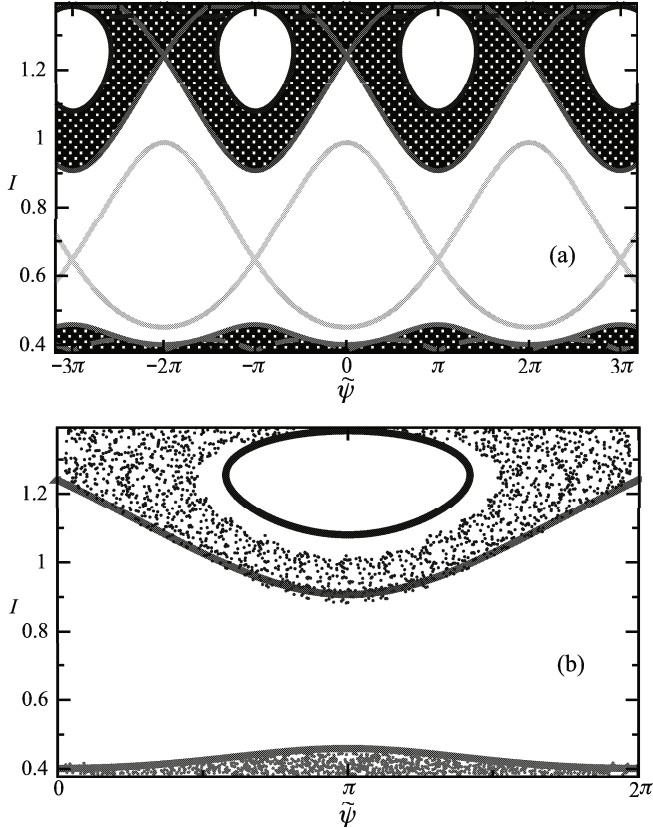


**Fig. 2.13** (a) Chaotic layers (shaded in green and blue, for the upper and lower layers respectively) in the plane of action  $I$  and slow angle  $\tilde{\psi}$ , as described by our theory. Parameters are the same as in Figs. 2.10(b) and 2.11(b). The lower and upper boundaries of the figure box coincide with  $I(E_b^{(1)})$  and  $I(E_b^{(2)})$  respectively. The resonance separatrices are drawn by the cyan and red solid lines (for the lower and upper resonances respectively). Dashed green and blue lines mark the curves  $I = I_{\text{GSS}}^{(l)}(\tilde{\psi}) \equiv I(E = E_b^{(1)} + \delta_l |\sin(\tilde{\psi})|)$  and  $I = I_{\text{GSS}}^{(u)}(\tilde{\psi}) \equiv I(E = E_b^{(2)} - \delta_u |\sin(\tilde{\psi})|)$  respectively, where  $\delta_l$  and  $\delta_u$  are the values of the separatrix split related to the lower and upper barrier respectively. The upper boundary of the lower layer is formed by the trajectory of the resonant Hamiltonian system (2.87) tangent to the curve  $I = I_{\text{GSS}}^{(l)}(\tilde{\psi})$ . The lower boundary of the upper layer is formed by the lower part of the upper (red) resonance separatrix. The periodic closed loops (solid blue lines) are the trajectories of the system (2.87) tangent to the curve  $I_{\text{GSS}}^{(u)}(\tilde{\psi})$ : they form the boundaries of the major stability islands inside the upper chaotic layer. (b) Comparison of the chaotic layers obtained from computer simulations (dots) with the theoretically calculated boundaries (solid lines) shown in the box (a). (Color version may be found in the online version of (Soskin et al., 2008a) as Fig. 8).

$$\delta_{\min}^{(l)} = \delta_s = \frac{\pi}{2\sqrt{2}} \frac{h}{\ln(\ln(1/\Phi))}. \quad (2.115)$$

Similar to the case of the odd spikes, the *maximal* deviation of the energy from the barrier (measured along the boundary) greatly exceeds both  $\delta_{\min}^{(l)}$  and  $\delta_l$ . As  $h \rightarrow h_{cr}^{(l)}$ , the maximum of the boundary approaches the saddle “*sl*”.

(2) *relatively large values of h*

If  $h > h_{cr}^{(l)}(\omega_f)$ , the previously described trajectory (either the tangent one or the separatrix, for the odd or even spike ranges respectively) is encompassed by the separatrix of the lower nonlinear resonance and typically forms the boundary of a major stability island inside the lower layer (reproduced periodically in  $\tilde{\psi}$  with the period  $2\pi$ ). The upper *outer* boundary of the layer is formed by the upper part of the *resonance separatrix*. This may be interpreted as the absorption of the lower resonance by the lower chaotic layer.

## 2. Upper layer

Let  $\omega_f$  be close to any of the spikes’ minima.

One of the key roles in the formation of the lower boundary of the layer is played by the angle-dependent quantity  $\delta_u |\sin(\tilde{\psi})|$  which we call the *generalized separatrix split* (GSS) for the upper layer;  $\delta_u$  is the separatrix split for the upper layer:  $\delta_u = |\varepsilon^{(up)}(\omega_f)|h$  with  $\varepsilon^{(up)}$  given by Eq. (2.204). Accordingly, we use the term “upper GSS curve” for the following curve in the  $I - \tilde{\psi}$  plane:

$$I = I_{\text{GSS}}^{(u)}(\tilde{\psi}) \equiv I(E_b^{(2)} - \delta_u |\sin(\tilde{\psi})|). \quad (2.116)$$

(1) *Relatively small values of h*

If  $h < h_{cr}^{(u)}(\omega_f)$ , where the critical value  $h_{cr}^{(u)}(\omega_f)$  is determined by Eq. (2.126) (its origin will be explained further), then there are some differences in the boundary formation in the frequency ranges of *odd* and *even* spikes: for odd spikes, the formation is similar to the one for even spikes in the lower-layer case and vice versa.

1) *Odd spikes*

In the case of odd spikes, the Hamiltonian (2.87) possesses saddles “*s*” in the close vicinity of the upper barrier, analogous to the saddles “*s*” near the lower barrier in the case of even spikes. Their angles are shifted by  $\pi$  from those of “*s*”:

$$\tilde{\psi}_s = \tilde{\psi}_s + \pi = \pi \frac{1 + (-1)^{\lfloor \frac{n}{4} \rfloor}}{2} + 2\pi m, \quad m = 0, \pm 1, \pm 2, \dots \quad (2.117)$$

The deviation of their energies from the upper barrier coincides, in the lowest-order approximation, with  $\delta_s$ :

$$\delta_{\tilde{s}} = \delta_s = \frac{\pi}{2\sqrt{2}} \frac{h}{\ln(\ln(1/\Phi))}. \quad (2.118)$$

The upper whiskers of the separatrix generated by these saddles intersect the upper GSS curve while the lower whiskers in the asymptotic limit do not intersect it. Thus, it is the lower whiskers of the separatrix which form the boundary of the chaotic layer in the asymptotic limit. The deviation of the energy from the upper barrier takes its minimal value (measured along the boundary) right on the saddle “ $\tilde{s}$ ”,

$$\delta_{\min}^{(u)} = \delta_s = \frac{\pi}{2\sqrt{2}} \frac{h}{\ln(\ln(1/\Phi))}. \quad (2.119)$$

The *maximal* deviation of the energy from the barrier (along the boundary) greatly exceeds both  $\delta_{\min}^{(u)}$  and  $\delta_u$ . As  $h \rightarrow h_{cr}^{(u)}$ , the maximum of the boundary approaches the saddle “ $su$ ”.

## 2) Even spikes

The boundary is formed by the trajectory of the Hamiltonian (2.87) *tangent* to the GSS curve. There are two tangencies in the angle range  $]-\pi, \pi[$ : they occur at the angles  $\pm \tilde{\psi}_t^{(u)}$  where  $\tilde{\psi}_t^{(u)}$  is determined by Eq. (2.202).

In the ranges of  $h$  and  $\omega_f$  relevant to the spike minimum, the expressions for  $\delta_u$  and  $\tilde{\psi}_t^{(u)}$  in the asymptotic limit  $\Phi \rightarrow 0$  are similar to the analogous quantities in the lower-layer case:

$$\delta_u = \sqrt{2}\pi h, \quad (2.120)$$

$$\tilde{\psi}_t^{(u)} = -(-1)^{[\frac{n}{4}]} \sqrt{\frac{n\pi}{8\ln(\frac{1}{\Phi})}} + \pi \frac{1 + (-1)^{[\frac{n}{4}]}]{2}. \quad (2.121)$$

Hence, the asymptotic value for the deviation of the tangency energy  $E_t^{(u)}$  from the upper barrier reduces to:

$$E_b^{(2)} - E_t^{(u)} \delta_u \left| \pi \frac{1 + (-1)^{[\frac{n}{4}]}]{2} - \tilde{\psi}_t^{(u)} \right| = \frac{\pi^{3/2}}{2} \frac{h}{\sqrt{\ln(1/\Phi)/n}}. \quad (2.122)$$

The maximal energy on the boundary,  $E_{\max}^{(u)}$ , corresponds to  $\tilde{\psi} = \pi(1 + (-1)^{[n/4]})/2$ . Thus, it can be found from the equality

$$\tilde{H}(I = I(E_{\max}^{(u)}), \tilde{\psi} = \pi(1 + (-1)^{[n/4]})/2) = \tilde{H}(I_t^{(u)} \equiv I(E_t^{(u)}), \tilde{\psi}_t^{(u)}). \quad (2.123)$$

At  $\Phi \rightarrow 0$ , Eq. (2.123) yields the following expression for the minimal deviation of energy from the barrier (measured along the boundary):

$$\delta_{\min}^{(u)} \equiv E_b^{(2)} - E_{\max}^{(u)} = (E_b^{(2)} - E_t^{(u)})/\sqrt{\epsilon} = \frac{\pi^{3/2}}{2e^{1/2}} \frac{h}{\sqrt{\ln(1/\Phi)/n}}. \quad (2.124)$$

### (2) Relatively large values of $h$

If  $h > h_{cr}^{(u)}(\omega_f)$  (cf. Fig. 2.13(a)), the previously described trajectory (either the tangent one or the separatrix, for the even and odd spikes ranges respectively) is encompassed by the separatrix of the upper nonlinear resonance and typically forms the boundary of a major stability island inside the upper layer (reproduced periodically in  $\tilde{\psi}$  with the period  $2\pi$ ). The lower *outer* boundary of the layer is formed in this case by the lower part of the *resonance separatrix*. This may be interpreted as the absorption of the upper resonance by the upper chaotic layer.

The self-consistent description of chaotic layers given above, and in more detail in the Appendix, is the first main result of this section. It provides a *rigorous basis* for our intuitive assumption that the minimal value of  $h$  at which the layers overlap corresponds to the reconnection of the nonlinear resonances with each other while the reconnected resonances touch one of the layers and also touch/overlap another layer. It is gratifying that we have obtained a *quantitative* theoretical description of the chaotic layer boundaries in the *phase space*, including even the major stability islands, that agrees well with the results of simulations as shown in Fig. 2.13(b). To the best of our knowledge it was the first ever (Soskin et al., 2008a) quantitative description of the layer boundaries in the phase space.

#### 2.4.1.4 Onset of global chaos: the spikes' minima

The condition for the merger of the lower resonance and the lower chaotic layer may be written as

$$\tilde{H}(I = I(E = E_b^{(1)} + \delta_{\min}^{(l)}), \tilde{\psi} = \pi(1 - (-1)^{[n/4]})/2) = \tilde{H}_{sl}. \quad (2.125)$$

The condition for the merger of the upper resonance and the upper chaotic layer may be written as

$$\tilde{H}(I = I(E = E_b^{(2)} - \delta_{\min}^{(u)}), \tilde{\psi} = \pi(1 + (-1)^{[n/4]})/2) = \tilde{H}_{su}. \quad (2.126)$$

For the onset of global chaos related to the spike minimum, either of Eqs. (2.125) and (2.126) should be combined with the condition of the separatrix reconnection (2.104). Let us seek first only the leading terms of  $h_s \equiv h_s(\Phi)$  and  $\omega_s \equiv \omega_s(\Phi)$ . Then (2.104) may be replaced by its lowest-order approximation (2.105) or, equivalently, (2.106). Using also the lowest-order approximation for the barriers ( $E_b^{(1,2)} \approx 1/2 \mp \Phi$ ), we reduce Eqs. (2.125), (2.126) respectively to

$$\tilde{H}(I = I(E = 1/2 - \Phi + \delta_{\min}^{(l)}), \tilde{\psi} = \pi(1 - (-1)^{[n/4]})/2) = 0, \quad (2.127)$$

$$\tilde{H}(I = I(E = 1/2 + \Phi - \delta_{\min}^{(u)}), \tilde{\Psi} = \pi(1 + (-1)^{[n/4]})/2) = 0, \quad (2.128)$$

where  $\delta_{\min}^{(l)}$  is given by (2.112) or (2.115) for the odd or even spikes respectively, while  $\delta_{\min}^{(u)}$  is given by (2.119) or (2.124) for the odd or even spikes respectively.

To the *leading* order, the solution  $(h_s^{(l)}, \omega_s^{(l)})$  of the system of Eqs. (2.106), (2.127) and the solution  $(h_s^{(u)}, \omega_s^{(u)})$  of the system of Eqs. (2.106), (2.128) turn out *identical*. For the sake of brevity, we derive below just  $(h_s^{(l)}, \omega_s^{(l)})$ , denoting the latter, in short, as  $(h_s, \omega_s)$ <sup>16</sup>.

The system of algebraic equations (2.106) and (2.127) is still too complicated for us to find its exact solution. However, we need only the *lowest-order* solution – and this simplifies the problem. Still, even this simplified problem is not trivial, both because the function  $h_s(\Phi)$  turns out to be non-analytic and because  $\Delta E^{(1)}$  in (2.106) is very sensitive to  $\omega_f$  in the relevant range. Despite these difficulties, we have found the solution in a *self-consistent* way, as briefly described below.

Assume that the asymptotic dependence  $h_s(\Phi)$  is:

$$h_s = a \frac{\Phi}{\ln(4\epsilon/\Phi)}, \quad (2.129)$$

where the constant  $a$  may be found from the asymptotic solution of (2.106), (2.127) and (2.129).

Substituting the energies  $E = 1/2 - \Phi + \delta_{\min}^{(l)}$  and  $E = 1/2 + \Phi - \delta_{\max}^{(u)}$  in (2.89) and taking account of (2.112), (2.115), (2.119), (2.124) and (2.129), we find that, both for the odd and even spikes, the inequality

$$\omega_m - \omega(E) \ll \omega_m \quad (2.130)$$

holds over the whole relevant range of energies, i.e. for

$$\Delta E \in [-\Phi + \delta_{\min}^{(l)}, \Phi - \delta_{\min}^{(u)}]. \quad (2.131)$$

Thus, the resonant approximation is valid over the whole range (2.131). Eq. (2.96) for  $q_n(E)$  is valid over the whole relevant range of energies too.

Consider Eq. (2.127) in an explicit form. Namely, we express  $\omega_f$  from (2.127), using Eqs. (2.87), (2.96), and (2.97), using also (2.112) or (2.115) for odd or even spikes and (2.129):

---

<sup>16</sup> With account taken of the next-order corrections, the spike minimum  $(h_s, \omega_s)$  coincides with  $(h_s^{(l)}, \omega_s^{(l)})$  in case of an odd spike, or with  $(h_s^{(u)}, \omega_s^{(u)})$  in case of an even spike. This occurs because, in case of odd spikes,  $|q_n(E)|$  increases/decreases as  $E$  approaches the relevant vicinity of the upper/lower barrier, while it is *vice versa* in the case of even spikes. And the larger  $|q_n|$  the further the resonance separatrix extends: in other words, the reconnection of the barrier chaotic layer with the resonance separatrix requires a smaller value of  $h$  at the barrier where  $|q_n|$ , in the relevant vicinity of the barrier, is larger.

$$\omega_f = \frac{n\pi}{2 \ln\left(\frac{4e}{\Phi}\right)} \left\{ 1 + \frac{h\sqrt{2}}{n\Phi} + O\left(\frac{1}{\ln^2(4e/\Phi)}\right) \right\}. \quad (2.132)$$

We emphasize that the value of  $\delta_{\min}^{(l)}$  enters explicitly only the term  $O(\dots)$  while, as is clear from the consideration below, this term does not affect the leading terms in  $(h_s, \omega_s)$ . Thus,  $\delta_{\min}^{(l)}$  does not affect the leading term of  $\omega_s$  at all, while it affects the leading term of  $h_s$  only *implicitly*:  $\delta_{\min}^{(l)}$  lies in the range of energies where  $nq_n(E) \approx \sqrt{2}$ . This latter quantity is present in the second term in the curly brackets in (2.132) and, as becomes clear from further consideration,  $h_s$  is proportional to it.

Substituting (2.132) into the expression for  $\Delta E^{(1)}$  in (2.106), using (2.129) and keeping only the leading terms, we obtain

$$\Delta E^{(1)} = \Phi \sqrt{1 - 4e^{c-2}}, \quad c \equiv \frac{2\sqrt{2}}{n} a. \quad (2.133)$$

Substituting  $\Delta E^{(1)}$  from (2.133) into Eq. (2.106) for  $h(\omega_f)$  and allowing for (2.129) once again, we arrive at a transcendental equation for  $c$ :

$$\ln\left(\frac{1 + \chi(c)}{1 - \chi(c)}\right) - 2\chi(c) = c, \quad \chi(c) \equiv \sqrt{1 - 4e^{c-2}}. \quad (2.134)$$

An approximate numerical solution of Eq. (2.134) is

$$c \simeq 0.179. \quad (2.135)$$

Thus, the final leading-order asymptotic formulæ for  $\omega_f$  and  $h$  in the minima of the spikes are the following:

$$\omega_{s0} \equiv \omega_{s0}^{(\frac{n+1}{2})} = n \frac{\pi}{2 \ln\left(\frac{4e}{\Phi}\right)}, \quad h_{s0} \equiv h_{s0}^{(\frac{n+1}{2})} = n \frac{c}{2\sqrt{2}} \frac{\Phi}{\ln\left(\frac{4e}{\Phi}\right)}, \quad (2.136)$$

$$n = 1, 3, 5, \dots, \quad \Phi \rightarrow 0,$$

where the constant  $c \simeq 0.179$  is the solution of Eq. (2.134).

*The self-consistent derivation of the explicit asymptotic formulæ for the minima of  $h_{gc}(\omega_f)$  constitutes the second main result of this section.* These formulae allow one to predict immediately the parameters for the weakest perturbation that may lead to global chaos.

#### 2.4.1.5 Numerical example and next-order corrections

For  $\Phi = 0.2$ , the numerical simulations give the following values for the frequencies at the minima of the first two spikes (see Fig. 2.9):

$$\omega_s^{(1)} \approx 0.4005 \pm 0.0005, \quad \omega_s^{(2)} \approx 1.24 \pm 0.005. \quad (2.137)$$

By the lowest-order formula (2.136), the values are:

$$\omega_{s0}^{(1)} \approx 0.393, \quad \omega_{s0}^{(2)} \approx 1.18, \quad (2.138)$$

in rather good agreement with the simulations.

The next-order correction for  $\omega_s$  can immediately be found from Eq. (2.132) for  $\omega_f$  and from Eq. (2.136) for  $h_{s0}$ , so that

$$\omega_{s1} \approx \omega_{s0} \left( 1 + \frac{c}{2 \ln\left(\frac{4e}{\Phi}\right)} \right) \approx \frac{n\pi \left( 1 + \frac{0.09}{\ln\left(\frac{4e}{\Phi}\right)} \right)}{2 \ln\left(\frac{4e}{\Phi}\right)}, \quad n = 1, 3, 5, \dots \quad (2.139)$$

The formula (2.139) agrees with the simulations even better than the lowest-order approximation:

$$\omega_{s1}^{(1)} \approx 0.402, \quad \omega_{s1}^{(2)} \approx 1.21. \quad (2.140)$$

For  $h$  in the spikes minima, the simulations give the following values (see Fig. 2.9):

$$h_s^{(1)} \approx 0.0049, \quad h_s^{(2)} \approx 0.03. \quad (2.141)$$

The values according to the lowest-order formula (2.52) are:

$$h_{s0}^{(1)} \approx 0.0032, \quad h_{s0}^{(2)} \approx 0.01. \quad (2.142)$$

The theoretical value  $h_{s0}^{(1)}$  gives reasonable agreement with the simulation value  $h_s^{(1)}$ . The theoretical value  $h_{s0}^{(2)}$  gives the correct order of magnitude for the simulation value  $h_s^{(2)}$ . Thus, the accuracy of the lowest-order formula (2.136) for  $h_s$  is much lower than that for  $\omega_s$ ; this is due to the steepness of  $h_{gc}(\omega_f)$  in the ranges of the spikes (the steepness, in turn, is due to the flatness of the function  $\omega(E)$  near its maximum). Moreover, as the number of the spike  $j$  increases, the accuracy of the lowest-order value  $h_{s0}^{(j)}$  significantly decreases. The latter can be explained as follows. For the next-order correction to  $h_{s0}^{(j)}$ , the dependence on  $\Phi$  reads as:

$$\frac{h_{s1}^{(j)} - h_{s0}^{(j)}}{h_{s0}^{(j)}} \propto \frac{1}{\ln(4e/\Phi)}. \quad (2.143)$$

At least some of the terms in this correction are positive and proportional to  $h_{s0}^{(j)}$  (e.g. due to the difference between the exact equation (2.99) and its approximate version (2.101)), while  $h_{s0}^{(j)}$  is proportional to  $n \equiv 2j - 1$ . Thus, for  $\Phi = 0.2$ , the relative correction for the 1st spike is  $\sim 0.25$  while the correction for the 2nd spike is a few times larger i.e.  $\sim 1$ . But the latter means that, for  $\Phi = 0.2$ , the asymptotic theory for the 2nd spike cannot pretend to be a quantitative description of  $h_s^{(2)}$ , but only provides the correct order of magnitude. Besides, if  $n > 1$  while  $\Phi$  exceeds some

critical value, then the search of the minimum involves Eq. (2.150) rather than Eq. (2.104), as explained below in Sect. 2.4.2 (cf. Figs. 2.15(b) and 2.16). Altogether, this explains why  $h_s^{(1)}$  is larger than  $h_{s0}^{(1)}$  only by 50% while  $h_s^{(2)}$  is larger than  $h_{s0}^{(2)}$  by 200%.

To provide a consistent explicit derivation of the correction to  $h_{s0}^{(j)}$  is complicated. A reasonable alternative may be a proper *numerical* solution of the algebraic system of Eqs. (2.104)<sup>17</sup> and (2.125) for the odd spikes, or (2.126) for the even spikes<sup>16</sup>. To this end, in Eqs. (2.104)<sup>17</sup> and (2.125) or (2.126) we use: (i) the exact values of the saddle energies obtained from the exact relations (2.100) instead of the approximate relations (2.101); (ii) the exact formula (2.88) for  $\omega(E)$  instead of the asymptotic expression (2.89); (iii) the exact functions  $q_n(E)$  instead of the asymptotic formula (2.86); (iv) the relation (111) and the calculation of the “tangent” state  $(\tilde{\psi}_t^{(l)}, I_t^{(l)})$  by Eqs. (2.172), (2.183) for the odd spikes, or relation (2.123) and the calculation of the “tangent” state  $(\tilde{\psi}_t^{(u)}, I_t^{(u)})$  by Eqs. (2.202)–(2.204) for the even spikes. Note that, to find the exact function  $q_n(E)$ , we substitute into the definition of  $q_n(E)$  in (2.87) the explicit<sup>18</sup> solution for  $q(E, \psi)$ :

$$\begin{aligned} q(E, \psi) &= \arcsin \left( \frac{\eta - \sqrt{2E} + \Phi}{1 - \eta} \right) & \text{for } \psi \in \left[ 0, \frac{\pi}{2} \right], \\ q(E, \psi) &= \pi - q(E, \pi - \psi) & \text{for } \psi \in \left[ \frac{\pi}{2}, \pi \right], \\ q(E, \psi) &= q(E, 2\pi - \psi) & \text{for } \psi \in [\pi, 2\pi], \\ \eta &\equiv \frac{1}{2}(\sqrt{2E} - \Phi + 1)\text{sn}^2 \left( \frac{2K}{\pi} \psi \right), \end{aligned} \quad (2.144)$$

where  $\text{sn}(x)$  is the elliptic sine (Abramovitz and Stegun, 1970) with the same modulus  $k$  as the full elliptic integral  $K$  defined in (2.88). The numerical solution described above gives:

$$\begin{aligned} \left( \omega_s^{(1)} \right)_{num} &\approx 0.401, & \left( h_s^{(1)} \right)_{num} &\approx 0.005, \\ \left( \omega_s^{(2)} \right)_{num} &\approx 1.24, & \left( h_s^{(2)} \right)_{num} &\approx 0.052. \end{aligned} \quad (2.145)$$

The agreement with the simulation results is: (i) excellent for  $\omega_s$  for the both spikes and for  $h_s$  for the 1st spike, (ii) reasonable for  $h_s$  for the 2nd spike. Thus, if  $\Phi$  is *moderately* small, a much more accurate prediction for  $h_s$  than that by the lowest-order formula is provided by the numerical procedure described above.

<sup>17</sup> For  $n > 1$ , it is also necessary to check if the solution lies above the line (2.150). If it does not, then (2.104) should be replaced here by (2.150).

<sup>18</sup> In the general case of an arbitrary potential  $U(q)$ , when the explicit expression for  $q(E, \psi)$  and  $\omega(E)$  cannot be obtained, these functions can be calculated numerically.

### 2.4.2 Theory of the spikes' wings

The goal of this section is to find the mechanisms responsible for the formation of the spikes' wings (i.e. the function  $h_{gc}(\omega_f)$  in the ranges of  $\omega_f$  slightly deviating from  $\omega_s^{(j)}$ ), and to provide for their theoretical description.

Before developing the theory, we briefly analyze the simulation data (Fig. 2.9), concentrating on the 1st spike. The left wing of the spike is smooth and nearly straight. The initial part of the right wing is also nearly straight<sup>19</sup>, though less steep. But at some small distance from  $\omega_s^{(1)}$  its slope changes jump-wisely by a few times: compare the derivative  $dh_{gc}/d\omega_f \approx 0.1$  at  $\omega_f = 0.4 \div 0.41$  (see the left inset in Fig. 2.9) and  $dh_{gc}/d\omega_f \approx 0.4$  at  $\omega_f = 0.45 \div 0.55$  (see the main part of Fig. 2.9). Thus, even prior to the theoretical analysis, one may assume that there are a number of different mechanisms responsible for formation of the wings.

Consider the arbitrary  $j$ th spike. We have shown in the previous section that, in the asymptotic limit  $\Phi \rightarrow 0$ , the minimum of the spike corresponds to the intersection between the line (2.104) with (2.125) or (2.126) for odd or even spikes respectively. We recall that: (i) Eq. (2.104) corresponds to the overlap in phase space between nonlinear resonances of the same order  $n \equiv 2j - 1$ ; (ii) Eq. (2.125) or (2.126) corresponds to the onset of the overlap between the resonance separatrix associated respectively with the lower or upper saddle and the chaotic layer associated with the lower or upper potential barrier; (iii) for  $\omega_f = \omega_s^{(j)}$ , the condition (2.125) or (2.126) also guarantees the overlap between the upper or lower resonance separatrix, respectively, and the chaotic layer associated with the upper or lower barrier<sup>16</sup>.

If  $\omega_f$  becomes slightly smaller than  $\omega_s^{(j)}$ , the resonances shift closer to the barriers while moving apart from each other. Hence, as  $h$  increases, the overlap of the resonances with the chaotic layers associated with the barriers occurs earlier than with each other. Therefore, at  $0 < \omega_s^{(j)} - \omega_f \ll \omega_m$ , the function  $h_{gc}(\omega_f)$  should correspond approximately to the reconnection of resonances of the order  $n \equiv 2j - 1$  as shown in Fig. 2.14(a). Fig. 2.15(a) demonstrates that even the asymptotic formula (2.106) for the separatrix reconnection line fits the left wing of the 1st spike quite well, and that the numerically calculated line (2.104) agrees with the simulations perfectly.

If  $\omega_f$  becomes slightly larger than  $\omega_s^{(j)}$  then, on the contrary, the resonances shift closer to each other and further from the barriers. Therefore, the mutual overlap of the resonances occurs at smaller  $h$  than the overlap between any of them and the chaotic layer associated with the lower/upper barrier as shown in Figs. 2.10(c) and 2.10(d) as well as 2.11(c) and 2.11(d). Hence, it is the latter overlap which determines the function  $h_{gc}(\omega_f)$  in the relevant range of  $\omega_f$  (Fig. 2.14(b)). Fig. 2.15 shows that  $h_{gc}(\omega_f)$  is indeed well-approximated in the close vicinity to the right from  $\omega_s^{(j)}$  by the numerical solution of Eq. (2.125) or (2.126), for an odd or even spike respectively and, for the 1st spike and the given  $\Phi$ , even by its asymptotic form,

<sup>19</sup> Provided  $h_{gc}(\omega_f)$  is smoothed over small fluctuations.

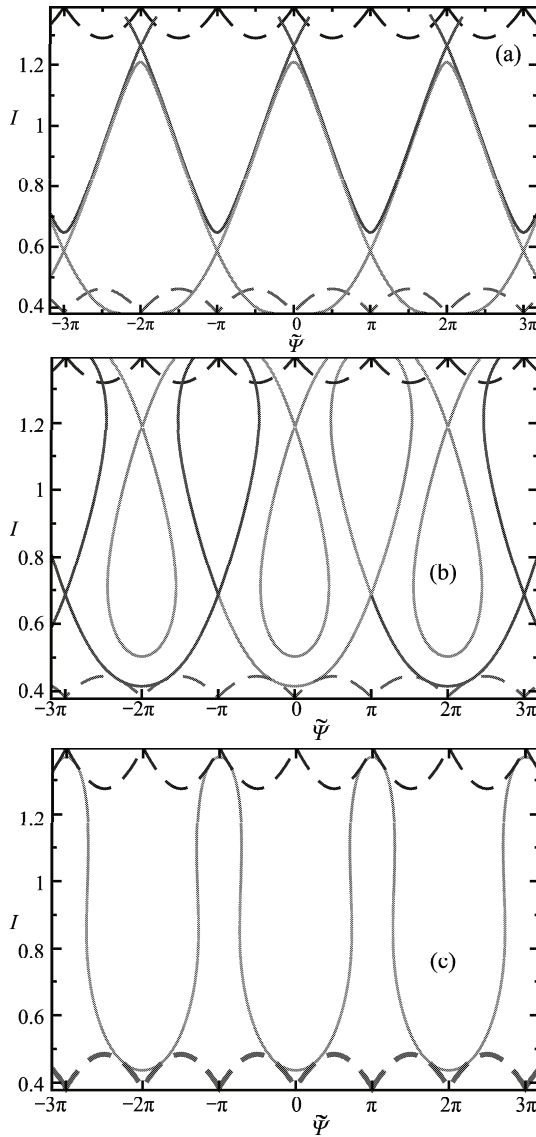


**Fig. 2.14** Illustrations of the mechanisms of the formation of the 1st spike wings and of the corresponding theoretical lines in Fig. 2.15(a). Boxes (a), (b) and (c) illustrate the lines of Eqs. (2.104), (2.125) and (2.148) respectively: the corresponding perturbation parameters are  $(\omega_f = 0.39, h = 0.0077)$ ,  $(\omega_f = 0.41, h = 0.00598)$  and  $(\omega_f = 0.43, h = 0.01009)$  respectively. Resonance separatrices are drawn in red and cyan. The dashed lines show the functions  $I_{\text{GSS}}^{(l)}(\tilde{\psi})$  and  $I_{\text{GSS}}^{(u)}(\tilde{\psi})$ . The black line in (c) is the trajectory of the resonant Hamiltonian system (2.87) which is tangent to both dashed lines. (Color version may be found in the online version of (Soskin et al., 2008a) as Fig. 9).

$$h \equiv h(\omega_f) = n \frac{-\Phi + \frac{\omega_f}{n\pi} \left[ \Phi \left\{ 2 \ln \left( \frac{4e}{\Phi} \right) + \ln \left( \frac{\Phi + \Delta E^{(1)}}{\Phi - \Delta E^{(1)}} \right) \right\} - 2 \Delta E^{(1)} \right]}{2\sqrt{2}},$$

$$\Delta E^{(1)} \equiv \sqrt{\Phi^2 - 64 \exp\left(-\frac{n\pi}{\omega_f}\right)}, n \equiv 2j - 1, \quad |\omega_f - \omega_s^{(j)}| \ll \omega_m. \quad (2.146)$$

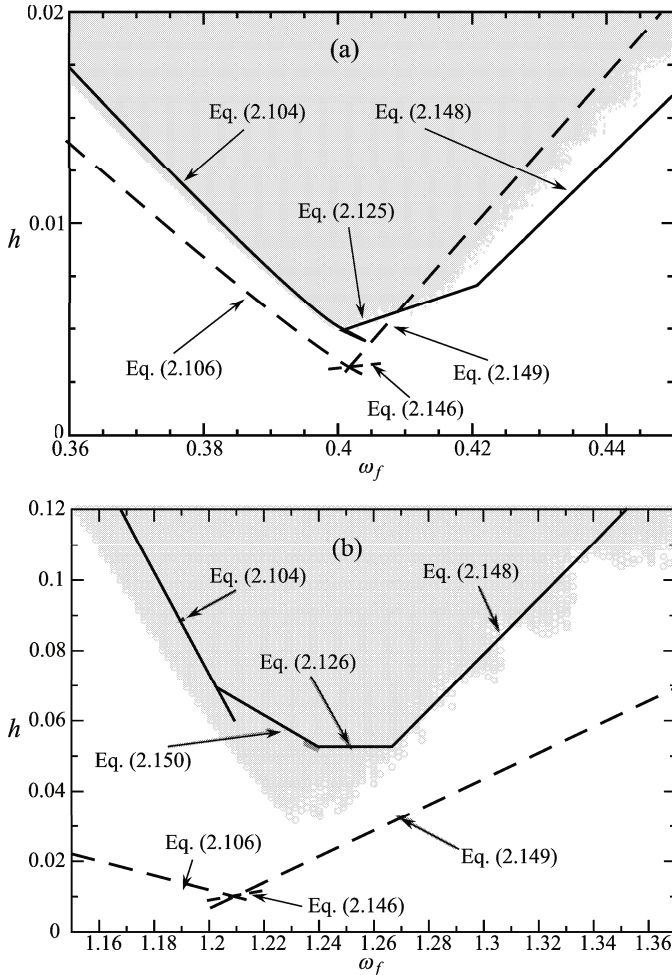


**Fig. 2.15** The 1st (a) and 2nd (b) spike in  $h_{gc}(\omega_f)$ : comparison between the results of the numerical simulations (the lower boundary of the shaded area) and the theoretical estimates. The estimates are indicated by the corresponding equation numbers and are drawn by different types of lines, in particular the dashed lines represent the explicit asymptote for the solid line of the same color. (Color version may be found in the online version of (Soskin et al., 2008a) as Fig. 10).

The mechanism described above determines  $h_{gc}(\omega_f)$  only in the close vicinity of  $\omega_s^{(j)}$ . If  $\omega_f/n$  becomes too close to  $\omega_m$  or exceeds it, then the resonances are not of immediate relevance: they may even disappear or, if they still exist, their closed loops shrink, so that they can no longer provide for connection of the chaotic layers in the relevant range of  $h$ . At the same time, the closeness of the frequency to  $\omega_m$  may still give rise to a large variation of action along the trajectory of the Hamiltonian system (2.87). For the odd/even spikes, the boundaries of the chaotic layers in the asymptotic limit  $\Phi \rightarrow 0$  are formed in this case by the trajectory of (2.87) which is tangent to the lower/upper GSS curves (for the lower/upper layer) or by the lower/upper part of the separatrix of (2.87) generated by the saddle “ $\tilde{s}$ ”/“ $s$ ” (for the upper/lower layer). The overlap of the layers occurs when these trajectories coincide with each other, which may be formulated as the equality of  $\tilde{H}$  in the corresponding tangency and saddle:

$$\begin{aligned}\tilde{H}(I_t^{(l)}, \tilde{\psi}_t^{(l)}) &= \tilde{H}(I_{\tilde{s}}, \tilde{\psi}_{\tilde{s}}) \quad \text{for } j = 1, 3, 5, \dots, \\ \tilde{H}(I_s, \tilde{\psi}_s) &= \tilde{H}(I_t^{(u)}, \tilde{\psi}_t^{(u)}) \quad \text{for } j = 2, 4, 6, \dots, \\ I_{\tilde{s}} &\equiv I(E_b^{(2)} - \delta_{\tilde{s}}), \quad I_s \equiv I(E_b^{(1)} + \delta_s).\end{aligned}\tag{2.147}$$

Note however that, for *moderately* small  $\Phi$ , the tangencies may be relevant both to the lower layer and to the upper one (see the Appendix). Indeed, such a case occurs for our example with  $\Phi = 0.2$ : see Fig. 2.14(c). Therefore, the overlap of the layers corresponds to the equality of  $\tilde{H}$  in the tangencies:

$$\tilde{H}(I_t^{(l)}, \tilde{\psi}_t^{(l)}) = \tilde{H}(I_t^{(u)}, \tilde{\psi}_t^{(u)}).\tag{2.148}$$

To the lowest order, Eqs. (2.147), (2.148) read as:

$$h \equiv h(\omega_f) = \frac{\sqrt{2}\Phi \ln\left(\frac{4c}{\Phi}\right)}{\pi} \left( \omega_f - \frac{n\pi}{2 \ln\left(\frac{4c}{\Phi}\right)} \right).\tag{2.149}$$

Both the line (2.148) and the asymptotic line (2.149) well agree with the part of the right wing of the 1st spike situated to the right from the fold at  $\omega_f \approx 0.42$  (Fig. 2.15(a)). The fold corresponds to the change of the mechanisms of the chaotic layers overlap.

If  $\Phi$  is moderately small while  $n > 1$ , the description of the far wings by the numerical lines (2.104) and (2.148) may be still quite good but the asymptotic lines (2.106) and (2.149) cannot pretend to describe the wings quantitatively any more (Fig. 2.15(b)). As for the minimum of the spike and the wings in its close vicinity, one more mechanism may become relevant for their formation as shown in Figs. 2.15(b) and 2.16. It may be explained as follows. If  $n > 1$ , then  $q_n(E)$  becomes zero in the close vicinity ( $\sim \Phi^2$ ) of the relevant barrier (the upper or lower barrier, in the case of even or odd spikes respectively: cf. Fig. 2.16). It follows from the equations of motion (2.98) that no trajectory can cross the line  $I = I_{q_n=0}$ . In the asymptotic limit  $\Phi \rightarrow 0$ , provided  $h$  is from the range relevant for the spike minimum, almost

the whole GSS curve is further from the barrier than the line  $I = I_{q_n=0}$ , and the latter becomes irrelevant. But, for a moderately small  $\Phi$ , the line may separate the whole GSS curve from the rest of the phase space. Then the resonance separatrix cannot connect to the GSS curve even if there is a state on the latter curve with the same value of  $\tilde{H}$  as on the resonance separatrix. For a given  $\omega_f$ , the connection then requires a higher value of  $h$ : for such a value, the GSS curve itself crosses the line  $I = I_{q_n=0}$ . In the relevant range of  $h$ , the resonance separatrix passes very close to this line, so that the connection is well approximated by the condition that the GSS curve *touches* this line (see the inset in Fig. 2.16):

$$\begin{aligned} \delta_u &= E_b^{(2)} - E_{q_{2j-1}=0} & \text{for } j &= 2, 4, 6, \dots, \\ \delta_l &= E_{q_{2j-1}=0} - E_b^{(1)} & \text{for } j &= 3, 5, 7, \dots \end{aligned} \quad (2.150)$$

This mechanism is relevant to the formation of the minimum of the 2nd spike at  $\Phi = 0.2$ , and in the close vicinity of the spike on the left (Fig. 2.15(b)).

Finally, let us find explicitly the *universal asymptotic shape* of the spike in the vicinity of its minimum. First, we note that the lowest-order expression (2.146) for the spike between the minimum and the fold can be written as the *half-sum* of the expressions (2.106) and (2.149) (which represent the lowest-order approximations for the spike to the left of the minimum, and to the right of the fold respectively). Thus, all three lines (2.106), (2.146) and (2.149) intersect at a single point. This means that, in the asymptotic limit  $\Phi \rightarrow 0$ , the fold merges with the minimum:  $\omega_f$  and  $h$  in the fold asymptotically approach  $\omega_s$  and  $h_s$  respectively. Thus, though the fold is a generic feature of the spikes, it is not of major significance: the spike is formed basically from two straight lines. The ratio between their slopes is universal.

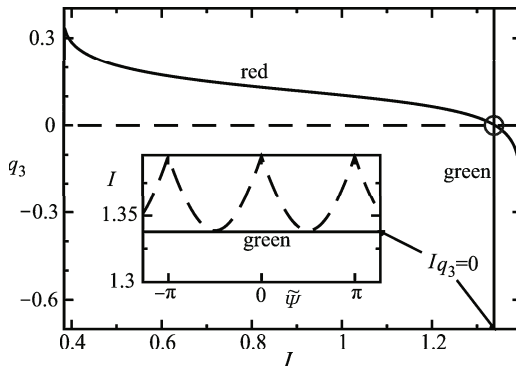


**Fig. 2.16** Amplitude of the 3rd Fourier harmonic as a function of action (solid red line). The dashed black line shows the zero level. Its intersection with the solid red line is marked by the circle. The green line indicates the value of action where  $q_3 = 0$ . The inset illustrates the line (2.150) in Fig. 2.15(b): the GSS curve touches the horizontal line  $I = I_{q_3=0}$ . (Color version may be found in the online version of (Soskin et al., 2008a) as Fig. 11).

So, introducing a proper scaling, we reduce the spike shape to the universal function (Fig. 2.17):

$$\begin{aligned}
 \tilde{h}(\Delta\tilde{\omega}_f) &= \tilde{h}^{(lw)}(\Delta\tilde{\omega}_f) \equiv 1 - \sqrt{1 - 4e^{c-2}}\Delta\tilde{\omega}_f \approx \\
 &\approx 1 - 0.593\Delta\tilde{\omega}_f \quad \text{for } \Delta\tilde{\omega}_f < 0, \\
 \tilde{h}(\Delta\tilde{\omega}_f) &= \tilde{h}^{(rw)}(\Delta\tilde{\omega}_f) \equiv 1 + \Delta\tilde{\omega}_f \quad \text{for } \Delta\tilde{\omega}_f > 0, \\
 & \\
 \tilde{h}^{(fold)}(\Delta\tilde{\omega}_f) &= \frac{\tilde{h}^{(lw)}(\Delta\tilde{\omega}_f) + \tilde{h}^{(rw)}(\Delta\tilde{\omega}_f)}{2} \\
 &\equiv 1 + \frac{1 - \sqrt{1 - 4e^{c-2}}}{2}\Delta\tilde{\omega}_f \approx 1 + 0.203\Delta\tilde{\omega}_f, \\
 & \\
 \tilde{h} &\equiv \frac{h}{h_{s0}}, \quad \Delta\tilde{\omega}_f \equiv \frac{\omega_f - \omega_{s1}}{\omega_{s1} - \omega_{s0}}, \quad \Phi \rightarrow 0,
 \end{aligned} \tag{2.151}$$

where  $\omega_{s0}$  and  $h_{s0}$  are the lowest-order expressions (2.136) respectively for the frequency and amplitude in the spike minimum,  $\omega_{s1}$  is the expression (2.139) for the frequency in the spike minimum, including the first-order correction, and  $c$  is a constant (2.135).

In addition to the left and right wings of the universal shape (the solid lines in Fig. 2.17), we include in (2.151) the function  $\tilde{h}^{(fold)}(\Delta\tilde{\omega}_f)$  (the dashed line in Fig. 2.17): its purpose is to show, on one hand, that the fold merges asymptotically with the minimum but, on the other hand, that the fold is generic and the slope of the spike between the minimum and the fold has a universal ratio to any of the slopes of the major wings.

Even for a moderately small  $\Phi$ , as in our example, the ratios between the three slopes related to the 1st spike in the simulations are reasonably well reproduced

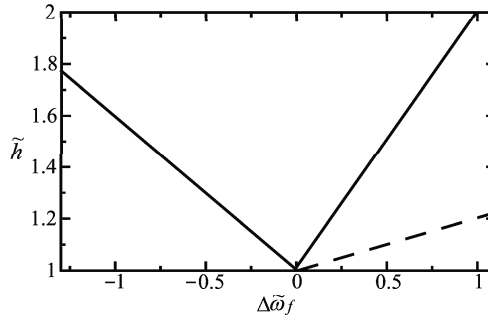


**Fig. 2.17** The universal shape of the spike minimum (2.151) (solid lines). The dashed line indicates the universal slope of the spike in between the minimum and the fold, which have merged in the universal (asymptotic) function (151). (Color version may be found in the online version of (Soskin et al., 2008a) as Fig. 12).

by those in Eq. (2.151): cf. Figs. 2.15(a) and 2.17. It follows from (2.151) that the asymptotic scaled shape is universal i.e. independent of  $\Phi$  (but still assuming the asymptotic limit  $\Phi \rightarrow 0$ ),  $n$  or any other parameter.

*The description of the wings of the spikes near their minima, in particular the derivation of the spike universal shape, constitutes the third main result of this section.*

### 2.4.3 Generalizations and applications

The *facilitation of the onset of global chaos* between adjacent separatrices has a number of possible generalizations and applications. We discuss one of the applications in Sect. 2.5, but first list some of generalizations below.

1. The spikes in  $h_{gc}(\omega_f)$  may occur for an *arbitrary Hamiltonian* system with two or more separatrices. The asymptotic theory can be generalized accordingly.

2. The absence of pronounced spikes at *even* harmonics  $2j\omega_m$  is explained by the symmetry of the potential (2.84): the even Fourier harmonics of the coordinate,  $q_{2j}$ , are equal to zero. For time-periodic perturbation of the dipole type, as in Eq. (2.85), there are no resonances of even order on account of this symmetry (Chirikov, 1979; Lichtenberg and Lieberman, 1992; Zaslavsky et al., 1991; Zaslavsky, 2007, 2005; Soskin et al., 2003). If either the potential is *non-symmetric*, or the additive perturbation of the Hamiltonian is not an *odd* function of the coordinate, then even-order resonances do exist, resulting in the presence of the spikes in  $h_{gc}(\omega_f)$  at  $\omega_f \approx 2j\omega_m$ .

3. There may also be an additional facilitation of the onset of global chaos that could reasonably be described as a “secondary” facilitation. Let the frequency  $\omega_f$  be close to the frequency  $\omega_s$  of the spike minimum, while the amplitude  $h$  be  $\sim h_s$  but still lower than  $h_{gc}(\omega_f)$ . Then there are two resonance separatrices in the  $I - \tilde{\psi}$  plane that are not connected by chaotic transport as shown in Fig. 2.11(b). This system possesses the zero-dispersion property. The trajectories of the resonant Hamiltonian (2.87) which start in between the separatrices oscillate in  $I$  (as well as in  $d\tilde{\psi}/dt$ ). The frequency  $\tilde{\omega}$  of such oscillations along a given trajectory depends on the corresponding value of  $\tilde{H}$  analogously to the way in which  $\omega$  depends on  $E$  for the original Hamiltonian  $H_0$ :  $\tilde{\omega}(\tilde{H})$  is equal to zero for the values of  $\tilde{H}$  corresponding to the separatrices (being equal in turn to  $\tilde{H}_{sl}$  and  $\tilde{H}_{su}$ : see Eq. (2.103)) while possessing a nearly rectangular shape in between, provided the quantity  $|\tilde{H}_{sl} - \tilde{H}_{su}|$  is much smaller than the variation of  $\tilde{H}$  within each of the resonances,

$$|\tilde{H}_{sl} - \tilde{H}_{su}| \ll \tilde{H}_{var} \sim |\tilde{H}_{sl} - \tilde{H}_{el}| \sim |\tilde{H}_{su} - \tilde{H}_{eu}|, \quad (2.152)$$

where  $\tilde{H}_{el}$  and  $\tilde{H}_{eu}$  are the values of  $\tilde{H}$  at the elliptic point of the lower and upper resonance respectively. The maximum of  $\tilde{\omega}(\tilde{H})$  in between  $\tilde{H}_{sl}$  and  $\tilde{H}_{su}$  is described by the asymptotic formula:

$$\tilde{\omega}_m \approx \frac{\pi}{\ln(\tilde{H}_{var}/|\tilde{H}_{sl} - \tilde{H}_{su}|)}. \quad (2.153)$$

If we additionally perturb the system in such a way that an additional time-periodic term of frequency  $\tilde{\omega}_f \approx \tilde{\omega}_m$  arises in the resonance Hamiltonian, then the chaotic layers associated with the resonance separatrices may be connected by chaotic transport even for a rather small amplitude of the additional perturbation, due to a scenario similar to the one described in this paper.

There may be various types of such additional perturbation (Soskin, unpublished). For example, one may *add* to  $H$  in Eq. (2.85) one more dipole time-periodic perturbation of *mixed* frequency (i.e.  $\approx \omega_m + \tilde{\omega}_m$ ). Alternatively, one may directly perturb the *angle* of the original perturbation by a *low-frequency* perturbation, i.e. the time-periodic term in  $H$  of Eq. (2.85) is replaced by the term

$$-hq \cos(\omega_f t + A \cos(\tilde{\omega}_f t)), \quad \omega_f \approx \omega_m, \quad \tilde{\omega}_f \approx \tilde{\omega}_m. \quad (2.154)$$

Recently discussed physical problems where a similar situation is relevant are: chaotic mixing and transport in a meandering jet flow (Prants et al., 2006) and reflection of light rays in a corrugated waveguide (Leonel, 2007).

4. If the time-periodic perturbation is *multiplicative* rather than additive, the resonances become *parametric* (cf. (Landau and Lifshitz, 1976)). Parametric resonance is more complicated and much less studied than nonlinear resonance. Nevertheless, the main mechanism for the onset of global chaos remains the same, namely the combination of the reconnection between resonances of the same order and of their overlap in energy with the chaotic layers associated with the barriers. At the same time, the frequencies of the main spikes in  $h_{gc}(\omega_f)$  may change (though still being related to  $\omega_m$ ). We consider below an example when the periodically driven parameter is<sup>20</sup>  $\Phi$  in (2.84). The Hamiltonian is

$$\begin{aligned} H &= p^2/2 + (\Phi - \sin(q))^2/2, \\ \Phi &= \Phi_0 + h \cos(\omega_f t), \quad \Phi_0 = \text{const} < 1. \end{aligned} \quad (2.155)$$

The term  $(\Phi - \sin(q))^2/2$  in  $H$  (2.155) may be rewritten as  $(\Phi_0 - \sin(q))^2/2 + (\Phi_0 - \sin(q))h \cos(\omega_f t) + h^2 \cos^2(\omega_f t)/2$ . The last term in the latter expression does not affect the equations of motion. Thus, we end up with an additive perturbation  $(\Phi_0 - \sin(q))h \cos(\omega_f t)$ . In the asymptotic limit  $\Phi_0 \rightarrow 0$ , the  $n$ th-order Fourier component of the function  $(\Phi_0 - \sin(q))$  can be shown to differ from zero only for the orders  $n = 2, 6, 10, \dots$ . Therefore one may expect the main spikes in  $h_{gc}(\omega_f)$  to be at frequencies twice larger than those for the dipole perturbation (2.85):

$$\omega_{sp}^{(j)} \approx 2\omega_s^{(j)} \approx 2(2j-1)\omega_m, \quad j = 1, 2, 3, \dots \quad (2.156)$$

This agrees well with the results of simulations (Fig. 2.18).

---

<sup>20</sup> In the case of a 2D electron gas in a magnetic superlattice, this may correspond e.g. to the time-periodic electric force applied perpendicular to the direction of the periodic magnetic field (Yevtushenko and Richter, 1998, 1999).

Moreover, the asymptotic theory for the dipole perturbation may immediately be generalized to the present case: it is necessary only to replace the Fourier component of the coordinate  $q$  by the Fourier component of the function  $(\Phi_0 - \sin q)$ :

$$(\Phi_0 - \sin(q))_n = \begin{cases} \frac{4}{\pi n} & \text{at } n = 2(2j - 1), \\ 0 & \text{at } n \neq 2(2j - 1), \end{cases} \quad j = 1, 2, 3, \dots, \quad \Phi_0 \rightarrow 0 \quad (2.157)$$

(cf. Eq. (2.96) for  $q_n$ ). We obtain:

$$\omega_{sp0} \equiv \omega_{sp0}^{(\frac{n+2}{4})} = n \frac{\pi}{2 \ln\left(\frac{4c}{\Phi_0}\right)}, \quad h_{sp0} \equiv h_{sp0}^{(\frac{n+2}{4})} = n \frac{c\pi}{8} \frac{\Phi_0}{\ln\left(\frac{4c}{\Phi_0}\right)}, \quad (2.158)$$

$$n = 2, 6, 10, \dots, \quad \Phi_0 \rightarrow 0,$$

where  $c$  is given in Eqs. (2.134) and (2.135).

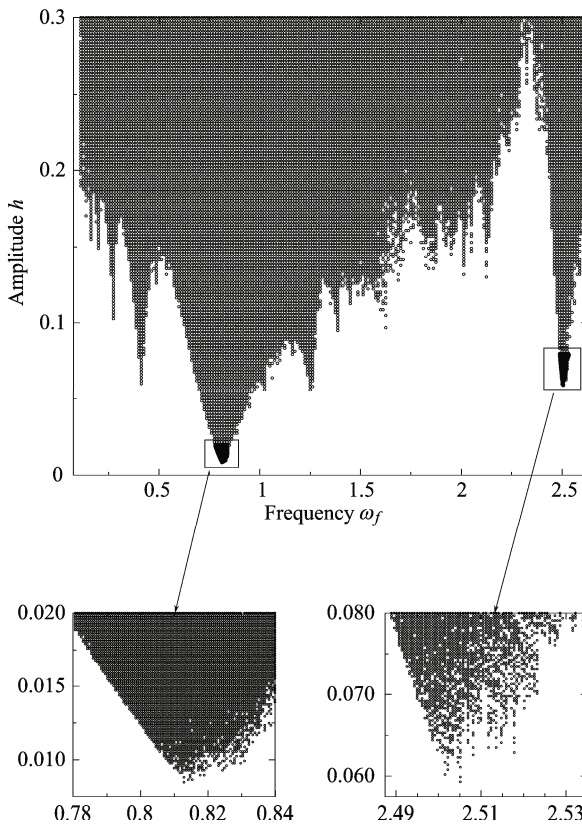


**Fig. 2.18** Diagram analogous to that in Fig. 2.9, but for the system (2.155) (with  $\Phi_0 = 0.2$ ).

For  $\Phi_0 = 0.2$ , Eq. (2.158) gives, for the 1st spike, values differing from the simulation data by about 3% in frequency and by about 10% in amplitude. Thus, the lowest-order formulae accurately describe the 1st spike even for a moderately small  $\Phi$ .

5. One more generalization relates to *multi-dimensional* Hamiltonian systems with two or more saddles with different energies: the perturbation may not necessarily be time-periodic, in this case. The detailed analysis has not yet been done.

The paper (Soskin et al., 2008a) presents a rather detailed discussion of possible applications to the electron gas in a magnetic superlattice, a spinning pendulum, cold atoms in an optical lattice as well as to problems of noise-induced escape and the stochastic web formation. We review briefly in the next section the further development of the latter application.

## 2.5 Enlargement of a low-dimensional stochastic web

The stochastic web concept dates back to the 1960s when Arnold showed (Arnold, 1964) that, in non-degenerate Hamiltonian systems of dimension exceeding 2, resonance lines necessarily intersect, forming an infinite-sized web in the Poincaré section. It provides in turn for a slow chaotic (sometimes called “stochastic”) diffusion for infinite distances in relevant dynamical variables.

It was discovered towards the end of 1980s (Zaslavsky et al., 1986; Chernikov et al., 1987a,b, 1988) that, in degenerate or nearly-degenerate systems, a stochastic web may arise even if the dimension is  $3/2$ . One of the archetypal examples of such a low-dimensional stochastic web arises in the 1D harmonic oscillator perturbed by a weak traveling wave the frequency of which coincides with a multiple of the natural frequency of the oscillator (Zaslavsky, 2007; Chernikov et al., 1987b; Zaslavsky et al., 1991). Perturbation plays a dual role: on the one hand, it gives rise to a slow dynamics characterized by an auxiliary Hamiltonian that possesses an infinite web-like separatrix; on the other hand, the perturbation destroys this self-generated separatrix, replacing it by a thin chaotic layer. Such a low-dimensional stochastic web may be relevant to a variety of physical systems and plays an important role in corresponding transport phenomena: see (Zaslavsky, 2007; Chernikov et al., 1987b; Zaslavsky et al., 1991) for reviews on relevant classical systems. In addition, there are quantum systems in which the dynamics of transport reduces to that in the classical model described above. The latter concerns e.g. nanometre-scale semiconductor superlattices with an applied voltage and magnetic field (Fromhold et al., 2001, 2004).

One might assume that, like the Arnold web, the low-dimensional stochastic web described above should be infinite, so that it can provide for transport between the centre of the web and states situated arbitrarily far away in coordinate and momentum. However the numerical integration of the equations of motion shows that this is not so: even for a rather non-weak perturbation, the real web is limited to the region within *a few* inner loops of the infinite web-like resonant separatrix (Fig. 2.19(a))

while chaotic layers associated with outer loops are distinctly separated from each other and from the web-like chaotic layer formed by the few inner loops. The reason is apparently as follows. The single infinite web-like separatrix is possessed by the resonant Hamiltonian only in the first-order approximation of the averaging method (Bogolyubov and Mitropolsky, 1961) whereas, with the account taken of the next-order approximations, the separatrix apparently splits into many separate complex loops successively embedded into each other. Non-resonant terms of the perturbation dress the separatrices by exponentially narrow chaotic layers. If the perturbation is not small, the chaotic layers manage to connect neighbouring separatrix loops situated close to the centre. However, the width of the chaotic layer decreases exponentially sharply as the distance from the centre grows (Zaslavsky, 2007; Chernikov et al., 1987b; Zaslavsky et al., 1991). As a result, the merger between chaotic layers associated with neighbouring loops takes place only within the few loops closest to the centre, provided that the perturbation is not exponentially strong.

If the resonance between the perturbation and the oscillator is inexact, or if the oscillator is nonlinear, the splitting between the neighbouring loops is typically much larger: it appears even in the first-order approximation of the averaging method (Zaslavsky, 2007; Chernikov et al., 1988; Zaslavsky et al., 1991). So the number of loops connected to the centre by chaotic transport is even smaller (Zaslavsky, 2007; Chernikov et al., 1988; Zaslavsky et al., 1991) than in the case of the exact resonance.

A natural question arises: how can the perturbation be modified in order for the transport to be unlimited or, at least, significantly extended? One of the answers was obtained in the very beginning of studies of the low-dimensional webs (Zaslavsky et al., 1986; Chernikov et al., 1987a): if the perturbation consists of repeated in time short kicks that are also periodic in space, and if the frequency of the kicks is equal to a multiple of the natural frequency, then a so-called uniform web covering the whole of phase space is formed. However such a perturbation is absent in many cases and, even where present, the chaotic transport is still exponentially slow if the perturbation is weak (Zaslavsky, 2007; Zaslavsky et al., 1991).

It is reasonable then to pose the following question: is it possible to obtain a web of form similar to the original one (Chernikov et al., 1987b) but substantially extended in phase space? A positive answer was suggested in (Soskin et al., 2008a) and explicitly realized recently (Soskin et al., 2009) using the following simple idea. The chaotic layer in the webs is *exponentially* narrow since the frequency of the non-resonant perturbation of the resonant Hamiltonian is necessarily much higher than the frequency of small eigenoscillation in the cell of the web-like separatrix (Zaslavsky, 2007; Zaslavsky et al., 1986; Chernikov et al., 1987a,b, 1988; Zaslavsky et al., 1991). So we need to modify the perturbation in such a way that the resonant Hamiltonian does not change while its perturbation contains, in addition to the conventional terms, a low-frequency one. One may do this modulating the wave angle with a low frequency or adding one more wave with the frequency slightly shifted from the original one. The latter option, together with a generalization for the uniform web leading to a huge enhancement of the chaotic transport through it, have

not yet been considered in detail while the work (Soskin et al., 2009, 2010b) and the present section concentrate on the former option since it may have immediate applications to nanometre-scale semiconductor superlattices in electric and magnetic fields (Fromhold et al., 2001, 2004).

### 2.5.1 Slow modulation of the wave angle

Fig. 2.19 demonstrates the validity of our idea. We integrate the equation

$$\ddot{q} + q = 0.1 \sin[15q - 4t - h \sin(0.02t)], \quad (2.159)$$

first for  $h = 0$  (i.e. for the conventional case with parameters as in (Zaslavsky, 2007; Chernikov et al., 1987b; Zaslavsky et al., 1991)), and secondly for  $h = 0.1$ . Although the modulation in the latter case is weak (its amplitude is about 63 times smaller than the  $2\pi$  period of the wave angle which is a characteristic scale in this problem), the resultant increase in the size of the web in coordinate and momentum is large: by a factor of  $\sim 6$ .

An analytic theory can be developed to account for these results. It can be generalized for the off-resonant case (Zaslavsky, 2007; Chernikov et al., 1988; Zaslavsky et al., 1991) too, using the general method developed in (Soskin et al., 2008a,b; Soskin and Mannella, 2009a,b) and described above in the previous sections.

It is anticipated that the method can also be generalized for uniform webs (Zaslavsky, 2007; Zaslavsky et al., 1986, 1991) too, leading to an exponentially strong enhancement of chaotic transport through them.

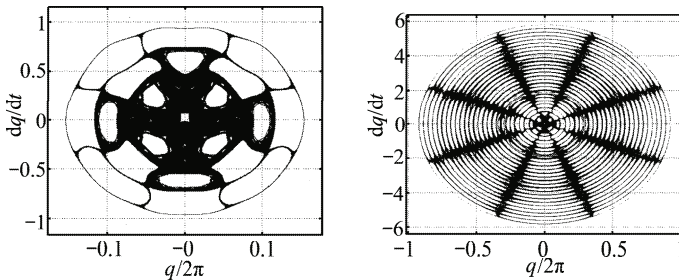


**Fig. 2.19** The Poincaré section for a trajectory of the system (2.159) with initial state  $q = 0.1$ ,  $\dot{q} = 0$  (at instants  $t_n = nT$  where  $T \equiv 2\pi/0.02$  is the period of the modulation and  $n = 1, 2, 3, \dots, 600000$ ) for  $h = 0$  (left panel) and  $h = 0.1$  (right panel). A symplectic integration scheme of the fourth order is used, with an integration step  $t_{int} = \frac{2\pi}{40000} \approx 1.57 \times 10^{-4}$ , so that the inaccuracy at each step is of the order of  $t_{int}^5 \approx \times 10^{-19}$ . The left panel corresponds to the example of the conventional case considered in (Zaslavsky, 2007; Chernikov et al., 1987b; Zaslavsky et al., 1991). The right panel demonstrates that the modulation, although weak, greatly enlarges the web sizes.

### 2.5.2 Application to semiconductor superlattices

The works (Fromhold et al., 2001, 2004) consider quantum electron transport in 1D semiconductor superlattices (SLs) on the nanometre scale, subject to a constant electric field along the SL axis and to a constant magnetic field. The spatial periodicity with a period of the nanometre scale gives rise to the onset of minibands for electrons. In the tight-binding approximation, the electron motion in the lowest mini-band is described by the following dispersion relation for the electron energy  $E$  versus momentum  $\mathbf{p}$ :

$$E(\mathbf{p}) = \frac{\Delta[1 - \cos(p_x d/\hbar)]}{2} + \frac{p_y^2 + p_z^2}{2m^*}, \quad (2.160)$$

where  $x$  is the direction along the SL axis,  $\Delta$  is the miniband width,  $d$  is the SL period,  $m^*$  is the electron effective mass for the motion in the transverse (i.e.  $y-z$ ) plane.

Thus, the quasi-classical motion of electron in an electric field  $\mathbf{F}$  and a magnetic field  $\mathbf{B}$  is described by the following equation:

$$\frac{d\mathbf{p}}{dt} = -e\{\mathbf{F} + [\nabla_{\mathbf{p}}E(\mathbf{p}) \times \mathbf{B}]\}, \quad (2.161)$$

where  $e$  is the electron charge

It was shown in (Fromhold et al., 2001) that, with a constant electric field along the SL axis  $\mathbf{F} = (-F_0, 0, 0)$  and a constant magnetic field with a given angle  $\theta$  to the axis  $\mathbf{B} = (B \cos(\theta), 0, B \sin(\theta))$ , the dynamics of the  $z$ -component of momentum  $p_z$  reduces to the equation of motion of an auxiliary harmonic oscillator in a plane wave. At certain values of the parameters, the ratio of the wave and oscillator frequencies takes integer values (like in Eq. (2.159) with  $h = 0$ ) which gives rise to the onset of the stochastic web, leading in turn to a delocalization of the electron in the  $x$ -direction and, as a result, to an increase of the dc-conductivity along the SL axis. The experiment (Fromhold et al., 2004) appears to provide evidence in favor of this exciting hypothesis.

At the same time, the finite size of the web and, yet more so, the exponentially fast decrease in the transport rate as the distance from the centre of the web increases, seems to put strong limitations on the use of the effect. We suggest a simple and efficient way to overcome these limitations. Indeed, one can show that, if we add to the original (constant) electric field  $F_0$  a small time-periodic (ac) component  $F_{ac} \sin(\Omega_{ac} t)$ , then the wave angle in the equation of motion of  $p_z$  is modulated by the term (cf. Eq. (2.159)):

$$h \sin(\Omega t) \equiv \frac{F_{ac}}{F_0} \frac{\Omega_0}{\Omega_{ac}} \sin\left(\frac{\Omega_{ac}}{\Omega_0} t\right), \quad \Omega_0 \equiv \frac{eF_0 d}{\hbar}. \quad (2.162)$$

This allows us to increase drastically the size of the web and the rate of chaotic transport through it. For example, for the case shown in Fig. 2.19, where we have an increase of the web size by a factor of  $6\times$ , it is sufficient to add an AC component of

the electric field with the frequency  $0.02 \cdot \Omega_0$  and an amplitude  $F_{ac} = 0.1 \cdot 0.02 \cdot F_0$  i.e. an amplitude smaller than that of the original constant field  $F_0$  by a factor of  $500\times$ .

### 2.5.3 Discussion

We have presented above just initial results on the subject (Soskin et al., 2009, 2010b). There are still many unsolved interesting problems:

1. It can be shown that, in the off-resonance case, there may be a facilitation of the onset of global chaos similar to that described in Sect. 2.4 above, i.e. the critical value of the modulation amplitude  $h$  required for the onset of global chaos between neighbouring separatrix loops possesses deep spikes (minima) as a function of the modulation frequency  $\Omega_{ac}$ . The detailed theory of this facilitation has yet to be developed.

2. Our conjecture that, in the resonant case, taking account of the next-order approximations of the averaging method could explain the split between different separatrix loops, should be proved rigorously. If the corresponding theory is developed, it will provide the possibility of calculating both the optimal modulation frequency, i.e. that at which the web sizes are maximal, for a given amplitude of modulation, and the maximum sizes themselves.

3. It would be interesting to study the case with an additive perturbation (rather than an angular modulation) in detail, both numerically and theoretically.

## 2.6 Conclusions

We have reviewed the recently developed method for the theoretical treatment of separatrix chaos in regimes when it involves resonance dynamics. It has been applied both to single-separatrix chaotic layers and to the onset of global chaos between two close separatrices. The method is based on a matching between the discrete chaotic dynamics of the separatrix map and the continuous regular dynamics of the resonance Hamiltonian. For single-separatrix chaos, the method has allowed:

1. Development of the first asymptotic (i.e. for  $h \rightarrow 0$ ) description of the high peaks in the width of the separatrix chaotic layer as a function of the perturbation frequency, thus describing its dominant feature and, in particular, its maxima.

2. Classification of all systems into two types, based on the asymptotic dependence of the maximum width on the perturbation amplitude  $h$ : the maximum width is proportional to  $h \ln(1/h)$  or  $h$  for systems of type I or type II respectively.

For systems with two or more separatrices, the method has allowed us to develop an accurate asymptotic theory of the facilitation of the onset of global chaos between neighbouring separatrices which occurs at frequencies close to multiples of a local

maximum in the eigenoscillation frequency as a function of the energy: the local maximum necessarily exists in the range between the separatrices.

Finally, for an oscillator perturbed by a plane wave of frequency equal to or close to the frequency of a small eigenoscillation, the method has allowed us to suggest how to enlarge substantially the size of the stochastic web using a rather weak perturbation, and it promises to provide an accurate theoretical description of the enlargement.

**Acknowledgements** We are very much indebted to George Zaslavsky: numerous discussions with him, and his friendly attitude and interest in our research, have greatly stimulated the work. We also acknowledge financial support from the grant within the Convention between the Institute of Semiconductor Physics and University of Pisa for 2008-2010, from a Royal Society International Joint Project grant 2007/R2-IJP, and from the German Physical Society grant SFB-TR12. Finally, S.M.S. acknowledges the hospitality of Pisa and Lancaster Universities during his visits to both places and, in turn, R.M. and P.V.E.McC. acknowledge the hospitality of the Institute of Semiconductor Physics during their visits there.

## 2.7 Appendix

This appendix follows the appendix of the paper (Soskin et al., 2008a). The chaotic layers of the system (2.85) associated with the separatrices of the unperturbed system (2.84) are described here by means of the separatrix map. To derive the map, we follow the method described in (Zaslavsky et al., 1991), but the analysis of the map significantly differs from formerly existing ones (Lichtenberg and Lieberman, 1992; Zaslavsky et al., 1991; Zaslavsky, 2007, 2005; Piftankin and Treschev, 2007) (cf. also the recently published paper (Shevchenko, 2008) where the analysis of the map has some similarity to ours but still differs significantly). Using our approach, we are able to calculate the chaotic layer boundaries in the *phase space* (rather than only in energy), throughout the resonance frequency ranges, and we can quantitatively describe the *transport* within the layer in a manner different from existing ones (cf. (Piftankin and Treschev, 2007; Rom-Kedar, 1994) and references therein).

### 2.7.1 Lower chaotic layer

We now present a detailed consideration of the lower chaotic layer. The upper layer may be considered in a very similar way.

### 2.7.1.1 Separatrix map

A typical form of trajectory  $\dot{q}(t)$  close to the inner separatrix (that corresponding to the lower potential barrier) is shown in Fig. 2.20. One can resolve pulses in  $\dot{q}(t)$ . Each of them consists of two approximately antisymmetric spikes<sup>21</sup>. The pulses are separated by intervals during which  $|\dot{q}|$  is relatively small. In general, successive intervals differ between each other. Let us introduce the pair of variables  $E$  and  $\varphi$ :

$$E \equiv H_0, \quad \varphi \equiv \omega_f t + \varphi_a, \tag{2.163}$$

where the constant  $\varphi_a$  may be chosen arbitrarily.

The energy  $E$  changes only during the pulses of  $\dot{q}(t)$  and remains nearly unchanged during the intervals between the pulses, when  $|\dot{q}(t)|$  is small (Zaslavsky et al., 1991). We assign numbers  $i$  to the pulses and introduce the sequences of  $(E_i, \varphi_i)$  corresponding to the initial instants  $t_i$  of the pulses. In such a way, we obtain the following map (cf. (Zaslavsky et al., 1991)):

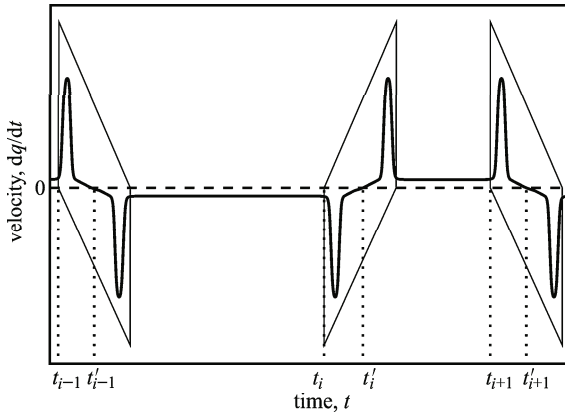


**Fig. 2.20** Schematic example of the time dependence of the velocity of the perturbed system (thick solid line) in the case when the energy of motion varies in the close vicinity of the top of the lower potential barrier. The dashed line marks the zero level of the velocity. Pulses of the velocity are schematically singled out by the parallelograms (drawn by a thin solid line). The two sequences of time instants  $(\dots, t_{i-1}, t_i, t_{i+1}, \dots)$  and  $(\dots, t'_{i-1}, t'_i, t'_{i+1}, \dots)$  correspond to beginnings and centers of the pulses, respectively.

<sup>21</sup> Spikes correspond to motion over any of the minima of the potential, first in one and then (after the reflection from one of the upper barriers) in the opposite direction. If  $\Phi$  is small, then the spikes within the pulse are separated by long intervals since the reflection point is situated close to the top of the upper barrier, where the motion is slow.

$$E_{i+1} = E_i + \Delta E_i, \quad \varphi_{i+1} = \varphi_i + \frac{\omega_f \pi (3 - \text{sign}(E_{i+1} - E_b^{(1)}))}{2\omega(E_{i+1})},$$

$$\Delta E_i \equiv h \int_{i\text{th pulse}} dt \dot{q}(t) \cos(\omega_f t), \quad (2.164)$$

where  $\int_{i\text{th pulse}}$  means integration over the  $i$ th pulse. Before deriving a more explicit expression for  $\Delta E_i$ , we make two remarks.

1. Let us denote with  $t'_i$  the instant within the  $i$ th pulse when  $\dot{q}$  is equal to zero (Fig. 2.20). The function  $\dot{q}(t - t'_i)$  is an odd function within the  $i$ th pulse and it is convenient to transform the cosine in the integrand in  $\Delta E_i$  (2.164) as

$$\begin{aligned} \cos(\omega_f t) &\equiv \cos(\omega_f(t - t'_i) + \omega_f t'_i) \\ &\equiv \cos(\omega_f(t - t'_i)) \cos(\omega_f t'_i) - \sin(\omega_f(t - t'_i)) \sin(\omega_f t'_i), \end{aligned}$$

and to put  $\varphi_a = \omega_f(t'_i - t_i)$ , so that  $\varphi_i \equiv \omega_f t'_i$ .

2. Each pulse of  $\dot{q}$  contains one positive and one negative spike. The first spike can be either positive or negative. If  $E$  changes during the given  $n$ th pulse so that its value at the end of the pulse is *smaller* than  $E_b^{(1)}$ , then the first spikes of the  $i$ th and  $(i + 1)$ st pulses have the *same* signs. On the contrary, if  $E$  at the end of the  $i$ th pulse is *larger* than  $E_b^{(1)}$ , then the first spikes of the  $i$ th and  $(i + 1)$ st pulses have *opposite* signs. Note that Fig. 2.20 corresponds to the case when the energy remains above  $E_b^{(1)}$  during the whole interval shown in the figure. This obviously affects the sign of  $\Delta E_i$ , and it may be explicitly accounted for in the map if we introduce a new discrete variable  $\sigma_i = \pm 1$  which characterizes the sign of  $\dot{q}$  at the beginning of a given  $i$ th pulse,

$$\sigma_i \equiv \text{sign}(\dot{q}(t_i)), \quad (2.165)$$

and changes from pulse to pulse as

$$\sigma_{i+1} = \sigma_i \text{sign}(E_b^{(1)} - E_{i+1}). \quad (2.166)$$

With account taken of the above remarks, we can rewrite the map (164) as follows:

$$\begin{aligned} E_{i+1} &= E_i + \sigma_i h \varepsilon^{(low)} \sin(\varphi_i), \\ \varphi_{i+1} &= \varphi_i + \frac{\omega_f \pi (3 - \text{sign}(E_{i+1} - E_b^{(1)}))}{2\omega(E_{i+1})}, \\ \sigma_{i+1} &= \sigma_i \text{sign}(E_b^{(1)} - E_{i+1}), \end{aligned} \quad (2.167)$$

$$\begin{aligned} \varepsilon^{(low)} &\equiv \varepsilon^{(low)}(\omega_f) = -\sigma_i \int_{i\text{th pulse}} dt \dot{q}(t - t'_i) \sin(\omega_f(t - t'_i)) \\ &\approx -2\sigma_i \int_{t'_i}^{t'_{i+1}} dt \dot{q}(t - t'_i) \sin(\omega_f(t - t'_i)). \end{aligned}$$

A map similar to (2.167) was introduced in (Zaslavsky and Filonenko, 1968), and it is often called the Zaslavsky separatrix map. It was re-derived mathematically rigorously in (Rom-Kedar, 1990); see also the recent mathematical review (Piftankin and Treschev, 2007). The latter review also describes generalizations of the Zaslavsky map as well as other types of separatrix map. The analysis presented below relates immediately to the Zaslavsky map but it is hoped that it will prove possible to generalize it for other types of separatrix maps too.

The variable  $\varepsilon^{(low)}$  introduced in (2.167) will be convenient for the further calculations since it does not depend on  $i$  in the lowest-order approximation. A quantity like  $\delta_l \equiv h|\varepsilon^{(low)}|$  is sometimes called the *separatrix split* (Zaslavsky, 2007) since it is conventionally assumed that the maximal deviation of energy on the chaotic trajectory from the separatrix energy is of the order of  $\delta_l$  (Lichtenberg and Lieberman, 1992; Zaslavsky et al., 1991; Zaslavsky, 2007, 2005). As in the main text, we shall use this term, but we emphasize that the maximal deviation may be much larger.

In the adiabatic limit  $\omega_f \rightarrow 0$ , the excess of the upper boundary  $E_{cl}^{(1)}$  of the lower layer over the lower barrier  $E_b^{(1)}$  does not depend on angle and is equal to  $2\pi h$  (cf. (Elskens and Escande, 1991)). But  $\omega_f$  relevant for the spike of  $h_{gc}(\omega_f)$  cannot be considered as an adiabatic frequency, despite its smallness, because it is close to  $\omega_m$  or to its multiple while all energies at the boundary lie in the range where the eigenfrequency is also close to  $\omega_m$ :

$$\omega_f \approx (2j-1)\omega_m \approx (2j-1)\omega(E_{cl}^{(1)}), \quad j = 1, 2, 3, \dots \quad (2.168)$$

The validity of (2.168) (confirmed by the results) is *crucial* for the description of the layer boundary in the relevant case.

### 2.7.1.2 Separatrix split

Let us evaluate  $\varepsilon^{(low)}$  explicitly. Given that the energy is close to  $E_b^{(1)}$ , the velocity  $\dot{q}(t-t'_i)$  in  $\varepsilon^{(low)}$  (2.167) may be replaced by the corresponding velocity along the separatrix associated with the lower barrier,  $\dot{q}_s^{(low)}(t-t'_i)$ , while the upper limit of the integral may be replaced by infinity. In the asymptotic limit  $\Phi \rightarrow 0$ , the interval between spikes within the pulse becomes infinitely long so that only the short ( $\sim \omega_0^{-1}$ ) intervals corresponding to the spikes contribute to the integral in  $\varepsilon^{(low)}$  (2.167). In the scale  $\omega_f^{-1}$ , they may be considered just as the two instants:

$$t_{sp}^{(1,2)} - t'_i \approx \pm \frac{\pi}{4\omega_m}, \quad \Phi \rightarrow 0. \quad (2.169)$$

In the definition of  $\varepsilon^{(low)}$  (2.167), we substitute the argument of the sine by the corresponding constants for the positive and negative spikes respectively:

$$\varepsilon^{(low)} \approx 2 \sin \left( \frac{\pi \omega_f}{4 \omega_m} \right) \int_{\text{positive spike}} dt \dot{q}_s^{(low)}(t - t'_i) \approx 2\pi \sin \left( \frac{\pi \omega_f}{4 \omega_m} \right), \quad (2.170)$$

$$\Phi \rightarrow 0.$$

In the derivation of the first equality in (2.170), we have also taken into account that the function  $\dot{q}_s^{(low)}(x)$  is odd. In the derivation of the second equality in (2.170), we have taken into account that the right turning point of the relevant separatrix is the top of the lower barrier and the distance between this point and the left turning point of the separatrix approaches  $\pi$  in the limit  $\Phi \rightarrow 0$ .

For the frequencies relevant to the minima of the spikes of  $h_{gc}(\omega_f)$ , i.e. for  $\omega_f = \omega_s^{(j)} \approx (2j - 1)\omega_m$ , we obtain:

$$\varepsilon^{(low)}(\omega_s^{(j)}) \approx 2\pi \sin \left( (2j - 1) \frac{\pi}{4} \right) = \sqrt{2}\pi(-1)^{\lfloor \frac{2j-1}{4} \rfloor}, \quad (2.171)$$

$$j = 1, 2, 3, \dots, \quad \Phi \rightarrow 0.$$

For moderately small  $\Phi$ , it is better to use the more accurate formula:

$$\varepsilon^{(low)}(\omega_f) = 2 \int_0^\infty dt \dot{q}_s^{(low)}(t) \sin(\omega_f t), \quad (2.172)$$

where the instant  $t = 0$  corresponds to the turning point of the separatrix to the left of the lower barrier, i.e.  $\dot{q}_s^{(low)}(t = 0) = 0$  while  $\dot{q}_s^{(low)} > 0$  for all  $t > 0$ . The dependence  $|\varepsilon^{(low)}(\omega_f)|$  by Eq. (2.172) is shown for  $\Phi = 0.2$  in Fig. 2.21(a). For small frequencies, the asymptotic formula (2.170) fits well the formula (2.172).

### 2.7.1.3 Dynamics of the map

Consider the *dynamics* of the map (2.167) when  $\omega_f$  is close to the spike's minima:  $\omega_f \approx n\omega_m$  where  $n \equiv 2j - 1$  while  $j = 1, 2, 3, \dots$ . Let the energy at the step  $i = -1$  be equal to  $E_b^{(1)}$ . The trajectory passing through the state with this energy is chaotic since  $(\omega(E))^{-1}$  diverges as  $E \rightarrow E_b^{(1)}$  and, therefore, the angle  $\varphi_{-1}$  is not correlated with the angle on the previous step  $\varphi_{-2}$ . The quantity  $\sigma_{-1}$  is not correlated with  $\sigma_{-2}$  either. Thus,  $\sin(\varphi_{-1})$  may take any value in the range  $[-1, 1]$  and  $\sigma_{-1}$  may equally take the values 1 or -1. Therefore, the energy may change on the next step by an arbitrary value in the interval  $[-h|\varepsilon^{(low)}|, h|\varepsilon^{(low)}|]$ . Thus,  $E_0 - E_b^{(1)}$  may have a positive value<sup>22</sup>  $\sim h|\varepsilon^{(low)}|$ . Then, the approximate equality  $n\omega(E_0) \approx \omega_m$  holds, provided that the value of  $h$  is from the relevant range. Allowing for this and recalling that we are interested only in those realizations of the map such that  $E_0 > E_b^{(1)}$ , the relevant realization of the map  $i = -1 \rightarrow i = 0$  may be written as:

<sup>22</sup> The latter is valid for any  $\varphi_{-1}$  except in the close vicinity of multiples of  $\pi$  while the state  $E_0, \varphi_0$  (2.167) in the latter range of  $\varphi_{-1}$  turns out irrelevant to the boundary, as shown further down.

$$\begin{aligned}
 E_0 &= E_b^{(1)} + \sigma_{-1} h \varepsilon^{(low)} \sin(\varphi_{-1}) = E_b^{(1)} + h |\varepsilon^{(low)} \sin(\varphi_{-1})|, \\
 \varphi_0 &\approx \varphi_{-1} + n\pi, \\
 \sigma_0 &= -\sigma_{-1}.
 \end{aligned}
 \tag{2.173}$$

One may expect that further evolution of the map will, for some time, approximately follow the trajectory of the system (2.87) with the initial energy  $E_0$  (2.173) and an arbitrary  $\varphi_{-1}$  and initial slow angle  $\psi$  somehow related to  $\varphi_0 \approx \varphi_{-1} + n\pi$ . Let us prove this explicitly.

Consider two subsequent iterations of the map (2.167):  $2i \rightarrow 2i + 1$  and  $2i + 1 \rightarrow 2i + 2$  with an arbitrary  $i \geq 0$ . While doing this, we shall assume the validity of (2.168) (it will be clarified below when this is true) from which it follows that: (i)  $\omega(E_{k+1}) \approx \omega(E_k)$ , (ii)  $\varphi_{k+1} - \varphi_k \approx n\pi \equiv (2j - 1)\pi$ . It will follow from the results that the neglected corrections are small in comparison with the characteristic scales of the variation of  $E$  and  $\varphi$  (cf. the conventional treatment of the nonlinear resonance dynamics (Chirikov, 1979; Lichtenberg and Lieberman, 1992; Zaslavsky et al., 1991; Zaslavsky, 2007, 2005; Soskin et al., 2003)). Furthermore it follows from

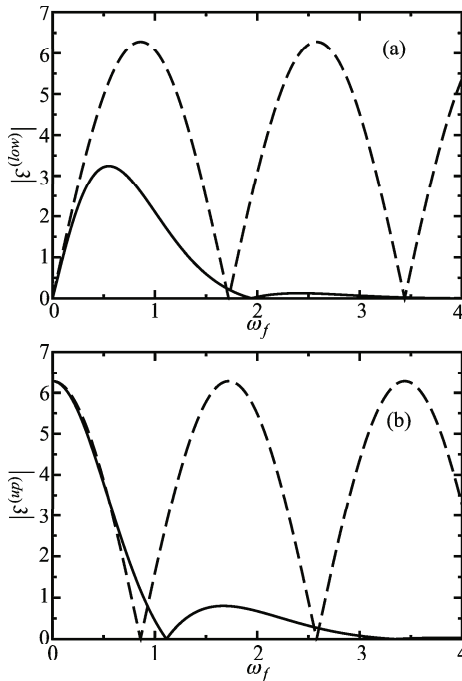


**Fig. 2.21** Theoretical estimates for the normalized separatrix split (for  $\Phi = 0.2$ ) as a function of the perturbation frequency, for the lower and upper layers in (a) and (b) respectively. The solid lines are calculated from Eqs. (2.172) and (2.204) for (a) and (b) respectively, while the dashed lines represent the asymptotic expressions (2.170) and (2.205) respectively.

(2.167) that, while the energy remains above the barrier energy,  $\sigma_k$  oscillates, so that  $\sigma_{2i} = \sigma_0$  and  $\sigma_{2i+1} = -\sigma_0$ . Then,

$$\begin{aligned} E_{2i+1} &= E_{2i} + \sigma_0 h \varepsilon^{(low)} \sin(\varphi_{2i}), \\ \varphi_{2i+1} &= \varphi_{2i} + \frac{\omega_f}{\omega(E_{2i+1})} \pi \approx \varphi_{2i} + n\pi + \pi \frac{\omega_f - n\omega(E_{2i})}{\omega(E_{2i})}, \end{aligned} \quad (2.174)$$

$$\begin{aligned} E_{2i+2} &= E_{2i+1} - \sigma_0 h \varepsilon^{(low)} \sin(\varphi_{2i+1}) \\ &= E_{2i+1} + \sigma_0 h \varepsilon^{(low)} \sin(\varphi_{2i+1} - n\pi) \approx E_{2i} + \sigma_0 2h \varepsilon^{(low)} \sin(\varphi_{2i}), \end{aligned} \quad (2.175)$$

$$\varphi_{2i+2} = \varphi_{2i+1} + \frac{\omega_f}{\omega(E_{2i+2})} \pi \approx \varphi_{2i} + 2\pi n + 2\pi \frac{\omega_f - n\omega(E_{2i})}{\omega(E_{2i})}$$

(the second equality in the map for  $E_{2i+2}$  takes into account that  $n$  is odd so that  $\sin(\varphi - n\pi) = -\sin(\varphi)$ .)

The quantity  $\varphi_{2i+2} - \varphi_{2i} - 2\pi n$  is small, so the map  $2i \rightarrow 2i + 2$  (2.175) may be approximated by differential equations for  $E_{2i}$  and  $\tilde{\varphi}_{2i} \equiv \varphi_{2i} - 2\pi ni$ :

$$\begin{aligned} \frac{dE_{2i}}{d(2i)} &= \sigma_0 h \varepsilon^{(low)} \sin(\tilde{\varphi}_{2i}), & \frac{d\tilde{\varphi}_{2i}}{d(2i)} &= \frac{\pi}{\omega(E_{2i})} (\omega_f - n\omega(E_{2i})), \\ \tilde{\varphi}_{2i} &\equiv \varphi_{2i} - 2\pi ni. \end{aligned} \quad (2.176)$$

Let us (i) use for  $\varepsilon^{(low)}$  the asymptotic formula (2.171), (ii) take into account that the increase of  $i$  by 1 corresponds to an increase of time by  $\pi/\omega(E)$ , and (iii) transform from the variables  $(E, \tilde{\varphi})$  to the variables  $(I, \tilde{\psi} \equiv n\pi(1 - \sigma_0)/2 - \tilde{\varphi})$ . Equations (2.176) reduce then to

$$\begin{aligned} \frac{dI}{dt} &= -h\sqrt{2}(-1)^{\lfloor \frac{n}{4} \rfloor} \sin(\tilde{\psi}), & \frac{d\tilde{\psi}}{dt} &= n\omega - \omega_f, \\ \tilde{\psi} &\equiv n\pi \frac{1 - \sigma_0}{2} - \tilde{\varphi}, & n &\equiv 2j - 1. \end{aligned} \quad (2.177)$$

Equations (2.177) are identical to the equations of motion of the system (2.87) in their lowest-order approximation, i.e. to equations (2.98) where  $q_n$  is replaced by its asymptotic value (2.96) and the last term in the right-hand part of the second equation is neglected, being of higher order in comparison with the term  $n\omega - \omega_f$ .

Apart from the formal identity of Eqs. (2.177) and (2.98),  $\tilde{\psi}$  in (2.177) and  $\tilde{\psi}$  in (2.98) are identical to each other. Necessarily  $t'_i$  corresponds to a turning point (see Fig. 2.20) while the corresponding  $\psi$  is equal to  $2\pi i$  or  $\pi + 2\pi i$  for the right and left turning points respectively (see (2.87)) i.e.  $\psi = 2\pi i + \pi(1 - \sigma_i)/2$ , so that  $\tilde{\psi}_{(2.98)} \equiv n\psi - \omega_f t = n\pi(1 - \sigma)/2 - \tilde{\varphi} \equiv \tilde{\psi}_{(2.177)}$ .

The relevant initial conditions for (2.177) follow from (2.173) and from the relationship between  $\tilde{\psi}$  and  $\varphi$ :

$$I(0) = I(E = E_b^{(1)} + h\sqrt{2\pi}|\sin(\tilde{\psi}(0))|), \quad (2.178)$$

while  $\tilde{\psi}(0) \equiv n\pi(1 - \sigma_0)/2 - \varphi_0$  may be an arbitrary angle from the ranges where

$$(-1)^{\lfloor n/4 \rfloor} \sin(\tilde{\psi}(0)) < 0. \quad (2.179)$$

For moderately small  $\Phi$ , it is better to use the more accurate dynamic equations (2.98) instead of (2.177) and the more accurate initial value of action instead of (2.178):

$$I(0) = I(E = E_b^{(1)} + \delta_l |\sin(\tilde{\psi}(0))|), \quad \delta_l \equiv h|\varepsilon^{(low)}|, \quad (2.180)$$

with  $\varepsilon^{(low)}$  calculated by (2.172).

We name the quantity  $\delta_l |\sin(\tilde{\psi})|$  the *generalized separatrix split* (GSS) for the lower layer. Unlike the conventional separatrix split  $\delta_l$  (Zaslavsky, 2007), it is *angle-dependent*. The curve  $I(\tilde{\psi}) = I(E = E_b^{(1)} + \delta_l |\sin(\tilde{\psi})|)$  may be called then the GSS curve for the lower barrier and denoted as  $I_{\text{GSS}}^{(l)}(\tilde{\psi})$ .

Finally, let us investigate an important issue: whether the transformation from the discrete separatrix map (i.e. (2.174) and (2.175)) to the differential equations (2.176) is valid for the very first step and, if it is so, for how long it is valid after that. The transformation is valid as long as  $\omega(E_k) \approx n\omega_f$  i.e. as long as  $E_k$  is not too close to the barrier energy  $E_b^{(1)}$ . At the step  $k = 0$ , the system stays at the GSS curve, with a given (random) angle  $\tilde{\psi}(0)$  from the range (2.179). Thus, at this stage, the relation (2.168) is certainly valid (for the relevant range of  $h$  and for any angle except for the close vicinity of the multiples of  $\pi$ ). The change of energy at the next step is positive too:

$$\begin{aligned} E_1 - E_0 &\equiv \sigma_0 h \varepsilon^{(low)} \sin(\tilde{\varphi}_0) \approx -\sigma_{-1} h \varepsilon^{(low)} \sin(\tilde{\varphi}_{-1} - n\pi) \\ &= \sigma_{-1} h \varepsilon^{(low)} \sin(\tilde{\varphi}_{-1}) \equiv E_0 - E_{-1} > 0. \end{aligned}$$

This may also be interpreted as a consequence of the first equation in (2.177) and of the inequality (2.179).

Hence, (2.168) is valid at the step  $k = 1$  too. Similarly, one can show that  $E_2 - E_1 > 0$ , etc. Thus, the transformation (2.174, 2.175)  $\rightarrow$  (2.176) is valid at this initial stage indeed, and the evolution of  $(E, \tilde{\varphi})$  does reduce to the resonant trajectory (2.14) with an initial angle from the range (2.179) and the initial action (2.180). This lasts until the resonant trajectory meets the GSS curve in the adjacent  $\pi$  range of  $\tilde{\psi}$  i.e. at  $t$  such that the state  $(I(t), \tilde{\psi}(t))$  satisfies the conditions:

$$I(t) = I_{\text{GSS}}^{(l)}(\tilde{\psi}(t)), \quad [\tilde{\psi}(t)/\pi] - [\tilde{\psi}(0)/\pi] = 1. \quad (2.181)$$

At this instant, the absolute value of the change of energy  $E_k$  in the separatrix map (2.174) is equal to  $E_k - E_b^{(1)}$  (just because the state belongs to the GSS curve) but the sign of this change is negative because the sign of  $\sin(\varphi_k)$  is opposite to that of  $\sin(\varphi_0)$ . Therefore, at the step  $k + 1$ , the system gets to the separatrix itself, and the

regular-like evolution stops: at the next step of the map, the system may either again get to the GSS curve but with a new (random) angle from the range (2.179), and start a new regular-like evolution as described above; or it may get to the similar GSS curve *below* the barrier and start an analogous regular-like evolution in the energy range below the barrier, until it stops in the same manner as described above, etc.

This approach makes it possible to describe all features of the transport within the chaotic layer. In the present context, it is most important to describe the *upper outer boundary* of the layer.

### 2.7.1.4 Boundary of the layer

We may now analyze the evolution of the boundary of the layer as  $h$  grows. Some of the stages of the evolution are illustrated by Figs. 2.13, 2.14 and 2.22.

It follows from the analysis carried out in the previous subsection that *any* state (in the  $I - \tilde{\psi}$  plane) lying beyond the GSS curve but belonging to any trajectory following Eqs. (2.98) which possesses common points with the GSS curve belongs to the chaotic layer: the system starting from such a state will, sooner or later, reach the separatrix where the chaotization will necessarily occur. Therefore, the *upper boundary* of the chaotic layer coincides with the trajectory following equations (2.98) with the initial action (2.180) and an initial angle  $\tilde{\psi}(0)$  from the range (2.179) such that the trajectory deviates from the barrier energy by more than does a trajectory (2.98)-(2.179)-(2.180) with any other initial angle. There may be only two topologically different options for such a trajectory: either it is *tangent* to the GSS curve, or it is the separatrix trajectory which *intersects* the GSS curve (some schematic examples are shown in Figs. 2.22(a) and (b) respectively; some real calculations are shown in Figs. 2.13 and 2.14).

#### 1. Relatively small $h$

Consider first values of  $h$  which are large enough for the condition (2.168) to be satisfied (the explicit criterion will be given in (2.192)) but which are smaller than the value  $h_{cr}^{(l)} \equiv h_{cr}^{(l)}(\omega_f)$  determined by Eq. (2.125) (its meaning is explained below). The further analysis within this range of  $h$  differs for the ranges of  $\omega_f$  relevant to *odd* and *even* spikes, and so we consider them separately.

##### (1) *Odd spikes*

The relevant frequencies are:

$$\omega_f \approx n\omega_m, \quad n \equiv 2j - 1, \quad j = 1, 3, 5, \dots \quad (2.182)$$

Let us seek the state  $\{I_t^{(l)}, \tilde{\psi}_t^{(l)}\}$  (with  $\tilde{\psi}_t^{(l)}$  within the range  $]0, \pi[$ ) where the resonant trajectory is *tangent* to the GSS curve. With this aim, we equalise both the ac-

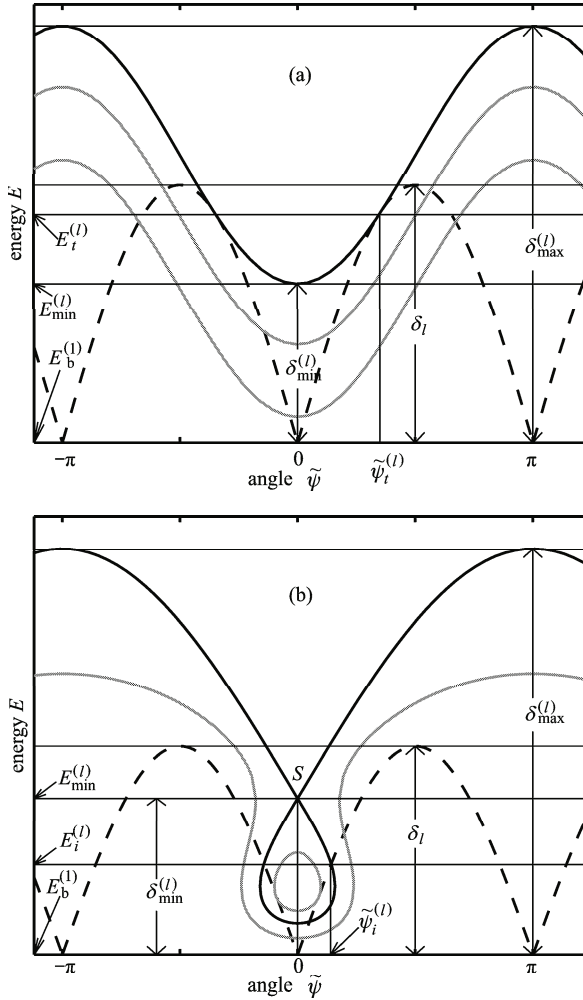


**Fig. 2.22** A schematic figure illustrating the formation of the boundary of the lower chaotic layer for  $h < h_{cr}^{(l)}(\omega_f)$  in the ranges of  $\omega_f$  relevant to (a) odd, and (b) even spikes. The dashed line shows the GSS curve in the energy-angle plane:  $E(\tilde{\psi}) = E_{GSS}^{(l)}(\tilde{\psi}) \equiv E_b^{(l)} + \delta_l |\sin(\tilde{\psi})|$ . Thicker solid lines show examples of those trajectories (2.98) which have points in common with the GSS curve. One of them (shown by the *black* line) relates to the formation of the upper boundary of the lower chaotic layer: in (a), the boundary is the trajectory *tangent* to the GSS curve; in (b), the boundary is the upper part of the *separatrix* generated by the saddle “s”. Relevant common points of the GSS curve and the thick *black* line have angles  $\pm \tilde{\psi}_i^{(l)}$  and energy  $E_i^{(l)}$  in the case (a), and angles  $\pm \tilde{\psi}_i^{(l)}$  and energy  $E_i^{(l)}$  in the case (b). The minimum and maximum deviation of energy on the boundary from the barrier energy are denoted as  $\delta_{min}^{(l)}$  and  $\delta_{max}^{(l)}$  respectively. The maximum deviation on the GSS curve is equal to  $\delta_l$ . (Color version may be found in the online version of (Soskin et al., 2008a) as Fig. 16).

tions and the derivatives of both curves. The equality of actions immediately yields  $I_t^{(l)}$  via  $\tilde{\psi}_t^{(l)}$ :  $I_t^{(l)} \equiv I(E = E_t^{(l)}) = I_{\text{GSS}}^{(l)}(\tilde{\psi}_t^{(l)})$ . The derivative along the GSS curve is obtained by differentiation of  $I_{\text{GSS}}^{(l)}(\tilde{\psi})$ . The derivative along a resonant trajectory can be found by dividing the first dynamic equation in (2.14) by the second one. Substituting the expression of  $I_t^{(l)}$  via  $\tilde{\psi}_t^{(l)}$  into the equality of the derivatives, we obtain a closed equation for  $\tilde{\psi}_t^{(l)}$ , and its solution immediately gives us the relevant  $\tilde{\psi}(0)$ :

$$\begin{aligned} & \left[ |\varepsilon^{(low)}| \cos(\tilde{\psi}_t^{(l)}) \left( 1 - \frac{\omega_f}{n\omega(E)} - h \frac{dq_n(E)}{dE} \cos(\tilde{\psi}_t^{(l)}) \right) + q_n(E) \sin(\tilde{\psi}_t^{(l)}) \right]_{E=E_t^{(l)}} \\ & = 0, \\ & E_t^{(l)} \equiv E_b^{(1)} + h|\varepsilon^{(low)}| \sin(\tilde{\psi}_t^{(l)}), \quad \tilde{\psi}_t^{(l)} \in [0, \pi], \\ & n \equiv 2j - 1, \quad j = 1, 3, 5, \dots, \quad \tilde{\psi}(0) = \tilde{\psi}_t^{(l)}. \end{aligned} \quad (2.183)$$

A careful analysis of the phase space structure shows that, in the present case (i.e. when  $h < h_{cr}^{(l)}(\omega_f)$  while  $j$  is odd), there is no separatrix of the resonant Hamiltonian (2.87) which would both intersect the GSS curve and possess points above the tangent trajectory<sup>23</sup>. Thus, for this range of  $h$ , the outer boundary of the chaotic layer is formed by the trajectory following the dynamical equations (2.98) with the initial angle given by (2.183) and the initial action by (2.180) (Fig. 2.22(a)).

Let us find the lowest-order solution of Eq. (2.183). We neglect the term  $1 - \omega_f/(n\omega(E))$  (the result will justify this) and use the lowest-order expression for the relevant quantities: namely, Eqs. (2.171) and (2.96) for  $\varepsilon^{(low)}$  and  $q_n$  respectively, and the lowest-order expression for  $dq_n/dE$  which can be derived from Eq. (2.95):

$$\begin{aligned} \frac{dq_n(E)}{dE} &= (-1)^{[\frac{n}{4}]} \frac{\pi}{4\sqrt{2} \left( E - E_b^{(1)} \right) \ln(\Phi^{-1})}, \\ n &\equiv 2j - 1, \quad E - E_b^{(1)} \ll \Phi \rightarrow 0. \end{aligned} \quad (2.184)$$

Then Eq. (2.183) reduces to the following equation

$$\tan^2(\tilde{\psi}_t^{(l)}) = \frac{n\pi}{8 \ln(\Phi^{-1})}. \quad (2.185)$$

The lowest-order solution of (2.185) in the range  $]0, \pi[$  is

$$\tilde{\psi}_t^{(l)} = (-1)^{[\frac{n}{4}]} \sqrt{\frac{n\pi}{8 \ln(1/\Phi)}} + \pi \frac{1 - (-1)^{[\frac{n}{4}]} }{2}. \quad (2.186)$$

<sup>23</sup> For odd numbers  $j \geq 3$ , there are separatrices which lie in the range of  $E$  where  $\omega(E) \ll \omega_m$  i.e. much closer to the barrier than the tangent trajectory: these separatrices are therefore irrelevant.

It follows from the definition  $E_t^{(l)}$  (2.183) and from (2.186) that the lowest-order expression for  $E_t^{(l)} - E_b^{(1)}$  is

$$E_t^{(l)} - E_b^{(1)} = \delta_l \sin(\tilde{\psi}_t^{(l)}) = \frac{\pi^{3/2}}{2} \frac{h}{\sqrt{\ln(1/\Phi)/n}}. \quad (2.187)$$

The next step is to find the *minimum* value of the energy on the boundary of the layer,  $E_{\min}^{(l)}$ . It follows from the analysis of the dynamical equations (2.98) that the corresponding angle  $\tilde{\psi}_{\min}$  is equal to 0 if  $\text{sign}(q_{2j-1}) > 0$  (i.e.  $j = 1, 5, 9, \dots$ ) or to  $\pi$  if  $\text{sign}(q_{2j-1}) < 0$  (i.e.  $j = 3, 7, 11, \dots$ ): cf. Fig. 2.8(a). Given that the Hamiltonian (2.87) is constant along any trajectory (2.98) while the boundary coincides with one such trajectory, the values of the Hamiltonian (2.87) in the states  $\{I(E_{\min}^{(l)}), \tilde{\psi} = \tilde{\psi}_{\min}\}$  and  $\{I_t^{(l)}, \tilde{\psi}_t^{(l)}\}$  should be equal to each other. In explicit form, this equality may be written as

$$\int_{E_{\min}^{(l)}}^{E_t^{(l)}} dE \left( 1 - \frac{\omega_f}{n\omega(E)} \right) - h \left( q_n(E_t^{(l)}) \cos(\tilde{\psi}_t^{(l)}) - (-1)^{[n/4]} q_n(E_{\min}^{(l)}) \right) = 0. \quad (2.188)$$

Let us find the lowest-order solution of Eq. (2.188). Assume that  $E_{\min}^{(l)}$  still belongs to the range of  $E$  where  $\omega(E) \approx \omega_m$  (the result will confirm this assumption). Then the integrand in (2.188) goes to zero in the asymptotic limit  $\Phi \rightarrow 0$ . Hence the integral may be neglected (again, to be justified by the result). The remaining terms in Eq. (2.188) should be treated very carefully. In particular, it is insufficient to use the lowest-order value (2.96) for  $q_n$  since it is the difference between  $q_n(E_t^{(l)})$  and  $q_n(E_{\min}^{(l)})$  that matters. Moreover, the approximate equality  $q_n(E_t^{(l)}) - q_n(E_{\min}^{(l)}) \approx dq_n(E_t^{(l)})/dE_t^{(l)}(E_t^{(l)} - E_{\min}^{(l)})$  does not apply here either since, as follows from Eq. (2.184), the derivative  $dq_n(E)/dE$  may vary strongly in the range  $[E_{\min}^{(l)}, E_t^{(l)}]$  if  $(E_t^{(l)} - E_{\min}^{(l)})/(E_{\min}^{(l)} - E_b^{(1)}) \gtrsim 1$  (again, to be justified by the result). That is why it is necessary to use the more accurate expression (2.95) for  $q_n$ . Allowing for the asymptotic expression (186) of  $\tilde{\psi}_t^{(l)}$  and keeping only the lowest-order terms, one can finally reduce Eq. (2.188) to the relation

$$\ln \left( \frac{E_t^{(l)} - E_b^{(1)}}{E_{\min}^{(l)} - E_b^{(1)}} \right) = \frac{1}{2}. \quad (2.189)$$

Substituting here the asymptotic value of  $E_t^{(l)}$  (2.187), we obtain the final lowest-order expression for the minimum deviation (along the boundary) of the energy from the barrier:

$$\delta_{\min}^{(l)} \equiv E_{\min}^{(l)} - E_b^{(1)} = (E_t^{(l)} - E_b^{(1)})/\sqrt{e} = \frac{\pi^{3/2}}{2e^{1/2}} \frac{h}{\sqrt{\ln(1/\Phi)/n}}. \quad (2.190)$$

It is necessary and sufficient that the condition  $\omega(E) \approx \omega_m$  is satisfied at the *minimal* and *maximal* energies of the boundary to ensure that the second equality in (2.168) holds true, i.e. that  $\omega(E)$  is close to  $\omega_m$  for *all* points of the boundary.

At the *minimal* energy, this condition is

$$\omega_m - \omega(E_b^{(1)} + \delta_{\min}^{(l)}) \ll \omega_m. \quad (2.191)$$

Eq. (2.191) determines the lower limit of the relevant range of  $h$ . The asymptotic form of (2.191) is:

$$\frac{\ln\left(\frac{\Phi\sqrt{\ln(1/\Phi)}}{h}\right)}{\ln(1/\Phi)} \ll 1. \quad (2.192)$$

We emphasize that any  $h$  of the order of  $h_{s0}$  (2.136) satisfies this condition. In the asymptotic limit  $\Phi \rightarrow 0$ , the left-hand part of Eq. (2.192) goes to zero.

As for the *maximal* energy, it may take values up to the energy of the lower saddle “ $sl$ ”, i.e.  $E_{sl}$  (2.102). Obviously, (2.168) is valid at this saddle, too.

## (2) Even spikes

The relevant frequencies are:

$$\omega_f \approx n\omega_m, \quad n \equiv 2j - 1, \quad j = 2, 4, 6, \dots \quad (2.193)$$

In this case,  $q_n(E)$  and  $dq_n(E)/dE$  have different signs for all  $E$  within the relevant range (i.e. where  $\omega(E) \approx \omega_m$ ,  $q_n(E) \approx q_n(E_m)$ ): cf. (2.96) and (2.184). Then, in the asymptotic limit  $\Phi \rightarrow 0$ , Eq. (2.183) for the tangency does not have any solution for  $\tilde{\psi}_t^{(l)}$  in the relevant range<sup>24</sup>. There may only be solutions very close to some of  $\pi$  integers, and the corresponding energies  $E_t^{(l)}$  are then very close to  $E_b^{(1)}$  i.e.  $\omega(E_t^{(l)}) \ll \omega_m$ : therefore they are irrelevant.

At the same time, unlike for the odd spikes, there exists a saddle with an angle

$$\tilde{\psi}_s^{(l)} = \pi \frac{1 - (-1)^{\lfloor \frac{n}{4} \rfloor}}{2}, \quad (2.194)$$

while the energy (which may be found as the appropriate solution of Eq. (2.99)) lies in the relevant vicinity of the lower barrier (Fig. 2.22(b)). In the lowest-order approximation, this saddle energy is:

$$E_s^{(l)} \equiv E_b^{(1)} + \delta_s, \quad \delta_s = \frac{\pi}{2\sqrt{2}} \frac{h}{\ln(\ln(4e/\Phi))}. \quad (2.195)$$

This saddle (denoted in Fig. 2.22(b) as “ $s$ ”) generates a separatrix. Its upper whiskers go to the similar adjacent saddles (shifted in  $\tilde{\psi}$  by  $2\pi$ ). In the asymp-

<sup>24</sup> In case of a *moderately* small  $\Phi$ , tangency may exist in the relevant range of energies. The boundary of the layer is then formed by the tangent trajectory.

otic limit  $\Phi \rightarrow 0$ , the upper whiskers are much steeper than the GSS curve and hence they do not intersect it<sup>25</sup>. The lower whiskers do intersect the GSS curve and, moreover, two intersections lie in the relevant energy range (Fig. 2.22(b)). Let us show this explicitly. We write the expression for the Hamiltonian (2.87) in the relevant vicinity of the barrier energy (i.e. where  $\omega_m - \omega(E) \ll \omega_m$ ), keeping in the expression both the lowest-order terms and the terms of next order (in particular, we use Eq. (2.95) for  $q_n(E)$  and take into account that  $0 < \sqrt{2} - nq_n(E) \ll \sqrt{2}$  for the relevant range of  $E$ ):

$$\begin{aligned} \tilde{H}(I = I(E = E_b^{(1)} + \delta), \tilde{\psi}) &= -\frac{n\delta \ln\left(\frac{2\Phi}{\delta}\right)}{2 \ln\left(\frac{4e}{\Phi}\right)} + \left(\omega_f - \frac{n\pi}{2 \ln\left(\frac{4e}{\Phi}\right)}\right) \frac{2\Phi}{\pi} \ln\left(\frac{4e}{\Phi}\right) - \\ &- (-1)^{[n/4]} h\sqrt{2} \left(1 + \frac{n\pi \ln\left(\frac{2\Phi}{\delta}\right)}{8 \ln\left(\frac{4e}{\Phi}\right)}\right) \cos(\tilde{\psi}), \end{aligned} \tag{2.196}$$

$\omega_m - \omega(E + \delta) \ll \omega_m$ .

The Hamiltonian  $\tilde{H}$  should possess equal values at the saddle “s” and at the intersections of the separatrix and the GSS curve. Let us denote the angle of the intersection in the range  $]0, \pi[$  as  $\tilde{\psi}_i^{(l)}$ , and let us denote the deviation of its energy  $E_i^{(l)}$  from  $E_b^{(1)}$  as  $\delta_i^{(l)} \equiv \delta_i \sin(\tilde{\psi}_i^{(l)})$ .

Assuming that  $|\tilde{\psi}_i^{(l)} - \tilde{\psi}_s^{(l)}| \ll 1$  (the result will confirm this) so that

$$\begin{aligned} \cos(\tilde{\psi}_i^{(l)}) &\approx (-1)^{[n/4]} (1 - (\tilde{\psi}_i^{(l)} - \tilde{\psi}_s^{(l)})^2/2) \\ &\approx (-1)^{[n/4]} (1 - (\delta_i^{(l)}/\delta_i)^2/2) \approx (-1)^{[n/4]} (1 - (\delta_i^{(l)}/h)^2/4), \end{aligned}$$

the equality of the values of  $\tilde{H}$  is:

$$\frac{n}{2 \ln\left(\frac{4e}{\Phi}\right)} \left( \delta_s \ln\left(\frac{2\Phi}{\delta_s}\right) - \delta_i^{(l)} \ln\left(\frac{2\Phi}{\delta_i^{(l)}}\right) \right) = h\sqrt{2} \frac{n\pi}{8} \frac{\ln\left(\frac{\delta_s}{\delta_i^{(l)}}\right)}{\ln\left(\frac{4e}{\Phi}\right)} - \frac{(\delta_i^{(l)})^2}{2\sqrt{2}h}. \tag{2.197}$$

Let us assume that, in the asymptotic limit  $\Phi \rightarrow 0$ ,  $\delta_i^{(l)} \ll \delta_s$  (the result will confirm this). Then the left-hand part is asymptotically smaller than the first term in the right-hand part. So, Eq. (2.197) implies, in the asymptotic limit, that the right-hand side equals zero. Expressing  $h$  via  $\delta_s$  from Eq. (2.195), we finally obtain a closed transcendental equation for  $\delta_s/\delta_i^{(l)}$ :

---

<sup>25</sup> In case of a *moderately* small  $\Phi$ , they may intersect the GSS curve. Then, the tangent trajectory lying above the separatrix necessarily exists, so the boundary of the layer is formed by this tangent trajectory.

$$\left(\frac{\delta_s}{\delta_i^{(l)}}\right)^2 \ln\left(\frac{\delta_s}{\delta_i^{(l)}}\right) = \frac{\pi \ln\left(\frac{4e}{\Phi}\right)}{n \left(\ln\left(\ln\left(\frac{4e}{\Phi}\right)\right)\right)^2} \equiv A. \quad (2.198)$$

In the asymptotic limit  $\Phi \rightarrow 0$ , the quantity  $A$  diverges and, hence, the lowest-order asymptotic solution of Eq. (2.198) reads as

$$\frac{\delta_s}{\delta_i^{(l)}} = \sqrt{\frac{2A}{\ln(A)}}. \quad (2.199)$$

Substituting here the expression (2.195) for  $\delta_s$  and the expression (2.198) for  $A$ , we obtain:

$$\delta_i^{(l)} = h \frac{1}{4} \sqrt{\frac{n\pi \ln\left(\ln\left(\frac{4e}{\Phi}\right)\right)}{\ln\left(\frac{4e}{\Phi}\right)}}. \quad (2.200)$$

Thus, we have proved the following asymptotic properties of the separatrix generated by the saddle “ $s$ ”: (i) the lower whiskers of the separatrix do intersect the GSS curve in the relevant range of  $E$  (i.e. where the resonant approximation is valid); and (ii) the upper whiskers of the separatrix do *not* intersect the GSS curve (there is no solution of Eq. (2.197) in the range  $\delta_i^{(l)} > \delta_s$ ). The former property confirms the self-consistency of the asymptotic theory for even spikes; the latter property means that the *upper outer boundary* of the lower chaotic layer is formed by the *upper whiskers of the separatrix generated by the saddle “ $s$ ”*.

Finally, we note explicitly that the minimal (along the boundary) deviation of energy from the barrier energy occurs exactly at the saddle “ $s$ ”, i.e.

$$\delta_{\min}^{(l)} = \delta_s. \quad (2.201)$$

## 2. Relatively large $h$

As  $h$  grows, the boundary of the layer rises while the lower part of the resonance separatrix, on the contrary, falls. They reconnect at the critical value of  $h$ ,  $h_{cr}^{(l)} \equiv h_{cr}^{(l)}(\omega_f)$ , determined by Eq. (2.125), which may be considered as the absorption of the resonance by the chaotic layer. If  $h$  grows further, then the GSS curve and the resonance separatrix intersect. As a result, the trajectory starting from the state of angle (2.183) and action (2.180), for odd spikes, or from the saddle “ $s$ ”, for even spikes, is *encompassed* by the resonance separatrix. So, it no longer forms the outer boundary of the layer. Rather it forms the inner boundary i.e. the boundary of the main island of stability inside the layer, repeated periodically in  $\tilde{\psi}$  with a period  $2\pi$  (cf. analogous islands in the upper layer in Fig. 2.13). Unless the lower chaotic layer reconnects with the upper one, the *outer* boundary of the lower layer is formed by the upper part of the *resonance separatrix*. The relevant initial angle  $\tilde{\psi}(0)$  on the GSS curve corresponds to the intersection of the GSS curve with the resonance separatrix (cf. the analogous situation for the upper layer in Fig. 2.13).

### 2.7.2 Upper chaotic layer

The upper chaotic layer may be treated analogously<sup>26</sup> to the lower layer. We present here only the results.

Similarly to the lower-layer case, one may consider the ranges of relatively small  $h$  (namely, smaller than  $h_{cr}^{(u)} \equiv h_{cr}^{(u)}(\omega_f)$  determined by Eq. (2.126)) and relatively large  $h$  (i.e.  $h > h_{cr}^{(u)}$ ). In the former range, the formation of the boundary occurs in a manner which is, in a sense, opposite to that for the lower-layer case. For even spikes, the lower outer boundary is formed by *tangency* while, for odd spikes, it is formed by the lower part of the *separatrix* generated by the saddle “ $s$ ”, analogous to the saddle “ $s$ ” in the lower-layer case<sup>27</sup>.

So, for even spikes, the angle of tangency  $\tilde{\psi}_t^{(u)}$  is determined by:

$$\left[ |\varepsilon^{(up)}| \cos(\tilde{\psi}_t^{(u)}) \left( 1 - \frac{\omega_f}{n\omega(E)} - h \frac{dq_n(E)}{dE} \cos(\tilde{\psi}_t^{(u)}) \right) - q_n(E) \sin(\tilde{\psi}_t^{(u)}) \right]_{E=E_t^{(u)}} = 0,$$

$$E_t^{(u)} \equiv E_b^{(2)} - h |\varepsilon^{(up)}| \sin(\tilde{\psi}_t^{(u)}) \quad \tilde{\psi}_t^{(u)} \in [0, \pi], \quad (2.202)$$

$$n \equiv 2j - 1, \quad j = 2, 4, 6, \dots, \quad \tilde{\psi}(0) = \tilde{\psi}_t^{(u)},$$

and  $\tilde{\psi}_t^{(u)}$  determines the tangency energy:

$$E_t^{(u)} = E_b^{(2)} - h |\varepsilon^{(up)}| \sin(\tilde{\psi}_t^{(u)}), \quad (2.203)$$

where the quantity  $\varepsilon^{(up)}$  is described by the formula

$$\varepsilon^{(up)}(\omega_f) = 2 \int_0^\infty dt \dot{q}_s^{(up)}(t) \cos(\omega_f t), \quad (2.204)$$

where  $\dot{q}_s^{(up)}(t)$  is the time dependence of the velocity along the separatrix associated with the upper barrier and the instant  $t = 0$  is chosen so that  $q_s^{(up)}(t = 0)$  is equal to the coordinate of the lower barrier while  $\dot{q}_s^{(up)} > 0$  for  $t \in [0, \infty[$ . The dependence  $|\varepsilon^{(up)}(\omega_f)|$  in Eq. (2.204) is shown for  $\Phi = 0.2$  in Fig. 2.21(b).

The asymptotic form of Eq. (2.204) is

<sup>26</sup> For any AC-driven spatially periodic Hamiltonian system, the *upper* energy boundary of the layer associated with the unbounded separatrix diverges in the adiabatic limit  $\omega_f \rightarrow 0$  (Soskin et al., 2005). However, this divergence is not relevant for the present problem for the following reasons. The lower chaotic layer relates to the *bounded* separatrix while, for the upper (unbounded) layer, it is the *lower* boundary of the layer which is relevant for the onset of global chaos in between the separatrices. Moreover, even for the upper boundary of the upper layer, the divergence is not yet manifested for the driving parameters  $(h, \omega_f)$  in the vicinity of the spikes minima (cf. (Soskin et al., 2005)).

<sup>27</sup> This tangency may exist for a *moderately* small  $\Phi$ . The boundary is then formed by the tangent trajectory rather than by the separatrix: see an example in Fig. 2.14(c).

$$\varepsilon^{(up)} \equiv \varepsilon^{(up)}(\omega_f) = 2\pi \cos\left(\frac{\pi\omega_f}{4\omega_m}\right). \quad (2.205)$$

For  $\omega_f = \omega_s^{(j)} \approx (2j-1)\omega_m$ , Eq. (2.204) reduces to

$$\begin{aligned} \varepsilon^{(up)}(\omega_s^{(j)}) &\approx 2\pi \cos\left((2j-1)\frac{\pi}{4}\right) = \sqrt{2}\pi(-1)^{\lfloor \frac{2j+1}{4} \rfloor}, \\ j &= 1, 2, 3, \dots, \quad \Phi \rightarrow 0. \end{aligned} \quad (2.206)$$

The lowest-order solution of (2.202) is given in Eq. (2.121), so that  $E_t^{(u)}$  is approximated by Eq. (2.122). The maximal energy on the lower boundary of the layer corresponds to  $\tilde{\psi}(t) = \pi$  if  $j = 2, 6, 10, \dots$  or 0 if  $j = 4, 8, 12, \dots$  and is determined by Eq. (2.123). The asymptotic value of the minimal deviation from the upper barrier of the energy at the boundary,  $\delta_{\min}^{(u)}$ , is given in Eq. (2.124).

For odd spikes, the boundary is formed by the lower part of the separatrix generated by the saddle “ $\tilde{s}$ ”. The angle of the saddle is given in Eq. (2.117) while the deviation of its energy from the barrier is approximated in lowest-order by Eq. (2.118).

As  $h$  grows, the boundary of the layer falls while the upper part of the upper resonance separatrix rises. They reconnect at  $h = h_{cr}^{(u)} \equiv h_{cr}^{(u)}(\omega_f)$ , as determined by Eq. (2.126), which may be considered as the absorption of the resonance by the layer.

For larger  $h$ , the boundary of the layer is formed by the lower part of the upper resonance separatrix (Fig. 2.13), unless the latter intersects the lower GSS curve (in which case,  $h_{cr}^{(u)}$  marks the onset of global chaos).

## References

- Abdullaev S.S., 2006, *Construction of Mappings for Hamiltonian Systems and Their Applications*, Springer, Berlin, Heidelberg.
- Abramovitz M. and Stegun I., 1970, *Handbook of Mathematical Functions*, Dover, New York.
- Andronov A.A., Vitt A.A. and Khaikin S.E., 1966, *Theory of Oscillators*, Pergamon, Oxford.
- Arnold V.I., 1964, Instability of dynamical systems with several degrees of freedom, *Sov. Math. Dokl.*, **5**, 581–585.
- Bogolyubov N.N. and Mitropolsky Yu.A., 1961, *Asymptotic Methods in the Theory of Nonlinear Oscillators*, Gordon and Breach, New York.
- Carmona H.A. et al., 1995, Two dimensional electrons in a lateral magnetic superlattice, *Phys. Rev. Lett.*, **74**, 3009–3012.

- Chernikov A.A. et al., 1987a, Minimal chaos and stochastic webs, *Nature*, **326**, 559–563.
- Chernikov A.A. et al., 1987b, Some peculiarities of stochastic layer and stochastic web formation, *Phys. Lett. A*, **122**, 39–46.
- Chernikov A.A. et al., 1988, Strong changing of adiabatic invariants, KAM-tori and web-tori, *Phys. Lett. A*, **129**, 377–380.
- Chirikov B.V., 1979, A universal instability of many-dimensional oscillator systems, *Phys. Rep.*, **52**, 263–379.
- del-Castillo-Negrete D., Greene J.M. and Morrison P.J., 1996, Area-preserving non-twist maps: periodic orbits and transition to chaos, *Physica D*, **61**, 1–23.
- Dullin H.R., Meiss J.D. and Sterling D., 2000, Generic twistless bifurcations, *Nonlinearity*, **13**, 203–224.
- Dykman M.I., Soskin S.M. and Krivoglaz M.A., 1985, Spectral distribution of a nonlinear oscillator performing Brownian motion in a double-well potential, *Physica A*, **133**, 53–73.
- Elskens Y. and Escande D.F., 1991, Slowly pulsating separatrices sweep homoclinic tangles where islands must be small: an extension of classical adiabatic theory, *Nonlinearity*, **4**, 615–667.
- Fromhold T.M. et al., 2001, Effects of stochastic webs on chaotic electron transport in semiconductor superlattices, *Phys. Rev. Lett.*, **87**, 046803-1-046803-4.
- Fromhold T.M. et al., 2004, Chaotic electron diffusion through stochastic webs enhances current flow in superlattices, *Nature*, **428**, 726–730.
- Gelfreich V., private communication.
- Gelfreich V.G. and Lazutkin V.F., 2001, Splitting of separatrices: perturbation theory and exponential smallness, *Russian Math. Surveys*, **56**, 499–558.
- Howard J.E. and Hohn S.M., 1984, Stochasticity and reconnection in Hamiltonian systems, *Phys. Rev. A*, **29**, 418–421.
- Howard J.E. and Humpherys J., 1995, Non-monotonic twist maps, *Physica*, **D 80**, 256–276.
- Landau L.D. and Lifshitz E.M., 1976, *Mechanics*, Pergamon, London.
- Leonel E.D., 2007, Corrugated Waveguide under Scaling Investigation, *Phys. Rev. Lett.*, **98**, 114102-1-114102-4.
- Lichtenberg A.J. and Leiberman M.A., 1992, *Regular and Stochastic Motion*, Springer, New York.
- Luo A.C.J., 2004, Nonlinear dynamics theory of stochastic layers in Hamiltonian systems, *Appl. Mech. Rev.*, **57**, 161–172.
- Luo A.C.J., Gu K. and Han R.P.S., 1999, Resonant-separatrix webs in stochastic layers of the Twin-Well duffing oscillator, *Nonlinear Dyn.*, **19**, 37–48.
- Morozov A.D., 2002, Degenerate resonances in Hamiltonian systems with 3/2 degrees of freedom, *Chaos*, **12**, 539–548.
- Neishtadt A.I., 1986, Change in adiabatic invariant at a separatrix, *Sov. J. Plasma Phys.*, **12**, 568–573.
- Neishtadt A.I., Sidorenko V.V. and Treschev D.V., 1997, Stable periodic motions in the problem on passage through a separatrix, *Chaos*, **7**, 2–11.

- Piftankin G.N. and Treschev D.V., 2007, Separatrix maps in Hamiltonian systems, *Russian Math. Surveys*, **62**, 219–322.
- Prants S.V., Budyansky M.V., Uleysky M.Yu. and Zaslavsky G.M., 2006, Chaotic mixing and transport in a meandering jet flow, *Chaos*, **16**, 033117-1-033117-8.
- Rom-Kedar V., 1990, Transport rates of a class of two-dimensional maps and flows, *Physica D*, **43**, 229–268.
- Rom-Kedar V., 1994, Homoclinic tangles—classification and applications, *Nonlinearity*, **7**, 441–473.
- Schmelcher P. and Shepelyansky D.L., 1994, Chaotic and ballistic dynamics for two-dimensional electrons in periodic magnetic fields, *Phys. Rev. B*, **49**, 7418–7423.
- Shevchenko I.I., 1998, Marginal resonances and intermittent Behaviour in the motion in the vicinity of a separatrix, *Phys. Scr.*, **57**, 185–191.
- Shevchenko I.I., 2008, The width of a chaotic layer, *Phys. Lett. A*, **372**, 808–816.
- Schmidt G.J.O., 1993, Deterministic diffusion and magnetotransport in periodically modulated magnetic fields, *Phys. Rev. B*, **47**, 13007–13010.
- Soskin S.M., Unpublished.
- Soskin S.M. and Mannella R., 2009a, New approach to the treatment of separatrix chaos, In Macucci C. and Basso G. (eds.) Noise and Fluctuations: 20 th International Conference on Noise and Fluctuations (ICNF-2009), AIP CONFERENCE PROCEEDINGS **1129**, 25–28, American Institute of Physics, Melville, New York.
- Soskin S.M. and Mannella R., 2009b, Maximal width of the separatrix chaotic layer, *Phys. Rev. E*, **80**, 066212-1-006212-1F.
- Soskin S.M., Mannella R., Arrayás M. and Silchenko A.N., 2001, Strong enhancement of noise-induced escape by transient chaos, *Phys. Rev. E*, **63**, 051111-1-051111-6.
- Soskin S.M., Mannella R. and McClintock P.V.E., 2003, Zero-Dispersion Phenomena in oscillatory systems, *Phys. Rep.*, **373**, 247–409.
- Soskin S.M., Yevtushenko O.M. and Mannella R., 2005, Divergence of the chaotic layer width and strong acceleration of the spatial chaotic transport in periodic systems driven by an adiabatic ac force, *Phys. Rev. Lett.*, **95**, 224101-1-224101-4.
- Soskin S.M., Mannella R. and Yevtushenko O.M., 2008a, Matching of separatrix map and resonant dynamics, with application to global chaos onset between separatrices, *Phys. Rev. E*, **77**, 036221-1-036221-29.
- Soskin S.M., Mannella R. and Yevtushenko O.M., 2008b, Separatrix chaos: new approach to the theoretical treatment. In: *Chandre C., Leoncini X., and Zaslavsky G.* (eds.) *Chaos, Complexity and Transport: Theory and Applications (Proceedings of the CCT-07)*, 119–128, World Scientific, Singapore.
- Soskin S.M., Khovanov I.A., Mannella R. and McClintock P.V.E., 2009, Enlargement of a low-dimensional stochastic web, Macucci C. and Basso G. (eds.) Noise and Fluctuations: 20 th International Conference on Noise and Fluctuations (ICNF-2009), AIP CONFERENCE PROCEEDINGS **1129**, 17–20, American Institute of Physics, Melville, New York.

- Soskin S.M., Yevtushenko O.M. and Mannella R., 2010a, Adiabatic divergence of the chaotic layer width and acceleration of chaotic and noise-induced transport, *Commun. Nonlinear Sci. Numer. Simulat.*, **15**, 16–23.
- Soskin S.M., McClintock P.V.E., Fromhold T.M., Khovamov I.A. and Mannella R., 2010b, Stochastic webs and quantum transport in superlattices: an introductory review, *Contemporary Physics*, **51**, 233–248.
- Vecheslavov V.V., 2004, Chaotic layer of a pendulum under low-and medium-frequency perturbations, *Tech. Phys.*, **49**, 521–525.
- Ye P.D. et al., 1995, Electrons in a periodic magnetic field induced by a regular array of micromagnets, *Phys. Rev. Lett.*, **74**, 3013–3016.
- Yevtushenko O.M. and Richter K., 1998, Effect of an ac electric field on chaotic electronic transport in a magnetic superlattice, *Phys. Rev. B*, **57**, 14839–14842.
- Yevtushenko O.M. and Richter K., 1999, AC-driven anomalous stochastic diffusion and chaotic transport in magnetic superlattices, *Physica*, **E 4**, 256–276.
- Zaslavsky G.M., 2005, *Hamiltonian Chaos and Fractional Dynamics*, Oxford University Press, Oxford.
- Zaslavsky G.M., 2007, *Physics of Chaos in Hamiltonian Systems*, 2nd ed., Imperial College Press, London.
- Zaslavsky G.M. and Filonenko N.N., 1968, Stochastic instability of trapped particles and conditions of application of the quasi-linear approximation, *Sov. Phys. JETP*, **27**, 851–857.
- Zaslavsky G.M. et al., 1986, Stochastic web and diffusion of particles in a magnetic field, *Sov. Phys. JETP*, **64**, 294–303.
- Zaslavsky G.M., Sagdeev R.D., Usikov D.A. and Chernikov A.A., 1991, *Weak Chaos and Quasi-Regular Patterns*, Cambridge University Press, Cambridge.

# Chapter 3

## Hamiltonian Chaos and Anomalous Transport in Two Dimensional Flows

Xavier Leoncini

**Abstract** In this chapter we discuss the dynamics of particles advected in regular and chaotic flows. We first address the dynamics of point vortices and show the great variety of the dynamics of three point vortices near the singularity giving rise to vortex collapse. We discuss the strong influence of the existence of a finite time singularity on the dynamics, especially on how the period of the motion evolves as we get closer to the singular conditions. We then analyze transport properties of passive tracers in various flows. We start with integrable flows governed by three vortices, then switch to chaotic flows generated by four and sixteen vortices, and end up with a turbulent flow governed by the Charney-Hasegawa-Mima. For all cases, anomalous superdiffusive transport with a characteristic exponent  $\mu \sim 1.5 - 1.8$  is observed. The origin of the anomaly is explained by the phenomenon of stickiness around coherent structures in regular flows, and by the presence of regular chaotic jets for the chaotic and turbulent ones. Finally we illustrate how the Hamiltonian nature of chaos can be used to localize 3-dimensional coherent structures or how to improve mixing properties in cellular flows while keeping the cellular structure of the flow.

### 3.1 Introduction

It was long believed that the deterministic character of Newton equations was the key to understanding the universe. In some sense, one would just have to understand and describe well enough a system to be able to solve the equations of motion and predict the future. However it has been clear now for more than a century that most dynamical systems do not lead to simple and regular solutions. Indeed one observe most of the time a strong sensitivity to initial conditions for solutions of a deter-

---

Xavier Leoncini  
Centre de Physique Théorique, Luminy Case 907, 13288 Marseille Cedex 9, France,  
e-mail: Xavier.Leoncini@cpt.univ-mrs.fr

ministic system, and unless having access to an exact and perfect description of our surrounding world, we cannot predict evolutions for large times. This fact may have generated some deceptions, but on the other hand the complexity arising from this sensitivity to initial conditions, chaos, allows to reconcile classical mechanics with thermodynamics. The discovery of the second principle of thermodynamics in the middle of the 19th century clearly defined the problem of the link between microscopic equation deriving from Hamiltonian dynamics which are time reversible and thermodynamics which evolves irreversibly towards a state which maximizes the entropy (disorder). To summarize, irreversibility is essentially observed for global ensembles variables. These are linked to the microscopic ones by statistical means, in this sense irreversibility gets a probabilistic nature, and can be expected to find its origin in the law of large numbers, which naturally applies to macroscopic systems. The switch from elementary particles governed by conservative Hamiltonian dynamics and statistics on phase space finds naturally its origin in the hypothesis of molecular chaos and sensitivity to initial conditions. Indeed the equations of motion are reversible but we need an exact knowledge of the system to invert time and any mistake made by some ideal non invading measurement will lead to disorder. These properties of the dynamics are intrinsic and are essentially due to the nonlinear form of the motion equations.

We observe actually the same phenomenon when we are interested in transport properties of an ensemble of particles. Chaos implies the impossible necessity of knowing exactly the initial conditions, hence using a statistical description of the ensemble is necessary and the evolution of the statistical distribution is studied to characterize transport. Most of the time, the transport law is linked to a diffusive phenomenon. If we consider transport of pollutants in a fluid, one must then also take into account the flow within the fluid as well as the molecular diffusion that takes place. Since molecular diffusion is related to microscopic chaos, we can imagine that a fluid particle (at the mesoscopic level) which is transported (advected) by the fluid can also have a chaotic dynamics, notably when the flow is turbulent. Hence an ensemble of fluid particles may also diffuse. We end up with some kind of Russian doll (matroshka) structure, with a diffusion at the microscopic scale with another one on top at the mesoscopic one.

In this chapter, we shall consider the dynamics of particles advected by different types of flow, with the perspective to understand transport properties for an ensemble of particles and eventually the control of transport. Indeed, the arguments which lead to diffusion phenomena can be mathematically well described if the motion of particles is sufficiently erratic and stochastic. However the presence of chaos, as we shall see, may not be sufficient to achieve diffusive transport. With this in mind, we will consider only the mesoscopic scale and ignore molecular diffusion. This choice can be justified in two ways, first depending on the advected quantity and the characteristics of the flow, one can assume that molecular characteristic time scales are negligible. Second, as we shall see, the advection of passive tracers in incompressible 2-dimensional flows belong to the class of low dimensional Hamiltonian systems, so we may be able to somewhat generalize the obtained results to other types of systems with equivalent Hamiltonian descriptions.

The chapter is organized as follows. First, we illustrate the phenomenon of chaotic advection, then we discuss the dynamics of point vortices and especially focus on the dynamics which can lead to three-vortex finite time singularity (collapse). Then we consider transport properties of passive tracers (fluid particles) in regular and chaotic flows. Finally we show possible ways to use chaotic advection phenomena to our advantage.

## 3.2 Point vortices and passive tracers advection

First, we will give some definitions.

### 3.2.1 Definitions

Let us consider a flow  $\mathbf{v}$  of an incompressible fluid ( $\nabla \cdot \mathbf{v} = 0$ ). A particle that is put in this flow will be considered a passive particle, if its presence in the fluid has no impact on the flow itself (or at first glance a negligible one). In these regards, one will be able to identify a passive particle with the so-called “fluid-particles”. In this setting the motion of the passive scalar (passive particle) can be inferred from a Lagrangian perspective. Indeed the speed of the passive particle has to be the speed of the flow itself, thus the trajectories are solutions of the following differential equation:

$$\dot{\mathbf{r}} = \mathbf{v}(\mathbf{r}, t), \quad (3.1)$$

where  $\mathbf{r} = (x, y, z)$  corresponds to the passive particle position. When we restrict ourselves to 2-dimensional flows one can easily rewrite Eqs. (3.1) using an Hamiltonian formalism. Since  $\nabla \cdot \mathbf{v} = 0$ , we can define up to some gradient a stream function  $\mathbf{H}$  such that  $\mathbf{v} = \nabla \wedge \mathbf{H}$ , and if we have a 2-dimensional system,  $\mathbf{H} = H \mathbf{e}_z$  resumes to a scalar function  $H$  where  $\mathbf{e}_z$  defines the normal of the two dimensional plane. In this setting Eqs. (3.1) become

$$\dot{x} = \frac{\partial H}{\partial y}, \quad \dot{y} = -\frac{\partial H}{\partial x}. \quad (3.2)$$

We shall notice that the couple  $(x, y)$  corresponds either to the canonical conjugate variables of the Hamiltonian and describe phase space, or the physical Cartesian coordinates of the particle. One notices here, one of the compelling properties of passive particle dynamics in 2-dimensional flows: a direct visualization of a Hamiltonian phase space by looking at the particles in the flow itself. This properties make these systems one of the ideal ones to confront low-dimensional Hamiltonian dynamics with real experiments.

In what follows we shall use the more usual notation  $\Psi$  for the stream function.

### 3.2.2 Chaotic advection

This phenomenon translates the fact that despite a laminar structure of the flow, passive particles or tracers have chaotic trajectories (Aref, 1984, 1990; Ottino, 1990). As a consequence mixing is considerably enhanced in chaotic regions of the flow, in the sense that chaotic motions mixes much faster than molecular diffusion (Ottino, 1989; Zaslavsky et al., 1991; Crisanti et al., 1991). For 2-dimensional incompressible flows, since chaos is generic for one degree of freedom time dependent Hamiltonian systems (usually know as systems with  $1 - \frac{1}{2}$  degree of freedom) one can expect to observe chaotic advection as soon as we have a time dependent flow. Such situations are quite generic and one observes in a multitude of physical systems and applications, for instance in geophysical flows or magnetized fusion plasmas (Brown and Smith, 1991; Behringer et al., 1991; Chernikov et al., 1990; Dupont et al., 1998; Crisanti et al., 1992; Carreras et al., 2003; Annibaldi et al., 2000; del Castillo-Negrete et al., 2004; Leoncini et al., 2005) or in chemical engineering (to enhance mixing of reactant) (Balasuriya, 2005; Stroock et al., 2002). In this sense chaotic advection reveals that the link between Eulerian and Lagrangian perspective are not as simple as one would like. And unfortunately from a mixing or transport point of view a Lagrangian approach is mandatory. We shall now start with a brief example describing chaotic advection.

#### 3.2.2.1 Example 1: advection in an array of vortices

Let us consider the following stream function

$$\Psi_0(x, y) = \alpha \sin x \sin y, \quad (3.3)$$

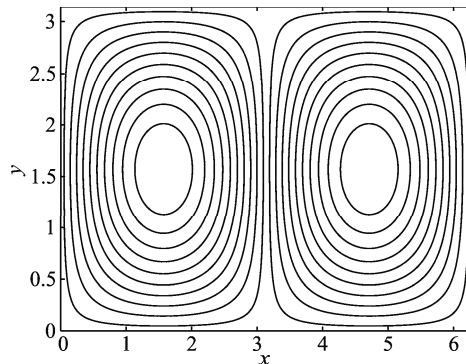


**Fig. 3.1** Trajectories of test particles and field lines of the flow (3.3). They do not depend on the value of  $\alpha$ .

which describes an array of alternating vortices emerging for instance from a convective instability such as Rayleigh-Bénard (Solomon and Gollub, 1988; Willaime et al., 1993; Solomon et al., 2003). Field lines of the velocity are represented for this flow in Fig. 3.1. Passive particles dynamics result from Hamiltonian dynamics governed by  $\Psi_0$ , thus from a system with one degree of freedom. In this setting

- Particle motion is integrable
- Particles trajectories are identical to velocity field lines (see Fig. 3.1)

### 3.2.2.2 Example 2: advection in an array of vortices

Now let us consider the stream function

$$\Psi_c(x, y, t) = \Psi_0(x + f, y), \quad (3.4)$$

with  $f = \varepsilon \sin \omega_0 t$  (Solomon and Gollub, 1988). We actually are perturbing the stream function (3.3), by making the array of vortices oscillate in the  $x$ -direction. With this perturbation, the flow is still regular but becomes time-dependent. Field lines are unchanged and are thus those represented in Fig. 3.1, but they oscillate in one direction with an amplitude  $\varepsilon$  and a pulsation  $\omega_0$ . However if we consider the dynamics of passive particles, we still have an Hamiltonian system, but a time-dependent one, and we have a  $1 - \frac{1}{2}$  degree of freedom which is generically chaotic. To summarize we have

- Field lines are just oscillating, the flow is laminar and simple (see Fig. 3.1)
- Instead the motion of tracers is chaotic (see Fig. 3.2).

We thus observe Hamiltonian chaos from a Lagrangian perspective even though the flow is extremely simple from the Eulerian one. And, since transport properties are

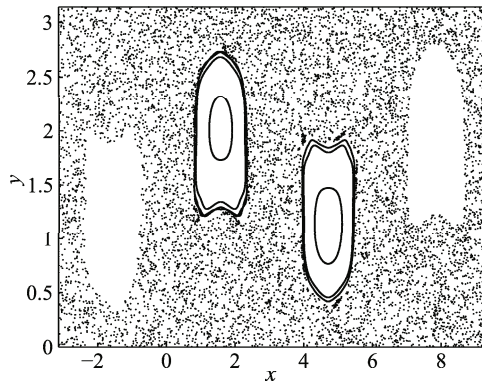


**Fig. 3.2** Poincaré section of particles trajectories advected by the flow governed by (3.4). Parameters used to compute trajectories and the figure are  $\alpha = 0.6$  et  $\varepsilon = 0.63$  et  $\omega_0 = 1$ .

more natural from the Lagrangian point of view, we have to take into account the chaotic dynamics of tracers to characterize transport in these type of systems.

### 3.3 A system of point vortices

In order to study chaotic advection and transport we will consider flows generated by point vortices. But first we will give some definitions.

#### 3.3.1 Definitions

Let us consider the Euler equation for the vorticity in a 2-dimensional incompressible flow

$$\frac{\partial \Omega}{\partial t} + [\Omega, \psi] = 0, \quad \Omega = -\nabla^2 \psi, \quad (3.5)$$

where  $\psi$  is the stream function,  $[\cdot, \cdot]$  and denotes the usual Poisson brackets. And let us consider a vorticity field given by a superposition of Dirac functions:

$$\Omega(\mathbf{x}, t) = \sum_{i=1}^N k_i \delta(\mathbf{x} - \mathbf{x}_i(t)). \quad (3.6)$$

Here,  $k_i$  designate the vorticity of the point vortex localized at point  $\mathbf{x}_i(t)$ . The vorticity is in fact directly associated with the circulation of the velocity field around the vortex. One shall notice that vorticity is zero everywhere but at the point where the point vortices are located (thus their name). This point vortex distribution is an exact solution of the Euler equation (in the weak sense) at the condition that the  $N$  positions of the vortices  $\mathbf{x}_i(t)$  follow a prescribed dynamics (Machioro and Pulvirenti, 1994). In fact one shows that

1. The system can be mapped to an  $N$ -body Hamiltonian dynamics
2. When we are considering the whole plane, the Hamiltonian writes

$$H = \frac{1}{2\pi} \sum_{i>j} k_i k_j \ln |z_i - z_j|, \quad (3.7)$$

where  $k_i z_i$  and  $\bar{z}_i$  are the canonically conjugate variables of the Hamiltonian (3.7) and locate the position  $\mathbf{x}_i(t)$  in the complex plane.

The Hamiltonian equations obtained from Hamiltonian (3.7) translate the fact that each vortex is advected by the velocity field generated by all other vortices. In the same spirit if we want the velocity field in any point of the plane we can get it using the stream function  $\Psi$  which writes

$$\Psi(z, \bar{z}, t) = -\frac{1}{2\pi} \sum_{i=1}^N k_i \ln |z - z_i(t)|, \quad (3.8)$$

and by computing its curl.

regarding the dynamics of point vortices, we can notice that the Hamiltonian (3.7) is invariant by translation and by rotation in the plane. The invariance by these continuous symmetry groups implies the existence of three extra integral of motions which are conserved quantities. The energy associated to the Hamiltonian being the fourth integral of motion. Translational and rotational invariance imply respectively the conservation of “momentum”

$$\mathbf{P} \equiv \sum_{i=1}^N k_i \mathbf{x}_i(t) = \text{const}, \quad (3.9)$$

and angular momentum of the vortices given by

$$L^2 \equiv \sum_{i=1}^N k_i \mathbf{x}_i^2(t) = \text{const}. \quad (3.10)$$

In fact only three of these four integrals are in involution (meaning that they reflect conditions which are truly independent). Given this, the system is integrable if the number of point vortices  $N$  is such that  $N \leq 3$ , on the other hand vortex motion is not integrable and consequently chaotic if  $N > 3$  (Novikov and Sedov, 1978; Aref and Pomphrey, 1980).

### 3.3.1.1 Scale invariance

Due to the specificity of the logarithmic interaction between vortices, it is possible to get another transformation which preserve the Hamiltonian (3.7). This last invariance however imposes a condition on the vorticities of the point vortices. Indeed if the condition

$$\sum_{i \neq j} k_i k_j = 0, \quad (3.11)$$

is satisfied, then the Hamiltonian becomes scale invariant. In order to get the condition (3.11) one can simply rescale all length by a constant global factor in Hamiltonian (3.7) to obtain the result. This last scale invariance property is important. As we shall see soon, it can imply the existence of singular solutions with finite time singularities.

### 3.3.1.2 Remarks 1

We shall notice that Hamiltonian (3.7) has not the classical form of a kinetic energy term to which one adds an interaction potential depending on positions. The canon-

ically conjugated variables are the space variables  $(k_i z_i, \bar{z}_i)$  in the complex plane or  $(k_i x_i, y_i)$  if one prefers Cartesian coordinates. The Hamiltonian is said to be non-separable. It is important also to notice that due to the logarithmic interaction, point vortex systems are counted among systems with long-range interactions. From this point of view the statistical physics approach to these type of problem is not trivial, and one is confronted to similar problem as for instance in gravitational systems.

### 3.3.1.3 Remarks 2

Vortices appear naturally in 2-dimensional turbulence (McWilliams, 1984). It is therefore important to have access to an exact solution of the Euler equation which can be used to model their behavior and dynamics. We shall however insist on the fact that more realistic fluid equations such as the Navier-Stokes one, include a dissipative term. Numerical simulations of such equation show that vortices do exist but have a spatial extension and are thus not localized on a point. Moreover it was observed numerically that when two vortices with same sign vorticity are sufficiently close to each other, a merging process occurs leaving only one larger vortex and that during this merging process dissipative effects are important. However point vortices model quite well the motion of vortices once these are quite localized and not too close to each other. It has also been observed that models of 2-dimensional turbulence using point vortices were giving the correct scaling laws, at the condition that the merging between vortices was taken into account in the model (Carnevale et al., 1991; Benzi et al., 1992).

## 3.4 Dynamics of systems with two or three point vortices

We shall here briefly describe the dynamics of two and three point vortices. In order to settle some points, we first recall the velocity field lines created by one point vortex are forming an ensemble of circles centered on the vortex itself. The norm of the speed decreases as  $1/r$  where  $r$  is the distance from the considered point vortex.

### 3.4.1 Dynamics of two vortices

The dynamics of a system composed of two point vortices summarizes as follows:

- If the center of vorticity defined by  $\mathbf{x}_c = \sum k_i \mathbf{x}_i(t) / \sum k_i$  exists ( $k_1 + k_2 \neq 0$ ), the vortices have a uniform circular motion around the center of vorticity (see Fig. 3.3).
- If we have a dipole ( $k_1 + k_2 = 0$ ), the dipole has a straight and uniform motion (see Fig. 3.4).
- For all situations the inter-vortex distance is constant.

This two vortex dynamics allows one to describe and understand what is the mutual influence of two vortices, which becomes important when the two vortices are more or less close to each other. However since inter-vortex distance is a constant of the motion, this dynamics does not allow vortices to come closer to each other to eventually merge. For this purpose we have to take into account three-body interactions: a three point vortex system which is also integrable.

### 3.4.2 Dynamics of three vortices

The motion of three point vortices even though integrable is quite complex to describe. For a global description of all available motions one can for instance have a look at (Aref, 1979; Tavantzis and Ting, 1988). To summarize in simpler way one has:

- The motion is generically either quasi-periodic or aperiodic.
- It is possible to observe finite-time singularities.
- Inter-vortex distance change: two vortices can get closer to each other.

In general aperiodic motion are not relevant if one is concerned with transport problems. Indeed they correspond to some kind of transient regime during which the vortices interact after which one or more vortices escape to infinity. We end up locally with a trivial system fully integrable from the transport point of view.

For quasi-periodic motion of the vortices, one can define a characteristic period of the motion. Indeed when looking at the triangle formed by the vortices one can define a period  $T$  after which the triangle has exactly the same shape (with the same vortices on top of the corners). The triangle has however been rotated by an angle  $\phi$  generically incommensurate with  $\pi$  around the center of vorticity. In what follows we shall often speak about the periodic motion of three point vortices keeping in mind that a rotation of angle  $\phi$  has been performed.

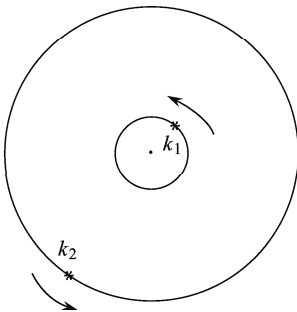


**Fig. 3.3** Dynamics of two point vortices, each vortex rotates around the center of vorticity.

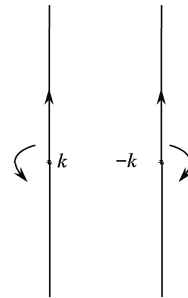


**Fig. 3.4** Dynamics of a dipole formed by two point vortices. Le motion is straight and uniform.

### 3.5 Vortex collapse and near collapse dynamics of point vortices

We shall now focus on a singular solution of three point vortex dynamics, namely the solution giving rise to finite time singularity and the collapse of the three vortices (Synge, 1949; Novikov and Sedov, 1979). Motivation for this study are quite varied. From one point of view, this singularity offers a pedagogical example of the limits of the Hamiltonian descriptions of classical motion. Indeed one switches from a three-body system with a phase space of six dimensions to a system with only one body and a phase space with two dimensions, and this in a finite time. And by analyzing the motion for conditions close to the collapse ones, we shall be able to describe the influence of the singularity on its neighboring solutions. Moreover, there is another interest in studying this solution. Indeed it has been shown for “real” systems (with extended vortices), that when the vortices are far from each other, vortex can come close to each other using a three body interaction following trajectories which are close to the collapse course (Dritschel and Zabusky, 1996). This phenomenon occur if the vortex concentration (number and spatial extension) is sufficiently small as it can occur in decaying 2-dimensional turbulence (see Fig. 3.5).

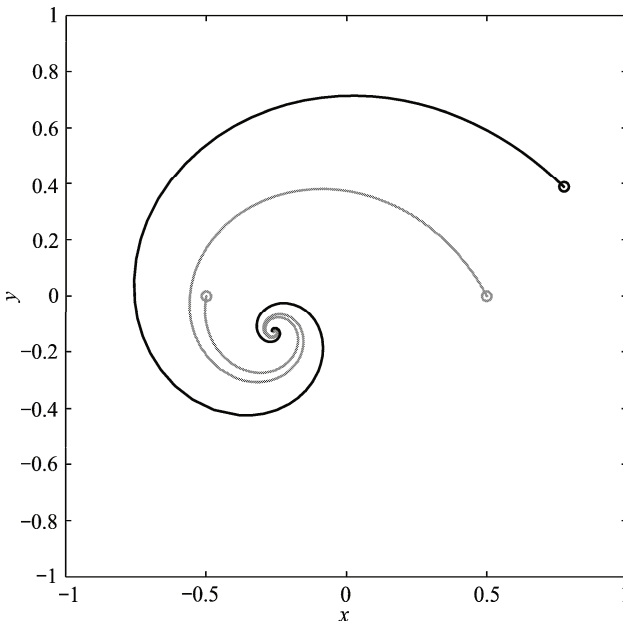


**Fig. 3.5** Collapse of three point vortices. An example of finite time singularity.

### 3.5.1 Vortex collapse

The conditions to observe the collapse of three point vortices can be written simply. First we need scale invariant dynamics. For three vortices, the scale free condition (3.11) takes the following form

$$\sum_{i=1}^3 \frac{1}{k_i} = 0. \quad (3.12)$$

One can notice that this condition implies the existence of a center of vorticity (where the vortices will collapse). The conservation of angular momentum implies another condition. It is convenient to rewrite this condition in order to get rid of the choice of a frame of reference, and thus to rewrite it using only inter-vortex distances which of course must be compatible with the vanishing of these if we want collapse

$$K = \left[ \left( \sum_i k_i \right) L^2 - P^2 \right] = \sum_{i \neq j} k_i k_j r_{ij}^2 = 0. \quad (3.13)$$

When these conditions are met, it is easy to show that the dynamics lead to a linear (in time) decrease of the area of the triangle formed by the vortices, and we end up with a finite time singularity where the three vortices merge (collapse) into the center of vorticity. To be more specific, due to the scale invariance the dynamics is self similar, meaning that as the area of the triangle is contracting, the shape of the triangle is unchanged. One also shall notice that since Hamiltonian dynamics are reversible one can also end up with an infinite dilatation of the triangle.

To summarize vortex collapse we shall insist on the fact that

- We observe a finite time singularity with a typical decrease of lengths as  $\sqrt{t_0 - t}$ .
- This singularity shows some limit of a full Hamiltonian description of three point vortices.
- We expect that close to collapse conditions will allow to bring vortices as close to each other as one desires.

### 3.5.2 Vortex dynamics in the vicinity of the singularity

Due to the specific singular nature of the collapse of vortices and its role played in bringing vortices close to each other we shall consider the dynamics in configurations which shall be close to the one giving rise to the singularity (Leoncini et al., 2000). For this purpose it is first useful to rewrite the Hamiltonian motion equation in a non-canonical form using the three inter-vortex distances  $R_1, R_2, R_3$ , and the area of the triangle  $A$

$$\begin{cases} k_1^{-1} R_1 \dot{R}_1 = A/\pi(R_2^{-2} - R_3^{-2}), \\ k_2^{-1} R_2 \dot{R}_2 = A/\pi(R_3^{-2} - R_1^{-2}), \\ k_3^{-1} R_3 \dot{R}_3 = A/\pi(R_1^{-2} - R_2^{-2}). \end{cases} \quad (3.14)$$

We shall as well, mainly to simplify the analysis, consider that two vortices are identical (have equal strength). Then after a small change of time scale which corresponds to choosing a reference in the intensity of vortex strengths  $k$ , we can choose

$$k_2 = k_3 = 1. \quad (3.15)$$

The collapse condition (3.12) imposes then a critical vorticity for the vortex 1,  $k_{1c} = -1/2$ . We shall therefore consider conditions for which the strength of vortex 1 is negative and close to the critical value. We use the notations

$$k \equiv |k_1|. \quad (3.16)$$

We perform then the following change of variables:  $X = R_1^2$ ,  $Y = R_2^2 R_3^2$ , and  $Z = R_2^2 + R_3^2$ . With these variables the constants of the motions rewrite

$$\begin{cases} \Lambda = e^{4\pi H} = Y^k/X, \\ K = X - kZ. \end{cases} \quad (3.17)$$

where the parameter  $\Lambda$  has been introduced to replace energy and simplify notations.

The dynamical equation for  $X$  is obtained by squaring the first of the motion equations (3.14):

$$\dot{X}^2 = \frac{4}{\pi^2} A^2 k^2 \frac{(R_2^2 + R_3^2)^2 - 4R_2^2 R_3^2}{R_2^4 R_3^4} = \frac{4}{\pi^2} A^2 k^2 \frac{Z^2 - 4Y}{Y^2}. \quad (3.18)$$

Then one uses the geometrical formulae for the triangle area  $A$

$$\begin{cases} A = \sqrt{Y} |\sin \theta|/2, \\ X = Z - 2\sqrt{Y} \cos \theta, \end{cases} \quad (3.19)$$

which leads us to

$$16A^2 = 4Y - (X - Z)^2. \quad (3.20)$$

We can then use the constant of the motion (3.17) to get

$$\dot{X}^2 = \frac{1}{4\pi^2} \frac{[4k^2 Y - (K - (1-k)X)^2][(K - X)^2 - 4k^2 Y]}{k^2 Y^2}, \quad (3.21)$$

where  $Y = (\Lambda X)^{1/k}$ . One can recognize a first integral of motion of a particle with mass 1 moving in a scalar potential  $V(X; \Lambda, K, k)$ , defined by

$$V(X; \Lambda, K, k) \equiv \frac{[(K - (1-k)X)^2 - 4k^2 Y][(X - K)^2 - 4k^2 Y]}{8\pi^2 k^2 Y^2}. \quad (3.22)$$

The equations of motion (3.21) can therefore be rewritten using an effective Hamiltonian

$$H_{eff}(P, X; \Lambda, K, k) \equiv P^2/2 + V(X; \Lambda, K, k) = 0, \quad (3.23)$$

and Hamilton's equations

$$\dot{X} = \partial H_{eff} / \partial P \equiv P, \quad \dot{P} = -\partial H_{eff} / \partial X. \quad (3.24)$$

The Hamiltonian (3.23) is separable and corresponds to a one degree of freedom system. Its study is therefore quite simple all the complexity being left out in the potential and how initial conditions of the vortices, the constants of motion, and vortex strengths are influencing it. A detailed study of all the type of motions can be found in Ref. (Leoncini et al., 2000).

To summarize, dynamics of point vortices in the vicinity of collapse conditions is like in the general case either aperiodic or periodic. One of the interesting point of the study developed in (Leoncini et al., 2000) is the rich variety of the asymptotic behavior of the period as the critical conditions are approached. Indeed depending on how these conditions are approached one finds

- A logarithmic growth of the period, which is reminiscent of the classical case of the conditions getting near an unstable equilibrium point.
- An algebraic growth of the period.
- An exponential growth of the period (see(Leoncini et al., 2001)).

This richness in the behavior characterizes the non-trivial influence of the final-time singularity. From this point on, event if one could argue that collapse condition are so precise that they correspond to a zero measure ensemble among all possibilities and that collapse course are very unlikely, one notices that the presence of the singularity has a strong impact on the dynamics in its neighborhood, and we shall for instance notice that its influence is much more complex than let us say being in the vicinity of a separatrix.

### 3.6 Chaotic advection and anomalous transport

In the previous section we have exhibited the phenomenon of chaotic advection and have briefly described the dynamics of system of point vortices. In this section we shall consider the transport properties of passive particles in order to get clues on the origin of so-called anomalous transport. We shall of course define what we mean by anomalous transport in what follows, but first we shall make a non-exhaustive and brief review of the problematic of transport problems in flows.

### 3.6.1 A brief history

As it always sometime necessary to put some kind of arbitrary beginning to a story we shall start by the problem of heat transport.

#### 3.6.1.1 Empirical laws of the 19th century

We are therefore on December 21st 1807 and after numerous recordings and experiments, Joseph Fourier gives his first results on heat transport also known as the Fourier law, written today as

$$\mathbf{j}_Q = -\lambda \nabla T, \quad (3.25)$$

where  $\mathbf{j}_Q$  denotes the heat current,  $\lambda$  is called the thermal conductivity and  $T$  is the temperature.

A little later in 1855 a German physiologist Adolf Fick finds a law, named the first Fick's law, which is formally identical to Fourier's law and which characterizes the transport of some constituents

$$\mathbf{j} = -D \nabla n, \quad (3.26)$$

here  $\mathbf{j}$  denotes matter current,  $D$  is the diffusion coefficient and  $n$  the concentration. He has the good idea to make a local balance using the principle that nothing is created and lost to arrive the same year at the second Fick's law, universally known as the heat equation or diffusion equation

$$\frac{\partial T}{\partial t} = D \Delta T. \quad (3.27)$$

All these results are empirical. We shall notice that the heat equation (3.27) is not reversible under time reversal. This irreversible evolution fits well the second principle of thermodynamics written by Carnot in 1824 and Clausius inequalities (1855).

We shall now make a little jump in time and skip a period which saw the definition of the Entropy function, and in which statistical physics started after through the works of Boltzmann and Maxwell to arrive at the beginning of the 20th century.

#### 3.6.1.2 Random walks and probabilities

Transport equation of heat or concentration are dealing with macroscopic (statistical) quantities, the link between microscopic and macroscopic will be done by Albert Einstein in one of his three seminal papers of 1905, the one dealing with Brownian motion. In fact and to be somewhat accurate, the first time a link was made between these transport equations and randomness goes back a few years earlier in 1900 when in his PhD dissertation entitled "Théorie de la Spéculation" Louis Bachelier linked the heat equation to a Wiener process.

These findings allowed in a certain way to reconcile microscopic and macroscopic physics. In a some sense one can grossly say that the microscopic and macroscopic worlds are linked by rolling some dice or in other words diffusion phenomena correspond to the macroscopic realization of an ensemble of microscopic random (drunk) walkers.

### 3.6.1.3 Classical deterministic dynamical systems

One problem still remains though. The microscopic world is supposed to be governed by conservative and time-reversible laws. For instance in the classical world one would assume the Newton equation to be valid in the microscopic realm. hence we know that:

1. Quantities are deterministic;
2. Motion is either uniform or accelerated.

One can then reasonable question the origin of the randomness of the microscopic walkers. It is then that sensibility to initial conditions exhibited by Poincaré for the N-body system reveals that the apparent deterministic character is an utopia. It is this phenomenon of unpredictability for large times due to the extreme sensitivity to initial conditions which are nowadays referred as chaotic phenomena or simply Chaos.

## 3.6.2 Definitions

We shall now move on by recalling briefly some results in order to introduce notions which will prove useful in what follows. The presented results will deliberately be shortly described and sometimes grossly. The aim is more to acquire quickly the notions in a simpler way even if this means some lack of rigor or mathematical detail.

### 3.6.2.1 The central limit theorem

We shall here present a version which shall be sufficient for the understanding of the problematic of this chapter. We consider a random process  $v$  and denote  $v(t)$  one of its realization. We introduce then another variable

$$x(t) = \delta t \sum_{t'=0}^t v(t'), \quad (3.28)$$

where  $\delta t$  is some (useless) constant which we choose to be positive. Then :

- If the temporal correlations of  $v$  decrease sufficiently fast then  $x(t)$  is a random process (in the sense of looses memory),

- and if the standard deviation of  $v(t)$  is finite,

the central limit theorem holds and  $x$  is a random process whose distribution tends towards a Gaussian one as  $t \rightarrow \infty$ .

This presentation of the theorem with  $\delta t$  reflects a Langevin perspective, with the transport problems discussed later on in mind. Let us consider a one dimensional trajectory  $x(t)$  where  $x$  corresponds to the position and let us call  $v(t)$  the speed. If we assume that we chosen the origin such that  $x(t = 0) = 0$ , we can write

$$x(t) = \int_0^t v(t') dt' \approx \delta t \sum_{t'=0}^t v(t'),$$

if  $\delta t$  is small enough.

### Remarks

1. The conditions necessary for the central limit theorem to hold are quite broad and often apply for many physical systems. In this point of view one refers to the Gaussian distribution as a general attractor of random processes.

2. We may as well notice that if initially  $v(t)$  is a Gaussian random variable then  $x(t)$  is also Gaussian. The Gaussian is therefore stable from the point of view of the addition. This property is not restricted to Gaussian variables but is in fact shared by all so-called Lévy  $\alpha$ -stable laws ( $0 < \alpha < 2$ ).

### 3.6.2.2 Lévy distributions

As just mentioned, there exists an ensemble of distributions of random variables which are said to be stable in regards to the addition operation. Stable means that the sum of random variables picked according to a given distribution results in a random variable whose distribution is of the same kind as the original one (like for the Gaussian). Paul Lévy has characterized all distribution stables by the addition (as for instance  $x$  is a sum of  $v$  in Eq. (3.28)). The ensemble of distributions said Lévy  $\alpha$ -stables are parameterized by a real number  $\alpha \in ]0, 2]$ . We list here below some of their properties.

The tails of Lévy distribution are of algebraic type and decay as  $x^{-(1+\alpha)}$ , (except for  $\alpha = 2$ , value for which the distribution is in fact the Gaussian one)

- This implies that the mean is not defined for  $1 \geq \alpha > 0$ .
- As well for  $2 > \alpha > 1$  the standard deviation of  $v(t)$  is infinite. This implies that events with large values of  $v(t)$  are statistically not negligible. From a physical standpoint, such events should not arise except if we can have large scale separation in the speeds of the problem dealt with. When we are dealing with transport properties one deals with this infinite problem by rescaling time by for instance introducing the notion of continuous time walker.

### 3.6.2.3 Classification of transport properties

Given the conditions to validate the central limit theorem previously mentioned we shall only obtain physically an anomalous behavior of transport properties (in the sense of non-Gaussian) only if time-correlations do not decay fast enough. One will then be able to talk about strong memory effects. Let us now specify what is meant by anomalous transport and what typical indicators are computed to characterize transport.

Traditionally transport properties of a system are characterized by monitoring the evolution of the second moment (variance) of the characteristic distribution. Even though from a practical point of view the first moment (the average) can have a prime importance (for instance for the transport of goods), from a classical mechanics perspective we try to define properties which have the same Galilean invariance as the motion equations have. Given a quantity  $X(t)$  with a given distribution (for instance  $X$  can be the position of one particle among a large number of them at time  $t$ ) we will focus on

$$M_2(t) = \langle |X(t) - \langle X(t) \rangle|^2 \rangle, \quad (3.29)$$

where  $\langle \cdot \rangle$  corresponds to an average over different realizations or constituents.

In these condition:

1. Transport is said to be diffusive if  $M_2 \sim t$ . It is for instance the case for an ensemble of random walkers moving with speeds distributed on a finite interval on a line (see the diffusion equation (3.27)). We remind the reader that the computation of only one moment is not sufficient to characterize the distribution, hence the diffusive character in the Gaussian sense is not granted even if the second moment evolves linearly with time, we however follow the habits and abusively will rely only on the second moment to name transport diffusive.

2. transport is said to be ballistic if  $M_2 \sim t^2$ . This type of behavior is typically expected for an integrable system. One can for instance think of an ensemble of regular walkers, each moving with its own constant speed, with again a distribution of speeds within a given interval, if all walkers have the same speed one finds of course  $M_2 = 0$ .

Given these two extremes we could expect in nature to observe:

$$M_2 \sim t^\mu \quad 0 < \mu < 2.$$

We could even get higher values of  $\mu$  due to acceleration, but we shall expect some saturation after a while in order to keep the range of velocity finite. When the exponent  $\mu$  is not equal to one, we are getting out of the context of the heat equation and transport is said to be anomalous.

### 3.6.2.4 Anomalous transport

We just have discussed the fact that transport in a complex system can be anomalous. To be more precise in the nomenclature, there exist a more fine classification of the

type of transport based on the value of the characteristic exponent of the evolution of the second moment. As already mentioned:

Transport is said to be anomalous if it is not diffusive in the sense  $\langle X^2 \rangle \sim t^\mu$ ,  $\mu \neq 1$

1. If  $\mu < 1$  transport is anomalous and one refers to it as sub-diffusion;
2. If  $\mu = 1$  transport is Gaussian and one refers to it as diffusion;
3. If  $\mu > 1$  transport is anomalous and one refers to it as super-diffusion.

### ***3.6.3 Anomalous transport in incompressible flows***

We are now going to address the problem of transport in various physical systems for which transport phenomena are essentially governed by advection phenomenon and for which anomalous transport has been observed either numerically or experimentally (Annibaldi et al., 2000; Chernikov et al., 1990; Zaslavsky et al., 1993; Schlesinger et al., 1993; Solomon et al., 1994; Leoncini et al., 2001; Leoncini and Zaslavsky, 2002; Leoncini et al., 2005; del Castillo-Negrete, 1998; Dickman, 2004). More precisely, we shall consider a model of 2-dimensional turbulence relevant for magnetically confined fusion plasmas or geophysical flows.

Both of these system present a strong anisotropy and some models can be done be built that reduce the problem to a 2-dimensional system. For the tokamaks, this reduction from 3 to 2 dimension is linked to the presence of a strong magnetic field, which confines particle along magnetic field lines. Since the magnetic field has no influence along the direction which is parallel to it (Laplace force), we are interested in transverse motion in the plane perpendicular to the field lines, and can in some case reduce the study to a 2-dimensional one. For geophysical flows, either the oceans or the atmosphere have a thickness of the order of a few tens of kilometers whiles their extension covers a few thousand ones, this fact allows approximation of the “shallow water” type and brings us back to two dimensions. In order to be more clear, the aspect ratio of the atmosphere or oceans are of the same order as those of a few pages of this book.

In these two types of system, transport is a key issue. For fusion machines, transport properties are intimately linked to confinement properties of the plasma and thus to the feasibility of a fusion reactor. Regarding geophysical flows, it can concern the level of concentration of salt in the ocean, traces of radio-active materials, temperature transport and of course transport of pollutants in the atmosphere and oceans.

To start the study of transport in these systems we shall start by a remark: in two dimensional turbulence one observes quasi-generically a self-organization due to the inverse cascade (McWilliams, 1984). This self-organization is characterized by the emergence of long lived coherent structures most notably vortices.

We are thus naturally inclined to ask what is the influence of these coherent structures on transport properties.

### 3.6.3.1 Modelling

The way we shall approach this problem is gradual. We shall start from first principles, meaning that we will consider the global evolution of an ensemble of particles with individual dynamics. It is important to mention that contrary to the more traditional approach of monitoring the evolution of a density or a concentration, our tackling of the problem takes into account the individual character of particle, hence we are not influenced by coarse graining effects or particle indifferenciation. These last two effects may indeed have a strong effect on anonymous transport properties, however we believe that by presupposing them we will also not be able to gain a finer and deeper understanding of some mechanisms which may govern the transport properties and thus the interpretation of the results. Of course this last statement would be pointless if our aim was just to get a model which reproduced well observed phenomena, but the ambition here is in the end to be able to control transport, hence a descriptive and not explicative modelling becomes inadequate.

In this same spirit of a deep understanding, we shall consider very simple modelling of the considered flows and take great care of understanding the transport properties in these flows. We shall then progressively move to more and more complex modelling of the flows and get closer to more realistic models.

Now before moving on we want to insist on the formal analogy which exists between geophysical flows and tokamak plasmas. Indeed the influences of the effects listed below are quasi-identical.

Geophysical flows	$\iff$	Tokamak plasma turbulence
Coriolis Force	$\iff$	Lorentz Force
Rossby waves	$\iff$	Drift waves
Charney-Obukhov Equation	$\iff$	Hasegawa-Mima Equation

And an equation describing plasma turbulence in a tokamak the so-called Hasegawa-Mima equation and one describing geophysical flows so-called the Charney equation are formally identical:

$$\partial_t \Omega + [\Omega, \Phi] = 0, \quad (3.30)$$

$$\Omega = \Phi - \lambda \Delta \Phi + gx, \quad (3.31)$$

only the scales and parameters have different physical meanings:  $\Phi$  is either the stream function or the electrostatic potential,  $\Omega$  is a generalized vorticity,  $\lambda^{1/2}$  is a characteristic screening length (Debye length or Rossby length), and  $g$  corresponds to either the presence of a density gradient or the local variation of the Coriolis force due to curvature.

To start our study we consider a very simple system, namely a system of point vortices. The motivation are based on the following already mentioned grounds, point vortices:

- are a good approximation of geophysical flows in some regimes,
- are an exact solution of the Euler equation,
- allow us to reduce the problem of the flow to a  $N$ -body Hamiltonian one.

Moreover to study transport in these system we are considering passive particles whose trajectories are computed using Eq.(3.1). Since the considered flows are time dependent we expect to observe chaotic advection phenomena. We then use numerics to compute the trajectories of particles and vortices.

Regarding this last point, it is mandatory to be more specific. Indeed as we have seen earlier on, the dynamics of passive tracers or point vortices is Hamiltonian for 2-dimensional flows. Hamiltonian dynamics are peculiar in the sense that they are preserving phase space volume and time-reversible, and there are conserved quantities. Since we are interested in transport properties, we have to compute trajectories over long times. It is then very important to carefully chose the algorithm which will be used for time integration of trajectories. Indeed most algorithms do not reproduce well the underlying symplectic structure of Hamilton's equations. For instance, it is now well know that typical Runge-Kutta scheme do not preserve phase space volume. For short time integrations, this is usually not a problem, but as soon as we consider asymptotic behaviors, these effects may actually totally bias the dynamics and by consequence transport properties. There exists however symplectic algorithms which have a symplectic structure. Of course, since we are dealing with discrete time and are facing Hamiltonian chaos we can not expect to reproduce "exactly" the continuous time dynamics, however we are using an iteration which will preserve well the original invariants of the dynamics, hence it is reasonable to expect that similar transport properties as the ones coming from the continuous time system will be numerically exhibited.

For the considered Hamiltonian, we have chosen to compute the trajectories using a sixth order symplectic scheme, namely the so-called Gauss-Legendre one (McLachlan and Atela, 1992). Since the Hamiltonians (3.2) and (3.7) are non-separable, we have no choice but to use this type of implicit algorithm.

### 3.6.4 Tracers (*passive particles*) dynamics

#### 3.6.4.1 Regular flows: particle's advection in a three point vortex system

We first start with the simplest case of a regular flow with vortices. In order to get some time dependence to avoid trivial results we are left with systems of three point vortices (if we had more the system would be chaotic). Also since we are interested in asymptotic transport properties we have considered a periodic motion of the vortices. Work related to transport for the case of three identical vortices can be found in (Kuznetsov and Zaslavsky, 1998, 2000). Here we want to have vortices of different signs and check the influence on transport of the finite time singularity (Leoncini et al., 2001), which also corresponds to real vortex trajectories when these are getting loser to each other (Dritschel and Zabusky, 1996). In order to check the

impact of the singularity we have considered configurations giving rise to periodic motion and which are getting closer and closer to the conditions (3.12 et 3.13).

Vortex motion being periodic, the stream function is time dependent, we are thus expecting Hamiltonian chaos for the passive tracers. To study this phenomenon it is useful to visualize phase space using a Poincaré section. With this in mind we define the following Poincaré map by

$$z_{n+1} = \hat{P}(z_n) = e^{-i\Theta} z(T, z_n),$$

where time is discrete and is now measured in number of periods ( $t_n = nT$ ). One notices also that since the vortex motion is in fact quasi-periodic, after each period a global rotation of angle  $\Theta$  is performed in order to make the triangle formed by the vortices invariant by the map. We have denoted  $z(T, z_n)$  the position in the complex plane at time  $t = T$  of a tracers which has an initial condition  $z_n$  at time  $t = 0$ , where  $T$  corresponds to one period of the triangle formed by the vortices.

For the case of identical vortices we have first considered conditions “far from collapse”  $k = -0.2$  ( $k_c = -1/2$  corresponds to the collapse). The Poincaré sections is displayed in Fig. 3.6. One can notice effectively the phenomenon of chaotic advection, in a large region usually referred to as the chaotic sea. We also observe regions where trajectories appear as regular (at least at first glance), which are referred as islands of stability in the literature, as most of the time an elliptic point corresponding to a stable periodic orbit lies at the center of the island. In the Fig. 3.6 the two identical vortices are marked with the  $+$  sign and the negative one with the  $o$  sign. Hence we notice the presence of islands of stability around the different vortices, in what follows we shall call these special islands vortex cores. Each core corresponds indeed to a quantity of fluid which is trapped around the vortex and stays in its vicinity with a more or less regular dynamics. We can also notice that the region surrounding the island localized in the lower-left part of the plot is darker than the stochastic sea. This translate a non homogeneous distribution of the trajectories in the chaotic sea and is a consequence of stickiness a phenomenon as we shall see at the origin of anomalous transport.

For comparison we have represented on Fig. 3.7, a Poincaré section resulting from a configuration close to collapse. We can notice that actually the phase space structure has not changed much, we find again, a stochastic sea and islands of stability. We however notice that the size of the cores is much smaller. In fact, a simple arguments can explain that the size of the cores is related to the minimum inter-vortex distance reached (Leoncini et al., 2001). We shall consider transport properties in these flows afterwards, but first we shall discuss chaotic flows.

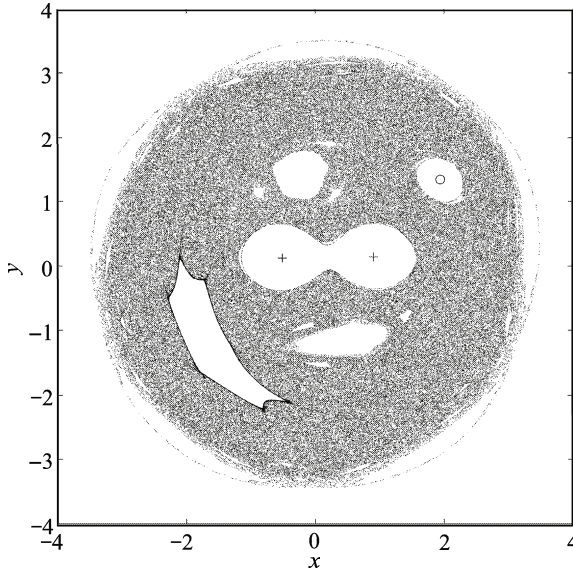


**Fig. 3.6** Poincaré section of a system of three point vortices with parameters far from the singularity. The constants of the motion of the three vortices are  $K = 0$ ,  $\Lambda = 0.9$ . Vorticities are  $(-0.2, 1, 1)$ . The resulting observed period is  $T = 10.73$ .

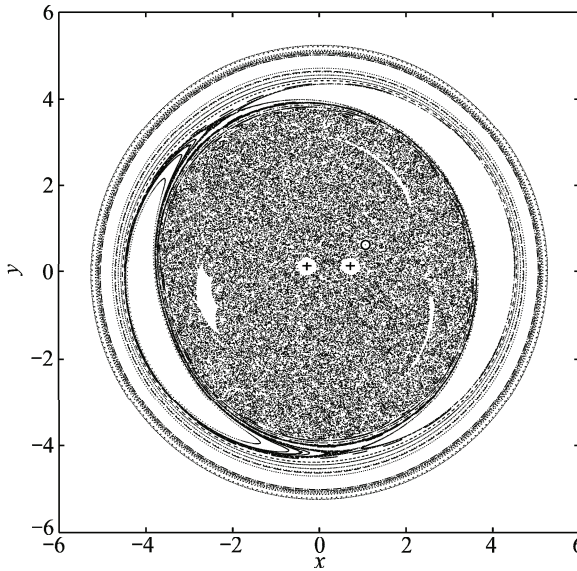


**Fig. 3.7** Poincaré section of a system of three point vortices with parameters far from the singularity. The constants of the motion of the three vortices are  $K = 0$ ,  $\Lambda = 0.9$ . Vorticities are  $(-0.41, 1, 1)$ . The resulting observed period is  $T = 36.86$ .

### 3.6.4.2 Chaotic flows

#### *Point vortex systems*

As mentioned when we have four vortices (Novikov and Sedov, 1978; Aref and Pomphrey, 1980; Laforgia et al., 2001), or more (Leoncini and Zaslavsky, 2002), the vortex motion itself becomes chaotic. The loss of quasi-periodicity does not allow to define a Poincaré map, and the global rotation invariance is likely to blur any attempt to have simple Poincaré sections. Visualization of tracers is thus limited and we are reduced to make snapshots of the system to visualize the positions of all tracers at a given time. For instance in Fig. 3.8 we have plotted snapshot obtained from a four point vortex system as well as one of sixteen vortices. Passive particles having been initially placed in a small region. We notice that the mixing appears as relatively homogeneous. We also notice the persistence of the “impenetrable” vortex core around the vortices, but do not see a priori any region of regular motion like in the three vortex system. We although can see some stickiness phenomenon around the vortex cores for four identical vortices in Fig. 3.8 The sticking mechanisms is related to some kind of peripheral trapping in the cores and has been identified in (Laforgia et al., 2001), it is intimately linked to the Hamiltonian dynamics of the vortices themselves. A form of stickiness exists indeed for the vortex dynamics, it took the form of two vortices getting close to each other and forming a pair (see Fig. 3.9). In this setting the vortices being close to each other and due to the logarithmic interaction between the two, we can portray the system as an integrable system of two vortices perturbed by the others. We are then in a close to integrable system, thus the notion of stickiness for this type of behavior. For the four vortex system stickiness is “degenerate”, indeed as the pair is formed, at large scales the pair looks like one vortex and we end up with a system of three vortices which is also integrable. This degeneracy gives rise to a special behavior of trapping times distribution with respect to systems with more vortices (Laforgia et al., 2001). For the system of 16 vortices, this stickiness phenomenon and pair formation is also observed, but we observe as well another form of stickiness with the formation of “triplets” which are also integrable subsystems.

We shall now discuss flows generated by Charney-Hasegawa-Mima.

The Charney-Hasegawa-Mima (CHM) equation

As already mentioned tokamak plasmas turbulence and geophysical flows can in some circumstances share in common a same dynamical equation as Eqs. (3.30) and (3.31), where  $\Phi$  is the stream function of the electric potential and  $\Omega$  is a generalized vorticity. One shall notice that when  $\lambda = g = 0$ , we end up with the Euler equation which admits point vortices as solutions. In fact only when  $g = 0$ , point vortex solutions still are valid. The existence of the  $\lambda \Delta \Phi$  term corresponds to some screening effect and vortex interaction is modified  $\log(r) \rightarrow K_0(r/\lambda^{1/2})$  where  $K_0$  is the zeroth order modified Bessel function, which becomes a logarithm for  $r \ll \sqrt{\lambda}$

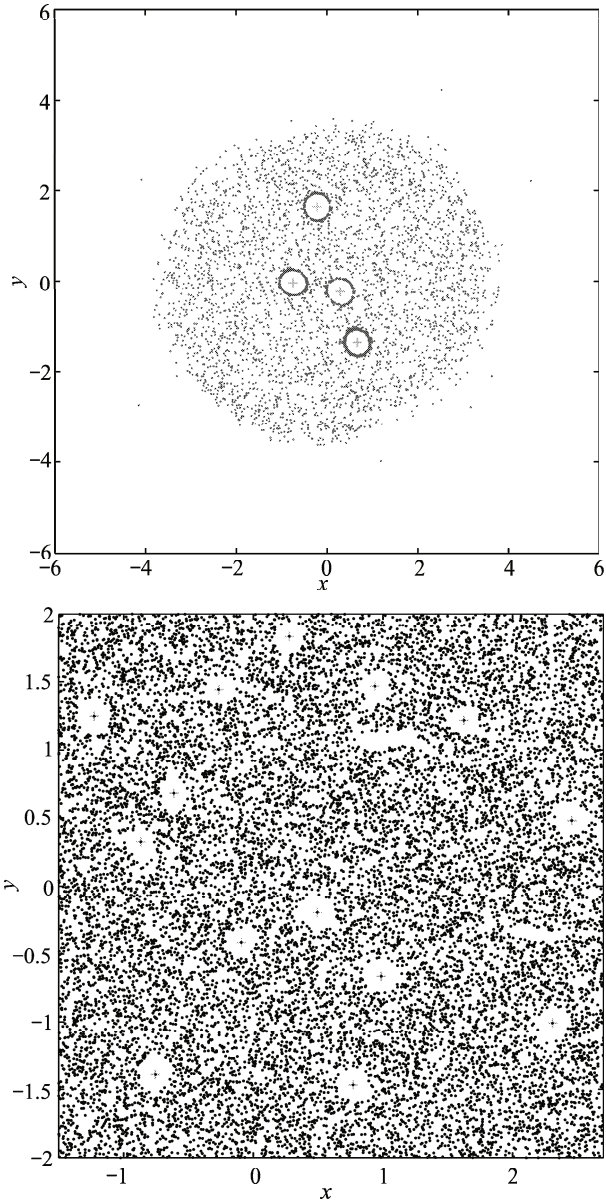


**Fig. 3.8** Snapshot of a system of point vortices and passive tracers. Top: system of four point vortices. Bottom: Local zoom of a snapshot of the system of sixteen point vortices. One can notice the presence of vortex cores surrounding the vortices. Also in the four point vortex system one observes stickiness around the cores. One can also guess the quasi-regular motion in the region far from where the vortices evolve (see (Boatto and Pierrehumbert, 1999)).

and exhibit exponential decay for  $r \gg \sqrt{\lambda}$ . The presence of a non zero  $g$  modifies drastically the solutions, indeed the  $g_x$  is non-local and from this fact Eq. (3.30) has then exact planar wave solutions with a given dispersion relation, but on the other hand localized point vortices are no more accepted. Moreover, the presence of this term introduces some anisotropy in the system.

To study transport in this system we have also had to simulate numerically the equation. Unfortunately the presence of a cascade towards small scales introduces some numerical instabilities. Hence to stabilize the code we have to introduce a dissipation term in the form of a viscous term  $\Delta\Omega$  which can cancel out the small scales problem. Moreover since we want to consider the flow for large times we also counterbalance the dissipation with some kind of source. Hence we rewrite the dynamical equation (3.30) as

$$\partial_t \Omega + [\Omega, \Phi] = 0 + \text{Source} + \text{Dissipation}. \quad (3.32)$$

To perform numerical simulation of this type of equation and study afterwards transport properties it is easier to consider periodic boundary conditions and use a pseudo-spectral scheme. We are then computing the non-linear evolution of a finite

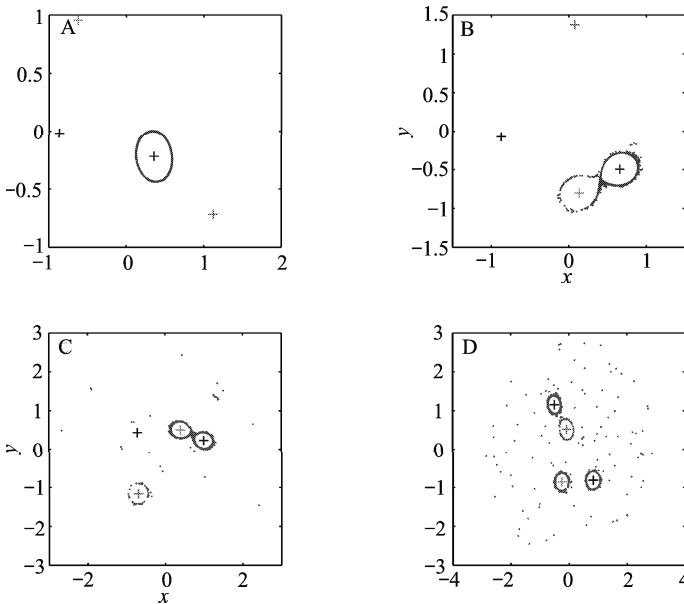


**Fig. 3.9** Visualization of four consecutive snapshots for a system of four point vortices with 1000 passive tracers, corresponding to four successive pair formations. Passive tracers were initially placed in the periphery of the core of one vortex. One can see that as the pairings occurs, the cores exchange particles, it is also during this pairing that some particle manage to escape. After four consecutive pairing all cores are “contaminated” and about 10% of the particles have escaped. Initial vortex positions are  $[(1.747, 1.203) (-\sqrt{2}/2, 0) (\sqrt{2}/2, 0) (0, -1)]$ . Particle are initially uniformly distributed on a circle of radius  $r = 0.27$  around the forth vortex.

number of modes. Hence when considering transport properties, it will be the transport of passive tracers in the flow generated by this finite number of modes which evolutions will be governed by Eq. (3.32). In order to characterize transport in these system, we can of course not cover all range of parameters and situations. So we have selected three different regimes with different parameters, as well as different dissipations and forcing terms, for which and for the time length of the simulation, the dynamical invariants of the dynamics, such as the energy or the enstrophy can be considered constant. The visualization of the scalar field  $\Delta\Phi$  has been reproduced on Figs. 3.10, 3.11, 3.12. We have a case with a very small dissipation (Fig. 3.10) and a few vortices, one with two strongly forced vortices (Fig. 3.11), and one case which is strongly anisotropic with intermediate forcing (Fig. 3.12).

From the point of view of the particle motion, we shall still remain with the Gauss-Legendre symplectic scheme, the Hamiltonian of the system being given by  $\Phi$ . Also, since we have concluded that eventual anomalous properties of transport are directly linked to memory effects and long lasting time-correlations, it is extremely important to be careful when computing the speed. Indeed the pseudo-spectral code gives access to the time evolution of a finite number of Fourier modes, or in real space it gives the values of the speed on specific grid points. In order to avoid any loss of memory resulting from a passive tracers moving from one small cell to another, we have to take into account all the Fourier modes (which is numerically costly), and not to interpolate from a finite number of point on the grid.

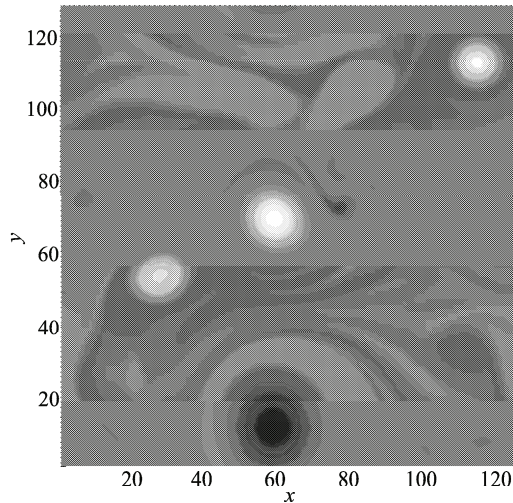


**Fig. 3.10** Scalar field  $\Delta\Phi$ , for a configuration with small dissipation and anisotropy.

### 3.6.5 Transport properties

We now focus on transport properties. First we define which quantities we shall consider in order to measure transport, and also which regions we are interested in.

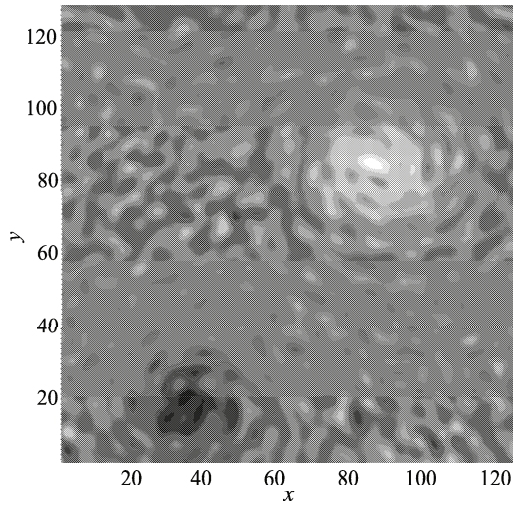


**Fig. 3.11** Scalar field  $\Delta\Phi$ , for a configuration with two large vortices and strong noisy forcing.

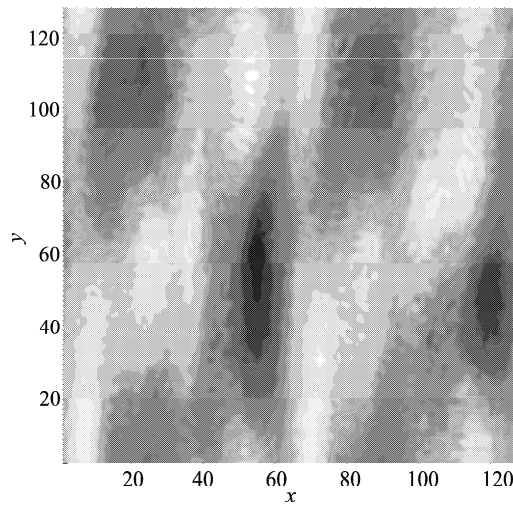


**Fig. 3.12** Scalar field  $\Delta\Phi$ , for a configuration with strong anisotropy.

### 3.6.5.1 Definitions and observations

When considering system of three point vortices, as those depicted in Figs 3.6 and 3.7, one can notice that the chaotic sea is finite. Moreover, transport properties are quite obvious when we are within an island of stability, thus we are interested in transport properties resulting from trajectories living in the chaotic sea which results from chaotic advection. Since the sea is bounded, it is of course not very useful to consider transport for long times based on particle positions (the sea being filled quite fast). We are thus considering transport properties based on the length of trajectories and measure the curvilinear arc-length, and the transport and dispersion associated to this quantity

$$s_i(t) = \int_0^t |v_i(\tau)| d\tau, \quad (3.33)$$

where  $v_i(\tau)$  is the speed of particle  $i$  at time  $\tau$ . Then to characterize and study transport we compute the moments

$$M_q(t) \equiv \langle |s(t) - \langle s(t) \rangle|^q \rangle, \quad (3.34)$$

where  $\langle \dots \rangle$  corresponds to ensemble averaging over different trajectories. And from the time evolution of these moments we “extract” a characteristic exponent

$$M_q(t) \sim t^{\mu(q)}. \quad (3.35)$$

In what follows and to be consistent across the different systems we consider everywhere transport properties related to the length of finite time trajectories.

### 3.6.5.2 Lévy flights

Before measuring the different moments, it is good to have an idea on how the lengths of trajectories evolve with time. We have drawn in Fig. 3.13 the relative evolution of the length with respect to the mean of an ensemble of 30 different particles in a flow generated by three point vortices. One can see in the figure that the time evolution is reminiscent of some random walks by parts. Indeed there are some parts where the evolution looks regular and ballistic before falling back to erratic again, and these regular parts can last relatively long times. This type of regular part behavior is usually referred to as Lévy flights. Indeed when we observe such large events, it usually means that they are not as improbable as a Gaussian would let us think, hence we may model it with random steps, but with step sizes taken from a Lévy distribution with infinite second moment. In fact to model this behavior gigantic steps are not compatible with finite speeds, thus we consider a Lévy walker, and put the constraint on time. For instance, one can think of two possible values for the speed of a walker  $\pm v$  and randomly pick according to a Lévy distribution how long the walker travel with that speed, before making another random pick. One talks then about continuous time random walks.

### 3.6.5.3 Transport characterization and moments

We shall now finally measure transport properties. As mentioned we shall consider system with increasing complexity, meaning first a system of three point vortices near collapse dynamics (Leoncini et al., 2001), then systems of four and sixteen identical vortices (Leoncini and Zaslavsky, 2002), and finally three different configuration of the Charney-Hasegawa-Mima (CHM)(Leoncini et al., 2005).

#### *Evolution of moments*

For the different considered cases we numerically compute the different moments (3.34). For this computation we typically consider an ensemble of about 500 trajectories, which have been computed for time scales of about  $10^4$  or more. The time step of the numerical integrator is  $10^{-2}$ , and characteristic Eulerian time scales (for instance the turn over vortex time) are about unity. Since we have only few trajectories, we have considered regimes which we may consider somewhat stationary from the transport perspective, in the sense that we considered that transport properties are invariant by time translation. This allows us to cut trajectories in pieces and thus to gain in the statistics up to relatively large times. It is important to mention that having few long trajectories is usually more relevant than a large number of them but for shorter times. Indeed assuming some ergodicity of the system, we are not sure that the ergodic measure is Lebesgue, however we know that long time trajectories should sample adequately the ergodic component, we may then expect that

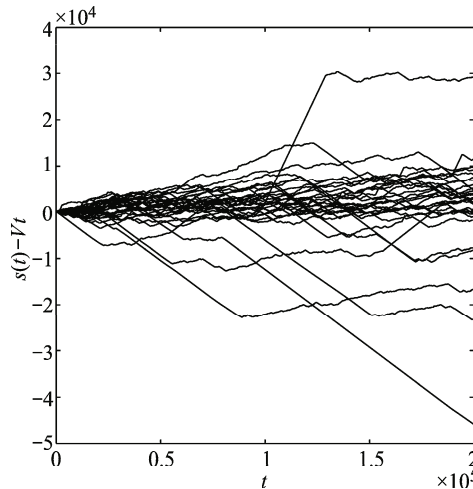


**Fig. 3.13** Deviation from average arc-length ( $s(t) - Vt$ ) versus time for an ensemble of 30 particles. We notice the presence of Lévy flights. The considered system for the flow is a three vortex one characterized by  $K = 0$ ,  $\Lambda = 0.9$ . The run is performed over 20000 periods. The average speed is  $V \approx 0.87$ . The vortex strength are  $(-0.2, 1, 1)$  and the quasi-period of the motion is  $T = 10.73$ .

large time transport properties will be better reproduced by using many portions of long trajectories rather than a large number of shorter ones.

In order to have an idea of the time behavior of the moments, we have reproduced on Fig. 3.14, the moments obtained from passive particle dynamics in the flow generated by CHM with low dissipation (Fig. 3.10). One can notice that the power-law behavior (3.35) is accurate except at very large times and for high moments. This problem can be understood by the fact that for large times we have only little statistics, and also by the fact that transport is anomalous, which can make a few events dominate transport properties, if the statistics is poor.

### Characterizing transport

To characterize transport we extract the exponent  $\mu(q)$  from the moment evolution and study how this function behaves in  $q$  (Castiglione et al., 1999; Ferrari et al., 2001). In fact in anomalous transport there are some nuances, indeed we may have self-similar anomalous transport properties or not, if not, one uses the term multi-fractal transport or strongly anomalous transport. The discrimination comes from the behavior of the function  $\mu(q)$ .

- If transport is Gaussian we have:  $\mu(q) = \lambda q$ ,  $\lambda = \frac{1}{2}$ .
- Transport is weakly anomalous or self-similar when:  $\mu(q) = \lambda q$ ,  $\lambda \neq \frac{1}{2}$ .
- And if the behavior of  $\mu(q)$  is non-linear we have then strongly anomalous or equivalently multi-fractal transport:  $\mu(q) \neq \lambda q$ .

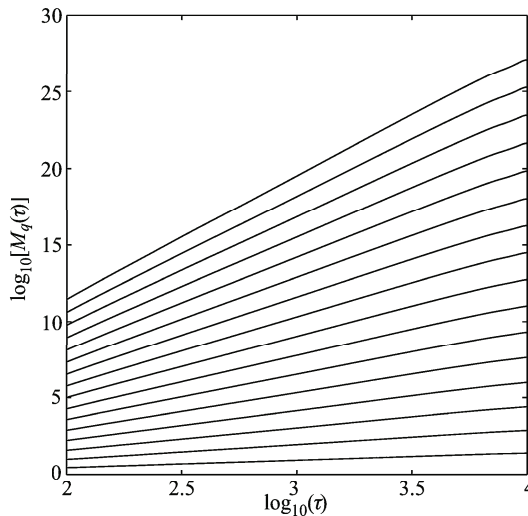


**Fig. 3.14** Time evolution of the moments  $M_q(t)$  for particles driven by the flow generated by Charney-Hasegawa-Mima with weak dissipation. We find the expected behavior:  $M_q(t) \sim t^{\mu(q)}$ . The moments for  $q = 0.5, 1, \dots, 8$  are represented.

We have reproduced in Fig. 3.15, the exponents observed in a system of three point vortices. One concludes that transport is super-diffusive ( $\mu(2) > 1$ ) and since  $\mu(q)$  is non-linear we have multi-fractal transport.

### *Summary of transport properties*

We can summarize the different results obtained for transport properties in the different systems (see (Leoncini et al., 2001; Leoncini and Zaslavsky, 2002; Leoncini et al., 2004, 2005)) in the following table:

	$\mu(2)$
3 vortices	$1.5 \pm 0.2$
4 vortices	1.82
16 vortices	1.77
CHM small dissipation	1.84
CHM noisy	1.70
CHM anisotropic	1.78

For all case we observe super-diffusive transport, and except maybe for the three point vortex systems, we may hypothesize that there is a probable universal value for the characteristic exponent of transport in these 2-dimensional flows. Moreover, for the 3 point vortex system, we had considered a different observable (see (Kuznetsov

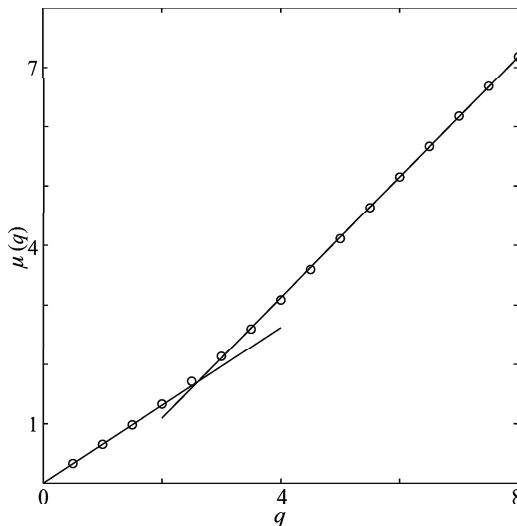


**Fig. 3.15** Behavior of the function  $\mu(q)$  versus moment order  $q$ , obtained for a system of three point vortices. The moments corresponding to order  $q = 1/2, \dots, 8$  are represented. We observe a non-linear behavior of  $\mu(q)$ . Transport is super-diffusive and multi-fractal. The slope for small moments is about 1.4 while it becomes 1 for high moments.

and Zaslavsky, 2000; Leoncini et al., 2001)) namely the number of turns around the center of vorticity, which may somewhat affect the value of the exponent when compared to arc-length. Also if we consider the nature of anomalous transport, we find that for point vortex flows the transport is multi-fractal (strong anomalous) (Leoncini and Zaslavsky, 2002; Leoncini et al., 2004), while for the flows resulting from CHM, we can not be as conclusive, but an analysis based on varying the total number of trajectories and the total computed time shows a trend that transport may be as well multi-fractal (Leoncini et al., 2005).

### 3.6.6 Origin of anomalous transport

We have just noticed in the considered two-dimensional flows some universality in the anomalous super-diffusive behavior of transport properties. It is then natural to question which phenomenon may be at the root of this observation.

#### 3.6.6.1 Regular flows

As shown in Fig. 3.13, the presence of Lévy flights seems to be intimately linked to the anomalous properties of transport. When the flows is regular and we can visualize phase space with a Poincaré section; the origin of the flights can be explained. Indeed, let us define an average speed over a time  $\tau$  with

$$\overline{v(\tau)} = \frac{1}{\tau} \int_t^{t+\tau} v(t') dt',$$

and let us consider the distribution of these averaged speeds for an ensemble of trajectories. We can reasonably expect that due to ergodicity in the chaotic sea, this distribution shall be sharper and sharper as  $\tau$  increases to become so delta function in the  $\tau \rightarrow \infty$  limit (see for instance (Leoncini et al., 2008) for details). We may however expect different peaks to arise, which would characterize the Lévy walkers, which we actually see in Fig. 3.16). We then localize with different colors in the phase space the regions visited by the portion of trajectories which contribute to a given peak (see right pictures in Fig. 3.16). It is then clear that the observed Lévy flights in Fig. 3.13 are a consequence of the phenomenon of stickiness. Stickiness is related to the fact that once a trajectory is in the vicinity of an island of stability it may (or may not if the island is not sticky) want to mimic trajectories which are inside the islands and become more or less regular for very large times. One can also notice on Fig. 3.16 that each peak corresponds to a specific sticking region in phase space, which actually explains the multi-fractal nature of transport in this three vortex system (Leoncini et al., 2001).

### 3.6.6.2 Notion of chaotic jet

When the flow is chaotic, we can not have access to phase space as easily as when we can define a Poincaré map, hence it becomes difficult to identify sticky regions. It is then useful to introduce the notion of chaotic jet (Leoncini and Zaslavsky, 2002,

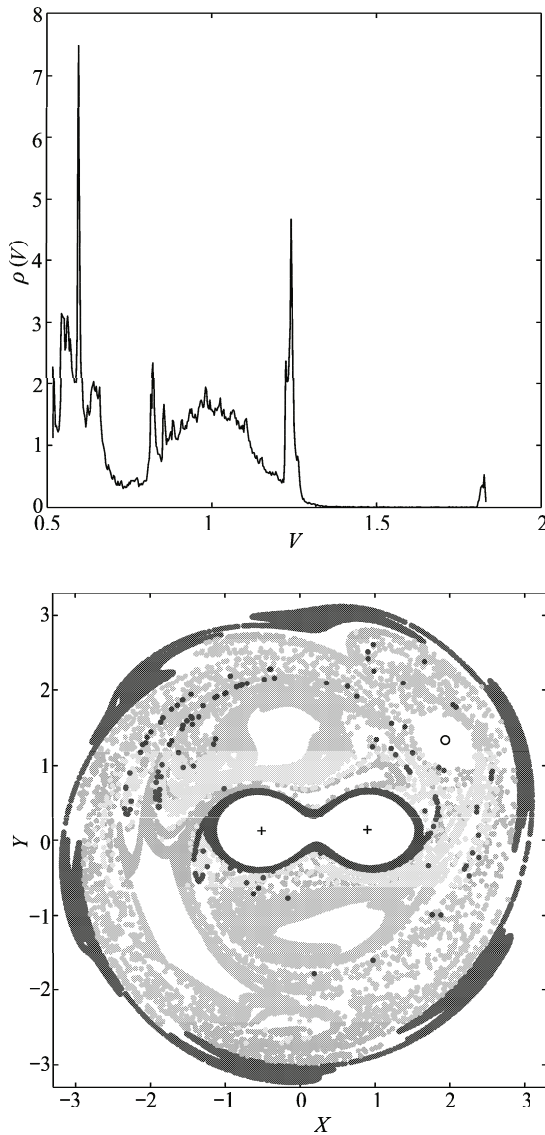


**Fig. 3.16** Top, distribution of speeds averaged over 20 periods. Bottom, localization of the regions contributing to the different peaks of the averaged speed distribution.

2003; Afraimovich and Zaslavsky, 2003)(See Fig. 3.17): We consider one special passive particle and place in its immediate neighborhood a few test (ghost) particles. We then measure the time/arc-length that the ghosts remain in the neighborhood of the chosen particle. We are then de facto interested in the relative dispersion of particles. From one point of view we can see this action as some kind of finite size Lyapunov exponent measurement, or take an other point of view and say that we are interested in the stability of a coarse grained trajectory. The implementation of this measurements stems from the fact that we expect long time trapping within jet when stickiness is observed, it however can be generalized to systems when we do not have access to an easy visualization of phase space. Note that computing chaotic jets properties can be included in a more general setting of measuring the  $\varepsilon$ -complexity (Afraimovich and Zaslavsky, 2003). When measured, we notice that the trapping time distribution within jets (see Fig. 3.18) displays a power-law decay with a characteristic exponent  $\gamma$ . For the system with sixteen vortices we have

- $\rho(\tau) \approx \tau^{-\gamma}$
- $\gamma \approx 2.82$
- $\gamma \approx 1 + \mu(2)$ .

In fact the  $\gamma = 1 + \mu$  law can be explained under certain conditions (see for instance (Leoncini et al., 2001; Leoncini and Zaslavsky, 2002)), when we reconcile the  $\gamma$  exponent to one related to the one observed in recurrence time distribution. The agreement with this law, indicate nevertheless that it is trapping times within jets which are at the origin of anomalous transport. And we can easily imagine that we indeed shall not observe a regular diffusion behavior if the dispersion of particles is not strong enough. We find again this behavior in CHM, except maybe for the strongly anisotropic situation (Leoncini et al., 2005).

Detection of jet using the method discussed earlier allows also to localize the origin of anomalous transport Indeed since particles when ghost particles are trapped for relatively large times in a jet (resulting in a contribution in the power-law tail), one can then start to localize the reference trajectory. Hence we are able to localize a non-dispersive jet for the system of sixteen vortices in Fig 3.19. For this jet, the influence of vortex cores is predominant, and one recovers the sticking phenomenon around coherent structures at the origin of anomalous transport. However for a jet identified in CHM the result is more surprising (see Fig 3.19). Indeed, one notices

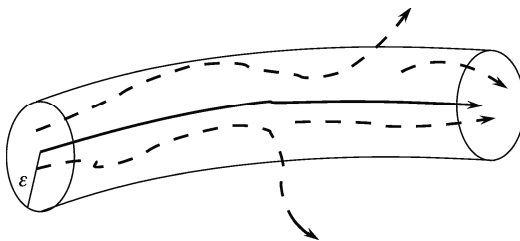


**Fig. 3.17** Schematic representation of a chaotic jet.

that even though coherent structures play definitively an important role, we notice that their influence is not restricted to their immediate individual periphery. Hence understanding transport properties is not limited to the presence of coherent structures but also to their eventual interactions or exchange of regular jets.

The notion of a jet is a priori not well defined, indeed it is subject to the introduction of two arbitrary quantities. For one part the radial extension of the jet  $\varepsilon$  around the reference trajectory and for the other part the initial distance  $\delta$  at which the ghost particles are placed. In order to see if these have an influence we can study the jet “structures”, meaning the evolution of ghosts relative to the reference tracers in a long lived jet. This “structure” is represented for the two mentioned jets in Fig. 3.20. In order to analyze the influence of delta, it appears clear that during the life of the jets, ghosts may come much closer to the reference trajectory (at least an order of magnitude closer). Also, and it is more visible for the jet in the vortex system (left in Fig. 3.20), that some kind of hierarchical structures appear. This underlines the fact that actually particles are trapped in different successive ( $\varepsilon$ -jets) scales. It is then reasonable to assess that the asymptotic properties of the tails of trapping time distributions are independent of  $\varepsilon$  and  $\delta$ . Of course we have to have considered these scales beyond any characteristic one of the system, i.e the size of the cores for instance. To conclude on the jet’s structure, it is important to mention that the relative dynamics of ghost tracers does not seem regular, and appears as chaotic, but that for relatively large times, chaos is confined on small scales, making thus the coarse grained  $\varepsilon$ -trajectory “regular”. This last statement is important as it shows that the computation of a Lyapunov exponent may lead to some misunderstandings such as extended chaos for instance.

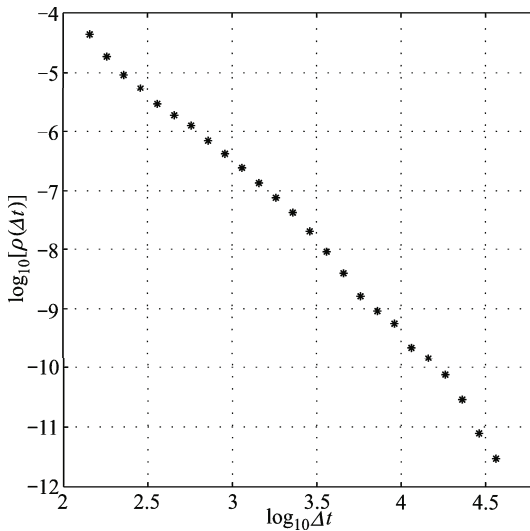


**Fig. 3.18** Tail of the distribution of trapping times within jets for the system of sixteen vortices. We observed a power law decay.

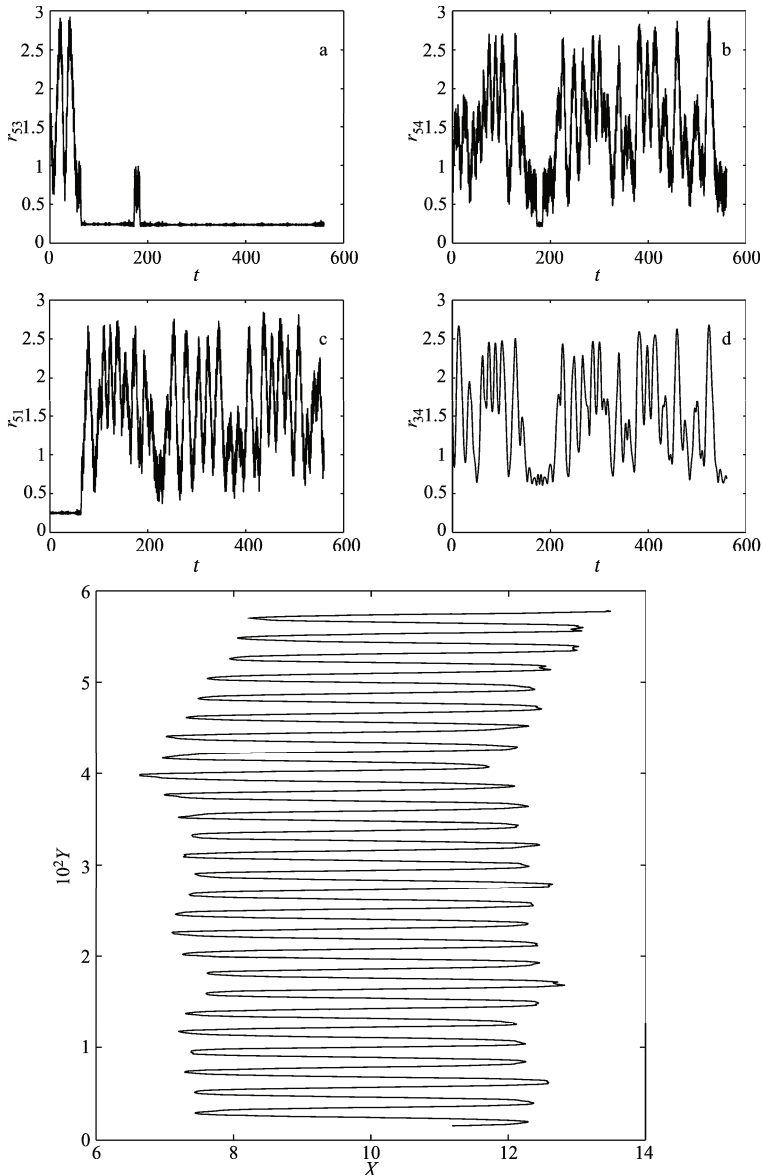


**Fig. 3.19** Localization of a non-dispersive (long-lived) jet in the system with sixteen vortices (top) and in the CHM noisy case (bottom). For the left figure, the distance between the passive tracer and three point vortices is presented on this first three plots on the top. We can see that the jet sticks around vortex cores. In the fourth plot we plotted the distance between two vortices which exchange the jet during the formation of a pair. For the CHM case, the jet is not trapped around one of the two vortices (see Fig. 3.11), but bounces back and forth between the two structures (recall the periodic boundary conditions of the flow).

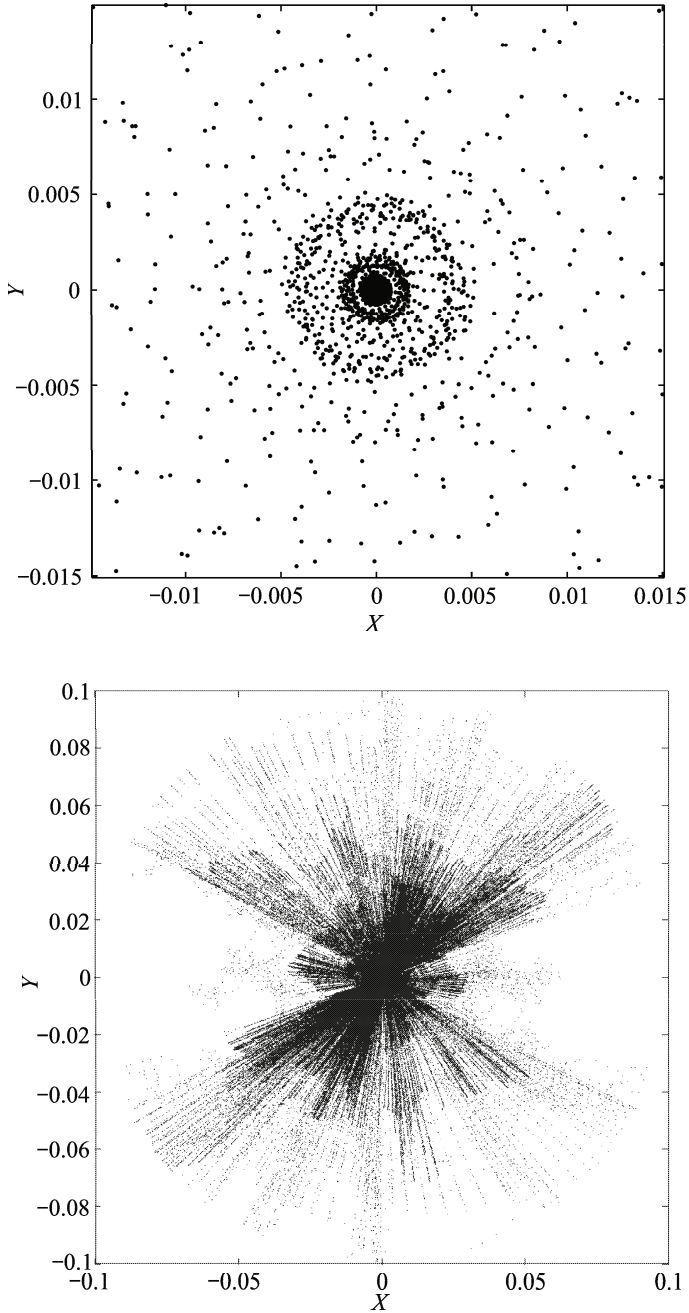


**Fig. 3.20** Structure of jets. Top for a jet in the system with 16 vortices and bottom for a jet in CHM (see Fig. 3.19)

### 3.6.7 *General remarks*

When we consider transport related problems in physics, we realize pretty soon that the range of applicability of the central limit theorem are quite broad and general. From this perspective, anomalous transport may be seen as some singular and exceptional behavior without any real consequences. One can though also asks ourselves if nature is really as simple as we want to represent it, or if it not our eyes and measuring instruments that give such a broad spectrum of applicability to this theorem, and in this perspective, we may want to sharpen our sight and tools to try to switch from description to explanation.

## 3.7 Beyond characterizing transport

We have up to now discussed transport problems in 2-dimensional flows and found out that the observed anomalous transport could be explained by chaotic advection and the emergence of coherent structures associated with the phenomenon of stickiness or chaotic jets. In this section we want to use the phenomenon of chaotic advection with two possible applications. In the first situation we shall consider stationary divergent free three dimensional field, and perform a transformation to fall back on a one and a half degree of freedom Hamiltonian, which we shall use to detect coherent Lagrangian structure in the flow. Then in a second part we shall see how we can use chaotic advection to achieve targeted mixing, meaning we want to achieve good mixing in a region of phase space confined by “virtual” (dynamical) barriers.

### 3.7.1 *Chaos of field lines*

In this first part we shall concentrate on the chaotic nature of field (stream) lines for a three dimensional incompressible and stationary flow which we note  $\mathbf{v}$  (Leoncini et al., 2006). Since the flow is considered stationary the fluid particles or tracer will follow the stream lines. The equation giving us the field lines equation is generically obtained by writing

$$\mathbf{v} \wedge d\mathbf{M} = \mathbf{0}. \quad (3.36)$$

### 3.7.2 *Local Hamiltonian dynamics*

We now briefly resume how to get the Hamiltonian chaotic character of field lines (Zaslavsky et al., 1991). Equations (3.36) can be rewritten as

$$\frac{dx}{v_x} = \frac{dy}{v_y} = \frac{dz}{v_z} = \frac{ds}{v} \quad (3.37)$$

then we assume that locally  $v_z \neq 0$  and we get rid of one equation

$$\begin{cases} dx/dz = v_x/v_z \\ dy/dz = v_y/v_z \end{cases}, \quad (3.38)$$

to get a dynamical system in two dimension.

Since the flow is incompressible (flux preserving) we have

$$\nabla \cdot \mathbf{v} = 0, \quad (3.39)$$

which implies the existence of a stream vector  $\xi$  such that

$$\nabla \wedge \xi = \mathbf{v}, \quad (3.40)$$

$\xi$  being defined up to some gradient, which we shall refer as a gauge condition.

Let us consider the vector  $\xi$  et rename its coordinates  $\xi_x = -p$ ,  $\xi_z = H$ , and let us reduce the gauge condition by choosing  $\xi_y = 0$ . Given Eq. (3.40), we end up with

$$\mathbf{v} = \left( \frac{\partial H}{\partial y}, -\frac{\partial H}{\partial x} - \frac{\partial p}{\partial z}, \frac{\partial p}{\partial y} \right). \quad (3.41)$$

Now let us recall Eqs. (3.38), but with a change of variables, namely instead of considering the triplet  $(x, y, z)$ , we use  $q = x$  and  $\tau = z$  to get to the triplet  $(q, p, \tau)$ . We shall use the notation  $\tilde{H}(p, q, \tau) = H(x, y, z)$ . This change of variables implies

$$\begin{cases} \partial_x f = \partial_q \tilde{f} + \frac{\partial p}{\partial x} \partial_p \tilde{f} \\ \partial_y f = v_z \partial_p \tilde{f} \end{cases}, \quad (3.42)$$

and now by using the expression of the speed (3.41) we end up with Hamilton's equations

$$\begin{cases} \dot{q} = \frac{\partial \tilde{H}}{\partial p}, \\ \dot{p} = -\frac{\partial \tilde{H}}{\partial q}. \end{cases} \quad (3.43)$$

### Consequences

- Field lines are generically chaotic for three dimensional divergence free fields.

Beyond this remark, we can also use this transformation to compute field lines numerically using a symplectic integrator. This algorithm insures us of a good preservation of the invariants of the systems and thus gives the assurance of having stream lines with the condition of having a divergence free field. Moreover we can think

of using the transformation to perform afterwards a Poincaré map and use them to localize 3-dimensional structures. It is important to insist that the change of variable is only locally valid, indeed the arrow of the effective time is not always defined. However we can use the fact that the choice of the direction  $z$  and the coordinate system is somewhat arbitrary, and we can for instance change labels or rotate it if we encounter such problems (Leoncini et al., 2006). We insist also on the fact that of course we have checked that such algorithmic procedure was giving better results than a direct integration of Eqs. (3.38) by a Runge-Kutta scheme. We now illustrate in what follows the obtained results for a simple example.

### 3.7.3 An ABC type flow

To illustrate the interest in performing the transformation to a Hamiltonian system we here consider an ABC (Arnold-Beltrami-Childress) type flow characterized by the following equations

$$\begin{aligned}v_x &= \cos(y) - \varepsilon \sin(z), \\v_y &= \sin(x) + \varepsilon \cos(z), \\v_z &= \cos(x) - \sin(y) + v_0,\end{aligned}\tag{3.44}$$

where  $v_0$  is a constant which allows to eventually get rid of the problem resulting from  $v_z$  being zero. The properties of this flow are known:

- If  $\varepsilon = 0$ , field lines are integrable (quasi-2D flow),
- If  $\varepsilon \neq 0$ , the flow is tri-dimensional and field lines are chaotic.

For the case  $\varepsilon = 0$ , we can see field lines in Fig. 3.21. We notice that in this case that when  $v_0 = 0$  all field lines are periodic and closed. We then consider a flow for which  $v_0 = 0$  and  $\varepsilon = 0.15$ . The Poincaré section is represented in Fig. 3.22.

We find then again the structure of phase space already observed in chaotic advection phenomena with a chaotic sea and islands of stability, which are a signature of Hamiltonian chaos in systems with one and a half degree of freedom. We note though some difference, indeed we have here  $v_0 = 0$ , we can then expect that  $v_z$  will change its sign and our fictitious time  $z$  is not anymore a regular growing monotonous function, hence the structure which gives rise to the regular tori on the Poincaré section may not have the expected cylindrical tubular form. We have therefore represented in Fig. 3.23, the regular field lines whose initial conditions are taken in the regular zone. One can see a delocalized structure which repeats itself periodically with time, but also a non-conventional localized structure, which reflect the local nature of the Hamiltonian formalism in this case. About these structure, we want to insist on their Lagrangian character and that from the Eulerian perspective, the velocity field is extremely simple.

We shall now move on to another potential application of chaotic advection. Namely, we shall use it to improve mixing properties of a given flow.

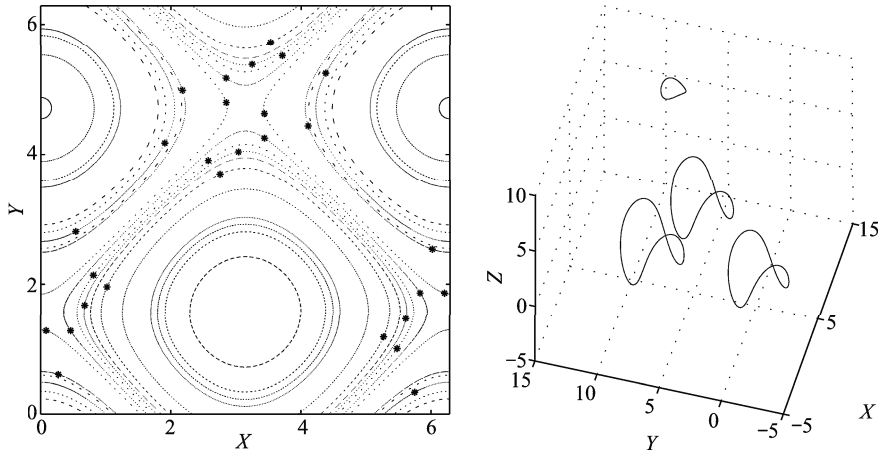


**Fig. 3.21** Left: Poincaré section of the ABC flow for the integrable case  $\varepsilon = 0$  for different values of  $v_0$  ranging from 3 to 0.01 ( $v_0 \rightarrow 0$ ), all trajectories are superposing themselves exactly. The \* signs correspond to the points obtained when  $v_0 = 0$ , field lines are periodic. Right: display of four different field lines for the case  $\varepsilon = 0$  and  $v_0 = 0$ . The lines are periodic and closed.

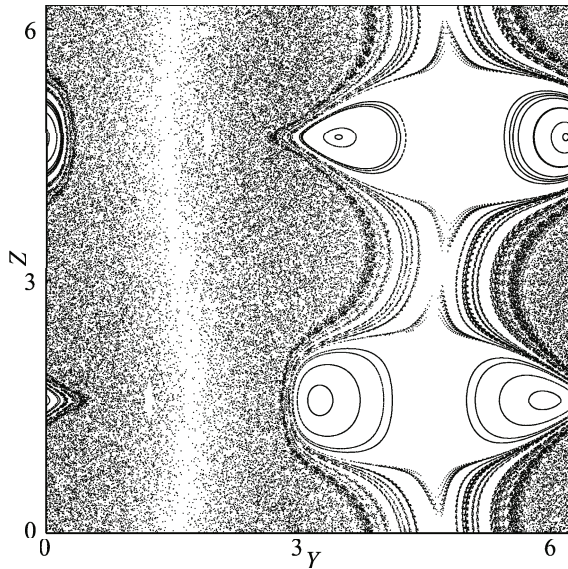


**Fig. 3.22** Poincaré section of the ABC flow for  $\varepsilon = 0.15$  and  $v_0 = 0$ . We observe Hamiltonian chaos and a mixed phase space with a stochastic sea and regular regions.

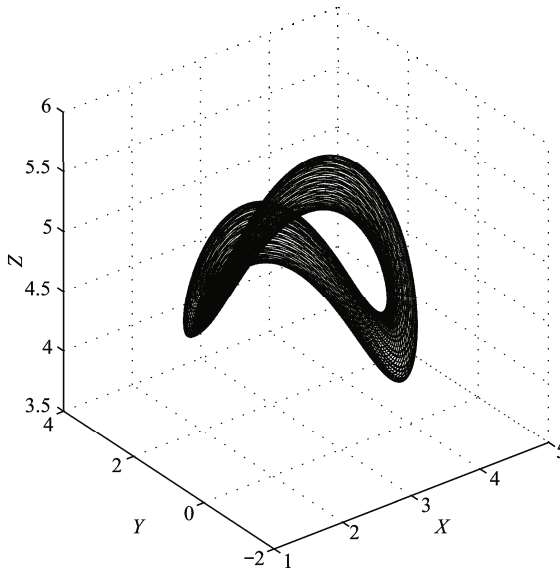
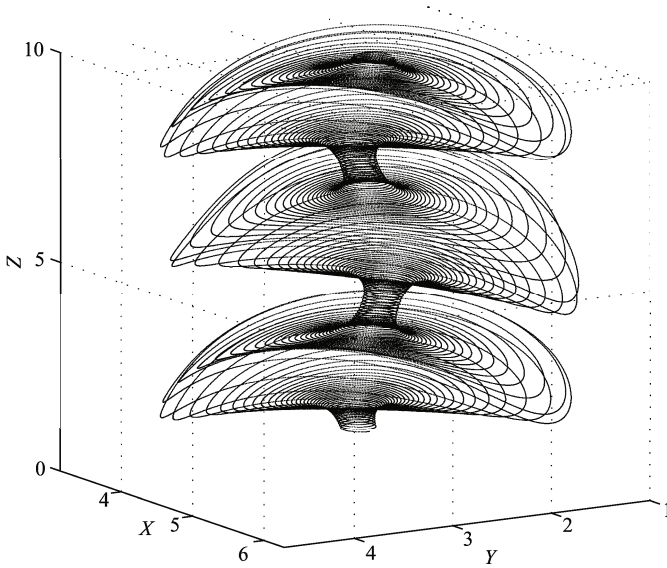


**Fig. 3.23** Top: Regular delocalized field line for the case  $\varepsilon = 0.15$  and  $\nu_0 = 0$ . Bottom: Regular localized field line for the case  $\varepsilon = 0.15$  and  $\nu_0 = 0$ , which is reminiscent of the observed behavior with  $\varepsilon = 0$ .

### 3.8 Targeted mixing in an array of alternating vortices

In order to improve mixing in fluids in non turbulent conditions (low Reynolds number), one possibility is to use chaotic advection (Aref, 1984). In this section we shall revisit the problem which we use to illustrate the phenomenon in the beginning of this chapter. We are thus considering the following integrable stream function which models an array of alternating vortices with slip boundary conditions

$$\Psi_0(x, y) = \alpha \sin x \sin y, \quad (3.45)$$

where  $x$  is the horizontal direction along the channel and  $y$  is the vertical one. The constant  $\alpha$  is the maximal value of the speed whose field lines have been represented in Fig. 3.1.

As already mentioned, passive particles are following stream lines given by  $\Psi_0$  because the dynamics resulting from Eq. (3.45) is integrable (we have a one degree of freedom Hamiltonian system). There is thus no mixing. The fluid is limited by two invariant surfaces  $y = \pi$  and  $y = 0$  corresponding at the top and bottom of the channel separating the vortices. The flow has periodic hyperbolic orbits on these two surfaces located in  $x = m\pi$  with  $m \in \mathbb{Z}$ . The phase space is then characterized by a chain of vortices with separatrices localized in  $x = m\pi$  with  $m \in \mathbb{Z}$ . From an experimental point of view, we can try to study the phenomenon of chaotic advection by introducing a time dependent perturbation of the flow  $f(x, y, t)$  in the stream function, in order to obtain a Hamiltonian system with one and a half degree of freedom. For instance the following stream function has been proposed to model a experimental situation

$$\Psi_1(x, y, t) = \alpha \sin(x + \varepsilon \sin \omega_0 t) \sin y, \quad (3.46)$$

where the perturbation is  $f = \varepsilon \sin \omega_0 t$  and describes lateral oscillations of the vortices (Willaime et al., 1993; Solomon and Gollub, 1988). The parameters  $\varepsilon$  and  $\omega_0$  are respectively the amplitude and pulsation of these lateral oscillations. Without loss of generality we set  $\omega_0 = 1$  (by a change of time scale). The field lines are identical as the one represented in Fig. 3.1 but oscillate periodically along the  $x$  direction along the channel. Passive tracers have now a non-integrable dynamics. As shown in Fig. 3.2, due to the presence of the perturbation the vertical heteroclinic connections (separatrices) between vortices have been destroyed. The stable and unstable manifolds intersect each other transversally and chaotic advection along the channel is triggered. Mixing has thus been enhanced. However we can see that islands of stability remain around the center of vortices. Mixing inside the rolls is thus only obtained through molecular diffusion, while tracers in the chaotic sea are advected along the channel without bounds. These conclusion are true for a large range of parameters, with of course some variations on the size and number of islands and size of the stochastic sea.

We can ask ourselves if by a more careful choice of the perturbation  $f$ , we could improve on mixing properties while avoiding the spreading along the channel (Toun-

sia Benzekri et al., 2006; Bachelard et al., 2007). In other words, the unperturbed flow has separatrices in  $x = m\pi$ , which were confining the flow in a cell, we are looking for a perturbation  $f$  which preserve the cellular structure of the flow while having a time dependency which maximizes mixing within the cell.

With this in mind, we shall start with a quite general approach and become more precise on the perturbation as we go along. We shall make a first simplification by considering  $f = f(y,t)$  and construct dynamical barriers. We consider therefore a generic integrable situation  $\Psi_0(x,y)$  which is periodic with period  $L = 2\pi$  in  $x$ , and such that  $\partial_x \Psi_0(x,0) = \partial_x \Psi_0(x,H) = 0$  for all  $x \in \mathbb{R}$  where  $H = \pi$  is the channel height. The perturbed stream function is given by Eq. (3.4) where  $f(y,t)$  is such that:

- Barriers whose equations are  $x = x_k(y,t)$  (for  $k \in \mathbb{Z}$ ) block chaotic advection along the  $x$  direction.

The equations of the barriers are  $x = x_k(y,t) = kL + \varphi(y,t)$  for  $k \in \mathbb{Z}$  where  $\varphi$  is function which we have to define. For this purpose we use Hamilton's equations

$$\begin{aligned}\dot{x} &= -\frac{\partial \Psi_c}{\partial y} = -\frac{\partial \Psi_0}{\partial y}(x+f,y) - \frac{\partial f}{\partial y} \frac{\partial \Psi_0}{\partial x}(x+f,y), \\ \dot{y} &= \frac{\partial \Psi_0}{\partial x}(x+f,y),\end{aligned}$$

and we impose that  $x_k$  is an invariant curve, which gives us the following dynamics for particles on the barrier

$$\dot{x} = \frac{\partial \varphi}{\partial t} + \dot{y} \frac{\partial \varphi}{\partial y}.$$

We then obtain:

$$\frac{\partial \varphi}{\partial t} + \frac{\partial}{\partial y} [\Psi_0(\varphi + f, y)] = 0. \quad (3.47)$$

We can for instance look for a solution for which the sum  $f + \varphi$  is only depending on time. We note  $\Phi(t)$  the sum, and the condition on  $\varphi$  is given by

$$\frac{\partial \varphi}{\partial t} = -\frac{\partial \Psi_0}{\partial y}(\Phi(t), y).$$

The above equation has as a solution

$$\varphi(y,t) = -\Gamma \partial_y \Psi_0(\Phi(t), y) + g(y),$$

where  $g$  is an arbitrary function and the linear operator  $\Gamma$  is a pseudo-inverse operator of  $\partial_t$ , meaning it acts on a function  $v(y,t) = \sum_k v_k e^{ikt}$  as

$$\Gamma v = \sum_{k \neq 0} \frac{v_k}{ik} e^{ikt}.$$

The perturbation  $f$  is then given by

$$f(y,t) = \Phi(t) + \Gamma \partial_y \Psi_0(\Phi(t), y) - g(y), \quad (3.48)$$

where  $\Phi$  is an arbitrary function of time and  $g$  function of  $y$ .

We now return to the array of alternating vortices (3.45) and trying to remain as close as possible to the already performed experimental setting, we choose  $\Phi(t) = \varepsilon \sin t$  and  $g(y) = 0$ .

The stream function modified by the perturbation (3.48) is then given by

$$\Psi_c(x, y, t) = \alpha \sin[x + \varepsilon \sin t + \alpha \cos y C_\varepsilon(t)] \sin y, \quad (3.49)$$

where

$$C_\varepsilon(t) = \sum_{n \geq 0} \frac{-2}{2n+1} \mathcal{J}_{2n+1}(\varepsilon) \cos(2n+1)t, \quad (3.50)$$

and  $\mathcal{J}_n$  (pour  $n \in \mathbb{N}$ ) are Bessel functions of the first kind.

We notice that  $y = 0$  and  $y = \pi$  are still defining borders of the stream function (3.49). This comes from the fact that we only modified the term with  $x$  in the original stream function. The stream lines are slightly modified (non-uniformly in  $y$ ) as can be seen on Figs. 3.24 (a) and (b) which represent the stream lines at two different times, respectively  $t = 0$  and  $t = 3\pi/4$ . Moreover the motion of the rolls remain horizontal, as is the case for the function  $\Psi_1$  given by Eq. (3.46). The fact that stream lines from the stream function (3.46) and those of the stream function (3.49) are alike, comes from the fact that the stream function  $\Psi_c$  is only a slight modification of  $\Psi_1$  (for small  $\alpha$ ) as we have  $|\Psi_c(x, y, t) - \Psi_1(x, y, t)| \leq \alpha^2 \varepsilon / 2$ .

We can also notice that the dynamics of tracers is totally different and show a high degree of mixing. Using the same values of  $\varepsilon$  and  $\alpha$  displayed in Fig. 3.2, Poincaré section of the dynamics governed by the stream function  $\Psi_c$  given by Eq. (3.49) is represented on Fig. 3.25. We notice that as expected there are invariant surfaces around  $x = 0 \pmod{2\pi}$  (bold curves) and that mixing within those barriers is considerably enhanced. The equation of these barriers in the  $x$  direction are known and given by

$$x = x_k(y, t) = 2k\pi - \alpha \cos y C_\varepsilon(t). \quad (3.51)$$

To be more precise, the barriers (3.51) are degenerate invariant tori as each of them is a heteroclinic connection between two periodic orbits (of period  $2\pi$ ), one located at  $y = 0$  et  $x(t) = -\alpha C_\varepsilon(t)$ , and the other at  $y = \pi$  and  $x(t) = \alpha C_\varepsilon(t)$ , both oscillating in opposite direction along the channel. Regarding the mixing inside the cell observed in Fig. 3.25, we also notice that regular trajectories observed with the stream function  $\Psi_1$  have been destroyed by the perturbation (see Fig. 3.2 to compare) for  $\varepsilon = 0.63$ . This means that the perturbation given by Eq. (3.48) creates two invariant surfaces around  $x = 0$  and  $x = 2\pi$ , and destabilizes the stable trajectories within the cell, most notably the regular motion near the former elliptic points close to  $x = \pi/2$  and  $x = 3\pi/2$ . A detail study on the parameters, and how optimal mixing within the cell can be obtained is given with great details in (Bachelard et al., 2007).

In order to simplify the perturbation and get a stream function which still mixes but may be more realizable experimentally, we can think of truncating the series (3.50) which gives the temporal behavior of the perturbation. For instance, we

consider a simplified perturbation by retaining only the first term in the series  $C_\varepsilon(t)$  which gives a stream function

$$\Psi_s(x, y, t) = \alpha \sin(x + \varepsilon \sin t - 2\alpha \mathcal{J}_1(\varepsilon) \cos y \cos t) \sin y. \quad (3.52)$$

The temporal dependence is much simplified as we are now left with only one cosine mode (to be compared with an infinite series). In order to check if this is still efficient, we computed the Poincaré section for the simplified stream function  $\Psi_s$  given by Eq. (3.52) for  $\alpha = 0.6$  and  $\varepsilon = 0.63$ , and for the naked eye, the section is identical as the one displayed in Fig. 3.25. Effective barriers are still there, and mixing are equivalent. In fact we may mention that if we consider very large times, some trajectories are escaping the cell, through holes which are present near the unstable periodic point (at the top and bottom of the barriers), the simplified perturbation remains however very efficient, especially since in any case molecular diffusion allows barrier crossing.

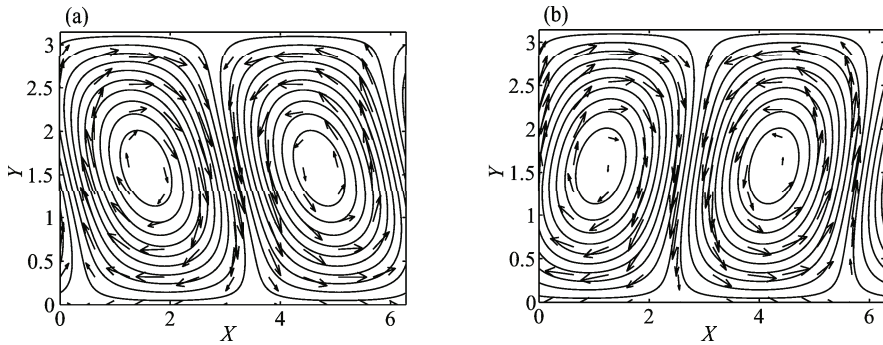


**Fig. 3.24** Stream lines of the stream function (3.49) for (a)  $t = 0$  and (b)  $t = 3\pi/4$ . Parameters are  $\alpha = 0.6$  et  $\varepsilon = 0.63$ .

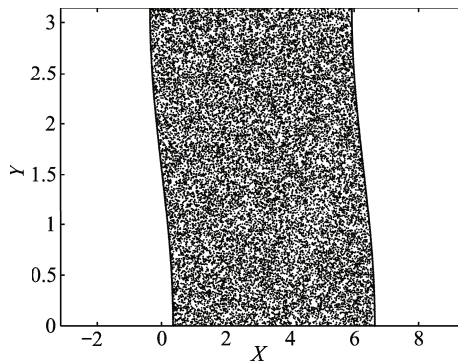


**Fig. 3.25** Poincaré section corresponding to a flow governed by the stream function (3.49). Parameters are  $\alpha = 0.6$ ,  $\varepsilon = 0.63$ .

To summarize, we have shown how in an array of alternating vortices corresponding to a cellular integrable system, we can use chaotic advection to trigger efficient mixing, while preserving the cellular structure of the flow (Tounsia Benzekri et al., 2006; Bachelard et al., 2007).

### 3.9 Conclusion

In this chapter we have discussed the dynamics of particles advected in regular and chaotic flows. We first have addressed the dynamics of point vortices and shown the great variety of the dynamics of three point vortices near the singularity giving rise to collapse. We have shown the strong influence of the existence of a finite time singularity on the dynamics, especially on how the period of the motion evolves as we get closer to the singular conditions. We have then studied transport properties of passive tracers in various flows. We have started with integrable flows governed by three vortices, then moved on to chaotic flows generated by four and sixteen vortices, to end up with a turbulent flow governed by the CHM equation. For all cases, we have observed anomalous superdiffusive transport with a characteristic exponent  $\mu \sim 1.5 - 1.8$ . We have explained the origin of the anomaly by the phenomenon of stickiness around coherent structures in regular flows, and by the presence of regular chaotic jets for the chaotic and turbulent ones. Finally we have illustrated how the Hamiltonian nature of chaos could be used to localize 3-dimensional coherent structures or how to improve mixing properties in cellular flows while keeping the cellular structure of the flow.

**Acknowledgements** I would like to express deep appreciation and gratitude to George Zaslavsky. He was one of my main collaborators, and most of the work presented in this chapter corresponds to common work, or work he inspired through our numerous and extremely fruitful discussions and exchanges. Most of the work presented in this chapter are shared with my co-authors: Olivier Agullo, Romain Bachelard, Sadruddin Benkadda, Tounsia Benzekri, Cristel Chandre, Leonid Kuznetsov, Antonio Laforgia, Magali Muraglia, Ouerdia Ourrad, Ricardo Lima, Michel Vittot and George Zaslavsky. I use this occasion to thank them again.

### References

- Afraimovich V. and Zaslavsky G.M., 2003, Space-time complexity in hamiltonian dynamics, *Chaos*, **13**, 519–532.
- Annibaldi S.V., Manfredi G., Dendy R.O. and Drury L.O’C., 2000, Evidence for strange kinetics in hasegawa-mima turbulent transport. *Plasma Phys. Control. Fusion*, **42**, L13–L22.
- Aref H., 1979, Motion of three vortices, *Phys. Fluids*, **22**, 393–400.
- Aref H., 1984, Stirring by chaotic advection, *J. Fluid Mech.*, **143**, 1–21.

- Aref H., 1990, Chaotic advection of fluid particles, *Phil. Trans. R. Soc. London A*, **333**, 273–288.
- Aref H. and Pumphrey N., 1980, Integrable and chaotic motion of four vortices, *Phys. Lett. A*, **78**, 297–300.
- Bachelard R., Benzekri T., Chandre C., Leoncini X. and Vittot M., 2007, Targeted mixing in an array of alternating vortices, *Phys. Rev. E*, **76**, 046217.
- Balasuriya S., 2005, Optimal perturbation for enhanced chaotic transport, *Physica D*, **202**, 155–176.
- Behringer R.P., Meyers S. and Swinney H.L., 1991, Chaos and mixing in geostrophic flow, *Phys. Fluids A*, **3**, 1243–1249.
- Benzekri T., Chandre C., Leoncini X., Lima R. and Vittot M., 2006, Chaotic advection and targeted mixing, *Phys. Rev. Lett.*, **96**, 124503.
- Benzi R., Colella M., Briscolini M. and Santangelo P., 1992, A simple point vortex model for two-dimensional decaying turbulence, *Phys. Fluids A*, **4**, 1036–1039.
- Boatto S. and Pierrehumbert R.T., 1999, Dynamics of a passive tracer in a velocity field of four identical point vortices, *J. Fluid Mech.*, **394**, 137–174.
- Brown M.G. and Smith K.B., 1991, Ocean stirring and chaotic low-order dynamics, *Phys. Fluids*, **3**, 1186–1192.
- Carnevale G.F., McWilliams J.C., Pomeau Y., Weiss J.B. and Young W.R., 1991, Evolution of vortex statistics in two dimensional turbulence, *Phys. Rev. Lett.*, **66**, 2735–2737.
- Carreras B.A., Lynch V.E., Garcia L., Edelman M. and Zaslavsky G.M., 2003, Topological instability along filamented invariant surfaces, *Chaos*, **13**, 1175–1187.
- Castiglione P., Mazzino A., Mutatore-Ginanneschi P. and Vulpiani A., 1999, On strong anomalous diffusion, *Physica D*, **134**, 75–93.
- Chernikov A.A., Petrovichev B.A., Rogal'sky A.V., Sagdeev R.Z. and Zaslavsky G.M., 1990, Anomalous transport of streamlines due to their chaos and their spatial topology, *Phys. Lett. A*, **144**, 127–133.
- Crisanti A., Falcioni M., Paladin G. and Vulpiani A., 1991, Lagrangian chaos: Transport, mixing and diffusion in fluids, *Riv. Nuovo Cimento*, **14**, 1–80.
- Crisanti A., Falcioni M., Provenzale A., Tanga P. and Vulpiani A., Dynamics of passively advected impurities in simple two-dimensional flow models, *Phys. Fluids A*, **4**, 1805–1820.
- del Castillo-Negrete D., 1998, Asymmetric transport and non-gaussian statistics of passive scalars in vortices in shear, *Phys. Fluids*, **10**, 576–594.
- del Castillo-Negrete D., Carreras B.A. and Lynch V.E., Fractional diffusion in plasma turbulence, *Phys. Plasmas*, **11**, 3854–3864.
- Dickman R., 2004, Fractal rain distributions and chaotic advection, *Brazilian Journal of Physics*, **34**, 337–346.
- Dritschel D.G. and Zabusky N.J., 1996, On the nature of the vortex interactions and models in unforced nearly inviscid two-dimensional turbulence, *Phys. Fluids*, **8**, 1252–1256.
- Dupont F., McLachlan R.I. and Zeitlin V., 1998, On possible mechanism of anomalous diffusion by rossby waves, *Phys. Fluids*, **10**, 3185–3193.

- Ferrari R., Manfroi A.J. and Young W.R., 2001, Strong and weakly self-similar diffusion, *Physica D*, **154**, 111–137.
- Kuznetsov L. and Zaslavsky G.M., 1998, Regular and chaotic advection in the flow field of a three-vortex system, *Phys. Rev. E*, **58**, 7330–7349.
- Kuznetsov L. and Zaslavsky G.M., 2000, Passive particle transport in three-vortex flow. *Phys. Rev. E*, **61**, 3777–3792.
- Laforgia A., Leoncini X., Kuznetsov L. and Zaslavsky G.M., 2001, Passive tracer dynamics in 4 point-vortex-flow, *Eur. Phys. J. B*, **20**, 427–440.
- Leoncini X., Agullo O., Benkadda S. and Zaslavsky G.M., 2005, Anomalous transport in charney-hasegawa-mima flows, *Phys. Rev. E*, **72**, 026218.
- Leoncini X., Kuznetsov L. and Zaslavsky G.M., 2000, Motion of three vortices near collapse. *Phys. Fluids*, **12**, 1911–1927.
- Leoncini X., Kuznetsov L. and Zaslavsky G.M., 2001, Chaotic advection near a 3-vortex collapse, *Phys. Rev. E*, **63**, 036224.
- Leoncini X. and Zaslavsky G.M., 2002, Jets, stickiness and anomalous transport, *Phys. Rev. E*, **65** 046216.
- Leoncini X., Agullo O., Muraglia M. and Chandre C., 2006, From chaos of lines to lagrangian structures in flux conservative fields, *Eur. Phys. J. B*, **53** 351–360.
- Leoncini X., Chandre C. and Ourrad O., 2008, Ergodicité, collage et transport anomal, *C. R. Mecanique*, **336**, 530–535.
- Leoncini X., Kuznetsov L. and Zaslavsky G.M., 2004, Evidence of fractional transport in point vortex flow, *Chaos, Solitons and Fractals*, **19**, 259–273.
- Leoncini X. and Zaslavsky G.M., 2003, Chaotic jets, *Communications in Nonlinear Science and Numerical Simulation*, **8**, 265–271.
- Machioro C. and Pulvirenti M., 1994, *Mathematical theory of incompressible non-viscous fluids*, Springer, New York.
- McLachlan R.I. and Atela P., 1992, The accuracy of symplectic integrators, *Non-linearity*, **5**, 541–562.
- McWilliams J.C., 1984, The emergence of isolated coherent vortices in turbulent flow, *J. Fluid Mech.*, **146**, 21–43.
- Novikov E.A. and Sedov Yu.B., 1978, Stochastic properties of a four-vortex system, *Sov. Phys. JETP*, **48**, 440–444.
- Novikov E.A. and Sedov Yu.B., 1979, Vortex collapse, *Sov. Phys. JETP*, **50**, 297–301.
- Ottino J.M., 1990, Mixing, chaotic advection and turbulence, *Ann. Rev. Fluid Mech.*, **22**, 207–253.
- Ottino J.M., 1989, *The Kinematics of mixing: stretching, chaos, and transport*, Cambridge University Press, Cambridge.
- Shlesinger M.F., Zaslavsky G.M., and Klafter J., 1993, *Nature*, **363**, 31–37.
- Solomon T.H. and Gollub J.P., 1988, Chaotic particle transport in rayleigh-bénard convection, *Phys. Rev. A*, **38**, 6280–6286.
- Solomon T.H., Miller N.S., Spohn C.J.L., and Moeur J.P., 2003, Lagrangian chaos: transport, coupling and phase separation, *AIP Conf. Proc.*, **676**, 195–206.
- Solomon T.H., Weeks E.R. and Swinney H.L., 1994, Chaotic advection in a two-dimensional flow: Lévy flights in and anomalous diffusion, *Physica D*, **76**, 70–84.

- Stroock A.D., Dertinger S.K.W., Ajdari A., Mezic I., Stone H.A. and Whitesides G.M., 2002, Chaotic mixer for microchannels, *Science*, **295**, 647–651.
- Synge J.L., 1949, On the motion of three vortices, *Can. J. Math.*, **1**, 257–270.
- Tavantzis J. and Ting L., 1988, The dynamics of three vortices revisited, *Phys. Fluids*, **31**, 1392–1409.
- Willaime H., Cardoso O. and Tabeling P., 1993, Spatiotemporel intermittency in lines of vortices, *Phys. Rev. E*, **48**, 288–295.
- Zaslavsky G.M., Sagdeev R.Z., Usikov D.A. and Chernikov A.A., 1991, *Weak Chaos and Quasiregular Patterns*, Cambridge University Press, Cambridge.
- Zaslavsky G.M., Stevens D. and Weitzner H., 1983, Self-similar transport in incomplete chaos, *Phys. Rev. E*, **48** 1683–1694.

# Chapter 4

## Hamiltonian Chaos with a Cold Atom in an Optical Lattice

S.V. Prants

**Abstract** We consider a basic model of the lossless interaction between a moving 2-level atom and a standing-wave single-mode laser field. Classical treatment of the translational atomic motion provides the semiclassical Hamilton-Schrödinger equations of motion which are a 5-dimensional nonlinear dynamical system with two integrals of motion. The atomic dynamics can be regular or chaotic (in the sense of exponential sensitivity to small variations in initial conditions and/or the system's control parameters) in dependence on values of the control parameters, the atom-field detuning and recoil frequency. We develop a semiclassical theory of the chaotic atomic transport in terms of a random walk of the atomic electric dipole moment  $u$  which is one of the components of a Bloch vector. Based on a jump-like behavior of this variable for atoms crossing nodes of the standing laser wave, we construct a stochastic map that specifies the center-of-mass motion. We find the relations between the detuning, recoil frequency and the atomic energy, under which atoms may move in a rigid optical lattice in a chaotic way. We obtain the analytical conditions under which deterministic atomic transport has fractal properties and explain a hierarchical structure of the dynamical fractals. Quantum treatment of the atomic motion in a standing wave is studied in the dressed state picture where the atom moves in two optical potentials simultaneously. If the values of the detuning and a characteristic atomic frequency are of the same order, than there is a probability of nonadiabatic transitions of the atom upon crossing nodes of the standing wave. At the same condition exactly, we observe sudden changes (jumps) in the atomic dipole moment  $u$  when the atom crosses the nodes. Those jumps are accompanied by splitting of atomic wave packets at the nodes. Such a proliferation of wave packets at the nodes of a standing wave is a manifestation of classical atomic chaotic transport. In particular, the effect of simultaneous trapping of an atom in a well of one of the optical potential and its flight in the other potential is a quantum analogue

---

S.V. Prants

Laboratory of Nonlinear Dynamical Systems, Pacific Oceanological Institute of the Russian Academy of Sciences, 43 Baltiiskaya st., 690041 Vladivostok, Russia,  
e-mail: prants@poi.dvo.ru

of a chaotic classical walking of an atom. At large values of the detuning, the quantum evolution is shown to be adiabatic in accordance with a regular character of the classical atomic motion.

## 4.1 Short historical background

The fundamental model for the interaction of a radiation with matter, comprising a collection of 2-level quantum systems coupled with a single-mode electromagnetic field, provides the basis for laser physics and describes a rich variety of nonlinear dynamical effects. The discovery that a single-mode laser, a symbol of coherence and stability, may exhibit deterministic instabilities and chaos is especially important since lasers provide nearly ideal systems to test general ideas in statistical physics. From the stand point of nonlinear dynamics, laser is an open dissipative system which transforms an external excitation into a coherent output in the presence of loss. In 1975 Haken (Haken, 1975) has shown that a single-mode, homogeneously broadened laser, operating on resonance with the gain center can be described in the rotating-wave approximation by three real semiclassical Maxwell-Bloch equations which are isomorphic to the famous Lorenz equations. Some manifestations of a Lorenz-type strange attractor and dissipative chaos have been observed with different types of lasers.

In the same time George Zaslavsky with co-workers (Belobrov et al., 1976) have studied interaction of an ensemble of 2-level atoms with their own radiation field in a perfect single-mode cavity without any losses and external excitations, which is known as the Dicke model (Dicke, 1954). They were able to demonstrate analytically and numerically dynamical instabilities and chaos of Hamiltonian type in a semiclassical version of the Dicke model without rotating-wave approximation. It was the first paper that opened the door to study Hamiltonian atomic chaos in the rapidly growing fields of cavity quantum electrodynamics, quantum and atomic optics. Semiclassical equations of motion for this system may be reduced to Maxwell-Bloch equations for three real independent variables which, in difference from the laser theory, do not include losses and pump. Those equations are, in general, nonintegrable, but they become integrable immediately after adopting the rotating-wave approximation (Jaynes and Cummings, 1963) that implies the existence of an additional integral of motion, conservation of the so-called number of excitations. Numerical experiments have shown that prominent chaos arises when the density of atoms is very large (approximately  $10^{20}$  cm<sup>3</sup> in the optical range (Belobrov et al., 1976)). The following progress in this field has been motivated, mainly, by a desire to find manifestations of Hamiltonian atomic chaos in the models more suitable for experimental implementations. Twenty years after that pioneer paper, manifestations of Hamiltonian chaos have been found in experiments with kicked cold atoms in a modulated laser field. Nowadays, a few groups in the USA, Australia, New Zealand, Germany, France, England, Italy and in other countries can perform

routine experiments on Hamiltonian chaos with cold atoms in optical lattices and traps (for a review see (Hensinger et al., 2003)).

In this paper we review some results on theory of Hamiltonian chaos with a single 2-level atom in a standing-wave laser field that have been obtained in our group in Vladivostok. In spite of we published with George only one paper on this subject (Prants et al., 2002), our work in this field has been mainly inspired by his paper (Belobrov et al., 1976) written in 1975 in Krasnoyarsk, Siberia.

## 4.2 Introduction

An atom placed in a laser standing wave is acted upon by two radiation forces, deterministic dipole and stochastic dissipative ones (Kazantsev et al., 1990). The mechanical action of light upon neutral atoms is at the heart of laser cooling, trapping, and Bose-Einstein condensation. Numerous applications of the mechanical action of light include isotope separation, atomic lithography and epitaxy, atomic-beam deflection and splitting, manipulating translational and internal atomic states, measurement of atomic positions, and many others. Atoms and ions in an optical lattice, formed by a laser standing wave, are perspective objects for implementation of quantum information processing and quantum computing. Advances in cooling and trapping of atoms, tailoring optical potentials of a desired form and dimension (including 1-dimensional optical lattices), controlling the level of dissipation and noise are now enabling the direct experiments with single atoms to study fundamental principles of quantum physics, quantum chaos, decoherence, and quantum-classical correspondence (for recent reviews on cold atoms in optical lattices see Ref. (Grynberg and Robilliard, 2001; Morsch and Oberthaler, 2006)).

Experimental study of quantum chaos has been carried out with ultracold atoms in  $\delta$ -kicked optical lattices (Moore et al., 1994; Robinson et al., 1995; Hensinger et al., 2003). To suppress spontaneous emission and provide a coherent quantum dynamics atoms in those experiments were *detuned far from the optical resonance*. Adiabatic elimination of the excited state amplitude leads to an effective Hamiltonian for the center-of-mass motion (Graham et al., 1992), whose 3/2 degree-of-freedom classical analogue has a mixed phase space with regular islands embedded in a chaotic sea. De Broglie waves of  $\delta$ -kicked ultracold atoms have been shown to demonstrate under appropriate conditions the effect of dynamical localization in momentum distributions which means the quantum suppression of chaotic diffusion (Moore et al., 1994; Robinson et al., 1995; Hensinger et al., 2003). Decoherence due to spontaneous emission or noise tend to suppress this quantum effect and restore classical-like dynamics. Another important quantum chaotic phenomenon with cold atoms in far-detuned optical lattices is a chaos-assisted tunneling. In experiments (Steck et al., 2001; Hensinger, 2001) ultracold atoms have been demonstrated to oscillate coherently between two regular regions in mixed phase space even though the classical transport between these regions is forbidden by a constant of motion (other than energy).

The transport of cold atoms in optical lattices has been observed to take the form of ballistic motion, oscillations in wells of the optical potential, Brownian motion (Chu et al., 1985), anomalous diffusion and Lévy flights (Bardou et al., 2002; Marksteiner et al., 1996). The Lévy flights have been found in the context of subrecoil laser cooling (Bardou et al., 2002) in the distributions of escape times for ultracold atoms trapped in the potential wells with momentum states close to the dark state. In those experiments the variance and the mean time for atoms to leave the trap have been shown to be infinite.

A new arena of quantum nonlinear dynamics with atoms in optical lattices is opened if we work *near the optical resonance* and take the dynamics of internal atomic states into account. A single atom in a standing-wave laser field may be semiclassically treated as a nonlinear dynamical system with coupled internal (electronic) and external (mechanical) degrees of freedom (Prants and Sirotkin, 2001; Prants and Kon'kov, 2001; Prants, 2002). In the semiclassical and Hamiltonian limits (when one treats atoms as point-like particles and neglects spontaneous emission and other losses of energy), a number of nonlinear dynamical effects have been analytically and numerically demonstrated with this system: chaotic Rabi oscillations (Prants and Sirotkin, 2001; Prants and Kon'kov, 2001; Prants, 2002), Hamiltonian chaotic atomic transport and dynamical fractals (Argonov and Prants, 2003; Prants and Uleysky, 2003; Argonov and Prants, 2007; Prants et al., 2006), Lévy flights and anomalous diffusion (Prants et al., 2002; Prants, 2002; Argonov and Prants, 2006). These effects are caused by local instability of the CM motion in a laser field. A set of atomic trajectories under certain conditions becomes exponentially sensitive to small variations in initial quantum internal and classical external states or/and in the control parameters, mainly, the atom-laser detuning. Hamiltonian evolution is a smooth process that is well described in a semiclassical approximation by the coupled Hamilton-Schrödinger equations. A detailed theory of Hamiltonian chaotic transport of atoms in a laser standing wave has been developed in our recent paper (Argonov and Prants, 2007).

## 4.3 Semiclassical dynamics

### 4.3.1 Hamilton-Schrödinger equations of motion

We consider a 2-level atom with mass  $m_a$  and transition frequency  $\omega_a$  in a 1-dimensional classical standing laser wave with the frequency  $\omega_f$  and the wave vector  $k_f$ . In the frame rotating with the frequency  $\omega_f$ , the Hamiltonian is the following:

$$\hat{H} = \frac{\hat{P}^2}{2m_a} + \frac{1}{2}\hbar(\omega_a - \omega_f)\hat{\sigma}_z - \hbar\Omega(\hat{\sigma}_- + \hat{\sigma}_+)\cos k_f\hat{X}. \quad (4.1)$$

Here  $\hat{\sigma}_{\pm,z}$  are the Pauli operators which describe the transitions between lower,  $|1\rangle$ , and upper,  $|2\rangle$ , atomic states,  $\Omega$  is a maximal value of the Rabi frequency. The laser

wave is assumed to be strong enough, so we can treat the field classically. Position  $\hat{X}$  and momentum  $\hat{P}$  operators will be considered in section “Semiclassical dynamics” as  $c$ -numbers,  $X$  and  $P$ . The simple wavefunction for the electronic degree of freedom is

$$|\Psi(t)\rangle = a(t)|2\rangle + b(t)|1\rangle, \quad (4.2)$$

where  $a$  and  $b$  are the complex-valued probability amplitudes to find the atom in the states  $|2\rangle$  and  $|1\rangle$ , respectively. Using the Hamiltonian (4.1), we get the Schrödinger equation

$$\begin{aligned} i\frac{da}{dt} &= \frac{\omega_a - \omega_f}{2}a - \Omega b \cos k_f X, \\ i\frac{db}{dt} &= \frac{\omega_f - \omega_a}{2}b - \Omega a \cos k_f X. \end{aligned} \quad (4.3)$$

Let us introduce instead of the complex-valued probability amplitudes  $a$  and  $b$  the following real-valued variables:

$$u \equiv 2\text{Re}(ab^*), \quad v \equiv -2\text{Im}(ab^*), \quad z \equiv |a|^2 - |b|^2, \quad (4.4)$$

where  $u$  and  $v$  are a synchronized (with the laser field) and a quadrature components of the atomic electric dipole moment, respectively, and  $z$  is the atomic population inversion.

In the process of emitting and absorbing photons, atoms not only change their internal electronic states but their external translational states change as well due to the photon recoil. In this section we will describe the translational atomic motion classically. The position and momentum of a point-like atom satisfy classical Hamilton equations of motion. Full dynamics in the absence of any losses is now governed by the Hamilton-Schrödinger equations for the real-valued atomic variables

$$\begin{aligned} \dot{x} &= \omega_r p, \quad \dot{p} = -u \sin x, \quad \dot{u} = \Delta v, \\ \dot{v} &= -\Delta u + 2z \cos x, \quad \dot{z} = -2v \cos x, \end{aligned} \quad (4.5)$$

where  $x \equiv k_f X$  and  $p \equiv P/\hbar k_f$  are normalized atomic center-of-mass position and momentum, respectively. Dot denotes differentiation with respect to the dimensionless time  $\tau \equiv \Omega t$ . The normalized recoil frequency,  $\omega_r \equiv \hbar k_f^2/m_a \Omega \ll 1$ , and the atom-field detuning,  $\Delta \equiv (\omega_f - \omega_a)/\Omega$ , are the control parameters. The system has two integrals of motion, namely the total energy

$$H \equiv \frac{\omega_r}{2} p^2 - u \cos x - \frac{\Delta}{2} z, \quad (4.6)$$

and the Bloch vector  $u^2 + v^2 + z^2 = 1$ . The conservation of the Bloch vector length follows immediately from Eqs. (4.4).

Equations (4.5) constitute a nonlinear Hamiltonian autonomous system with two and half degrees of freedom which, owing to two integrals of motion, move on a 3-dimensional hypersurface with a given energy value  $H$ . In general, motion in a 3-dimensional phase space is characterized by a positive Lyapunov exponent  $\lambda$ , a

negative exponent equal in magnitude to the positive one, and zero exponent. The maximum Lyapunov exponent characterizes the mean rate of the exponential divergence of initially close trajectories and serves as a quantitative measure of dynamical chaos in the system. The result of computation of the maximum Lyapunov exponent in dependence on the detuning  $\Delta$  and the initial atomic momentum  $p_0$  is shown in Fig. 4.1. Color in the plot codes the value of the maximum Lyapunov exponent  $\lambda$ . In white regions the values of  $\lambda$  are almost zero, and the atomic motion is regular in the corresponding ranges of  $\Delta$  and  $p_0$ . In shadowed regions positive values of  $\lambda$  imply unstable motion.

Figure 4.1 demonstrates that the center-of-mass motion becomes unstable if the dimensionless momentum exceeds the value  $p_0 \approx 300$  that corresponds (with our normalization) to the atomic velocity  $v_a \approx 3$  m/s for an atom with  $m_a \approx 10^{-22}$  g in the field with the wavelength close to the transition wavelength  $\lambda_a \simeq 800$  nm. With these estimates for the atomic and lattice parameters and  $\Omega/2\pi = 10^9$  HZ, one gets the normalized value of the recoil frequency equal to  $\omega_r = 10^{-5}$ . The detuning  $\Delta$  will be varied in a wide range, and the Bloch variables are restricted by the length of the Bloch vector.

### 4.3.2 Regimes of motion

The case of exact resonance,  $\Delta = 0$ , was considered in detail in Ref. (Prants and Sirotkin, 2001; Argonov and Prants, 2006). Now we briefly repeat the simple results for the sake of self-consistency. At zero detuning, the variable  $u$  becomes a constant,  $u = u_0$ , and the fast ( $u, v, z$ ) and slow ( $x, p$ ) variables are separated allowing one to integrate exactly the reduced equations of motion. The total energy (4.6) is equal to  $H_0 = H(u = u_0, \Delta = 0)$ , and the atom moves in a simple cosine potential  $u_0 \cos x$

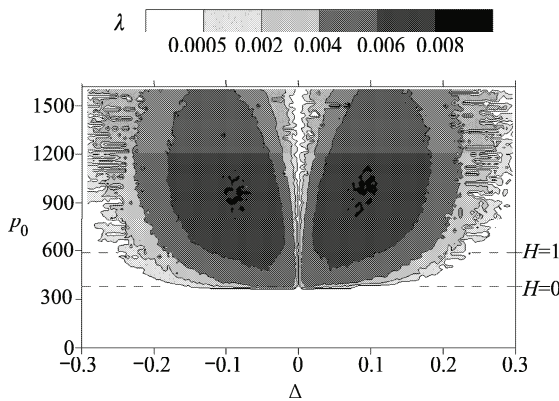


**Fig. 4.1** Maximum Lyapunov exponent  $\lambda$  vs atom-field detuning  $\Delta$  and initial atomic momentum  $p_0$ :  $\omega_r = 10^{-5}$ ,  $u_0 = z_0 = 0.7071$ ,  $v_0 = 0$ .

with three possible types of trajectories: oscillator-like motion in a potential well if  $H_0 < u_0$  (atoms are trapped by the standing-wave field), motion along the separatrix if  $H_0 = u_0$ , and ballistic-like motion if  $H_0 > u_0$ . The exact solution for the center-of-mass motion is easily found in terms of elliptic functions (see (Prants and Sirotkin, 2001; Argonov and Prants, 2006)).

As to internal atomic evolution, it depends on the translational degree of freedom since the strength of the atom-field coupling depends on the position of atom in a periodic standing wave. At  $\Delta = 0$ , it is easy to find the exact solutions of Eqs. (4.5)

$$\begin{aligned} v(\tau) &= \pm \sqrt{1-u^2} \cos \left( 2 \int_0^\tau \cos x d\tau' + \chi_0 \right), \\ z(\tau) &= \mp \sqrt{1-u^2} \sin \left( 2 \int_0^\tau \cos x d\tau' + \chi_0 \right), \end{aligned} \quad (4.7)$$

where  $u = u_0$ , and  $\cos[x(\tau)]$  is a given function of the translational variables only which can be found with the help of the exact solution for  $x$  (Prants and Sirotkin, 2001; Argonov and Prants, 2006). The sign of  $v$  is equal to that for the initial value  $z_0$  and  $\chi_0$  is an integration constant. The internal energy of the atom,  $z$ , and its quadrature dipole-moment component  $v$  could be considered as frequency-modulated signals with the instant frequency  $2\cos[x(\tau)]$  and the modulation frequency  $\omega_r p(\tau)$ , but it is correct only if the maximum value of the first frequency is much greater than the value of the second one, i. e., for  $|\omega_r p_0| \ll 2$ .

The maximum Lyapunov exponent  $\lambda$  depends both on the parameters  $\omega_r$  and  $\Delta$ , and on initial conditions of the system (4.5). It is naturally to expect that off the resonance atoms with comparatively small values of the initial momentum  $p_0$  will be at once trapped in the first well of the optical potential, whereas those with large values of  $p_0$  will fly through. The question is what will happen with atoms, if their initial kinetic energy will be close to the maximum of the optical potential. Numerical experiments demonstrate that such atoms will wander in the optical lattice with alternating trappings in the wells of the optical potential and flights over its hills. The direction of the center-of-mass motion of wandering atoms may change in a chaotic way (in the sense of exponential sensitivity to small variations in initial conditions). A typical chaotically wandering atomic trajectory is shown in Fig. 4.2.

It follows from (4.5) that the translational motion of the atom at  $\Delta \neq 0$  is described by the equation of a nonlinear physical pendulum with the frequency modulation

$$\ddot{x} + \omega_r u(\tau) \sin x = 0, \quad (4.8)$$

where  $u$  is a function of all the other dynamical variables.

### 4.3.3 Stochastic map for chaotic atomic transport

Chaotic atomic transport occurs even if the normalized detuning is very small,  $|\Delta| \ll 1$  (Fig. 4.1). Under this condition, we will derive in this section approximate equations for the center-of-mass motion. The atomic energy at  $|\Delta| \ll 1$  is given with a good accuracy by its resonant value  $H_0$ . Returning to the basic set of the equations of motion (4.5), we may neglect the first right-hand term in the fourth equation since it is very small as compared with the second one there. However, we cannot now exclude the third equation from the consideration. Using the solution (4.7) for  $v$ , we can transform this equation as

$$\dot{u} = \pm \Delta \sqrt{1 - u^2} \cos \chi, \quad \chi \equiv 2 \int_0^\tau \cos x d\tau' + \chi_0. \quad (4.9)$$

Far from the nodes of the standing wave, Eq. (4.9) can be approximately integrated under the additional condition,  $|\omega_r p| \ll 1$ , which is valid for the ranges of the parameters and the initial atomic momentum where chaotic transport occurs. Assuming  $\cos x$  to be a slowly-varying function in comparison with the function  $\cos \chi$ , we obtain far from the nodes the approximate solution for the  $u$ -component of the atomic dipole moment

$$u \approx \sin \left( \pm \frac{\Delta}{2 \cos x} \sin \chi + C \right), \quad (4.10)$$

where  $C$  is an integration constant. Therefore, the amplitude of oscillations of the quantity  $u$  for comparatively slow atoms ( $|\omega_r p| \ll 1$ ) is small and of the order of  $|\Delta|$  far from the nodes.

At  $|\Delta| = 0$ , the synchronized component of the atomic dipole moment  $u$  is a constant whereas the other Bloch variables  $z$  and  $v$  oscillate in accordance with the solution (4.7). At  $|\Delta| \neq 0$  and far from the nodes, the variable  $u$  performs shallow os-

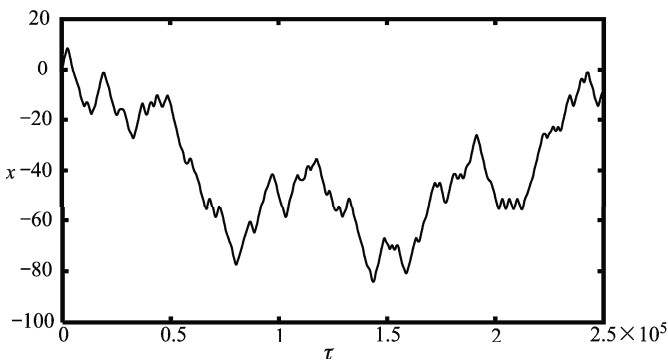


**Fig. 4.2** Typical atomic trajectory in the regime of chaotic transport:  $x_0 = 0$ ,  $p_0 = 300$ ,  $z_0 = -1$ ,  $u_0 = v_0 = 0$ ,  $\omega_r = 10^{-5}$ ,  $\Delta = -0.05$ .

cillations for the natural frequency  $|\Delta|$  is small as compared with the Rabi frequency. However, the behavior of  $u$  is expected to be very special when an atom approaches to any node of the standing wave since near the node the oscillations of the atomic population inversion  $z$  slow down and the corresponding driving frequency becomes close to the resonance with the natural frequency. As a result, sudden “jumps” of the variable  $u$  are expected to occur near the nodes. This conjecture is supported by the numerical simulation. In Fig. 4.3 we show a typical behavior of the variable  $u$  for a comparatively slow and slightly detuned atom. The plot clearly demonstrates sudden “jumps” of  $u$  near the nodes of the standing wave and small oscillations between the nodes.

Approximating the variable  $u$  between the nodes by constant values, we can construct a discrete mapping (Argonov and Prants, 2007)

$$u_m = \sin(\Theta \sin \phi_m + \arcsin u_{m-1}), \quad (4.11)$$

where  $\Theta \equiv |\Delta| \sqrt{\pi / \omega_r p_{\text{node}}}$  will be called an angular amplitude of the jump,  $u_m$  is a value of  $u$  just after the  $m$ -th node crossing,  $\phi_m$  are random phases to be chosen in the range  $[0, 2\pi]$ , and  $p_{\text{node}} \equiv \sqrt{2H / \omega_r}$  is the value of the atomic momentum at the instant when the atom crosses a node (which is the same with a given value of the energy  $H$  for all the nodes). With given values of  $\Delta$ ,  $\omega_r$ , and  $p_{\text{node}}$ , the map (4.11) has been shown numerically to give a satisfactory probabilistic distribution of magnitudes of changes in the variable  $u$  just after crossing the nodes. The stochastic map (4.11) is valid under the assumptions of small detunings ( $|\Delta| \ll 1$ ) and comparatively slow atoms ( $|\omega_r p| \ll 1$ ). Furthermore, it is valid only for those ranges of the control parameters and initial conditions where the motion of the basic system (4.5) is unstable. For example, in those ranges where all the Lyapunov exponents are zero,  $u$  becomes a quasi-periodic function and cannot be approximated by the map.

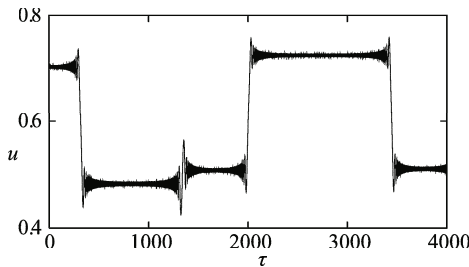


**Fig. 4.3** Typical evolution of the atomic dipole-moment component  $u$  for a comparatively slow and slightly detuned atom:  $x_0 = 0$ ,  $p_0 = 550$ ,  $v_0 = 0$ ,  $u_0 = z_0 = 0.7071$ ,  $\omega_r = 10^{-5}$ ,  $\Delta = -0.01$ .

#### 4.3.4 Statistical properties of chaotic transport

With given values of the control parameters and the energy  $H$ , the center-of-mass motion is determined by the values of  $u_m$  (see Eq. (4.8)). One can obtain from the expression for the energy (4.6) the conditions under which atoms continue to move in the same direction after crossing a node or change the direction of motion not reaching the nearest antinode. Moreover, as in the resonance case, there exist atomic trajectories along which atoms move to antinodes with the velocity going asymptotically to zero. It is a kind of separatrix-like motion with an infinite time of reaching the stationary points.

The conditions for different regimes of motion depend on whether the crossing number  $m$  is even or odd. Motion in the same direction occurs at  $(-1)^{m+1}u_m < H$ , separatrix-like motion — at  $(-1)^{m+1}u_m = H$ , and turns — at  $(-1)^{m+1}u_m > H$ . It is so because even values of  $m$  correspond to  $\cos x > 0$ , whereas odd values — to  $\cos x < 0$ . The quantity  $u$  during the motion changes its values in a random-like manner (see Fig. 4.3) taking the values which provide the atom either to prolong the motion in the same direction or to turn. Therefore, atoms may move chaotically in the optical lattice. The chaotic transport occurs if the atomic energy is in the range  $0 < H < 1$ . At  $H < 0$ , atoms cannot reach even the nearest node and oscillate in the first potential well in a regular manner (see Fig. 4.1). At  $H > 1$ , the values of  $u$  are always satisfy to the flight condition. Since the atomic energy is positive in the regime of chaotic transport, the corresponding conditions can be summarized as follows: at  $|u| < H$ , atom always moves in the same direction, whereas at  $|u| > H$ , atom either moves in the same direction, or turns depending on the sign of  $\cos x$  in a given interval of motion. In particular, if the modulus of  $u$  is larger for a long time then the energy value, then the atom oscillates in a potential well crossing two times each of two neighbor nodes in the cycle.

The conditions stated above allow to find a direct correspondence between chaotic atomic transport in the optical lattice and stochastic dynamics of the Bloch variable  $u$ . It follows from Eq. (4.11) that the jump magnitude  $u_m - u_{m-1}$  just after crossing the  $m$ -th node depends nonlinearly on the previous value  $u_{m-1}$ . For analyzing statistical properties of the chaotic atomic transport, it is more convenient to introduce the map for  $\arcsin u_m$  (Argonov and Prants, 2007)

$$\theta_m \equiv \arcsin u_m = \Theta \sin \phi_m + \arcsin u_{m-1}, \quad (4.12)$$

where the jump magnitude does not depend on a current value of the variable. The map (4.12) visually looks as a random motion of the point along a circle of unit radius (Fig. 4.4). The vertical projection of this point is  $u_m$ . The value of the energy  $H$  specifies four regions, two of which correspond to atomic oscillations in a well, and two other ones — to ballistic motion in the optical lattice.

We will call “a flight” such an event when atom passes, at least, two successive antinodes (and three nodes). The continuous flight length  $L > 2\pi$  is a distance between two successive turning points at which the atom changes the sign of its ve-

locity, and the discrete flight length is a number of nodes  $l$  the atom crossed. They are related in a simple way,  $L \simeq \pi l$ , for sufficiently long flight.

Center-of-mass oscillations in a well of the optical potential will be called “a trapping”. At extremely small values of the detuning, the jump magnitudes are small and the trapping occurs, largely, in the  $2\pi$ -wide wells, i. e., in the space interval of the length  $2\pi$ . At intermediate values of the detuning, it occurs, largely, in the  $\pi$ -wide wells, i. e. in the space interval of the length  $\pi$ . Far from the resonance,  $|\Delta| \gtrsim 1$ , trapping occurs only in the  $\pi$ -wide wells. Just like to the case of flights, the number of nodes  $l$ , atom crossed being trapped in a well, is a discrete measure of trapping.

The PDFs for the flight  $P_{\text{fl}}(l)$  and trapping  $P_{\text{tr}}(l)$  events were analytically derived to be exponential in a case of large jumps (Argonov and Prants, 2007). In a case of small jumps, the kind of the statistics depends on additional conditions imposed on the atomic and lattice parameters, and the distributions  $P_{\text{fl}}(l)$  and  $P_{\text{tr}}(l)$  were analytically shown to be either practically exponential or functions with long power-law segments with the slope  $-1.5$  but exponential “tails”. The comparison of the PDFs computed with analytical formulas, the stochastic map, and the basic equations of motion has shown a good agreement in different ranges of the atomic and lattice parameters (Argonov and Prants, 2007). We will use the results obtained to find the analytical conditions, under which the fractal properties of the chaotic atomic transport can be observed, and to explain the structure of the corresponding dynamical fractals.

Since the period and amplitude of the optical potential and the atom-field detuning can be modified in a controlled way, the transport exponents of the flight and trapping distributions are not fixed but can be varied continuously, allowing to explore different regimes of the atomic transport. Our analytical and numerical results with the idealized system have shown that deterministic atomic transport in an optical lattice cannot be just classified as normal and anomalous one. We have found that the flight and trapping PDFs may have long algebraically decaying seg-

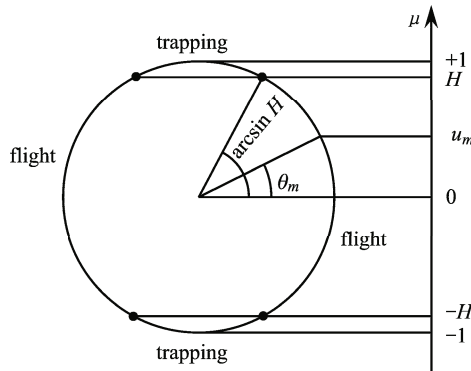


**Fig. 4.4** Graphic representation for the maps of  $u_m$  and  $\theta_m \equiv \arcsin u_m$ .  $H$  is a given value of the atomic energy. Atoms either oscillate in optical potential wells (trapping) or fly through the optical lattice (flight).

ments and a short exponential “tail”. It means that in some ranges of the atomic and lattice parameters numerical experiments reveal anomalous transport with Lévy flights. The transport exponent equal to  $-1.5$  means that the first, second, and the other statistical moments are infinite for a reasonably long time. The corresponding atomic trajectories computed for this time are self-similar and fractal. The total distance, that the atom travels for the time when the flight PDF decays algebraically, is dominated by a single flight. However, the asymptotic behavior is close to normal transport. In other ranges of the atomic and lattice parameters, the transport is practically normal both for short and long times.

### 4.3.5 Dynamical fractals

Various fractal-like structures may arise in chaotic Hamiltonian systems (Gaspard et al., 1998; Zaslavsky et al., 2005). In Ref. (Prants and Uleysky, 2003; Argonov and Prants, 2003, 2006; Prants et al., 2006) we have found numerically fractal properties of chaotic atomic transport in cavities and optical lattices. In this section we apply the analytical results of the theory of chaotic transport, developed in the preceding sections, to find the conditions under which the dynamical fractals may arise.

We place atoms one by one at the point  $x_0 = 0$  with a fixed positive value of the momentum  $p_0$  and compute the time  $T$  when they cross one of the nodes at  $x = -\pi/2$  or  $x = 3\pi/2$ . In these numerical experiments we change the value of the atom-field detuning  $\Delta$  only. All the initial conditions  $p_0 = 200$ ,  $z_0 = -1$ ,  $u_0 = v_0 = 0$  and the recoil frequency  $\omega_r = 10^{-5}$  are fixed. The exit time function  $T(\Delta)$  in Fig. 4.5 demonstrates an intermittency of smooth curves and complicated structures that cannot be resolved in principle, no matter how large the magnification factor. The second and third panels in Fig. 4.5 demonstrate successive magnifications of the detuning intervals shown in the upper panel. Further magnifications reveal a self-similar fractal-like structure that is typical for Hamiltonian systems with chaotic scattering (Gaspard et al., 1998; Budyansky et al., 2004). The exit time  $T$ , corresponding to both the smooth and unresolved  $\Delta$  intervals, increases with increasing the magnification factor. Theoretically, there exist atoms never crossing the border nodes at  $x = -\pi/2$  or  $x = 3\pi/2$  in spite of the fact that they have no obvious energy restrictions to do that. Tiny interplay between chaotic external and internal atomic dynamics prevents those atoms from leaving the small space region.

Various kinds of atomic trajectories can be characterized by the number of times  $m$  atom crosses the central node at  $x = \pi/2$  between the border nodes. There are also special separatrix-like trajectories along which atoms asymptotically reach the points with the maximum of the potential energy, having no more kinetic energy to overcome it. In difference from the separatrix motion in the resonant system ( $\Delta = 0$ ), a detuned atom can asymptotically reach one of the stationary points even if it was trapped for a while in a well. Such an asymptotic motion takes an infinite time, so the atom will never reach the border nodes.

The smooth  $\Delta$  intervals in the first-order structure (Fig. 4.5, upper panel) correspond to atoms which never change the direction of motion ( $m = 1$ ) and reach the border node at  $x = 3\pi/2$ . The singular points in the first-order structure with  $T = \infty$ , which are located at the border between the smooth and unresolved  $\Delta$  intervals, are generated by the asymptotic trajectories. Analogously, the smooth  $\Delta$  intervals in the second-order structure (second panel in Fig. 4.5) correspond to the 2-nd order ( $m = 2$ ) trajectories, and so on.

The set of all the values of the detunings, generating the separatrix-like trajectories, was shown to be a countable fractal in Refs. (Argonov and Prants, 2003, 2006), whereas the set of the values generating dynamically trapped atoms with  $m = \infty$  seems to be uncountable. The exit time  $T$  depends in a complicated way not only on the values of the control parameters but on initial conditions as well.

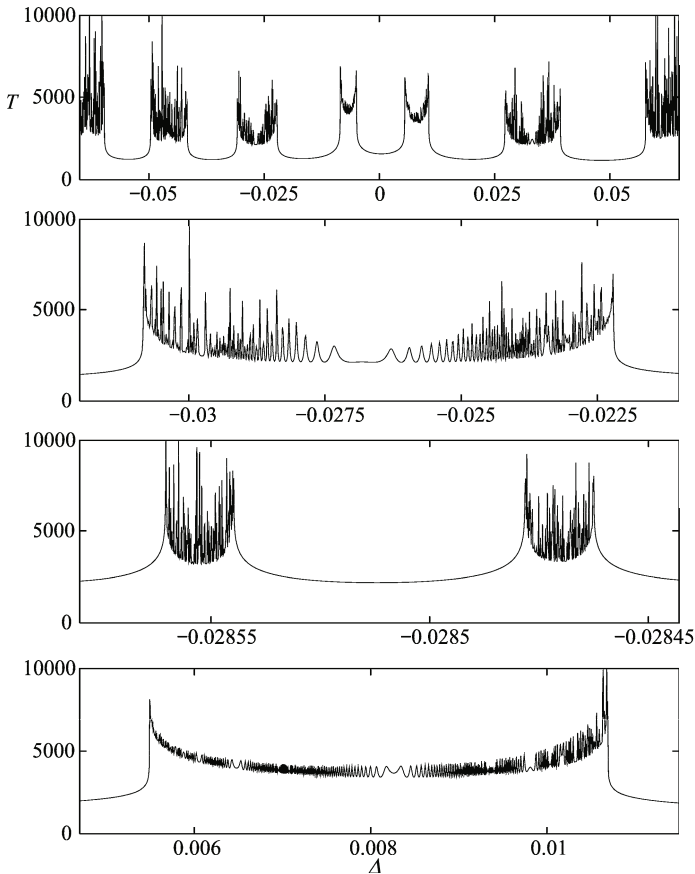


**Fig. 4.5** Fractal-like dependence of the time of exit of atoms  $T$  from a small region in the optical lattice on the detuning  $\Delta$ :  $p_0 = 200$ ,  $z_0 = -1$ ,  $u_0 = v_0 = 0$ . Magnifications of the detuning intervals are shown.

In Fig. 4.6 (Argonov and Prants, 2006) we presented a 2-dimensional image of the time of exit  $T$  in the space of the initial atomic momentum  $p_0$  and the atom-field detuning  $\Delta$ . A self-similarity of this function is evident.

The length of all smooth segments in the  $m$ -th order structure in Fig. 4.5 is proportional to the number of atoms  $N(m)$  leaving the space  $[-\pi/2, 3\pi/2]$  after crossing the central node  $m$  times. An exponential scaling  $N(m) \sim \exp(-\gamma m)$  has been found numerically with  $\gamma \simeq 1$ . The trapping PDFs, computed with the basic and reduced equations of motion at the detunings in the range shown in Fig. 4.5, have been found to have exponential tails. It is well known (Gaspard et al., 1998) that Hamiltonian systems with fully developed chaos demonstrate, as a rule, exponential decay laws, whereas the systems with a mixed phase space (containing islands of regular motion) usually have more slow algebraic decays due to the effect of stickiness of trajectories to the boundaries of such islands (Zaslavsky et al., 2005). We have not found visible regular islands in our system at the values of the control parameters used to compute the fractal in Fig. 4.5 and we may conclude that the exponential scaling is a result of completely chaotic wandering of atoms in the space interval  $[-\pi/2, 3\pi/2]$  resembling chaotic motion in hyperbolic systems.

The fractal-like structure with smooth and unresolved components may appear if atoms have an alternative either to turn back or to prolong the motion in the same direction just after crossing the node at  $x = \pi/2$ . For the first-order structure in the upper panel in Fig. 4.5, it means that the internal variable  $u$  of an atom, just after crossing the node for the first time ( $\cos x < 0$ ), satisfies either to the condition  $u_1 < H$  (atom moves in the same direction), or to the condition  $u_1 > H$  (atom turns back). If  $u_1 = H$ , then the exit time  $T$  is infinite. The jumps of the variable  $u$  after crossing the node are deterministic but sensitively dependent on the values of the control parameters and initial conditions. We have used this fact when introducing the stochastic map. Small variations in these values lead to oscillations of the quantity  $\arcsin u_1$  around the initial value  $\arcsin u_0$  with the angular amplitude  $\Theta$ . If this amplitude is large enough, then the sign of the quantity  $u_1 - H$  alternates and we obtain alternating smooth (atoms reach the border  $x = 3\pi/2$  without changing their direction of motion) and unresolved (atoms turns a number of times before exit) components of the fractal-like structure.

If the values of the parameters admit large jump magnitudes of the variable  $u$ , then the dynamical fractal arises in the energy range  $0 < H < 1$ , i. e., at the same condition under which atoms move in the optical lattice in a chaotic way. In a case of small jump magnitudes, fractals may arise if the initial value of an atom  $u_0$  is close enough to the value of the energy  $H$ , i. e., the atom has a possibility to overcome the value  $u = H$  in a single jump. Therefore, the condition for appearing in the fractal  $T(\Delta)$  the first-order structure with singularities is the following:

$$|\arcsin u_0 - \arcsin H| < \Theta. \quad (4.13)$$

The generation of the second-order structure is explained analogously. If an atom made a turn after crossing the node for the first time, then it will cross the node for the second time. After that, the atom either will turn or cross the border node at

$x = -\pi/2$ . What will happen depends on the value of  $u_2$ . However, in difference from the case with  $m = 1$ , the condition for appearing an infinite exit time with  $m = 2$  is  $u_2 = -H$ . Furthermore, the previous value  $u_1$  is not fixed (in difference from  $u_0$ ) but depends on the value of the detuning  $\Delta$ . In any case we have  $u_1 > H$  since the second-order structure consists of the trajectories of those atoms which turned after the first node crossing. In order for an atom would be able to turn after the second node crossing, the magnitude of its variable  $u$  should change sufficiently to be in the range  $u_2 < -H$ . The atoms, whose variables  $u$  could not “jump” so far,

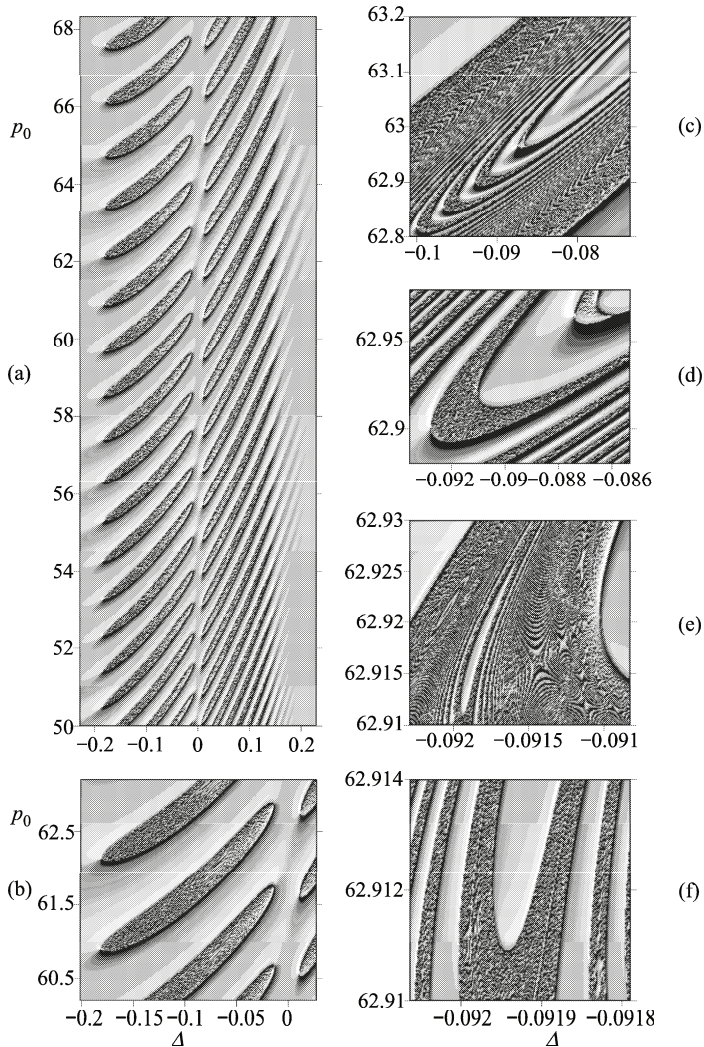


**Fig. 4.6** The scattering function in the regime of chaotic wandering. The time of exit  $T$  vs the detuning  $\Delta$  and the initial momentum  $p_0$ . The function is shown in a shaded relief regime.

leave the space  $[-\pi/2, 3\pi/2]$ . The singularities are absent in the middle segment of the second-order structure shown in the second panel in Fig. 4.5 because all the corresponding atoms left the space after the second node crossing. The variable  $u_2$  oscillates with varying  $\Delta$  generating oscillations of the exit time. The condition for appearing singularities in the second-order structure is the following:

$$2 \arcsin H < \Theta. \quad (4.14)$$

With the values of the parameters taken in the simulation, we get the energy  $H = 0.2 + \Delta/2$ . It is easy to obtain from the inequality (4.14) the approximate value of the detuning  $|\Delta| \approx 0.0107$  for which the second-order singularities may appear. In the lower panel in Fig. 4.5 one can see this effect. No additional conditions are required for generating the structures of the third and the next orders.

Inequality (4.14) is opposite to the inequality that determines the condition for appearing power law decays in the flight PDF. Therefore, dynamical fractal may appear in those ranges of the control parameters where the Lévy flights are impossible and vice versa. However, the trapping PDF may have a power law decay. Inequality (4.14) in difference from (4.13) is strongly related with the chosen concrete scheme for computing exit times. It is not required with other schemes, say, with three antinodes between the border nodes.

## 4.4 Quantum dynamics

In this section we will treat atomic translational motion quantum mechanically, i. e., atom is supposed to be not a point particle but a wave packet. The corresponding Hamiltonian  $\hat{H}$  has the form (4.1) with  $\hat{X}$  and  $\hat{P}$  being the position and momentum operators. We will work in the momentum space with the state vector

$$|\Psi(t)\rangle = \int [a(P,t)|2\rangle + b(P,t)|1\rangle] dP, \quad (4.15)$$

which satisfies to the Schrödinger equation

$$i\hbar \frac{d|\Psi\rangle}{dt} = \hat{H}|\Psi\rangle. \quad (4.16)$$

The normalized equations for the probability amplitudes have the form

$$\begin{aligned} i\dot{a}(p) &= \frac{1}{2}(\omega_r p^2 - \Delta)a(p) - \frac{1}{2}[b(p+1) + b(p-1)], \\ i\dot{b}(p) &= \frac{1}{2}(\omega_r p^2 + \Delta)b(p) - \frac{1}{2}[a(p+1) + a(p-1)], \end{aligned} \quad (4.17)$$

with the same normalization and the control parameters as in the semiclassical theory. When deriving (4.17), we used the following property of the momentum oper-

ator  $\hat{P}$ :

$$\cos k_f \hat{X} |P\rangle \equiv \frac{1}{2} \left( e^{ik_f \hat{X}} + e^{-ik_f \hat{X}} \right) |P\rangle = \frac{1}{2} (|P + \hbar k_f\rangle + |P - \hbar k_f\rangle). \quad (4.18)$$

Equations (4.17) are an infinite-dimensional set of ordinary differential complex-valued equations of the first order with coupled amplitudes  $a(p \pm n)$  and  $b(p \pm m)$ . To characterize the internal atomic state, let us introduce the following variables;

$$\begin{aligned} u(\tau) &\equiv 2 \operatorname{Re} \int dx [a(x, \tau) b^*(x, \tau)], \\ v(\tau) &\equiv -2 \operatorname{Im} \int dx [a(x, \tau) b^*(x, \tau)], \\ z(\tau) &\equiv \int dx [|a(x, \tau)|^2 - |b(x, \tau)|^2], \end{aligned} \quad (4.19)$$

which are quantum versions of the Bloch components (4.4), and we denote them by the same letters.

## 4.5 Dressed states picture and nonadiabatic transitions

Interpretation of the atomic wave-packet motion in a standing-wave field is greatly facilitated in the basis of atomic dressed states which are eigenstates of a 2-level atom in a laser field. The adiabatic dressed states

$$\begin{aligned} |+\rangle_{\Delta} &= \sin \Theta |2\rangle + \cos \Theta |1\rangle, \quad |-\rangle_{\Delta} = \cos \Theta |2\rangle - \sin \Theta |1\rangle, \\ \tan \Theta &\equiv \frac{\Delta}{2 \cos x} - \sqrt{\left( \frac{\Delta}{2 \cos x} \right)^2 + 1} \end{aligned} \quad (4.20)$$

are eigenstates at a nonzero detuning. The corresponding values of the quasienergy are

$$E_{\Delta}^{(\pm)} = \pm \sqrt{\frac{\Delta^2}{4} + \cos x}. \quad (4.21)$$

Figure 4.7 shows a spatial variation of the quasienergies along the standing-wave axis. It follows from Eqs.(4.20) and (4.21) that, in general case, atom moves in the two potentials  $E_{\Delta}^{(\pm)}$  simultaneously.

At exact resonance,  $\Delta = 0$ , the dressed states have the simple form

$$|+\rangle = \frac{1}{\sqrt{2}} (|1\rangle + |2\rangle), \quad |-\rangle = \frac{1}{\sqrt{2}} (|1\rangle - |2\rangle) \quad (4.22)$$

and are called diabatic states. The resonant potentials,  $E_0^{(\pm)} = \pm \cos x$ , cross each other at the nodes of the standing wave,  $x = \pi/2 + \pi m$ , ( $m = 0, \pm 1, \dots$ ). What will happen if we place the centroid of an atomic wave packet exactly at the node,  $x_0 =$

$\pi/2$ , in the ground state  $|1\rangle$  and suppose its initial mean momentum to be zero,  $p_0 = 0$ ? The initial ground state is the superposition of the diabatic states:  $|1\rangle = (|+\rangle + |-\rangle)/\sqrt{2}$ . One part of the initial wave packet at the top of the potential  $E_0^{(+)}$  will start to move to the right under the action of the gradient force  $F^{(+)} = -dE_0^{(+)}/dx = \sin x$ , and another one — to the left to be forced by  $F^{(-)} = -\sin x$  (see Fig. 4.7). It is the well-known optical Stern-Gerlach effect (Kazantsev et al., 1974, 1990; Sleator et al., 1992). If the maximal expected value of the atomic kinetic energy does not exceed the potential one, the atom will be trapped in the potential well. Two splitted components of the initial wave packet will oscillate in the well with the period of oscillations

$$T \simeq 4\sqrt{\frac{\pi}{\omega_r}}. \quad (4.23)$$

The wave packet, with  $p_0 = 0$ , placed at the antinode, say, at  $x_0 = 0$ , is simultaneously at the top of the potential  $E_0^{(+)}$  and at the bottom of  $E_0^{(-)}$ . Therefore, its  $|+\rangle$ -component will slide down the both sides of the potential curve  $E_0^{(+)}$ , and the  $|-\rangle$ -component will oscillate around  $x = 0$  (see Fig. 4.7).

Out off resonance,  $\Delta \neq 0$ , the atomic wave packet moves in the bipotential  $E_\Delta^{(\pm)}$  (4.21). The distance between the quasienergy curves is minimal at the nodes of the standing wave and equal to  $\Delta$  (see Fig. 4.7). The spatial period and the modulation depth of the resonant potentials  $E_0^{(\pm)}$  are twice as much as those for the nonresonant potentials  $E_\Delta^{(\pm)}$ .

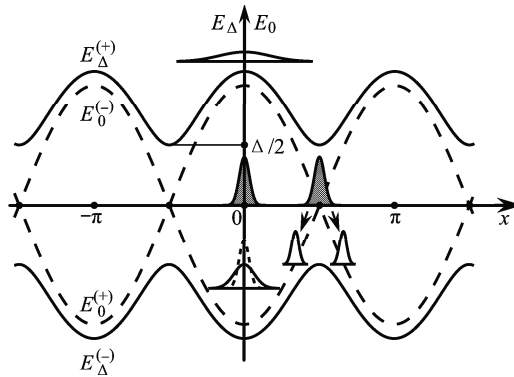


**Fig. 4.7** Resonant  $E_0^{(\pm)}$  and nonresonant  $E_\Delta^{(\pm)}$  potentials for an atom in a standing wave. The optical Stern-Gerlach effect in the resonant  $E_0^{(\pm)}$  potential is shown: splitting of an atomic wave packet launched at the node of the wave ( $x_0 = \pi/2$ ,  $p_0 = 0$ ). The wave packet, placed initially at the antinode ( $x_0 = 0$ ,  $p_0 = 0$ ), appears to be simultaneously at the top of  $E_0^{(+)}$  and the bottom of  $E_0^{(-)}$  potentials. Its  $|+\rangle$ -component slides down both the sides of  $E_0^{(+)}$  and the  $|-\rangle$ -component oscillates at the bottom of  $E_0^{(-)}$ .

The probability of nonadiabatic transitions between the dressed states  $|+\rangle_\Delta$  and  $|-\rangle_\Delta$  can be estimated in a simple way. The time of flight over a short distance  $\delta x$  in neighbourhood of a node is  $\delta x/\omega_r p_{\text{node}}$ . If the time of transition between the quasienergy levels,  $2/\Delta$ , is of the order of the flight time, the transition probability is close to 1. It is easy to get the characteristic frequency of atomic motion from that condition (Kazantsev et al., 1990)

$$\Delta_0 = \sqrt{\omega_r p_{\text{node}}}, \quad (4.24)$$

where  $p_{\text{node}}$  is a value of the momentum in the vicinity of a node.

Depending on the relation between  $\Delta$  and  $\Delta_0$ , there are three typical cases.

1. If  $|\Delta| \ll \Delta_0$ , the nonadiabatic transition probability between the states  $|+\rangle_\Delta$  and  $|-\rangle_\Delta$  upon crossing any node is close to 1. However, the diabatic states  $|+\rangle$  and  $|-\rangle$  are not mixed, and atom moves in one of optical resonant potentials.
2. If  $|\Delta| \simeq \Delta_0$ , the probabilities to change or not to change a given adiabatic state upon crossing any node are of the same order.
3. If  $|\Delta| \gg \Delta_0$ , the nonadiabatic transition probability is exponentially small, and atom moves in one of the nonresonant potentials.

### 4.5.1 Wave packet motion in the momentum space

The atom at  $\tau = 0$  is supposed to be prepared as a Gaussian wave packet in the momentum space

$$a_0(p) = 0, \quad b_0(p) = \frac{1}{\sqrt{\sqrt{\pi}\Delta p}} \exp \left[ -\frac{(p-p_0)^2}{2(\Delta p)^2} - i(p-p_0)x_0 \right], \quad (4.25)$$

with the momentum width  $\Delta p = 10$  corresponding to the spatial width  $\Delta X = \lambda_f/40\pi$  that is much smaller than the optical wavelength  $\lambda_f$ . We compute the probability to find a 2-level atom at the moment of time  $\tau$  with the momentum  $p$

$$W(p, \tau) = |a(p, \tau)|^2 + |b(p, \tau)|^2, \quad (4.26)$$

by integrating Eqs.(4.17) with the initial condition (4.25). The recoil frequency,  $\omega_r = 10^{-5}$ , is fixed and the centroid of the wave packet is placed at the antinode  $x_0 = 0$ , in all the numerical experiments.

#### 4.5.1.1 Adiabatic evolution at exact resonance

At exact resonance,  $\Delta = 0$ , the wave functions of the diabatic states  $|+\rangle$  and  $|-\rangle$  evolve independently, each one evolves in its own potential  $E_0^{(+)}$  and  $E_0^{(-)}$ , respectively. The atom, prepared initially in the ground state  $|1\rangle = (|+\rangle + |-\rangle)/\sqrt{2}$  with

the mean initial momentum  $p_0 = 800$ , will start to move from the top of  $E_0^{(+)}$  and the bottom of  $E_0^{(-)}$  potentials (see Fig.4.7). Thus, the initial wave packet will split into two components  $|+\rangle$  and  $|-\rangle$ . Time evolution of the probability function (4.26) for each of the components is shown in Fig.4.8. Pay, please, attention that the values of  $p$  on this and similar plots increase downwards. Color in this figure codes the values of  $W(p, \tau)$ . The  $|+\rangle$ -component (the lower trajectory in the figure) slides down the curve  $E_0^{(+)}$  and, therefore, moves with an increasing velocity up to the next antinode at  $x = \pi$ , and then it slows down approaching the antinode at  $x = 2\pi$ . The atom moves in the positive direction of the axis  $x$  and the process repeats periodically with the period  $\tau_0^{(+)} = 2\pi/\omega_r \bar{p}_{0,2\pi}^{(+)} \simeq 690$ , where  $\bar{p}_{0,2\pi}^{(+)}$  is a mean momentum of the  $|+\rangle$ -component upon the atomic motion between 0 and  $2\pi$ .

The  $|-\rangle$ -component (the upper trajectory in Fig.4.8) moves upward the potential curve  $E_0^{(-)}$  and slows down up to reaching the top of  $E_0^{(-)}$  at  $x = \pi$ . Then it moves with an increasing momentum up to  $x = 2\pi$ . Since the mean momentum of the  $|-\rangle$ -component is smaller than that of the  $|+\rangle$  one, the corresponding period is longer,  $\tau_0^{(-)} \simeq 980$ .

#### 4.5.1.2 Proliferation of wave packets at the nodes of the standing wave

New features in propagation of atomic wave packets through the standing wave appear under the condition  $\Delta \simeq \Delta_0$ . Using the semiclassical expression for the total atomic energy (4.6), let us estimate the value of the atomic momentum at the nodes

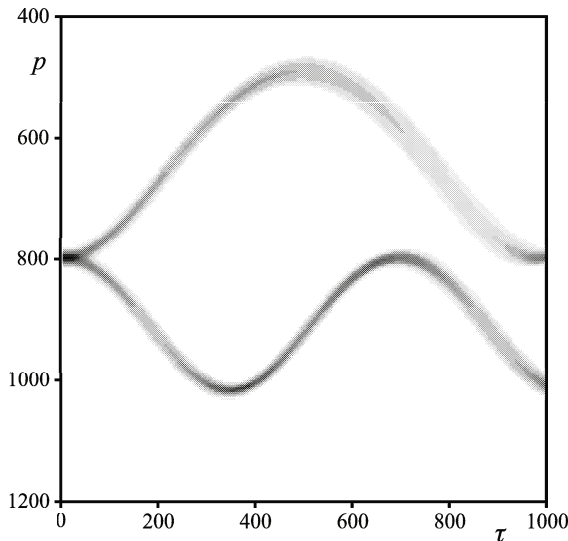


**Fig. 4.8** Time dependence of the momentum probability function  $W(p, \tau)$  for a ballistic atom at resonance prepared initially in the ground state ( $\Delta = 0$ ,  $\omega_r = 10^{-5}$ ,  $x_0 = 0$ ,  $p_0 = 800$ ).

of the standing wave if the detuning is not large,  $|\Delta| \ll 1$ . If the atom is prepared initially in the state  $|+\rangle$ , i.e.,  $u_0 = 1$ ,  $z_0 = 0$ , and  $x_0 = 0$  then we have  $H = H_0 = 2.2$  at  $p_0 = 800$ . Since the total energy is a constant, we get immediately from Eq. (4.6)

$$p_{\text{node}} \simeq \sqrt{2H/\omega_r} \simeq 665. \quad (4.27)$$

Using the same formula (4.6), we get the values of the minimal and maximal momenta if the atom starts to move with the initial mean momentum  $p_0 = 800$ :  $p_{\text{min}} \simeq \sqrt{2(H_0 - 1)/\omega_r} \simeq 490$  and  $p_{\text{max}} \simeq \sqrt{2(H_0 + 1)/\omega_r} \simeq 800$ .

The formula (4.24) gives us the value of the characteristic frequency under the chosen conditions,  $\Delta_0 \simeq 0.08$ . We fix  $\Delta = 0.05$  in this section, so  $\Delta \simeq \Delta_0$ . The initial state  $|+\rangle$  is the following superposition of the adiabatic states:

$$|+\rangle = \frac{1}{\sqrt{2}}[(\cos\Theta + \sin\Theta)|+\rangle_{\Delta} + (\cos\Theta - \sin\Theta)|-\rangle_{\Delta}]. \quad (4.28)$$

With the help of (4.21) we can estimate the mixing angle at  $\Delta = 0.05$  to be equal to  $\theta \simeq -\pi/4$ . Then it follows from (4.28) that  $|+\rangle \simeq |-\rangle_{\Delta}$ , i. e., practically all the wave packet is initially at the bottom of the potential  $E_{\Delta}^{(-)}$  (Fig. 4.7). Figure 4.9 demonstrates that the wave packet really slows down, and its centroid intersects the node  $x = \pi/2$  at  $\tau_1^{(-)} \simeq 215$ . Under the condition  $\Delta \simeq \Delta_0$ , the atom has a probability to change the potential for another one upon crossing a node and a probability to stay in its present potential. This is exactly what we see in Fig. 4.9: the wave packet splits at the node  $x = \pi/2$  with the  $|-\rangle$ -component moving down in the potential  $E_{\Delta}^{(-)}$  (see the lower trajectory in this figure) and the  $|+\rangle$ -component moves up the curve  $E_{\Delta}^{(+)}$  with a decreasing momentum (see the upper trajectory). Just after crossing the node, the most part of the probability density moves in the potential  $E_{\Delta}^{(-)}$  because the corresponding probability is larger. The  $|-\rangle$ -component increases its velocity upon approaching the antinode at  $x = \pi$  and then slows down up to the second node at  $x = 3\pi/2$  where it splits into two components at  $\tau_2^{(-)} \simeq 640$ . After that, one of the components will move in the potential  $E_{\Delta}^{(+)}$  decreasing the velocity up to the next antinode at  $x = 2\pi$ , and the other one will move in  $E_{\Delta}^{(-)}$  increasing its velocity in the same space interval. The probability density of this  $|-\rangle$ -component is only a few percents, and we draw a solid curve along this trajectory in order to visualize the motion.

The  $|+\rangle$ -component of the packet, splitted after crossing the first node at  $x = \pi/2$ , has a smaller mean momentum than the  $|-\rangle$ -one. Therefore, it reaches the second node later, at  $\tau_2^{(+)} \simeq 800$ , where it splits into two parts: the upper  $|+\rangle$ -component will move in the potential  $E_{\Delta}^{(+)}$  and the lower  $|-\rangle$ -one — in  $E_{\Delta}^{(-)}$ . Such a proliferation of atomic wave packets takes places upon crossing all the next nodes of the standing wave.

The moment of time  $\tau_n^{(\pm)}$ , when the centroids of the  $|\pm\rangle$ -components cross the  $n$ -th node, can be estimated by the simple formula (we suppose that the centroid of

the atomic wave packet was at  $x = 0$  at  $\tau = 0$ ):

$$\omega_r \bar{p}_{n-1, n}^{(\pm)} \tau_n^{(\pm)} = (2n - 1) \frac{\pi}{2}, \quad n = 2, 3, \dots, \quad (4.29)$$

where  $\bar{p}_{n-1, n}^{(\pm)}$  is a mean momentum of the  $|\pm\rangle$ -components upon their movement between  $(n - 1)$ -th and  $n$ -th nodes. This quantity for the  $|-\rangle$ -component, moving between  $x = 0$  and  $x = \pi/2$ , is  $\bar{p}_{0,1}^{(-)} = (p_0 + p_{\text{node}})/2 \simeq 732.5$ . So, the centroid of this wave packet crosses the first node at  $\tau_1^{(-)} \simeq 214$ . The lower  $|-\rangle$ -component crosses the second node at  $x = 3\pi/2$  at  $\tau_2^{(-)} \simeq 642$ . For the upper  $|+\rangle$ -component we get  $\bar{p}_{1,2}^{(+)} = (p_{\text{node}} + p_{\text{min}})/2 \simeq 577.5$  and  $\tau_2^{(+)} \simeq 815$ . All the other moments of time,  $\tau_n^{(\pm)}$ , can be estimated in the same way. The estimates obtained fit well the numerical data (see Fig. 4.9). The interference fringes on the upper trajectory at  $\tau \simeq 1000$  and  $p \simeq 500$  and on the lower one at  $\tau \simeq 900$  and  $p \simeq 800$  reflect the fine-scale splitting of the corresponding wave packets.

Let us now compute the probability map for the atom prepared initially in the ground state  $|1\rangle$  which has the following form in the adiabatic state basis:

$$|1\rangle = \cos \Theta |+\rangle_{\Delta} - \sin \Theta |-\rangle_{\Delta}. \quad (4.30)$$

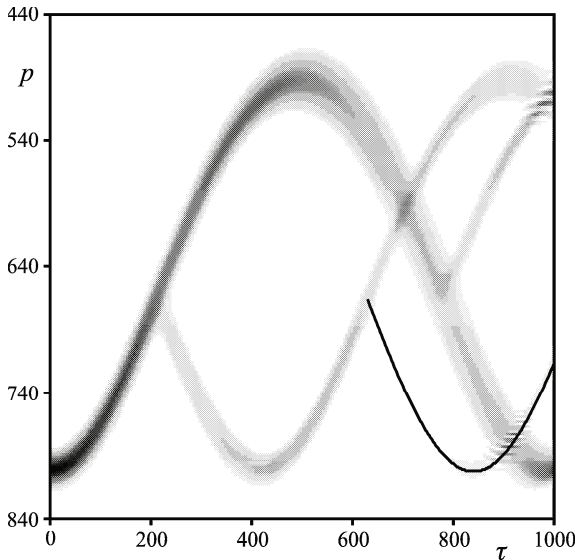


**Fig. 4.9** Proliferation of atomic wave packets at the nodes of the standing wave at the detuning  $\Delta = 0.05$ . The atom is prepared initially in the dressed state  $|+\rangle$ . Other conditions are the same as in Fig. 4.8.

It follows from (4.21) that (4.30) is almost a 50%–50% superposition of the  $|+\rangle_\Delta$  and  $|-\rangle_\Delta$  states. All the other conditions are assumed to be the same as before. The atomic wave packet splits from the beginning into two components with the  $|+\rangle$ -one sliding down the curve  $E_\Delta^{(+)}$  (the lower trajectory in Fig. 4.10) and the  $|-\rangle$ -one climbing over the potential  $E_\Delta^{(-)}$  (the upper trajectory). Each of the components splits at the first node with a small time difference between the events. The subsequent proliferation of the wave packets occurs for the upper and lower parts of the probability density independently on each other in accordance with the same scenario as described above. In difference from the preceding case, the atom, prepared initially in the ground state, acquired the values of the momentum that are larger than the initial momentum  $p_0 = 800$ .

The nonadiabatic transitions are accompanied by drastic changes in the internal state of the atom which is characterized by the values of the synphased component of the electric dipole moment  $u$  and the population inversion  $z$ . In Fig. 4.11 we demonstrate their behavior for the atom prepared initially in the state  $|+\rangle$ . Both the variables change their values abruptly in the time intervals with the centers at  $\tau \simeq 215, 640$  and  $815$ , i. e., when the centroids of the atomic wave packets cross the first two nodes.

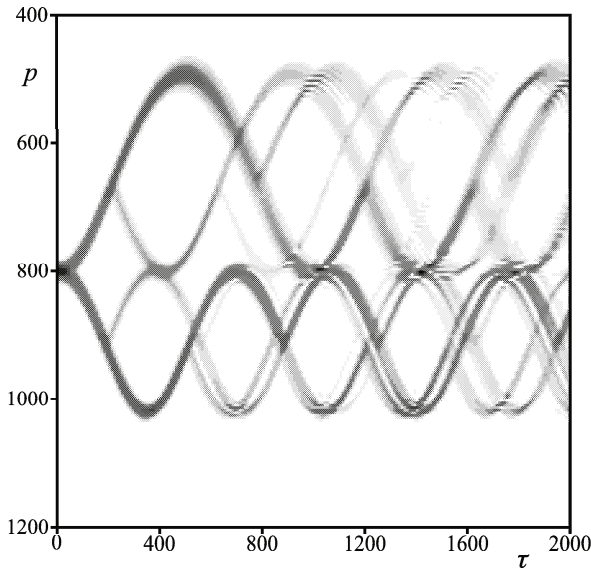


**Fig. 4.10** The same as in Fig. 4.9 but for the atom prepared initially in the ground state.

### 4.5.1.3 Adiabatic motion at large detunings

For comparison with the results of the preceding section, we demonstrate in Fig. 4.12 the evolution of the momentum distribution function  $W(p, \tau)$  with the ground in-

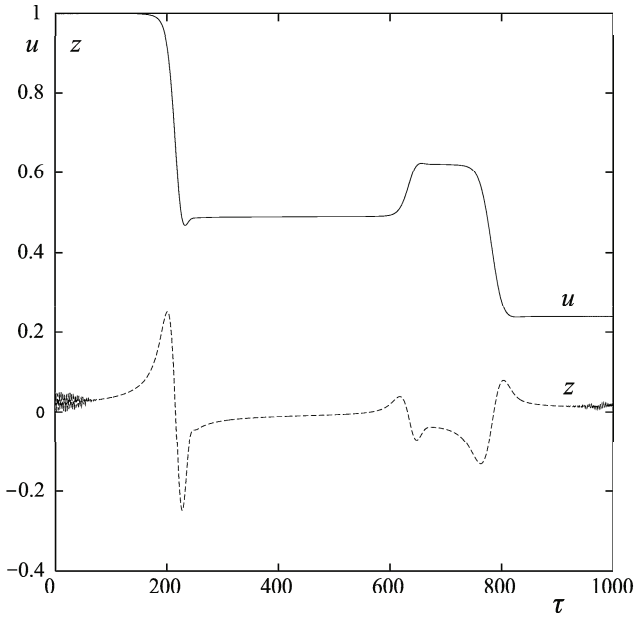


**Fig. 4.11** Time dependence of the dipole moment  $u$  and the population inversion  $z$  at the same conditions as in Fig. 4.9.

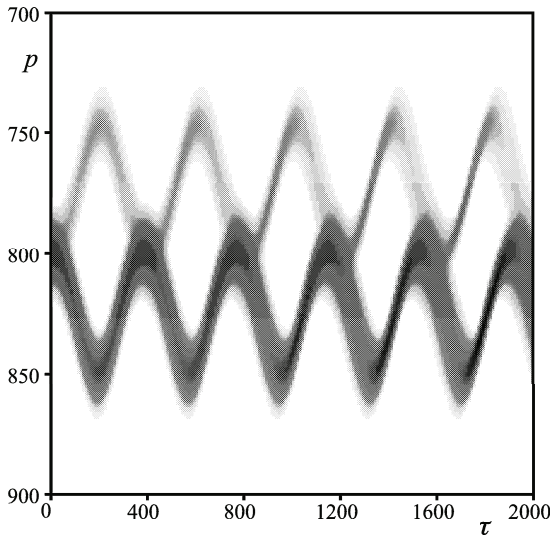


**Fig. 4.12** Adiabatic evolution of the momentum probability function  $W(p, \tau)$  for a ballistic atom at the large detuning  $\Delta = 2$ .

tial state at  $\Delta = 2$  and the other same conditions as in the preceding section. The detuning  $\Delta = 2$  is large as compared to the characteristic frequency  $\Delta_0 \simeq 0.09$  that is estimated from (4.24) at  $p_0 = 800$ . It follows from (4.20) and (4.21) that at  $\Delta = 2$

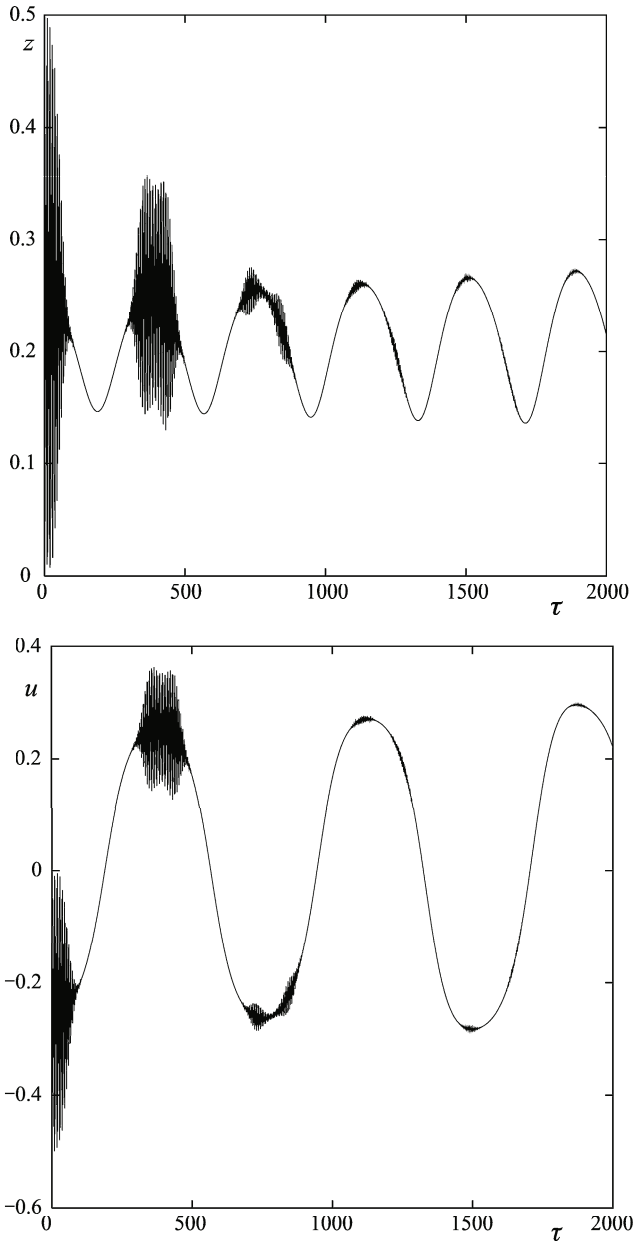


**Fig. 4.13** The same as in Fig.4.11 but at the large detuning  $\Delta = 2$ .

the initial state  $|1\rangle$  is a superposition of approximately 70% of the state  $|+\rangle_\Delta$  and  $\sim 30\%$  of the state  $|-\rangle_\Delta$ . So the main part of the initial packet begins to move in the potential  $E_\Delta^{(+)}$  increasing the momentum upon approaching the node at  $x = \pi/2$ , and the other part moves in  $E_\Delta^{(-)}$  decreasing the momentum in the same space interval (see Fig. 4.12). Upon crossing the nodes, the probability of transition between the states  $|\pm\rangle_\Delta$  is small if  $|\Delta| \gg \Delta_0$ , and each of the component will continue to move in its own potential. The process is repeated and we see the periodic variations of the mean momentum of each of the components. The same picture is observed if we take the state  $|+\rangle = (|1\rangle + |2\rangle)/\sqrt{2}$  as the initial one. At  $\Delta = 2$ , the state  $|+\rangle$  is a mix of 70% of  $|-\rangle_\Delta$  and 30% of  $|+\rangle_\Delta$ , so the main part of the initial  $|+\rangle$  wave packet will move in the potential  $E_\Delta^{(-)}$ . The evolution of the internal atomic variables  $z$  and  $u$  is shown in Fig. 4.13. There are no jumps of  $z$  and  $u$  when the atom crosses nodes. Instead of that, we see fast oscillations of those variables when the atom crosses the first antinodes.

Thus, at  $|\Delta| \gg \Delta_0$ , there are no nonadiabatic transitions due to the corresponding small probability and, therefore, no proliferation of wave packets at the nodes. The evolution of the atomic wave packet is adiabatic.

#### 4.5.1.4 An atom can fly and be trapped simultaneously

An intriguing effect of simultaneous trapping of an atom in a well of the optical potential and its ballistic flight through the optical lattice is observed at comparatively small values of the detuning. Let us prepare an atom in the ground state  $|1\rangle$  with such a mean initial value of the momentum  $p_0$  that its  $|-\rangle$ -component would not be able to overcome the barrier of the potential  $E_\Delta^{(-)}$  but its  $|+\rangle$ -component would have a sufficient kinetic energy to overcome the barrier of the  $E_\Delta^{(+)}$  potential. Now one could expect periodic oscillations in the first well of the potential  $E_\Delta^{(-)}$  and a simultaneous ballistic flight in the  $E_\Delta^{(+)}$  potential with a proliferation of wave packets of the  $|+\rangle$ -component at the nodes of the standing wave.

Figure 4.14 demonstrates this effect at  $p_0 = 300$ ,  $\Delta = -0.05$  and the same other conditions as before. We see that the momentum of the  $|-\rangle$ -component (the upper trajectory in this figure) oscillates in the range  $(300, -300)$ , and this component is trapped in the first well  $(-\pi/2 \leq x \leq \pi/2)$ . Whereas the  $|+\rangle$ -component moves in the positive direction splitting at each node. Estimates of the period of oscillations of the  $|-\rangle$ -component,  $T \simeq 2240$ , with the help of (4.23) and of the time when the centroid of the  $|+\rangle$ -component crosses the first node,  $\tau_1^{(+)} \simeq 380$  (formula (4.29)), fit well the data in Fig. 4.14.

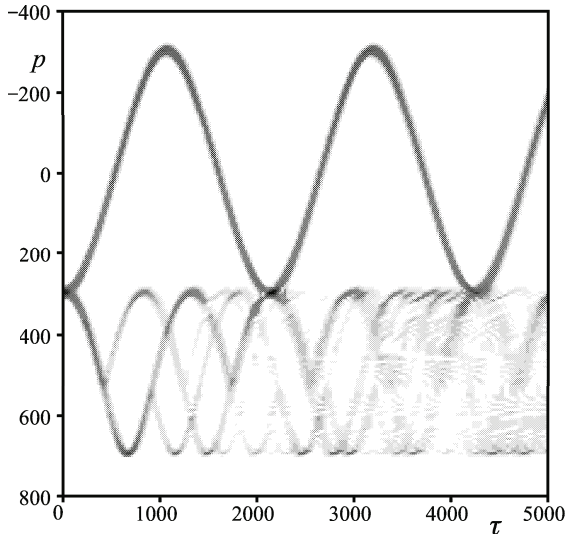


**Fig. 4.14** Effect of simultaneous trapping of an atom in a well of the optical potential and its flight through the wave. The ground initial state,  $\Delta = -0.05$ ,  $p_0 = 300$ .

## 4.6 Quantum-classical correspondence and manifestations of dynamical chaos in wave-packet atomic motion

Dynamical chaos in classical systems is characterized by exponentially fast divergence of initially close trajectories in a bounded phase space. Such a behavior is possible because of the continuity of the classical phase space whose points (therefore, classical system's states) can be arbitrary close to each other. The trajectory concept is absent in quantum mechanics whose phase space is not continuous due to the Heisenberg uncertainty relation. The evolution of an isolated quantum system is unitary, and there can be no chaos in the sense of exponential sensitivity of its states to small variations in initial conditions. What is usually understood under “quantum chaos” is special features of the unitary evolution of a quantum system in the range of its parameter values and initial conditions at which its classical analogue is chaotic.

The question “what happens to classical motion in the quantum world” is a core of the problem of quantum-classical correspondence. In spite of years of discussions from the beginning of the quantum era, it is still unclear how classical features appear from the underlying quantum equations. It is especially difficult to specify what happens to classical dynamical chaos in the quantum world (Berman and Zaslavsky, 1978; Casati et al., 1979; Zaslavsky, 1981; Gutzwiller, 1990; Reichl, 1992; Haake, 1991; Stöckmann, 1999). The interest to the problem of “quantum chaos” is motivated by our desire to understand the quantum origin of the observed classical chaos.

In this section we establish a correspondence between the quantized motion of a 2-level atom in a standing laser wave and its semiclassical analogue considered in the third section. Semiclassical equations (4.5) represent a nonlinear dynamical system with positive values of the maximal Lyapunov exponent in a wide range of the initial conditions and control parameters  $\omega_r$  and  $\Delta$ . In other words, trajectories in the 5-dimensional phase space are exponentially sensitive to small variations in initial conditions and/or parameters in those ranges. That local dynamical instability is a reason for chaotic Rabi oscillations and chaotic motion of the atomic center of mass discussed in the third section. In particular, it has been found that an atom is able to walk chaotically in a strictly periodic optical lattice without any noise or other random processes (see Fig. 4.2). The chaotic behavior is caused by jumps of the electric-dipole moment  $u$  at the nodes of the standing wave (Fig. 4.3). It follows from Eqs. (4.5) that this quantity governs the atomic momentum. A stochastic map for the quantity  $u$  (4.11) allowed to derive analytic expressions for probability density functions of the atomic trapping and flight events that have been shown to fit well numerical simulation (Argonov and Prants, 2007).

It has been shown that sudden changes in the behavior of  $u$  take place when we quantized the atomic motion (see Fig. 4.11) under the condition  $\Delta \simeq \Delta_0$ . Those changes are more smooth than the jumps of  $u$  in the semiclassical case because a delocalized wave packet crosses a node for a finite time interval. The quantum analysis provides a clear reason for those jumps at  $\Delta \simeq \Delta_0$ , namely, it is nonadiabatic transitions between the quasienergy states  $|+\rangle_\Lambda$  and  $|-\rangle_\Lambda$  which occur when an atom crosses any node of the standing wave. Those jumps are accompanied by splitting of wave packets at the nodes. We may conclude that the proliferation of wave packets at the nodes of the standing wave is a manifestation of classical chaotic transport of an atom in an optical lattice that has been shown in Refs. (Argonov and Prants, 2003, 2006, 2007) to take place in exactly the same ranges of initial conditions and control parameters. In particular, the effect of simultaneous trapping of an atom in a well of the optical potential and its flight in the same potential (Fig. 4.14) is a quantum analogue of a chaotic walking of an atom shown in Fig. 4.2.

In conclusion we would like to discuss briefly the role of dissipation. We did not take into account any losses in our treatment. Coherent evolution of the atomic state in a near-resonant standing-wave laser field is interrupted by spontaneous emission events at random moments of times. The semiclassical Hamiltonian evolution between these events has been shown to be regular or chaotic depending on the values of the detuning  $\Delta$  and the initial momentum  $p_0$ . We stress that dynamical chaos may happen without any noise and any modulation of the lattice parameters. It is a specific kind of dynamical instability in the fundamental interaction between the matter and radiation.

Dissipative transport of spontaneously emitting atoms in a 1D standing-wave laser field has been studied in detail in Ref. (Argonov and Prants, 2008) in the regimes where the underlying semiclassical Hamiltonian dynamics is regular and chaotic. A Monte Carlo stochastic wavefunction method was applied to simulate semiclassically the atomic dynamics with coupled internal and translational degrees of freedom. It has been shown in numerical experiments and confirmed analytically

that chaotic atomic transport can take the form either of ballistic motion or a random walking with specific statistical properties. The character of spatial and momentum diffusion in the ballistic atomic transport was shown to change abruptly in the atom-laser detuning regime where the Hamiltonian dynamics is irregular in the sense of dynamical chaos. A clear correlation between the behavior of the momentum diffusion coefficient and Hamiltonian chaos probability has been found.

What one could expect if spontaneous emission would be taken into consideration with our fully quantum equations of motion? Any act of spontaneous emission interrupts a coherent evolution of an atom at a random time moment and is accompanied by a momentum recoil and a sudden transition of the atom into the ground state which is a superposition of the dressed states. The coherent evolution starts again after that. A collapse of the atomic wave function and a splitting of atomic wave packets are expected just after any spontaneous emission event. That additional splitting of wave packets at random time moments, besides of their proliferation at the nodes of a standing wave at  $\Delta \simeq \Delta_0$ , can improve the quantum-classical correspondence in the regime of Hamiltonian chaos.

**Acknowledgements** I thank L. Konkov and M. Uleysky for their help in preparing some figures. This work was supported by the Russian Foundation for Basic Research (project no. 09-02-00358) and by the Program “Fundamental Problems of Nonlinear Dynamics” of the Russian Academy of Sciences.

## References

- Argonov V.Yu. and Prants S.V., 2003, Fractals and chaotic scattering of atoms in the field of a stationary standing light wave, *JETP*, **96**, 832–845. [*Zh. Eksp. Teor. Fiz.*, **123**, 946–961, (2003)].
- Argonov V.Yu. and Prants S.V., 2006, Nonlinear coherent dynamics of an atom in an optical lattice, *J. Russ. Laser Res.*, **27**, 360–378.
- Argonov V.Yu. and Prants S.V., 2007, Theory of chaotic atomic transport in an optical lattice, *Phys. Rev. A*, **75**, art. 063428.
- Argonov V.Yu. and Prants S.V., 2008, Theory of dissipative chaotic atomic transport in an optical lattice, *Phys. Rev. A*, **78**, art. 043413.
- Bardou F., Bouchaud J.P., Aspect A. and Cohen-Tannoudji C., 2002, *Lévy Statistics and Laser Cooling*, Cambridge University Press, Cambridge.
- Belobrov P.I., Zaslavskii G.M. and Tartakovskii G.Kh., 1976, Stochastic destruction of bound states in a system of atoms interacting with a radiation, *Zh. Eksp. Teor. Fiz.*, **71**, 1799–1812. [*Sov. Phys. JETP*, **44**, 945–957, (1976)].
- Berman G.P. and Zaslavsky G.M., 1978, Condition of stochasticity in quantum nonlinear systems, *Physica A*, **91**, 450–460.
- Budyansky M.V., Uleysky M.Yu. and Prants S.V., 2004, Chaotic scattering, transport, and fractals in a simple hydrodynamic flow, *J. Exper. Theor. Phys.*, **99**, 1018–1027. [*Zh. Eksp. Teor. Fiz.*, **126**, 1167–1179, (2004)].

- Casati G., Chirikov B.V., Izrailev F.M. and Ford J., 1979, Stochastic behavior in classical and quantum hamiltonian Systems, *Lecture Notes in Physics*, Springer, Berlin.
- Chu S., Hollberg L., Bjorkholm J.E., Cable A. and Ashkin A., 1985, Three-dimensional viscous confinement and cooling of atoms by resonance radiation pressure, *Phys. Rev. Lett.*, **55**, 48–51.
- Dicke R.M., 1954, Coherence in spontaneous radiation, *Phys. Rev.*, **93**, 99–110.
- Gaspard P., 1998, *Chaos, Scattering and Statistical Mechanics*, Cambridge University Press, Cambridge.
- Gould P.L., Ruff G.A. and Pritchard D.E., 1986, Diffraction of atoms by light: The near-resonant Kapitza-Dirac effect, *Phys. Rev. Lett.*, **56**, 827–830.
- Graham R., Schlautmann M. and Zoller P., 1992, Dynamical localization of atomic-beam deflection by a modulated standing light wave, *Phys. Rev. A*, **45**, R19–RR22.
- Grynberg G. and Robilliard C., 2001, Cold atoms in dissipative optical lattices, *Phys. Rep.*, **355**, 335–451.
- Gutzwiller M., 1990, *Chaos in Classical and Quantum Mechanics*, Springer, New York.
- Haake F., 1991, *Quantum Signatures of Chaos*, Springer, Berlin.
- Haken H., 1975, Analogy between higher instabilities in fluids and lasers, *Phys. Lett. A*, **53**, 77–78.
- Hensinger W.K. et al., 2001, Dynamical tunnelling of ultracold atoms, *Nature*, **412**, 52–55.
- Hensinger W.K. et al., 2003, Experimental tests of quantum nonlinear dynamics in atom optics, *J. Opt. B: Quantum Semiclass. Opt.*, **5**, R83–R120.
- Jaynes E.T., Cummings F.W., 1963, Comparison of quantum and semiclassical theories with application to the beam maser, *Proc. IEEE*, **51**, 89–109.
- Kazantsev A.P., 1975, Recoil effect in a strong resonant field, *Sov. Phys. JETP*, **40**, 825–831. [*Zh. Eksp. Teor. Fiz.*, **67**, 1660–1666, (1974)].
- Kazantsev A.P., Surdutovich G.I. and Yakovlev V.P., 1990, *Mechanical Action of Light on Atoms*, World Scientific, Singapore.
- Marksteiner S., Ellinger K. and Zoller P., 1996, Anomalous diffusion and Levy walks in optical lattices, *Phys. Rev. A*, **53**, 3409–3430.
- Moore F.L., Robinson J.C., Bharucha C., Williams P.E. and Raizen M.G., 1994, Observation of dynamical localization in atomic momentum transfer: a new testing ground for quantum chaos, *Phys. Rev. Lett.*, **73**, 2974–2977.
- Morsch O. and Oberthaler M., 2006, Dynamics of Bose-Einstein condensates in optical lattices, *Rev. Mod. Phys.*, **78**, 179–215.
- Moskowitz P.E., Gould P.L., Atlas S.R. and Pritchard D.E., 1983, Diffraction of an atomic beam by standing-wave radiation, *Phys. Rev. Lett.*, **51**, 370–373.
- Prants S.V., 2002, Fractals and flights of atoms in cavities, *JETP Letters*, **75**, 651–658. [*Pis'ma ZhETF*, **75**, 777–785 (2002)].
- Prants S.V., Edelman M. and Zaslavsky G.M., 2002, Chaos and flights in the atom-photon interaction in cavity QED, *Phys. Rev. E*, **66**, art. 046222.

- Prants S.V., Uleysky M.Yu. and Argonov V.Yu., 2006, Entanglement, fidelity, and quantum-classical correlations with an atom moving in a quantized cavity field, *Phys. Rev. A*, **73**, 023807.
- Prants S.V. and Kon'kov L.E., 2001, Chaotic motion of atom in the coherent field of a standing light wave, *JETP Lett.*, **73**, 180–183. [*Pis'ma ZhETF*, **73**, 200, (2001)].
- Prants S.V. and Sirotkin V.Yu., 2001, Effects of the Rabi oscillations on the atomic motion in a standing-wave cavity, *Phys. Rev. A*, **64**, art. 033412.
- Prants S.V. and Uleysky M.Yu., 2003, Atomic fractals in cavity quantum electrodynamics, *Phys. Lett. A*, **309**, 357–362.
- Reichl L.E., 1992, *The Transition to Chaos in Conservative Classical Systems: Quantum Manifestations*, Springer, New York.
- Robinson J.C., Bharucha C., Moore F.L., Jahnke R., Georgakis G.A., Niu Q., Raizen M.G. and Bala Sundaram, 1995, Atom optics realization of the quantum  $\delta$ -kicked rotor, *Phys. Rev. Lett.*, **74**, 4598–4601.
- Sleator T., Pfau T., Balykin V., Carnal O. and Mlynek J., 1992, Experimental demonstration of the optical Stern-Gerlach effect, *Phys. Rev. Lett.*, **68**, 1996–1999.
- Steck D.A. et al., 2001, Observation of chaos-assisted tunneling between islands of stability, *Science*, **293**, 274–278.
- Stöckmann H.-J., 1999, *Quantum Chaos: An Introduction*, Cambridge University Press, Cambridge.
- Zaslavsky G.M., 1981, Stochasticity in quantum systems, *Phys. Rep.*, **80**, 157–250.
- Zaslavsky G.M., 2005, *Hamiltonian Chaos and Fractional Dynamics*, Oxford University Press, Oxford.

# Chapter 5

## Using Stochastic Webs to Control the Quantum Transport of Electrons in Semiconductor Superlattices

T.M. Fromhold<sup>1</sup>, A.A. Krokhin<sup>2</sup>, S. Bujkiewicz<sup>1,3</sup>, P.B. Wilkinson<sup>1,4</sup>, D. Fowler, A. Patanè<sup>1</sup>, L. Eaves<sup>1</sup>, D.P.A. Hardwick<sup>1</sup>, A.G. Balanov<sup>5</sup>, M.T. Greenaway<sup>1</sup>, A. Henning<sup>1</sup>

**Abstract** We show that electrons in a semiconductor superlattice can be used to realize and exploit the unique dynamics of the driven harmonic oscillator that were discovered and explored by George Zaslavsky and colleagues. Under the action of an electric and tilted magnetic field, the semiclassical dynamics of electrons in an energy band of the superlattice exhibit non-KAM chaos, which strongly affects the electrical conductivity. At certain critical field parameters, the electron trajectories change abruptly from fully localized to completely unbounded, and map out intricate stochastic webs in phase space, which act as conduction channels for the electrons. Delocalization of the electron paths produces a series of strong resonant peaks in the electron drift velocity versus electric field curves. We use these drift velocity characteristics to make self-consistent drift-diffusion calculations of the current-voltage and differential conductance-voltage curves of the superlattices, which agree well with our experimental data and reveal strong resonant features originating from the sudden delocalization of the stochastic single-electron paths. We show that this delocalization has a pronounced effect on the distribution of space charge and electric field domains within the superlattices. Inter-miniband tunneling greatly reduces the amount of space-charge buildup, thus enhancing the domain structure and both the strength and number of the current resonances.

---

<sup>1</sup>School of Physics & Astronomy, University of Nottingham, Nottingham NG7 2RD, UK  
e-mail: mark.fromhold@nottingham.ac.uk

<sup>2</sup>Department of Physics, University of North Texas, P.O. Box 311427, Denton, TX 76203, USA

<sup>3</sup>Present address: Centre for Biostatistics and Genetic Epidemiology, Department of Health Sciences, University of Leicester, University Road, Leicester LE1 7RH, UK

<sup>4</sup>Present address: British Geological Survey, Kingsley Dunham Centre, Keyworth NG12 5GG, UK

<sup>5</sup>Department of Physics, Loughborough University, Leicestershire, LE11 3TU, UK

## 5.1 Introduction

In this chapter, we show how the intricate phase space structure of the driven harmonic oscillator (Sagdeev et al., 1998; Vasiliev et al., 1989; Beloshapkin et al., 1989; Zaslavsky et al., 1991; Shlesinger et al., 1993; Zaslavsky et al., 2004; Luo, 2004; Kamenev and Berman, 2000; Karney and Bers, 1977; Chia et al., 1996; Gardiner et al., 1997; Demikhovskii et al., 1999, 2002; Robnik and Romanovski, 2008; Soskin et al., 2009b), which was identified and extensively studied by George Zaslavsky and co-workers (Sagdeev et al., 1998; Vasiliev et al., 1989; Beloshapkin et al., 1989; Zaslavsky et al., 1991; Shlesinger et al., 1993; Zaslavsky et al., 2004; Luo, 2004; Kamenev and Berman, 2000), can greatly enhance electron transport in semiconductor superlattices (SLs) (Wacker, 2002; Esaki and Tsu, 1970; Shik, 1975; Ignatov et al., 1991; Kastrup, 1994; Canali et al., 1996; Zhang et al., 1996; Alekseev et al., 1996; Luo et al., 1998; Schomburg et al., 1998; Schöll, 2001; Amann et al., 2002; Alekseev and Kusmartsev, 2002; Patanè et al., 2002; Shimada et al., 2003; Savvidis et al., 2004; Raspopin et al., 2005; Bonilla and Grahn, 2005; Fromhold et al., 2001; Kuraguchi et al., 2002; Fromhold et al., 2004; Stapleton et al., 2004; Hardwick et al., 2006; Kosevich et al., 2006; Fowler et al., 2007; Balanov et al., 2008; Soskin et al., 2009a; Greenaway et al., 2009; Hyart et al., 2009; Hardwick, 2007). In particular, we show that the electrical current through the SL can be modulated by using an applied bias voltage and a tilted magnetic field to switch on and off stochastic web patterns, which thread the electron phase space and act as a network of conduction channels through which the electrons can propagate in real space. When the web is switched on, the electrons can undergo chaotic diffusive motion along its filaments, thereby producing a sharp increase in the measured and calculated current flow. Consequently, non-KAM chaos provides a new and, in principle, extremely sensitive mechanism for controlling SL conductivity (Fromhold et al., 2001; Kuraguchi et al., 2002; Fromhold et al., 2004; Stapleton et al., 2004; Hardwick et al., 2006; Kosevich et al., 2006; Fowler et al., 2007; Balanov et al., 2008; Soskin et al., 2009a; Greenaway et al., 2009; Hyart et al., 2009; Hardwick, 2007).

In semiconductor physics, chaotic electron transport has been explored using a variety of 2-dimensional billiard structures (Stöckmann, 1999; Nakamura and Harayama, 2003; Marcus et al., 1992; Chang et al., 1994; Folk et al., 1996; Ketzmerick, 1996; Sachrajda et al., 1998; Bird et al., 1999; Micolich et al., 2001; Marlow et al., 2006), antidot arrays (Stöckmann, 1999; Nakamura and Harayama, 2003; Weiss et al., 1991; Fleischmann et al., 1992; Weiss et al., 1993), SLs (Kastrup, 1994; Zhang et al., 1996; Alekseev et al., 1996; Luo et al., 1998) and resonant tunneling diodes containing a wide quantum well enclosed by two tunnel barriers (Stöckmann, 1999; Fromhold et al., 1994, 1995a,b; Shepelyansky and Stone, 1995; Müller et al., 1995; Wilkinson et al., 1996; Monteiro and Dando, 1996; Fromhold et al., 1997a,b; Monteiro et al., 1997a,b; Narimanov et al., 1998; Narimanov and Stone, 1998a,b; Saraga and Monteiro, 1998a; Saraga et al., 1998; Saraga and Monteiro, 1998b; Bogomolny and Rouben, 1998, 1999; Fromhold et al., 2002). Figure 5.1 shows a schematic diagram of a quantum well formed by molecular beam epitaxy (MBE) in which layers of undoped GaAs (salmon) and (AlGa)As or AlAs (blue) are alternatively deposited

on a heavily-doped GaAs substrate (yellow). Each layer of (AlGa)As acts as a potential barrier to electron motion perpendicular to the plane of the layers. Between the barriers there is a GaAs quantum well, whose interfaces are flat to the precision of a single atomic layer.

Despite the diversity of experimental studies of quantum chaos in semiconductor nanostructures, they all involve systems in which the transition to chaos occurs by the gradual and progressive destruction of stable orbits in response to an increasing perturbation. To illustrate this, Fig. 5.2 shows Poincaré sections calculated for electrons in the 30 nm wide quantum well of a resonant tunneling diode with a magnetic field  $\mathbf{B}$  tilted at an angle  $\theta$  to the normal to the well walls, i.e. to the  $x$ -axis (Fromhold et al., 2002). The scattered points indicate the momentum components  $p_y$  and  $p_z$  in the plane of the well for each bounce of the electron off the left-hand barrier. When

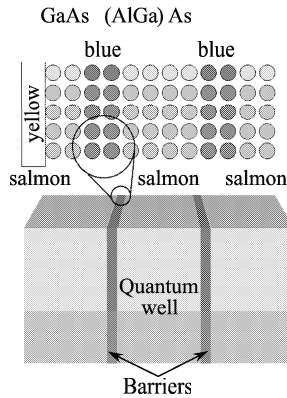


**Fig. 5.1** Schematic diagram of a semiconductor quantum well structure fabricated by molecular beam epitaxy. Upper part of figure: schematic illustration of the deposition of atoms onto a semiconductor substrate (yellow) to form layers of GaAs (salmon) and (AlGa)As (blue). Lower part of figure: the GaAs layers form a square quantum well enclosed by two (AlGa)As tunnel barriers.

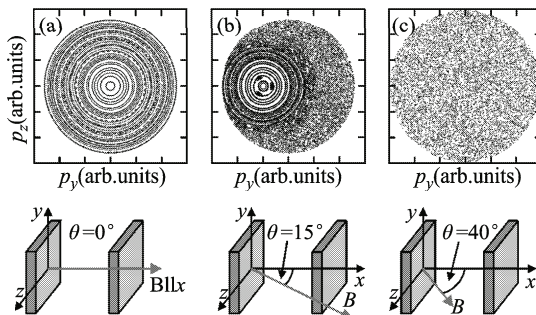


**Fig. 5.2** Black dots: Poincaré sections calculated by plotting the momentum components ( $p_y, p_z$ ) each time an electron collides with the left-hand barrier of a 30 nm wide quantum well (barriers, shown by shaded shapes in lower part of figure, lie in the  $y-z$  plane) with a magnetic field  $B=12$  T applied at an angle  $\theta =$  (a)  $0^\circ$ , (b)  $15^\circ$  and (c)  $40^\circ$  to the  $x$ -axis (Fromhold et al., 2002).

$\theta = 0^\circ$  (see Fig. 5.2(a)), the points lie on a series of concentric circles because the electrons undergo cyclotron motion in the plane of the well (Fromhold et al., 2002). As  $\theta$  increases from  $0^\circ$ , the regular parts of the phase space slowly shrink. When  $\theta = 15^\circ$  (see Fig. 5.2(b)), there is a mixed stable-chaotic phase space in which the islands of stability are surrounded by a chaotic sea. But when  $\theta$  reaches  $40^\circ$  (see Fig. 5.2(c)), all stable islands have disappeared, leaving only a chaotic sea, which corresponds to strongly chaotic classical trajectories (Fromhold et al., 2002). This gradual onset of chaos occurs for all systems used in previous quantum chaos experiments, which obey the KAM theorem (Fromhold et al., 2001, 2004; Stöckmann, 1999).

However, by connecting a series of quantum wells together to form a superlattice, it is possible to create a much rarer type of “weak” chaos—studied by Zaslavsky and co-workers (Sagdeev et al., 1998; Vasiliev et al., 1989; Beloshapkin et al., 1989; Zaslavsky et al., 1991; Shlesinger et al., 1993; Zaslavsky et al., 2004; Luo, 2004; Kamenev and Berman, 2000) for driven harmonic oscillator systems that do not obey the KAM theorem—which is characterized by abrupt delocalization of the classical paths. The theory of such “non-KAM” chaos is of great interest due to diverse applications in, for example, plasma physics, tokamak fusion, turbulent fluid dynamics, ion traps, quasicrystals and ultra-cold atoms in optical lattices (Sagdeev et al., 1998; Vasiliev et al., 1989; Beloshapkin et al., 1989; Zaslavsky et al., 1991; Shlesinger et al., 1993; Zaslavsky et al., 2004; Luo, 2004; Kamenev and Berman, 2000; Karney and Bers, 1977; Chia et al., 1996; Gardiner et al., 1997; Demikhovskii et al., 1999, 2002; Robnik and Romanovski, 2008; Soskin et al., 2009b; Hensinger et al., 2001; Steck et al., 2001; Scott et al., 2002). However, it has proven difficult to realize and explore the rich phase space structure of a driven harmonic oscillator in experiment.

In the next section, we describe the growth and structure of semiconductor SLs and describe their unique energy band structure, which enables the creation of non-KAM chaos for semiclassical trajectories generated by the bands. The physics of non-KAM chaos in this experimentally-realizable system may have wider relevance by providing new insights into more exotic areas of research, for example the quantum dynamics of ultracold atoms in a laser field.

## 5.2 Superlattice structures

SLs comprise alternating layers of two or more different semiconductor materials, which produce a sandwich-like structure containing a series of quantum wells, as shown schematically in Fig. 5.3(a) for a GaAs/(AlGa)As SL (Wacker, 2002). The layer structure produces a periodic square potential (see Fig. 5.3(b)) for conduction electrons moving along the  $x$ -direction perpendicular to the layers, which are typically between 1 and 10 nm thick. Usually, a SL contains a chain of between 10 and 100 quantum wells, though in Fig. 5.3 we only shown 3 wells for clarity. Tunneling through the barriers couples the wells and thereby broadens their quantized energy

levels into bands, known as “minibands” (Wacker, 2002). The blue rectangles in Fig. 5.3(b) show schematically the energy range of the two lowest minibands.

To observe non-KAM chaos, we used two different SL structures. In this section, we focus on the first type of structure, henceforth known as SL1, whose composition is described in detail elsewhere (Patanè et al., 2002; Fromhold et al., 2004). We describe the second SL structure (SL2) in Sect. 5.7. SL1 has a spatial period  $a = 8$  nm and contains 14 QWs. The density of  $n$ -type doping in the SL layers is  $N = 3 \times 10^{16} \text{ cm}^{-3}$ . The solid black curve in Fig. 5.4 shows the potential energy of an electron at the conduction band edge versus position  $x$  through the SL. For clarity, only 3 of the 14 quantum wells are shown. The unusual feature of this SL is that at

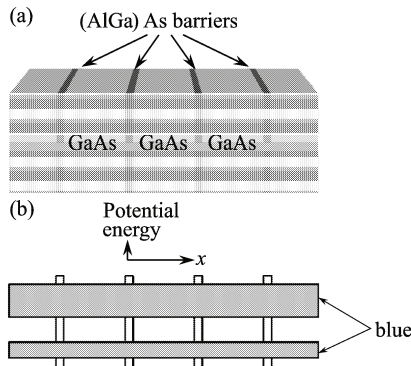


**Fig. 5.3** (a) Schematic diagram of a semiconductor SL formed by epitaxial growth of a series of quantum wells (only three shown for simplicity). (b) Electron potential energy versus position,  $x$ , through the SL. Blue areas represent the two lowest minibands for electron motion along  $x$ .

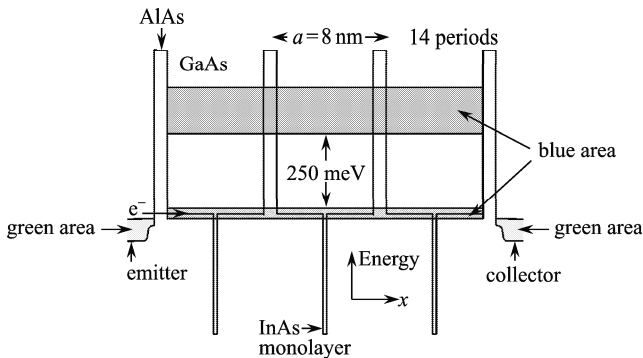


**Fig. 5.4** Schematic variation of the electronic potential energy with position  $x$  through GaAs/AlAs/InAs SL1. The AlAs layers act as potential barriers and the InAs monolayer produces a square potential notch at the center of the GaAs quantum well. Blue areas represent the two lowest minibands, which are separated by a large energy gap of 250 meV. Green areas represent electron gases in the emitter and collector contacts. Electrons are injected from the emitter (left-hand) contact into the lowest miniband. Further details of SL1 are given in (Patanè et al., 2002; Fromhold et al., 2004).

the center of each GaAs quantum well, there is an InAs monolayer, which produces a notch in the conduction band edge. Since this notch coincides with the antinode in the ground state wavefunction of the quantum well, its effect is to lower the energy of the first miniband (lower blue rectangle in Fig. 5.4) down to the bottom of the quantum well (Patanè et al., 2002). This ensures that the edge of the miniband lies close to the chemical potential in the emitter contact (left-hand green region in Fig. 5.4), which facilitates electron injection.

By contrast, the InAs layer has almost no effect on the energy of the second miniband (upper blue rectangle in Fig. 5.4) because it is located at the node in the first excited state of the quantum well.

We now consider more quantitatively the effect of the InAs layer on the miniband energies. To do this, Fig. 5.5 shows energy versus crystal momentum,  $p_x$ , dispersion relations calculated for the first and second minibands of SL1 containing the InAs layer (red curves) and for a SL that is identical except that the InAs layer is replaced by GaAs (black curves) (Patanè et al., 2002; Fromhold et al., 2004). The dispersion relations are shown within the first Brillouin zone of the SL, whose width is inversely proportional to the SL period,  $a$ . Since  $a$  greatly exceeds the lattice constant of bulk GaAs, the SL Brillouin zone is much smaller than for bulk GaAs and is therefore known as a minizone. Comparison of the red and black curves in Fig. 5.5 reveals that including the InAs layer lowers the first miniband by approximately 70 meV, but has almost no effect on the second miniband. Consequently, the InAs layer has two key effects. Firstly it lowers the first miniband, which facilitates electron injection into the miniband from the emitter contact. Secondly, it increases the miniband gap energy (separation between the first and second minibands) to 250 meV, which reduces inter-miniband tunneling when a bias voltage is applied to the SL, thus ensuring that a single band transport picture is appropriate.

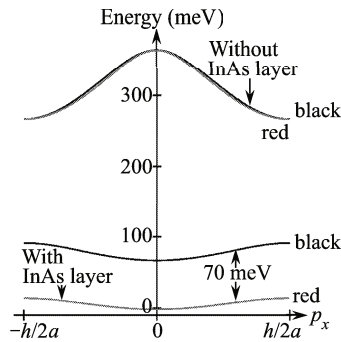


**Fig. 5.5** Red curves: energy versus crystal momentum,  $p_x$ , dispersion relations calculated for the two lowest minibands of the GaAs/AlAs/InAs SL1 shown in Fig. 5.4. Black curves: energy versus  $p_x$  curves calculated for the two lowest minibands of a SL that is identical to SL1 except that the InAs monolayer is replaced by GaAs.

### 5.3 Semiclassical electron dynamics

In this section we consider the semiclassical dynamics of an electron confined to the lowest miniband of SL1. The miniband states are delocalized Bloch functions specified by the crystal momentum  $\mathbf{p} = (p_x, p_y, p_z)$ . Within the tight-binding approximation, the energy-crystal momentum dispersion relation for the lowest miniband is  $E(\mathbf{p}) = \Delta[1 - \cos(p_x a/\hbar)]/2 + (p_y^2 + p_z^2)/2m^*$ , where  $\Delta = 19$  meV is the miniband width and  $m^*$  (equal to 0.067 times the free electron mass) is the electronic effective mass for motion in the  $y-z$  plane. The crystal momentum component,  $p_x$ , lies within the first SL minizone.

The electron moves under the action of an electric field  $\mathbf{F} = (-F, 0, 0)$ , applied anti-parallel to the  $x$  axis, created by a voltage,  $V$ , applied between the emitter and collector contacts, and a tilted magnetic field  $\mathbf{B} = (B \cos \theta, 0, B \sin \theta)$  (Fig. 5.6 inset). In a semiclassical picture, the force produced by  $\mathbf{F}$  and  $\mathbf{B}$  changes the electron's crystal momentum at a rate

$$\frac{d\mathbf{p}}{dt} = -e[\mathbf{F} + (\nabla_{\mathbf{p}}E(\mathbf{p}) \times \mathbf{B})], \quad (5.1)$$

where  $e$  is the electronic charge. In component form, Equation (5.1) can be written as

$$\dot{p}_x = eF - \bar{\omega}_c p_y \tan \theta, \quad (5.2)$$

$$\dot{p}_y = \frac{a\Delta m^* \bar{\omega}_c}{2\hbar} \sin\left(\frac{p_x a}{\hbar}\right) \tan \theta - \bar{\omega}_c p_z, \quad (5.3)$$

$$\dot{p}_z = \bar{\omega}_c p_y, \quad (5.4)$$

where the left-hand terms are time derivatives of the crystal momentum components and  $\bar{\omega}_c = eB \cos \theta / m^*$  is the cyclotron frequency corresponding to the magnetic field component along the  $x$ -axis. It follows from Eqs. (5.2)–(5.4) that

$$\ddot{p}_z + \bar{\omega}_c^2 p_z = C \sin(Kp_z - \omega_B t - \phi), \quad (5.5)$$

where  $C = (-m^* \bar{\omega}_c^2 a \Delta \tan \theta) / 2\hbar$ ,  $K = a \tan \theta / \hbar$ , and  $\omega_B = eFa/\hbar$  is the Bloch frequency. The phase,  $\phi = a(p_x(t=0) + p_z(t=0) \tan \theta) / \hbar$ , depends on the initial conditions and equals zero for electrons starting from rest (Fromhold et al., 2001, 2004). In the absence of scattering, Equation (5.5) fully describes the electron motion because its solution,  $p_z(t)$ , uniquely determines all of the other dynamical variables, in particular the electron orbits in real space (Fromhold et al., 2004). Consequently, the dynamics of a miniband electron in a tilted  $\mathbf{B}$ -field are exactly equivalent to a 1-dimensional driven harmonic oscillator: a text book system that exhibits non-KAM chaos and is characterized by intricate phase space patterning, as we discuss below (Sagdeev et al., 1998; Vasiliev et al., 1989; Beloshapkin et al., 1989; Zaslavsky et al., 1991; Shlesinger et al., 1993; Zaslavsky et al., 2004; Luo, 2004; Kamenev and Berman, 2000; Karney and Bers, 1977; Chia et al., 1996; Gardiner et al., 1997; Demikhovskii et al., 1999, 2002; Robnik and Romanovski, 2008; Soskin

et al., 2009b). The system does not obey the KAM theorem because the harmonic oscillator is degenerate as, physically, its oscillation frequency is independent of energy.

Equation (5.5) reveals that even though the applied electric and magnetic fields are stationary, they act like a time-dependent monochromatic wave. In Eq. (5.5), the amplitude of the plane wave can be increased by increasing  $B$  and/or the mini-band width,  $\Delta$ , and is maximal when  $\theta = 45^\circ$ . The wavenumber and THz-range angular frequency of the plane wave can be controlled independently by changing  $\theta$  and  $F$  respectively. This is a crucial difference from cyclotron motion driven by an electromagnetic wave whose wavenumber and frequency cannot, of course, be independently tuned.

In our analysis, we first solve Eq. (5.5) numerically to obtain  $p_z(t)$ , which we then use to determine the other crystal momentum components (see (Balanov et al., 2008; Hardwick, 2007) for details)

$$\begin{aligned} p_x &= p_x(t=0) + eFt - (p_z - p_z(t=0)) \tan \theta, \\ p_y &= \frac{\dot{p}_z}{\bar{\omega}_c}, \end{aligned} \quad (5.6)$$

and the electron velocity components

$$\dot{x} = \frac{a\Delta}{2\hbar} \sin(Kp_z - \omega_B t + \phi), \quad \dot{y} = \frac{\dot{p}_z}{\bar{\omega}_c m^*}, \quad \dot{z} = \frac{p_z}{m^*}. \quad (5.7)$$

We now consider electron orbits in the  $x-z$  plane, in which the magnetic field lies (Fig. 5.6 inset), calculated for field values  $F = 3.6 \times 10^6 \text{ Vm}^{-1}$  and  $B = 11 \text{ T}$  taken from experiment (Fromhold et al., 2004). Qualitatively similar trajectories occur for a wide range of other field parameters. When  $\theta = 0^\circ$ , the plane wave on the right-hand side of Eq. (5.5) has zero amplitude, which means that the  $x-z$  motion is separable. Consequently, the electrons execute cyclotron motion about the magnetic field ( $x$ -) axis, and Bloch oscillations along the  $x$ -direction with a peak-to-peak amplitude equal to  $\Delta/eF$ . The Bloch and cyclotron orbits add to produce a regular bounded trajectory in the  $x-z$  plane, which resembles a Lissajous figure (see Fig. 5.6(a)). When  $\theta$  is increased to  $30^\circ$ , the harmonic oscillator on the left-hand side of Eq. (5.5) is only weakly perturbed by the plane wave driving term on the right-hand side. The electron orbits therefore remain stable and regular (see Fig. 5.6(b)) and are qualitatively similar to the cyclotron-Bloch oscillations shown in Fig. 5.6(a). For  $\theta = 45^\circ$ , the plane wave in Eq. (5.5) has maximal amplitude. As a consequence, it strongly perturbs the harmonic oscillator and thus drives some of the electron orbits chaotic (see Fig. 5.6(c)). Although these chaotic trajectories extend across approximately 10 periods, they remain localized within a finite range of the SL axis. But if  $\theta$  is increased to  $60^\circ$  so that  $\omega_B = 3\bar{\omega}_c$ , the chaotic orbits are no longer bounded and extend arbitrarily far through the SL (see Fig. 5.6(d)).

Figure 5.7 shows a 3-dimensional representation of the unbounded chaotic orbit followed by an electron starting from rest when  $\omega_B = 3\bar{\omega}_c$ . The tube lies along the electron trajectory and changes color from green to red as time increases. Initially,

the orbit weaves a basket-like pattern (predominantly colored green) towards the left-hand side of the figure. But eventually, the electron breaks away from this trajectory and follows the more open cyclotron-like path (red) towards the right-hand side of the figure.

More generally, the chaotic orbits are unbounded whenever  $\omega_B = r\bar{\omega}_c$ , where  $r$  is an integer. When this resonance condition is satisfied, the electron trajectories map

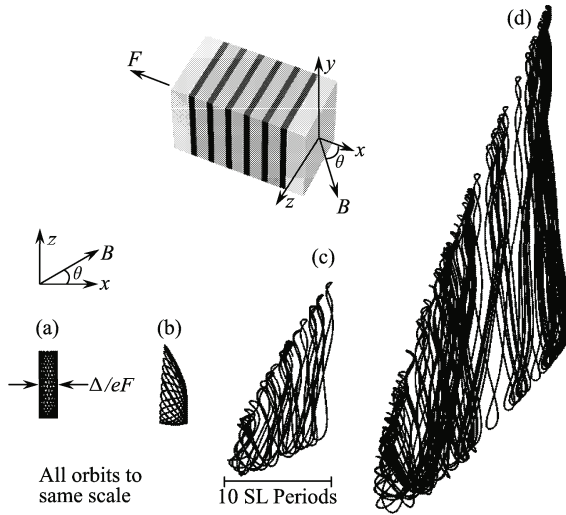


**Fig. 5.6** Electron orbits in the  $x-z$  plane (axes inset) calculated for SL1 with  $F = 3.6 \times 10^6 \text{ Vm}^{-1}$ ,  $B = 11 \text{ T}$  and  $\theta =$  (a)  $0^\circ$  showing peak-to-peak amplitude ( $\Delta/eF$ ) of Bloch oscillations, (b)  $30^\circ$ , (c)  $45^\circ$ , (d)  $60^\circ$  (corresponding to  $r = 3$  resonance). Inset: schematic diagram showing orientation of co-ordinate axes,  $\mathbf{F}$ , and  $\mathbf{B}$  relative to SL layers (shaded).

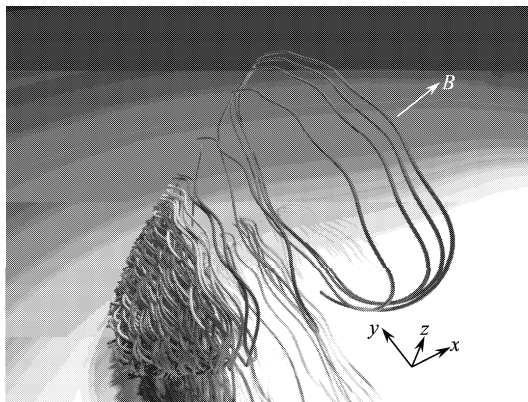


**Fig. 5.7** 3-dimensional representation (axes and orientation of  $\mathbf{B}$  shown inset) of an unbounded chaotic trajectory, which lies at the center of the colored tube, calculated for SL1 when  $\omega_B = 3\bar{\omega}_c$ . As time increases, the color of the orbit changes from green to red. (color plot in the book end)

out intricate stochastic web patterns (Sagdeev et al., 1998; Vasiliev et al., 1989; Beloshapkin et al., 1989; Zaslavsky et al., 1991; Shlesinger et al., 1993; Zaslavsky et al., 2004; Luo, 2004; Kamenev and Berman, 2000; Karney and Bers, 1977; Chia et al., 1996; Gardiner et al., 1997; Demikhovskii et al., 1999, 2002; Robnik and Romanovski, 2008; Soskin et al., 2009b) in the phase space of the underlying driven harmonic oscillator (see Eq. (5.5)). The stochastic web shown in Fig. 5.8(a) corresponds to the  $r = 3$  resonance and is constructed by plotting the momentum components  $p_y \propto \dot{p}_z$  and  $p_z$  at discrete equally-spaced times (Fromhold et al., 2001, 2004; Hardwick, 2007). Since the width of the filaments decreases exponentially with distance from the web center (Zaslavsky et al., 1991), we have used orbits with several different initial conditions to construct the filaments. The filaments of the stochastic web are extensions of the chaotic sea visible at the center of the Poincaré section, where the electrons have low energy and momentum and are therefore strongly perturbed by the plane wave in Eq. (5.5).

Of crucial importance for understanding the significance of this phase space structure is that the distance of each point from the center of the web is proportional to  $\sqrt{x}$  (Fromhold et al., 2004). So as the electron travels further through the SL, it produces points further from the center of the section (Fromhold et al., 2004). The electrons are driven out along the radial filaments of the web by the resonant absorption of energy from the plane wave in Eq. (5.5), and so progress rapidly through the SL. Physically, as the electron moves through the SL down the potential energy gradient created by  $\mathbf{F}$ , the kinetic energy that it gains from  $\mathbf{F}$  is transferred into the  $y - z$  plane by the tilted  $\mathbf{B}$ -field. Consequently, the electron's  $y - z$  momentum increases and, as it does so, the electron moves away from the central part of the stochastic web along one of the six radial filaments. Since the web extends to infinity, the chaotic electron orbits are unbounded on resonance and should therefore produce a large direct current. But moving  $F$  slightly off resonance destroys the stochastic web by breaking the radial filaments (see Fig. 5.8(b)). This localizes the electron orbits spatially (see Fig. 5.6(c)) and should therefore suppress the current flow.

Consequently, non-KAM chaos provides a new and, in principle, extremely sensitive mechanism for modulating the electrical conductivity of a SL. Indeed, in the absence of scattering, stochastic web formation would change the SL from an insulator to a conductor at discrete field values for which the resonance condition  $\omega_B = r\bar{\omega}_c$  ( $r = 1, 2, 3, \dots$ ) is satisfied.

## 5.4 Electron drift velocity

In a real semiconductor device, the electrons are scattered by phonons, charged impurities, and roughness of the interfaces between the barriers and quantum wells. However, at low temperatures and high electric fields, conduction electrons have mean free paths  $l \gg a$  and, for short period SLs, comparable to the entire width of the SL layer region. This regime is called the quasi-ballistic domain.

In polar semiconductors such as GaAs and AlAs, an important electron scattering mechanism is scattering by longitudinal optic (LO) phonons of energy  $\hbar\omega_L$ . By carrying out experiments at low temperatures, we eliminate the LO phonon “absorption” transitions. By designing our SL with  $\Delta < \hbar\omega_L$ , we can also greatly reduce the effect of LO phonon emission (except by a small number of hot electrons in the upper miniband, which could relax into the lower miniband by LO phonon emission). Therefore, in any realistic model of the electrical properties of a SL in the non-KAM chaos regime, we need to include the effects of scattering. We do this by using the velocity integral method (Esaki and Tsu, 1970).

Specifically, to quantify the effect of stochastic-web-assisted transport on the electrical characteristics of real SL structures, we used the semiclassical trajectories to calculate the electron drift velocity

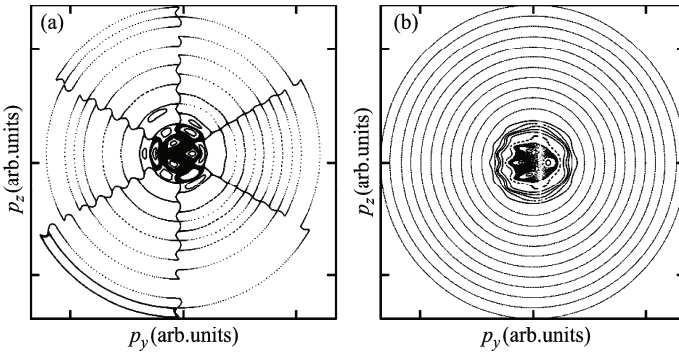


**Fig. 5.8** Poincaré sections showing electron momentum components ( $p_y, p_z$ ) plotted at time intervals of  $2\pi/\omega_c$  (a) on resonance ( $r = 3$ ) showing stochastic web, (b) off resonance ( $r$  irrational) showing sea of chaos bounded by islands of stability (Fromhold et al., 2001).

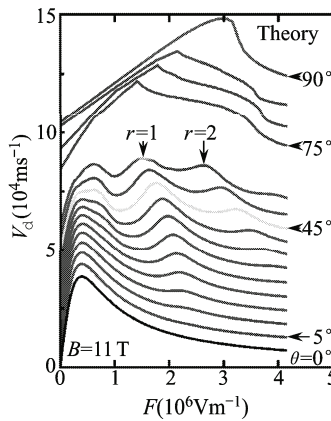


**Fig. 5.9**  $v_d(F)$  curves calculated for SL1 with  $B = 11 \text{ T}$ , and  $\theta = 0^\circ$  (bottom trace) to  $90^\circ$  (top trace) at  $5^\circ$  intervals. Curves for  $\theta = 60^\circ$  to  $70^\circ$  are omitted. Arrows mark  $r = 1$  and  $r = 2$  resonant peaks created by chaos-assisted transport through stochastic webs.

$$v_d = \frac{1}{\tau} \int_0^{\infty} \exp\left(\frac{-t}{\tau}\right) v_x(t) dt, \quad (5.8)$$

where the electron scattering time,  $\tau$ , determined from experiment, includes contributions from both elastic and inelastic scattering processes (Fromhold et al., 2004) and  $v_x(t) = \dot{x}$  is determined from Eqs. (5.5) and (5.7). Figure 5.9 shows  $v_d(F)$  curves calculated using Eq. (5.8) for  $\theta = 0^\circ$  (bottom trace) to  $90^\circ$  (top trace) at  $5^\circ$  intervals.

When  $\theta = 0^\circ$  (lower curve in Fig. 5.9), the  $v_d(F)$  curve is identical to that predicted by the famous Esaki-Tsu model (Esaki and Tsu, 1970). The peak drift velocity occurs when  $\omega_B \tau = 1$  because, then, the electron scatters approximately half-way up the miniband where the electron velocity is maximal. As  $F$  increases beyond the Esaki-Tsu peak, more and more electrons complete Bloch oscillations before scattering, which increasingly localizes their trajectories, thus reducing  $v_d$ .

When  $\theta = 90^\circ$  (upper curve in Fig. 5.9) the electron orbits remain regular but the peak  $v_d$  value occurs at higher  $F$  than for  $\theta = 0^\circ$ . This shift of the peak position occurs because the magnetic field bends the electron trajectory, thereby reducing the average electron velocity along the SL axis. As a result,  $F$  must be increased in order for  $v_d$  to attain its maximal value (Fromhold et al., 2001).

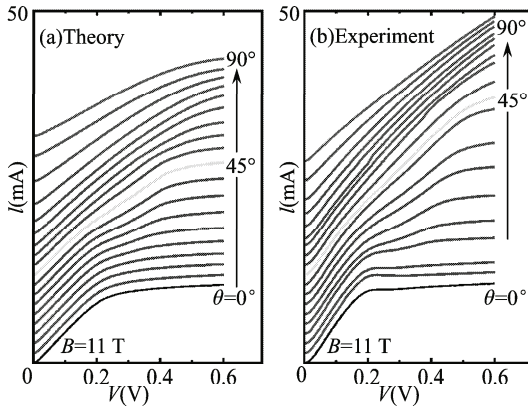
As  $\theta$  increases from  $0^\circ$  to  $55^\circ$ , additional peaks emerge in the  $v_d(F)$  curves at  $F$  values (marked by arrows in Fig. 5.9) for which  $\omega_B = r\omega_c$ , where  $r = 1$  or  $2$ . When this resonance condition is satisfied, the electron phase space is threaded by a stochastic web, which delocalizes the electron trajectories spatially (see Fig. 5.6(d)), and therefore enhances  $v_d$ . The positions of the resonant peaks in the  $v_d(F)$  curves can be altered by simply changing  $\theta$ .

## 5.5 Current-voltage characteristics: theory and experiment

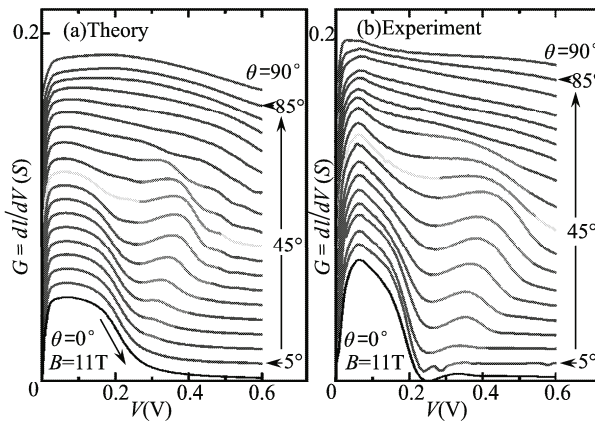
In this section, we consider how the resonances in  $v_d(F)$  that result from the formation of stochastic webs in the electron phase space manifest themselves in the current-voltage,  $I(V)$ , characteristics of the SL measured in experiment and simulated theoretically. In our theoretical analysis, we used the  $v_d(F)$  curves as a basis for making drift-diffusion calculations of the  $I(V)$  characteristics of SL1. These calculations involve obtaining self-consistent solutions of the Poisson and current continuity equations throughout the SL (Fromhold et al., 2004; Greenaway et al., 2009).

Figure 5.10(a) shows  $I(V)$  curves calculated for  $\theta = 0^\circ$  (bottom trace) to  $90^\circ$  (top trace). The curves are offset vertically and shown at  $5^\circ$  intervals. When  $\theta = 0^\circ$  and  $90^\circ$ , the calculated  $I(V)$  curves are knee shaped: approximately linear at low  $V$  and then flattening when  $V$  becomes high enough for  $F$  to reach the Esaki-Tsu peak in  $v_d(F)$  (lower trace in Fig. 5.9). In each case, at high  $V$ ,  $I$  is almost constant because the decrease in  $v_d(F)$  that occurs at high  $F$  is compensated by an increase in the number of conduction electrons in the miniband, as we explain further in Sects. 5.6 and 5.7.

For  $0^\circ \leq \theta \leq 55^\circ$ , the slope of each  $I(V)$  curve increases when  $V$  reaches  $\approx 250$  mV both in our calculations (see Fig. 5.10(a)) and in the corresponding experimental data (see Fig. 5.10(b)) measured at a lattice temperature  $T = 4.2$  K. When  $V$  increases above  $\approx 250$  mV, there is a region of enhanced current, which gives rise to a strong resonant peak (red in Fig. 5.11) in the differential conductance  $G = dI/dV$  versus  $V$  curves that are calculated (see Fig. 5.11(a)) and measured experimentally (see Fig. 5.11(b)). The amplitude of the resonant peak decreases as  $\theta$  approaches  $0^\circ$ , where the small remnant feature shown at  $V \approx 325$  mV in the lower trace of Fig. 5.11(b) is a Stark-cyclotron resonance, originating from weak elastic scattering be-



**Fig. 5.10**  $I(V)$  curves (a) calculated and (b) measured at  $T = 4.2$  K for SL1 with  $B = 11$  T, and  $\theta = 0^\circ$  (bottom trace) to  $90^\circ$  (top trace) at  $5^\circ$  intervals.



**Fig. 5.11**  $G(V)$  curves (a) calculated and (b) measured at  $T = 4.2$  K for SL1 with  $B = 11$  T, and  $\theta = 0^\circ$  (bottom trace) to  $90^\circ$  (top trace) at  $5^\circ$  intervals. Curves for  $\theta = 0^\circ, 45^\circ$ , and  $90^\circ$  are shown black, green, and brown, respectively. The  $G(V)$  curves reveal strong resonant peaks (red). Arrow in (a) indicates region of decreasing conductance associated with the onset of Bloch oscillations (color plot in the book end).

tween the quantized states produced by  $\mathbf{B} \parallel \mathbf{F}$  (Canali et al., 1996). The electric field quantizes the energy associated with motion along the SL axis into a Wannier-Stark ladder. Neighboring levels are equally spaced by  $\hbar\omega_B$ . Motion in the  $y-z$  plane is quantized by the magnetic field into Landau levels, separated by  $\hbar\bar{\omega}_c$ . At the applied voltage for which the Wannier-Stark and Landau levels are equally spaced, the electrons can undergo elastic scattering between the lowest Wannier-Stark states in adjacent quantum wells and, during each scattering event, the Landau level index increases by 1 to ensure energy conservation. This process is related to inter-Landau-level transitions in a single quantum well with a tilted magnetic field applied (Leadbeater et al., 1989, 1991).

The Stark-cyclotron resonance observed when  $\theta = 0^\circ$  has a *purely quantum mechanical* origin because it requires energy level quantization. By contrast, the much stronger resonant peak observed in  $G(V)$  when  $\theta \neq 0^\circ$  can be explained within a semiclassical miniband transport model and originates from non-KAM chaos. In both the theory and experiment, this peak occurs near the bias voltage for which  $\omega_B = \bar{\omega}_c$ , which means that the phase space is threaded by a stochastic web. The electrons undergo rapid diffusive motion through the web and through the SL itself, thereby generating the resonant peak in both the calculated and measured  $G(V)$  curves. This result demonstrates that chaos-assisted transport through stochastic-webs, which has been of great theoretical interest since the pioneering work of Zaslavsky and co-workers in the mid 1980s (Sagdeev et al., 1998; Vasiliev et al., 1989; Beloshapkin et al., 1989; Zaslavsky et al., 1991), can strongly affect and control the electrical behavior of a real semiconductor device.

Despite the good quantitative agreement between theory and experiment, the form of the  $I(V)$  curves in Fig. 5.10 is, at first sight, surprising for the following reason. If  $F$  is uniform throughout the SL and proportional to  $V$ ,  $I(V) = ANev_d(F)$ , where  $A$  is the cross-sectional area of the SL. This means that the  $I(V)$  curves should have exactly the same shape as the  $v_d(F)$  curves shown in Fig. 5.9 and therefore contain two strong resonant peaks when  $\theta \approx 45^\circ$ . But, as is clear from Fig. 5.10, the  $I(V)$  curves do *not* have the same form  $v_d(F)$ . Indeed, we have to differentiate the  $I(V)$  curves in order to observe clear resonant peaks and, even then, we only see a single peak in the  $G(V)$  curves when  $\omega_B = \bar{\omega}_c$ .

The reason for this difference is that  $F$  is *not* uniform throughout the SL, as we explain in the next section.

## 5.6 Electrostatics and charge domain structure

To illustrate the highly non-uniform electric field profile through SL1, the surface plot in Fig. 5.12(a) shows  $r = \omega_B/\bar{\omega}_c \propto F$  calculated as a function of  $V$  and position ( $x$ ) through the SL from the emitter contact (Position 0 nm) to the collector contact (Position 120 nm) when  $\theta = 45^\circ$ . The most striking feature of this surface plot is the dramatic increase of  $F$ , which occurs towards the collector contact at high  $V$ . This increase occurs because  $v_d$  decreases monotonically at high  $F$  (5.9). As electrons

start to build up in the SL layers, they make  $F$  increase with position through the SL. When  $F$  becomes high enough, this reduces the local electron drift velocity, and so the density of electrons,  $n_d$ , must increase in order to maintain current continuity through the SL. This accumulation of electrons, which appears as the large spike in the surface plot of  $n_d$  versus  $V$  and position shown in Fig. 5.12(b), further increases  $F$ , making it highly non-uniform for  $V \geq 0.3$  V.

The sharply-peaked electric field profile shown in Fig. 5.12(a) is similar to that found when  $\theta = 0^\circ$  (Wacker, 2002). In addition, there is a broad plateau region in the surface plot, in which  $F$  is pinned near the value required to satisfy the  $r = 1$  resonance condition ( $r = 1$  along the lowest white contour in Fig. 5.12(a)) so that  $\omega_B = \bar{\omega}_c$ . Within this plateau region,  $r = 1$  throughout most of the SL, which ensures that we see a strong  $r = 1$  resonant peak in the corresponding  $G(V)$  curve (shown green in Fig. 5.11(a)). By contrast, near the  $r = 2$  resonance (white contour marked by arrow in Fig. 5.12(a)),  $F$  varies rapidly with position, meaning that the resonance condition is not satisfied across an extended region of the SL. Consequently, we see no  $r = 2$  peak in the corresponding  $G(V)$  curve for SL1.

To see more conductance resonances, we therefore need to suppress the accumulation of electrons near the collector contact and thus ensure that  $F$  is more uniform through the SL. We achieved this in a real SL structure through miniband engineering, as described in the next section.

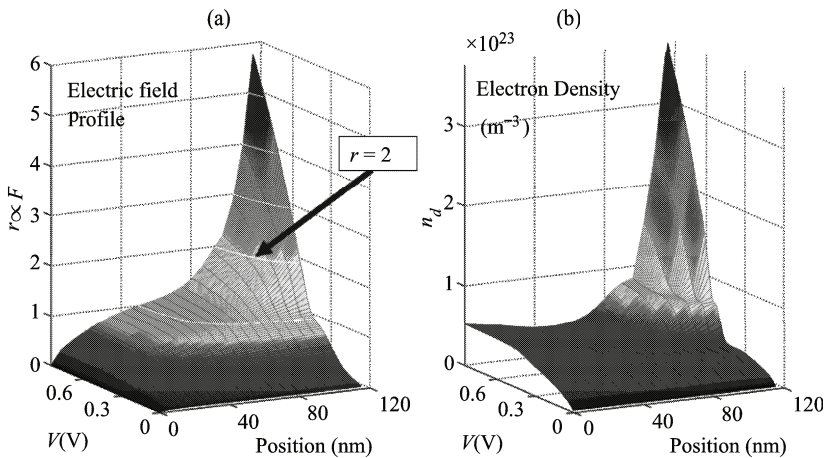


**Fig. 5.12** Surface plots showing (a)  $r \propto F$ , (b) electron density,  $n_d$ , calculated versus  $V$  and position ( $x$ ) through SL1 for  $B = 11$  T and  $\theta = 0^\circ$ . Contours in (a) show integer values of  $r$ , with  $r = 2$  contour arrowed.

## 5.7 Tailoring the SL structure to increase the number of conductance resonances

To reduce the accumulation of electrons in the SL layers, we fabricated a GaAs/(AlGa)As SL, henceforth known as SL2 and shown schematically in Fig. 5.13, in which the energy gap between the first and second minibands is only 60 meV: approximately four times smaller than in SL1 (Hardwick et al., 2006). This narrow gap allows electrons to tunnel from the first miniband (of width  $\Delta = 11$  meV) into the second miniband and thus flow through the SL rather than accumulating towards the collector contact. In SL2, there is no InAs layer to lower the first miniband. Instead, to facilitate electron injection into the miniband, the emitter contact has a 3% Al content, which raises the conduction band edge just enough to bring the Fermi energy in the emitter contact (left-hand green region in Fig. 5.13) into alignment with the miniband.

Figure 5.14 shows surface plots of electron density,  $n_d$ , calculated versus  $V$  and position,  $x$ , through (a) SL1, (b) SL2 when  $\theta = 45^\circ$ . For SL2 (see Fig. 5.14(b)), there is very little electron accumulation towards the collector contact. Instead, the surface plot reveals small ridges (red) of electron accumulation, which separate regions of constant electron density. Within these regions, the corresponding surface plot of  $r = \omega_B / \tilde{\omega}_c \propto F$  versus  $V$  and position through the SL (see Fig. 5.15) reveals two well defined plateaux in which  $F$  is pinned at the  $r = 1$  and  $r = 2$  resonances.

The narrow miniband gap of SL2 enables electrons to tunnel from the first to the second miniband at high  $F$ , which causes  $v_d(F)$  to *increase* at high  $F$ , thus ensuring that there is far less electron accumulation in SL2 than in SL1. Due to the interminiband tunneling, we cannot use a single band picture to describe the transport and electrostatic properties of SL2. Instead, we used wavepacket dynamics, constructing an initial state from (along the  $x$  direction) a superposition of

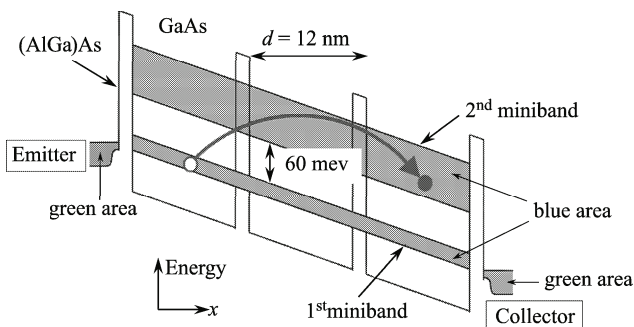


**Fig. 5.13** Schematic variation of the electronic potential energy with position  $x$  through GaAs/(AlGa)As SL2 (Hardwick et al., 2006). For simplicity, band bending and electric field variations produced by the accumulation of electrons is not shown. The (AlGa)As layers act as potential barriers, which separate adjacent GaAs quantum wells. Blue areas represent the two lowest minibands, whose separation is small enough (60 meV) to enable inter-miniband tunneling. Green areas represent electron gases in the emitter and collector contacts.

Wannier-functions near the bottom of the lowest miniband and (along the  $z$  direction) the lowest Landau state. Motion along the  $y$  direction, which separates from that in the  $x - z$  plane (Fromhold et al., 2004; Hardwick, 2007) (see also Section 5.8), was described by a plane wave. The Wannier function basis spanned enough  $p_x$  states to ensure that the initial state extends across several (approximately 8) SL periods. We then determined the time evolution of the wavepacket in the  $x - z$  plane, by solving the time-dependent Schrödinger equation, and calculated the mean position of the wavepacket,  $\langle \mathbf{R}(t) \rangle = (\langle x(t) \rangle, \langle z(t) \rangle)$  and its time derivative  $d\langle \mathbf{R}(t) \rangle / dt = \langle \mathbf{v}(t) \rangle = (\langle v_x(t) \rangle, \langle v_z(t) \rangle) = (d\langle x(t) \rangle / dt, d\langle z(t) \rangle / dt)$ . By replacing the semiclassical velocity,  $v_x(t)$ , in Eq. (5.8), by the quantum-mechanical expectation value,  $\langle v_x(t) \rangle$ , we were able to calculate  $v_d(F)$  curves, and hence determine

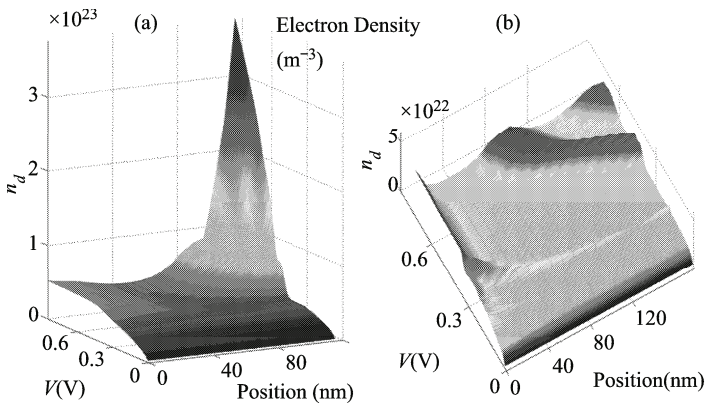


**Fig. 5.14** Surface plots showing electron density calculated versus  $V$  and position ( $x$ ) through (a) SL1 with  $B = 11$  T, (b) SL2 with  $B = 14$  T.  $\theta = 45^\circ$ .

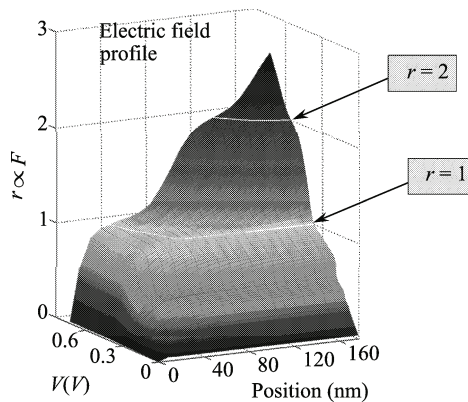


**Fig. 5.15** Surface plot showing  $r \propto F$  calculated versus  $V$  and position ( $x$ ) through SL2 for  $B = 14$  T and  $\theta = 45^\circ$ . Contours show integer values of  $r$ , with  $r = 1$  and  $2$  contours arrowed. Plateaux are electric field domains. At the boundary between adjacent domains, there is a large accumulation of electrons (ridges in Fig. 5.14(b)).

both  $I(V)$  and the electrostatic properties of the SL (for example, the surface plots shown in Fig. 5.14(b) and in Fig. 5.15), via a formalism that explicitly includes interminiband tunneling.

Figure 5.16 shows  $v_d(F)$  curves (offset vertically for clarity) determined from the wavepacket dynamics for  $\theta = 0^\circ$  (lower curve) to  $\theta = 55^\circ$  (upper curve). At low  $F$ , interminiband tunneling is negligible and so the quantum-mechanical expectation value  $\langle \mathbf{R}(t) \rangle$  coincides with the semiclassical trajectory  $(x(t), z(t))$  obtained by solving Eqs. (5.5) and (5.7). Consequently, the wavepacket dynamics reveals precisely the same stochastic web-induced  $v_d$  resonant peaks obtained from the semiclassical transport equations. In Fig. 5.16, the  $r = 1$  and  $r = 2$  peaks are marked by the left and right arrows respectively. At high  $F$ , the wavepacket dynamics exhibit strong interminiband tunneling, which causes  $v_d$  to *increase* with increasing  $F$ . This contrasts with the monotonic *decrease* obtained from the semiclassical dynamics, shown for  $\theta = 0^\circ$  by the red dotted curve in Fig. 5.16, which do not incorporate inter-miniband tunneling. As discussed above, the increase of  $v_d$  at high  $F$  due to interminiband tunneling suppresses accumulation of electrons (Fig. 5.14(b)), thus ensuring that  $F$  pins to the values required to satisfy the  $r = 1$  and  $r = 2$  resonance condition throughout much of the SL (plateaux in Fig. 5.15). As a consequence, the  $I(V)$  and  $G(V)$  curves measured for SL2 reveal stronger resonances, and more of them, than for SL1.

To illustrate this, Fig. 5.17(a) shows  $I(V)$  curves measured for SL2 for  $B = 14$  T and  $\theta = 0^\circ$  (bottom trace) to  $90^\circ$  (top trace) at  $5^\circ$  intervals for  $T = 4.2$  K. The  $r = 1$  resonant feature, clearly visible for  $V \approx 0.2 - 0.4$  V, is far stronger than observed for SL1 (Fig. 5.10(b)) and actually triples the current flow even at room temperature. The  $I(V)$  curves calculated from the wavepacket dynamics (Fig. 5.17(b)) are in broad agreement with the experimental data and, in particular, reveal strong resonant enhancement of the current due to stochastic-web-assisted transport when  $r = 1$ . Whereas the derivative plots,  $G(V)$ , measured experimentally for SL1 reveal *only* the  $r = 1$  resonant peak (red in Figs. 5.11(b) and 5.18(a), which show the same

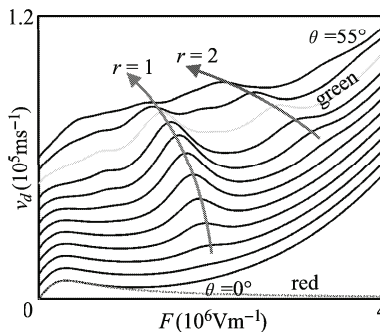


**Fig. 5.16**  $v_d(F)$  curves (solid) calculated for SL2 with  $B = 14$  T, and  $\theta = 0^\circ$  (bottom trace) to  $55^\circ$  (top trace) at  $5^\circ$  intervals. Curve for  $\theta = 45^\circ$  is shown green. Arrows mark  $r = 1$  and  $r = 2$  resonant peaks created by chaos-assisted transport through stochastic webs. Red dotted curve shows  $v_d(F)$  calculated for  $\theta = 0^\circ$  in the absence of inter-miniband tunneling.

data), for SL2 there are *two* distinct conductance peaks, shown red and purple in Fig. 5.18(b), which correspond to the  $r = 1$  and  $r = 2$  resonances, respectively.

### 5.8 Energy eigenstates and Wigner functions

We now consider how the onset of non-KAM chaos in the semiclassical electron trajectories manifests itself in the quantized energy eigenstates of the system. To do this, we represent the tilted magnetic field by the vector potential  $\mathbf{A} = [0, B(x \sin \theta - z \cos \theta), 0]$ . In this gauge, the Hamiltonian operator

$$\hat{H} = (\hat{\mathbf{p}} + e\mathbf{A})^2/2m^* + V_{SL}(x) - eFx, \tag{5.9}$$

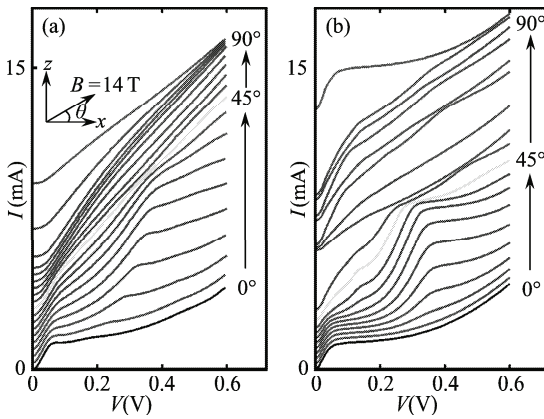


**Fig. 5.17**  $I(V)$  curves for SL2 (a) measured at  $T = 4.2$  K (b) calculated for  $B = 14$  T and  $\theta = 0^\circ$  (bottom trace) to  $90^\circ$  (top trace) at  $5^\circ$  intervals. Inset in (a): orientation of  $B$  in  $x - z$  plane.

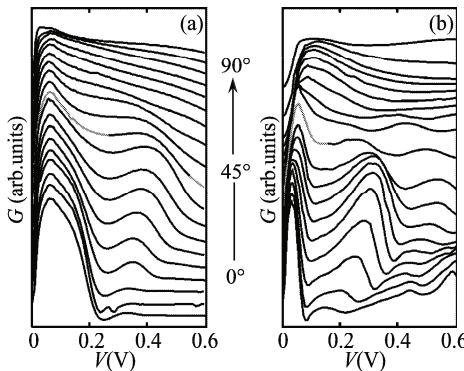


**Fig. 5.18**  $G(V)$  curves measured at  $T = 4.2$  K for (a) SL1 with  $B = 11$  T, (b) SL2 with  $B = 14$  T and  $\theta = 0^\circ$  (bottom trace) to  $90^\circ$  (top trace) at  $5^\circ$  intervals.

is invariant under translation along  $y$ . In Eq. (5.9),  $\hat{\mathbf{p}}$  is the canonical momentum operator and  $V_{SL}(x)$  is the periodic SL potential. Since  $\hat{H}$  does not depend on  $y$ , the energy eigenfunctions of the system can be written in the form  $\Psi(x, z)\exp(ik_y y)$ , where  $\Psi(x, z)$  is an eigenfunction of the Hamiltonian obtained by replacing  $\hat{p}_y$  by  $\hbar k_y = 0$  in Eq. (5.9), i.e. taking the constant canonical momentum component,  $k_y$  to equal 0. To calculate the eigenfunctions,  $\Psi(x, z)$ , we diagonalized the Hamiltonian taking a basis of Wannier functions along  $x$  and simple harmonic oscillator states along  $z$  (Fromhold et al., 2004).

When  $\theta = 0^\circ$ , the eigenfunctions comprise Wannier-Stark states along  $x$  and Landau states along  $z$ . Figure 5.19(a) shows the probability density of one of these eigenstates, which is localized within the turning points of the corresponding semiclassical orbit shown overlaid in the  $x - z$  plane. To relate the probability distribution directly to the underlying semiclassical phase space, we calculated Wigner functions,  $W(p_y, p_z)$ , of the quantized eigenstates (Fromhold et al., 2004, 2002).

Wigner functions are often used in quantum chaos theory, as well as in semiconductor device modelling, because they are quantum-mechanical analogues of classical Poincaré sections (Reichl, 1998). To demonstrate this analogy, Fig. 5.19(b) shows  $W(p_y, p_z)$  calculated for the eigenstate shown in Fig. 5.19(b). Its ring pattern coincides exactly with the circular island in the corresponding Poincaré section (see Fig. 5.19(c)), which is produced by the orbit shown overlaid in Fig. 5.19(a), whose cyclotron energy equals the energy of the lateral Landau state.

When  $\theta \neq 0^\circ$ , the link between the semiclassical electron trajectories and corresponding quantum wavefunctions becomes more subtle and interesting. For example, at the  $r = 1$  resonance (i.e.  $\omega_B = \bar{\omega}_c$ ) for  $B = 8$  T and  $\theta = 15^\circ$ , the probability density distribution of the eigenstate shown in Fig. 5.20(a) extends across many SL periods just like the unbounded semiclassical orbit shown overlaid. By contrast,

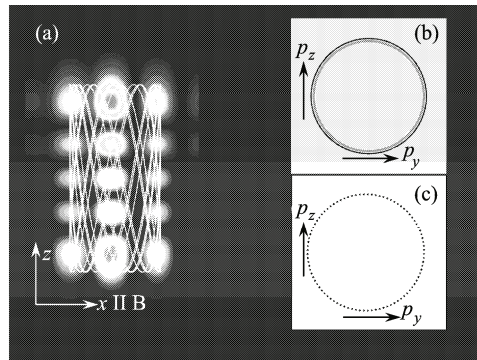


**Fig. 5.19** (a) Yellow curve: classical electron trajectories for SL1 in the  $x$ - $z$  plane (axes inset) overlaid on a corresponding plot of  $|\Psi(x, z)|^2$  (blue zero, red high) at  $B = 8$  T and  $\theta = 0^\circ$ . (b) Wigner function values (red large positive, light green = 0, blue large negative) in  $(p_y, p_z)$  plane (axes inset) corresponding to the energy eigenfunction shown in (a) and to the Poincaré section shown in (c) (color plot in the book end).

moving off resonance strongly localizes both the semiclassical orbits and the corresponding quantized eigenstates, as shown in Fig. 5.20(b), for example.

The highly extended wavefunction shown in Fig. 5.20(a) is, to good approximation, a superposition of the lowest Wannier-Stark states in each quantum well plus a series of lateral Landau states. Moving left to right from one well to the next, the Landau level index increases from 0 to 1,2,3,...,15. The wavefunction has such a simple form for the following reason. Since  $\theta$  is only  $15^\circ$ , the  $z$ -component of  $\mathbf{B}$  is also small. Consequently, it acts only as a perturbation to the Wannier-Stark ladder and the Landau levels produced by the  $\mathbf{B}$ -field component along the  $x$  direction. But on resonance, when the Wannier-Stark and Landau levels are equally spaced, the perturbation has a dramatic effect because it couples Landau states in adjacent wells whose quantum numbers differ by one and thus forms extended eigenstates like that shown in Fig. 5.20(a). However, even though the extended wavefunction seems to be shaped by purely quantum-mechanical coupling of adjacent Landau states, there is a great deal of classical information embedded within it, which can be extracted by calculating its Wigner function. The saddle-shaped pattern in the Wigner function shown in Fig. 5.21(a) closely resembles the central part of the stochastic web shown in Fig. 5.21(b), which forms in the corresponding classical phase space.

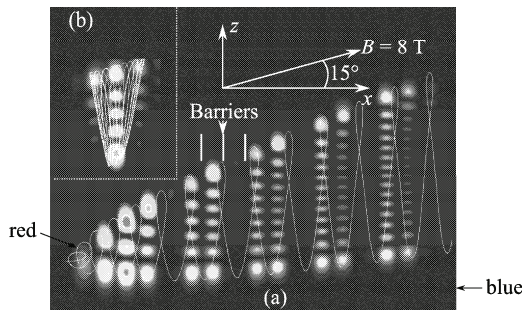


**Fig. 5.20** Yellow curves: classical electron trajectories for SL1 in the  $x$ - $z$  plane (axes inset) overlaid on corresponding plots of  $|\Psi(x, z)|^2$  (blue zero, red high) (a) on resonance ( $r = 1$ ), (b) off resonance ( $r$  irrational).  $B = 8$  T,  $\theta = 15^\circ$  (color plot in the book end).

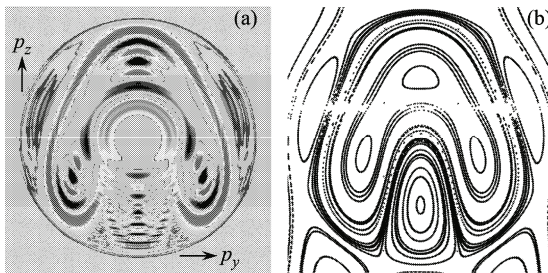


**Fig. 5.21** (a) Wigner function plot for the energy eigenstate of SL1 shown in Fig. 5.20(a) (red large positive, light green = 0, blue large negative). The Wigner function is shown in the  $(p_y, p_z)$  plane (axes inset) and corresponds to the Poincaré section shown in (b) (color plot in the book end).

Consequently, electron transport through stochastic webs provides a classical interpretation of the inter-Landau level transitions that occur at small tilt angles, thereby producing highly delocalized eigenfunctions.

At higher  $\theta$ , the  $z$ -component of  $\mathbf{B}$  couples the motion along the  $x$ - and  $z$ -directions so strongly that it produces chaotic semiclassical paths and highly irregular energy eigenfunctions, like that shown in Fig. 5.22(a) at the  $r = 1$  resonance. The probability density distribution in Fig. 5.22(a) reflects the shape of the unstable

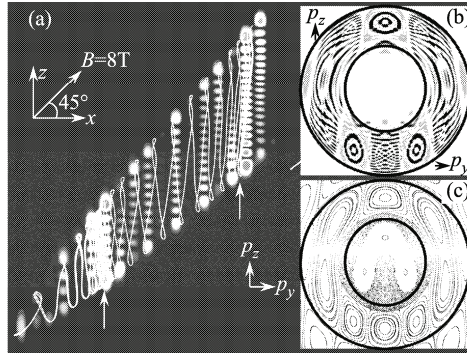


**Fig. 5.22** (a) Yellow curve: semiclassical electron trajectory for SL1 in the  $x$ - $z$  plane (axes inset) overlaid on a corresponding plot of  $|\Psi(x,z)|^2$  (blue zero, red high) at the  $r = 1$  resonance for  $B = 8$  T and  $\theta = 45^\circ$ . Red arrows mark regions of high probability density, where, in addition, the orbital loops are closely packed. (b) Wigner function values (red large positive, light green = 0, blue large negative) in  $(p_y, p_z)$  plane (axes inset) corresponding to the energy eigenfunction shown in (a) and to the Poincaré section shown in (c). Solid black lines in (b) [marked by red arrows] and (c) highlight ring-shaped stochastic web filaments (color plot in the book end).

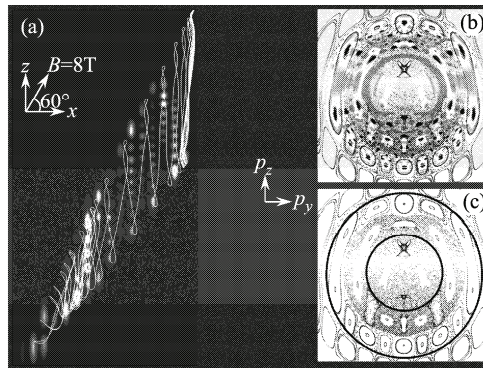


**Fig. 5.23** (a) Yellow curve: classical electron trajectories for SL1 in the  $x$ - $z$  plane (axes inset) overlaid on a corresponding plot of  $|\Psi(x,z)|^2$  (blue zero, red high) at the  $r = 2$  resonance for  $B = 8$  T and  $\theta = 60^\circ$ . (b) Wigner function values (red large positive, light green = 0, blue large negative) in  $(p_y, p_z)$  plane (axes inset) corresponding to the energy eigenfunction shown in (a) and to the Poincaré section shown in (c) and also overlaid in (b). Solid black lines in (c) highlight ring-shaped stochastic web filaments (color plot in the book end).

semiclassical orbit shown overlaid and cannot be interpreted as a simple superposition of Landau and Wannier-Stark states. In this high  $\theta$  regime, the similarity between the semiclassical paths and quantum wavefunctions is striking. In particular, in Fig. 5.22(a) ( $\theta = 45^\circ$ ), the probability density is high (red) in two distinct regions, where the overlaid orbital loops are more densely packed. The corresponding Wigner function shown in Fig. 5.22(b) clearly reveals filaments of the stochastic web shown in Fig. 5.22(c), in particular the two ring-shaped filaments highlighted by the black circles, plus the islands of stability enmeshed by the stochastic web. When the electron trajectory lies on one of the two ring-shaped web filaments, the electron's  $x$  co-ordinate (proportional to the square of the distance from the center of the web) is confined to a narrow range of values, which correspond to the two regions of densely-packed orbital loops marked by the red arrows in Fig. 5.22(a). The left-hand (right-hand) arrows in Fig. 5.22(a) mark parts of the trajectory where the electron is pinned within the first (second) rings in the stochastic web (marked by red arrows in Fig. 5.22(b)).

Similar localized regions of high probability density and of compressed orbital loops can be seen in Fig. 5.23(a) for the  $r = 2$  resonance at  $\theta = 60^\circ$ . These concentrations occur when the electron is trapped on two of the ring-shaped filaments of the stochastic web shown in Fig. 5.23(b) and (c) (ring positions marked by black circles), and is therefore unable to progress through the SL. But when the electron eventually transfers onto the radial filaments, it shifts rapidly along the  $x$ -direction, following the widely-spaced orbital loops in Fig. 5.23(a), which correspond to low probability density. The Wigner function in Fig. 5.23(b) is concentrated along the filaments of the stochastic web and also reveals fine details of the stable islands enclosed by those filaments, in particular the island chains formed towards the bottom of the Poincaré section in Fig. 5.23(c) and also overlaid in Fig. 5.23(b).

## 5.9 Summary and outlook

We have shown that electrons in a biased SL with an applied tilted magnetic field provide an experimentally-accessible non-KAM chaotic system in which, unusually, the chaotic trajectories have an intrinsically quantum-mechanical origin: miniband dispersion. Despite involving only *stationary* electric and magnetic fields, this 3-dimensional system is dynamically equivalent to a 1-dimensional simple harmonic oscillator driven by a *time-dependent* plane wave. In effect, the applied fields act on the electrons like a THz wave whose wavelength and frequency can be tuned independently by changing, respectively, the orientation of the magnetic field or the strength of the electric field. Consequently, non-KAM chaos for miniband electrons in a *multi-well* SL is fundamentally different from the quantum effects, such as wavefunction scarring, associated with classical Hamiltonian chaos in a *single* quantum well (Stöckmann, 1999; Fromhold et al., 1994, 1995a,b; Shepelyansky and Stone, 1995; Müller et al., 1995; Wilkinson et al., 1996; Monteiro and Dando, 1996; Fromhold et al., 1997a,b; Monteiro et al., 1997a,b; Narimanov et al., 1998;

Narimanov and Stone, 1998a,b; Saraga and Monteiro, 1998a; Saraga et al., 1998; Saraga and Monteiro, 1998b; Bogomolny and Rouben, 1998, 1999; Fromhold et al., 2002).

When the cyclotron and Bloch frequencies are commensurate, the electron phase space is threaded by a stochastic web, which spatially delocalizes the electrons. This unique feature of non-KAM chaos produces strong resonant peaks in the experimental and theoretical  $I(V)$  and  $G(V)$  curves, with the most striking resonant features being observed for a SL with a narrow energy gap between the first and second minibands, which promotes inter-miniband tunneling and therefore reduces charge accumulation. In such structures, stochastic web formation strongly affects the collective behavior of the electrons, creating a series of electric field domains (plateaux in Fig. 5.15), whose structure can be controlled by changing  $B$  and/or  $\theta$  (Hardwick et al., 2006). Although the parameters of the SLs considered in this paper are designed to suppress LO phonon emission, the residual impurity and interface roughness scattering can mask some of the subtle features of non-KAM chaos. Nevertheless, its effects remain clearly discernable in the  $I(V)$  curves measured for our SL devices. Analogous experiments on ultracold atoms in optical lattices with oblique magnetic confinement may be able to detect far richer quantum manifestations of non-KAM chaos because the atoms can undergo almost no scattering (Scott et al., 2002).

Recent work (Greenaway et al., 2009) has shown that the modulation of the  $v_d(F)$  curves that accompanies resonant stochastic web formation can induce multiple *propagating* electric field domains in the SL, which increase both the amplitude and frequency (into the THz regime) of the associated temporal current oscillations: effects that should be experimentally observable in existing SLs. Stochastic-web-assisted transport thus opens routes to controlling the form and *collective* dynamics of charge domains in SLs, and hence enhancing the GHz-THz performance of the devices, by using *single-electron* miniband transport to tailor  $v_d(F)$ .

Similar dynamics can occur in other spatially periodic systems in which wave interference gives rise to band transport phenomena, for example ultracold atoms in an optical lattice (Scott et al., 2002) and light propagating through spatially-modulated photonic crystals (Wilkinson and Fromhold, 2003). The beautiful stochastic web patterns that George Zaslavsky discovered in the phase space of the driven harmonic oscillator could therefore provide a generic and, in principle, extremely sensitive mechanism for controlling the transmission of quantum or electromagnetic waves through engineered lattice structures.

**Acknowledgements** The work was supported by the UK Engineering and Physical Sciences Research Council. We acknowledge Professor M. Henini (University of Nottingham) who grew the MBE SL samples used in our experiments and Dr R. Airey (University of Sheffield) for sample processing.

## References

- Alekseev K.N., Berman G.P., Campbell D.K., Cannon E.H. and Cargo M.C., 1996, Dissipative chaos in semiconductor superlattice, *Phys. Rev. B*, **54**, 10625–10636.
- Alekseev K.N., Kusmartsev F.V., 2002, Pendulum limit, chaos and phase-locking in the dynamics of ac-driven semiconductor superlattice, *Phys. Lett. A*, **305**, 281–288.
- Amann A., Schlesner J., Wacker A. and Schöll E., 2002, Chaotic front dynamics in semiconductor superlattices, *Phys. Rev. B*, **65**, 193313–193316.
- Balanov A.G., Fowler D., Patané A., Eaves L. and Fromhold T.M., 2008, Bifurcations and chaos in semiconductor superlattices with a tilted magnetic field, *Phys. Rev. E*, **77**, 026209–026221.
- Beloshapkin V.V. et al., 1989, Chaotic streamlines in pre-turbulent states, *Nature*, **337**, 133–137.
- Bird J.P., Akis R., Ferry D.K., Vasileska D., Cooper J., Aoyagi Y. and Sugano T., 1999, Lead-orientation-dependent wave function scarring in open quantum dots, *Phys. Rev. Lett.*, **82**, 4691–4694.
- Bogomolny E.B. and Rouben D.C., 1998, Semiclassical description of resonant tunneling, *Europhys. Lett.*, **43**, 111–116.
- Bogomolny E.B. and Rouben D.C., 1999, Semiclassical description of resonant tunneling, *European Physical Journal B*, **9**, 695–718.
- Bonilla L.L. and Grahn H.T., 2005, Non-linear dynamics of semiconductor superlattices, *Rep. Prog. Phys.*, **68**, 577–683.
- Canali L., Lazzarino M., Sorba L. and Beltram F., 1996, Stark-cyclotron resonance in a semiconductor superlattice, *Phys. Rev. Lett.*, **76**, 3618–3621.
- Chang A.M., Baranger H.U., Pfeiffer L.N. and West K.W., 1994, Weak-localization in chaotic versus nonchaotic cavities—a striking difference in the line-shape, *Phys. Rev. Lett.*, **73**, 2111–2114.
- Chia P.-K., Schmitz L. and Conn R.W., 1996, Stochastic ion behavior in subharmonic and superharmonic electrostatic waves, *Phys. Plasmas*, **3**, 1545–1568.
- Demikhovskii V.Ya., Kamenev D.I. and Luna-Acosta G.A., 1999, Quantum weak chaos in a degenerate system, *Phys. Rev. E*, **59**, 294–302.
- Demikhovskii V.Ya., Izrailev F.M. and Malyshev A.I., 2002, Manifestation of Arnol'd diffusion in quantum systems, *Phys. Rev. Lett.*, **88**, 154101–154104.
- Esaki L. and Tsu R., 1970, Superlattice and negative differential conductivity in semiconductors, *IBM J. Res. Develop.*, **14**, 61–65.
- Fleischmann R., Geisel T. and Ketzmerick R., 1992, Magnetoresistance due to chaos and nonlinear resonances in lateral surface superlattices, *Phys. Rev. Lett.*, **68**, 1367–1370.
- Folk J.A., Patel S.R., Godijn S.F., Huibers A.G., Cronenwett S.M., Marcus C.M., Campman K. and Gossard A.C., 1996, Statistics and parametric correlations of Coulomb blockade peak fluctuations in quantum dots, *Phys. Rev. Lett.*, **76**, 1699–1702.
- Fowler D., Hardwick D.P.A., Patané A., Greenaway M.T., Balanov A.G., Fromhold T.M., Eaves L., Henini M., Kozlova N., Freudenberger J. and Mori N., 2007,

- Magnetic-field-induced miniband conduction in semiconductor superlattices, *Phys. Rev. B*, **76**, 245303–245308.
- Fromhold T.M., Eaves L., Sheard F.W., Leadbeater M.L., Foster T.J. and Main P.C., 1994, Magnetotunneling spectroscopy of a quantum-well in the regime of classical chaos, *Phys. Rev. Lett.*, **72**, 2608–2611.
- Fromhold T.M., Wilkinson P.B., Sheard F.W., Eaves L., Miao J., and Edwards G., 1995, Manifestations of classical chaos in the energy-level spectrum of a quantum-well, *Phys. Rev. Lett.*, **75**, 1142–1145.
- Fromhold T.M., Fogarty A., Eaves L., Sheard F.W., Henini M., Foster T.J., Main P.C. and Hill G., 1995, Evidence for quantum states corresponding to families of stable and chaotic classical orbits in a wide potential well, *Phys. Rev. B*, **51**, 18029–18032.
- Fromhold T.M., Wilkinson P.B., Sheard F.W. and Eaves L., 1997, Precursors and transition to chaos in a quantum well in a tilted magnetic field, *Phys. Rev. Lett.*, **78**, 2865–2865.
- Fromhold T.M., Wilkinson P.B., Eaves L., Sheard F.W., Main P.C., Henini M., Carter M.J., Miura N. and Takamasu T., 1997, Manifestations of quantum chaos in resonant tunnelling, *Chaos, Solitons & Fractals*, **8**, 1381–1411. Special Edition on Chaos and Quantum Transport in Mesoscopic Cosmos, edited by K. Nakamura.
- Fromhold T.M., Krokhin A.A., Tench C.R., Bujkiewicz S., Wilkinson P.B., Sheard F.W. and Eaves L., 2001, Effects of stochastic webs on chaos electron transport in semiconductor superlattices, *Phys. Rev. Lett.*, **87**, 046803–046806.
- Fromhold T.M., Wilkinson P.B., Hayden R.K., Eaves L., Sheard F.W., Miura N. and Henini M., 2002, Tunneling spectroscopy of mixed stable-chaotic electron dynamics in a quantum well, *Phys. Rev. B*, **65**, 155312–155323.
- Fromhold T.M., Patanè A., Bujkiewicz S., Wilkinson P.B., Fowler D., Sherwood D., Stapleton S.P., Krokhin A.A., Eaves L., Henini M., Sankeshwar N.S. and Sheard F.W., 2004, Chaotic electron diffusion through stochastic webs enhances current flow in superlattices, *Nature*, **428**, 726–730.
- Gardiner S.A., Cirac J.I. and Zoller P., 1997, Quantum chaos in an ion trap: The delta-kicked harmonic oscillator, *Phys. Rev. Lett.*, **79**, 4790–4793.
- Greenaway M.T., Balanov A.G., Schöll E. and Fromhold T.M., 2009, Controlling and enhancing terahertz collective electron dynamics in superlattices by chaos-assisted miniband transport, *Phys. Rev. B*, **80**, 205318–205322.
- Hardwick D.P.A., 2007, Quantum and semiclassical calculations of electron transport through a stochastic system, *PhD Thesis*, University of Nottingham.
- Hardwick D.P.A., Naylor S.L., Bujkiewicz S., Fromhold T.M., Fowler D., Patanè A., Eaves L., Krokhin A.A., Wilkinson P.B., Henini M. and Sheard F.W., 2006, Effect of inter-miniband tunneling on current resonances due to the formation of stochastic conduction networks in superlattices, *Physica E*, **32**, 285–288.
- Hensinger W.K., Häffner H., Browaeys A., Heckenberg N.R., Helmerson K., McKenzie C., Milburn G.J., Phillips W.D., Rolston S.L., Rubinsztein-Dunlop H. and Upcroft B., 2001, Dynamical tunnelling of ultracold atoms, *Nature*, **412**, 52–55.

- Hyart T., Mattas J. and Alekseev K.N., 2009, Model of the influence of an external magnetic field on the gain of terahertz radiation from semiconductor superlattices, *Phys. Rev. Lett.*, **103**, 117401–117404.
- Ignatov A.A., Dodin E.P. and Shashkin V.I., 1991, Transient response theory of semiconductor superlattices: connection with Bloch oscillations, *Mod. Phys. Lett. B*, **5**, 1087–1094.
- Kamenev D.I. and Berman G.P., 2000, *Quantum Chaos: a Harmonic Oscillator in Monochromatic Wave*, Rinton Press, Princeton, New Jersey.
- Karney C.F.F. and Bers A., 1977, Stochastic ion heating by a perpendicularly propagating electrostatic wave, *Phys. Rev. Lett.*, **39**, 550–554.
- Kastrup J., Grahn H.T., Ploog K.H., Pregel F., Wacker A. and Schöll E., 1994, Multistability of the current-voltage characteristics in doped GaAs-AlAs superlattices, *Appl. Phys. Lett.*, **65**, 1808–1810.
- Ketzmerick R., 1996, Fractal conductance fluctuations in generic chaotic cavities, *Phys. Rev. B*, **54**, 10841–10844.
- Kosevich Y.A., Hummel A.B., Roskos H.G. and Köhler K., 2006, Ultrafast Fiske effect in semiconductor superlattices, *Phys. Rev. Lett.*, **96**, 137403–137406.
- Kuraguchi M., Ohmichi E., Osada T. and Shiraki Y., 2002, Relationship between Stark-cyclotron resonance and angular dependent magnetoresistance oscillations, *Physica E*, **12**, 264–266.
- Leadbeater M.L., Alves E.S., Eaves L., Henini M., Hughes O.H., Celeste A., Portal J.C., Hill G. and Pate M.A., 1989, Magnetic field studies of elastic scattering and optic-phonon emission in resonant-tunneling devices, *Phys. Rev. B*, **39**, 3438–3441.
- Leadbeater M.L., Sheard F.W. and Eaves L., 1991, Inter-Landau-level transitions of resonantly tunneling electrons in tilted magnetic-fields, *Semicond. Sci. Tech.*, **6**, 1021–1024.
- Luo A.C., 2004, Nonlinear dynamics theory of stochastic layers in Hamiltonian systems, *Applied Mechanics Review*, **57**, 161–172.
- Luo K.J., Grahn H.T., Ploog K.H. and Bonilla L.L., 1998, Explosive bifurcation to chaos in weakly coupled semiconductor superlattices, *Phys. Rev. Lett.*, **81**, 1290–1293.
- Marcus C.M., Rimberg A.J., Westervelt R.M., Hopkins P.F. and Gossard A.C., 1992, Conductance fluctuations and chaotic scattering in ballistic microstructures, *Phys. Rev. Lett.*, **69**, 506–509.
- Marlow C.A. et al., 2006, Unified model of fractal conductance fluctuations for diffusive and ballistic semiconductor devices, *Phys. Rev. B*, **73**, 195318–195324.
- Micolich A.P. et al., 2001, Evolution of fractal patterns during a classical-quantum transition, *Phys. Rev. Lett.*, **87**, 036802–036805.
- Monteiro T.S. and Dando P.A., 1996, Chaos in a quantum well in tilted fields: A scaling system, *Phys. Rev. E*, **53**, 3369–3373.
- Monteiro T.S., Delande D., Fisher A.J. and Boebinger G.S., 1997, Bifurcations and the transition to chaos in the resonant-tunneling diode, *Phys. Rev. B*, **56**, 3913–3921.

- Monteiro T.S., Delande D. and Connerade J.P., 1997, Have quantum scars been observed, *Nature*, **387**, 863–864.
- Müller G., Boebinger G.S., Mathur H., Pfeiffer L.N. and West K.W., 1995, Precursors and transition to chaos in a quantum-well in a tilted magnetic-field, *Phys. Rev. Lett.*, **75**, 2875–2878.
- Narimanov E.E., Stone A.D. and Boebinger G.S., 1998, Semiclassical theory of magnetotransport through a chaotic quantum well, *Phys. Rev. Lett.*, **80**, 4024–4027.
- Narimanov E.E. and Stone A.D., 1998, Theory of the periodic orbits of a chaotic quantum well, *Phys. Rev. B*, **57**, 9807–9848.
- Narimanov E.E. and Stone A.D., 1998, Origin of strong scarring of wave functions in quantum wells in a tilted magnetic field, *Phys. Rev. Lett.*, **80**, 49–52.
- Nakamura K. and Harayama T., 2003, *Quantum Chaos and Quantum Dots*, Oxford University Press, Oxford.
- Patanè A. et al., 2002, Tailoring the electronic properties of GaAs/AlAs superlattices by InAs layer insertions, *Appl. Phys. Lett.*, **81**, 661–663.
- Raspopin A.S., Zharov A.A and Cui H.L., 2005, Spectrum of electromagnetic excitations in a dc-biased semiconductor superlattice, *J. App. Phys.*, **98**, 103517–103522.
- Reichl L.E., 1998, *A Modern Course in Statistical Physics 2nd Ed.*, John Wiley & Sons Inc., New York.
- Robnik M. and Romanovski V.G. (Eds.), 2008, Energy evolution and exact analysis of the adiabatic invariants in time-dependent linear oscillator, *AIP Conf. Proc. Series Vol. 1076*, 185–212, AIP, Melville, New York.
- Sachrajda A.S., Ketzmerick R., Gould C., Feng Y., Kelly P.J., Delage A. and Wasilewski Z., 1998, Fractal conductance fluctuations in a soft-wall stadium and a Sinai billiard, *Phys. Rev. Lett.*, **80**, 1948–1951.
- Sagdeev R.Z., Usikov D.A. and Zaslavsky G.M., 1988, *Nonlinear Physics*, Harwood Academic Publishers, NY.
- Saraga D.S. and Monteiro T.S., 1998, Quantum chaos with nonperiodic, complex orbits in the resonant tunneling diode, *Phys. Rev. Lett.*, **81**, 5796–5799.
- Saraga D.S. and Monteiro T.S., 1998, Quantum wells in tilted fields: Semiclassical analysis and experimental evidence for effects “beyond” periodic orbits, *Phys. Rev. E*, **57**, 5252–5265.
- Saraga D.S., Monteiro T.S. and Rouben D.C., 1998, Periodic orbit theory for resonant tunneling diodes: Comparison with quantum and experimental results, *Phys. Rev. E*, **58**, 2701–2704.
- Savvidis P.G., Kolasa B., Lee G. and Allen S.J., 2004, Resonant crossover of terahertz loss to the gain of a Bloch oscillating InAs/AlSb superlattice, *Phys. Rev. Lett.*, **92**, 196802–196805.
- Schöll E., 2001, *Nonlinear Spatio-temporal Dynamics and Chaos in Semiconductors*, Nonlinear Science Series, Vol. 10, Cambridge University Press, Cambridge.
- Schomburg E., Grenzer J., Hofbeck K., Blomeier T., Winnerl S., Brandl S., Ignatov A.A., Renk K.F., Pavel’ev D.G., Koschurinov Y., Ustinov V., Zhukov A., Kovsch

- A., Ivanov S. and Kop'ev P.S., 1998, Millimeter wave generation with a quasi planar superlattice electronic device, *Solid-State Electronics*, **42**, 1495–1498.
- Scott R.G., Bujkiewicz S., Fromhold T.M., Wilkinson P.B. and Sheard F.W., 2002, Effects of chaotic energy-band transport on the quantized states of ultracold sodium atoms in an optical lattice with a tilted harmonic trap, *Phys. Rev. A.*, **66**, 023407–023415.
- Shepelyansky D.L. and Stone A.D., 1995, Chaotic Landau-level mixing in classical and quantum-wells, *Phys. Rev. Lett.*, **74**, 2098–2101.
- Shik A.Y., 1975, Superlattices—periodic semiconductor structures (review), *Sov. Phys. Semicond.*, **8**, 1195–1209.
- Shimada Y., Hirakawa K., Odnoblioudov M. and Chao K.A., 2003, Terahertz conductivity and possible Bloch gain in semiconductor superlattices, *Phys. Rev. Lett.*, **90**, 046806–046809.
- Shlesinger M.F., Zaslavsky G.M. and Klafter J., 1993, Strange kinetics, *Nature*, **363**, 31–37.
- Soskin S.M., Khovanov I.A., Mannella R. and McClintock P.V.E., 2009, M. Macucci and G. Basso, eds., Acceleration of the chaotic and noise-induced transport in adiabatically driven spatially periodic systems, *Noise and Fluctuations: 20th International Conference on Noise and Fluctuations (ICNF-2009)*, AIP, Melville, New York, vol. 1129, 17–20.
- Soskin S.M., McClintock P.V.E., Fromhold T.M., Khovanov I.A. and Mannella R., 2009, Stochastic webs and quantum transport in superlattices: an introductory review, *Contemporary Physics*, to be published.
- Stapleton S.P., Bujkiewicz S., Fromhold T.M., Wilkinson P.B., Patanè A., Eaves L., Krokhn A.A., Henini M., Sankeshwar N.S. and Sheard F.W., 2004, Use of stochastic web patterns to control electron transport in semiconductor superlattice, *Physica D*, **199**, 166–172.
- Steck D.A., Oskay W.H. and Raizen M.G., 2001, Observation of chaos-assisted tunneling between islands of stability, *Science*, **293**, 274–278.
- Stöckmann H.-J., 1999, *Quantum Chaos: An Introduction*, Cambridge University Press, Cambridge.
- Vasiliev A.A., Zaslavsky G.M., Natenzon M.Y., Neishtadt A.I., Petrovichev B.A., Sagdeev R.Z. and Chernikov A.A., 1989, Attractors and stochastic attractors of motion in a magnetic-field, *Sov. Phys. JETP*, **67**, 2053. [*Zh. Eksp. Teor. Fiz.*, **94**, 170, (1988)]
- Wacker A., 2002, Semiconductor superlattices: A model system for nonlinear transport, *Phys. Rep.*, **357**, 1–111.
- Weiss D., Roukes M.L., Menshig A., Grambow P., von Klitzing K. and Weimann G., 1991, Electron pinball and commensurate orbits in a periodic array of scatterers, *Phys. Rev. Lett.*, **66**, 2790–2793.
- Weiss D., Richter K., Menshig A., Bergmann R., Schweizer H., von Klitzing K., and Weimann G., 1993, Quantized periodic-orbits in large antidot arrays, *Phys. Rev. Lett.*, **70**, 4118–4121.
- Wilkinson P.B. and Fromhold T.M., 2003, Chaotic ray dynamics in slowly varying two-dimensional photonic crystals. *Opt. Lett.*, **28**, 1034–1036.

- Wilkinson P.B., Fromhold T.M., Eaves L., Sheard F.W., Miura N. and Takamasu T., 1996, Observation of 'scarred' wavefunctions in a quantum well with chaotic electron dynamics, *Nature*, **380**, 608–610.
- Zaslavsky G.M., Sagdeev R.Z., Usikov D.A. and Chernikov A.A., 1991, *Weak Chaos and Quasi-Regular Patterns*, Cambridge University Press, Cambridge.
- Zaslavsky G.M., 2004, *Hamiltonian Chaos and Fractional Dynamics*, Oxford University Press, Oxford.
- Zhang Y., Kastrup J., Klann R., Ploog K.H. and Grahn H.T., 1996, Synchronization and chaos induced by resonant tunneling in GaAs/AlAs superlattices, *Phys. Rev. Lett.*, **77**, 3001–3004.

# Chapter 6

## Chaos in Ocean Acoustic Waveguide

A.L. Virovlyansky

**Abstract** At the end of 1980s it was realized that the phenomenon of ray chaos to a significant extent determines the long range sound propagation in the ocean. In this Chapter we consider the chaotic ray motion and its manifestations in the modal structure of the wave field in a deep water acoustic waveguide. It is assumed that the ray and wave chaos is caused by the sound speed fluctuations induced by random internal waves.

### 6.1 Introduction

Long-range sound propagation in the ocean is possible due to the existence of a natural refractive waveguide called the underwater sound channel (USC) (Brekhovskikh and Lysanov, 1991; Jensen et al., 1994; Flatte et al., 1979). The point is that the vertical sound speed profile in a deep ocean usually has a minimum at a depth of about 1 km. Therefore, part of the sound energy is captured within the water bulk which prevents it from the interaction with the lossy bottom. Since the dissipation in sea water at frequencies  $O(100 \text{ Hz})$  is rather small, low frequency sound waves captured in the USC can propagate with comparatively low attenuation over distances of order thousands of kilometers (Munk et al., 1994). In the ocean acoustics such distances are termed the megameter ranges.

Wave fields in the USCs are governed by the linear wave equation. Therefore, they can be described using standard methods traditionally employed in other waveguide media. Extensive theoretical and experimental studies of long range sound propagation in the ocean have been carried out for sixty years. Already in the middle 1980s this topic was considered well understood. However, in the last

---

A.L. Virovlyansky  
Institute of Applied Physics, Russian Academy of Science,  
46 Ul'yanov Street, 603950 Nizhny Novgorod, Russia,  
e-mail: viro@hydro.appl.scinnov.ru

two decades it turned out that there exists a factor, earlier not taken into consideration, which to a significant extent determines the structure of the wave field at long ranges. This is the phenomenon of ray chaos whose significance was realized at the end of the 1980s (Palmer et al., 1988; Abdullaev and Zaslavsky, 1991; Palmer et al., 1991; Smith et al., 1992; Tappert and Tang, 1996).

The phenomenon of ray chaos and its manifestations at a finite wavelength—the so-called wave chaos—have well-known prototypes in mechanics: the dynamical chaos and the quantum chaos (Reichl, 1992). The point is that the same Hamilton equations describe a ray trajectory in an inhomogeneous waveguide and a nonlinear oscillator under the action of a nonstationary (deterministic) external force. The situation where the oscillator behaves in a quasi-random way is typical (Zaslavsky, 1985; Lichtenberg and Lieberman, 1992). Investigation of the phase space of such an oscillator is a classical problem of the theory of dynamic chaos. The objects studied by the theory of quantum chaos are the systems whose classical analogs exhibit a chaotic behavior.

A significant contribution to understanding the role of ray and wave chaos in the waveguide propagation was given in works of G. Zaslavsky. In a series of papers written by S. Abdullaev and G. Zaslavsky in the 1980s it was shown how the methods derived in the theory of dynamical and quantum chaos can be applied for the description of wave fields in range-dependent waveguides. Their results are summarized in review (Abdullaev and Zaslavsky, 1991) and monograph (Abdullaev, 1993). In the 1990s G. Zaslavsky turned his attention to problems related to manifestations of the chaotic ray motions in the ocean acoustics. This topic became an important direction of his research activity (Abdullaev and Zaslavsky, 1991; Smirnov et al., 2001, 2002; Brown et al., 2003; Smirnov et al., 2004, 2005a,b; Virovlyanskii and Zaslavsky, 2007).

First works on studying the ray chaos in ocean acoustic waveguides were based on highly idealized environmental models with range-periodic perturbation (Palmer et al., 1988; Abdullaev and Zaslavsky, 1991; Smith et al., 1992). The point is that the chaotic ray dynamics in range-periodic waveguides can be examined by direct application of methods borrowed from the theory of dynamical chaos, such, for example, as the method of Poincaré map.

Later on, more realistic waveguide models with a random perturbation of the sound speed field were explored (Brown and Viechnicki, 1998; Beron-Vera et al., 2003). In a deep ocean, it is generally believed that the sound speed inhomogeneities induced by internal waves are the dominant cause of the acoustic fluctuations at long ranges (Flatte et al., 1979). In the presence of random internal waves the ray paths become extremely sensitive to variations of the initial conditions: vertical separation between the paths with close starting parameters, on the average, grows with range  $r$  as  $\exp(\nu r)$ , where  $\nu$  is the Lyapunov exponent. For realistic models of deep water waveguides the values of  $\nu$  are on the order of  $1/100 \text{ km}^{-1}$  (Simmen et al., 1997; Beron-Vera et al., 2003). At ranges  $O(1000 \text{ km})$  the ray chaos is well developed and it cannot be ignored when describing the long range sound propagation in the ocean.

In recent years it has been demonstrated that the ray-based description of the sound field in a deep water acoustic waveguide can properly predict many important

features of the arrival pattern at megameter ranges. Numerical results obtained in the scope of the geometrical optics approximation are consistent with both parabolic-equation-based simulations and field experiments (Worcester et al., 1999; Colosi et al., 1999; Beron-Vera et al., 2003). Simulations show that even at distances  $O(1000 \text{ km})$  effects of ray scattering may dominate diffractive effects (Simmen et al., 1997). These results stimulate the developing of ray-based approaches for the analysis of long range sound propagation.

In this paper we review a statistical approach derived in Refs. (Virovlyansky, 2005b; Virovlyansky et al., 2007) for description of the chaotic ray dynamics in a waveguide with a perturbation of the sound speed field caused by random internal waves. Following Ref. (Virovlyansky et al., 2009; Virovlyansky, 2006), we also consider the manifestations of ray chaos in the modal structure of the sound field. A more detailed discussion of these issues is given in monograph (Makarov et al., 2010).

Traditional approaches for describing stochastic ray dynamics in a waveguide with random inhomogeneities are associated with ideas of the study of wave propagation in random media (WPRM) (Flatte et al., 1979; Rytov et al., 1978). It should be emphasized that the theory of WPRM and the theory of ray chaos investigate the ray structure from different and complementary viewpoints. Let us formulate the difference in statements of problems in these two approaches (Virovlyanskii and Zaslavsky, 2007; Virovlyansky et al., 2007).

(i) The description of WPRM is based on the notion of statistical ensemble. The latter consists of infinitely many realizations of the waveguide specified by different  $\delta c(r, z)$ . Statistical characteristics of a ray with given starting parameters  $z_0$  and  $\chi_0$ —initial depth and grazing angle, respectively, — are determined by averaging over rays with the same initial parameters in all realizations.

(ii) The theory of ray chaos deals with a *deterministic* medium. In our case the latter is specified by a *single* realization of random perturbation. At ranges  $r \gg \nu^{-1}$  initially close ray paths become practically independent and the averaging over their starting parameters can be considered as the statistical averaging.

An approximate analytical description of chaotic ray structure in a deep water environment was derived in Refs. (Virovlyansky, 2005b,a; Virovlyansky et al., 2007). This was done using the Hamiltonian formalism expressed in terms of the action-angle variables  $(I, \theta)$ . These variables are a convenient tool for studying oscillations of particles (in mechanics) and rays (in wave theory) (Abdullaev and Zaslavsky, 1991; Landau and Lifshitz, 1976). The action variable  $I$  determines both ray amplitude and cycle length while the angle variable  $\theta$  (it should not be confused with the ray grazing angle) determines the position of a current ray point within the cycle. The angle variable  $\theta$  may be interpreted as a phase of an oscillating ray path. The use of the action-angle variables has the following three important advantages.

First, the statistical description of rays in a waveguide with a perturbation caused by random internal waves is greatly simplified due to the fact that  $\theta$  rapidly randomizes and already at comparatively short ranges (hundreds of kilometers) for most rays it becomes more or less uniformly distributed on  $(0, 2\pi)$ . Then the problem reduces to investigation of a slow diffusion of action  $I$  described by the Fokker-Planck

equation. A similar approach is commonly applied in the studies of dynamical chaos (Lichtenberg and Lieberman, 1992). In Refs. (Virovlyansky, 2005b,a; Virovlyansky et al., 2007) it was shown that irregular range variations of action in a realistic environmental model may be approximated by a random Wiener process representing the simplest model of diffusion (Gardiner, 1985). This yields a simple stochastic ray theory which allows one to derive analytical estimates characterizing the chaotic ray dynamics.

Second, the action-angle variables are a convenient tool for studying the ray travel times, that is arrival times of sound pulses coming through individual ray paths. In the methods of ocean acoustic tomography and thermometry these quantities are used as input parameters in reconstructing the variations of temperature fields (Munk and Wunsch, 1979; Worcester et al., 1999). In Refs. (Virovlyansky, 2003; Virovlyansky et al., 2007) it is demonstrated that the variations of ray travel times caused by weak fluctuations of sound speed are expressed through variations of the action and angle variables. This allows one to apply to stochastic ray theory to studying fluctuations of the ray travel times.

Third, the use of the action-angle variables allows one to establish a simple link between the ray and mode representations of the wave field. The normal mode is formed by contribution from rays whose action variables at the observation range satisfy the quantization rule (Virovlyansky et al., 2005, 2009). It turns out that the mode amplitudes can be expressed through parameters of the ray paths. This ray-based approach for the description of the modal structure allows one to apply the stochastic ray theory for description of normal modes under conditions of wave chaos.

The paper is organized as follows. Section 6.2 includes a background material. We present the basic equations for the description of the wave field; introduce the the Hamiltonian formalism in terms of the momentum-position and action-angle variables; discuss the ray-based approach for the evaluation of mode amplitudes. Statistical approach for the description of chaotic rays is formulated in Sect. 6.3. It is applied to the evaluation of the probability density functions of different ray parameters and evaluation of the coarse-grained distribution of the sound energy. Section 6.4 is concerned with statistics of ray travel times. Our attention is focused on the distribution of ray arrivals in the time-depth plane. In Sect. 6.5 it is shown that an approximate analytical description of the modal structure at megameter ranges can be obtained by combining relations expressing mode amplitudes through parameters of ray paths, and stochastic ray theory. We present analytical estimates for the coarse-grained distribution of the sound energy over normal mode. We also estimate the spread and bias of sound pulses carried by individual modes due to scattering at random inhomogeneities. In Sect. 6.6 the results of this work are summarized.

## 6.2 Basic equations

In this section the main equations governing the sound wave field are presented. Our analysis is based on the standard parabolic equation obtained from the linear

wave equation in the small-angle approximation. The ray and modal representations of the wave field are introduced. In describing the ray representation we use the Hamiltonian formalism expressed in terms of the momentum-position and action-angle canonical variables. It is shown that even in a range-dependent waveguide the amplitudes of normal modes can be (approximately) expressed through parameters of ray paths, that is, through solutions of the Hamilton (ray) equations.

### 6.2.1 Parabolic equation approximation

In what follows we shall study the ray structure of acoustic field in a simple but realistic 2-dimensional environmental model. The sound speed field  $c(r, z)$  ( $r$  is range and  $z$  is depth) in this model is presented in the form

$$c(r, z) = \bar{c}(z) + \delta c(r, z), \quad (6.1)$$

where  $\bar{c}(z)$  is a smooth (unperturbed) background profile and  $\delta c(r, z)$  is a weak range-dependent perturbation caused by random internal waves (Flatte et al., 1979). The  $z$ -axis is directed upward and the sea surface is located at  $z = 0$ .

Sound wave field  $v$  as a function of  $r$ ,  $z$ , and time  $t$  can be represented as

$$v(r, z, t) = \int d\Omega \tilde{v}(r, z, \Omega) e^{-i\Omega t}, \quad (6.2)$$

with  $\tilde{v}$  governed by the Helmholtz equation (Brekhovskikh and Lysanov, 1991; Jensen et al., 1994)

$$\frac{\partial^2 \tilde{v}}{\partial r^2} + \frac{\partial^2 \tilde{v}}{\partial z^2} + \frac{\Omega^2}{c^2} \tilde{v} = 0. \quad (6.3)$$

At distances on the order of hundreds kilometers the sound field is formed by waves propagating at small grazing angles. Only such waves survive at so long ranges. In the small angle approximation Eq. (6.3) can be replaced by the parabolic equation (Brekhovskikh and Lysanov, 1991; Jensen et al., 1994; Simmen et al., 1997). Represent  $\tilde{v}$  as

$$v(r, z, \Omega) = r^{-1/2} u(r, z, \Omega) e^{ikr}, \quad (6.4)$$

where  $k = \Omega/c_0$  is a wave number in a reference medium with the sound speed  $c_0$ , and  $u(r, z, \Omega)$  is an envelope function. On neglecting the second derivative of  $u$  with respect to  $r$ , we arrive at the standard parabolic equation (Brekhovskikh and Lysanov, 1991; Tappert, 1977)

$$2ik \frac{\partial u}{\partial r} + \frac{\partial^2 u}{\partial z^2} - 2k^2 [U(z) + V(r, z)] u = 0, \quad (6.5)$$

where

$$U(z) = \frac{1}{2} \left( 1 - \frac{c_0^2}{\bar{c}^2(z)} \right), \quad V(r, z) \simeq \frac{\delta c(r, z)}{c_0}. \quad (6.6)$$

Transient wave field excited by a pulse source can be synthesized out of solutions of Eq. (6.5) at different carrier frequencies as

$$v(r, z, t) = r^{-1/2} \int d\Omega' u(r, z, \Omega') s(\Omega') e^{i\Omega'(r/c_0 - t)}, \quad (6.7)$$

where  $s(\Omega)$  is the spectrum of an initially radiated pulse.

Note that Eq. (6.5) formally coincides with the time-dependent Schrödinger equation. In this analogy  $r$  plays a role of time and  $k^{-1}$  associates with the Planck constant. However, it is difficult to generalize this analogy between the quantum mechanics and wave theory to the case of a transient wave field. The integration over  $\Omega$  in Eq. (6.7) formally corresponds to integration over the Plank constant.

### 6.2.2 Geometrical optics. Hamiltonian formalism

In the geometrical optics approximation the solution to Eq. (6.5) is expressed through parameters of ray trajectories (Abdullaev and Zaslavsky, 1991; Brown and Viechnicki, 1998; Simmen et al., 1997; Beron-Vera et al., 2003). In the unperturbed waveguide ( $V = 0$ ) the ray path obeys the Hamilton equations  $dz/dr = \partial H / \partial p$  and  $dp/dr = -\partial H / \partial z$ , where  $H = p^2/2 + U(z)$  is an unperturbed Hamiltonian and  $p$  is the momentum. The latter is related to the ray grazing angle  $\chi$  through  $p = \tan \chi$ . In the presence of perturbation  $H$  should be replaced by  $H + V$ .

In deep water acoustic waveguides the sound speed profile at any cross-section ( $r = \text{const}$ ) usually has a minimum at a depth of about 1 km (Brekhovskikh and Lysanov, 1991). Then  $U$  represents a “potential well” whose parameters may vary with range  $r$ . Since  $r$  is a time-like variable, our Hamiltonian system formally coincides with that describing a mechanical particle oscillating in a time-dependent potential well.

The contribution from a single ray to the total wave field is

$$u(r, z, \Omega) = A(r, z) \exp [ikS(r, z)], \quad (6.8)$$

where  $A$  and  $S$  are the ray amplitude and eikonal, respectively. The eikonal  $S$  is an analog to Hamilton’s principal function in classical mechanics and it is given by an integral

$$S = \int [p dz - (H + V) dr] \quad (6.9)$$

running over the ray path (Landau and Lifshitz, 1976; Simmen et al., 1997).

The amplitude  $A$  also can be expressed through solutions of the Hamilton (ray) equations (Brekhovskikh and Lysanov, 1991). In the case of a point source whose wave field satisfies parabolic equation (6.5) with an initial condition

$$u(0, z_s, \Omega) = \delta(z - z_s), \quad (6.10)$$

all rays escape the same point  $(0, z_s)$  with different starting momenta  $p_0$ . Then

$$A = \sqrt{\frac{k}{2\pi i |\partial z / \partial p_0|}}. \quad (6.11)$$

Rays arriving at a given observation point are called the *eigenrays*. Equations (6.8) and (6.11) determine the contribution to the total wave field from an individual eigenray.

**Action-angle variables.** Consider an unperturbed waveguide and for simplicity assume that the function  $U(z)$  has a single minimum. In this (range-independent) waveguide each ray is periodic and the Hamiltonian  $H$  remains constant along the trajectory. The action variable  $I$  is defined as an integral over a cycle of the ray path (Abdullaev and Zaslavsky, 1991; Landau and Lifshitz, 1976)

$$I = \frac{1}{2\pi} \oint p dz = \frac{1}{\pi} \int_{z_{\min}}^{z_{\max}} dz \sqrt{2[H - U(z)]}, \quad (6.12)$$

where  $z_{\min}$  and  $z_{\max}$  are the lower and upper turning depths, respectively, satisfying the condition  $U(z) = H$ . Equation (6.12) defines function  $H(I)$  expressing the Hamiltonian as a function of action. The canonical transformation

$$p = p(I, \theta), \quad z = z(I, \theta) \quad (6.13)$$

connecting the position-momentum and action-angle variables is defined by equations  $p = \partial G / \partial z$  and  $\theta = \partial G / \partial I$ , where  $G(I, z)$  is a generating function. For  $p > 0$

$$G(I, z) = \int_{z_{\min}}^z dz P(I, z), \quad P(I, z) = \sqrt{2[H(I) - U(z)]}. \quad (6.14)$$

If  $p < 0$ ,  $G(I, z)$  should be replaced by  $2\pi I - G(I, z)$ . The angle variable  $\theta$  can be interpreted as a phase of the ray path. The so-defined  $\theta$  will be called the wrapped angle variable. It belongs to an interval from 0 to  $2\pi$ . To make  $\theta$  continuous, its value should be increased by  $2\pi$  at the beginning of each new cycle. This is a standard procedure (Landau and Lifshitz, 1976). It makes the angle variable  $\theta$  unwrapped.

According to the Liouville theorem the Jacobian of any canonical transformation is equal to unity (Landau and Lifshitz, 1976). Thus, we have

$$\frac{\partial(I(p, z), \theta(p, z))}{\partial(p, z)} = \frac{\partial(p(I, \theta), z(I, \theta))}{\partial(I, \theta)} = 1. \quad (6.15)$$

The canonical transformation determined for the unperturbed waveguide, formally, can be used in the perturbed waveguide (with  $V \neq 0$ ), as well. In the presence of perturbation the ray equations take the form

$$\frac{dI}{dr} = -\frac{\partial V}{\partial \theta}, \quad (6.16)$$

and

$$\frac{d\theta}{dr} = \omega + \frac{\partial V}{\partial I}, \quad (6.17)$$

where  $\omega(I) = dH(I)/dI$  is the spatial angular frequency of the ray path oscillation in the unperturbed waveguide. The cycle length of the unperturbed path is  $D(I) = 2\pi/\omega(I)$ .

In what follows we will use functions  $I(r, I_0, \theta_0)$  and  $\theta(r, I_0, \theta_0)$  to denote the action and angle of the ray path at range  $r$ . Arguments  $I_0$  and  $\theta_0$  are initial values of these variables at  $r = 0$ . Sometimes it will be more convenient to use similar functions  $I(r, p_0, z_0)$  and  $\theta(r, p_0, z_0)$  where  $p_0$  and  $z_0$  are initial momentum and coordinate of the ray path, respectively.

**Ray travel times.** A signal arriving at the observation point through a particular ray path—we call it the *ray pulse*—can be evaluated by substituting Eq. (6.8) into Eq. (6.7). Since both  $A$  and  $S$  do not depend on  $\Omega$  it is easy to see that the travel time of a ray pulse is

$$t = (r + S)/c_0. \quad (6.18)$$

In the unperturbed waveguide, from Eqs. (6.9) and (6.12) it follows that at one cycle of oscillations the eikonal of a ray with action  $I$  increases by  $2\pi[I - H(I)/\omega(I)]$ . Therefore at a long range  $r$  the travel time is approximately equal to

$$\bar{t}(I, r) = [1 + I\omega(I) - H(I)]r/c_r. \quad (6.19)$$

### 6.2.3 Modal representation of the wave field

The wave field at any range point can be presented in the form of decomposition

$$u(r, z, \Omega) = \sum_m a_m(r, \Omega) \varphi_m(z, \Omega), \quad (6.20)$$

where  $\varphi_m(z, \Omega)$  are eigenfunctions of the Sturm–Liouville problem in the unperturbed waveguide (Brekhovskikh and Lysanov, 1991; Brekhovskikh and Godin, 1999). Each term in this sum describes a normal mode. For simplicity, we restrict our attention to modes with turning points within the water bulk. In the WKB approximation the  $m$ -th eigenfunction is determined by parameters of an unperturbed ray path whose action variable—we denote it by  $I_{m\Omega}$ —satisfies the quantization rule (Brekhovskikh and Lysanov, 1991; Brekhovskikh and Godin, 1999; Landau and Lifshitz, 1977)

$$I_{m\Omega} = \frac{m - 1/2}{k} = \frac{m - 1/2}{\Omega} c_0, \quad m = 1, 2, \dots \quad (6.21)$$

The eigenfunction of the  $m$ -th mode between its turning points can be presented as (Brekhovskikh and Lysanov, 1991; Brekhovskikh and Godin, 1999; Landau and Lifshitz, 1977)

$$\varphi_m(z, \Omega) = \varphi_m^+(z, \Omega) + \varphi_m^-(z, \Omega), \quad (6.22)$$

where

$$\varphi_m^\pm(z, \Omega) = [D(I_{m\Omega})P(I_{m\Omega}, z)]^{-1/2} \exp\{\pm i[kG(I_{m\Omega}, z) - \pi/4]\}. \quad (6.23)$$

#### 6.2.4 Ray-based description of normal modes

The ray-based description of mode amplitudes  $a_m(r, \Omega)$  can be derived by projecting the ray representation of the wave field onto normal modes and evaluating the corresponding integrals using the stationary phase technique. A detailed discussion of this issue is given in Refs. (Berman and Zaslavsky, 1979; Virovlyansky and Zaslavsky, 1999; Virovlyansky, 2000; Virovlyansky et al., 2005; Virovlyansky, 2006). It turns out that each modes is formed by contributions from rays—we will call them the *mode rays*—whose actions at the observation range  $r$  satisfy the condition

$$I(r, I_0, \theta_0) = I_{m\Omega}. \quad (6.24)$$

It should be emphasized, that at different frequencies this condition singles out different rays. In this sense, the mode rays are frequency dependent.

If the action of the ray path is expressed by function  $I(r, p_0, z_0)$  Eq. (6.24) translates to

$$I(r, p_0, z_0) = I_{m\Omega}. \quad (6.25)$$

We will consider two types of sources.

**Point source.** In this case the wave field is a solution of Eq. (6.5) with initial condition (6.10) and all the rays start from a depth  $z_s$ . Then according to Eq. (6.25) we get the condition

$$I(r, p_0, z_s) = I_{m\Omega} \quad (6.26)$$

defining the starting momenta of mode rays. Take one of these rays and denote its coordinate at the range of observation by  $Z_{m\Omega}$ . Its contribution to the mode amplitude is (Virovlyansky and Zaslavsky, 1999; Virovlyansky, 2000; Virovlyansky et al., 2005; Virovlyansky, 2006)

$$a_m(r, \Omega) = Q \exp[i(\Phi + \beta)], \quad (6.27)$$

where

$$\Phi = k[S(r, Z_{m\Omega}) + \sigma G(I_{m\Omega}, Z_{m\Omega})], \quad (6.28)$$

$\sigma = -\text{sgn} p$ ,  $p$  is the momentum of the mode ray,

$$Q = \frac{1}{\sqrt{2\pi |\partial I(r, p_0, z_s) / \partial p_0|}}, \quad (6.29)$$

$\beta$  is a constant that does not depend on frequency. An explicit expression for  $\beta$  is given in Refs. (Virovlyansky and Zaslavsky, 1999; Virovlyansky, 2000; Virovlyansky et al., 2005; Virovlyansky, 2006).

**Single-mode source.** In this case

$$u(0, z, \Omega) = \varphi_{m_0}(z, \Omega). \quad (6.30)$$

Rays escape from depths  $z_0$  between turning points of the  $m_0$ -th mode. There are two rays escaping each  $z_0$  with starting momenta  $p_0 = \pm P(I_{m_0\Omega}, z_0)$ . All rays have the same initial action  $I_{m_0\Omega}$ . The condition that singles out the mode rays follows from Eq. (6.24) as

$$I(r, I_{m_0\Omega}, \theta_0) = I_{m_0\Omega}. \quad (6.31)$$

It determines  $\theta_0$  (an hence  $z_0$ ) corresponding to mode rays. A contribution from an individual mode ray to  $a_m$  has the form of Eq. (6.27) with the same expression for the phase  $\Phi$  and

$$Q = \frac{1}{\sqrt{2\pi k} |\partial I(r, I_{m_0\Omega}, \theta_0) / \partial \theta_0|} \exp[\pm ikG(I_{m_0\Omega}, z_0)]. \quad (6.32)$$

The mode amplitude is evaluated by summing up contributions from all the mode rays.

## 6.3 Ray chaos

In this section we construct a statistical description of the chaotic ray dynamics in a realistic model of the underwater acoustic waveguide with a sound speed fluctuation induced by random internal waves. The use of the action-angle variables greatly simplifies the analysis. It turns out that the range dependence of the action variable can be modeled by a random Wiener process. Then the angle variable is modeled by an integral of this process. In this approximation, surprisingly simple analytical estimates for statistical characteristics of ray parameters are derived. It is shown how this result can be applied for estimating the sound intensity smoothed over the depth with a sufficiently large smoothing scale.

### 6.3.1 Statistical description of chaotic rays

Statistical description of chaotic rays is based on a property of the chaotic ray dynamics called *mixing* (Lichtenberg and Lieberman, 1992; Sagdeev et al., 1988). Take a bundle of rays starting from a small area of the phase space  $\mathcal{R}$  centered at a point  $(p_0, z_0)$ . The square of  $\mathcal{R}$  denote by  $S_{\mathcal{R}}$ . At ranges  $r \gg v^{-1}$  points depicting the ray paths in the phase plane are scattered over much larger area  $\mathcal{R}'$ . Consider a

small portion of this area  $\Delta\mathcal{R}'$  centered at an observation point  $(p, z)$ . A fraction of trajectories arriving at  $\Delta\mathcal{R}'$  may be treated as an expectancy of hitting this area. In order to quantify this statement, introduce a function

$$P_{pz|p_0z_0}(p, z, r|p_0, z_0) = \frac{1}{S_{\mathcal{R}}} \times \iint_{\mathcal{R}} dp'_0 dz'_0 \delta(z - z(r, p'_0, z'_0, 0)) \delta(p - p(r, p'_0, z'_0, 0)), \quad (6.33)$$

which may be interpreted as a conditional probability density function (PDF) of ray coordinates in the phase plane. Then an integral over the area  $\Delta\mathcal{R}'$

$$P_{\Delta\mathcal{R}'} = \int_{\Delta\mathcal{R}'} dp dz P_{pz|p_0z_0}(p, z, r - r_0|p_0, z_0) \quad (6.34)$$

determines the probability that a ray path starting from  $(p_0, z_0)$  arrives at  $\Delta\mathcal{R}'$ . The mixing phenomenon manifests itself in the fact that at long ranges  $P_{\Delta\mathcal{R}'}$  weakly depends on the size and shape of  $\mathcal{R}$ . When  $r$  tends to infinity and sizes of  $\mathcal{R}$  tend to zero the dependence of  $P_{\Delta\mathcal{R}'}$  on the shape of  $\mathcal{R}$  vanishes. But at finite ranges  $r$  we cannot take too small  $\mathcal{R}$ 's and consider probabilities of hitting too small  $\Delta\mathcal{R}'$ 's.

In a similar way we define a conditional PDF  $P_{I\theta|I_0\theta_0}(I, \theta, r|I_0, \theta_0)$  for the action-angle variables. The connection between PDFs  $P_{pz|p_0z_0}$  and  $P_{I\theta|I_0\theta_0}$  is readily established using standard formulas of the probability theory. Equation (6.13) formally determines a nonlinear change of variables. The Liouville theorem (6.15) simplifies the application of standard relations and we arrive at

$$P_{pz|p_0z_0}(p, z, r|p_0, z_0) = P_{I\theta|I_0\theta_0}(I(p, z), \theta(p, z), r|I(p_0, z_0), \theta(p_0, z_0)). \quad (6.35)$$

The PDF introduced by Eq. (6.33) can be used for any environmental model in which rays exhibit chaotic behavior. But the application of this approach in a waveguide representing a realization of a random medium may have the following specific feature (Virovlyansky, 2006; Virovlyanskii and Zaslavsky, 2007; Virovlyansky et al., 2007, 2009). At long ranges initially close ray paths diverge so significantly that they are spaced apart from each other by intervals exceeding correlation scales of the medium. Then the rays travel through practically independent inhomogeneities and behave as if they propagate in different realizations of the medium. Therefore it is natural to expect that the averaging over initial conditions may give results close to those obtained by the ensemble averaging. It means that the PDF defined by Eq. (6.33) may comparatively weakly depend on a particular realization of the waveguide. Numerical simulations show that this is the case for our environmental model (see below).

### 6.3.2 Environmental model

In numerical simulations presented below we use an environmental model with an unperturbed profile  $\bar{c}(z)$  (borrowed from Ref. (Colosi and Flatté, 1996)) shown in the left panel of Fig. 6.1. It represents the Munk profile (Brekhovskikh and Lysanov, 1991; Flatte et al., 1979)

$$c_0(z) = c_0 [1 + \varepsilon(e^\eta - \eta - 1)], \quad \eta = 2(z - z_a)/Q \quad (6.36)$$

with parameters  $c_0 = 1.5$  km/s,  $\varepsilon = 0.00238$ ,  $Q = 0.485$  km, and  $z_a = -0.7$  km.

It is assumed that the weak perturbation  $\delta c(r, z)$  is caused by random internal waves with statistics determined by the empirical Garrett-Munk spectrum (Flatte et al., 1979). To generate realizations of a random field  $\delta c(r, z)$  we apply a numerical technique developed by J. Colosi and M. Brown (Colosi and Brown, 1998). Realizations of  $\delta c(r, z)$  have been computed using Eq. (19) from (Colosi and Brown, 1998). Components of wave number vectors in the horizontal plane belong to the interval from  $2\pi/100$  km<sup>-1</sup> to  $2\pi/4$  km<sup>-1</sup>. An rms amplitude of the perturbation scales in depth like  $\exp(3z/2L)$ , where  $L = 1$  km, and its surface-extrapolated value is about 0.5 m/s. Depth dependencies of  $\delta c$  at three different ranges are shown in the right panel of Fig. 6.1.

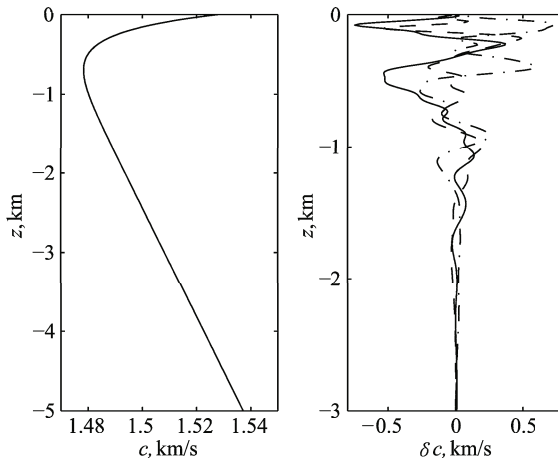


**Fig. 6.1** Unperturbed sound speed profile  $\bar{c}(z)$  (left panel) and perturbation  $\delta c$  in vertical sections of the waveguide at three different ranges (right panel).

### 6.3.3 Wiener process approximation

In (Virovlyansky, 2005b, 2006; Virovlyansky et al., 2007; Virovlyanskii and Zaslavsky, 2007) it is shown that an analytical estimate of the above PDF can be obtained by replacing the Hamilton (ray) equations (6.16) and (6.17) with simple stochastic Langevin equations. The point is that due to the smallness of perturbation  $\delta c$ , the action variable  $I$  weakly varies at the longitudinal correlation scales  $l_r$  of the sound speed fluctuations. Therefore, the right-hand side of Eq. (6.16) may be approximated by a delta-correlated random function  $\xi(r)$  with statistical moments

$$\langle \xi \rangle = 0, \quad \langle \xi(r)\xi(r') \rangle = B\delta(r-r'). \quad (6.37)$$

The values of  $B$  were estimated numerically for a few typical deep water waveguides (Virovlyansky, 2005b, 2006; Virovlyansky et al., 2007; Virovlyanskii and Zaslavsky, 2007; Udovidchenkov and Brown, 2008). They turned out to be of order  $10^{-7}$  km. In the environmental model described in Sect. 6.3.2,  $B$  is about  $1.4 \times 10^{-7}$  km for practically all the ray paths.

Represent the action and angle variables of a ray path in the form

$$I(r, I_0, \theta_0) = I_0 + x(r), \quad \theta(r, I_0, \theta_0) = \theta_0 + \omega(I_0)r + y(r), \quad (6.38)$$

where  $x(r)$  and  $y(r)$  are random functions describing the deviation of the ray path from its unperturbed position. They are determined by stochastic Langevin equations

$$\frac{dx}{dr} = \xi, \quad (6.39)$$

and

$$\frac{dy}{dr} = \omega'(I_0)x \quad (6.40)$$

which approximate Eqs. (6.16) and (6.17), respectively. Here and in what follows we use the notation  $\omega'(I) = d\omega(I)/dI$ . Equation (6.40) is derived by neglecting the derivative  $\partial V/\partial I$  in the right hand-side of Eq. (6.17) and replacing  $\omega(I)$  by  $\omega(I_0) + \omega'(I_0)x$ .

At short ranges where the ray action is still close to its starting value, the deviation of the ray path from its unperturbed position is determined by the random increment of the angle variable  $y$ . According to Eq. (6.40) the rms value of  $y$  is proportional to the derivative  $\omega'(I_0)$  which is defined by the unperturbed sound speed profile  $\bar{c}(z)$ . This means that the parameter  $\omega'(I_0)$  to a significant extent determines the sensitivity of a ray path to the sound speed fluctuations. This conclusion is consistent with results obtained in Refs. (Beron-Vera and Brown, 2003, 2004; Brown et al., 2005; Rypina and Brown, 2007; Udovidchenkov and Brown, 2008), where the authors argue that the sensitivity of the ray path is controlled by the stability parameter of the background sound speed profile

$$\alpha = \frac{I\omega'(I)}{\omega(I)}. \quad (6.41)$$

Numerical results presented in the above papers, show that ray instability increases with increasing magnitude of  $\alpha$ .

Since  $B$  in our environmental model can be approximated by the constant, both Langevin equations are readily solved. The deviation of action  $x(r)$  is expressed by a random Wiener process (Gardiner, 1985). It is a zero mean Gaussian process whose statistical characteristics are defined by the correlation function  $\langle x(r)x(r') \rangle = B \min(r, r')$ . The deviation of the angle variable is given by relations

$$y(r) = \omega'(I_0)\eta(r), \quad \eta(r) = \int_0^r dr' x(r'), \quad (6.42)$$

that is,  $y(r)$  is described by an integral of the Wiener process. The approach based on Eqs. (6.37)–(6.40) we call the Wiener process approximation.

Using the standard relations of the probability theory, it is easy to show that the conditional PDF of action  $I$  at range  $r$ , i.e., the PDF of  $I$  given that at  $r = 0$  this variable equals  $I_0$ , is

$$P_{I|I_0}(I, r|I_0) = \frac{1}{\sqrt{2\pi Br}} \exp \left[ -\frac{(I - I_0)^2}{2Br} \right]. \quad (6.43)$$

In the scope of our approach statistical characteristics of the action variable does not depend on the starting angle  $\theta_0$ .

There is a subtlety to this result. According to Eq. (6.43), action  $I$  may take on both positive and negative values. But the action is nonnegative by definition. According to Eq. (6.43) this condition is met for most rays if  $I_0$  exceeds  $\sqrt{Br}$ . At megameter ranges this occurs for rays with grazing angles  $\chi_a$  at the sound channel axis  $z = z_a$  satisfying the condition

$$|\chi_a| > 5^\circ. \quad (6.44)$$

For treating flat rays our approach should be modified as it is discussed in Refs. (Virovlyansky, 2005b, 2006; Virovlyansky et al., 2007; Virovlyanskii and Zaslavsky, 2007).

The standard deviations of the action and angle variables for steep rays satisfying condition (6.44) are

$$\sigma_I \equiv \langle (I - I_0)^2 \rangle^{1/2} = (Br)^{1/2}. \quad (6.45)$$

and

$$\sigma_\theta \equiv \langle y^2 \rangle^{1/2} = |\omega'(I_0)| (B/3)^{1/2} r^{3/2}. \quad (6.46)$$

In the Wiener process approximation Eq. (6.35) translates to

$$P_{pz|p_0z_0}(p, z, r|p_0, z_0) = \frac{1}{2\pi} P_{I|I_0}(I(p, z), r|I(p_0, z_0)). \quad (6.47)$$

### 6.3.4 Distribution of ray parameters

Function  $P_{pz|p_0z_0}(p, z, r|p_0, z_0)$  describes statistics of rays starting from a small area of the phase plane centered at point  $(p_0, z_0)$ . In the case of a point source set at a depth  $z_s$  we have a family of rays whose starting points in the phase plane  $p - z$  form a segment of straight line determined by the relations  $z_0 = z_s$  and  $-p_{\max} < p_0 < p_{\max}$ . In order to describe the statistical characteristics of these rays, let us assume that the quantity  $\eta(p_0)dp_0$  defines a fraction of rays with starting momenta from an interval  $(p_0, p_0 + dp_0)$ . The function  $\eta(p_0)$  is determined by the radiation pattern of a particular source. Formally considering  $\eta(p_0)$  as a PDF of the initial momentum  $p_0$  and exploiting Eqs. (6.33), (6.45), and (6.47) we can find PDFs of  $I$ ,  $p$ , and  $z$  at ranges  $r \gg v^{-1}$  (Virovlyansky, 2005b; Virovlyansky et al., 2007). PDF of action is

$$P_I(I, r) = \int dp_0 \eta(p_0) P_{I|I_0}(I, r|I(p_0, z_s)). \quad (6.48)$$

Exploiting standard formulas of the probability theory and the Liouville theorem (6.15), we obtain a joint PDF of  $p$  and  $z$ :

$$P_{pz}(p, z, r) = \frac{1}{2\pi} P_I(I(p, z), r). \quad (6.49)$$

Equations (6.48) and (6.49) yield a PDF of momentum

$$P_p(p, r) = \frac{1}{2\pi} \int dp_0 dz \eta(p_0) P_{I|I_0}(I(p, z), r|I(p_0, z_s)), \quad (6.50)$$

and depth

$$P_z(z, r) = \frac{1}{2\pi} \int dp_0 dp \eta(p_0) P_{I|I_0}(I(p, z), r|I(p_0, z_s)). \quad (6.51)$$

To check the above relations we have traced 50000 rays escaping a source set at depth  $z_0 = z_a$  with initial momenta uniformly distributed in an interval  $(-p_{\max}, p_{\max})$ , with  $p_{\max} = 0.22$  corresponding to a maximum launch angle  $\chi_{\max} = 12.5^\circ$ . In this case  $\eta(p_0) = (2p_{\max})^{-1}$ . Smooth lines in Fig. 6.2 show PDFs of  $I$  (a),  $\theta$  (b),  $p$  (c), and  $z$  (d) at a range of 3000 km obtained in the Wiener process approximation, that is evaluated by formulas (6.48), (6.50), and (6.51). For the wrapped angle variable  $\theta$  the uniform distribution is expected. The smooth curves are compared to stairstep graphs representing distributions (normalized histograms) of the same quantities obtained by direct numerical ray tracing for two different realizations of  $\delta c(r, z)$ . It is clear that predictions made in the Wiener process approximation are in good agreement with the results of ray tracing. In these figures we see that, consistent with our expectation, distributions of ray parameters weakly depend on particular realizations of perturbation.

### 6.3.5 Smoothed intensity of the wave field

At ranges  $O(1000 \text{ km})$ , where the ray chaos is well developed, the wave field at any observation point is formed by a huge number of chaotic eigenrays. A coarse-grained distribution of the sound field intensity determined as

$$J(r, z) = \frac{1}{\sqrt{2\pi}\Delta_z} \int dz' |u(r, z')|^2 \exp \left[ -\frac{(z - z')^2}{2\Delta_z^2} \right], \quad (6.52)$$

where  $\Delta_z$  is a smoothing scale, may be estimated by an incoherent summation of contributions from these eigenrays. According to Eq. (6.11), a sum of their intensities can be presented in the form

$$\begin{aligned} |u(r, z)|^2 &= \sum_j \frac{k}{2\pi |\partial z / \partial p_0|} \Big|_{p_0=p_{0,j}} \\ &= \frac{k}{2\pi} \int dp_0 \delta(z - z(r, p_0, z_s)), \end{aligned} \quad (6.53)$$

where the index  $j$  in the middle expression numbers the eigenrays. Let us show that under conditions of a well developed ray chaos the integral in Eq. (6.53) can be presented in the form of a statistical average.

As above, we assume that the initial momenta  $p_0$  of rays leaving the source lie within an interval  $(-p_{\max}, p_{\max})$ . Let us divide this interval into a set of small subintervals with end points  $p_j, j = 1, \dots, N$ . Then the last expression in Eq. (6.53) can

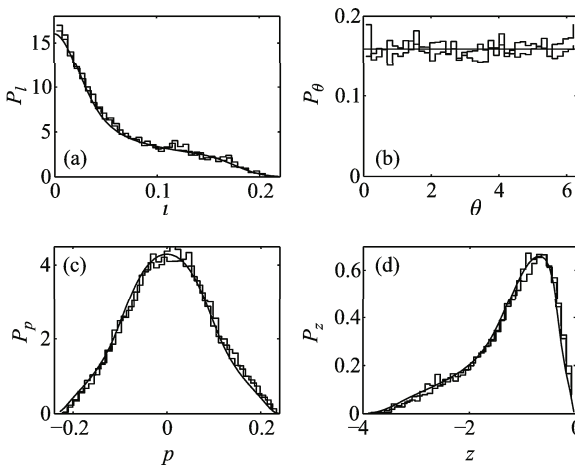


**Fig. 6.2** Distributions of ray parameters at  $r = 3000 \text{ km}$ . Smooth curves show PDFs of  $I$  (a),  $\theta$  (b),  $p$  (c), and  $z$  (d) evaluated analytically in the Wiener process approximation for rays escaping a point source set at a depth  $z_s = -0.7 \text{ km}$ . Stairstep graphs present normalized histograms, obtained by numerical ray tracing in waveguides with two different realizations of perturbation  $\delta c(r, z)$ .

be presented as a sum of integrals over these subinterval

$$|u(r, z)|^2 = \frac{k}{2\pi} \sum_{j=1}^{N-1} \int_{p_{j-1}}^{p_j} dp_0 \delta(z - z(r, p_0, z_s)). \tag{6.54}$$

Making use of Eqs. (6.33) and (6.47) yields

$$\begin{aligned} \int_{p_j}^{p_{j+1}} dp_0 \delta(z - z(r, p_0, z_s)) &= (p_{j+1} - p_j) \int dp P_{pz|p_0z_0}(p, z|p_j, z_s) \\ &= \frac{p_{j+1} - p_j}{2\pi} \int dp P_{I|I_0}(I(p, z), r|I(p_j, z_s)). \end{aligned} \tag{6.55}$$

Substituting Eq. (6.55) into Eq. (6.54) and replacing  $p_{j+1} - p_j$  by  $dp_0$  we find

$$|u(r, z)|^2 = \frac{k}{(2\pi)^2} \int dp_0 dp P_{I|I_0}(I(p, z), r|I(p_j, z_s)). \tag{6.56}$$

This relation can be rewritten in the form

$$|u(r, z)|^2 = \frac{p_{\max} k}{\pi} P_z(z, r), \tag{6.57}$$

where  $P_z(z, r)$  is determined by Eq. (6.51) with  $\eta(p_0) = (2p_{\max})^{-1}$ . Insertion of Eq. (6.57) into Eq. (6.52) yields (Virovlyansky, 2005b)

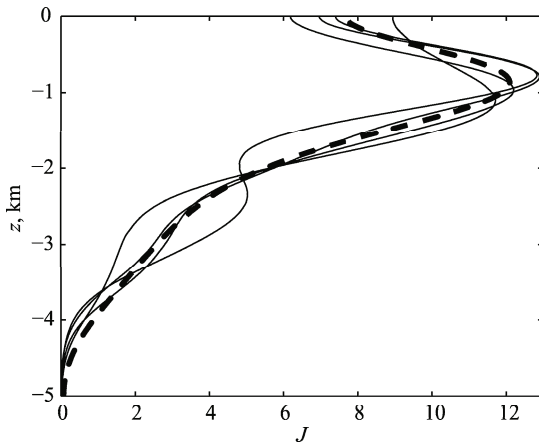


**Fig. 6.3** Smoothed intensity  $J$  at 3000 km versus depth  $z$ . The carrier frequency is  $f = 75$  Hz. Dashed line: prediction of Eq. (6.58). Thin solid lines: results of numerical solving the parabolic equation for 4 realizations of the random perturbation.

$$J(r, z) = \frac{2kp_{\max}}{(2\pi)^{3/2} \Delta_z} \int dz' e^{-\frac{(z-z')^2}{2\Delta_z^2}} P_z(z', r). \quad (6.58)$$

Figure 6.3 compares the prediction of Eq. (6.58) (dashed line) with results obtained by numerical solving the parabolic equation at a carrier frequency of 75 Hz for four realizations of the random perturbation. The wave field is excited by a point source set at the sound channel axis  $z_a$ . The smoothing scale  $\Delta_z = 0.4$  km. It is seen that Eq. (6.58) gives a rough estimate of the smoothed intensity.

## 6.4 Ray travel times

In this section we study how the chaotic ray motion manifests itself in the distribution of ray arrivals in the time–depth plane. It turns out that chaotic rays whose trajectories have equal number of turning points has close travel times. This phenomenon sheds new light on the surprising stability of the early portion of the arrival pattern observed in both numerical simulations and field experiments. It is shown how the stochastic ray theory described in Sect. 6.3 can be used for obtaining analytical estimates characterizing the statistics of ray travel times.

### 6.4.1 Timefront

Now we turn our attention to the ray travel times, that is, arrival times of sound pulses coming through individual ray paths. In the ocean acoustics, a distribution of ray travel times at a given observation range most frequently is characterized by the so-called *timefront* representing ray arrivals in the time–depth plane. Figure 6.4 presents timefronts in the unperturbed (upper panel) and perturbed (lower panel) waveguides at the range 3000 km constructed by tracing numerically a fan of 120000 rays escaping a point source set at depth  $z_s = -0.7$  km. Starting momenta of the fan rays uniformly fill an interval corresponding to launch angles  $\pm 12.5^\circ$ . Time is reckoned from  $r/c_0$ , which is the arrival time of an axial ray.

The timefront in a range-independent waveguide has the well-known accordion-like shape consisting of smooth segments (branches) (Simmen et al., 1997; Brekhovskikh and Lysanov, 1991). Each segment is formed by points corresponding to arrivals of rays with the same identifier  $\pm M$ , where  $M$  is the number of ray turning points and symbols  $+$  and  $-$  correspond to rays starting upward and downward, respectively. So, we can associate each segment with a particular identifier. Identifiers for some segments in the unperturbed waveguide are indicated in the upper panels of Fig. 6.3. It is seen that the travel time grows with  $M$ . This is a typical situation for a deep water waveguide (Brekhovskikh and Lysanov, 1991): steep rays usually have greater cycle lengths (smaller  $M$ ) and arrive earlier than flat ones.

In the lower panel of Fig. 6.3 we see that in the presence of weak range-dependent inhomogeneities the structure of the timefront becomes more complicated: instead of infinitely thin segments of smooth curves, we have some areas filled with randomly scattered points. Although we observe the scattered points only because our fan is far too sparse to resolve what should be unbroken curves, the appearance of such regions indicates the presence of chaotic rays.

Even in the presence of perturbation giving rise to ray chaos, segments of the timefront formed by early arriving steep rays reveal a remarkable stability. The early portion of the timefront still “remembers” its structure in the unperturbed waveguide. This property is well-known and it has been observed in both numerical simulations and field experiments (Simmen et al., 1997; Worcester et al., 1999; Colosi et al., 1999; Brown and Viechnicki, 1998).

Points depicting arrivals of rays with the given identifier are scattered in the vicinity of the corresponding unperturbed segment. A group of arrivals formed by rays with the same identifier produces a fuzzy versions of an unperturbed segment (Beron-Vera et al., 2003). We shall call such groups of points in the time-depth plane, the fuzzy segments. In the lower panel of Fig. 6.3 an example of the fuzzy segment is shown by thick points. This segment is associated with identifier +140. Its unperturbed counterpart in the upper panel is marked by a thick solid line.

Travel times of eigenrays arriving at a point receiver set at a depth  $z_r$  are determined by intersections of the timefront and horizontal line  $z = z_r$ . Intersection

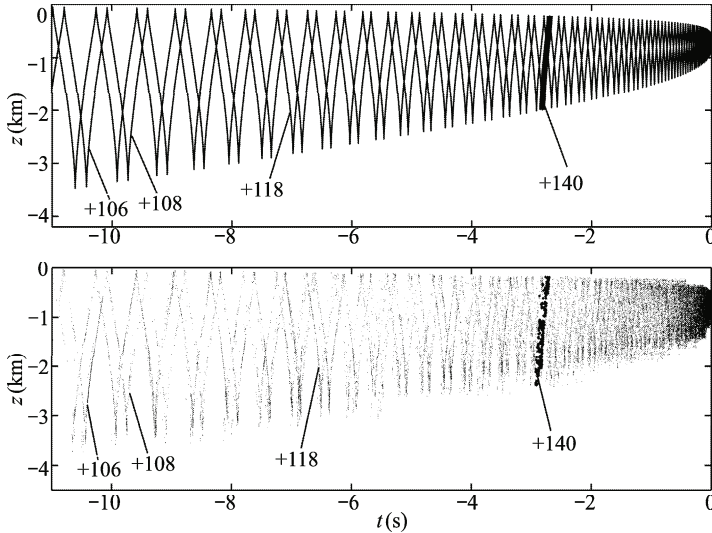


**Fig. 6.4** Timefronts in the unperturbed (upper panel) and perturbed (lower panel) waveguide: depth versus ray travel time at 3000 km for a point source set at  $z_s = 0.7$  km. Identifiers of rays forming some particular segments are indicated next to the corresponding segments. In the lower panel, arrivals with identifier +140 are marked by thick points. In the upper panel, arrivals with this identifier are depicted by a thick solid line.

with each fuzzy segment gives a compact cluster of travel times representing arrivals of eigenrays with an identifier associated with the segment. The effect of the internal-wave-induced perturbation on eigenrays may be interpreted in the following way (Beron-Vera et al., 2003). In the presence of perturbation, the unperturbed eigenray splits into a bundle of new eigenrays with the same identifier as the original one. Travel times of the new eigenrays form a cluster. Correspondingly, the ray pulse coming to the observation point through an unperturbed eigenray turns into what we will call the fuzzy ray pulse representing a superposition of pulses coming through the eigenrays belonging to the bundle. The observation that the travel times of chaotic ray paths may cluster and be relatively stable was first made in (Palmer et al., 1991; Tappert and Tang, 1996).

### 6.4.2 Statistics of ray travel times

Statistical description of ray travel times under conditions of ray chaos can be obtained by combining the stochastic ray theory discussed in Sect. 6.3 and approximate analytical estimates for the difference between travel times of chaotic and regular rays derived in (Virovlyansky, 2003, 2005a). This approach gives a quantitative explanation for the effect of clustering (Virovlyansky, 2006; Virovlyansky et al., 2007).

Consider perturbed and unperturbed rays escaping a point source at equal launch angles. Initial action and angle variables of these two rays denoted  $I_0$  and  $\theta_0$ , respectively. In (Virovlyansky, 2003, 2005a) it was shown that even at ranges  $O(1000 \text{ km})$  the difference in travel times of these rays,  $\Delta t$ , can be approximately estimated as

$$\Delta t = \tau_G + \tau_N + \tau_I + \tau_V, \quad (6.59)$$

where

$$\tau_G = [G(z, I_0) - G(\bar{z}, I_0)] / c_0, \quad (6.60)$$

$z$  and  $\bar{z}$  are coordinates of perturbed and unperturbed rays, respectively, at the observation range;

$$\tau_N = 2\pi\Delta N I_0 / c_0, \quad (6.61)$$

$\Delta N$  is the difference between numbers of minima (numbers of cycles) of perturbed and unperturbed ray paths;

$$\tau_I = \frac{\omega'(I_0)}{2c_0} \int_0^r [I(r') - I_0]^2 dr', \quad (6.62)$$

and

$$\tau_V = -\frac{1}{c_0} \int_0^r V(I_0, \theta(r'), r') dr. \quad (6.63)$$

Functions  $I(r)$  and  $\theta(r)$  in Eqs. (6.62) and (6.63) present the range-dependencies of action and angle variables, respectively, along the perturbed ray path.

At comparatively short ranges  $O(100 \text{ km})$  both rays follow practically the same path. Then  $\Delta N = 0$ ,  $z \simeq \bar{z}$ ,  $I(r') \simeq I_0$  and terms  $\tau_G$ ,  $\tau_N$  and  $\tau_I$  on the right of Eq. (6.59) are negligible. Equation (6.59) reduces to a well known relation (Flatte et al., 1979)

$$\Delta t \simeq \tau_V \simeq -\frac{1}{c_0^2} \int_0^r \delta c(r, z_0(r)) dr, \quad (6.64)$$

where the integration goes along the unperturbed path  $z_0(r)$ . In this case the travel time variations are caused by sound speed fluctuations crossed by the unperturbed ray. A detailed analysis of statistical characteristics of  $\tau_V$  have been done in Ref. (Flatte et al., 1979). The rms variations of  $\tau_V$  grows with range as  $r^{1/2}$ .

At ranges  $O(1000 \text{ km})$  perturbed and unperturbed paths with equal starting parameters are no longer close and usually have different numbers of cycles ( $\Delta N \neq 0$ ) (Beron-Vera et al., 2003; Virovlyansky, 2003, 2005a). For steep rays with large starting actions  $I_0$  the main contribution to  $\Delta t$  at long ranges comes from the term  $\tau_N$  (Virovlyansky, 2003, 2005a). From Eqs. (6.12) and (6.14) it follows that  $2\pi I_0 > G(I_0, z)$  and, hence,  $\tau_G < \tau_N$ . Therefore the term  $\tau_N$  may be used as a rough estimates of  $\Delta t$  for steep rays. For flat rays (small  $I_0$ ), both  $\tau_N$  and  $\tau_G$  become negligible as compared to  $\tau_I$ . Since the latter typically exceeds  $\tau_V$ , the relation

$$\Delta t = \tau_N + \tau_I \quad (6.65)$$

gives a rough estimate of  $\Delta t$  at ranges  $O(1000 \text{ km})$  for rays with arbitrary launch angles.

To apply the Wiener process approximation for description of  $\Delta t$  we approximate  $\Delta N$  by  $y/(2\pi)$ . This yields

$$\tau_N = y(r)I_0/c_0. \quad (6.66)$$

According to (6.38) and (6.62)

$$\tau_I = \frac{\omega'(I_0)}{2c_0} \int_0^r x^2(r') dr'. \quad (6.67)$$

An analytical estimate for the rms value of  $\Delta t$  can be easily derived for steep rays. In this case  $\Delta t \simeq \tau_N$  and  $\langle \Delta t \rangle = 0$ . Combining Eqs.(6.46) and (6.66) yields a standard deviation of  $\Delta t$

$$\sigma_{\Delta t} = |\omega'(I_0)| \frac{r^{3/2}}{c_0} \left(\frac{B}{3}\right)^{1/2}. \quad (6.68)$$

According to Eq. (6.68) the rms spread of travel times grows with range like  $r^{3/2}$ . The same range dependence was found by other authors (Beron-Vera and Brown, 2004). It should be emphasized that  $\sigma_{\Delta t}$  estimates the spread of travel times for a bundle of rays escaping a point source with starting actions close to  $I_0$ . At a long observation range these (initially close) rays diverge and can have different identifiers.

The above formulas for the ray travel times can be applied for estimating the width of a timefront segment. Figure 6.5 shows an expanded view of the unperturbed and perturbed segments with identifier +140 marked in Fig. 6.4 by thick line (upper panel) and thick points (lower panel). The quantity  $\tau_i$  (see Fig. 6.5) represents a time delay between the arrival of  $i$ -th ray contributing to the given fuzzy segment and the unperturbed segment corresponding to the same identifier. In fact,  $\tau_i$  is a difference in travel times of perturbed and unperturbed rays escaping a point source and arriving at the same observation point ( $z = \bar{z}$ ) with equal identifiers. Setting  $\tau_G = \tau_N = 0$  and neglecting  $\tau_V$ , from Eqs. (6.59)-(6.63) we find (Virovlyansky, 2003, 2005a)

$$\tau_i = \frac{\omega'(\bar{I}_M)}{2c_0} \int_0^r [I(r') - \bar{I}_M]^2 dr', \tag{6.69}$$

where  $I(r)$  is an action of the  $i$ -th perturbed ray as a function of range, and  $\bar{I}_M$  is the mean action of rays forming the unperturbed segment. According to Eq. (6.69) the sign of  $\tau_i$  is determined by the sign of  $\omega'(\bar{I}_M)$ . For typical deep water waveguides the cycle length grows with launch angle  $|\chi|$  and therefore  $\omega'(I)$  is negative. Then  $\tau_i < 0$  and the perturbed segment is biased toward early times (Virovlyansky, 2003, 2005a). Let us emphasize that this statement is valid only at long enough ranges where  $|\tau_i|$  for most rays exceeds  $|\tau_V|$ . At short ranges, where  $\tau_V$  dominates, there exists a different mechanism of bias. It is discussed in Ref. (Codona et al., 1985).

Since all (or almost all)  $\tau_i$  have the same sign, both width and bias of a fuzzy segment are characterized by the quantity

$$\delta\tau_{\text{mean}} = N^{-1} \sum_{i=1}^N \tau_i. \tag{6.70}$$

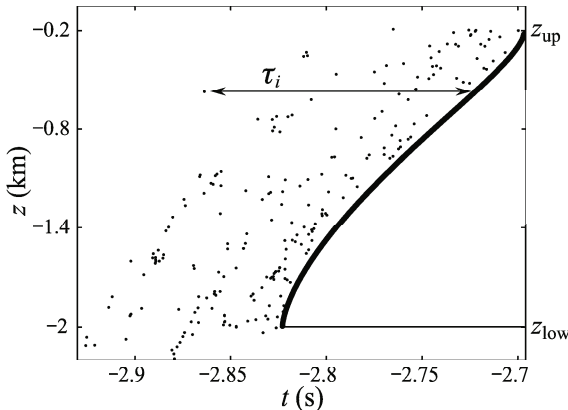


**Fig. 6.5** Arrivals of rays with the identifier +140 at the range 3000 km are shown in the time-depth plane. Points and solid line depict arrivals with and without internal waves present, respectively.

Summation is taken over rays belonging to the selected fuzzy segment and arriving at depths in an interval  $z_{\text{low}} < z < z_{\text{up}}$ , where  $z_{\text{low}}$  and  $z_{\text{up}}$  are depths of lower and upper ends of the unperturbed segment, respectively. A thin solid line in Fig. 6 shows  $\delta\tau_{\text{mean}}$  for segments with identifiers  $+M$  for  $M = 110, 111, \dots, 185$  obtained by direct ray tracing. Values of  $\delta\tau_{\text{mean}}$  for segments with identifiers  $+M$  and  $-M$  are close for most  $M$  (not shown).

The value of  $\tau_i$  can be estimated in the Wiener process approximation. The action  $I(r)$  in Eq. (6.69) should be represented as  $I_0 + x(r)$ , where  $I_0$  is the stating value and  $x(r)$  is a realization of a Wiener process subject to a constraint which accounts for the fact that the ray trajectory has a given identifier. In Ref. (Virovlyansky, 2005a) it is shown how this constraint can be taken into account and  $\delta\tau_{\text{mean}}$  for steep rays is estimated as

$$\delta\tau_{\text{mean}} = \frac{\omega'(\bar{I}_M)}{12c_0} Br^2. \quad (6.71)$$

In Fig. 6.6 this dependence for segments with  $M < 160$  is displayed by a thick solid line. Segments with larger  $M$  are formed by flat rays. Figure 6.6 demonstrates that predictions (numerical and analytical) obtained in the Wiener process approximation agree fairly well with results of direct ray tracing. Equation (6.71) also estimates the width of a cluster of ray travel times formed by eigenrays with a given identifier. Note that at the range 3000 km the spread predicted by Eq. (6.68) for a bundle of ray paths with close launch angles, but without restrictions on their final depths and identifiers, is on the order of 1 s. According to results presented in Fig. 6.6, this is much more than the width of a fuzzy timefront segment.

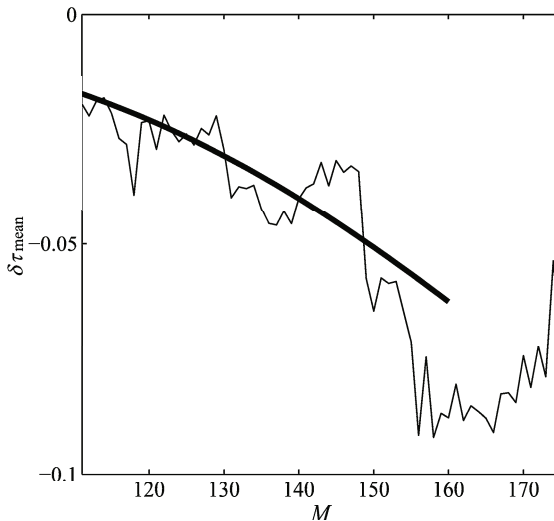


**Fig. 6.6** Mean bias of the fuzzy segment at the sound channel axis as a function of number of ray turning points,  $M$ . The plot is constructed for rays starting upward. Thin solid line: direct ray tracing. Thick solid line: analytical estimate (6.71).

## 6.5 Modal structure of the wave field under conditions of ray chaos

In this section we explore the influence of the random perturbation on the modal structure of the wave field. This problem is solved by combining two results: (i) relations from Sec. 6.2.4 expressing mode amplitudes through parameters of ray paths and (ii) stochastic ray theory from Sec. 6.3.1. For a monochromatic wave field, a simple analytical estimate is obtained for a coarse-grained distribution of acoustic energy between normal modes. Significant attention is paid to a study of the mode pulses, that is, sound pulses carried by individual modes. Analytical estimates for the spread of a mode pulse and the bias of its mean travel time in the presence of internal waves are derived.

### 6.5.1 Coarse-grained energy distribution between normal modes

First, consider the modal structure of a monochromatic wave field. Squared mode amplitudes  $|a_m(r, \Omega)|^2$  we will call the mode intensities. Our task will be to derive an analytical expression for a smoothed mode intensity

$$J_m(r, \Omega) = \sum_{m'} |a_{m'}(r, \Omega)|^2 e^{-\frac{(m-m')^2}{2\mu^2}} \bigg/ \sum_{m'} e^{-\frac{(m-m')^2}{2\mu^2}}, \quad (6.72)$$

where  $\mu$  is a smoothing scale. Under conditions of ray chaos, the number of mode rays contributing to a given mode at a long range becomes very large. Then it is natural to expect that a rough estimate of  $J_m(r, \Omega)$  may be obtained by incoherent summation of these rays. Numerical results presented in Refs. (Virovlyansky and Zaslavsky, 2000; Virovlyansky, 2000) support this expectation. Analytical evaluation of an incoherent sum of mode rays expressing  $J_m(r, \Omega)$  may be performed on the basis of the stochastic ray theory derived in Sect. 6.3.1. This approach allows one to replace the summation of rays by statistical averaging.

For a single mode source determined by Eq. (6.30) an incoherent sum of mode rays representing the mode intensity, according to Eqs. (6.27) and (6.32), can be presented in the form

$$\begin{aligned} |a_m(r, \Omega)|^2 &= \frac{1}{2\pi k} \sum_j \frac{1}{|\partial I(r, I_{m_0\Omega}, \theta_0) / \partial \theta_0|_{\theta_0=\theta_{0,j}}} \\ &= \frac{1}{2\pi k} \int_0^{2\pi} d\theta_0 \delta(I_{m\Omega} - I(r, I_{m_0\Omega}, \theta_0)), \end{aligned} \quad (6.73)$$

where the index  $j$  in the middle expression numbers the contributing mode rays. The integral in the last expression can be treated in the same manner as the integral on the right of Eq. (6.53). Dividing the interval of integration into small subintervals,

we note that the integral over each subinterval once again has the form similar to that of Eq. (6.33). For a subinterval  $(\theta_0, \theta_0 + \delta\theta)$  we have

$$\frac{1}{\delta\theta} \int_{\theta_0}^{\theta_0 + \delta\theta} d\theta_0 \delta(I_{m\Omega} - I(r, I_{m_0\Omega}, \theta_0)) = P_I(I_{m\Omega}, r | I_{m_0\Omega}). \quad (6.74)$$

Since the right hand side does not depend on  $\theta_0$  we get

$$|a_m(r, \Omega)|^2 = \frac{1}{k} P_I(r, I_{m\Omega} | I_{m_0\Omega}). \quad (6.75)$$

According to Eq. (6.21) the summation over  $m$  in Eq. (6.72) may be approximately replaced by an integration over the action variable. Assuming  $m \gg \mu$  we can formally extend the integration over  $m'$  to the infinite limits. Then

$$\begin{aligned} \sum_{m'} e^{-\frac{(m-m')^2}{2\mu^2}} &= \int_{-\infty}^{\infty} dm' e^{-\frac{(m-m')^2}{2\mu^2}} \\ &= k \int_{-\infty}^{\infty} dI' e^{-\frac{k^2(I_{m\Omega} - I')^2}{2\mu^2}} = \sqrt{2\pi}\mu. \end{aligned} \quad (6.76)$$

Substituting this in Eq. (6.72) and replacing the summation over  $m$  by integration over  $I$ , as in Eq. (6.76), we get

$$\begin{aligned} J_m(r, \Omega) &= \frac{1}{\sqrt{2\pi}\mu} \int dI' P_I(r, I' | I_{m_0\Omega}) \\ &\quad \times \exp\left[-\frac{k^2(I_{m\Omega} - I')^2}{2\mu^2}\right]. \end{aligned} \quad (6.77)$$

Substituting Eq. (6.43) yields

$$J_m(r, \Omega) = \frac{1}{\sqrt{2\pi}(\mu^2 + k^2Br)} \exp\left[-\frac{(m - m_0)^2}{2(\mu^2 + k^2Br)}\right]. \quad (6.78)$$

This result is valid only for high modes. At a carrier frequency of 75 Hz the condition (6.44) in our environmental model is met only for mode rays corresponding to  $m > 7$ . For treating low modes one should use Eq. (6.77) with a generalized version of formula for  $P_I(r, I | I_0)$  that describes both steep and flat rays (Virovlyansky, 2006; Virovlyansky et al., 2007). Note that according to Eq. (6.78) at very long ranges the number of effectively excited modes grows like  $r^{1/2}$ . In (Morozov and Colosi, 2007) a similar range dependence was observed in numerical simulations.

To check the validity of Eq. (6.78) we have solved (numerically) the parabolic equation (6.5) at a carrier frequency of 75 Hz with an initial condition  $u(0, z) = \varphi_{24}(z)$ . Mode intensities at range  $r = 3000$  km are shown in the upper panel of Fig. 6.7 for two realizations of random perturbation. The lower panel presents results for the smoothed mode intensities evaluated with a smoothing scale  $\mu = 4$ . Thin solid

lines graph  $J_m$  for four realizations of perturbation (values of  $|a_m|^2$  for two of them are presented in the upper panel). The heavy dashed line shows the prediction of Eq. (6.78). It is seen that the smoothed mode intensity weakly depends on a particular realization of perturbation and our analytical estimate is in a reasonable agreement with simulations.

In (Virovlyansky, 2006) it is shown that the wave field excited by a point source can be treated in a similar way.

### 6.5.2 Transient wave field

We now turn our attention to studying the modal structure of a narrow-band pulse signal radiated by a point source. Our task is to derive a ray-based description of what we call the mode pulses, that is pulses carried by individual modes. The mode pulse is defined as

$$\psi_m(t, r, \Omega) = \int d\Omega' a_m(r, \Omega') s(\Omega - \Omega') e^{i\Omega'(r/c_0 - t)}, \quad (6.79)$$

where  $a_m(r, \Omega')$  are mode amplitudes of the wave field satisfying the parabolic equation (6.5) with an initial condition (6.10), and

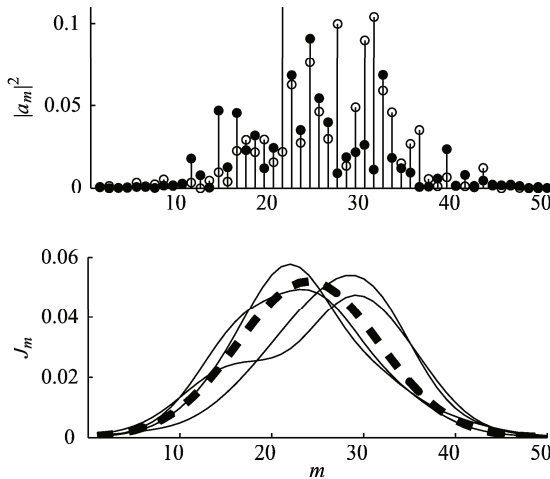


**Fig. 6.7** Mode intensities at range 3000 km for a single mode source exciting the 24-th mode ( $u(0, z) = \varphi_{24}(z)$ ) at a carrier frequency of 75 Hz. *Upper panel.* Open and solid circles show mode intensities for two realizations of perturbation (6.5). *Lower panel.* Smoothed mode intensities computed for four realizations of the perturbation (thin solid lines) and prediction of Eq. (6.78) (heavy dashed line). The smoothing scale is  $\Delta_M = 4$ .

$$s(\Omega) = \frac{1}{\sqrt{2\pi}\Delta\Omega} \exp\left(-\frac{\Omega^2}{2\Delta\Omega^2}\right) \quad (6.80)$$

is a weighting function. This definition implies that the point source emits sound pulse  $\tilde{s}(t) = \exp(-i\Omega t - \Delta\Omega^2 t^2/2)$ , whose bandwidth and duration we estimate as  $\delta\Omega = \sqrt{2\pi}\Delta\Omega$  and  $\tau_s = 2\pi/\delta\Omega = \sqrt{2\pi}/\Delta\Omega$ , respectively. It is assumed that the radiated wave field is recorded on a long vertical array and at each frequency is decomposed into a sum of normal modes (Wage et al., 2003). Then the mode pulses are synthesized in accord with Eq. (6.79). The argument  $\Omega$  of function  $\psi_m$  indicates the central frequency of an emitted signal. Each mode pulse is a wave packet spreading with range.

### Arrival time of an instantaneous frequency

As in the case of monochromatic source we will proceed from the ray-based representation of the mode amplitude described in Sect. 6.2.4. Take a mode ray contributing to the  $m$ -th mode at a central frequency of emitted pulse  $\Omega$ . Its starting momentum—denote it by  $p_0^*$ —satisfies condition (6.26), i.e.,  $I(r, p_0^*, z_s) = I_{m\Omega}$ . It is natural to assume that there exists a bundle of rays with starting momenta from a small interval centered at  $p_0^*$  which are mode rays for the  $m$ -th mode at frequencies close to  $\Omega$ : for a ray escaping the source with momentum  $p_0^* + \delta p$  there exists frequency  $\Omega'$  such that  $I(r, p_0^* + \delta p, z_s) = I_{m\Omega'}$ . The contribution from this bundle to the mode pulse is given by an integral

$$\delta\psi_m(r, t) = \int d\Omega' s(\Omega - \Omega') Q \exp\{i\Phi - i\Omega' t + i\beta\} \quad (6.81)$$

obtained by insertion of Eq. (6.27) into Eq. (6.79). At long ranges the phase  $\Phi$  rapidly varies with  $\Omega'$  and the spreading of the wave packet  $\delta\psi_m(r, t)$  can be investigated using the stationary phase technique. The stationary phase point is determined by the condition

$$t = \partial\Phi/\partial\Omega'. \quad (6.82)$$

Frequency  $\Omega'$  satisfying this equation is interpreted as an instantaneous frequency of the wave packet at time  $t$ . For a given  $\Omega'$  Eq. (6.82) predicts the arrival time of a constituent of the mode pulse with this instantaneous frequency.

Since  $\beta$  does not depend on frequency, from Eqs. (6.28) and (6.21) we find

$$\frac{\partial\Phi}{\partial\Omega'} = \frac{1}{c_0} [r + S(r, Z_{m\Omega'})] + t_1 + t_2, \quad (6.83)$$

where

$$t_1 = \frac{1}{c_0} \left[ \frac{\partial S(r, z)}{\partial z} + \sigma \frac{\partial G(z, l)}{\partial z} \right]_{z=Z_{m\Omega'}, l=I_{m\Omega'}} \frac{\partial Z_{m\Omega'}}{\partial\Omega'}, \quad (6.84)$$

and

$$t_2 = \frac{\sigma}{c_0} \left[ G(Z_{m\Omega'}, I_{m\Omega'}) - I_{m\Omega'} \left. \frac{\partial G(Z_{m\Omega'}, I)}{\partial I} \right|_{I=I_{m\Omega'}} \right]. \quad (6.85)$$

Term  $t_1$  vanishes because, as it is shown in (Virovlyansky et al., 2005; Virovlyansky, 2006), the quantity in square brackets in Eq. (6.84) is identically zero. According to Eqs. (6.12), (6.14), and (6.21)  $G(z, I)$  is a monotonic function of  $I$  and  $G(Z_{m\Omega'}, I_{m\Omega'})$  is always less than  $mT'c_0/2$ , where  $T' = 2\pi/\Omega'$ . Therefore, typically, the magnitude of  $t_2$  is a few time less than  $mT'/2$ . We will see that this is significantly less than the mode pulse length. Therefore, the arrival time of a fragment of the wave packet  $\delta\psi_m(r, t)$  with an instantaneous frequency  $\Omega'$  can be estimated as

$$t(r, \Omega', m) = \frac{1}{c_0} [r + S(r, Z_{m\Omega'})]. \quad (6.86)$$

We will call this quantity the arrival time of an instantaneous frequency  $\Omega'$ . It is the travel time of a sound pulse through the mode ray corresponding to given  $r$ ,  $m$ , and  $\Omega'$ .

Two comments concerning this result are noteworthy. First, a geometrical ray may be the mode ray for more than one mode. This occurs if its action  $I$  at the observation range satisfies the condition  $I = I_{m_1\Omega_1} = I_{m_2\Omega_2}$  where  $m_1 \neq m_2$  and both  $\Omega_1$  and  $\Omega_2$  belong to the frequency band of a radiated signal. Second, generally at the observation range there are several rays with equal travel times and different actions. It means that, typically, the instantaneous frequency of the mode pulse cannot be defined: at any moment  $t$  the pulse is a superposition of signals with different instantaneous frequencies.

### Mode pulse in a range-independent waveguide

In the unperturbed (range-independent) waveguide the action variable remains constant along the ray path, so that function  $I(r, p_0, z_s)$  does not depend on  $r$ . Since  $I$  is a monotonically increasing function of  $|p_0|$ , the condition (6.25) with  $z_0 = z_s$  at any range is met for  $p_0 = \pm\sqrt{2[H_0(I_{m\Omega'}) - U(z_s)]}$ . This means that for any mode  $m$  at each frequency  $\Omega'$  there are two mode rays. Their travel times are close and can be estimated using the approximate formula (6.19). Using Eq. (6.87), the arrival time of an instantaneous frequency  $\Omega'$  may be estimated as

$$\bar{t}(I_{m\Omega'}, r) = [1 + \omega(I_{m\Omega'})I_{m\Omega'} - H(I_{m\Omega'})]r/c_0. \quad (6.87)$$

This expression immediately gives the known WKB formula for the group slowness  $W_{m\Omega'} = \bar{t}(I_{m\Omega'}, r)/r$  (Munk and Wunsch, 1983; Brown et al., 1996).

### Mode pulses in the presence of internal waves

At long ranges where the chaos is well developed, the mode pulse is formed by many mode rays. We will sum up their contributions incoherently. Our task will be to derive an approximate analytical description of a smoothed mode pulse defined as

$$Y_m(r, \Omega, t) = \frac{1}{\sqrt{2\pi}\Delta_t} \int dt' |\psi_m(r, \Omega, t')|^2 \exp\left[-\frac{(t-t')^2}{2\Delta_t^2}\right], \quad (6.88)$$

where  $\Delta_t$  is a smoothing scale. Substituting Eqs. (6.79) and (6.80) into (6.88) we get

$$Y_m(r, \Omega, t) = \frac{1}{2\pi\Delta_\Omega^2} \int d\Omega_1 d\Omega_2 a_m(r, \Omega_1 + \Omega_2/2) a_m^*(r, \Omega_1 - \Omega_2/2) \times \exp\left[-i\Omega_r t - \frac{(\Omega - \Omega_1)^2}{\Delta_\Omega^2} - \frac{1}{2} \left(\frac{1}{2\Delta_\Omega^2} + \Delta_t^2\right) \Omega_2^2\right]. \quad (6.89)$$

Once again present the mode amplitude  $a_m(r, \Omega)$  as a sum of contributions from mode rays expressed by Eq. (6.27). An interval of integration over  $\Omega_2$  is of order  $\max(\Delta_\Omega, \Delta_t^{-1})$ . Assuming that this interval is sufficiently small, we will use an approximation

$$a_m(r, \Omega_1 + \Omega_2/2) a_m^*(r, \Omega_1 - \Omega_2/2) = \frac{1}{2\pi |\partial I(r, p_0, z_s)/\partial p_0|_{p_0=p_{0\Omega_1}}} e^{i\Omega_2 \partial \Phi(\Omega_1)/\partial \Omega_1}, \quad (6.90)$$

where the symbol  $p_{0\Omega_1}$  denotes the starting momentum of a mode ray contributing to the  $m$ -th mode at frequency  $\Omega_1$ . The action variable of this ray at the range of observation, according to Eq. (6.21), is

$$I = mc_r/\Omega_1. \quad (6.91)$$

Equation (6.90) is our main approximation. It implies that (i) the mode pulse is a superposition of (practically independent) pulses associated with bundles of mode rays described above, and (ii) contributions from these pulses are summed up incoherently.

Substituting Eq. (6.90) in (6.89) and integrating over  $\Omega_2$  yields

$$Y_m(r, \Omega, t) = \frac{1}{(2\pi)^{3/2} \Delta_\Omega \sqrt{1/2 + \Delta_\Omega^2 \Delta_t^2}} \int \frac{d\Omega_1}{|\partial I/\partial p_0|_{p_0=p_{0\Omega_1}}} \times \exp\left[-\frac{[t-t(r, \Omega_1, m)]^2}{2\Delta_t^2 + \Delta_\Omega^{-2}} - \frac{(\Omega - \Omega_1)^2}{\Delta_\Omega^2}\right]. \quad (6.92)$$

From Eq. (6.91) it follows that  $d\Omega_1 = -mc_r I^{-2} dI$ . Using this relation we can change the variable of integration in Eq. (6.92) from  $\Omega_1$  to  $p_0$ . Then

$$Y_m(r, \Omega, t) = \frac{c_r m}{(2\pi)^{3/2} \Delta_\Omega \sqrt{1/2 + \Delta_\Omega^2 \Delta_t^2}} \int \frac{dp_0}{I^2(r, p_0, z_s)} \times \exp \left[ -\frac{[t - t(r, p_0, z_s)]^2}{2\Delta_t^2 + \Delta_\Omega^{-2}} - \frac{[\Omega - mc_r/I(r, p_0, z_s)]^2}{\Delta_\Omega^2} \right]. \quad (6.93)$$

Equation (6.93) presents the smoothed mode pulse as an integral over all ray paths escaping the point source. From Sect. 6.3 we know that under conditions of ray chaos the integration over the ray starting momenta can be interpreted as the statistical averaging. Smoothed mode pulse  $Y_m(r, \Omega, t)$  can be evaluated in the same manner as the smoothed intensity of the wave field  $J(r, z)$  (Sect. 6.3.5) and the smoothed mode intensity  $J_m(r, \Omega)$  (Sect. 6.5.1). This was done in Ref. (Virovlyansky et al., 2009). Omitting details of a somewhat cumbersome calculation, we present the final result obtained for a narrow band pulse ( $\Delta_\Omega \ll \Omega$ ):

$$Y_m(r, \Omega, t) = \frac{1}{(2\pi)^{3/2} \Delta_\Omega \sqrt{Br}} \int \frac{dp_0}{\sqrt{2\Delta_t^2 + \Delta_\Omega^{-2} + Br^3 \gamma^2(I_0)}/6} \times \exp \left\{ -\frac{[t - \bar{t}(I_0) - \gamma(I_0)r(I_{m\Omega} - I_0)/2]^2}{2\Delta_t^2 + \Delta_\Omega^{-2} + \gamma^2(I_0)Br^3/6} - \frac{(I_{m\Omega} - I_0)^2}{2Br} \right\}, \quad (6.94)$$

where

$$\gamma(I) = \frac{I}{c_0} \frac{d\omega(I)}{dI}. \quad (6.95)$$

Like Eq. (6.78), this expression is valid only for modes formed by steep rays satisfying condition (6.44). At frequencies of about 75 Hz this condition is met for modes with  $m > 7$ .

Thus, we have two approximate formulas for the smoothed mode pulse given by Eqs. (6.93) and (6.94). Equation (6.93) expresses  $Y_m(r, \Omega, t)$  through solutions of the ray equations (ray paths) and it depends on a particular realization of perturbation. In contrast, Eq. (6.94) is an analytical estimate independent of a particular realization of  $\delta c$ . In Fig. 6.8 predictions of Eqs. (6.93) and (6.94) are compared to results of simulations performed by solving (numerically) the parabolic equation (6.5). A point source has been set at the sound channel axis  $z = z_a$ . The simulations have a center frequency of 75 Hz, and a smoothing scale  $\Delta_t = 0.1$  s. The envelope of an emitted signal is determined by Eq. (6.80) with  $\Delta_\Omega/(2\pi) = 2$  Hz. The effective bandwidth of the emitted pulse is about 5 Hz. Smoothed mode pulses for  $m = 11, 21, 31,$  and  $41$  at the observation range 3000 km are shown by thin solid lines. In order to apply Eq. (6.93) we have traced numerically 50000 rays leaving the point source with initial momenta  $p_0$  uniformly filling an interval corresponding to launch angles  $\pm 14^\circ$ . Replacing the integral over  $p_0$  in Eq. (6.93) with a sum over the computed ray paths yields pulses shown in Fig. 6.8 by dashed lines. Predictions of Eq. (6.94) in Fig. 6.8 are presented by thick solid lines. It is seen that both our approximate formulas are too rough and cannot give a detailed description of the smoothed

mode pulse. Nevertheless, they are able to predict the spread of the pulse and its bias caused by the random perturbation.

Let us determine the bias,  $\delta t_{m\Omega}$ , and spread,  $\tau_{m\Omega}$ , of the mode pulse as

$$\delta t_{m\Omega} = \langle t - \bar{t}(I_{m\Omega}) \rangle_{m\Omega} \tag{6.96}$$

and

$$\tau_{m\Omega}^2 = \langle [t - \bar{t}(I_{m\Omega})]^2 \rangle_{m\Omega}, \tag{6.97}$$

where the symbol  $\langle \dots \rangle_{m\Omega}$  denotes the averaging over the smoothed mode pulse so that

$$\langle q(t) \rangle_{m\Omega} \equiv \int dt q(t) Y_m(r, \Omega, t) / \int dt Y_m(r, \Omega, t). \tag{6.98}$$

The quantities  $\delta t_{m\Omega}$  and  $\tau_{m\Omega}$  can be evaluated in two ways: using Eq. (6.93) or (6.94). In (Virovlyansky et al., 2009) it is shown that the expressions for bias and spread following from Eq. (6.94) in the case of high modes reduce to simple (albeit rough) analytical estimates

$$\delta t_{m\Omega} = \frac{g(I_m)\gamma(I_m)B}{2q(I_m)} r^2, \tag{6.99}$$

where  $g(I) = d^2 p_0(I)/dI^2$  (function  $p_0(I)$  expresses starting momentum  $p_0$  in the unperturbed waveguide as a function of action  $I$ ), and

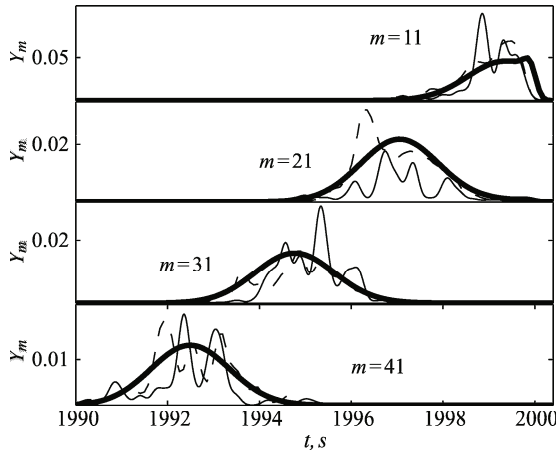


**Fig. 6.8** The smoothed mode pulses at 3000 km for  $m = 11, 21, 31,$  and  $41$ . Parabolic equation based simulations (thin solid lines) are compared to predictions of Eqs. (6.93) (dashed lines) and (6.94) (heavy solid lines).

$$\tau_{m\Omega} = \frac{|\gamma(I_{m\Omega})|B^{1/2}r^{3/2}}{\sqrt{3}}. \tag{6.100}$$

Equation (6.100) has a simple physical meaning. It represents the spread of travel times of mode rays contributing to the  $m$ -th modes. In our environmental model at the frequency 75 Hz estimates (6.99) and (6.100) can be used only for modes with  $m > 14$ . Equation (6.100) can be obtained as an estimate for the spread of travel times of mode rays contributing to the  $m$ -th mode pulse. In (Virovlyansky et al., 2006; Virovlyansky, 2006) this was done proceeding from the ray-mode relations and Eq. (6.68). An alternative derivation was given in Ref. (Udovidchenkov and Brown, 2008).

**Numerical example.** To check the applicability of the above results we have performed the parabolic equation simulation of 100 sound pulses with equal envelope functions  $s(\Omega)$  but different central frequencies uniformly filling an interval of 66 to 84 Hz. The bandwidth of each pulse is determined by the same constant  $\Delta\Omega/(2\pi) = 2$  Hz as in Fig. 6.8. This simulation has been performed for four realizations of perturbation  $\delta c$ . Then we have evaluated the biases,  $\delta t_{m\Omega}$ , and spreads,  $\tau_{m\Omega}$ , at the range 3000 km for  $m = 1, \dots, 50$ , and for 100 values of  $\Omega$  corresponding to the above central frequencies. Values of  $\delta t_{m,\Omega}$  and  $\tau_{m,\Omega}$  averaged over the 100

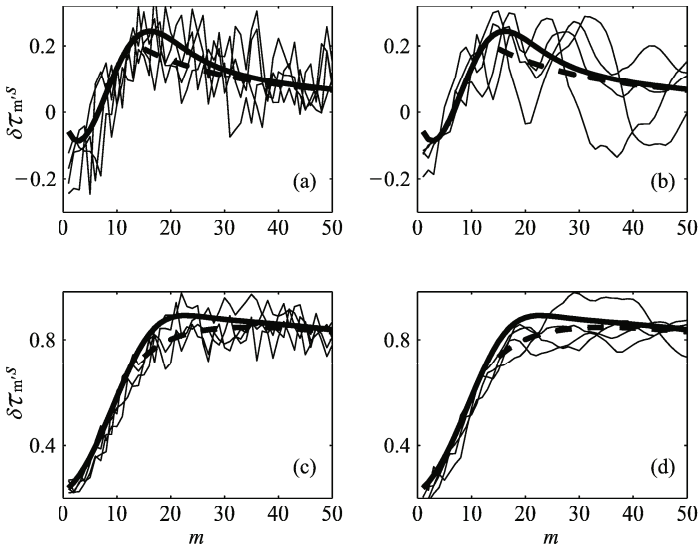


**Fig. 6.9** Biases (upper row of plots) and spreads (lower row) of mode pulses at 3000 km. Heavy solid lines present analytical predictions for the bias ((a) and (b)) and spread ((c) and (d)) at 75 Hz. Heavy dashed line show simplified analytical estimates for the same quantities. Thin solid lines graph frequency averaged biases,  $\delta t_m$ , and spreads,  $\tau_m$ , obtained by parabolic equation simulation ((a) and (c)) and predicted on the basis of a numerical ray tracing ((b) and (d)) for four realizations of the perturbation.

frequencies we will call the frequency averaged bias and spread and denote by  $\delta t_m$  and  $\tau_m$ , respectively.

The estimates of  $\delta t_{m\Omega}$  and  $\tau_{m\Omega}$  for the same  $m$  and  $\Omega$  have been obtained on the basis of ray tracing. In each of the four realizations of our random waveguide 50000 rays with the same starting parameters as indicated in Sec. 6.4 have been traced numerically. Then estimates of  $\delta t_{m\Omega}$ ,  $\tau_{m\Omega}$ ,  $\delta t_m$ , and  $\tau_m$  have been calculated on the basis of Eqs. (6.93) and (6.96). Thin solid lines in Fig. 6.9a and 6.9b show the frequency averaged bias  $\delta t_m$  obtained using the parabolic equation simulation and numerical ray tracing, respectively, for four realizations of  $\delta c$ . A heavy solid line, the same in both plots, depicts an analytical estimates of  $\delta t_{m\Omega}$  at a frequency of 75 Hz predicted by Eqs. (6.94) and (6.96). The simplified analytical estimate (6.100) at 75 Hz is shown by a heavy dashed line. Fig. 6.9c and 6.9d present similar results for the spread. A heavy solid line is an analytical estimate of  $\tau_{m\Omega}$  at 75 Hz given by Eqs. (6.94) and (6.97). A heavy dashed line is a simplified analytical estimate given by Eq. (6.100).

The agreement between simulations and theory based estimates is seen to be good for the spread. It is somewhat surprising that in spite of the restriction indicated after Eq. (6.94) the analytical estimate based on Eqs. (6.94) and (6.97) are valid not only for the high modes. The predictions of bias are less accurate. They can be considered only as order-of-magnitude estimates.

## 6.6 Conclusion

We considered the chaotic ray motion in a realistic model of the ocean acoustic waveguide and manifestations of this phenomenon in a modal structure of the wave field. It is shown that the chaotic ray dynamics in a single realization of the random medium can be described using a statistical approach introduced in Sect. 6.3. In the scope of this approach, any statistical characteristic of a ray path starting from the given point  $(p_0, z_0)$  is determined by averaging over a bundle of rays starting from a small area centered at this point. The bundle plays the role of a statistical ensemble. The Hamilton (ray) equations are approximated by stochastic Langevin equations (6.39) and (6.40) whose solutions are readily expressed through a random Wiener process representing the simplest model of diffusion. In the Wiener process approximation, the PDFs of ray parameters may be obtained analytically. At megameter ranges, where the ray chaos is well developed, the wave field at any observation point is formed by contributions from a large number of chaotic rays. Incoherent summation of their intensities gives a coarse-grained distribution of the wave field intensity. The sum over chaotic rays can be expressed through integration over their starting parameters. In our approach, this integration is interpreted as the statistical averaging. This yields an analytical estimate for the smoothed intensity of the sound field.

In Sect. 6.4 we studied the properties of ray travel times. The most important of them is a close connection between the travel time and the identifier of the ray

path. This property manifests itself in the effect of clustering. A weak perturbation causes an eigenray to split into a cluster of eigenrays whose travel time spread is small and whose centroid has a travel time that is close to that of the eigenray in the background environment. All the eigenrays belonging to the cluster have the same identifier as the original unperturbed one. Due to the effect of clustering, the timefront remains relatively stable even at megameter ranges. The presence of sound speed fluctuations causes only the diffusion of the timefront segments and their bias toward early times. Segments formed by the early arriving steep rays remain almost unaffected. Quantitative explanation of the clustering effect is based on Eqs. (6.59)–(6.63) connecting the differences between travel times of perturbed and unperturbed rays and variations the ray paths. This formulas combined with the stochastic ray theory derived in Sect. 6.3 yield estimates for the spread and bias of the timefront segment.

Manifestations of the chaotic ray dynamics in the modal structure of the wave field is studied using the ray-based formalism for description of mode amplitudes presented in Sect. 6.2.4. In the scope of this approach the amplitude of the  $m$ -th mode is formed by contributions from rays—we call them the mode rays—whose action variables at the observation range up to a (frequency dependent) multiplicative constant are approximately equal to  $m$ . Under conditions of ray chaos, the number of mode rays contributing to the given mode exponentially grows with range. At long ranges the coarse-grained distribution of mode intensities can be evaluated by incoherent ray summation. Analytical estimate for the coarse-grained distribution of acoustic energy between normal modes is obtained by combining the ray-based formalism and the stochastic ray theory based on the Wiener process approximation. The ray-based formalism derived for the monochromatic wave field can be applied for studying the transient wave field, as well. It turned out that the arrival time of a fragment of the  $m$ -th mode pulse with an instantaneous frequency  $\Omega$  is approximately equal to the travel time of a mode ray contributing to the  $m$ -th mode at this frequency. Our analysis of the transient wave field is based on this fact. It allows one to apply the stochastic ray theory for the description of mode pulses. This approach yields estimates for the spread and bias of the mode pulse caused by random internal waves.

A major limitation of our approach is an insufficient understanding of its applicability conditions. This is a common problem for practically all ray-based approaches. But in our case an additional difficulty arises due to the conjecture that the averaging over ray starting parameters may be replaced by the statistical averaging. Obviously, this may be done only when evaluating smoothed characteristics of the wave field. However the question of selecting proper smoothing scales remains open and requires a further investigation. The smoothing scales used in our calculations were selected empirically.

**Acknowledgements** The work was supported by the Grants No. 07-02-00255 and 08-05-00596 from the Russian Foundation for Basic Research, the Program “Fundamentals of acoustic diagnostics of artificial and natural media” of Physical Sciences Division of Russian Academy of Sciences, and the Leading Scientific Schools grant 1055.2008.2.

## References

- Abdullaev S.S., 1993, *Chaos and dynamics of rays in waveguide media*. Edited by G. Zaslavsky, Gordon and Breach Science Publishers, New York.
- Abdullaev S.S. and Zaslavsky G.M., 1991, Classical nonlinear dynamics and chaos of rays in wave propagation problems in inhomogeneous media, *Usp. Fiz. Nauk*, **161**, 1–43. [*Sov. Phys. Usp.*, 38, 645 (1991)]
- Beron-Vera F.J. and Brown M.G., 2003, Ray stability in weakly range-dependent sound channels, *J. Acoust. Soc. Am.*, **114**, 123–130.
- Beron-Vera F.J. and Brown M.G., 2004, Travel time stability in weakly range-dependent sound channels. *J. Acoust. Soc. Am.*, **115**, 1068–1077.
- Berman G.P. and Zaslavsky G.M., 1979, Condition of stochasticity in quantum nonlinear systems, *Physica A*, **97**, 367–382.
- Beron-Vera F.J., Brown M.G., Colosi J.A., Tomsovic S., Virovlyansky A.L., Wolfson M.A. and Zaslavsky G.M., 2003, Ray dynamics in a long-range acoustic propagation experiment, *J. Acoust. Soc. Am.*, **114**, 1226–1242.
- Brekhovskikh L.M. and Godin O.A., 1999, *Acoustics of Layered Media. II: Point Sources and Bounded Beams*, Springer, Berlin.
- Brekhovskikh L.M. and Lysanov Yu.P., 1991, *Fundamentals of Ocean Acoustics*, Springer, Berlin.
- Brown M.G., Viechnicki J. and Tappert F.D., 1996, On the measurement of modal group time delays in the deep ocean, *J. Acoust. Soc. Am.*, **100**, 2093–2102.
- Brown M.G., Colosi J.A., Tomsovic S., Virovlyansky A.L., Wolfson M.A. and Zaslavsky G.M., 2003, Ray dynamics in long-range deep ocean sound propagation, *J. Acoust. Soc. Am.*, **113**, 2533–2547.
- Brown M.G., Beron-Vera F.J., Rypina I. and Udovydchenkov I.A., 2005, Rays, modes, wavefield structure, and wavefield stability, *J. Acoust. Soc. Am.*, **117** Pt. 2, 1607–1609.
- Brown M.G. and Viechnicki J., 1998, Stochastic ray theory for long-range sound propagation in deep ocean environment, *J. Acoust. Soc. Am.*, **104**, 2090–2104.
- Codona J.L., Creamer D.B., Flatté S.M., Frehlich R.G. and Henyey F.S., 1985, Average arrival time of wave pulses through continuous random media, *Phys. Rev. Lett.*, **55**, 9–12.
- Colosi J.A. and Brown M.G., 1998, Efficient numerical simulation of stochastic internal-wave-induced sound-speed perturbation field, *J. Acoust. Soc. Am.*, **103**, 2232–2235.
- Colosi J.A., Scheer E.K., Flatte S.M., Cornuelle B.D., Dzieciuch M.A., Munk W.H., Worcester P.F., Howe B.M., Mercer J.A., Spindel R.C., Metzger K., Birdsall T. and Baggeroer A.B., 1999, Comparisons of measured and predicted acoustic fluctuations for a 3250-km propagation experiment in the eastern north pacific ocean, *J. Acoust. Soc. Am.*, **105**, 3202–3218.
- Colosi J.A. and Flatté S.M., 1996, Mode coupling by internal waves for multimeter acoustic propagation in the ocean, *J. Acoust. Soc. Am.*, **100**, 3607–3620.

- Flatte S.M., Dashen R., Munk W.M., Watson K.M. and Zakhariassen F., 1979, *Sound Transmission Through a Fluctuating Ocean*, Cambridge University Press, London.
- Gardiner C.W., 1985, *Handbook of Stochastic Methods for Physics, Chemistry and the Natural Sciences*, Springer, New York.
- Jensen F.B., Kuperman W.A., Porter M.B. and Schmidt H., 1994, *Computational Ocean Acoustics*, AIP, Woodbury, New York.
- Landau L.D. and Lifshitz E.M., 1976, *Mechanics, 3rd edition*, Pergamon Press, Oxford.
- Landau L.D. and Lifshitz E.M., 1977, *Quantum mechanics*, Pergamon Press, Oxford.
- Lichtenberg A.J. and Lieberman M.A., 1992, *Regular and Chaotic Dynamics (Applied Mathematical Sciences, Vol 38)*, Springer, New York.
- Makarov D., Prants S., Virovlyansky A. and Zaslavsky G., 2010, *Ray and Wave Chaos in Ocean Acoustics*, World Scientific, New Jersey.
- Morozov A.K. and Colosi J.A., 2007, Stochastic differential equation analysis for sound scattering by random internal waves in the ocean, *Acous. Physics*, **53**, 335–347.
- Munk W.H., Spindel R.S., Baggeroer A. and Birdsall T.G., 1994, The heard island feasibility test, *J. Acoust. Soc. Am.*, **96**, 2330–2342.
- Munk W. and Wunsch C., 1979, Ocean acoustic tomography: A scheme for large scale monitoring, *Deep-Sea Res.*, **26**, 123–161.
- Munk W. and Wunsch C., 1983, Ocean acoustic tomography: rays and modes, *Rev. Geophys. and Space. Phys.*, **21**, 1–37.
- Palmer D.R., Brown M.G., Tappert F.D. and Bezdek H.F., 1988, Classical chaos in nonseparable wave propagation problems, *Geophys. Res. Lett.*, **15**, 569–572.
- Palmer D.R., Georges T.M. and Jones R.M., 1991, Classical chaos and the sensitivity of the acoustic field to small-scale ocean structure, *Comput. Phys. Commun.*, **65**, 219–223.
- Reichl L.E., 1992, *The Transition to Chaos in Conservative Classical Systems: Quantum Manifestations*, Springer, New York.
- Rypina I.I. and Brown M.G., 2007, On the width of a ray, *J. Acoust. Soc. Am.*, **122**, 1440–1448.
- Rytov S.M., Kravtsov Yu.A., and Tatarsky V.I., 1978, *Introduction to statistical radiophysics. Part II*, Nauka, Moscow.
- Sagdeev R.Z., Usikov D.A. and Zaslavsky G.M., 1988, *Nonlinear Physics: From the Pendulum to Turbulence and Chaos*, Harwood Academic, Switzerland.
- Smirnov I.P., Virovlyansky A.L. and Zaslavsky G.M., 2001, Theory and applications of ray chaos to underwater acoustics, *Phys. Rev. E*, **64**, 036221.
- Smirnov I.P., Virovlyansky A.L. and Zaslavsky G.M., 2002, Sensitivity of ray travel times, *Chaos*, **12**, 617–635.
- Smirnov I.P., Virovlyansky A.L. and Zaslavsky G.M., 2004, Wave chaos and mode-medium resonances at long range sound propagation in the ocean, *Chaos*, **14**, 317–322.

- Smirnov I.P., Virovlyansky A.L. and Zaslavsky G.M., 2005a, Ray chaos, travel time modulation, and sensitivity to the initial conditions. *J. Acoust. Soc. Am.*, **117**, Pt. 2:1595–1606.
- Smirnov I.P., Virovlyansky A.L., Edelman M. and Zaslavsky G.Z., 2005b, Chaos-induced intensification of wave scattering, *Phys. Rev. E*, **72**, 026206.
- Smith K.B., Brown M.G. and Tappert F.D., Ray chaos in underwater acoustics, *J. Acoust. Soc. Am.*, **91**, 1939–1949.
- Simmen J., Flatte S.M. and Wan G.-Y., 1997, Wavefront folding, chaos, and diffraction for sound propagation through ocean internal waves, *J. Acoust. Soc. Am.*, **102**, 239–255.
- Tappert F.D., 1977, The parabolic approximation method, In J.B. Keller and J.S. Papadakis, editors, *Lecture Notes in Physics No. 70, Wave Propagation and Underwater Acoustics*, 224–284. Springer, Berlin.
- Tappert F.D. and Tang X., 1996, Ray chaos and eigenrays, *J. Acoust. Soc. Am.*, **99**, 185–195.
- Udovidchenkov I.A. and Brown M.G., 2008, Modal group time spreads in weakly range-dependent deep ocean environments, *J. Acoust. Soc. Am.*, **123**, 41–50.
- Virovlyansky A.L., 2000, Manifestation of ray stochastic behavior in a modal structure of the wave field, *J. Acoust. Soc. Am.*, **108**, 84–95.
- Virovlyansky A.L., 2003, Ray travel times at long ranges in acoustic waveguides, *J. Acoust. Soc. Am.*, **113**, 2523–2532.
- Virovlyansky A.L., 2005a, Signal travel times along chaotic rays in long-range sound propagation in the ocean, *Acoustical Physics*, **51**, 271–281.
- Virovlyansky A.L., 2005b, Statistical description of ray chaos in an underwater acoustic waveguide, *Acoustical Physics*, **51**, 71–80.
- Virovlyansky A.L., 2006, *Ray theory of Long-range Sound Propagation in the Ocean*, Institute of Applied Physics, Nizhny Novgorod.
- Virovlyansky A.L., Kazarova A.Yu. and Lyubavin L.Ya., 2005, Ray-based description of normal mode amplitudes in a range-dependent waveguide, *Wave motion*, **42**, 317–334.
- Virovlyansky A.L., Kazarova A.Yu. and Lyubavin L.Ya., 2006, *Ocean Acoustics, Proceedings of the 11th L.M. Brekhovskikh Conference*, chapter Modal structure of the field under conditions of wave chaos, 40–43, GEOS, Moscow.
- Virovlyansky A.L., Kazarova A.Yu. and Lyubavin L.Ya., 2007, Statistical description of chaotic rays in a deep water acoustic waveguide, *J. Acoust. Soc. Am.*, **121**, 2542–2552.
- Virovlyansky A.L., Kazarova A.Yu. and Lyubavin L.Ya., 2009, Ray-based description of normal modes in a deep ocean acoustic waveguide, *J. Acoust. Soc. Am.*, **125**, 1362–1373.
- Virovlyansky A.L. and Zaslavsky G.M., 1999, Wave chaos in terms of normal modes, *Phys. Rev. E*, **59**, 1656–1668.
- Virovlyansky A.L. and Zaslavsky G.M., 2000, Evaluation of the smoothed interference pattern under conditions of ray chaos, *Chaos*, **10**, 211–223.
- Virovlyanskii A.L. and Zaslavsky G.Z., 2007, Ray and wave chaos in problems of sound propagation in the ocean, *Acoustical Physics*, **53**, 282–297.

- Wage K.E., Baggeroer A.B. and Preisig J.C., 2003, Modal analysis of broadband acoustic receptions at 3515-km range in the north pacific using short-time fourier techniques, *J. Acoust. Soc. Am.*, **113**, 801–817.
- Worcester P.F., Cornuelle B.D., Dzieciuch M.A., Munk W.H., Howe M., Mercer A., Spindel R.C., Colosi J.A., Metzger, Birdsall T. and Baggeroer A.B., 1999, A test of basin-scale acoustic thermometry using a large- aperture vertical array at 3250-km range in the eastern north pacific ocean, *J. Acoust. Soc. Am.*, **105**, 3185–3201.
- Zaslavsky G.M., 1985, *Chaos in Dynamical Systems*, Harwood Academic, New York.

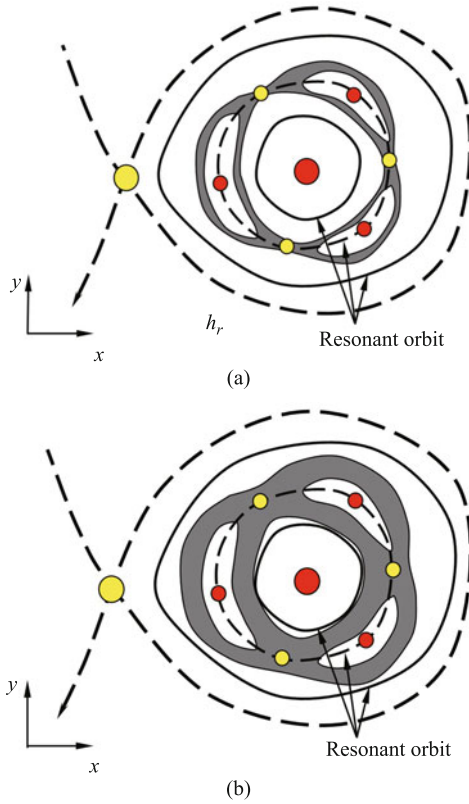


**Fig. 1.9** Resonant layer in nonlinear Hamiltonian systems with separatrix: (a) appearance and (b) disappearance. The solid and hollow circles represent the center and hyperbolic points. The irregular small circles are the sub-resonances in the neighborhood of the primary resonance.

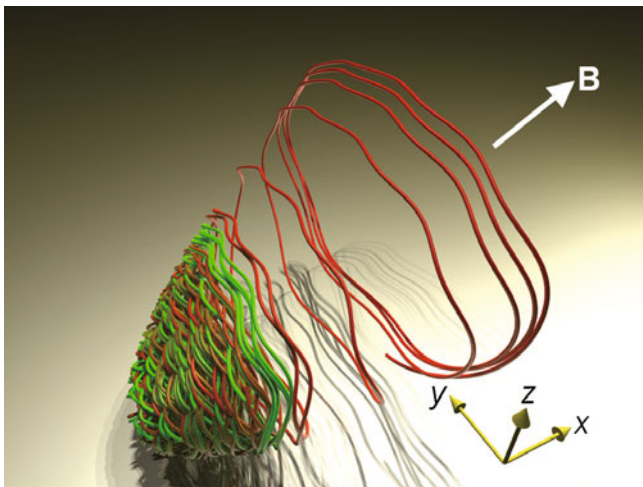


**Fig. 5.7** Three-dimensional representation (axes and orientation of  $\mathbf{B}$  shown inset) of an unbounded chaotic trajectory, which lies at the center of the colored cube, calculated for SL1 when  $\omega_B = 3\bar{\omega}_c$ . As time increases, the color of the orbit changes from green to red.

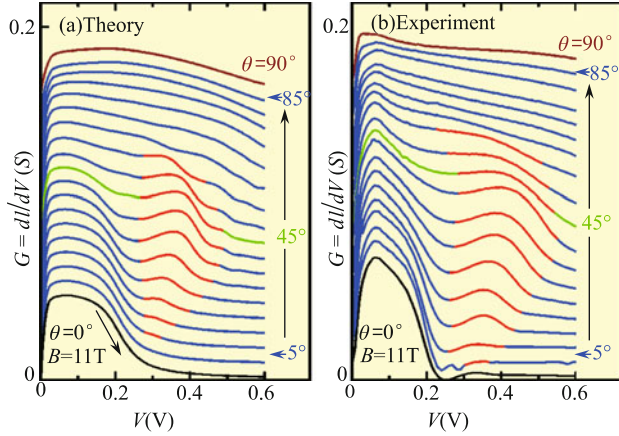


**Fig. 5.11**  $G(V)$  curves (a) calculated and (b) measured at  $T = 4.2$  K for SL1 with  $B = 11$  T, and  $\theta = 0^\circ$  (bottom trace) to  $90^\circ$  (top trace) at  $5^\circ$  intervals. Curves for  $\theta = 0^\circ, 45^\circ$ , and  $90^\circ$  are shown black, green, and brown, respectively. The  $G(V)$  curves reveal strong resonant peaks (red). Arrow in (a) indicates region of decreasing conductance associated with the onset of Bloch oscillations.

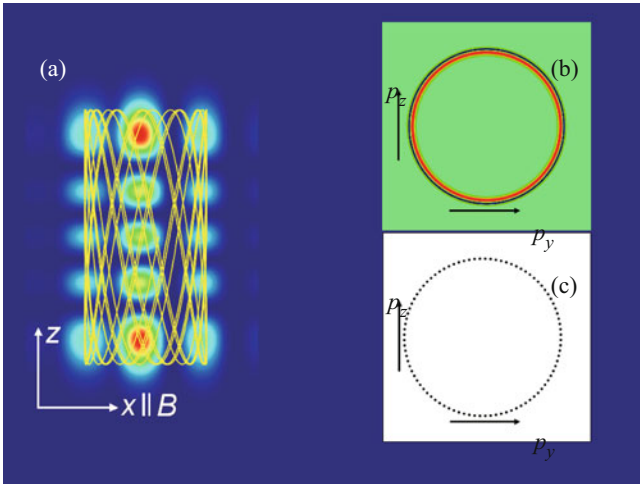


**Fig. 5.19** (a) Yellow curve: classical electron trajectories for SL1 in the  $x - z$  plane (axes inset) overlaid on a corresponding plot of  $|\Psi(x, z)|^2$  (blue zero, red high) at  $B = 8$  T and  $\theta = 0^\circ$ , (b) Wigner function values (red large positive, light green = 0, blue large negative) in  $(p_y, p_z)$  plane (axes inset) corresponding to the energy eigenfunction shown in (a) and to the Poincaré section shown in (c).

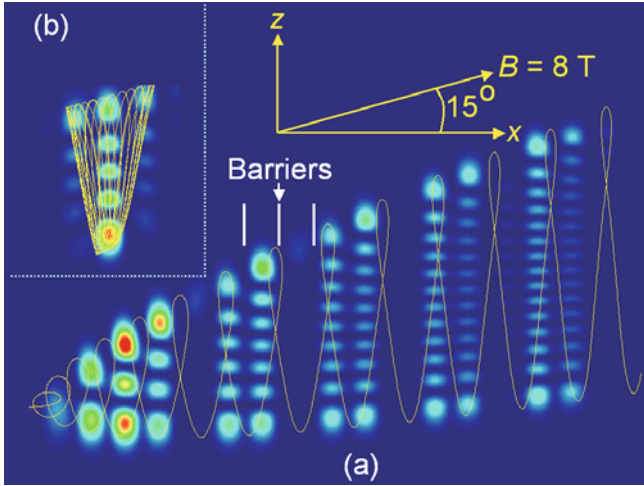


**Fig. 5.20** Yellow curves: classical electron trajectories for SL1 in the  $x-z$  plane (axes inset) overlaid on corresponding plots of  $|\Psi(x,z)|^2$  (blue zero, red high) (a) on resonance ( $r = 1$ ), (b) off resonance ( $r$  irrational).  $B = 8\text{T}$ ,  $\theta = 15^\circ$ .

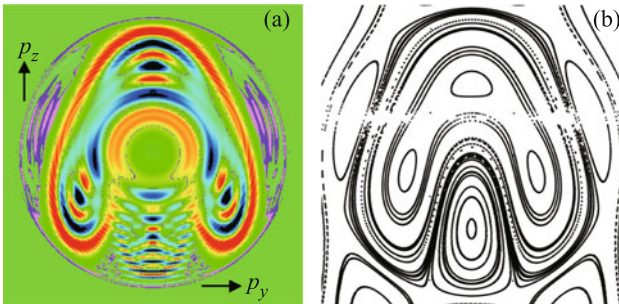


**Fig. 5.21** (a) Wigner function plot for the energy eigenstate of SL1 shown in Fig. 5.20 (a) (red large positive, light green=0, blue large negative). The Wigner function is shown in the  $(p_y, p_z)$  plane (axes inset) and corresponds to the Poincaré section shown in (b).

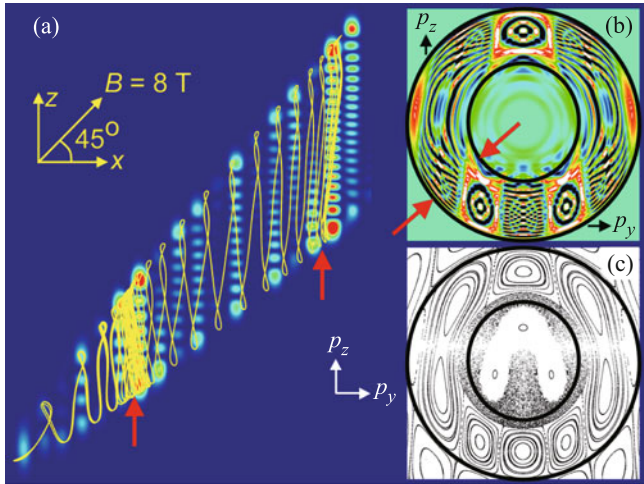


**Fig. 5.22** (a) Yellow curve: senriclassical electron trajectory for SL1 in the  $x-z$  plane (axes inset) overlaid on a corresponding plot of  $|\Psi(x,z)|^2$  (blue zero, red high) at the  $r = 1$  resonance for  $B = 8\text{ T}$  and  $\theta = 45^\circ$ . Red arrows mark regions of high probability density, where, in addition, the orbital loops are closely packed. (b) Wigner function values (red large positive, light green=0, blue large negative) in  $(p_y, p_z)$  plane (axes inset) corresponding to the energy eigenfunction shown in (a) and to the Poincaré section shown in (c). Solid black lines in (b) [marked by red arrows] and (c) highlight ring-shaped stochastic web filaments.

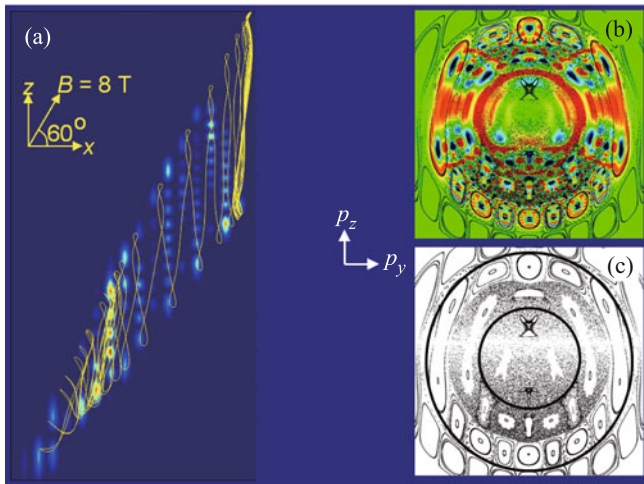


**Fig. 5.23** (a) Yellow curve: classical electron trajectories for SL1 in the  $x-z$  plane (axes inset) overlaid on a corresponding plot of  $|\Psi(x,z)|^2$  (blue zero, red high) at the  $r = 2$  resonance for  $B = 8\text{ T}$  and  $\theta = 60^\circ$ . (b) Wigner function values (red large positive, light green=0, blue large negative) in  $(p_y, p_z)$  plane (axes inset) corresponding to the energy eigenfunction shown in (a) and to the Poincaré section shown in (c) and also overlaid in (b). Solid black lines in (c) highlight ring-shaped stochastic web filaments.

# Nonlinear Physical Science

---

*(Series Editors: Albert C.J. Luo, Nail H. Ibragimov)*

**Nail. H. Ibragimov/ Vladimir. F. Kovalev:** Approximate and Renormgroup Symmetries

**Abdul-Majid Wazwaz:** Partial Differential Equations and Solitary Waves Theory

**Albert C.J. Luo:** Discontinuous Dynamical Systems on Time-varying Domains

**Anjan Biswas/ Daniela Milovic/ Matthew Edwards:** Mathematical Theory of Dispersion-Managed Optical Solitons

**Meike Wiedemann/ Florian P.M. Kohn/ Harald Rosner/ Wolfgang R.L. Hanke :** Self-organization and Pattern-formation in Neuronal Systems under Conditions of Variable Gravity

**Vasily E. Tarasov:** Fractional Dynamics

**Vladimir V. Uchaikin:** Fractional Derivatives in Physics

**Albert C.J. Luo:** Nonlinear Deformable-body Dynamics

**Ivo Petras:** Fractional Order Nonlinear Systems

**Albert C.J. Luo / Valentin Afraimovich (Editors):** Hamiltonian Chaos Beyond the KAM Theory

**Albert C.J. Luo / Valentin Afraimovich (Editors):** Long-range Interaction, Stochasticity and Fractional Dynamics

**Albert C. J. Luo / Jian-Qiao Sun(Editors):** Complex Systems with Fractionality, Time-delay and Synchronization

**Fečkan Michal:** Bifurcation and Chaos in Discontinuous and Continuous Systems